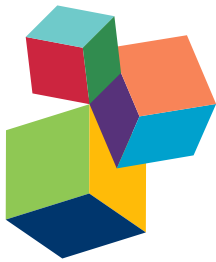


# **EXPLORING CANCER METABOLIC REPROGRAMMING THROUGH MOLECULAR IMAGING**

**EDITED BY:** Franca Podo, Zaver M. Bhujwalla and Egidio Iorio

**PUBLISHED IN:** Frontiers in Oncology





# frontiers

## **Frontiers Copyright Statement**

© Copyright 2007-2017 Frontiers Media SA. All rights reserved.

All content included on this site, such as text, graphics, logos, button icons, images, video/audio clips, downloads, data compilations and software, is the property of or is licensed to Frontiers Media SA ("Frontiers") or its licensees and/or subcontractors. The copyright in the text of individual articles is the property of their respective authors, subject to a license granted to Frontiers.

The compilation of articles constituting this e-book, wherever published, as well as the compilation of all other content on this site, is the exclusive property of Frontiers. For the conditions for downloading and copying of e-books from Frontiers' website, please see the Terms for Website Use. If purchasing Frontiers e-books from other websites or sources, the conditions of the website concerned apply.

Images and graphics not forming part of user-contributed materials may not be downloaded or copied without permission.

Individual articles may be downloaded and reproduced in accordance with the principles of the CC-BY licence subject to any copyright or other notices. They may not be re-sold as an e-book.

As author or other contributor you grant a CC-BY licence to others to reproduce your articles, including any graphics and third-party materials supplied by you, in accordance with the Conditions for Website Use and subject to any copyright notices which you include in connection with your articles and materials.

All copyright, and all rights therein, are protected by national and international copyright laws.

The above represents a summary only. For the full conditions see the Conditions for Authors and the Conditions for Website Use.

**ISSN 1664-8714**

**ISBN 978-2-88945-234-7**

**DOI 10.3389/978-2-88945-234-7**

## **About Frontiers**

Frontiers is more than just an open-access publisher of scholarly articles: it is a pioneering approach to the world of academia, radically improving the way scholarly research is managed. The grand vision of Frontiers is a world where all people have an equal opportunity to seek, share and generate knowledge. Frontiers provides immediate and permanent online open access to all its publications, but this alone is not enough to realize our grand goals.

## **Frontiers Journal Series**

The Frontiers Journal Series is a multi-tier and interdisciplinary set of open-access, online journals, promising a paradigm shift from the current review, selection and dissemination processes in academic publishing. All Frontiers journals are driven by researchers for researchers; therefore, they constitute a service to the scholarly community. At the same time, the Frontiers Journal Series operates on a revolutionary invention, the tiered publishing system, initially addressing specific communities of scholars, and gradually climbing up to broader public understanding, thus serving the interests of the lay society, too.

## **Dedication to quality**

Each Frontiers article is a landmark of the highest quality, thanks to genuinely collaborative interactions between authors and review editors, who include some of the world's best academicians. Research must be certified by peers before entering a stream of knowledge that may eventually reach the public - and shape society; therefore, Frontiers only applies the most rigorous and unbiased reviews.

Frontiers revolutionizes research publishing by freely delivering the most outstanding research, evaluated with no bias from both the academic and social point of view.

By applying the most advanced information technologies, Frontiers is catapulting scholarly publishing into a new generation.

## **What are Frontiers Research Topics?**

Frontiers Research Topics are very popular trademarks of the Frontiers Journals Series: they are collections of at least ten articles, all centered on a particular subject. With their unique mix of varied contributions from Original Research to Review Articles, Frontiers Research Topics unify the most influential researchers, the latest key findings and historical advances in a hot research area! Find out more on how to host your own Frontiers Research Topic or contribute to one as an author by contacting the Frontiers Editorial Office: [researchtopics@frontiersin.org](mailto:researchtopics@frontiersin.org)

# EXPLORING CANCER METABOLIC REPROGRAMMING THROUGH MOLECULAR IMAGING

Topic Editors:

**Franca Podo**, Istituto Superiore di Sanità, Italy

**Zaver M. Bhujwalla**, The Johns Hopkins University School of Medicine, USA

**Egidio Iorio**, Istituto Superiore di Sanità, Italy



Cover Photo: "Evoking interactive pathways in a metabolic network" by Giuseppe Fossati

Lenz cloth composition (14.0×11.5 cm)  
San Donato Milanese Exhibition, 2013,  
Milan, Italy.

Courtesy by the Artist to Frontiers in Oncology, Research Topic "Exploring Cancer Metabolic Reprogramming through Molecular Imaging".

signatures of malignancy that are providing a strong foundation for improving cancer diagnosis and monitoring tumor response to therapy using appropriate molecular imaging approaches. In particular, the recent evolution of positron emission tomography (PET), magnetic resonance spectroscopy (MRS), magnetic resonance spectroscopic imaging (MRSI), functional magnetic resonance imaging (fMRI) and optical imaging technologies, combined with complementary cellular imaging approaches, have created new ways to explore and monitor the effects of

The inclusion of oncogene-driven reprogramming of energy metabolism within the list of cancer hallmarks (Hanahan and Weinberg, Cell 2000, 2011) has provided major impetus to further investigate the existence of a much wider metabolic rewiring in cancer cells, which not only includes deregulated cellular bioenergetics, but also encompasses multiple links with a more comprehensive network of altered biochemical pathways. This network is currently held responsible for redirecting carbon and phosphorus fluxes through the biosynthesis of nucleotides, amino acids, lipids and phospholipids and for the production of second messengers essential to cancer cells growth, survival and invasiveness in the hostile tumor environment. The capability to develop such a concerted rewiring of biochemical pathways is a versatile tool adopted by cancer cells to counteract the host defense and eventually resist the attack of anticancer treatments.

Integrated efforts elucidating key mechanisms underlying this complex cancer metabolic reprogramming have led to the identification of new

metabolic reprogramming in cancer at clinical and preclinical levels. Thus, the progress of high-tech engineering and molecular imaging technologies, combined with new generation genomic, proteomic and phosphoproteomic methods, can significantly improve the clinical effectiveness of image-based interventions in cancer and provide novel insights to design and validate new targeted therapies.

The Frontiers in Oncology Research Topic “Exploring Cancer Metabolic Reprogramming Through Molecular Imaging” focusses on current achievements, challenges and needs in the application of molecular imaging methods to explore cancer metabolic reprogramming, and evaluate its potential impact on clinical decisions and patient outcome. A series of reviews and perspective articles, along with original research contributions on humans and on preclinical models have been conceretedly included in the Topic to build an open forum on perspectives, present needs and future challenges of this cutting-edge research area.

**Citation:** Podo, F., Bhujwalla, Z. M., Iorio, E., eds. (2017). Exploring Cancer Metabolic Reprogramming Through Molecular Imaging. Lausanne: Frontiers Media. doi: 10.3389/978-2-88945-234-7

# Table of Contents

- 07 Editorial: Exploring Cancer Metabolic Reprogramming through Molecular Imaging**  
Franca Podo, Zaver M. Bhujwalla and Egidio Iorio  
**Exploring the Links of Cancer Metabolic Reprogramming with Tumor Progression and Response to Therapy Using Molecular Imaging Approaches: Present Views and Perspectives**
- 11 Potential Clinical Roles for Metabolic Imaging with Hyperpolarized [1-<sup>13</sup>C]Pyrurate**  
Eva M. Serrao and Kevin M. Brindle
- 17 Positron Emission Tomography Imaging of Tumor Cell Metabolism and Application to Therapy Response Monitoring**  
Amarnath Challapalli and Eric O. Aboagye
- 37 <sup>13</sup>C MRS and LC-MS Flux Analysis of Tumor Intermediary Metabolism**  
Alexander A. Shestov, Seung-Cheol Lee, Kavindra Nath, Lili Guo, David S. Nelson, Jeffrey C. Roman, Dennis B. Leeper, Mariusz A. Wasik, Ian A. Blair and Jerry D. Glickson
- 60 Molecular Imaging of Metabolic Reprograming in Mutant IDH Cells**  
Pavithra Viswanath, Myriam M. Chaumeil and Sabrina M. Ronen
- 68 Targeting Phospholipid Metabolism in Cancer**  
Menglin Cheng, Zaver M. Bhujwalla and Kristine Glunde
- 85 The Tumor Microenvironment Modulates Choline and Lipid Metabolism**  
Noriko Mori, Flonné Wildes, Tomoyo Takagi, Kristine Glunde and Zaver M. Bhujwalla
- 95 Characterization of the Tumor Microenvironment and Tumor–Stroma Interaction by Non-invasive Preclinical Imaging**  
Nirilanto Ramamonjisoa and Ellen Ackerstaff
- 117 Potential of Induced Metabolic Bioluminescence Imaging to Uncover Metabolic Effects of Antiangiogenic Therapy in Tumors**  
Stefano Indraccolo and Wolfgang Mueller-Klieser
- 123 Activation of Phosphatidylcholine-Specific Phospholipase C in Breast and Ovarian Cancer: Impact on MRS-Detected Choline Metabolic Profile and Perspectives for Targeted Therapy**  
Franca Podo, Luisa Paris, Serena Cecchetti, Francesca Spadaro, Laura Abalsamo, Carlo Ramoni, Alessandro Ricci, Maria Elena Pisanu, Francesco Sardanelli, Rossella Canese and Egidio Iorio

**131 Metabolic Imaging to Assess Treatment Response to Cytotoxic and Cytostatic Agents**

Natalie J. Serkova and S. Gail Eckhardt

**Challenges and Future Directions in the Application of Metabolic Imaging Approaches to Preclinical Models and to Cancer Patients**

**Breast Cancer**

**140 Estrogen Receptor-Targeted Contrast Agents for Molecular Magnetic Resonance Imaging of Breast Cancer Hormonal Status**

Adi Pais and Hadassa Degani

**153 Key Players in Choline Metabolic Reprograming in Triple-Negative Breast Cancer**

Egidio Iorio, Maria José Caramujo, Serena Cecchetti, Francesca Spadaro, Giulia Carpinelli, Rossella Canese and Franca Podo

**161 Impact of Freezing Delay Time on Tissue Samples for Metabolomic Studies**

Tonje H. Haukaas, Siver A. Moestue, Riyas Vettukattil, Beathe Sitter, Santosh Lamichhane, Remedios Segura, Guro F. Giskeødegård and Tone F. Bathen

**170 Metabolic Study of Breast MCF-7 Tumor Spheroids after Gamma Irradiation by  $^1\text{H}$  NMR Spectroscopy and Microimaging**

Alessandra Palma, Sveva Grande, Anna Maria Luciani, Vladimír Mlynárik, Laura Guidoni, Vincenza Viti and Antonella Rosi

**179 Glycerophosphocholine and Glycerophosphoethanolamine Are Not the Main Sources of the In Vivo  $^{31}\text{P}$  MRS Phosphodiester Signals from Healthy Fibroglandular Breast Tissue at 7 T**

Wybe J. M. van der Kemp, Bertine L. Stehouwer, Jurgen H. Runge, Jannie P. Wijnen, Aart J. Nederveen, Peter R. Luijten and Dennis W. J. Klomp

**186 Potential of Diffusion-Weighted Imaging in the Characterization of Malignant, Benign, and Healthy Breast Tissues and Molecular Subtypes of Breast Cancer**

Uma Sharma, Rani G. Sah, Khushbu Agarwal, Rajinder Parshad, Vurthaluru Seenu, Sandeep R. Mathur, Smriti Hari and Naranamangalam R. Jagannathan

**197 Clinical Breast MR Using MRS or DWI: Who Is the Winner?**

Francesco Sardanelli, Luca Alessandro Carbonaro, Stefania Montemezzi, Carlo Cavedon and Rubina Manuela Trimboli

**Ovarian Cancer**

**205 Choline Metabolism Alteration: A Focus on Ovarian Cancer**

Marina Bagnoli, Anna Granata, Roberta Nicoletti, Balaji Krishnamachary, Zaver M. Bhujwalla, Rossella Canese, Franca Podo, Silvana Canevari, Egidio Iorio and Delia Mezzanzanica

**212 In vivo Magnetic Resonance Metabolic and Morphofunctional Fingerprints in Experimental Models of Human Ovarian Cancer**

Rossella Canese, Delia Mezzanzanica, Marina Bagnoli, Stefano Indraccolo, Silvana Canevari, Franca Podo and Egidio Iorio

**219 Effect of Pantethine on Ovarian Tumor Progression and Choline Metabolism**

Marie-France Penet, Balaji Krishnamachary, Flonne Wildes, Yelena Mironchik, Delia Mezzanzanica, Franca Podo, Max de Reggi, Bouchra Gharib and Zaver M. Bhujwalla

## **Prostate Cancer**

- 228 *Tissue Microstructure Is Linked to MRI Parameters and Metabolite Levels in Prostate Cancer***

Kirsten Margrete Selnæs, Riyas Vettukattil, Helena Bertilsson, Alan J. Wright, Arend Heerschap, Anders Angelsen, May-Britt Tessem and Tone Frost Bathen

- 235 *Metabolic Imaging in Prostate Cancer: Where We Are***

Claudia Testa, Cristian Pultrone, David Neil Manners, Riccardo Schiavina and Raffaele Lodi



# Editorial: Exploring Cancer Metabolic Reprogramming through Molecular Imaging

Franca Podo<sup>1\*</sup>, Zaver M. Bhujwalla<sup>2</sup> and Egidio Iorio<sup>1</sup>

<sup>1</sup>Istituto Superiore di Sanità, Rome, Italy, <sup>2</sup>The Johns Hopkins University School of Medicine, Baltimore, MD, USA

**Keywords:** editorial, energy metabolism, cancer metabolic reprogramming, molecular imaging, imaging methods

## Editorial on the Research Topic

### Exploring Cancer Metabolic Reprogramming through Molecular Imaging

## OPEN ACCESS

### Edited by:

Giuseppe Esposito,  
MedStar Georgetown University  
Hospital, USA

### Reviewed by:

Giuseppe Esposito,  
MedStar Georgetown University  
Hospital, USA

Deborah K. Hill,

Norwegian University of Science and  
Technology (NTNU), Norway

Santosh Kumar Bharti,

Johns Hopkins School of Medicine,  
USA

### \*Correspondence:

Franca Podo  
franca.podo@alice.it,  
franca.podo@iss.it

### Specialty section:

This article was submitted to Cancer  
Imaging and Diagnosis,  
a section of the journal  
*Frontiers in Oncology*

**Received:** 03 January 2017

**Accepted:** 11 April 2017

**Published:** 26 April 2017

### Citation:

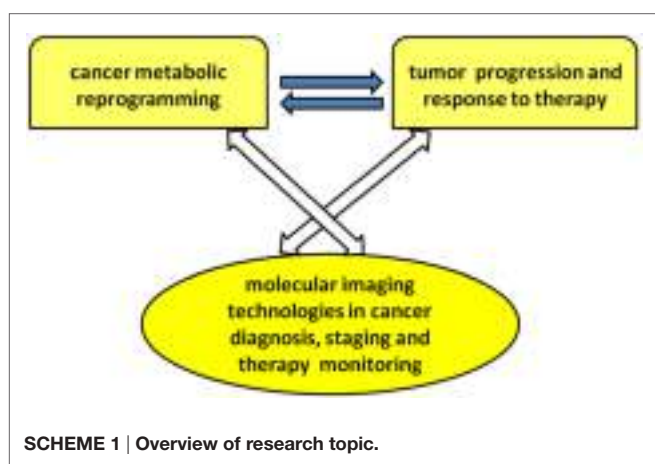
Podo F, Bhujwalla ZM and Iorio E  
(2017) Editorial: Exploring Cancer  
Metabolic Reprogramming through  
Molecular Imaging.  
*Front. Oncol.* 7:79.  
doi: 10.3389/fonc.2017.00079

## BACKGROUND AND PURPOSE OF THE TOPIC

Oncogene-driven reprogramming of energy metabolism has been added in 2011 to the list of general cancer hallmarks originally introduced by Hanahan and Weinberg to rationalize the complexities of neoplastic diseases (1, 2). However, a growing body of evidence points today to the more general vision of a wider cancer metabolic reprogramming not restricted to the deregulated cellular bioenergetics linked to aerobic glycolysis (Warburg effect), but encompassing a more complex network of concerted biochemical reactions. This wider metabolic network is responsible for the redirection of carbon and phosphorus fluxes through pathways involved in nucleotide, neutral lipid, and phospholipid biosynthesis, as well as in the oncogene-driven production of second messengers essential to cell growth and tumor invasiveness in a hostile tumor environment. Multiple efforts addressed to elucidate the key mechanisms of this more comprehensive metabolic rewiring recently led to the identification of novel signatures of malignancy, thus providing the grounds for improving cancer diagnosis and monitoring tumor response to therapy using advanced molecular imaging approaches. Among these, magnetic resonance spectroscopy (MRS) and magnetic resonance spectroscopic imaging, positron emission tomography (PET), functional MR imaging, and optical imaging technologies, combined with latest-generation cellular imaging approaches, currently offer powerful means to explore and monitor the effects of cancer metabolic reprogramming, a most versatile molecular machinery to counteract the effects of the microenvironment and eventually resist the attack of anticancer treatments. The progress of high-tech engineering and molecular imaging methods, combined with genomic, proteomic, and phosphor-proteomic approaches, are progressively improving the effectiveness of image-based clinical examinations and provide the basis to design and preclinically evaluate new targeted anticancer therapies.

The present research topic focuses on current achievements, challenges, and needs in the application of molecular imaging methods to explore different aspects of cancer metabolic reprogramming, with the final goal of improving individualized therapeutic decisions and patient outcome. Major attention has been focused on the links among oncogene-driven metabolic reprogramming, tumor progression, and response to therapy, as well as on the evolving capabilities of metabolic imaging technologies in cancer diagnosis, staging, and therapy monitoring (see **Scheme 1**).

The topic hosted 22 scientific contributions covering in a concerted manner these cutting-edge and cross-fertilizing research fields, including three general reviews, one opinion article, one perspective article, eight minireviews, and nine original articles, together with a combined list of over 90 keywords in oncology and metabolic imaging.



## EXPLORING THE LINKS OF CANCER METABOLIC REPROGRAMMING WITH TUMOR PROGRESSION AND RESPONSE TO THERAPY USING MOLECULAR IMAGING APPROACHES: PRESENT VIEWS AND PERSPECTIVES

As noted in the opinion article by Serrao and Brindle, clinical oncology relies increasingly on biomedical imaging, with anatomical imaging, especially computed tomography (CT) and MRI, forming the mainstay of patient assessment, from diagnosis to treatment monitoring. However, the need for further improvements in specificity and sensitivity, coupled with imaging techniques that are reaching their limit of clinically attainable spatial resolution, has resulted in the emergence and growing use of imaging techniques with additional functional read-outs, such as 2-deoxy-2<sup>[18]F</sup>fluoro-D-glucose (<sup>18</sup>FDG)-PET and multiparametric MRI. These techniques add a new dimension to our understanding of the biological behavior of tumors, allowing a more personalized approach to patient management.

Compared to normal differentiated cells, cancer cells require a metabolic reprogramming to support their high proliferation rates and survival. A rewiring of energy metabolism through the Warburg effect is essential to generate the required biomass, including membrane biosynthesis, and to overcome bioenergetic and redox stress. Both established and evolving radioprobes developed in association with PET to detect tumor cell metabolism, and effects of treatment have been reviewed by Challapalli and Aboagye. In addition to providing us with opportunities for examining the complex regulation of reprogrammed energy metabolism in living subjects, the PET methods open up opportunities for monitoring pharmacological activity of new therapies that directly or indirectly inhibit tumor cell metabolism.

<sup>1</sup>H-MRS measurements have also been used to investigate tumor metabolism for diagnostic purposes. However, clinical applications of MRS have been hampered by low sensitivity and consequently low spatial and temporal resolution. Nuclear spin hyperpolarization of <sup>13</sup>C-labeled substrates by dynamic nuclear polarization (DNP) radically increases the sensitivity of these

substrates to detection by <sup>13</sup>C MRS (3). DNP has rejuvenated interest in MRS measurements of tissue metabolism, as overviewed by Serrao and Brindle, with a focus on the potential clinical role for metabolic imaging with hyperpolarized [1-<sup>13</sup>C]pyruvate. Successful translation of this technique to the clinic was achieved recently with measurements of [1-<sup>13</sup>C]pyruvate metabolism in prostate cancer (4).

An original research article by Glickson and colleagues (Shestopal et al.) on <sup>13</sup>C MRS and LC-MS flux analysis of tumor intermediary metabolism presented the first validated metabolic network model for analysis of flux through key pathways of tumor intermediary metabolism including glycolysis, the oxidative and non-oxidative arms of the pentose pyrophosphate shunt, and the TCA cycle, as well as its anaplerotic pathways, pyruvate malate shuttling, glutaminolysis, and fatty acid biosynthesis and oxidation. Two models, respectively called bonded cumomer analysis for application to <sup>13</sup>C MRS data and fragmented cumomer analysis for mass spectrometric data, are refined and efficient forms of isotopomer analysis that can be readily expanded to incorporate glycogen, phospholipid and other pathways, thereby encompassing all the key pathways of tumor intermediary metabolism. Results validated with melanoma and lymphoma cell models suggest the potential translation of these methods to *in situ* investigations on human cancer reprogramming using MRS with stable <sup>13</sup>C isotopically labeled substrates on instruments operating at high magnetic fields ( $\geq 7$  T), possibly in combination with FDG-PET and hyperpolarized <sup>13</sup>C MRS methods.

Mutations in metabolic enzymes involved in cell bioenergetics but not directly responsible for aerobic glycolysis may also play an important role in cancer metabolic reprogramming. Notably, mutations in the metabolic enzyme isocitrate dehydrogenase (IDH), whose wild-type form catalyzes the interconversion of isocitrate to  $\alpha$ -ketoglutarate, have recently been identified as drivers in the development of several tumor types. In particular, cytosolic IDH1 is mutated in 70–90% of low-grade gliomas and secondary glioblastomas, and mitochondrial IDH2 is mutated in about 20% of acute myeloid leukemia cases. An article by Ronen and colleagues (Viswanath et al.) provides a timely overview of the metabolic changes observed in mutant IDH cells and the various molecular imaging methods that have been used to characterize these changes. The review describes how metabolic imaging has helped shed light on the basic biology of mutant IDH cells and how this information can be leveraged to identify new therapeutic targets and develop new clinically translatable imaging methods to detect and monitor mutant IDH tumors *in vivo*.

As reviewed by Glunde and colleagues (Cheng et al.), recent evidence suggests that cancer cells undergo metabolic reprogramming beyond aerobic glycolysis and bioenergetic rewiring, in the course of tumor development and progression. Starting from pioneering studies at the end of the last century (5–7), a progressive awareness has been built on the impact of the MRS-detectable aberrant tumor phospholipid metabolism on oncogene-driven cell signaling perturbations, which lead to altered cell proliferation and block of cell differentiation (8, 9). In this context, all cancers tested so far display abnormal choline and ethanolamine phospholipid metabolism, which has been detected with numerous MRS approaches in cells, animal models of cancer, and the tumors

of cancer patients. Since the discovery of this metabolic hallmark of cancer, many studies have been performed to elucidate the molecular origins of deregulated choline metabolism, to identify targets for cancer treatment, and to develop MRS approaches that detect choline and ethanolamine compounds for clinical use in diagnosis and treatment monitoring. Several enzymes in choline, recently also ethanolamine, and phospholipid metabolism [including choline kinase alpha (ChK $\alpha$ ), phospholipase D1, phosphatidylcholine-specific phospholipase C (PC-PLC), sphingomyelinases, choline transporters, glycerophosphodiesterases, phosphatidylethanolamine N-methyltransferase, and ethanolamine kinase] have been shown to be involved in carcinogenesis and tumor progression, suggesting their potential use as targets for anticancer therapy, either alone or in combination with other chemotherapeutic approaches.

Besides aerobic glycolysis and altered choline metabolism, tumors are often characterized by peculiar microenvironment features such as hypoxia, vascular abnormalities, and low extracellular pH (pHe). The impact of these tumor characteristics has been investigated extensively in the context of tumor development, progression, and treatment response, resulting in a number of non-invasive imaging biomarkers. As highlighted by Ramamonyisoa and Ackerstaff, additional emerging evidence reveals that the interaction between tumor and stroma cells can alter tumor metabolism (leading to metabolic reprogramming) as well as tumor growth and vascular features. The review summarizes the current efforts to clarify how non-invasive multimodal imaging can help to characterize tumor–stroma interaction and understand its role in the development, progression, and treatment response of tumors.

The potential of induced metabolic bioluminescence imaging (imBI) to uncover metabolic effects of antiangiogenic therapy in tumors has been overviewed by Indraccolo and Mueller-Klieser. Tumor heterogeneity at the genetic level has been illustrated by a multitude of studies on the genomics of cancer, but whether tumors can be heterogeneous at the metabolic level is an issue that has been less systematically investigated so far. A burning related question is whether the metabolic features of tumors can change following either natural tumor progression (i.e., in primary tumors versus metastasis) or therapeutic interventions. In this regard, recent findings by independent teams indicate that antiangiogenic drugs cause metabolic perturbations in tumors, as well as metabolic adaptations associated with increased malignancy. ImBI is an imaging technique that enables detection of key metabolites associated with glycolysis, including lactate, glucose, pyruvate, and ATP in tumor sections. Signals captured by imBI can be used to visualize the topographic distribution of these metabolites and quantify their absolute amount. ImBI can be very useful for metabolic classification of tumors and to track metabolic changes in the glycolytic pathway associated with certain therapies. Imaging of the metabolic changes induced by antiangiogenic drugs in tumors by imBI or other emerging technologies is a valuable tool to uncover molecular sensors engaged by metabolic stress and offers an opportunity to understand how metabolism-based approaches could improve cancer therapy.

A perspective article by Podo and colleagues entitled “Activation of phosphatidylcholine-specific phospholipase C in breast and ovarian cancer: impact on MRS-detected choline

metabolic profile and perspectives for targeted therapy” (Podo et al.) provides an overview of recent findings on functional and metabolic features of PC-PLC in breast and ovarian cancer cells in terms of (a) activation, protein overexpression, and subcellular redistribution of this enzyme in cancer cells compared with non-tumoral counterparts; (b) relative contributions of ChK $\alpha$  and PC-PLC to the intracellular MRS-detected phosphocholine pool; (c) interaction of PC-PLC with ErbB receptors’ family members such as human epidermal growth factor receptor 2 (HER2) and human epidermal growth factor receptor 1 (HER1, EGFR); and (d) effects of PC-PLC inhibition on HER2 overexpression, cell proliferation, and cell differentiation (10, 11). This body of evidence points to PC-PLC as a potential target for newly designed therapies, whose effects can be preclinically and clinically monitored by molecular imaging methods.

The unique capabilities of metabolic imaging to assess treatment response to cytotoxic and cytostatic agents were reviewed by Serkova and Eckhardt. For several decades, cytotoxic chemotherapeutic agents were considered the basis of anticancer treatment for patients with metastatic tumors. A decrease in tumor burden, assessed by volumetric CT and MRI, according to the Response Evaluation Criteria in Solid Tumors (RECIST), was considered as a radiological response to cytotoxic chemotherapies. In addition to RECIST-based dimensional measurements, a metabolic response to cytotoxic drugs can be assessed by PET using  $^{18}\text{F}$ -fluorothymidine ( $^{18}\text{FLT}$ ) as a radioactive tracer for drug-disrupted DNA synthesis. The decreased  $^{18}\text{FLT}$ -PET uptake is often seen concurrently with increased apparent diffusion coefficients by diffusion-weighted MRI (DWI) due to chemotherapy-induced changes in tumor cellularity. Recently, the discovery of molecular origins of tumorigenesis led to the introduction of novel signal transduction inhibitors (STIs). STIs are targeted cytostatic agents; their effect is based on a specific biological inhibition with no immediate cell death. As such, tumor size is no longer a sensitive end point for a treatment response to STIs; novel physiological imaging end points are needed. For receptor tyrosine kinase inhibitors, as well as modulators of the downstream signaling pathways, an almost immediate inhibition in glycolytic activity (the Warburg effect) and phospholipid turnover (the Kennedy pathway) has been seen by metabolic imaging in the first 24 h of treatment. The quantitative imaging end points by MRS and metabolic PET (including  $^{18}\text{FDG}$  and total choline) provide an early treatment response to targeted STIs, before a reduction in tumor burden can be seen.

## CHALLENGES AND FUTURE DIRECTIONS IN THE APPLICATION OF METABOLIC IMAGING APPROACHES TO PRECLINICAL MODELS AND TO CANCER PATIENTS

A series of 13 original articles or minireviews focused on MRI and metabolic imaging studies on cell-based models, dissected tissue specimens, and *in vivo* tissues especially in breast (Pais and Degani; Iorio et al.; Mori et al.; Haukaas et al.; Palma et al.; van der Kemp et al.; Sharma et al.; Sardanelli et al.), ovarian (Bagnoli et al.; Canese et al.; Penet et al.), and prostate cancers (Mori et al.; Selnaes et al.; Testa et al.).

The reported studies on breast cancer highlight relevant issues concerning development of quantitative molecular imaging methods that specifically detect estrogen receptor (ER) *in vivo* using novel ER-targeted contrast agents (Pais and Degani); identification of key players in choline metabolic reprogramming in triple negative breast cancer (Iorio et al.); influence of the tumor microenvironment on choline and lipid metabolism (Mori et al.); impact of freezing delay time on tissue samples for metabolomic studies (Haukaas et al.); monitoring of metabolic changes induced by gamma irradiation on breast tumor spheroids using <sup>1</sup>H NMR spectroscopy and microimaging (Palma et al.); identification of <sup>31</sup>P MRS phosphodiester signals of human fibroglandular breast tissue at ultrahigh field (van der Kemp et al.); and evaluation of the potential of DWI in the characterization of malignant, benign, and healthy breast tissues and molecular subtypes of breast cancer (Sharma et al.). An article entitled “Clinical breast MR using MRS or DWI: Who is the winner?” by Sardanelli et al. provides a critical summary of secondary evidence on two different *in vivo* non-contrast molecular imaging approaches, <sup>1</sup>H MRS and DWI, with special focus on the translational perspective toward clinical feasibility and applicability.

Regarding epithelial ovarian carcinoma (EOC), a highly heterogeneous and lethal malignancy characterized by late diagnosis, frequent relapse, and development of chemoresistance, Bagnoli and colleagues reviewed the role of ChK $\alpha$  in sustaining the cancer “cholinic phenotype” (Bagnoli et al.). The article shows that ChK $\alpha$  inhibition, besides reducing ovarian cancer aggressiveness, increases disease sensitivity to drug treatment sparing normal cells and therefore opening a new therapeutic window. An abnormal tCho profile along with altered levels of other metabolites has also been detected in human EOC xeno-grafts, as reviewed by Canese and colleagues (Canese et al.). This molecular imaging study provides a more extensive picture of tumor metabolism in EOC models *in vivo*, potentially opening the way to a multiple metabolic targeting. Furthermore, DWI is

suggested as a potential tool for better differentiating malignant from benign tissues and possibly distinguishing cytotoxic from cytostatic treatment effects. New therapeutic strategies are urgently needed to improve survival of ovarian cancer patients. The effect of pantethine (precursor of vitamin B5 and active moiety of coenzyme A) on ovarian tumor progression and choline metabolism has been investigated by (Penet et al.) using MRI and high-resolution <sup>1</sup>H MRS in a orthotopic ovarian cancer model. Pantethine treatment resulted in slower tumor progression, decreased levels of phosphocholine and phosphatidylcholine, and reduced metastases and ascites occurrence.

MRI can portray spatial variations in tumor heterogeneity, architecture, and tumor microenvironment, key biological features of prostate cancer. An original research article by Selnaes et al. focused on the relationships between MRI parameters measured on prostate cancer patients *in vivo*, individual metabolites measured *ex vivo* in prostatectomy specimens, and quantitative histopathology (Selnaes et al.). Last, but not least, Testa and colleagues reviewed the recent literature regarding molecular imaging methods developed and used to improve diagnosis and staging of prostate cancer (Testa et al.). The encouraging progress of *in vivo* metabolic imaging approaches nowadays points to the need of harmonized and shared protocols to increase the applicability of these technologies to a clinical setting. Furthermore, the use of well-characterized preclinical models that closely mirror the pathogenesis of human prostate cancer (e.g., the murine TRAMP model) allows for further progress in the comparative evaluation of DWI versus other molecular imaging approaches in assessing different stages of this disease (12).

## AUTHOR CONTRIBUTIONS

All authors listed, have made substantial, direct and intellectual contribution to the work, and approved it for publication.

## REFERENCES

1. Hanahan D, Weinberg RA. Hallmarks of cancer: the next generation. *Cell* (2011) 5:646–74. doi:10.1016/j.cell.2011.02.013
2. Hanahan D, Weinberg RA. The hallmarks of cancer. *Cell* (2000) 1:57–70. doi:10.1016/S0092-8674(00)81683-9
3. Ardenkjær-Larsen JH, Fridlund B, Gram A, Hansson G, Hansson L, Lerche MH, et al. Increase in signal-to-noise ratio of > 10,000 times in liquid-state NMR. *Proc Natl Acad Sci U S A* (2003) 100:10158–63. doi:10.1073/pnas.1733835100
4. Nelson SJ, Kurhanewicz J, Vigneron DB, Larson PE, Harzstark AL, Ferrone M, et al. Metabolic imaging of patients with prostate cancer using hyperpolarized [1-<sup>13</sup>C]pyruvate. *Sci Transl Med* (2013) 5:198ra108. doi:10.1126/scitranslmed.3006070
5. Negendank W. Studies of human tumors by MRS: a review. *NMR Biomed* (1992) 5:303–24. doi:10.1002/nbm.1940050518
6. Podo F. Tumour phospholipid metabolism. *NMR Biomed* (1999) 12:413–39. doi:10.1002/(SICI)1099-1492(199911)12:7<413::AID-NBM587>3.3.CO;2-L
7. Aboagye EO, Bhujwalla ZM. Malignant transformation alters membrane choline phospholipid metabolism of human mammary epithelial cells. *Cancer Res* (1999) 59:80–4.
8. Glunde K, Bhujwalla ZM, Ronen SM. Choline metabolism in malignant transformation. *Nat Rev Cancer* (2011) 11:835–48. doi:10.1038/nrc3162
9. Podo F, Canevari S, Canese R, Pisano ME, Ricci A, Iorio E. MR evaluation of response to targeted treatment in cancer cells. *NMR Biomed* (2011) 24:648–72. doi:10.1002/nbm.1658
10. Paris L, Cecchetti S, Spadaro F, Abalsamo L, Lugini L, Pisano ME, et al. Inhibition of phosphatidylcholine-specific phospholipase C downregulates HER2 overexpression on plasma membrane of breast cancer cells. *Breast Cancer Res* (2010) 12:R27. doi:10.1186/bcr2575
11. Abalsamo L, Spadaro F, Bozzuto G, Paris L, Cecchetti S, Lugini L, et al. Inhibition of phosphatidylcholine-specific phospholipase C results in loss of mesenchymal traits in metastatic breast cancer cells. *Breast Cancer Res* (2012) 14:R50. doi:10.1186/bcr3151
12. Hill DK, Kim E, Teruel JR, Jamin Y, Widerøe M, Søgaard CD, et al. Diffusion-weighted MRI for early detection and characterization of prostate cancer in the transgenic adenocarcinoma of the mouse prostate model. *J Magn Reson Imaging* (2016) 43:1207–17. doi:10.1002/jmri.25087

**Conflict of Interest Statement:** The authors declare that the research was conducted in the absence of any commercial or financial relationships that could be construed as a potential conflict of interest.

The reviewer, SB, declared a shared affiliation and a past coauthorship with one of the authors, ZB, to the handling editor, who ensured that the process nevertheless met the standards of a fair and objective review.

Copyright © 2017 Podo, Bhujwalla and Iorio. This is an open-access article distributed under the terms of the Creative Commons Attribution License (CC BY). The use, distribution or reproduction in other forums is permitted, provided the original author(s) or licensor are credited and that the original publication in this journal is cited, in accordance with accepted academic practice. No use, distribution or reproduction is permitted which does not comply with these terms.



# Potential Clinical Roles for Metabolic Imaging with Hyperpolarized [1-<sup>13</sup>C]Pyruvate

Eva M. Serrao<sup>1,2</sup> and Kevin M. Brindle<sup>1,2\*</sup>

<sup>1</sup> Li Ka Shing Centre, Cancer Research UK Cambridge Institute, University of Cambridge, Cambridge, UK, <sup>2</sup> Department of Biochemistry, University of Cambridge, Cambridge, UK

**Keywords:** cancer, metabolism, imaging, hyperpolarized, pyruvate, therapy monitoring

Clinical oncology relies increasingly on biomedical imaging, with anatomical imaging, especially using CT and <sup>1</sup>H-MRI, forming the mainstay of patient assessment, from diagnosis to treatment monitoring. However, the need for further improvements in specificity and sensitivity, coupled with imaging techniques that are reaching their limit of clinically attainable spatial resolution, has resulted in the emergence and growing use of imaging techniques with additional functional readouts, such as <sup>18</sup>FDG-PET and multiparametric MRI. These techniques add a new dimension to our understanding of the biological behavior of tumors, allowing a more personalized approach to patient management.

An important functional imaging target in cancer is metabolism. PET measurements of <sup>18</sup>Fluorodeoxyglucose uptake (<sup>18</sup>FDG-PET), a <sup>18</sup>F-labeled glucose analog, and <sup>1</sup>H-MRS measurements, have both been used to investigate tumor metabolism for diagnostic purposes. However, clinical applications of MRS have been hampered by low sensitivity and consequently low spatial and temporal resolution (1). Nuclear spin hyperpolarization of <sup>13</sup>C-labeled substrates, using dynamic nuclear polarization (DNP), which radically increases the sensitivity of these substrates to detection by <sup>13</sup>C MRS (2), has created a renewed interest in MRS measurements of tissue metabolism. Successful translation of this technique to the clinic was achieved recently with measurements of [1-<sup>13</sup>C]pyruvate metabolism in prostate cancer (3) (see Figure 1). We explore here the potential clinical roles for metabolic imaging with hyperpolarized [1-<sup>13</sup>C]pyruvate.

## OPEN ACCESS

### Edited by:

Franca Podo,  
Istituto Superiore di Sanità, Italy

### Reviewed by:

Natalie Julie Serkova,  
University of Colorado, USA

Sarah Nelson,  
University of California San Francisco,  
USA

### \*Correspondence:

Kevin M. Brindle  
kmb1001@cam.ac.uk

### Specialty section:

This article was submitted to Cancer Imaging and Diagnosis, a section of the journal Frontiers in Oncology

**Received:** 23 December 2015

**Accepted:** 28 February 2016

**Published:** 11 March 2016

### Citation:

Serrao EM and Brindle KM (2016) Potential Clinical Roles for Metabolic Imaging with Hyperpolarized [1-<sup>13</sup>C]Pyruvate.

Front. Oncol. 6:59.

doi: 10.3389/fonc.2016.00059

## DYNAMIC NUCLEAR POLARIZATION

Dynamic nuclear polarization, which can increase the signal-to-noise ratio in the solution-state <sup>13</sup>C MR experiment by 10<sup>4</sup>- to 10<sup>5</sup>-fold (4), has enabled *in vivo* imaging of various metabolites and their enzymatic conversion into other species, as well as metabolic fluxes in central metabolic pathways, such as glycolysis (5–7) and the tricarboxylic acid cycle (8–10). The principle limitation of the technique is the short half-life of the polarization; for [1-<sup>13</sup>C]pyruvate *in vivo*, this is typically between 30 and 40 s, which means that the hyperpolarized signal will last for 2–3 min. Therefore, the substrate, whose metabolism is to be imaged, must be transferred promptly from the polarizer, injected intravenously, and then transit quickly *via* the circulation to the tissue of interest, where it should be taken up and metabolized rapidly (11, 12). To date, numerous molecules, in addition to <sup>13</sup>C-labeled pyruvate, have been successfully hyperpolarized and their metabolism imaged, including [1,4-<sup>13</sup>C<sub>2</sub>]fumarate, as a marker of cell necrosis (13, 14); [U-<sup>2</sup>H,

**Abbreviations:** <sup>18</sup>FDG, <sup>18</sup>Fluorodeoxyglucose; MRS, magnetic resonance spectroscopy; MRSI, magnetic resonance spectroscopic imaging; PET, positron emission tomography.

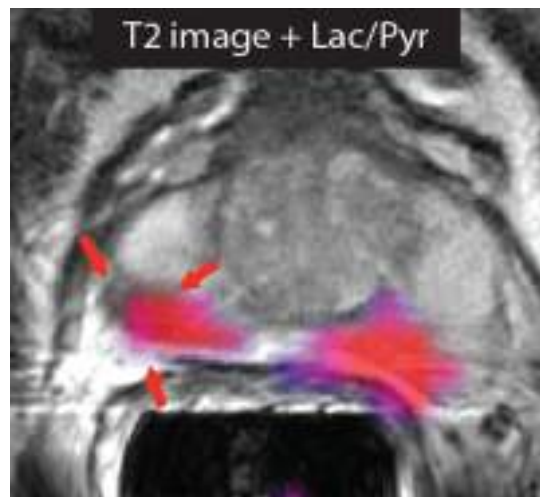


**FIGURE 1 | Imaging prostate cancer with hyperpolarized [1-<sup>13</sup>C]pyruvate.** The T<sub>2</sub>-weighted image of a patient with biopsy-proven bilateral prostate cancer showed only a unilateral decrease in signal intensity. However, the metabolic image ([1-<sup>13</sup>C]lactate/[1-<sup>13</sup>C]pyruvate ratio) detected disease on both the right and left sides of the prostate. Reproduced from Nelson et al. (3) with permission.

U-<sup>13</sup>C]glucose for assessment of glycolytic and pentose phosphate pathway activities and for detecting early treatment response (7); <sup>13</sup>C-labeled bicarbonate for *in vivo* mapping of pH (15); and <sup>13</sup>C-labeled urea as a marker of perfusion (16), among others (13, 16–18). Despite initial interest in vascular imaging (19–21), the main focus has been on imaging metabolism in tumors (13, 17, 22) and cardiac tissue (23–27).

## PYRUVATE

Pyruvate is an important intermediate in many biochemical pathways (28). As an end product of glycolysis, pyruvate can be reduced by NADH to generate lactate, in the readily reversible reaction catalyzed by lactate dehydrogenase, or transaminated by glutamate, in the reversible reaction catalyzed by alanine aminotransferase (ALT), to form alanine. In tissues with high levels of mitochondrial activity, such as heart muscle, pyruvate may be irreversibly decarboxylated to form carbon dioxide in the reaction catalyzed by the mitochondrial pyruvate dehydrogenase (PDH) complex (26). Since increased aerobic glycolysis is a well-recognized hallmark of cancer (29, 30), this has made it an attractive pathway to probe for diagnostic and treatment monitoring purposes (3, 17, 31).

## Potential Clinical Roles

Preclinical studies have demonstrated that hyperpolarized [1-<sup>13</sup>C]pyruvate is a promising probe for oncological imaging, with increased lactate labeling observed in tumors as compared to normal tissues (31, 32). The substrate has the potential to be used in many steps of patient management. A recent study

demonstrated the potential of hyperpolarized [1-<sup>13</sup>C]pyruvate as an imaging biomarker for early detection and secondary screening of pancreatic cancer, where a decrease in the hyperpolarized [1-<sup>13</sup>C]alanine/[1-<sup>13</sup>C]lactate ratio was observed in the progression from precursor lesions to adenocarcinoma (33). In another study, [1-<sup>13</sup>C]pyruvate detected metabolic changes prior to tumor formation (34). Additionally, in the first reported clinical trial in prostate cancer, increased lactate labeling was observed in histologically confirmed areas of disease that were not identifiable by conventional <sup>1</sup>H-MRI measurements (3) (**Figure 1**). The few studies that have explored the role of [1-<sup>13</sup>C]pyruvate in grading and prognosis, which were in the transgenic mouse model of prostate adenocarcinoma (TRAMP), have also produced promising results (35, 36). Tumor grading by biopsy can sometimes be difficult depending on the accessibility of the organ of interest. Translation of the DNP technique to the clinic may allow more accurate targeting of biopsy procedures. Since lactate labeling is increased in regions of hypoxia, the technique also has the potential to be used for treatment planning in radiotherapy (37, 38). Clinical assessments of tumor responses to treatment are still based largely on observed changes in tumor size (39). However, this might not always be appropriate, particularly for detection of early responses or if the drug does not result in tumor shrinkage, for example, in the case of antiangiogenic drugs (40, 41). Additionally, treatment assessment using <sup>18</sup>FDG-PET is difficult in some organs, e.g., prostate and brain, due to both low tumor uptake and increased background uptake, respectively (40). Evaluation of treatment response is likely to be the clinical scenario where hyperpolarized [1-<sup>13</sup>C]pyruvate will have the most impact, as it could lead to immediate changes in clinical management, allowing the clinician to change a non-responding patient to a more effective drug at an early stage (40). Early assessment of treatment response could also be used to accelerate the introduction of new drugs into the clinic by providing an indication of drug efficacy in early stage clinical trials. In support of this are numerous studies showing early decreases in hyperpolarized <sup>13</sup>C-labeled exchange between injected [1-<sup>13</sup>C]pyruvate and the endogenous lactate pool in a range of cancer models following treatment with cytotoxic chemotherapy (17, 42), targeted drugs (43–45), and radiotherapy (41, 46, 47).

There is as yet no direct evidence to support the suggestion that residual disease/recurrence can be identified by increased lactate labeling. However, observations of increased lactate labeling in areas of disease and following disease progression (3, 33) make this likely. There is, however, evidence that hyperpolarized [1-<sup>13</sup>C]pyruvate can be used to assess normal tissue toxicity, with an increase in the [1-<sup>13</sup>C]lactate/[1-<sup>13</sup>C]pyruvate ratio occurring in radiation-induced lung injury (48, 49).

## ADVANTAGES OF METABOLIC IMAGING WITH [1-<sup>13</sup>C]PYRUVATE

### Advantages Compared to <sup>18</sup>FDG-PET

Metabolic imaging of cancer in the clinic has principally been with <sup>18</sup>FDG-PET, which has been used to stage tumors

and to assess treatment response. Despite its high sensitivity and capability to provide whole-body images, the use of ionizing radiation is a drawback, limiting its application in children and women of reproductive age, and when multiple investigations are needed, for example, as might be required for guiding treatment in an individual patient. A similar clinical role can be envisaged for [1-<sup>13</sup>C]pyruvate as has been established for <sup>18</sup>FDG-PET. Both techniques can be used to detect increased glycolytic flux (50) and have been shown to be comparably sensitive in detecting tumor response to treatment (51). However, since hyperpolarized [1-<sup>13</sup>C]pyruvate effectively detects lactate accumulation (11), a defining feature of cancer metabolism, i.e., the failure to oxidize pyruvate in the presence of oxygen and reduce it instead to lactate (the “Warburg Effect”), this means that hyperpolarized [1-<sup>13</sup>C]pyruvate may be more specific for detecting cancer than <sup>18</sup>FDG-PET. The latter detects only elevated levels of glucose uptake, which is a feature of many normal tissues and cancer, for example, the brain. The specificity of cancer detection by hyperpolarized [1-<sup>13</sup>C]pyruvate may be confounded, however, by the presence of hypoxia, which will also lead to lactate accumulation and increased lactate labeling (38). Another drawback of imaging with hyperpolarized [1-<sup>13</sup>C]pyruvate is that the short half-life of the polarization precludes whole-body imaging.

## Advantages Compared to <sup>1</sup>H MRS

<sup>1</sup>H-MR spectroscopy and spectroscopic imaging measurements of tissue metabolite profiles are label-free and have found some applications, for example, in identifying different types of brain tumor (52). A notable example is the detection of 2-hydroxyglutarate, which can be used to identify glioblastomas with isocitrate dehydrogenase mutations (IDH) (53). <sup>1</sup>H MRSI has also proved to be important in the prostate, where it can improve the specificity of detection and determination of tumor extent when combined with other MR imaging sequences (54). However, detectable metabolites are present in only millimolar concentrations, as compared to tissue water protons, which are present at ~80M, which results in long data acquisition times and limited spatial resolution. In addition, data processing can be more complex and the biochemical information provided may be unfamiliar to many clinicians, which has limited routine clinical application. Moreover, <sup>1</sup>H MR spectroscopy and spectroscopic images of metabolite profiles provide a static picture of tumor metabolism. On the other hand, imaging with hyperpolarized <sup>13</sup>C-labeled substrates provides dynamic metabolic flux information in the form of images that can be acquired at relatively high spatial and temporal resolutions and therefore should provide an improved assessment of tumor behavior. Additionally, coinjection of different hyperpolarized substrates could also provide additional functional information in the same acquisition, e.g., pyruvate for assessing glycolytic activity and urea for assessing tumor perfusion (55).

## COMBINING METABOLIC IMAGING WITH HYPERPOLARIZED [1-<sup>13</sup>C]PYRUVATE WITH NEW TECHNOLOGIES

### PET-MRI

This is an emerging combined imaging modality with significant potential for clinical assessment of cancer patients (56). Simultaneous PET-MR measurements with hyperpolarized <sup>13</sup>C- and <sup>18</sup>F-labeled substrates would allow a multiparametric assessment of the primary lesion and its metastases in a single imaging session, which potentially could be used to identify imaging-based phenotypes that have prognostic value and which may give a more specific readout of treatment response. For example, PET measurements of <sup>18</sup>FDG uptake assess just the first three steps in tumor glucose metabolism, i.e., delivery *via* the bloodstream, uptake on the glucose transporters, and phosphorylation and trapping in the reaction catalyzed by hexokinase. <sup>13</sup>C MRSI measurements of the exchange of hyperpolarized <sup>13</sup>C-labeled exchange between injected [1-<sup>13</sup>C]pyruvate and the endogenous lactate pool again assess delivery *via* the bloodstream and effectively the last two steps in the glycolytic pathway, i.e., the steps catalyzed by lactate dehydrogenase and the plasma membrane monocarboxylate transporters. Therefore, by combining <sup>18</sup>FDG-PET and hyperpolarized [1-<sup>13</sup>C]pyruvate measurements, we may be able to assess flux in the entire glycolytic pathway, for example, increased mitochondrial oxidation of pyruvate may have no effect on <sup>18</sup>FDG uptake but could decrease <sup>13</sup>C labeling of lactate. There are other PET probes of tumor metabolism that could also be used alongside hyperpolarized [1-<sup>13</sup>C]pyruvate, and which could provide complementary information. These include <sup>11</sup>C-acetate, as a marker of fatty acid synthesis, and labeled glutamine, which can be used to assess glutaminolysis; both of which are upregulated in tumor cells (57, 58). These PET probes may be especially useful in tumors where <sup>18</sup>FDG is ineffective, e.g., in prostate tumors (59) and in gliomas (60), and where the corresponding hyperpolarized <sup>13</sup>C-labeled probes are limited. For example, the metabolism of hyperpolarized [1-<sup>13</sup>C]acetate has been detected *in vivo* (61); however, the short lifetime of the hyperpolarization means that it could not be used to monitor fatty acid synthesis, where PET studies with [1-<sup>11</sup>C]acetate in animal tumor models have shown that it can take over 60 min before there is substantial incorporation into the fatty acid pool (62). In the case of [5-<sup>13</sup>C] glutamine, a relatively short hyperpolarization lifetime and slow metabolism (63) has precluded imaging *in vivo* (64).

### Liquid Biopsies

Blood and urine biomarkers, obtained from “liquid biopsies,” are also evolving, providing information in a non-invasive way allied to the advantages of collection simplicity and relatively low cost. Many body fluid biomarkers have been reported for different types of cancer; however, few have become established in the clinic, usually because they lack specificity. A recent promising example is a panel of three urine biomarkers for early detection of pancreatic cancer (65). Rapid advances in DNA sequencing technology have allowed somatic mutations present in tumor cells to

be detected and tracked in blood-borne circulating tumor DNA (ctDNA). These fragments of DNA, which have been detected with most types of cancer, have been demonstrated to have potential roles in early detection, staging, and in detecting response to therapy and acquired resistance to treatment (66, 67). Although measurements with hyperpolarized <sup>13</sup>C-labeled cell substrates and these new circulating biomarkers are still their infancy it seems likely that they will provide complementary information, for example, in the assessment of tumor heterogeneity.

## CONCLUSION AND FUTURE DIRECTIONS

Imaging with hyperpolarized <sup>13</sup>C-labeled cell substrates has the potential to become a powerful tool in many steps of clinical evaluation, allowing a more personalized approach to treatment. The first clinical trial established the feasibility of imaging human tumors with hyperpolarized [1-<sup>13</sup>C]pyruvate. Since this substrate can be used to assess glycolysis, which is upregulated in many tumors, then this should make it a very general tool for oncological imaging in the clinic. Despite the biological insights that imaging with hyperpolarized <sup>13</sup>C-labeled substrates promises to deliver in the clinic, it will nevertheless have to prove itself against

established and emerging clinical techniques, demonstrating that it can provide unique information that changes clinical practice.

## AUTHOR CONTRIBUTIONS

Both authors listed, have made substantial, direct, and intellectual contribution to the work, and approved it for publication. .

## ACKNOWLEDGMENTS

Work in KB's laboratory is supported by a Cancer Research UK Programme grant (17242) and the CRUK-EPSRC Imaging Centre in Cambridge and Manchester (16465). Clinical studies are funded by a Strategic Award from the Wellcome Trust (095962). ES was a recipient of a fellowship from the European Union Seventh Framework Programme (FP7/2007-2013) under the Marie Curie Initial Training Network *METAFUX* (project number 264780). ES also acknowledges the educational support of the Programme for Advanced Medical Education from Calouste Gulbenkian Foundation, Champalimaud Foundation, Ministerio de Saude, and Fundacao para a Ciencia e Tecnologia, Portugal.

## REFERENCES

- Glunde K, Bhujwalla ZM. Metabolic tumor imaging using magnetic resonance spectroscopy. *Semin Oncol* (2011) **38**:26–41. doi:10.1053/j.seminoncol.2010.11.001
- Ardenkjær-Larsen JH, Fridlund B, Gram A, Hansson G, Hansson L, Lerche MH, et al. Increase in signal-to-noise ratio of >10,000 times in liquid-state NMR. *Proc Natl Acad Sci U S A* (2003) **100**:10158–63. doi:10.1073/pnas.1733835100
- Nelson SJ, Kurhanewicz J, Vigneron DB, Larson PE, Harzstark AL, Ferrone M, et al. Metabolic imaging of patients with prostate cancer using hyperpolarized [1-<sup>13</sup>C]pyruvate. *Sci Transl Med* (2013) **5**:198ra108. doi:10.1126/scitranslmed.3006070
- Brindle KM, Bohndiek SE, Gallagher FA, Kettunen MI. Tumor imaging using hyperpolarized <sup>13</sup>C magnetic resonance spectroscopy. *Magn Reson Med* (2011) **66**:505–19. doi:10.1002/mrm.22999
- Meier S, Karlsson M, Jensen PR, Lerche MH, Duus JO. Metabolic pathway visualization in living yeast by DNP-NMR. *Mol Biosyst* (2011) **7**:2834–6. doi:10.1039/c1mb05202k
- Harris T, Degani H, Frydman L. Hyperpolarized <sup>13</sup>C NMR studies of glucose metabolism in living breast cancer cell cultures. *NMR Biomed* (2013) **26**:1831–43. doi:10.1002/nbm.3024
- Rodrigues TB, Serrao EM, Kennedy BW, Hu DE, Kettunen MI, Brindle KM. Magnetic resonance imaging of tumor glycolysis using hyperpolarized <sup>13</sup>C-labeled glucose. *Nat Med* (2014) **20**:93–7. doi:10.1038/nm.3416
- Schroeder MA, Atherton HJ, Ball DR, Cole MA, Heather LC, Griffin JL, et al. Real-time assessment of Krebs cycle metabolism using hyperpolarized <sup>13</sup>C magnetic resonance spectroscopy. *FASEB J* (2009) **23**:2529–38. doi:10.1096/fj.09-129171
- Merritt ME, Harrison C, Sherry AD, Malloy CR, Burgess SC. Flux through hepatic pyruvate carboxylase and phosphoenolpyruvate carboxykinase detected by hyperpolarized <sup>13</sup>C magnetic resonance. *Proc Natl Acad Sci U S A* (2011) **108**:19084–9. doi:10.1073/pnas.1111247108
- Chen AP, Hurd RE, Schroeder MA, Lau AZ, Gu YP, Lam WW, et al. Simultaneous investigation of cardiac pyruvate dehydrogenase flux, Krebs cycle metabolism and pH, using hyperpolarized [1,2-<sup>13</sup>C]pyruvate in vivo. *NMR Biomed* (2012) **25**:305–11. doi:10.1002/nbm.1749
- Gallagher FA, Bohndiek SE, Kettunen MI, Lewis DY, Soloviev D, Brindle KM. Hyperpolarized <sup>13</sup>C MRI and PET: *in vivo* tumor biochemistry. *J Nucl Med* (2011) **52**:1333–6. doi:10.2967/jnumed.110.085258
- Brindle KM. Imaging metabolism with hyperpolarized <sup>13</sup>C-labeled cell substrates. *J Am Chem Soc* (2015) **137**:6418–27. doi:10.1021/jacs.5b03300
- Gallagher FA, Kettunen MI, Hu DE, Jensen PR, Zandt RI, Karlsson M, et al. Production of hyperpolarized [1,4-<sup>13</sup>C<sub>2</sub>]malate from [1,4-<sup>13</sup>C<sub>2</sub>]fumarate is a marker of cell necrosis and treatment response in tumors. *Proc Natl Acad Sci U S A* (2009) **106**:19801–6. doi:10.1073/pnas.0911447106
- Clawson MR, Kettunen MI, Hu DE, Mathews RJ, Witney TH, Kennedy BW, et al. Magnetic resonance imaging with hyperpolarized [1,4-<sup>13</sup>C<sub>2</sub>]fumarate allows detection of early renal acute tubular necrosis. *Proc Natl Acad Sci U S A* (2012) **109**:13374–9. doi:10.1073/pnas.1205539109
- Gallagher FA, Kettunen MI, Day SE, Hu DE, Ardenkjær-Larsen JH, Zandt R, et al. Magnetic resonance imaging of pH *in vivo* using hyperpolarized <sup>13</sup>C-labelled bicarbonate. *Nature* (2008) **453**:940–3. doi:10.1038/nature07017
- Wilson DM, Keshari KR, Larson PE, Chen AP, Hu S, Van Criekinge M, et al. Multi-compound polarization by DNP allows simultaneous assessment of multiple enzymatic activities *in vivo*. *J Magn Reson* (2010) **205**:141–7. doi:10.1016/j.jmr.2010.04.012
- Day SE, Kettunen MI, Gallagher FA, Hu DE, Lerche M, Wolber J, et al. Detecting tumor response to treatment using hyperpolarized <sup>13</sup>C magnetic resonance imaging and spectroscopy. *Nat Med* (2007) **13**:1382–7. doi:10.1038/nm1650
- Kurhanewicz J, Vigneron DB, Brindle K, Chekmenev EY, Comment A, Cunningham CH, et al. Analysis of cancer metabolism by imaging hyperpolarized nuclei: prospects for translation to clinical research. *Neoplasia* (2011) **13**:81–97. doi:10.1593/neo.101102
- Golman K, Ardenkjær-Larsen JH, Svensson J, Axelsson O, Hansson G, Hansson L, et al. <sup>13</sup>C-angiography. *Acad Radiol* (2002) **9**(Suppl 2):S507–10. doi:10.1016/S1076-6332(03)80278-7
- Svensson J, Mansson S, Johansson E, Petersson JS, Olsson LE. Hyperpolarized <sup>13</sup>C MR angiography using trueFISP. *Magn Reson Med* (2003) **50**:256–62. doi:10.1002/mrm.10530
- Mansson S, Johansson E, Magnusson P, Chai CM, Hansson G, Petersson JS, et al. <sup>13</sup>C imaging—a new diagnostic platform. *Eur Radiol* (2006) **16**:57–67. doi:10.1007/s00330-005-2806-x
- Chen AP, Albers MJ, Cunningham CH, Kohler SJ, Yen YF, Hurd RE, et al. Hyperpolarized <sup>13</sup>C spectroscopic imaging of the TRAMP mouse at 3T—initial experience. *Magn Reson Med* (2007) **58**:1099–106. doi:10.1002/mrm.21256
- Merritt ME, Harrison C, Storey C, Jeffrey FM, Sherry AD, Malloy CR. Hyperpolarized <sup>13</sup>C allows a direct measure of flux through a single

- enzyme-catalyzed step by NMR. *Proc Natl Acad Sci U S A* (2007) **104**:19773–7. doi:10.1073/pnas.0706235104
24. Golman K, Petersson JS, Magnusson P, Johansson E, Akeson P, Chai CM, et al. Cardiac metabolism measured noninvasively by hyperpolarized <sup>13</sup>C MRI. *Magn Reson Med* (2008) **59**:1005–13. doi:10.1002/mrm.21460
  25. Merritt ME, Harrison C, Storey C, Sherry AD, Malloy CR. Inhibition of carbohydrate oxidation during the first minute of reperfusion after brief ischemia: NMR detection of hyperpolarized <sup>13</sup>CO<sub>2</sub> and H<sup>13</sup>CO<sub>3</sub>. *Magn Reson Med* (2008) **60**:1029–36. doi:10.1002/mrm.21760
  26. Schroeder MA, Cochlin LE, Heather LC, Clarke K, Radda GK, Tyler DJ. *In vivo* assessment of pyruvate dehydrogenase flux in the heart using hyperpolarized carbon-13 magnetic resonance. *Proc Natl Acad Sci U S A* (2008) **105**:12051–6. doi:10.1073/pnas.0805953105
  27. Dodd MS, Atherton HJ, Carr CA, Stuckey DJ, West JA, Griffin JL, et al. Impaired *in vivo* mitochondrial Krebs cycle activity after myocardial infarction assessed using hyperpolarized magnetic resonance spectroscopy. *Circ Cardiovasc Imaging* (2014) **7**:895–904. doi:10.1161/CIRCIMAGING.114.001857
  28. Denton RM, Halestrap AP. Regulation of pyruvate metabolism in mammalian tissues. *Essays Biochem* (1979) **15**:37–77.
  29. Gatenby RA, Gillies RJ. Why do cancers have high aerobic glycolysis? *Nat Rev Cancer* (2004) **4**:891–9. doi:10.1038/nrc1478
  30. Hanahan D, Weinberg RA. Hallmarks of cancer: the next generation. *Cell* (2011) **144**:646–74. doi:10.1016/j.cell.2011.02.013
  31. Golman K, Zandt RI, Lerche M, Pehrson R, Ardenkjaer-Larsen JH. Metabolic imaging by hyperpolarized <sup>13</sup>C magnetic resonance imaging for *in vivo* tumor diagnosis. *Cancer Res* (2006) **66**:10855–60. doi:10.1158/0008-5472.CAN-06-2564
  32. Park I, Larson PE, Zierhut ML, Hu S, Bok R, Ozawa T, et al. Hyperpolarized <sup>13</sup>C magnetic resonance metabolic imaging: application to brain tumors. *Neuro Oncol* (2010) **12**:133–44. doi:10.1093/neuonc/nop043
  33. Serrao EM, Kettunen MI, Rodrigues TB, Dzien P, Wright AJ, Gopinathan A, et al. MRI with hyperpolarised [1-<sup>13</sup>C]pyruvate detects advanced pancreatic preneoplasia prior to invasive disease in a mouse model. *Gut* (2015) **65**(3):465–75. doi:10.1136/gutjnl-2015-310114
  34. Hu S, Balakrishnan A, Bok RA, Anderton B, Larson PE, Nelson SJ, et al. <sup>13</sup>C-pyruvate imaging reveals alterations in glycolysis that precede c-Myc-induced tumor formation and regression. *Cell Metab* (2011) **14**:131–42. doi:10.1016/j.cmet.2011.04.012
  35. Albers MJ, Bok R, Chen AP, Cunningham CH, Zierhut ML, Zhang VY, et al. Hyperpolarized <sup>13</sup>C lactate, pyruvate, and alanine: noninvasive biomarkers for prostate cancer detection and grading. *Cancer Res* (2008) **68**:8607–15. doi:10.1158/0008-5472.CAN-08-0749
  36. Chen AP, Bok R, Zhang V, Xu D, Veeraraghavan S, Hurd RE, et al. Serial hyperpolarized <sup>13</sup>C 3D-MRSI following therapy in a mouse model of prostate cancer. *Proc Int Soc Mag Reson Med* (2008) **16**:888.
  37. Krishna MC, Matsumoto S, Saito K, Matsuo M, Mitchell JB, Ardenkjaer-Larsen JH. Magnetic resonance imaging of tumor oxygenation and metabolic profile. *Acta Oncol* (2013) **52**:1248–56. doi:10.3109/0284186X.2013.819118
  38. Bluff JE, Reynolds S, Metcalf S, Alizadeh T, Kazan SM, Bucur A, et al. Measurement of the acute metabolic response to hypoxia in rat tumours *in vivo* using magnetic resonance spectroscopy and hyperpolarised pyruvate. *Radiother Oncol* (2015) **116**:392–9. doi:10.1016/j.radonc.2015.03.011
  39. Eisenhauer EA, Therasse P, Bogaerts J, Schwartz LH, Sargent D, Ford R, et al. New response evaluation criteria in solid tumours: revised RECIST guideline (version 1.1). *Eur J Cancer* (2009) **45**:228–47. doi:10.1016/j.ejca.2008.10.026
  40. Brindle K. New approaches for imaging tumour responses to treatment. *Nat Rev Cancer* (2008) **8**:94–107. doi:10.1038/nrc2289
  41. Bohndiek SE, Kettunen MI, Hu DE, Brindle KM. Hyperpolarized <sup>13</sup>C spectroscopy detects early changes in tumor vasculature and metabolism after VEGF neutralization. *Cancer Res* (2012) **72**:854–64. doi:10.1158/0008-5472.CAN-11-2795
  42. Witney TH, Kettunen MI, Hu DE, Gallagher FA, Bohndiek SE, Napolitano R, et al. Detecting treatment response in a model of human breast adenocarcinoma using hyperpolarised [1-<sup>13</sup>C]pyruvate and [1,<sup>13</sup>C<sub>2</sub>]fumarate. *Br J Cancer* (2010) **103**:1400–6. doi:10.1038/sj.bjc.6605945
  43. Bohndiek SE, Kettunen MI, Hu DE, Witney TH, Kennedy BW, Gallagher FA, et al. Detection of tumor response to a vascular disrupting agent by hyperpolarized <sup>13</sup>C magnetic resonance spectroscopy. *Mol Cancer Ther* (2010) **9**:3278–88. doi:10.1158/1535-7163.MCT-10-0706
  44. Dafni H, Larson PE, Hu S, Yoshihara HA, Ward CS, Venkatesh HS, et al. Hyperpolarized <sup>13</sup>C spectroscopic imaging informs on hypoxia-inducible factor-1 and myc activity downstream of platelet-derived growth factor receptor. *Cancer Res* (2010) **70**:7400–10. doi:10.1158/0008-5472.CAN-10-0883
  45. Ward CS, Venkatesh HS, Chaumeil MM, Brandes AH, Vancriekinge M, Dafni H, et al. Noninvasive detection of target modulation following phosphatidylinositol 3-kinase inhibition using hyperpolarized <sup>13</sup>C magnetic resonance spectroscopy. *Cancer Res* (2010) **70**:1296–305. doi:10.1158/0008-5472.CAN-09-2251
  46. Day SE, Kettunen MI, Cherukuri MK, Mitchell JB, Lizak MJ, Morris HD, et al. Detecting response of rat C6 glioma tumors to radiotherapy using hyperpolarized [1-<sup>13</sup>C]pyruvate and <sup>13</sup>C magnetic resonance spectroscopic imaging. *Magn Reson Med* (2011) **65**:557–63. doi:10.1002/mrm.22698
  47. Saito K, Matsumoto S, Takakusagi Y, Matsuo M, Morris HD, Lizak MJ, et al. <sup>13</sup>C-MR spectroscopic imaging with hyperpolarized [1-<sup>13</sup>C]pyruvate detects early response to radiotherapy in SCC tumors and HT-29 tumors. *Clin Cancer Res* (2015) **21**(22):5073–81. doi:10.1158/1078-0432.ccr-14-1717
  48. Thind K, Chen A, Friesen-Waldner L, Ouriadov A, Scholl TJ, Fox M, et al. Detection of radiation-induced lung injury using hyperpolarized <sup>13</sup>C magnetic resonance spectroscopy and imaging. *Magn Reson Med* (2013) **70**:601–9. doi:10.1002/mrm.24525
  49. Thind K, Jensen MD, Hegarty E, Chen AP, Lim H, Martinez-Santiesteban F, et al. Mapping metabolic changes associated with early radiation induced lung injury post conformal radiotherapy using hyperpolarized <sup>13</sup>C-pyruvate magnetic resonance spectroscopic imaging. *Radiother Oncol* (2014) **110**:317–22. doi:10.1016/j.radonc.2013.11.016
  50. Menzel MI, Farrell EV, Janich MA, Khegai O, Wiesinger F, Nekolla S, et al. Multimodal assessment of *in vivo* metabolism with hyperpolarized [1-<sup>13</sup>C]MR spectroscopy and <sup>18</sup>F-FDG PET imaging in hepatocellular carcinoma tumor-bearing rats. *J Nucl Med* (2013) **54**:1113–9. doi:10.2967/jnumed.112.110825
  51. Witney TH, Kettunen MI, Day SE, Hu D, Neves AA, Gallagher FA, et al. A comparison between radiolabeled fluorodeoxyglucose uptake and hyperpolarized <sup>13</sup>C-labeled pyruvate utilization as methods for detecting tumor response to Treatment12. *Neoplasia* (2009) **11**:574–82. doi:10.1593/neo.09254
  52. Horska A, Barker PB. Imaging of brain tumors: MR spectroscopy and metabolic imaging. *Neuroimaging Clin N Am* (2010) **20**:293–310.1. doi:10.1016/j.nic.2010.04.003
  53. Choi C, Ganji SK, Deberardinis RJ, Hatanpaa KJ, Rakheja D, Kovacs Z, et al. 2-hydroxyglutarate detection by magnetic resonance spectroscopy in IDH-mutated patients with gliomas. *Nat Med* (2012) **18**:624–9. doi:10.1038/nm.2682
  54. Johnson LM, Turkbey B, Figg WD, Choyke PL. Multiparametric MRI in prostate cancer management. *Nat Rev Clin Oncol* (2014) **11**:346–53. doi:10.1038/nrclinonc.2014.69
  55. von Morze C, Larson PE, Hu S, Yoshihara HA, Bok RA, Goga A, et al. Investigating tumor perfusion and metabolism using multiple hyperpolarized <sup>13</sup>C compounds: HP001, pyruvate and urea. *Magn Reson Imaging* (2012) **30**:305–11. doi:10.1016/j.mri.2011.09.026
  56. Rosenkrantz AB, Friedman K, Chandarana H, Melsaether A, Moy L, Ding YS, et al. Current status of hybrid PET/MRI in oncologic imaging. *AJR Am J Roentgenol* (2016) **206**(1):162–72. doi:10.2214/ajr.15.14968
  57. Hensley CT, Wasti AT, Deberardinis RJ. Glutamine and cancer: cell biology, physiology, and clinical opportunities. *J Clin Invest* (2013) **123**:3678–84. doi:10.1172/JCI69600
  58. Hosios AM, Vander Heiden MG. Acetate metabolism in cancer cells. *Cancer Metab* (2014) **2**:27. doi:10.1186/s40170-014-0027-y
  59. Grassi I, Nanni C, Allegri V, Morigi JJ, Montini GC, Castellucci P, et al. The clinical use of PET with <sup>11</sup>C-acetate. *Am J Nucl Med Mol Imaging* (2012) **2**:33–47.
  60. Venneti S, Dunphy MP, Zhang H, Pitter KL, Zanzonico P, Campos C, et al. Glutamine-based PET imaging facilitates enhanced metabolic evaluation of gliomas *in vivo*. *Sci Transl Med* (2015) **7**:274ra217. doi:10.1126/scitranslmed.aaa1009
  61. Bastiaansen JA, Cheng T, Mishkovsky M, Duarte JM, Comment A, Gruetter R. *In vivo* enzymatic activity of acetylCoA synthetase in skeletal muscle revealed

- by <sup>13</sup>C turnover from hyperpolarized [1-<sup>13</sup>C]acetate to [1-<sup>13</sup>C]acetyl carnitine. *Biochim Biophys Acta* (2013) **1830**:4171–8. doi:10.1016/j.bbagen.2013.03.023
62. Lewis DY, Boren J, Shaw GL, Bielik R, Ramos-Montoya A, Larkin TJ, et al. Late imaging with [1-<sup>11</sup>C]acetate improves detection of tumor fatty acid synthesis with PET. *J Nucl Med* (2014) **55**:1144–9. doi:10.2967/jnumed.113.134437
63. Gallagher FA, Kettunen MI, Day SE, Lerche M, Brindle KM. <sup>13</sup>C MR spectroscopy measurements of glutaminase activity in human hepatocellular carcinoma cells using hyperpolarized <sup>13</sup>C-labeled glutamine. *Magn Reson Med* (2008) **60**:253–7. doi:10.1002/mrm.21650
64. Cabella C, Karlsson M, Canape C, Catanzaro G, Colombo Serra S, Miragoli L, et al. *In vivo* and *in vitro* liver cancer metabolism observed with hyperpolarized [5-<sup>13</sup>C] glutamine. *J Magn Reson* (2013) **232**:45–52.1. doi:10.1016/j.jmr.2013.04.010
65. Radon TP, Massat NJ, Jones R, Alrawashdeh W, Dumartin L, Ennis D, et al. Identification of a three-biomarker panel in urine for early detection of pancreatic adenocarcinoma. *Clin Cancer Res* (2015) **21**:3512–21. doi:10.1158/1078-0432.CCR-14-2467
66. Murtaza M, Dawson SJ, Tsui DW, Gale D, Forshaw T, Piskorz AM, et al. Non-invasive analysis of acquired resistance to cancer therapy by sequencing of plasma DNA. *Nature* (2013) **497**:108–12. doi:10.1038/nature12065
67. Bettegowda C, Sausen M, Leary RJ, Kinde I, Wang Y, Agrawal N, et al. Detection of circulating tumor DNA in early- and late-stage human malignancies. *Sci Transl Med* (2014) **6**:224ra224. doi:10.1126/scitranslmed.3007094

**Conflict of Interest Statement:** KB's lab has a research agreement with GE Healthcare (GEH) and holds patents on DNP technology with GHE.

Copyright © 2016 Serrao and Brindle. This is an open-access article distributed under the terms of the Creative Commons Attribution License (CC BY). The use, distribution or reproduction in other forums is permitted, provided the original author(s) or licensor are credited and that the original publication in this journal is cited, in accordance with accepted academic practice. No use, distribution or reproduction is permitted which does not comply with these terms.



# Positron Emission Tomography Imaging of Tumor Cell Metabolism and Application to Therapy Response Monitoring

Amarnath Challapalli<sup>1</sup> and Eric O. Aboagye<sup>2\*</sup>

<sup>1</sup>Department of Clinical Oncology, Bristol Cancer Institute, Bristol, UK, <sup>2</sup>Department of Surgery and Cancer, Imperial College London, London, UK

## OPEN ACCESS

**Edited by:**

Zaver Bhujwalla,  
Johns Hopkins University School of  
Medicine, USA

**Reviewed by:**

Sridhar Nimmagadda,  
Johns Hopkins University, USA  
Marie-France Penet,  
Johns Hopkins University School of  
Medicine, USA

**\*Correspondence:**

Eric O. Aboagye  
eric.aboagye@imperial.ac.uk

**Specialty section:**

This article was submitted to Cancer  
Imaging and Diagnosis,  
a section of the journal  
*Frontiers in Oncology*

**Received:** 25 November 2015

**Accepted:** 12 February 2016

**Published:** 29 February 2016

**Citation:**

Challapalli A and Aboagye EO (2016)  
Positron Emission Tomography  
Imaging of Tumor Cell Metabolism  
and Application to Therapy Response  
Monitoring.  
*Front. Oncol.* 6:44.  
doi: 10.3389/fonc.2016.00044

Cancer cells do reprogram their energy metabolism to enable several functions, such as generation of biomass including membrane biosynthesis, and overcoming bioenergetic and redox stress. In this article, we review both established and evolving radioprobes developed in association with positron emission tomography (PET) to detect tumor cell metabolism and effect of treatment. Measurement of enhanced tumor cell glycolysis using 2-deoxy-2-[<sup>18</sup>F]fluoro-D-glucose is well established in the clinic. Analogs of choline, including [<sup>11</sup>C]choline and various fluorinated derivatives are being tested in several cancer types clinically with PET. In addition to these, there is an evolving array of metabolic tracers for measuring intracellular transport of glutamine and other amino acids or for measuring glycogenesis, as well as probes used as surrogates for fatty acid synthesis or precursors for fatty acid oxidation. In addition to providing us with opportunities for examining the complex regulation of reprogrammed energy metabolism in living subjects, the PET methods open up opportunities for monitoring pharmacological activity of new therapies that directly or indirectly inhibit tumor cell metabolism.

**Keywords:** tumor metabolism, positron emission tomography, choline, acetate, methionine, glutamine

## INTRODUCTION

Mammalian cells possess molecular machineries that regulate their proliferation, differentiation, and death. Malignant transformation is a multistep process involving genetic alterations, disruption of regulatory circuits, and dynamic changes in the genome. It has been suggested that malignant growth is governed by six essential alterations in cell physiology: self-sufficiency in growth signals, insensitivity to growth-inhibitory (antigrowth) signals, evasion of programmed cell death (apoptosis), limitless replicative potential, sustained angiogenesis, and tissue invasion and metastasis (1). Recent advances led to the notion that progressive evolution of normal cells to a neoplastic state involves not only the successive acquisition of hallmark capabilities but also contributions of recruited normal cells (which form tumor-associated stroma, constituting the “tumor microenvironment”) (2).

Metabolic reprogramming is an important property of the cancer cells. In the presence of abundant nutrients, oncogenic signaling facilitates assimilation of carbons into macromolecules, such as lipids, proteins, and nucleic acids. The net result of this is to support cell growth and proliferation. Glucose and glutamine are abundant nutrients, and both feed into multiple nodes of central metabolism. Glutamine also provides two nitrogen atoms for synthesis of hexosamines,

nucleotides, and amino acids, all of which are also required for growth (3). Among the host of pathways altered in cancer, glucose and glutamine metabolism are consistently reprogrammed by mutations in *MYC*, *TP53*, the Ras-related oncogenes, and the LKB1-AMP kinase (AMPK) and PI3 kinase (PI3K) signaling pathways. Oncogenic Ras increases both glucose uptake via enhanced expression of glucose transporter (GLUT) 1, and utilization (4), in addition to regulating glutamine metabolism, promoting cell survival and growth (5). Increased *MYC* also enhances glycolysis, and glutamine catabolism, resulting in cell growth (6).

The hallmarks of cancer are all linked to proliferation of cancer cells, thus making cell proliferation an important capability leading to immortalization and generation of macroscopic tumors. The framework of hallmarks assumes a homogeneous population of cancer cells and considers the hallmarks as distinct entities, with a one-to-one relation between oncogenic events (the inducers), the signaling pathways (transmission), and the hallmarks (the effects). However, one oncogenic event, or one signaling cascade, could induce several hallmarks accounting for the dynamic and spatial heterogeneity of tumors (7). This heterogeneity provides a framework to interpret pathological, diagnostic, and therapeutic observations of tumors and supports the need for non-invasive serial studies on the whole tumor mass and the use of simultaneous, multi-targeted therapies for treating cancer.

Routine clinical evaluation of cancer therapeutics involves assessment of the change in tumor burden (anatomical measurements). Tumor shrinkage (objective response) and time to disease progression are both important endpoints, as these have been linked to an improvement in overall survival or other time to event measures in randomized phase III studies (8). These measures also determine the efficacy of drugs under study. In order to have standardized and widely accepted criteria for measurement of response to allow comparisons to be made across studies, the Response Evaluation Criteria in Solid Tumors (RECIST) criteria were formulated (9). These criteria have been widely adopted for trials where the primary endpoints are objective response or disease progression. Since the introduction of RECIST in 2000, the increasing utilization of imaging technologies, such as MRI, FDG positron emission tomography (PET), and targeted cytostatic therapies, have prompted an update in the guidelines (RECIST v1.1) (10). The definitions of the criteria used to determine objective tumor response for target lesions are as follows:

- 1) Complete response (CR): disappearance of all target lesions. Any pathological lymph nodes (whether target or non-target) must have reduction in short axis to <10 mm.
- 2) Partial response (PR): at least a 30% decrease in the sum of diameters of target lesions, taking as reference the baseline sum diameters.
- 3) Progressive disease (PD): at least a 20% increase in the sum of diameters of target lesions, taking as reference the smallest sum on study (this includes the baseline sum if that is the smallest on study). In addition to the relative increase of 20%, the sum must also demonstrate an absolute increase of at least 5 mm. (Note: the appearance of one or more new lesions is also considered progression.)

- 4) Stable disease (SD): neither sufficient shrinkage to qualify for PR nor sufficient increase to qualify for PD, taking as reference the smallest sum diameters while on study.

RECIST has limitations due to its reliance on changes in tumor size with therapy. First, uni-dimensional measurements may be apparent only after three to four cycles of chemotherapy. In non-responders, this means subjecting patients to cumulative toxicity of three to four cycles of treatment with little benefit. Moreover, the change in the tumor diameter may be non-uniform. Second, changes in measurements of smaller lesions are not reliable (11). Third, cytostatic treatments may not necessarily cause a decrease in tumor size or volume. Use of functional imaging overcomes several of these limitations. The use of PET has, for example, resulted in accurate imaging of subtle tumor biologic changes and the detection of early response to anti-cancer therapy (12). Tumors having increased metabolic activity may take up greater amounts of a radioactive tracer as compared to adjacent normal tissues; in that regard, sub-millimeter tumors have been known to show significant radiotracer uptake for certain tracers (13). Similarly, any change in metabolic or signaling pathway activity consequent to successful treatment could result in changes in uptake of the tracer on PET (14). Thus, PET is a useful tool in oncology to image certain metabolic pathways and response to therapy.

This review gives an overview of metabolic processes imaged by PET focusing on both established and evolving radioprobes to detect tumor glycolysis, choline metabolism, intracellular transport of glutamine, and other amino acids, as well as fatty acid metabolism (Figure 1). In particular, we emphasize the role of radiolabeled choline, acetate, and amino acid tracers for monitoring efficacy or predicting response to new therapies that directly or indirectly inhibit tumor cell metabolism.

## METHODOLOGY

A comprehensive PubMed literature search was performed, identifying articles relating to PET imaging in malignant disease, particularly those reporting on response assessment with radiolabeled tracers, focusing on [<sup>11</sup>C]- and [<sup>18</sup>F]-labeled choline, acetate, methionine, and glutamine derivatives, up to July 2015. Search terms that were used to identify such articles were “acetate,” “choline,” “methionine,” “glutamine,” “tryptophan,” “FACBC,” and “PET” or “positron emission tomography.” Original publications were selected for inclusion in this review.

## OVERVIEW OF PATHWAYS TRACED BY PET IMAGING

### Glycolysis and Glycolysis-Linked Metabolic Pathways

A review of metabolism will be incomplete without reference to glycolysis. Energy production in normal cells is predominantly the result of oxidative phosphorylation, as opposed to glycolysis. However, tumor cells predominantly use glycolysis as a means to energy production irrespective of oxygen levels. Aerobic

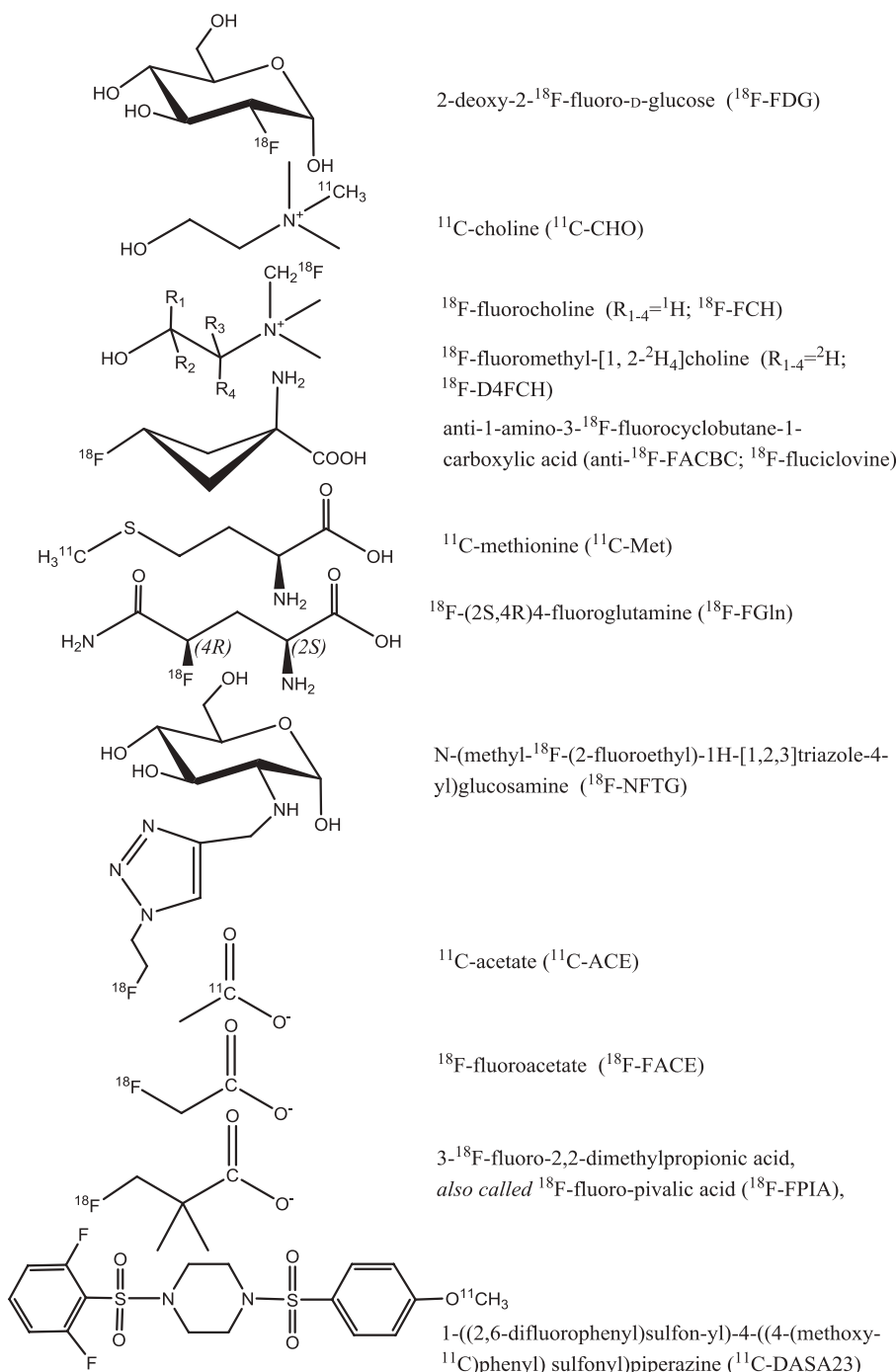


**FIGURE 1 | Radiotracers utilized in the imaging of tumor cell metabolism.**

glycolysis (AG) refers to glucose utilization in excess of that needed for oxidative phosphorylation, despite sufficient oxygen to metabolize glucose to carbon dioxide and water. AG plays an important role in the biosynthesis of glycogen, proteins, lipids, and nucleic acids (15). AG, also known as the Warburg effect, supports the biosynthetic requirements of proliferating cancer cells (16). PET using 2-deoxy-2-[<sup>18</sup>F]fluoro-D-glucose ([<sup>18</sup>F]

FDG) has been widely used in the evaluation of various tumor types on the basis that an increase in AG will be reflected in an increase in the total glucose consumption of the tissue.

In a large pooled review of over 18,000 patient studies, it was shown that [<sup>18</sup>F]FDG PET has a sensitivity of 84% and a specificity of 88% for tumor detection (17). [<sup>18</sup>F]FDG PET has also been evaluated in response assessment following treatment with

conventional chemotherapeutic agents both in the preclinical (18) and in the clinical setting (19–25), with the premise that decreases in glycolysis may occur in tumors that are sensitive to the applied cancer therapeutics and that the tumors that are resistant to treatment will show unchanged glucose metabolism. The prediction of treatment response has also been analyzed in many studies following treatment with different targeted therapies, e.g., monoclonal antibodies and small molecules inhibitors (26). However, [<sup>18</sup>F]FDG PET has the following limitations: (1) False positive uptake in some benign processes, such as infection and inflammatory lesions (27); (2) low sensitivity in well-differentiated/low-grade tumors that have relatively low glucose metabolism such as carcinoid tumors, bronchoalveolar cell carcinoma, and renal cell carcinoma (RCC) (28–30); (3) low sensitivity in hypocellular cancers, such as desmoplastic or mucinous tumors (31); (4) increased [<sup>18</sup>F]FDG accumulation in some normal body regions, such as lymphoid tissue and brown fat (32); and (5) lack of clinical utility due to high urinary excretion and low expression of GLUT in prostate cancer (PCa) (30). Thus, newer radiotracers to image tumors accurately are being developed to address these shortcomings, as well as explore other metabolic pathways of tumors that can be imaged using PET. Two evolving imaging strategies somewhat linked to glycolysis will be discussed next.

Further to the Warburg effect, the final rate-limiting step in AG, catalyzed by pyruvate kinase (PK), controls the balance between energy production and metabolic precursor synthesis. The M2 isoform of PK (PKM2) is preferentially expressed in cancer cells and channels glycolytic intermediates into pentose phosphate pathway for nucleotide synthesis (33). PKM2 can be allosterically regulated to assume a high- or low-activity state. In cancer cells, there is downregulation of PK activity favoring a microenvironment that is conducive to cell proliferation. 1-((2,6-difluorophenyl)sulfonyl)-4-((methoxy-<sup>11</sup>C)phenoxy)sulfonylpiperazine ([<sup>11</sup>C]DASA-23) (Figure 1) has been developed as a non-invasive PET probe to measure activity of PKM2 in pre-clinical glioblastoma models (34). Witney and co-workers have demonstrated that [<sup>11</sup>C]DASA-23 improved tumor visualization and predicted response to PKM2 activator, which resulted in loss of PET signal. The clinical translation of these findings is eagerly awaited.

Another glycolysis-linked pathway that has come to the fore is glycogenesis. Glycogen, the principal glucose store in mammalian cells, is synthesized from uridine diphosphate glucose (UDP-glucose) catalyzed by glycogen synthase (GS). Tumor cells originating from epithelial tissues, especially in the quiescent state also accumulate glycogen, in addition to increased glycolytic flux (35, 36). In order to gain biological insight into the role of glycogenesis, PET with [<sup>18</sup>F]-N-(methyl-(2-fluoroethyl)-1H[1,2,3]triazole-4-yl) glucosamine (<sup>18</sup>F)NFTG has been studied (37). The authors showed that glycogen levels, [<sup>18</sup>F]NFTG, but not [<sup>18</sup>F]FDG uptake, increased proportionately with cell density and G1/G0 arrest. This increase in glycogen levels and [<sup>18</sup>F]NFTG uptake has potential application in the assessment of oncogenic pathways related to glycogenesis and the detection of post-treatment tumor quiescence. However, there have been no studies evaluating response to therapy.

## Choline Metabolism: Choline PET

Choline is a precursor of phosphatidylcholine (PC), an essential component of phospholipids in the cell membrane (38) and is required for structural stability and cell growth. It is also essential for the synthesis of neurotransmitters such as acetylcholine (by reaction of choline with acetyl-CoA), and production of potent lipid mediators, such as platelet-activating factor. Choline kinase (CHK) is the first enzyme in the Kennedy pathway (39), and is responsible for the *de novo* synthesis of PC. CHK phosphorylates choline to phosphocholine (PCho), the rate-limiting step in the Kennedy pathway. PCho is further phosphorylated to cytidine diphosphate-choline (CDP-choline) by the enzyme cytidylyltransferase and then to other intermediates before being incorporated into cell membrane phospholipids as PC. Malignant transformation is associated with enhanced choline transport and utilization, characterized in a large part by increased CHKα expression, which leads to a phenotype of increased radiolabeled choline uptake (40, 41).

### Choline Tracers

Choline has been radiolabeled with [<sup>11</sup>C], [<sup>18</sup>F] for tracing choline transport and phosphorylation in several tumor types. In one of the first studies, Hara and colleagues showed that phosphorylation led to intracellular retention of the carbon label [<sup>11</sup>C] in PCa (42), thus enabling imaging of this metabolic pathway. The same group also showed that [<sup>11</sup>C]choline had good uptake in brain tumors with almost negligible activity in the blood after 5 min (43). This work inspired others to use [<sup>11</sup>C]choline as a PET radiotracer to image other tumors, including renal (30), esophageal (44–48), and non-small cell lung cancer (NSCLC) (44). [<sup>11</sup>C]choline is particularly useful in PCa as there is negligible urinary bladder excretion, a challenge with [<sup>18</sup>F]FDG. The utility of [<sup>11</sup>C]choline in visualizing and staging PCa has been extensively reported (42, 49).

[<sup>18</sup>F]Fluorocholine ([<sup>18</sup>F]FCH) was developed to overcome the short physical half-life of carbon-11 (20.4 min). The longer half-life (109.8 min) of [<sup>18</sup>F] was deemed potentially advantageous in permitting late imaging of tumors when sufficient clearance of parent tracer in systemic circulation had occurred. Since DeGrado and co-workers first reported the use of [<sup>18</sup>F]FCH (50), the tracer has proven safe for human administration (51) and has been extensively used in patients for diverse pathologies.

[<sup>11</sup>C]Choline (and fluoro-analog) is, however, readily oxidized to [<sup>11</sup>C]betaine by choline oxidase mainly in kidney and liver tissues, with metabolites detectable in plasma soon after injection of the radiotracer (52–54). This makes discrimination of the relative contributions of parent radiotracer from catabolites difficult when a late imaging protocol is used. A more metabolically stable [<sup>18</sup>F] choline analog, [<sup>18</sup>F]fluoromethyl-[1,2-<sup>2</sup>H]<sub>4</sub>choline ([<sup>18</sup>F]D4-FCH), based on the deuterium isotope effect (55) has been developed. The simple substitution of deuterium [<sup>2</sup>D] for hydrogen [<sup>1</sup>H] and the presence of [<sup>18</sup>F] improve the stability of the compound and reduce degradation of the parent tracer (54, 56, 57). This modification is hypothesized to increase the net availability of the parent tracer for phosphorylation and trapping within cells leading to a better signal-to-background contrast, thus improving tumor detection sensitivity of PET. [<sup>18</sup>F]D4-FCH has been validated for imaging tumors preclinically (56, 57). [<sup>18</sup>F]D4-FCH injection was also found to be safe and well tolerated in healthy volunteers with a

favorable dosimetry profile (58). Further clinical studies are now underway to evaluate the utility of [<sup>18</sup>F]D4-FCH in cancer patients.

As the large proportion of studies evaluating response with choline radiotracers has been conducted in PCa – a disease that is managed by a plethora of agents, including androgen deprivation therapy (ADT), radiotherapy (RT), and chemotherapy – this will be the main aspect of the review although other malignancies will be briefly discussed.

## Preclinical Studies

Radiolabeled choline uptake has been extensively investigated in cells and animal models of cancer to determine factors that

affect intrinsic uptake and allow interpretation of clinical findings (**Table 1**).

Hara and colleagues demonstrated that androgen depletion markedly suppressed the uptake of [<sup>3</sup>H]choline in androgen-dependent LNCaP cells but not in androgen-independent PC3 cells (59). Anti-androgens were subsequently shown to modulate choline uptake in androgen-dependent cell lines and also inhibit proliferation (60, 61). Regarding chemotherapy, the effects of docetaxel have been studied by Krause et al. (62), who showed a reduction in the mean [<sup>11</sup>C]choline uptake in PC3 xenograft mouse model as early as 1 week after initiation of docetaxel. A significant reduction of mean tracer uptake of 45% was associated with a mean

**TABLE 1 | Response assessment: preclinical studies.**

	Cell lines/animal models	Outcome
<b>CHOLINE PET</b>		
<b>Prostate</b>		
Hara et al. (59)	LNCaP cells, PC3 cells	Androgen depletion markedly suppressed the uptake of [ <sup>3</sup> H]choline in androgen-dependent LNCaP cells but not in androgen-independent PC3 cells
Al-Saeedi et al. (60)	PC3 cells	Flutamide inhibited tumor cell growth and proliferation Flutamide might inhibit proliferation by an androgen-independent mechanism
Holzapfel et al. (64)	LNCaP cells, PC3 cells Dose of RT – 6 Gy	Transient increase in [ <sup>3</sup> H]choline uptake seen in PC3 cells (maximum at 24 h). Significant decrease in uptake seen in LNCaP cells (minimum at 48 h)
Krause et al. (62)	PC3 cells, subcutaneous 13 NMRI (nu/nu) mice	Reduction in the mean [ <sup>11</sup> C]choline uptake (tumor-to-muscle ratio: TMR) as early as 1 week after initiation of docetaxel [ <sup>11</sup> C]choline PET/CT might be a useful tool for monitoring responses to taxane-based chemotherapy
Fei et al. (65)	PC3, CWR22 cells athymic nude mice	For treated tumors, normalized [ <sup>11</sup> C]choline uptake decreased significantly 24 and 48 h after photodynamic therapy (PDT), associated with decrease in PSA levels. [ <sup>11</sup> C]Choline PET has the potential to determine whether a PDT-treated tumor responds to treatment within 48 h after therapy
Emonds et al. (61)	LNCaP, PC346C cells PC3, PC346DCC cells	Androgens modulated the uptake of [ <sup>11</sup> C]choline in PC346C cells but not in PC3 cells Anti-androgen (Bicalutamide) reduced the uptake in PC346C cells
Schwarzenbock et al. (63)	LNCaP cells SCID-mice	[ <sup>11</sup> C]choline has the potential for use in the early monitoring of the therapeutic effect of docetaxel
<b>Breast</b>		
Al-Saeedi et al. (83)		Incorporation of radiolabeled choline in tumor cells has been shown to be associated with proliferation
<b>ACETATE PET</b>		
<b>Prostate</b>		
Oyama et al. (94)	CWR22 androgen-dependent cells Nude mice	[ <sup>18</sup> F]FDG PET detected metabolic changes within days of androgen ablation in a murine model of prostate cancer, whilst there was no significant difference in [ <sup>11</sup> C]acetate uptake
Vavere et al. (96)	LNCaP, PC3, 22Rv1 Male nu/nu mice	Demonstrating that the FASN inhibitor C75 could reduce [ <sup>11</sup> C]acetate SUV by up to 60% in prostate cancer xenografts
Yoshii et al. (95)	LNCaP, PC3, 22Rv1, and DU145 cells	Evaluated method to predict FASN-targeted therapy outcome using radiolabeled acetate uptake. They demonstrated that uptake of radiolabeled acetate reflects FASN expression and sensitivity to FASN-targeted therapy with orlistat, indicating uptake of radiolabeled acetate is a useful predictor of FASN-targeted therapy outcome
Emonds et al. (93)	LAPC-4 (androgen sensitive), 22Rv1 cells (androgen-independent) Nude mice	They found that ADT significantly decreased the uptake of [ <sup>11</sup> C]choline and [ <sup>18</sup> F]FDG but not uptake of [ <sup>11</sup> C]acetate after 5d of ADT Concluded that [ <sup>11</sup> C]acetate uptake occurs independently of androgens and thus may be more favorable for detecting tumor viability during or following ADT
<b>METHIONINE PET</b>		
<b>Brain</b>		
Sato et al. (125)	Glioma model	The metabolic changes following intraperitoneal chemotherapy were seen immediately as a sharp fall in [ <sup>14</sup> C]thymidine (dTdh) and [ <sup>18</sup> F]fluoro-2'-deoxyuridine ([ <sup>18</sup> F]FUDR) uptake and a moderate fall for [ <sup>14</sup> C]methionine whereas decrease in [ <sup>3</sup> H]deoxyglucose (DG) were seen 1 week after chemotherapy
Reinhardt et al. (123)	AH109A hepatoma cells Donryu rats	[ <sup>11</sup> C]Methionine PET has been sensitive enough to detect and differentiate viable cancer cells in a residual tumor mass as compared to FDG and thymidine, 6 days after one to eight doses of 5 Gy <sup>60</sup> Co radiotherapy (RT)

(Continued)

**TABLE 1 | Continued**

Cell lines/animal models	Outcome
Sasajima et al. (124) <i>In vitro and in vivo</i> Sprague-Dawley rats	The [ <sup>3</sup> H]TdR accumulation rate and amino acid tracer trans-1-amino-3-fluoro-1-[ <sup>14</sup> C]-cyclobutanecarboxylic acid [ <sup>14</sup> C]FACBC and [ <sup>3</sup> H]Met uptake significantly decreased 48 and 72 h, respectively, after temozolomide (TMZ) treatment in C6 but not C6R cells. The decrease in uptake was seen before morphological changes on MRI. Anti-[ <sup>14</sup> C]FACBC and [ <sup>3</sup> H]Met could be a sensitive and precise imaging biomarker for tumor extent visualization and response assessment in glioma patients.
Ono et al. (121) Human Glioblastoma, U87MG (U87) cells U87 and U87R F344/N-mu rats	PET with amino acid tracers (1-amino-3-[ <sup>18</sup> F]fluorocyclobutanecarboxylic acid ( <sup>[18</sup> F]FACBC) and [ <sup>11</sup> C]Methionine) provides useful information on the early response of glioblastomas to single-agent [TMZ, interferon- $\beta$ (IFN), and bevacizumab (Bev)] and combination therapy in glioblastoma
<b>Breast</b>	
Paquette et al. (122) MC7-L1 (ER+) and MC7-L1 ER $\alpha$ -knockdown cell lines Balb/c mice	Letrozole and Fulvestrant reduced glucose uptake/consumption (FDG) and protein synthesis ( <sup>[11</sup> C]Methionine) in ER+ tumors, but not so in ER $\alpha$ KD tumors
<b>Radiotherapy effect</b>	
Kubota et al. (118) AH109A hepatoma cells Donryu rats	A rapid reduction in [ <sup>11</sup> C]methionine uptake following therapy in animal studies was demonstrated
Schaider et al. (126) SW707 colon cancer cells	In an experimental tumor model, MET uptake showed a rapid decrease after irradiation and was followed by necrosis and progressive tumor shrinkage
Murayama et al. (120) SCCV11, murine squamous cell carcinoma cell line C3H/HeN mice	Tumor uptake was decreased with all the tracers (FDG, [ <sup>11</sup> C]Methionine, FLT, [ <sup>18</sup> F]FMT) after were treated with a single dose of x-ray irradiation at 2, 6, 20, or 60 Gy. Significant positive correlations were found between ligand uptake and tumor volume for [ <sup>18</sup> F]FMT
<b>Gynecological</b>	
Higashi et al. (116) Human ovarian carcinoma cell line (HTB77IP3)	Early assessment of human adenocarcinoma response to radiotherapy by FDG, Thymidine, and [ <sup>11</sup> C]methionine PET may be confounded by a normal increase in tracer uptake post-irradiation (30 Gy <sup>60</sup> Co irradiation), despite a 6.25-fold decline in viable cell numbers
Trencsenyi et al. (127) A2780AD/A2780 human ovarian carcinoma and KB-V1/KB-3-1 human epidermoid adenocarcinoma tumor CB-17 SCID mice	FDG, FLT, [ <sup>11</sup> C]Methionine and [ <sup>18</sup> F]fluoroazomycin-arabinofuranoside ( <sup>[18</sup> F]FAZA) are suitable PET tracers for the diagnosis and <i>in vivo</i> follow-up of the efficacy of tumor chemotherapy (doxorubicin) in both Pgp(+) and Pgp(−) human tumor xenografts by mini PET
<b>Myeloma</b>	
Luckerath et al. (119) OPM2, MM.1S myeloma cell lines NOD.CB17-Prkdc <sup>scid</sup> /NCrHsd mice	[ <sup>11</sup> C]Methionine is superior to FDG (30–79% reduction in [ <sup>11</sup> C]Methionine uptake) in very early assessment (24h post) of response to Bortezomib

tumor growth inhibition of 20%. They concluded that [<sup>11</sup>C]choline might be a useful tool for monitoring responses to taxane-based chemotherapy in patients with advanced PCa. These findings were confirmed by Schwarzenböck et al. in a LNCaP-xenograft mouse model (63). Thus, labeled choline uptake is intrinsically responsive to anti-androgen therapy and chemotherapy.

Regarding RT, Holzapfel et al. have studied the effect of 6 Gy of radiation on PC3 and LNCaP cells, *in vitro* (64). Radiation-induced effects were variable with a transient increase in radiotracer uptake in androgen-independent PC3 cells but a decrease in androgen-dependent LNCaP cells. In both cell lines, modulation of tracer uptake was dose-independent following irradiation with 2–12 Gy with a mean increase to 120% in PC3 cells and a mean decrease to 74% in LNCaP cells. The authors suggested that changes of tumor choline uptake monitored by PET after RT may be due to a combination of factors, including therapeutic efficacy and altered tracer transport in cancer cells as a consequence of irradiation. Photodynamic therapy (PDT) responses have also been evaluated. Fei and co-workers evaluated the potential use of [<sup>11</sup>C]choline PET to monitor early tumor response to PDT

in animal models. For treated tumors, normalized [<sup>11</sup>C]choline uptake decreased significantly at 24 and 48 h after PDT, associated with decreases in prostate-specific antigen (PSA) levels. The authors concluded that [<sup>11</sup>C]choline PET has the potential to determine response in a PDT-treated tumor within 48 h after therapy (65).

### Clinical Studies

To date, only anecdotal reports (50, 66) and two small clinical studies (67, 68) have assessed the role of [<sup>11</sup>C]choline PET as a method to monitor the therapeutic effects of ADT (Table 2). Fuccio et al. (67) retrospectively evaluated the effect of 6 months of androgen deprivation (Zoladex in 12 and Bicalutamide in 2 patients) in 14 PCa patients with recurrence after radical prostatectomy. They concluded that androgen deprivation significantly decreases [<sup>11</sup>C] choline uptake in androgen-sensitive patients. In another study in six primary PCa patients having bicalutamide therapy, Giovacchini et al. (68) showed an average reduction of 45% in the [<sup>11</sup>C]choline uptake (SUV<sub>max</sub> from 11.8 to 6.4) corresponding to a 78% decrease in PSA following a median of 4 months of therapy. A similar

**TABLE 2 | Choline PET response assessment: clinical studies.**

	Sample size	Outcome
<b>CHOLINE PET/CT</b>		
<b>Prostate</b>		
De Grado et al. (50)	1	60% reduction in choline uptake in the primary tumor and the bony metastases with androgen deprivation therapy (ADT) in patient with bone metastases from PCa
Giovacchini et al. (68)	6	45% reduction in the [ <sup>11</sup> C]choline uptake ( $SUV_{max}$ ) from 11.8 to 6.4 with a 78% decrease in PSA with a median of 4 months of bicalutamide therapy in patients with primary prostate cancer
Beheshti et al. (72, 73)	38	Demonstrated that reduced [ <sup>18</sup> F]FCH uptake is seen in PCa patients who respond to the hormone therapy often without any significant morphological CT changes
De Waele et al. (66)	1	Initial uptake in prostate and multiple iliac nodes in locally advanced disease, disappeared after 6 months of therapy with leuprorelin and flutamide
Fuccio et al. (67)	14	Six months of androgen deprivation significantly decreases [ <sup>11</sup> C]choline uptake in patients with recurrence after radical prostatectomy
Casamassima et al. (70)	25	High dose of radiotherapy is effective in eradication of limited nodal recurrences
Kwee et al. (76)	8	Plasma cfDNA content and FCH PET/CT-detected tumor activity are potential candidate markers of therapeutic response in castrate resistant prostate cancer (CRPC)
Amani et al. (71)	11	Intra-prostatic [ <sup>11</sup> C]choline uptake (as measured by $SUV_{max}$ and TMR) significantly decreased during and after RT
Challapalli et al. (69)	10	[ <sup>11</sup> C]choline uptake in prostate tumors, determined by [ <sup>11</sup> C]choline PET/CT, is sensitive to ADT and RT, and could be used as an objective quantitative tool for response assessment
De Giorgi et al. (79)	43	Early FCH PET/CT can predict clinical outcome (Progression free and overall survival: PFS and OS) than PSA response in patients on Abiraterone
Caffo et al. (77)	31	Enzalutamide induces volume reductions in primary tumors and metabolic changes in metastatic lesions as detected by [ <sup>18</sup> F]FCH PET/CT
De Giorgi et al. (78)	36	Combination of changes in [ <sup>18</sup> F]FCH PET/CT and decrease in PSA level in patients on enzalutamide could be a valid tool to predict PFS in metastatic CRPC patients
Miyazaki et al. (80)	2	[ <sup>18</sup> F]FCH PET/CT detected changes in bone metastatic activity midway during treatment with radium-223 dichloride. Whole-body tumor burden decreased in one patient, while a heterogeneous tumor response was observed in the other. Corresponding normalization and persistent elevation in serum alkaline phosphatase levels were observed in these cases, respectively
<b>Renal cell cancer</b>		
Middendorp et al. (86)	2	[ <sup>18</sup> F]FEC PET/CT before and 10 weeks after two cycles of tyrosine kinase inhibitor therapy showed progression in one patient and partial response in the other
<b>Brain</b>		
Parashar et al. (81)	14 (various tumor sites)	[ <sup>18</sup> F]FCH PET/CT is potentially a predictive biomarker for early detection (after 3–4 weeks) of RT/CRT response in patients with lesions in base of tongue, tonsil, nodes, hypopharynx, maxilla, palate, lung, pancreas, brain, uterus, and rectum with 88% patients had response (complete and partial response: CR and PR)
Panagiotidis et al. (82)	1	Simultaneous PET/MRI with [ <sup>18</sup> F]choline in a patient with pineal germ cell tumor demonstrated a reduction in both size and radiotracer activity of the mass after chemotherapy
<b>Breast</b>		
Kenny et al. (85)	2	[ <sup>11</sup> C]choline uptake was lower in two patients responding to trastuzumab treatment, suggesting that [ <sup>11</sup> C]choline PET may be useful in detecting the response of breast cancer to trastuzumab treatment

magnitude of reduction in  $SUV_{ave}$  and  $SUV_{max}$  in the prostate tumors corresponding to 94% reduction in PSA was shown by Challapalli and co-workers, in patients having neoadjuvant ADT (69).

There is paucity of data on use of [<sup>11</sup>C]choline PET to monitor response to RT. Based on 2-month post-RT [<sup>11</sup>C]choline PET/CT reductions, Casamassima and colleagues inferred that high-dose RT was effective in eradication of limited nodal recurrences (70). More recently, in a study of 11 patients with intermediate-risk PCa, Amani and co-workers evaluated sequential [<sup>11</sup>C]choline PET/CT scans before and up to 12 months after completion of RT (74 Gy/37 fractions). None of the patients received hormonal therapy. They concluded that RT significantly decreased intra-prostatic [<sup>11</sup>C]choline uptake (as measured by  $SUV_{max}$  and tumor-to-muscle ratio (TMR)) (71). Thus, the concern that RT

might increase labeled choline transport does not appear to occur in patients at clinically relevant doses. Furthermore, in a proof of concept study, Challapalli and co-workers showed that choline uptake in prostate tumors, determined by [<sup>11</sup>C] choline PET/CT, is sensitive to ADT and RT, and could be used as an objective quantitative tool for response assessment. ADT decreased tumor-imaging variables –  $SUV_{60,ave}$ ,  $SUV_{60,max}$ , TMR<sub>ave</sub>, and TMR<sub>max</sub> – by 26–60%. RT also decreased [<sup>11</sup>C]choline uptake within primary prostate tumors (though of lesser magnitude: 12–27%), compared to that seen with ADT, except for TMR<sub>max</sub> where a significant reduction (40%) was seen (Figure 2) (69). Similarly, Beheshti and colleagues demonstrated that reduced [<sup>18</sup>F]FCH uptake is seen in PCa patients who respond to the hormone therapy often without any significant morphological

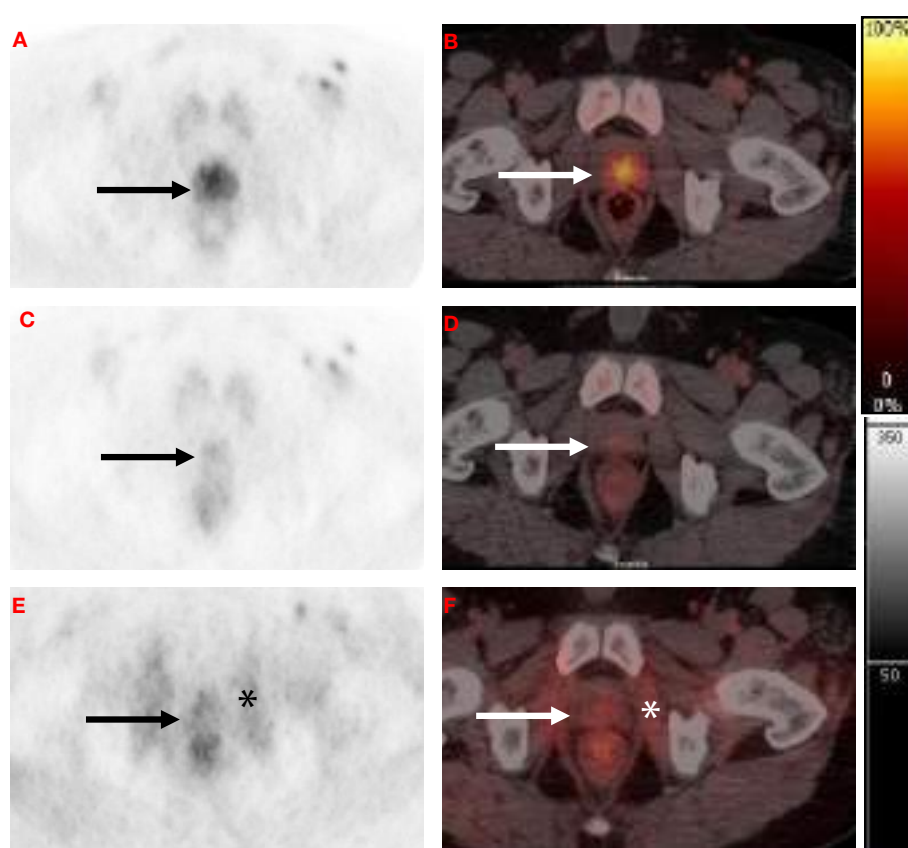


**FIGURE 2 | Axial [<sup>11</sup>C]choline PET and fused PET/CT at level of the prostate.** **(A,B)** Baseline scan with focal activity in the peripheral zone (black and white arrows). **(C,D)** Post-neoadjuvant androgen deprivation therapy (NAD) scan (8–10 weeks after initiating NAD) with a marked reduction in [<sup>11</sup>C]choline uptake in the peripheral zone. **(E,F)** Post- radiotherapy combined with concurrent androgen deprivation therapy (RT-CAD) scan (4 months after completion of RT-CAD) with a further reduction in prostate activity and increased obturator internus muscular activity (black and white asterisk).

CT changes (72, 73). These studies show the potential of radiolabeled choline to detect response of early PCa to therapies used routinely in the clinic.

Chemotherapy, Radium-223, and drugs interfering with androgen receptor (AR) machinery, such as enzalutamide and abiraterone, are the main stay of treatments in metastatic castrate resistant prostate cancer (mCRPC). Currently, there is excessive reliance on changes in serum PSA as an indicator of therapeutic efficacy and there are no predictive diagnostic tools to identify an early objective response in patients with mCRPC treated with abiraterone acetate or enzalutamide, although AR splice variants detectable in circulating tumor cells (CTCs) are evolving (74). The Prostate Cancer Clinical Trials Working Group recommends waiting 12 weeks before the first evaluation of response to ensure adequate drug exposure (75). Therefore, studies investigating new biomarkers for outcome prediction and disease monitoring are urgently needed. To this effect, labeled choline PET is under evaluation to assess therapeutic response.

Kwee and colleagues evaluated effects of docetaxel chemotherapy on circulating cell-free DNA (cfDNA) and [<sup>18</sup>F]FCH PET/CT uptake in CRPC. Tumor-derived plasma cfDNA concentrations increased significantly after one and three treatment cycles,

possibly due to post-chemotherapy necrotic cell lysis. Lower cfDNA concentrations at baseline were found to be associated with PET responses as measured after the third chemotherapy cycle. They concluded that it is feasible to annotate potential tumor sources of cfDNA using [<sup>18</sup>F]FCH PET/CT imaging, and that plasma cfDNA content and [<sup>18</sup>F]FCH PET/CT-detected tumor activity are potential response markers in CRPC (76). Caffo et al. showed that enzalutamide induces volume reductions in primary tumors and metabolic changes in metastatic lesions as detected by [<sup>18</sup>F]FCH PET/CT (77). In a proof of principle study, De Giorgi et al. evaluated [<sup>18</sup>F]FCH PET/CT as an early predictor of outcome in mCRPC patients treated with enzalutamide (78). They concluded that the combination of [<sup>18</sup>F]FCH PET/CT and decrease in PSA level could be a valid tool to predict progression-free survival (PFS) in mCRPC patients.

In a similar study with abiraterone, De Giorgi et al. demonstrated that early [<sup>18</sup>F]FCH PET/CT can predict clinical outcome (PFS and overall survival: OS) than PSA response in patients on abiraterone. Using fairly arbitrary thresholds for change in SUV (as specified in European Organization for Research and Treatment of Cancer (EORTC) guidelines), a PSA decline  $\geq 50\%$  was shown to be associated with the [<sup>18</sup>F]FCH PET/CT response

(12/42)/non-response (18/42) in 71% of patients (79). Miyazaki and co-workers evaluated acute changes in net metabolically active tumor volume (MATV) and total lesion activity (TLA) detected by [<sup>18</sup>F]FCH PET/CT imaging midway during treatment with radium-223 dichloride, in two patients. After the third dose of radium-223 dichloride, near-total disappearance of abnormal skeletal activity was observed in one case, while a heterogeneous tumor response was observed in the other (80). It can be summarized that, while being a proliferation-independent phenotype (13), changes in labeled choline uptake reflects response to therapy although the optimal time still needs to be clarified.

### Non-Prostate Tumors

In addition to PCa, radiolabeled choline has been utilized in other tumor histotypes. Parashar et al. explored whether [<sup>18</sup>F]FCH PET could serve as a predictive biomarker for early detection of RT/chemo-radiotherapy (CRT) response in patients with lesions at the base of the tongue, tonsil, nodes, hypopharynx, maxilla, palate, lung, pancreas, brain, uterus, and rectum. They demonstrated reductions in SUV<sub>max</sub> in 88% of lesions (CR: 7/16 and PR: 7/16) and concluded that changes in SUV<sub>max</sub> after 3–4 weeks of initiation of RT were predictive of final outcome (81). Panagiotidis and co-workers showed that simultaneous PET/MRI with [<sup>18</sup>F]FCH in a patient with pineal germ cell tumor demonstrated a reduction in both size and radiotracer activity of the mass after chemotherapy (82).

While the choline phenotype has been reported as being proliferation independent in PCa (13), the phenotype is intrinsically associated with proliferation in breast cancer cells (83). In particular, PCho formation is linked to the activity of mitogen-activated protein kinase (MAPK) signaling function (84). It was, thus, postulated that therapy response in breast cancer might be accompanied by predictable changes in the tumor retention of [<sup>11</sup>C]choline. In a clinical study involving breast cancer patients receiving trastuzumab, [<sup>11</sup>C]choline uptake decreased in two patients responding to trastuzumab compared to non-responders (85). Regarding targeted therapies, Middendorp et al. also evaluated use of [<sup>18</sup>F]fluoroethylcholine (FEC) PET/CT in staging and monitoring therapy response of advanced RCC before and 10 weeks after two cycles of tyrosine kinase inhibitor (TKI) therapy. FEC PET/CT showed heterogeneous changes, with progression in one patient and a PR in the second patient, which were concordant with the RECIST response (86). Thus, changes in uptake of labeled choline in non-prostate histotypes also appear to reflect therapy response.

## Fatty Acid Metabolism

### Fatty Acid Synthesis: Acetate PET

Cancer cells are dependent on their ability to gain access to energy and substrate precursors, by reprogramming the normal metabolic pathways required for the proliferation and survival of tumor cells, to synthesize proteins, nucleotides, and lipids (87). Cancer cells are also characterized by a lipogenic phenotype (88), and often require that fatty acids be generated *de novo* to maintain proliferation and viability. As a result, fatty acid biosynthesis has gained significance as a potential therapeutic target in multiple cancers.

Acetate is metabolized in the tricarboxylic acid (TCA) cycle yielding CO<sub>2</sub> and water (89). However, in cancer cells, acetate is preferentially utilized for fatty acid synthesis as a component of acetyl-CoA. Intracellularly, acetate is converted to acetyl-CoA by acetyl-CoA synthase (ACeS), and fed into the fatty acid synthesis pathway. [<sup>11</sup>C]Acetate PET was originally used to assess myocardial function (90). In myocardial tissues, carbons derived from [<sup>11</sup>C]acetate are incorporated into CO<sub>2</sub> during the TCA cycle, allowing for PET visualization of oxygen consumption. However, in tumor cells, [<sup>11</sup>C]acetate is incorporated into membrane lipids due to over-expression of fatty acid synthase (FASN). This property is exploited for tumor imaging with [<sup>11</sup>C]acetate (91). The majority of studies analyzing the efficacy of [<sup>11</sup>C]acetate PET in tumors have focused on the detection of PCa (91). In addition to PCa, there are a number of other tumor types in which [<sup>11</sup>C]acetate PET shows high contrast, including hepatocellular carcinoma (HCC), thymomas, renal cancers, brain tumors, and bronchioloalveolar carcinoma (92). These studies demonstrate that [<sup>11</sup>C]acetate is useful in diagnosis, staging, and predicting disease progression in certain cancers, and it is logical that [<sup>11</sup>C]acetate could also be used to stratify patients for specific therapies, as well as a method to monitor response to therapy.

### Preclinical Studies

Emonds et al. evaluated the effect of 5 days of ADT on the uptake of [<sup>11</sup>C]acetate, together with [<sup>18</sup>F]FDG and [<sup>11</sup>C]choline *in vivo*. They found that ADT significantly decreased the uptake of [<sup>11</sup>C]choline and tended to decrease [<sup>18</sup>F]FDG uptake. [<sup>11</sup>C]Acetate uptake was unaffected by ADT in both PCa xenograft models [LAPC-4 (androgen sensitive), 22Rv1 cells (androgen-independent)]. The authors concluded that [<sup>11</sup>C]acetate uptake occurs independently of androgens and, thus, may be more favorable for detecting tumor viability during or following ADT (93). These findings were corroborated by Oyama et al. who also showed that [<sup>18</sup>F]FDG PET, detected metabolic changes within days of androgen ablation, while there was no significant difference in [<sup>11</sup>C]acetate uptake in a murine model of PCa (94).

[<sup>11</sup>C]Acetate PET could potentially be used as a surrogate for monitoring FASN activity as the incorporation of [<sup>11</sup>C]acetate into membrane lipids is regulated by FASN expression. There is potential that this approach may be an effective means to validate FASN inhibitors as they progress through clinical development. Yoshii et al. (95) evaluated a method to predict FASN-targeted therapy outcome using radiolabeled acetate uptake in LNCaP, PC3, 22Rv1, and DU145 cells. They demonstrated that uptake of radiolabeled acetate reflects FASN expression and sensitivity to FASN-targeted therapy with orlistat. Furthermore, Vavere et al. demonstrated that the FASN inhibitor C75 could reduce [<sup>11</sup>C]acetate uptake by up to 60% in PCa xenografts (96). While these studies are promising (Table 1), it has been noted recently that optimal acquisition of [<sup>11</sup>C]acetate images may require late imaging (~90 min) to increase sensitivity toward lipid incorporation (97).

### Clinical Studies

Yu and co-workers, tested the feasibility of [<sup>11</sup>C]acetate PET imaging to assess response to therapy in men with bone metastatic PCa. Patients were imaged before and 6–12 weeks after initial

ADT for new metastatic PCa or after first-line chemotherapy with docetaxel for CRPC. Changes in qualitative assessment and tumor:normal uptake ratio correlated with clinical response criteria. They concluded that [<sup>11</sup>C]acetate PET scanning was highly accurate for determining response to treatment in patients with bone metastases (98). Regarding therapy planning, Gomez and co-workers reported that [<sup>11</sup>C]acetate PET aids in detection of lymph node metastases especially in high risk PCa patients and led to changes of radiation therapy treatment field/volume or dose in about one-third of the patients (37%). Changes in [<sup>11</sup>C] acetate may serve as a tool for monitoring radiation therapy response (99).

There are anecdotal reports of [<sup>11</sup>C]acetate PET monitoring response in RCC and meningiomas. Maleddu et al. suggested that [<sup>11</sup>C]acetate PET could predict response to sunitinib as early as 2 weeks after therapy initiation (100). In the evaluation of meningiomas, Liu RS et al. demonstrated that [<sup>11</sup>C]acetate had good sensitivity for detection of meningiomas compared to [<sup>18</sup>F]FDG, and concluded that [<sup>11</sup>C]acetate performed better in monitoring five patients who had received gamma-knife surgery (101). [<sup>11</sup>C] acetate PET has also been used in assessing response to therapy in multiple myeloma. Bone marrow histology and whole-body (WB) MRI were used as comparators. In 13 patients who had repeat examination after induction therapy, visual and quantitative analysis, suggested a higher detection rate for both diffuse and focal myeloma lesions at diagnosis. After treatment, a 66% reduction in SUV<sub>max</sub> was seen in patients with at least a very good PR ( $\geq 90\%$  reduction in M-protein) versus a 34% reduction in those with a PR ( $\geq 50\%$  reduction in M-protein). They concluded that [<sup>11</sup>C]acetate may be valuable for response assessment (102). In aggregate, the initial data with [<sup>11</sup>C]acetate for monitoring response is promising (Table 3) but the short half-life of the tracer may reduce sensitivity for imaging lipid incorporation, and its use is limited to centers with in-house cyclotron. Moreover, acetate is not specific to fatty acid synthesis, it also serves as a substrate for protein acetylation, and is utilized in cholesterol synthesis.

#### **[<sup>18</sup>F]Fluoroacetate**

[<sup>18</sup>F]Fluoroacetate ([<sup>18</sup>F]FACE), a [<sup>18</sup>F]fluorinated acetate analog (t<sub>1/2</sub>: 110 min), which is putatively converted to fatty acids and incorporated into lipids, has been tested as an alternative PET tracer for imaging fatty acid synthesis. However, there are only limited clinical reports using [<sup>18</sup>F]FACE for oncologic diagnosis of patients with cancer (103, 104), thus far with no studies evaluating therapy response.

#### **Fatty Acid Oxidation: [<sup>18</sup>F]Fluoropivalic Acid PET**

In addition to fatty acid synthesis, the critical nature of fatty acid oxidation for cancer cells survival has been recognized (105). Short-chain carboxylates, including acetate, propionate, butyrate, and the non-natural substrate pivalate (trimethylacetate) use the early steps of the fatty acid oxidation pathway involving acyl-CoA and acyl-carnitine synthesis (106). A new radioprobe, 3-<sup>18</sup>F-fluoro-2,2-dimethylpropionic acid, also called [<sup>18</sup>F]fluoropivalic acid ([<sup>18</sup>F]FPIA), for imaging the early steps of the fatty acid oxidation pathway has been validated and has shown promise for cancer detection (107). Further studies are eagerly awaited.

## **Amino Acid Metabolism**

Amino acids play an important role in the synthesis of a variety of nitrogen-containing compounds, such as proteins and nucleotides during cell growth, and their increased transport and utilization are associated with early events in carcinogenesis (108). Natural amino acids are transported into cells by specific carrier-mediated transport systems and further incorporated into proteins and intermediary metabolites to different extents. Thus, investigators have studied the utility of several radiolabeled natural amino acids (including methionine, glycine, tyrosine, phenylalanine, and leucine) as tumor-imaging agents with PET (109). Amino acid scanning provides higher contrast between tumor and normal brain compared to [<sup>18</sup>F]FDG PET, due to the low uptake of amino acids in normal brain. However, of the several amino acid tracers investigated for tumor imaging, only a few have been evaluated beyond the initial feasibility studies in human patients.

#### **Glutamine**

Glutamine is the most abundant amino acid in plasma and occupies a unique niche in intermediary metabolism by providing a major inter-organ shuttle for both nitrogen and carbon (110). This makes it essential for cell proliferation by contributing to synthesis of nucleic acids, proteins, and hexosamines. Loss of amino and amido groups in glutamine produces alpha-ketoglutarate that also promotes cell growth, anaplerosis and adenosine-tri-phosphate (ATP) generation (111). Malignant transformation, involving enhanced c-Myc expression, increases glutamine metabolism by increased expression of cell surface transporters (112, 113).

**TABLE 3 | Acetate PET response assessment: clinical studies.**

	Sample size	Outcome
<b>Renal cell cancer</b>		
Maleddu et al. (100)	1	[ <sup>11</sup> C]acetate PET could predict response to sunitinib as early as 2 weeks after therapy initiation
<b>Brain</b>		
Liu et al. (101)	22	[ <sup>11</sup> C]acetate had a good sensitivity in detection, of meningioma compared to [ <sup>18</sup> F]FDG. [ <sup>11</sup> C] acetate performed better in monitoring five patients who had received gamma-knife surgery
<b>Prostate</b>		
Yu et al. (98)	6	[ <sup>11</sup> C]acetate PET scanning was highly accurate for determining the response to treatment in prostate cancer patients with bone metastases
Gomez et al. (99)	19	Changes in [ <sup>11</sup> C]acetate may serve as a tool for monitoring radiation therapy response in high risk prostate cancer
<b>Myeloma</b>		
Lin et al. (102)	15	Visual and quantitative analysis showed a higher detection rate of myeloma lesions at diagnosis than using [ <sup>18</sup> F]FDG. After treatment, a 66% reduction in SUV <sub>max</sub> was seen in patients with at least a very good partial response versus a 34% reduction in those with a PR. They concluded that [ <sup>11</sup> C]acetate may be valuable for response assessment

Glutamine metabolism lends itself to evaluation by PET imaging, most relevant in non-[<sup>18</sup>F]FDG avid tumors, such as prostate, bronchoalveolar carcinomas, carcinoid tumors, and low-grade lymphomas. These malignancies may use glutamine as an alternative nutrient source and as such are more easily detected by a glutamine-based tracer. Venneti and co-workers, for example demonstrated that PET imaging *in vivo* with the glutamine analog 4-[<sup>18</sup>F]-*(2S,4R)*-fluoroglutamine ([<sup>18</sup>F]FGln) facilitates clear tumor delineation due to high tumor-to-background ratio. Chemo/radiation therapy reduced [<sup>18</sup>F]FGln tumor uptake, which was associated with decreased tumor burden, confirmed on autoradiography. In contrast, there were no anatomical or structural changes seen on T2-weighted MRI sequences, within the same time frame. These findings were translated into humans (six patients) and an increased [<sup>18</sup>F]FGln uptake was seen in patients with progressive brain tumors, but not in patients with SD (114).

## Methionine

Methionine, an essential sulfur amino acid, is necessary for growth and development. It plays an important role in protein

synthesis and is a predominant methyl group donor for multiple metabolic pathways. Malignant transformation enhances demand for methionine in cancer cells caused by increased fluxes in the pathways of protein synthesis, transmethylation, and transsulfuration. This forms the basis for higher uptake of labeled methionine in tumors.

Currently, PET using L-[methyl-<sup>11</sup>C]-methionine (<sup>11</sup>C-methionine) is the most popular amino acid imaging modality for tumors, although its use is restricted to PET centers with an on-site cyclotron facility. <sup>11</sup>C-methionine PET has been extensively studied in gliomas. Its role in initial diagnosis, differentiation of tumor recurrence from radiation injury, grading, prognostication, tumor extent delineation, biopsy planning, surgical resection and RT planning has been evaluated (115). A number of oncologic imaging studies have evaluated the role of <sup>11</sup>C-methionine in response assessment and have been described in detail in the preclinical setting (116–127) (Table 1) and in patients (128–170) (Table 4). While most studies have focused on non-hematological solid tumors, multiple myeloma also represents an evolving area of interest. In this case, preclinical

**TABLE 4 | Methionine PET response assessment: clinical studies.**

	Sample size	Outcome
<b>Brain</b>		
Bergstrom et al. (128)	400	In a large series of pituitary adenomas and in some meningiomas, a decrease in the uptake of [ <sup>11</sup> C]methionine after medical therapy has been shown to represent a positive treatment effect. [ <sup>11</sup> C]methionine PET method does have potential for the evaluation of treatment effects
Kubota et al. (117)	70	[ <sup>11</sup> C]Methionine seemed to have a higher potential for rapid tumor monitoring than FDG after radiotherapy, and the effect was radiation-dose dependent
Sato et al. (159)	1	Serial [ <sup>11</sup> C]methionine PET imaging in low-grade astrocytoma permits evaluation of changes after radio-chemotherapy treatment in patients in whom CT has revealed no notable changes
Wurker et al. (169)	5	A dose-dependent decline in [ <sup>11</sup> C]methionine uptake with a greater decrease in tumors with high basal uptake of [ <sup>11</sup> C]methionine
Voges et al. (167)	10	One year after seed implantation of <sup>125</sup> I for brachytherapy in treatment of cerebral glioma, there were no changes in glucose metabolism, but a significant decline of [ <sup>11</sup> C]methionine uptake was seen [ <sup>11</sup> C]methionine PET may improve tumor delineation, and allows monitoring of therapeutic effects following brachytherapy
Roelcke et al. (158)	30	No significant difference in [ <sup>11</sup> C]methionine and [ <sup>18</sup> F]FDG tracer uptake between tumors with or without adjuvant radiotherapy after surgery for low-grade astrocytomas
Shintani et al. (161)	1	Serial [ <sup>11</sup> C]methionine PET in a biopsy-proven case of gliomatosis cerebri (GC) suggested initial hypermetabolism, associated with increase in cerebral blood flow (shown on [ <sup>15</sup> O]water PET) that normalized 6 months after completion of radiotherapy
Nuutinen et al. (155)	13	[ <sup>11</sup> C]methionine PET improves tumor visualization in patients with low-grade glioma and signifies better prognosis in patients with low tumor uptake at baseline. Stable or decreasing uptake of [ <sup>11</sup> C]methionine in tumor area after radiotherapy signifies a favorable outcome
Gudjonsson et al. (135)	19	Stereotactic proton beam irradiation of meningiomas had an inhibitory effect (average 19.4% reduction in uptake after 36-month of follow-up) on the [ <sup>11</sup> C]methionine uptake in meningiomas, although tumor size remained unchanged (CT/MRI)
Sorensen et al. (162)	2	A prompt reduction in [ <sup>11</sup> C]methionine uptake was seen within d of starting therapy in two children with prolactinomas
Muhr et al. (152)	12	During IFN-alpha treatment, [ <sup>11</sup> C]methionine PET demonstrated a mean relative percentage of reduction in the uptake ratio (MRelR) of 22.3% in meningiomas
Herholz et al. (137)	1	Estimated a reduction rate in [ <sup>11</sup> C]methionine defined active tumor volume of approximately 2.4% per day in a case of anaplastic oligoastrocytoma after procarbazine, CCNU, and vincristine (PCV) chemotherapy
Tang et al. (164)	7	A significant reduction in [ <sup>11</sup> C]methionine uptake and a semiquantitative index based on both [ <sup>11</sup> C]methionine uptake and [ <sup>11</sup> C]methionine defined volume was noted in low-grade oligodendrogloma patients after chemotherapy with PCV regime. Prediction of long-term outcome and effect on high-grade gliomas could not be assessed
Ribom et al. (157)	32	[ <sup>11</sup> C]methionine PET may be a promising surrogate endpoint after treatment of grade II gliomas. An increase in [ <sup>11</sup> C]methionine uptake or [ <sup>11</sup> C]methionine defined volume on follow-up scans was associated with a reduced time to progression of disease in patients with histologically confirmed supratentorial WHO grade II gliomas

(Continued)

**TABLE 4 | Continued**

<b>Sample size</b>	<b>Outcome</b>
Nariai et al. (153)	194 Patients with high-grade glioma showed a significantly decreased post-irradiation tumor-to-normal tissue ratio of [ <sup>11</sup> C]methionine uptake compared with the pre-treatment value
Galldiks et al. (131)	15 [ <sup>11</sup> C]methionine PET performed before and after the third cycle of temozolomide (TMZ) chemotherapy in patients with malignant gliomas, showed a significantly longer median time to progression in patients with decline in [ <sup>11</sup> C]methionine uptake than in those with increasing [ <sup>11</sup> C]methionine uptake (23 versus 3.5 months)
Kawai et al. (143)	3 [ <sup>11</sup> C]methionine PET findings suggested presence of increased tumor activity in patients with germinomas in the basal ganglia or thalamus after the initial treatment, which gradually decreased during the course of intensive therapy in these patients
Galldiks et al. (132)	1 [ <sup>11</sup> C]methionine PET metabolic activity showed a continuous decline of tumor volume, over a 2-year period, below the threshold of significant [ <sup>11</sup> C]methionine uptake in patient with glioblastoma multiforme (GBM), treated with surgery, radiosurgery, and maintenance of imatinib and hydroxyurea
Lee et al. (146)	3 A gradual decrease of [ <sup>11</sup> C]methionine uptake in basal ganglia germinoma during the course of treatment was seen but the temporal pattern of [ <sup>11</sup> C]methionine uptake during the treatment was not evaluated
Jang et al. (140)	4 After high-dose methotrexate chemotherapy for primary CNS Lymphoma (PCNSL), [ <sup>11</sup> C]methionine PET displayed complete disappearance of abnormal uptake in all four patients, corroborated on post-treatment MRI and clinical follow-up in three patients
Galldiks et al. (133)	1 A continuous decline in metabolically active tumor volume after stereotaxy-guided laser-induced interstitial thermotherapy (LITT) was observed in a patient with a recurrent GBM, suggesting that [ <sup>11</sup> C]methionine PET could be useful for monitoring the short-term therapeutic effects of LITT
Miwa et al. (151)	42 Metastatic lesions demonstrated significant decreases in [ <sup>11</sup> C]methionine uptake (quantitative analysis) following stereotactic radiation therapy with intensity modulated radiation therapy (SRT-IMRT: 25–35 Gy in five fractions) in metastatic brain tumors
Chiba et al. (130)	14 A voxel-wise parametric response map (PRM) analysis of [ <sup>11</sup> C]methionine PET could be useful for monitoring treatment response in immunotherapy for malignant gliomas
<b>Head and neck</b>	
Lindholm et al. (150)	15 In patients with squamous cell carcinomas of the head and neck region treated with preoperative radiotherapy (dose of 61–73 Gy), [ <sup>11</sup> C]methionine PET demonstrated a significantly lower [ <sup>11</sup> C]methionine uptake in tumors showing a histopathological response when examined before and 5–42 days after radiotherapy
Nuutinen (154)	15 A significant decrease in [ <sup>11</sup> C]methionine uptake was seen during the first 2–3 weeks after radiotherapy of head and neck cancer, but the rate of decrease in tracer uptake could not distinguish between relapsing disease and locally controlled disease
Chesnay et al. (129)	13 Reduction in [ <sup>11</sup> C]methionine PET accumulation after the completion of one course of chemotherapy for hypopharynx squamous cancer correlated significantly with a reduction in the tumor mass, as measured by MRI at the completion of three courses of chemotherapy
Hasebe et al. (136)	39 [ <sup>11</sup> C]methionine PET allowed for a prediction of the therapeutic efficacy of carbon-ion radiotherapy (CIRT) in head and neck adenocarcinomas. Tumor-to-normal tissue ratio pre-treatment (TNR <sub>pre</sub> ) was significantly associated with metastasis and disease-specific survival, while the TNR post-treatment (TNR <sub>post</sub> ) was associated with the local recurrence, metastasis, and disease-specific survival
Toubaru et al. (165)	67 [ <sup>11</sup> C]methionine PET or PET/CT prior to and 1 month after the completion of CIRT for adenoid cystic carcinoma of the head and neck, showed a significant decrease in TNR after treatment
<b>Breast</b>	
Huovinen et al. (138)	8 A reduction in [ <sup>11</sup> C]methionine uptake predicted clinical target stability or regression of metastasis, while an increase uptake predicted progressive disease when evaluated at 7 weeks after radiotherapy, hormonal therapy, or chemotherapy for metastatic breast cancer
Jansson et al. (141)	16 [ <sup>11</sup> C]methionine PET predicted response in 67% (8/12) of clinical responders as early as 6–13 days after the first course of chemotherapy.
Lindholm et al. (149)	13 [ <sup>11</sup> C]methionine PET showed significant reduction in uptake (30–54%) in all six responding metastatic sites, whereas the decrease in uptake was lower in magnitude or showed an increase in stable or non-responding lesions, in metastatic breast cancer patients treated with polychemotherapy or hormones
<b>Bladder</b>	
Letocha et al. (148)	4 [ <sup>11</sup> C]methionine PET identified patients who progressed after chemotherapy for localized or metastatic bladder cancer
Katz et al. (142)	1 In a patient with metastatic transitional cell carcinoma (TCC) unfit for platinum-based chemotherapy, being treated with Sunitinib, [ <sup>11</sup> C]methionine PET showed a significantly decreased metabolic uptake in bone and lymph nodes 28 days after sunitinib initiation without any objective morphological changes, corroborated by objective tumor reduction on CT at 2 months after therapy initiation

(Continued)

**TABLE 4 | Continued**

Sample size	Outcome
<b>Choroidal melanoma</b>	
Tamura K (163)	1 [ <sup>11</sup> C]methionine PET uptake when evaluated visually and semiquantitatively showed a significant decrease in tumor-to-brain ratio at ≥6 months after therapy and disappeared in 50% of the patients at 12 months after carbon-ion therapy
<b>Soft tissue sarcoma</b>	
Zhang et al. (170)	[ <sup>11</sup> C]methionine PET was of prognostic value in patients with bone and soft tissue sarcoma treated by CIRT
Ghigi et al. (134)	9 The percentage variation in histological response (tumor grade regression) and SUVmax of [ <sup>18</sup> F]FDG before and after neoadjuvant chemo-radiotherapy seems to discriminate between partial and complete response better than [ <sup>11</sup> C]methionine
<b>Rectal cancer</b>	
Wieder et al. (168)	26 [ <sup>11</sup> C]methionine PET aided tumor visualization, but the degree of reduction in [ <sup>11</sup> C]methionine uptake post chemo-radiation did not correlate with the tumor response measured by pathologic evaluation. [ <sup>11</sup> C]methionine PET may not be a good method for evaluating the response of radiotherapy in rectal cancer
Koizumi et al. (144)	53 [ <sup>11</sup> C]methionine PET uptake decreased with CIRT but there were no significant correlations between imaging variables (SUV, tumor-to-normal tissue ratio) and other clinical parameters (distant metastasis and survival) in patients with rectal cancer
<b>Lung cancer</b>	
Kubota et al. (145)	21 A significant decrease in [ <sup>11</sup> C]methionine uptake in responding human lung tumors 2 weeks after radiotherapy or chemotherapy, and the decrease preceded the shrinkage in tumor volume measured with CT
Ishimori et al. (139)	9 [ <sup>11</sup> C]methionine PET did not provide additional information over FDG PET in lung cancer treated with stereotactic radiotherapy (SRT). Decline in [ <sup>11</sup> C]methionine PET activity reflects acute reaction to SRT and the increase in activity in later time points denotes radiation-induced pneumonitis
<b>Lymphoma</b>	
Leskinen-Kallio et al. (147)	1 Demonstrated a decrease in [ <sup>11</sup> C]methionine uptake with chemotherapy and radiotherapy in a patient with non-Hodgkin's lymphoma (NHL)
Sawataishi et al. (160)	2 [ <sup>11</sup> C]methionine PET improved lesion delineation compared to CT/MRI in PCNSL and predicted presence of residual tumors after radiotherapy in lesions involuting on CT
Ogawa et al. (156)	10 [ <sup>11</sup> C]methionine PET is useful for the delineation of CNS lymphoma and for monitoring the therapeutic effect of irradiation. The extent of [ <sup>11</sup> C]methionine accumulation in tumor tissue markedly decreased after radiation therapy
Tsuyuguchi et al. (166)	1 [ <sup>11</sup> C]methionine PET is helpful in assessing the effect of chemotherapy earlier than is feasible with other methods in malignant scalp lymphoma

studies demonstrate superiority of [<sup>11</sup>C]methionine to [<sup>18</sup>F]FDG in monitoring novel anti-myeloma therapy involving proteasome inhibition (119).

### Leucine Analogs

Leucine is one of the preferential amino acid required for proliferating tumor cells and is, therefore, of interest in molecular imaging of anabolic cancer processes. 1-Amino-3-[<sup>18</sup>F]fluorocyclobutane-1-carboxylic acid (anti-[<sup>18</sup>F]FACBC), a synthetic non-natural leucine analog, has been widely studied in imaging brain (171, 172), prostate tumors (173, 174), and pulmonary lesions (175). The non-natural amino acids are not metabolized but are taken up through both the L-type transporter and the energy-dependent A-type transporter (176). The tracer accumulation in PCa cells correlates with the expression level of the alanine, serine, and cysteine preferring system-mediated amino acid transport with the large neutral amino acid transporter (LAT1) as an important transport system (177, 178). There are only two preclinical studies that evaluated the role of anti-[<sup>18</sup>F]FACBC in predicting response [Table 1; (121, 124)] and in these cases anti-[<sup>18</sup>F]FACBC PET provided useful information on early response. Future studies are eagerly awaited.

### Tryptophan Analogs

Tryptophan is an essential amino acid required for biosynthesis of proteins, serotonin, and niacin in the brain and other tissues (179). The amino acid PET tracer alpha-[<sup>11</sup>C]methyl-L-tryptophan (AMT) is transported in tumor tissue by LAT1 but is not incorporated into proteins (180). Instead, AMT is utilized by the kynurenine immunomodulatory pathway (181). Under pathological conditions, induction of this pathway's rate-limiting enzyme, indoleamine 2,3-dioxygenase (IDO), leads to increased metabolism of tryptophan and, thus, AMT accumulation (182). Tryptophan analogs have been widely studied in imaging high-grade gliomas (182, 183), CRPC (184), and neuroendocrine tumors (185). In a case report, Peng and co-workers suggested that AMT PET may be useful for assessing progression and therapeutic response of optic glioma (186). Further studies are eagerly awaited.

## DISCUSSION

Several metabolic pathways are deranged in cancer in a proliferation-dependent or proliferation-independent manner. These metabolic pathways, particularly enhanced glycolysis,

offer the opportunity to detect cancer often with high contrast. In this review article, we discuss about the role of established and evolving metabolism tracers for prediction/monitoring response to therapy. The effect of drug or radiation therapy on each metabolic phenotype ought to be carefully considered to enable assignment of biological and clinical relevance to the changes seen. Notably, these therapies may directly or indirectly inhibit tumor cell metabolism, or indeed the changes may simply reflect loss of cell viability and influence the timing of post-treatment scanning. For [<sup>18</sup>F]FDG PET, the effect of the so-called targeted or biologic therapies on response monitoring has been reviewed (26) with the suggestion that the drugs may directly affect GLUT/hepatocyte kinase expression or activity with changes occurring within hours to days after initiating treatment. This type of information is less mature when other metabolism tracers are considered. For example, as discussed above, only a few studies have attempted to directly link the biology of androgen deprivation to changes in the tumor labeled choline signal. Regarding imaging variables, different variables have been used in the assessment of non-FDG tracers (see **Tables 1–4**). Some of these variables, e.g., TMR, may be considered, for instance, when RT is the choice of therapy to account for the effect of radiation on normal tissues.

Whatever the mechanism of signal change, be it direct or via loss of cell viability, it is important to consider the intrinsic variability of the quantitative measure, as well as that magnitude of change (threshold) for response. For [<sup>18</sup>F]FDG uptake, the intrinsic measurement variability (without treatment) ranges from 10 to 20% in different tumor phenotypes (187, 188). Based on pooling together reproducibility data, a consensus for quantifying PET response by EORTC PET study group was reached (189). The tumor responses were graded as follows:

- 1) Complete metabolic response (CMR): complete resolution of FDG uptake.
- 2) Partial metabolic response (PMR): a decrease (across all lesions) of minimum of 15% in tumor SUV after one cycle or >25% after more than one cycle of chemotherapy.
- 3) Stable metabolic disease (SMD): an increase of <25% or a decrease of <15% in SUV, and no visible increase in extent of FDG tumor uptake (20% in longest dimension).
- 4) Progressive metabolic disease (PMD): an increase in FDG tumor SUV of >25% within tumor region defined on baseline scan; visible increase in extent of FDG tumor uptake (20% in longest dimension) or appearance of new FDG uptake in metastatic lesions.

More recently, PET Response Criteria in Solid Tumors (PERCIST) guidelines have been formulated (190). These are based on the premise that cancer response as assessed by PET is a continuous and time-dependent variable. The tumor responses were graded as follows:

- 1) CMR: visual disappearance of all metabolically active tumors.
- 2) PMR: more than a 30% decline and a 0.8-unit decline in SUL<sub>peak</sub> between the most intense lesion before treatment and the most

intense lesion after treatment, although not necessarily the same lesion.

- 3) SMD: not CMR, PMR, or PMD.
- 4) PMD: more than a 30% and 0.8-unit increase in SUL<sub>peak</sub> or new lesions, if confirmed. A >75% increase in total lesion glycolysis is also proposed as another metric of progression.

The PERCIST criteria differ from the EORTC criteria in that the SUV is normalized to the lean body mass and five tumors (up to two per organ) with the most intense [<sup>18</sup>F]FDG uptake lesions being considered target lesions; SUL<sub>mean</sub> is the recommended imaging variable, as it has better test-retest variability (8–10%), is statistically less susceptible to variance, and is less subjective due to clear definition of target lesions.

Notably, these criteria are specific for [<sup>18</sup>F]FDG PET and may differ for other tracers. For example, Kenny and co-workers have evaluated the reproducibility of [<sup>11</sup>C]choline in breast cancer (85). A decrease of 40% for SUV<sub>30min</sub>, and 24% for SUV<sub>60min</sub>, was classified statistically as response. However, it is not clear if these criteria could be widely applied across different tumor sites or across different PET tracers, as the intrinsic variability may be isotope, patient, or scanner related.

In the future, further evaluation is required to assess the role of metabolic-PET imaging in assessing response to treatment and follow-up after treatment. These include what the optimal time (early or delayed) for performing the scan after treatment is, what the relevant imaging variables for predicting response are, how often to scan, whether imaging sensitivity and specificity are sufficient to predict response or progression, and whether changes in imaging variables can be used as surrogates for predicting patient outcomes. Future studies will need to be designed to establish the answers to these questions.

## CONCLUSION

In this article, we aimed to give an overview of metabolic processes imaged by PET and focused on both established and evolving radioprobes to detect tumor glycolysis, choline metabolism, intracellular transport of glutamine, and other amino acids, as well as fatty acid metabolism. In particular, we emphasize the role of radiolabeled choline, acetate, and amino acid tracers for monitoring efficacy or predicting response to new therapies that directly or indirectly inhibit tumor cell metabolism. The optimal imaging time point, pertinent imaging variable, and criteria for response will require further interrogation.

## AUTHOR CONTRIBUTIONS

AC and EA have contributed to the conception, layout of the review, and reviewed and proof read.

## FUNDING

EA's laboratory receives core funding from Cancer Research UK and the UK Medical Research Council.

## REFERENCES

1. Hanahan D, Weinberg RA. The hallmarks of cancer. *Cell* (2000) **100**(1):57–70. doi:10.1016/S0092-8674(00)81683-9
2. Hanahan D, Weinberg RA. Hallmarks of cancer: the next generation. *Cell* (2011) **144**(5):646–74. doi:10.1016/j.cell.2011.02.013
3. DeBerardinis RJ, Cheng T. Q's next: the diverse functions of glutamine in metabolism, cell biology and cancer. *Oncogene* (2010) **29**(3):313–24. doi:10.1038/onc.2009.358
4. Ying H, Kimmelman AC, Lyssiotis CA, Hua S, Chu GC, Fletcher-Sananikone E, et al. Oncogenic Kras maintains pancreatic tumors through regulation of anabolic glucose metabolism. *Cell* (2012) **149**(3):656–70. doi:10.1016/j.cell.2012.01.058
5. Son J, Lyssiotis CA, Ying H, Wang X, Hua S, Ligorio M, et al. Glutamine supports pancreatic cancer growth through a KRAS-regulated metabolic pathway. *Nature* (2013) **496**(7443):101–5. doi:10.1038/nature12040
6. Wise DR, DeBerardinis RJ, Mancuso A, Sayed N, Zhang XY, Pfeiffer HK, et al. Myc regulates a transcriptional program that stimulates mitochondrial glutaminolysis and leads to glutamine addiction. *Proc Natl Acad Sci U S A* (2008) **105**(48):18782–7. doi:10.1073/pnas.0810199105
7. Floor SL, Dumont JE, Maenhaut C, Raspe E. Hallmarks of cancer: of all cancer cells, all the time? *Trends Mol Med* (2012) **18**(9):509–15. doi:10.1016/j.molmed.2012.06.005
8. Buyse M, Thirion P, Carlson RW, Burzykowski T, Molenberghs G, Piedbois P. Relation between tumour response to first-line chemotherapy and survival in advanced colorectal cancer: a meta-analysis. Meta-Analysis Group in Cancer. *Lancet* (2000) **356**(9227):373–8. doi:10.1016/S0140-6736(00)02528-9
9. Therasse P, Arbuck SG, Eisenhauer EA, Wanders J, Kaplan RS, Rubinstein L, et al. New guidelines to evaluate the response to treatment in solid tumors. European Organization for Research and Treatment of Cancer, National Cancer Institute of the United States, National Cancer Institute of Canada. *J Natl Cancer Inst* (2000) **92**(3):205–16. doi:10.1093/jnci/92.3.205
10. Eisenhauer EA, Therasse P, Bogaerts J, Schwartz LH, Sargent D, Ford R, et al. New response evaluation criteria in solid tumours: revised RECIST guideline (version 1.1). *Eur J Cancer* (2009) **45**(2):228–47. doi:10.1016/j.ejca.2008.10.026
11. Revel MP, Bissery A, Bienvenu M, Aycard L, Lefort C, Frija G. Are two-dimensional CT measurements of small noncalcified pulmonary nodules reliable? *Radiology* (2004) **231**(2):453–8. doi:10.1148/radiol.2312030167
12. Dose Schwarz J, Bader M, Jenicke L, Hemminger G, Janicke F, Avril N. Early prediction of response to chemotherapy in metastatic breast cancer using sequential 18F-FDG PET. *J Nucl Med* (2005) **46**(7):1144–50.
13. Contractor K, Challapalli A, Barwick T, Winkler M, Hellawell G, Hazell S, et al. Use of [11C]choline PET-CT as a noninvasive method for detecting pelvic lymph node status from prostate cancer and relationship with choline kinase expression. *Clin Cancer Res* (2011) **17**(24):7673–83. doi:10.1158/1078-0432.CCR-11-2048
14. Juweid ME, Cheson BD. Positron-emission tomography and assessment of cancer therapy. *N Engl J Med* (2006) **354**(5):496–507. doi:10.1056/NEJMra050276
15. Lunt SY, Vander Heiden MG. Aerobic glycolysis: meeting the metabolic requirements of cell proliferation. *Annu Rev Cell Dev Biol* (2011) **27**:441–64. doi:10.1146/annurev-cellbio-092910-154237
16. Vander Heiden MG, Cantley LC, Thompson CB. Understanding the Warburg effect: the metabolic requirements of cell proliferation. *Science* (2009) **324**(5930):1029–33. doi:10.1126/science.1160809
17. Gambhir SS, Czernin J, Schwimmer J, Silverman DH, Coleman RE, Phelps ME. A tabulated summary of the FDG PET literature. *J Nucl Med* (2001) **42**(5 Suppl):1S–93S.
18. Jensen MM, Kjaer A. Monitoring of anti-cancer treatment with (18)F-FDG and (18)F-FLT PET: a comprehensive review of pre-clinical studies. *Am J Nucl Med Mol Imaging* (2015) **5**(5):431–56.
19. Maffiione AM, Marzola MC, Capirci C, Colletti PM, Rubello D. Value of (18)F-FDG PET for predicting response to neoadjuvant therapy in rectal cancer: systematic review and meta-analysis. *AJR Am J Roentgenol* (2015) **204**(6):1261–8. doi:10.2214/AJR.14.13210
20. Pasha MA, Marcus C, Fakhry C, Kang H, Kiess AP, Subramaniam RM. FDG PET/CT for management and assessing outcomes of squamous cell cancer of the oral cavity. *AJR Am J Roentgenol* (2015) **205**(2):W150–61. doi:10.2214/AJR.14.13830
21. Kwee RM, Marcus C, Sheikbahaei S, Subramaniam RM. PET with fluorodeoxyglucose F 18/computed tomography in the clinical management and patient outcomes of esophageal cancer. *PET Clin* (2015) **10**(2):197–205. doi:10.1016/j.cpet.2014.12.003
22. Sheikbahaei S, Marcus C, Hafezi-Nejad N, Taghipour M, Subramaniam RM. Value of FDG PET/CT in patient management and outcome of skeletal and soft tissue sarcomas. *PET Clin* (2015) **10**(3):375–93. doi:10.1016/j.cpet.2015.03.003
23. Sheikbahaei S, Marcus C, Subramaniam RM. 18F FDG PET/CT and head and neck cancer: patient management and outcomes. *PET Clin* (2015) **10**(2):125–45. doi:10.1016/j.cpet.2014.12.001
24. El-Galaly TC, Hutchings M. Imaging of non-Hodgkin lymphomas: diagnosis and response-adapted strategies. *Cancer Treat Res* (2015) **165**:125–46. doi:10.1007/978-3-319-13150-4\_5
25. Meignan M, Itti E, Gallamini A, Younes A. FDG PET/CT imaging as a biomarker in lymphoma. *Eur J Nucl Med Mol Imaging* (2015) **42**(4):623–33. doi:10.1007/s00259-014-2973-6
26. Contractor KB, Aboagye EO. Monitoring predominantly cytostatic treatment response with 18F-FDG PET. *J Nucl Med* (2009) **50** (Suppl 1):97S–105S. doi:10.2967/jnumed.108.057273
27. van Waarde A, Elsinga PH. Proliferation markers for the differential diagnosis of tumor and inflammation. *Curr Pharm Des* (2008) **14**(31):3326–39. doi:10.2174/138161208786549399
28. Fleming IN, Gilbert FJ, Miles KA, Cameron D. Opportunities for PET to deliver clinical benefit in cancer: breast cancer as a paradigm. *Cancer Imaging* (2010) **10**:144–52. doi:10.1102/1470-7330.2010.0020
29. Higashi K, Ueda Y, Seki H, Yuasa K, Oguchi M, Noguchi T, et al. Fluorine-18-FDG PET imaging is negative in bronchioloalveolar lung carcinoma. *J Nucl Med* (1998) **39**(6):1016–20.
30. Schoder H, Larson SM. Positron emission tomography for prostate, bladder, and renal cancer. *Semin Nucl Med* (2004) **34**(4):274–92. doi:10.1053/j.semnuclmed.2004.06.004
31. Higashi T, Saga T, Nakamoto Y, Ishimori T, Fujimoto K, Doi R, et al. Diagnosis of pancreatic cancer using fluorine-18 fluorodeoxyglucose positron emission tomography (FDG PET) – usefulness and limitations in “clinical reality”. *Ann Nucl Med* (2003) **17**(4):261–79. doi:10.1007/BF02988521
32. Wechalekar K, Sharma B, Cook G. PET/CT in oncology – a major advance. *Clin Radiol* (2005) **60**(11):1143–55. doi:10.1016/j.crad.2005.05.018
33. Liu VM, Vander Heiden MG. The role of pyruvate kinase M2 in cancer metabolism. *Brain Pathol* (2015) **25**(6):781–3. doi:10.1111/bpa.12311
34. Witney TH, James ML, Shen B, Chang E, Pohling C, Arksey N, et al. PET imaging of tumor glycolysis downstream of hexokinase through noninvasive measurement of pyruvate kinase M2. *Sci Transl Med* (2015) **7**(310):310ra169. doi:10.1126/scitranslmed.aac6117
35. Cheng KW, Agarwal R, Mitra S, Lee JS, Carey M, Gray JW, et al. Rab25 increases cellular ATP and glycogen stores protecting cancer cells from bioenergetic stress. *EMBO Mol Med* (2012) **4**(2):125–41. doi:10.1002/emmm.201100193
36. Takahashi S, Satomi A, Yano K, Kawase H, Tanimizu T, Tuji Y, et al. Estimation of glycogen levels in human colorectal cancer tissue: relationship with cell cycle and tumor outgrowth. *J Gastroenterol* (1999) **34**(4):474–80. doi:10.1007/s00530050299
37. Witney TH, Carroll L, Alam IS, Chandrashekran A, Nguyen QD, Sala R, et al. A novel radiotracer to image glycogen metabolism in tumors by positron emission tomography. *Cancer Res* (2014) **74**(5):1319–28. doi:10.1158/0008-5472.CAN-13-2768
38. Zeisel SH. Dietary choline: biochemistry, physiology, and pharmacology. *Annu Rev Nutr* (1981) **1**:95–121. doi:10.1146/annurev.nu.01.070181.000523
39. Gibellini F, Smith TK. The Kennedy pathway – de novo synthesis of phosphatidylethanolamine and phosphatidylcholine. *IUBMB Life* (2010) **62**(6):414–28. doi:10.1002/iub.354
40. Ackerstaff E, Pflug BR, Nelson JB, Bhujwalla ZM. Detection of increased choline compounds with proton nuclear magnetic resonance spectroscopy subsequent to malignant transformation of human prostatic epithelial cells. *Cancer Res* (2001) **61**(9):3599–603.
41. Glunde K, Bhujwalla ZM, Ronen SM. Choline metabolism in malignant transformation. *Nat Rev Cancer* (2011) **11**(12):835–48. doi:10.1038/nrc3162

42. Hara T, Kosaka N, Kishi H. PET imaging of prostate cancer using carbon-11-choline. *J Nucl Med* (1998) **39**(6):990–5.
43. Hara T, Kosaka N, Shinoura N, Kondo T. PET imaging of brain tumor with [methyl-11C]choline. *J Nucl Med* (1997) **38**(6):842–7.
44. Ramirez de Molina A, Sarmentero-Estrada J, Belda-Iniesta C, Taron M, Ramirez de Molina V, Cejas P, et al. Expression of choline kinase alpha to predict outcome in patients with early-stage non-small-cell lung cancer: a retrospective study. *Lancet Oncol* (2007) **8**(10):889–97. doi:10.1016/S1470-2045(07)70279-6
45. Tian M, Zhang H, Higuchi T, Oriuchi N, Endo K. Oncological diagnosis using (11)C-choline-positron emission tomography in comparison with 2-deoxy-2-[<sup>18</sup>F] fluoro-D-glucose-positron emission tomography. *Mol Imaging Biol* (2004) **6**(3):172–9. doi:10.1016/j.mibio.2004.02.003
46. Tamura K, Yoshikawa K, Tsujii H, Murata H. [Diagnosis of esophageal cancer using positron emission tomography]. *Nippon Geka Gakkai Zasshi* (2002) **103**(4):325–30.
47. Jager PL, Que TH, Vaalburg W, Pruim J, Elsinga P, Plukker JT. Carbon-11 choline or FDG-PET for staging of oesophageal cancer? *Eur J Nucl Med* (2001) **28**(12):1845–9. doi:10.1007/s002590100655
48. Kobori O, Kirihara Y, Kosaka N, Hara T. Positron emission tomography of esophageal carcinoma using (11)C-choline and (18)F-fluorodeoxyglucose: a novel method of preoperative lymph node staging. *Cancer* (1999) **86**(9):1638–48. doi:10.1002/(SICI)1097-0142(19991101)86:9<1638::AID-CNCR4>3.0.CO;2-U
49. Reske SN, Blumstein NM, Neumaier B, Gottfried HW, Finsterbusch F, Kocot D, et al. Imaging prostate cancer with 11C-choline PET/CT. *J Nucl Med* (2006) **47**(8):1249–54.
50. DeGrado TR, Coleman RE, Wang S, Baldwin SW, Orr MD, Robertson CN, et al. Synthesis and evaluation of 18F-labeled choline as an oncologic tracer for positron emission tomography: initial findings in prostate cancer. *Cancer Res* (2001) **61**(1):110–7.
51. Treglia G, Giovannini E, Di Franco D, Calcagni ML, Rufini V, Picchio M, et al. The role of positron emission tomography using carbon-11 and fluorine-18 choline in tumors other than prostate cancer: a systematic review. *Ann Nucl Med* (2012) **26**(6):451–61. doi:10.1007/s12149-012-0602-7
52. Bansal A, Shuyan W, Hara T, Harris RA, Degrado TR. Biodisposition and metabolism of [(18)F]fluorocholine in 9L glioma cells and 9L glioma-bearing fisher rats. *Eur J Nucl Med Mol Imaging* (2008) **35**(6):1192–203. doi:10.1007/s00259-008-0736-y
53. Roivainen A, Forsback S, Gronroos T, Lehtokoinen P, Kahkonen M, Sutinen E, et al. Blood metabolism of [methyl-11C]choline; implications for in vivo imaging with positron emission tomography. *Eur J Nucl Med* (2000) **27**(1):25–32. doi:10.1007/PL00006658
54. Smith G, Zhao Y, Leyton J, Shan B, Nguyen QD, Perumal M, et al. Radiosynthesis and pre-clinical evaluation of [(18)F]fluoro-[1,2-(2)H(4)]choline. *Nucl Med Biol* (2011) **38**(1):39–51. doi:10.1016/j.nucmedbio.2010.06.012
55. Gadda G. pH and deuterium kinetic isotope effects studies on the oxidation of choline to betaine-aldehyde catalyzed by choline oxidase. *Biochim Biophys Acta* (2003) **1650**(1–2):4–9. doi:10.1016/S1570-9639(03)00188-2
56. Leyton J, Smith G, Zhao Y, Perumal M, Nguyen QD, Robins E, et al. [18F] fluoromethyl-[1,2-2H4]-choline: a novel radiotracer for imaging choline metabolism in tumors by positron emission tomography. *Cancer Res* (2009) **69**(19):7721–8. doi:10.1158/0008-5472.CAN-09-1419
57. Witney TH, Alam IS, Turton DR, Smith G, Carroll L, Brickute D, et al. Evaluation of deuterated 18F- and 11C-labeled choline analogs for cancer detection by positron emission tomography. *Clin Cancer Res* (2012) **18**(4):1063–72. doi:10.1158/1078-0432.CCR-11-2462
58. Challapalli A, Sharma R, Hallett WA, Kozlowski K, Carroll L, Brickute D, et al. Biodistribution and radiation dosimetry of deuterium-substituted 18F-fluoromethyl-[1,2-2H4]choline in healthy volunteers. *J Nucl Med* (2014) **55**(2):256–63. doi:10.2967/jnumed.113.129577
59. Hara T, Bansal A, DeGrado TR. Effect of hypoxia on the uptake of [methyl-<sup>3</sup>H] choline, [1-<sup>14</sup>C] acetate and [<sup>18</sup>F]FDG in cultured prostate cancer cells. *Nucl Med Biol* (2006) **33**(8):977–84. doi:10.1016/j.nucmedbio.2006.08.002
60. Al-Saeedi F. Effects of flutamide on [methyl-(3)H]-choline uptake in human prostate cancer-3 cells: a pilot study. *Curr Ther Res Clin Exp* (2007) **68**(4):226–41. doi:10.1016/j.curtheres.2007.08.003
61. Emonds KM, Swinnen JV, van Weerden WM, Vanderhoydonc F, Nuyts J, Mortelmans L, et al. Do androgens control the uptake of 18F-FDG, 11C-choline and 11C-acetate in human prostate cancer cell lines? *Eur J Nucl Med Mol Imaging* (2011) **38**(10):1842–53. doi:10.1007/s00259-011-1861-6
62. Krause BJ, Souvatzoglou M, Herrmann K, Weber AW, Schuster T, Buck AK, et al. [11C]Choline as pharmacodynamic marker for therapy response assessment in a prostate cancer xenograft model. *Eur J Nucl Med Mol Imaging* (2010) **37**(10):1861–8. doi:10.1007/s00259-010-1493-2
63. Schwarzenbock S, Sachs D, Souvatzoglou M, Schuster T, Nawroth R, Weirich G, et al. [(1)C]choline as a pharmacodynamic marker for docetaxel therapy. Response assessment in a LNCaP prostate cancer xenograft mouse model. *Nuklearmedizin* (2013) **52**(4):141–7. doi:10.3413/Nukmed-0521-12-07
64. Holzapfel K, Müller S, Seidl C, Grosu A-L, Schwaiger M, Senekowitsch-Schmidtke R. Effects of irradiation on the [Methyl-&lt;&gt;3&lt;/&gt;H]choline uptake in the human prostate cancer cell lines LNCaP and PC3. *Strahlenther Onkol* (2008) **184**(6):319–24. doi:10.1007/s00066-008-1799-1
65. Fei B, Wang H, Wu C, Chiu SM. Choline PET for monitoring early tumor response to photodynamic therapy. *J Nucl Med* (2010) **51**(1):130–8. doi:10.2967/jnumed.109.067579
66. De Waele A, Van Binnebeek S, Mottaghay FM. Response assessment of hormonal therapy in prostate cancer by [11C] choline PET/CT. *Clin Nucl Med* (2010) **35**(9):701–3. doi:10.1097/RNU.0b013e3181e9faf5
67. Fuccio C, Schiavina R, Castellucci P, Rubello D, Martorana G, Celli M, et al. Androgen deprivation therapy influences the uptake of 11C-choline in patients with recurrent prostate cancer: the preliminary results of a sequential PET/CT study. *Eur J Nucl Med Mol Imaging* (2011) **38**(11):1985–9. doi:10.1007/s00259-011-1867-0
68. Giovacchini G, Picchio M, Coradeschi E, Scattoni V, Bettinardi V, Cozzarini C, et al. [(11)C]choline uptake with PET/CT for the initial diagnosis of prostate cancer: relation to PSA levels, tumour stage and anti-androgenic therapy. *Eur J Nucl Med Mol Imaging* (2008) **35**(6):1065–73. doi:10.1007/s00259-008-0716-2
69. Challapalli A, Barwick T, Tomasi G, O'Doherty M, Contractor K, Stewart S, et al. Exploring the potential of [11C]choline-PET/CT as a novel imaging biomarker for predicting early treatment response in prostate cancer. *Nucl Med Commun* (2014) **35**(1):20–9. doi:10.1097/MNM.0000000000000014
70. Casamassima F, Masi L, Menichelli C, Bonucci I, Casamassima E, Lazzeri M, et al. Efficacy of eradication radiotherapy for limited nodal metastases detected with choline PET scan in prostate cancer patients. *Tumori* (2011) **97**(1):49–55.
71. Amanie J, Jans HS, Wuest M, Pervez N, Murtha A, Usmani N, et al. Analysis of intraprostatic therapeutic effects in prostate cancer patients using [(11)C]-choline pet/ct after external-beam radiation therapy. *Curr Oncol* (2013) **20**(2):104–10. doi:10.3747/co.20.1217
72. Beheshti M, Vali R, Waldenberger P, Fitz F, Nader M, Hammer J, et al. The use of F-18 choline PET in the assessment of bone metastases in prostate cancer: correlation with morphological changes on CT. *Mol Imaging Biol* (2009) **11**(6):446–54. doi:10.1007/s11307-009-0217-0
73. Beheshti M, Vali R, Waldenberger P, Fitz F, Nader M, Loidl W, et al. Detection of bone metastases in patients with prostate cancer by 18F fluorocholine and 18F fluoride PET-CT: a comparative study. *Eur J Nucl Med Mol Imaging* (2008) **35**(10):1766–74. doi:10.1007/s00259-008-0788-z
74. Antonarakis ES, Lu C, Wang H, Luber B, Nakazawa M, Roeser JC, et al. AR-V7 and resistance to enzalutamide and abiraterone in prostate cancer. *N Engl J Med* (2014) **371**(11):1028–38. doi:10.1056/NEJMoa1315815
75. Scher HI, Halabi S, Tannock I, Morris M, Sternberg CN, Carducci MA, et al. Design and end points of clinical trials for patients with progressive prostate cancer and castrate levels of testosterone: recommendations of the Prostate Cancer Clinical Trials Working Group. *J Clin Oncol* (2008) **26**(7):1148–59. doi:10.1200/JCO.2007.12.4487
76. Kwee S, Song MA, Cheng I, Loo L, Tiirkainen M. Measurement of circulating cell-free DNA in relation to 18F-fluorocholine PET/CT imaging in chemotherapy-treated advanced prostate cancer. *Clin Transl Sci* (2012) **5**(1):65–70. doi:10.1111/j.1752-8062.2011.00375.x
77. Cafo O, Maines F, Donner D, Vecchia A, Chierichetti F, Galligioni E. Impact of enzalutamide administration on primary prostate cancer volume: a metabolic evaluation by choline positron emission tomography in castration-resistant prostate cancer patients. *Clin Genitourin Cancer* (2014) **12**(5):312–6. doi:10.1016/j.clgc.2014.03.004

78. De Giorgi U, Caroli P, Scarpi E, Conteduca V, Burgio SL, Menna C, et al. (18)F-fluorocholine PET/CT for early response assessment in patients with metastatic castration-resistant prostate cancer treated with enzalutamide. *Eur J Nucl Med Mol Imaging* (2015) **42**(8):1276–83. doi:10.1007/s00259-015-3042-5
79. De Giorgi U, Caroli P, Burgio SL, Menna C, Conteduca V, Bianchi E, et al. Early outcome prediction on 18F-fluorocholine PET/CT in metastatic castration-resistant prostate cancer patients treated with abiraterone. *Oncotarget* (2014) **5**(23):12448–58. doi:10.18632/oncotarget.2558
80. Miyazaki KS, Kuang Y, Kwee SA. Changes in skeletal tumor activity on (18)F-choline PET/CT in patients receiving (223)radium radionuclide therapy for metastatic prostate cancer. *Nucl Med Mol Imaging* (2015) **49**(2):160–4. doi:10.1007/s13139-014-0314-0
81. Parashar B, Wernicke AG, Rice S, Osborne J, Singh P, Nori D, et al. Early assessment of radiation response using a novel functional imaging modality – [18F]fluorocholine PET (FCH-PET): a pilot study. *Discov Med* (2012) **14**(74):13–20.
82. Panagiotidis E, Shankar A, Afqaq A, Bomanji J. Assessing therapy response of secreting pineal germ cell tumor on simultaneous 18F-choline PET/MRI. *Clin Nucl Med* (2014) **39**(9):e387–8. doi:10.1097/RNU.0000000000000231
83. Al-Saeedi F, Welch AE, Smith TA. [<sup>3</sup>H]Choline incorporation into MCF7 tumour cells: correlation with proliferation. *Eur J Nucl Med Mol Imaging* (2005) **32**(6):660–7. doi:10.1007/s00259-004-1707-6
84. Lodi A, Woods SM, Ronen SM. MR-detectable metabolic consequences of mitogen-activated protein kinase kinase (MEK) inhibition. *NMR Biomed* (2014) **27**(6):700–8. doi:10.1002/nbm.3109
85. Kenny LM, Contractor KB, Hinz R, Stebbing J, Palmieri C, Jiang J, et al. Reproducibility of [11C]choline-positron emission tomography and effect of trastuzumab. *Clin Cancer Res* (2010) **16**(16):4236–45. doi:10.1158/1078-0432.CCR-10-0468
86. Middendorp M, Mauthe L, Sauter B, Vogl TJ, Grunwald F. Initial experience with 18F-fluoroethylcholine PET/CT in staging and monitoring therapy response of advanced renal cell carcinoma. *Ann Nucl Med* (2010) **24**(6):441–6. doi:10.1007/s12149-010-0375-9
87. DeBerardinis RJ, Lum JJ, Hatzivassiliou G, Thompson CB. The biology of cancer: metabolic reprogramming fuels cell growth and proliferation. *Cell Metab* (2008) **7**(1):11–20. doi:10.1016/j.cmet.2007.10.002
88. Swinnen JV, Brusselmans K, Verhoeven G. Increased lipogenesis in cancer cells: new players, novel targets. *Curr Opin Clin Nutr Metab Care* (2006) **9**(4):358–65. doi:10.1097/01.mco.0000232894.28674.30
89. Landau BR. Acetate's metabolism, CO<sub>2</sub> production, and the TCA cycle. *Am J Clin Nutr* (1991) **53**(4):981–2.
90. Brown M, Marshall DR, Sobel BE, Bergmann SR. Delineation of myocardial oxygen utilization with carbon-11-labeled acetate. *Circulation* (1987) **76**(3):687–96. doi:10.1161/01.CIR.76.3.687
91. Mohsen B, Giorgio T, Rasoul ZS, Werner L, Ali GR, Reza DK, et al. Application of C-11-acetate positron-emission tomography (PET) imaging in prostate cancer: systematic review and meta-analysis of the literature. *BJU Int* (2013) **112**(8):1062–72. doi:10.1111/bju.12279
92. Grassi I, Nanni C, Allegri V, Morigi JJ, Montini GC, Castellucci P, et al. The clinical use of PET with (11)C-acetate. *Am J Nucl Med Mol Imaging* (2012) **2**(1):33–47.
93. Emonds KM, Swinnen JV, Lerut E, Koole M, Mortelmans L, Mottaghay FM. Evaluation of androgen-induced effects on the uptake of [18F]FDG, [11C] choline and [11C]acetate in an androgen-sensitive and androgen-independent prostate cancer xenograft model. *EJNMMI Res* (2013) **3**(1):31. doi:10.1186/2191-219X-3-31
94. Oyama N, Kim J, Jones LA, Mercer NM, Engelbach JA, Sharp TL, et al. MicroPET assessment of androgenic control of glucose and acetate uptake in the rat prostate and a prostate cancer tumor model. *Nucl Med Biol* (2002) **29**(8):783–90. doi:10.1016/S0969-8051(02)00346-3
95. Yoshii Y, Furukawa T, Oyama N, Hasegawa Y, Kiyono Y, Nishii R, et al. Fatty acid synthase is a key target in multiple essential tumor functions of prostate cancer: uptake of radiolabeled acetate as a predictor of the targeted therapy outcome. *PLoS One* (2013) **8**(5):e64570. doi:10.1371/journal.pone.0064570
96. Vavere AL, Kridel SJ, Wheeler FB, Lewis JS. 1-11C-acetate as a PET radiopharmaceutical for imaging fatty acid synthase expression in prostate cancer. *J Nucl Med* (2008) **49**(2):327–34. doi:10.2967/jnumed.107.046672
97. Lewis DY, Boren J, Shaw GL, Bielik R, Ramos-Montoya A, Larkin TJ, et al. Late imaging with [1-(11)C]acetate improves detection of tumor fatty acid synthesis with PET. *J Nucl Med* (2014) **55**(7):1144–9. doi:10.2967/jnumed.113.134437
98. Yu EY, Muzy M, Hackenbrach JA, Rezvani BB, Link JM, Montgomery RB, et al. C11-acetate and F-18 FDG PET for men with prostate cancer bone metastases: relative findings and response to therapy. *Clin Nucl Med* (2011) **36**(3):192–8. doi:10.1097/RNU.0b013e318208f140
99. Hinojosa Gomez J, Blake M, Hernandez JO, Balam J, Teh BS. C11-acetate positron emission tomography (PET) for prostate cancer patients undergoing radiation therapy. *Int J Radiat Oncol* (2012) **84**(3):S371–2. doi:10.1016/j.ijrobp.2012.07.981
100. Maleddu A, Pantaleo MA, Castellucci P, Astorino M, Nanni C, Nannini M, et al. 11C-acetate PET for early prediction of sunitinib response in metastatic renal cell carcinoma. *Tumori* (2009) **95**(3):382–4.
101. Liu RS, Chang CP, Guo WY, Pan DH, Ho DM, Chang CW, et al. 1-11C-acetate versus 18F-FDG PET in detection of meningioma and monitoring the effect of gamma-knife radiosurgery. *J Nucl Med* (2010) **51**(6):883–91. doi:10.2967/jnumed.109.070565
102. Lin C, Ho CL, Ng SH, Wang PN, Huang Y, Lin YC, et al. (11)C-acetate as a new biomarker for PET/CT in patients with multiple myeloma: initial staging and postinduction response assessment. *Eur J Nucl Med Mol Imaging* (2014) **41**(1):41–9. doi:10.1007/s00259-013-2520-x
103. Ho CL, Cheung MK, Chen S, Cheung TT, Leung YL, Cheng KC, et al. [18F] fluoroacetate positron emission tomography for hepatocellular carcinoma and metastases: an alternative tracer for [11C]acetate? *Mol Imaging* (2012) **11**(3):229–39.
104. Takemoto K, Hatano E, Nishii R, Kagawa S, Kishibe Y, Takahashi M, et al. Assessment of [(18)F]-fluoroacetate PET/CT as a tumor-imaging modality: preclinical study in healthy volunteers and clinical evaluation in patients with liver tumor. *Ann Nucl Med* (2014) **28**(4):371–80. doi:10.1007/s12149-014-0823-z
105. Carracedo A, Cantley LC, Pandolfi PP. Cancer metabolism: fatty acid oxidation in the limelight. *Nat Rev Cancer* (2013) **13**(4):227–32. doi:10.1038/nrc3483
106. Bastiaansen JA, Cheng T, Mishkovsky M, Duarte JM, Comment A, Gruetter R. In vivo enzymatic activity of acetylCoA synthetase in skeletal muscle revealed by (13)C turnover from hyperpolarized [1-(13)C]acetate to [1-(13)C]acetyl carnitine. *Biochim Biophys Acta* (2013) **1830**(8):4171–8. doi:10.1016/j.bbagen.2013.03.023
107. Witney TH, Pisaneschi F, Alam IS, Trousil S, Kaliszczak M, Twyman F, et al. Preclinical evaluation of 3-18F-fluoro-2,2-dimethylpropionic acid as an imaging agent for tumor detection. *J Nucl Med* (2014) **55**(9):1506–12. doi:10.2967/jnumed.114.140343
108. Isselbacher KJ. Increased uptake of amino acids and 2-deoxy-D-glucose by virus-transformed cells in culture. *Proc Natl Acad Sci U S A* (1972) **69**(3):585–9. doi:10.1073/pnas.69.3.585
109. Jager PL, Vaalburg W, Pruijm J, de Vries EG, Langen KJ, Piers DA. Radiolabeled amino acids: basic aspects and clinical applications in oncology. *J Nucl Med* (2001) **42**(3):432–45.
110. Albano F, Anelli L, Zagaria A, Coccaro N, D'Addabbo P, Liso V, et al. Genomic segmental duplications on the basis of the t(9;22) rearrangement in chronic myeloid leukemia. *Oncogene* (2010) **29**(17):2509–16. doi:10.1038/onc.2009.524
111. DeBerardinis RJ, Mancuso A, Daikhin E, Nissim I, Yudkoff M, Wehrli S, et al. Beyond aerobic glycolysis: transformed cells can engage in glutamine metabolism that exceeds the requirement for protein and nucleotide synthesis. *Proc Natl Acad Sci U S A* (2007) **104**(49):19345–50. doi:10.1073/pnas.0709747104
112. Rajagopalan KN, DeBerardinis RJ. Role of glutamine in cancer: therapeutic and imaging implications. *J Nucl Med* (2011) **52**(7):1005–8. doi:10.2967/jnumed.110.084244
113. Zhu A, Lee D, Shim H. Metabolic positron emission tomography imaging in cancer detection and therapy response. *Semin Oncol* (2011) **38**(1):55–69. doi:10.1053/j.seminoncol.2010.11.012
114. Venneti S, Dunphy MP, Zhang H, Pitter KL, Zanzonico P, Campos C, et al. Glutamine-based PET imaging facilitates enhanced metabolic evaluation of gliomas *in vivo*. *Sci Transl Med* (2015) **7**(274):274ra17. doi:10.1126/scitranslmed.aaa1009

115. Singhal T, Narayanan TK, Jain V, Mukherjee J, Mantil J. <sup>11</sup>C-L-methionine positron emission tomography in the clinical management of cerebral gliomas. *Mol Imaging Biol* (2008) **10**(1):1–18. doi:10.1007/s11307-007-0115-2
116. Higashi K, Clavo AC, Wahl RL. In vitro assessment of 2-fluoro-2-deoxy-D-glucose, L-methionine and thymidine as agents to monitor the early response of a human adenocarcinoma cell line to radiotherapy. *J Nucl Med* (1993) **34**(5):773–9.
117. Kubota K, Ishiwata K, Kubota R, Yamada S, Tada M, Sato T, et al. Tracer feasibility for monitoring tumor radiotherapy: a quadruple tracer study with fluorine-18-fluorodeoxyglucose or fluorine-18-fluorodeoxyuridine, L-[methyl-<sup>14</sup>C]methionine, [6-<sup>3</sup>H]thymidine, and gallium-67. *J Nucl Med* (1991) **32**(11):2118–23.
118. Kubota K, Kubota R, Yamada S, Tada M. Effects of radiotherapy on the cellular uptake of carbon-14 labeled L-methionine in tumor tissue. *Nucl Med Biol* (1995) **22**(2):193–8. doi:10.1016/0969-8051(94)00099-6
119. Luckeath K, Lapa C, Albert C, Herrmann K, Jorg G, Samnick S, et al. <sup>11</sup>C-Methionine-PET: a novel and sensitive tool for monitoring of early response to treatment in multiple myeloma. *Oncotarget* (2015) **6**(10):8418–29. doi:10.18632/oncotarget.3053
120. Murayama C, Harada N, Kakiuchi T, Fukumoto D, Kamijo A, Kawaguchi AT, et al. Evaluation of D-18F-FMT, 18F-FDG, L-<sup>11</sup>C-MET, and 18F-FLT for monitoring the response of tumors to radiotherapy in mice. *J Nucl Med* (2009) **50**(2):290–5. doi:10.2967/jnumed.108.057091
121. Ono T, Sasajima T, Doi Y, Oka S, Ono M, Kanagawa M, et al. Amino acid PET tracers are reliable markers of treatment responses to single-agent or combination therapies including temozolomide, interferon-beta, and/or bevacizumab for glioblastoma. *Nucl Med Biol* (2015) **42**(7):598–607. doi:10.1016/j.nucmedbio.2015.01.008
122. Paquette M, Tremblay S, Benard F, Lecomte R. Quantitative hormone therapy follow-up in an ER+/ERalphaKD mouse tumor model using FDG and [<sup>11</sup>C]-methionine PET imaging. *EJNMMI Res* (2012) **2**(1):61. doi:10.1186/2191-219X-2-61
123. Reinhardt MJ, Kubota K, Yamada S, Iwata R, Yaegashi H. Assessment of cancer recurrence in residual tumors after fractionated radiotherapy: a comparison of fluorodeoxyglucose, L-methionine and thymidine. *J Nucl Med* (1997) **38**(2):280–7.
124. Sasajima T, Ono T, Shimada N, Doi Y, Oka S, Kanagawa M, et al. Trans-1-amino-3-18F-fluorocyclobutanecarboxylic acid (anti-18F-FACBC) is a feasible alternative to <sup>11</sup>C-methyl-L-methionine and magnetic resonance imaging for monitoring treatment response in gliomas. *Nucl Med Biol* (2013) **40**(6):808–15. doi:10.1016/j.nucmedbio.2013.04.007
125. Sato K, Kameyama M, Ishiwata K, Katakura R, Yoshimoto T. Metabolic changes of glioma following chemotherapy: an experimental study using four PET tracers. *J Neurooncol* (1992) **14**(1):81–9. doi:10.1007/BF00170948
126. Schaidler H, Haberkorn U, Berger MR, Oberdorfer F, Morr I, van Kaick G. Application of alpha-aminoisobutyric acid, L-methionine, thymidine and 2-fluoro-2-deoxy-D-glucose to monitor effects of chemotherapy in a human colon carcinoma cell line. *Eur J Nucl Med* (1996) **23**(1):55–60. doi:10.1007/BF01736990
127. Trencsenyi G, Marian T, Lajtos I, Krasznai Z, Balkay L, Emri M, et al. <sup>18</sup>FDG, [<sup>18</sup>F]FLT, [<sup>18</sup>F]FAZA, and <sup>11</sup>C-methionine are suitable tracers for the diagnosis and in vivo follow-up of the efficacy of chemotherapy by miniPET in both multidrug resistant and sensitive human gynecologic tumor xenografts. *Biomed Res Int* (2014) **2014**:787365. doi:10.1155/2014/787365
128. Bergstrom M, Muhr C, Lundberg PO, Langstrom B. PET as a tool in the clinical evaluation of pituitary adenomas. *J Nucl Med* (1991) **32**(4):610–5.
129. Chesnay E, Babin E, Constans JM, Agostini D, Bequignon A, Regeasse A, et al. Early response to chemotherapy in hypopharyngeal cancer: assessment with (<sup>11</sup>C)-methionine PET, correlation with morphologic response, and clinical outcome. *J Nucl Med* (2003) **44**(4):526–32.
130. Chiba Y, Kinoshita M, Okita Y, Tsuoboi A, Isohashi K, Kagawa N, et al. Use of (<sup>11</sup>C)-methionine PET parametric response map for monitoring WT1 immunotherapy response in recurrent malignant glioma. *J Neurosurg* (2012) **116**(4):835–42. doi:10.3171/2011.12.JNS111255
131. Galldiks N, Kracht LW, Burghaus L, Thomas A, Jacobs AH, Heiss WD, et al. Use of <sup>11</sup>C-methionine PET to monitor the effects of temozolamide chemotherapy in malignant gliomas. *Eur J Nucl Med Mol Imaging* (2006) **33**(5):516–24. doi:10.1007/s00259-005-0002-5
132. Galldiks N, Ullrich R, Schroeter M, Fink GR, Kracht LW. Imaging biological activity of a glioblastoma treated with an individual patient-tailored, experimental therapy regimen. *J Neurooncol* (2009) **93**(3):425–30. doi:10.1007/s11060-008-9790-3
133. Galldiks N, von Tempelhoff W, Kahraman D, Kracht LW, Vollmar S, Fink GR, et al. <sup>11</sup>C-methionine positron emission tomographic imaging of biologic activity of a recurrent glioblastoma treated with stereotaxy-guided laser-induced interstitial thermotherapy. *Mol Imaging* (2012) **11**(4):265–71.
134. Ghigi G, Micera R, Maffione AM, Castellucci P, Cammelli S, Ammendolia I, et al. <sup>11</sup>C-methionine vs. <sup>18</sup>F-FDG PET in soft tissue sarcoma patients treated with neoadjuvant therapy: preliminary results. *In Vivo* (2009) **23**(1):105–10.
135. Gudjonsson O, Blomquist E, Lilja A, Ericson H, Bergstrom M, Nyberg G. Evaluation of the effect of high-energy proton irradiation treatment on meningiomas by means of <sup>11</sup>C-L-methionine PET. *Eur J Nucl Med* (2000) **27**(12):1793–9. doi:10.1007/s002590000335
136. Hasebe M, Yoshikawa K, Ohashi S, Toubaru S, Kawaguchi K, Sato J, et al. A study on the prognostic evaluation of carbon ion radiotherapy for head and neck adenocarcinoma with C-11 methionine PET. *Mol Imaging Biol* (2010) **12**(5):554–62. doi:10.1007/s11307-010-0318-9
137. Herholz K, Kracht LW, Heiss WD. Monitoring the effect of chemotherapy in a mixed glioma by C-11-methionine PET. *J Neuroimaging* (2003) **13**(3):269–71. doi:10.1111/j.1552-6569.2003.tb00190.x
138. Huovinen R, Leskinen-Kallio S, Nagren K, Lehtinen P, Ruotsalainen U, Teras M. Carbon-11-methionine and PET in evaluation of treatment response of breast cancer. *Br J Cancer* (1993) **67**(4):787–91. doi:10.1038/bjc.1993.143
139. Ishimori T, Saga T, Nagata Y, Nakamoto Y, Higashi T, Mamede M, et al. <sup>18</sup>F-FDG and <sup>11</sup>C-methionine PET for evaluation of treatment response of lung cancer after stereotactic radiotherapy. *Ann Nucl Med* (2004) **18**(8):669–74. doi:10.1007/BF02985960
140. Jang SJ, Lee KH, Lee JY, Choi JY, Kim BT, Kim SJ, et al. (<sup>11</sup>C)-methionine PET/CT and MRI of primary central nervous system diffuse large B-cell lymphoma before and after high-dose methotrexate. *Clin Nucl Med* (2012) **37**(10):e241–4. doi:10.1097/RNU.0b013e318252d1ea
141. Jansson T, Westlin JE, Ahlstrom H, Lilja A, Langstrom B, Bergh J. Positron emission tomography studies in patients with locally advanced and/or metastatic breast cancer: a method for early therapy evaluation? *J Clin Oncol* (1995) **13**(6):1470–7.
142. Katz L, Choueiri TK, Bellmunt J. (<sup>11</sup>C)-methionine positron-emission tomography and computed tomography (PET-CT) in evaluating metastatic transitional cell carcinoma response to sunitinib therapy. *BJU Int* (2010) **106**(9):1249–50. doi:10.1111/j.1464-410X.2010.09732.x
143. Kawai N, Miyake K, Yamamoto Y, Nishiyama Y, Maeda Y, Kageji T, et al. Use of <sup>11</sup>C-methionine positron emission tomography in basal germinoma: assessment of treatment response and residual tumor. *Childs Nerv Syst* (2009) **25**(7):845–53. doi:10.1007/s00381-009-0841-7
144. Koizumi M, Saga T, Yoshikawa K, Suzuki K, Yamada S, Hasebe M, et al. <sup>11</sup>C-methionine-PET for evaluation of carbon ion radiotherapy in patients with pelvic recurrence of rectal cancer. *Mol Imaging Biol* (2008) **10**(6):374–80. doi:10.1007/s11307-008-0156-1
145. Kubota K, Yamada S, Ishiwata K, Ito M, Fujiwara T, Fukuda H, et al. Evaluation of the treatment response of lung cancer with positron emission tomography and L-[methyl-<sup>11</sup>C]methionine: a preliminary study. *Eur J Nucl Med* (1993) **20**(6):495–501. doi:10.1007/BF00175162
146. Lee J, Lee BL, Yoo KH, Sung KW, Koo HH, Lee SJ, et al. Atypical basal ganglia germinoma presenting as cerebral hemiatrophy: diagnosis and follow-up with <sup>11</sup>C-methionine positron emission tomography. *Childs Nerv Syst* (2009) **25**(1):29–37. doi:10.1007/s00381-008-0674-9
147. Leskinen-Kallio S, Minn H, Joensuu H. PET and [<sup>11</sup>C]methionine in assessment of response in non-Hodgkin lymphoma. *Lancet* (1990) **336**(8724):1188. doi:10.1016/0140-6736(90)92799-N
148. Letocha H, Ahlstrom H, Malmstrom PU, Westlin JE, Fasth KJ, Nilsson S. Positron emission tomography with L-methyl-<sup>11</sup>C-methionine in the monitoring of therapy response in muscle-invasive transitional cell carcinoma of the urinary bladder. *Br J Urol* (1994) **74**(6):767–74. doi:10.1111/j.1464-410X.1994.tb07123.x
149. Lindholm P, Lapela M, Nagren K, Lehtinen P, Minn H, Jyrkkio S. Preliminary study of carbon-11 methionine PET in the evaluation of early

- response to therapy in advanced breast cancer. *Nucl Med Commun* (2009) **30**(1):30–6. doi:10.1097/MNM.0b013e328313b7bc
150. Lindholm P, Leskinen-Kallio S, Grenman R, Lehtikoinen P, Nagren K, Teras M, et al. Evaluation of response to radiotherapy in head and neck cancer by positron emission tomography and [11C]methionine. *Int J Radiat Oncol Biol Phys* (1995) **32**(3):787–94. doi:10.1016/0360-3016(95)00007-L
  151. Miwa K, Matsuo M, Shinoda J, Aki T, Yonezawa S, Ito T, et al. Clinical value of [(1)<sup>11</sup>C]methionine PET for stereotactic radiation therapy with intensity modulated radiation therapy to metastatic brain tumors. *Int J Radiat Oncol Biol Phys* (2012) **84**(5):1139–44. doi:10.1016/j.ijrobp.2012.02.032
  152. Muhr C, Gudjonsson O, Lilja A, Hartman M, Zhang ZJ, Langstrom B. Meningioma treated with interferon-alpha, evaluated with [(1)<sup>11</sup>C]-L-methionine positron emission tomography. *Clin Cancer Res* (2001) **7**(8):2269–76.
  153. Nariai T, Tanaka Y, Wakimoto H, Aoyagi M, Tamaki M, Ishiwata K, et al. Usefulness of L-[methyl-<sup>11</sup>C] methionine-positron emission tomography as a biological monitoring tool in the treatment of glioma. *J Neurosurg* (2005) **103**(3):498–507. doi:10.3171/jns.2005.103.3.0498
  154. Nuutinen J, Jyrkkio S, Lehtikoinen P, Lindholm P, Minn H. Evaluation of early response to radiotherapy in head and neck cancer measured with [11C]methionine-positron emission tomography. *Radiother Oncol* (1999) **52**(3):225–32. doi:10.1016/S0167-8140(99)00091-2
  155. Nuutinen J, Sonninen P, Lehtikoinen P, Sutinen E, Valavaara R, Eronen E, et al. Radiotherapy treatment planning and long-term follow-up with [(1)<sup>11</sup>C] methionine PET in patients with low-grade astrocytoma. *Int J Radiat Oncol Biol Phys* (2000) **48**(1):43–52. doi:10.1016/S0360-3016(00)00604-0
  156. Ogawa T, Kanno I, Hatazawa J, Inugami A, Fujita H, Shimosegawa E, et al. Methionine PET for follow-up of radiation therapy of primary lymphoma of the brain. *Radiographics* (1994) **14**(1):101–10. doi:10.1148/radiographics.14.1.8128041
  157. Ribom D, Schoenmaekers M, Engler H, Smits A. Evaluation of <sup>11</sup>C-methionine PET as a surrogate endpoint after treatment of grade 2 gliomas. *J Neurooncol* (2005) **71**(3):325–32. doi:10.1007/s11060-004-2031-5
  158. Roelcke U, von Ammon K, Hausmann O, Kaech DL, Vanloffeld W, Landolt H, et al. Operated low grade astrocytomas: a long term PET study on the effect of radiotherapy. *J Neurol Neurosurg Psychiatry* (1999) **66**(5):644–7. doi:10.1136/jnnp.66.5.644
  159. Sato K, Kameyama M, Kayama T, Yoshimoto T, Ishiwata K, Ito M. Serial positron emission tomography imaging of changes in amino acid metabolism in low grade astrocytoma after radio- and chemotherapy – case report. *Neurol Med Chir (Tokyo)* (1995) **35**(11):808–12. doi:10.2176/nmc.35.808
  160. Sawataishi J, Mineura K, Sasajima T, Kowada M, Sugawara A, Shishido F. Effects of radiotherapy determined by <sup>11</sup>C-methyl-L-methionine positron emission tomography in patients with primary cerebral malignant lymphoma. *Neuroradiology* (1992) **34**(6):517–9. doi:10.1007/BF00598964
  161. Shintani S, Tsuruoka S, Shiigai T. Serial positron emission tomography (PET) in gliomatosis cerebri treated with radiotherapy: a case report. *J Neurol Sci* (2000) **173**(1):25–31. doi:10.1016/S0022-5110(99)00296-8
  162. Sorensen J, Savitcheva II, Engler H, Langstrom B. 3. Utility of PET and <sup>11</sup>C-methionine in the paediatric brain tumors. *Clin Positron Imaging* (2000) **3**(4):157. doi:10.1016/S1095-0397(00)00069-8
  163. Tamura K, Yoshikawa K, Ishikawa H, Hasebe M, Tsuji H, Yanagi T, et al. Carbon-11-methionine PET imaging of choroidal melanoma and the time course after carbon ion beam radiotherapy. *Anticancer Res* (2009) **29**(5):1507–14.
  164. Tang BN, Sadeghi N, Branle F, De Witte O, Wikler D, Goldman S. Semiquantification of methionine uptake and flair signal for the evaluation of chemotherapy in low-grade oligodendrogloma. *J Neurooncol* (2005) **71**(2):161–8. doi:10.1007/s11060-004-9654-4
  165. Toubaru S, Yoshikawa K, Ohashi S, Tanimoto K, Hasegawa A, Kawaguchi K, et al. Accuracy of methionine-PET in predicting the efficacy of heavy-particle therapy on primary adenoid cystic carcinomas of the head and neck. *Radiat Oncol* (2013) **8**:143. doi:10.1186/1748-717X-8-143
  166. Tsuyuguchi N, Hakuba A, Okamura T, Ochi H, Suzuki T, Sunada I. PET for diagnosis of malignant lymphoma of the scalp: comparison of [11C]methyl-L-methionine and [<sup>18</sup>F]fluoro-2-deoxyglucose. *J Comput Assist Tomogr* (1997) **21**(4):590–3. doi:10.1097/00004728-199707000-00011
  167. Voges J, Herholz K, Holzer T, Wurker M, Bauer B, Pietrzik U, et al. <sup>11</sup>C-methionine and <sup>18</sup>F-2-fluorodeoxyglucose positron emission tomography: a tool for diagnosis of cerebral glioma and monitoring after brachytherapy with <sup>125</sup>I seeds. *Stereotact Funct Neurosurg* (1997) **69**(1–4 Pt 2):129–35. doi:10.1159/000099864
  168. Wieder H, Ott K, Zimmermann F, Nekarda H, Stollfuss J, Watzlowik P, et al. PET imaging with [11C]methyl-L-methionine for therapy monitoring in patients with rectal cancer. *Eur J Nucl Med Mol Imaging* (2002) **29**(6):789–96. doi:10.1007/s00259-002-0779-4
  169. Wurker M, Herholz K, Voges J, Pietrzik U, Treuer H, Bauer B, et al. Glucose consumption and methionine uptake in low-grade gliomas after iodine-125 brachytherapy. *Eur J Nucl Med* (1996) **23**(5):583–6. doi:10.1007/BF00833397
  170. Zhang H, Yoshikawa K, Tamura K, Tomemori T, Sagou K, Tian M, et al. [(1)<sup>11</sup>C]methionine positron emission tomography and survival in patients with bone and soft tissue sarcomas treated by carbon ion radiotherapy. *Clin Cancer Res* (2004) **10**(5):1764–72. doi:10.1158/1078-0432.CCR-0190-3
  171. Ono M, Oka S, Okudaira H, Schuster DM, Goodman MM, Kawai K, et al. Comparative evaluation of transport mechanisms of trans-1-amino-3-[(1)<sup>18</sup>F]fluorocyclobutanecarboxylic acid and L-[methyl-(1)<sup>11</sup>C]methionine in human glioma cell lines. *Brain Res* (2013) **1535**:24–37. doi:10.1016/j.brainres.2013.08.037
  172. Shoup TM, Olson J, Hoffman JM, Votaw J, Eshima D, Eshima L, et al. Synthesis and evaluation of [<sup>18</sup>F]1-amino-3-fluorocyclobutane-1-carboxylic acid to image brain tumors. *J Nucl Med* (1999) **40**(2):331–8.
  173. Savir-Baruch B, Schuster DM, Jarkas N, Master VA, Nieh PT, Halkar RK, et al. Pilot evaluation of anti-1-amino-2-[<sup>18</sup>F] fluorocyclopentane-1-carboxylic acid (anti-2-[<sup>18</sup>F] FACPC) PET-CT in recurrent prostate carcinoma. *Mol Imaging Biol* (2011) **13**(6):1272–7. doi:10.1007/s11307-010-0445-3
  174. Schuster DM, Votaw JR, Nieh PT, Yu W, Nye JA, Master V, et al. Initial experience with the radiotracer anti-1-amino-3-<sup>18</sup>F-fluorocyclobutane-1-carboxylic acid with PET/CT in prostate carcinoma. *J Nucl Med* (2007) **48**(1):56–63.
  175. Amzat R, Taleghani P, Miller DL, Beitzler JJ, Bellamy LM, Nye JA, et al. Pilot study of the utility of the synthetic PET amino-acid radiotracer anti-1-amino-3-[(<sup>18</sup>F)fluorocyclobutane-1-carboxylic acid for the noninvasive imaging of pulmonary lesions. *Mol Imaging Biol* (2013) **15**(5):633–43. doi:10.1007/s11307-012-0606-7
  176. Huang C, McComathy J. Radiolabeled amino acids for oncologic imaging. *J Nucl Med* (2013) **54**(7):1007–10. doi:10.2967/jnumed.112.113100
  177. Oka S, Okudaira H, Yoshida Y, Schuster DM, Goodman MM, Shirakami Y. Transport mechanisms of trans-1-amino-3-fluoro[1-(14)C]cyclobutane-carboxylic acid in prostate cancer cells. *Nucl Med Biol* (2012) **39**(1):109–19. doi:10.1016/j.nucmedbio.2011.06.008
  178. Okudaira H, Shikano N, Nishii R, Miyagi T, Yoshimoto M, Kobayashi M, et al. Putative transport mechanism and intracellular fate of trans-1-amino-3-<sup>18</sup>F-fluorocyclobutanecarboxylic acid in human prostate cancer. *J Nucl Med* (2011) **52**(5):822–9. doi:10.2967/jnumed.110.086074
  179. Peters JC. Tryptophan nutrition and metabolism: an overview. *Adv Exp Med Biol* (1991) **294**:345–58. doi:10.1007/978-1-4684-5952-4\_32
  180. Diksic M, Nagahiro S, Sourkes TL, Yamamoto YL. A new method to measure brain serotonin synthesis in vivo. I. Theory and basic data for a biological model. *J Cereb Blood Flow Metab* (1990) **10**(1):1–12. doi:10.1038/jcbfm.1990.1
  181. Chugani DC, Muzik O. Alpha-[C-11]methyl-L-tryptophan PET maps brain serotonin synthesis and kynurenine pathway metabolism. *J Cereb Blood Flow Metab* (2000) **20**(1):2–9. doi:10.1097/00004647-200001000-00002
  182. Juhasz C, Chugani DC, Muzik O, Wu D, Sloan AE, Barger G, et al. In vivo uptake and metabolism of alpha-[<sup>11</sup>C]methyl-L-tryptophan in human brain tumors. *J Cereb Blood Flow Metab* (2006) **26**(3):345–57. doi:10.1038/sj.jcbfm.9600199
  183. Christensen M, Kamson DO, Snyder M, Kim H, Robinette NL, Mittal S, et al. Tryptophan PET-defined gross tumor volume offers better coverage of initial progression than standard MRI-based planning in glioblastoma patients. *J Radiat Oncol* (2014) **3**(2):131–8. doi:10.1007/s13566-013-0132-5
  184. Kalkner KM, Gimman C, Nilsson S, Bergstrom M, Antoni G, Ahlstrom H, et al. Positron emission tomography (PET) with <sup>11</sup>C-5-hydroxytryptophan (5-HTP) in patients with metastatic hormone-refractory prostatic adenocarcinoma. *Nucl Med Biol* (1997) **24**(4):319–25. doi:10.1016/S0969-8051(97)00064-4
  185. Koopmans KP, Neels OC, Kema IP, Elsinga PH, Sluiter WJ, Vanghillewe K, et al. Improved staging of patients with carcinoid and islet cell tumors with <sup>18</sup>F-dihydroxy-phenylalanine and <sup>11</sup>C-5-hydroxy-tryptophan positron

- emission tomography. *J Clin Oncol* (2008) **26**(9):1489–95. doi:10.1200/JCO.2007.15.1126
186. Peng F, Juhasz C, Bhamhani K, Wu D, Chugani DC, Chugani HT. Assessment of progression and treatment response of optic pathway glioma with positron emission tomography using alpha-[(11)C]methyl-L-tryptophan. *Mol Imaging Biol* (2007) **9**(3):106–9. doi:10.1007/s11307-007-0090-7
187. Minn H, Zasadny KR, Quint LE, Wahl RL. Lung cancer: reproducibility of quantitative measurements for evaluating 2-[F-18]-fluoro-2-deoxy-D-glucose uptake at PET. *Radiology* (1995) **196**(1):167–73. doi:10.1148/radiology.196.1.7784562
188. Weber WA, Ziegler SI, Thodtmann R, Hanuske AR, Schwaiger M. Reproducibility of metabolic measurements in malignant tumors using FDG PET. *J Nucl Med* (1999) **40**(11):1771–7.
189. Young H, Baum R, Cremerius U, Herholz K, Hoekstra O, Lammertsma AA, et al. Measurement of clinical and subclinical tumour response using [18F]-fluorodeoxyglucose and positron emission tomography: review and 1999 EORTC recommendations. European Organization for Research and Treatment of Cancer (EORTC) PET Study Group. *Eur J Cancer* (1999) **35**(13):1773–82. doi:10.1016/S0959-8049(99)00229-4
190. Wahl RL, Jacene H, Kasamon Y, Lodge MA. From RECIST to PERCIST: evolving considerations for PET response criteria in solid tumors. *J Nucl Med* (2009) **50**(Suppl 1):122S–50S. doi:10.2967/jnumed.108.057307

**Conflict of Interest Statement:** The authors declare that the research was conducted in the absence of any commercial or financial relationships that could be construed as a potential conflict of interest.

Copyright © 2016 Challapalli and Aboagye. This is an open-access article distributed under the terms of the Creative Commons Attribution License (CC BY). The use, distribution or reproduction in other forums is permitted, provided the original author(s) or licensor are credited and that the original publication in this journal is cited, in accordance with accepted academic practice. No use, distribution or reproduction is permitted which does not comply with these terms.



# **<sup>13</sup>C MRS and LC–MS Flux Analysis of Tumor Intermediary Metabolism**

**Alexander A. Shestov<sup>1\*</sup>, Seung-Cheol Lee<sup>1</sup>, Kavindra Nath<sup>1</sup>, Lili Guo<sup>2</sup>, David S. Nelson<sup>1</sup>, Jeffrey C. Roman<sup>1</sup>, Dennis B. Leeper<sup>3</sup>, Mariusz A. Wasik<sup>4</sup>, Ian A. Blair<sup>2</sup> and Jerry D. Glickson<sup>1,5\*</sup>**

<sup>1</sup> Laboratory of Molecular Imaging, Department of Radiology, Perelman School of Medicine, University of Pennsylvania, Philadelphia, PA, USA, <sup>2</sup> Department of Systems Pharmacology and Translational Therapeutics, Center for Cancer Pharmacology, Perelman School of Medicine, University of Pennsylvania, Philadelphia, PA, USA, <sup>3</sup> Department of Radiation Oncology, Thomas Jefferson University, Philadelphia, PA, USA, <sup>4</sup> Laboratory Medicine, Department of Pathology, Perelman School of Medicine, University of Pennsylvania, Philadelphia, PA, USA, <sup>5</sup> Department of Biochemistry and Biophysics, Perelman School of Medicine, University of Pennsylvania, Philadelphia, PA, USA

## OPEN ACCESS

### **Edited by:**

Zaver Bhujwalla,  
Johns Hopkins University  
School of Medicine, USA

### **Reviewed by:**

Cigdem Soydal,  
Ankara University Medical Faculty,  
Turkey  
Noriko Mori,  
Johns Hopkins University, USA

### **\*Correspondence:**

Alexander A. Shestov  
*ashestov@mail.med.upenn.edu;*  
Jerry D. Glickson  
*glickson@mail.med.upenn.edu*

### **Specialty section:**

This article was submitted to  
Cancer Imaging and Diagnosis,  
a section of the journal  
*Frontiers in Oncology*

**Received:** 29 March 2016

**Accepted:** 23 May 2016

**Published:** 15 June 2016

### **Citation:**

Shestov AA, Lee SC, Nath K, Guo L, Nelson DS, Roman JC, Leeper DB, Wasik MA, Blair IA and Glickson JD (2016) <sup>13</sup>C MRS and LC–MS Flux Analysis of Tumor Intermediary Metabolism. *Front. Oncol.* 6:135.  
doi: 10.3389/fonc.2016.00135

We present the first validated metabolic network model for analysis of flux through key pathways of tumor intermediary metabolism, including glycolysis, the oxidative and non-oxidative arms of the pentose pyrophosphate shunt, the TCA cycle as well as its anaplerotic pathways, pyruvate–malate shuttling, glutaminolysis, and fatty acid biosynthesis and oxidation. The model that is called Bonded Cumomer Analysis for application to <sup>13</sup>C magnetic resonance spectroscopy (<sup>13</sup>C MRS) data and Fragmented Cumomer Analysis for mass spectrometric data is a refined and efficient form of isotopomer analysis that can readily be expanded to incorporate glycogen, phospholipid, and other pathways thereby encompassing all the key pathways of tumor intermediary metabolism. Validation was achieved by demonstrating agreement of experimental measurements of the metabolic rates of oxygen consumption, glucose consumption, lactate production, and glutamate pool size with independent measurements of these parameters in cultured human DB-1 melanoma cells. These cumomer models have been applied to studies of DB-1 melanoma and DLCL2 human diffuse large B-cell lymphoma cells in culture and as xenografts in nude mice at 9.4 T. The latter studies demonstrate the potential translation of these methods to *in situ* studies of human tumor metabolism by MRS with stable <sup>13</sup>C isotopically labeled substrates on instruments operating at high magnetic fields ( $\geq 7$  T). The melanoma studies indicate that this tumor line obtains 51% of its ATP by mitochondrial metabolism and 49% by glycolytic metabolism under both euglycemic (5 mM glucose) and hyperglycemic conditions (26 mM glucose). While a high level of glutamine uptake is detected corresponding to ~50% of TCA cycle flux under hyperglycemic conditions, and ~100% of TCA cycle flux under euglycemic conditions, glutaminolysis flux and its contributions to ATP synthesis were very small. Studies of human lymphoma cells demonstrated that inhibition of mammalian target of rapamycin (mTOR) signaling produced changes in flux through the glycolytic, pentose shunt, and TCA cycle pathways that were evident within 8 h of treatment and increased at 24 and 48 h. Lactate was demonstrated to be a suitable biomarker of mTOR inhibition that could readily be monitored by <sup>1</sup>H MRS and perhaps also by FDG-PET and hyperpolarized <sup>13</sup>C MRS methods.

**Keywords:** metabolic modeling, sensitivity analysis, cancer metabolism, isotopomer, metabolic flux analysis, isotopomer, <sup>13</sup>C magnetic resonance spectroscopy, <sup>13</sup>C liquid chromatography-mass spectrometry

## INTRODUCTION

Tumor intermediary metabolism provides the energy required to sustain cancer cells over their entire life span. This energy is utilized to maintain cation pumps, including the pumps that eliminate cytotoxic drugs contributing to multi-drug resistance. It also provides energy for cellular motility during metastasis. Tumor metabolism also provides key metabolic precursors for DNA, protein, and lipid synthesis during cellular replication. Delineation of flux through these critical metabolic pathways provides an invaluable tool, complementary to genomic information, for cancer diagnosis as well as prediction and early detection of therapeutic response. Tracing these metabolic pathways was first accomplished through the use of radioactive isotopic labels, but monitoring of flux through these pathways has more recently been achieved by analysis of stable  $^{13}\text{C}$  isotope kinetics labeling detected with metabolomic tools – magnetic resonance spectroscopy (MRS) and liquid chromatography–mass spectrometry (LC–MS) – the former providing a potentially non-invasive but relatively insensitive method for imaging metabolism and the latter providing a much more sensitive but invasive approach. Analysis of these dynamic isotopolome (labeled metabolome) data used to require solution of hundreds of differential equations that could only be accomplished with the help of supercomputers (1), but today can be readily accomplished with laptop computers virtually in real time. This problem has been solved for normal organs, such as the heart (1–6), brain (7–9), and liver (10–12); our goal here is to describe the first validated solution of the problem for tumors.

We present data on human DB-1 melanoma and models of various non-Hodgkin's lymphomas (NHLs). DB-1 melanoma has served as the principal tumor model on which this technology has been developed and validated (13, 14). This technology has been applied to isolated perfused tumor cells grown *ex vivo* as monolayers on solid microcarrier beads in a bioreactor system or in flasks and to *in vivo* xenografts in mice. Isotope exchange has been monitored non-invasively *in vivo* or in intact cells by  $^{13}\text{C}$  MRS and invasively by LC–MS following *ex vivo* extraction. The NHL models have been examined by similar methods except that because they are anchorage independent, they had to be immobilized by encapsulation in agarose beads or studied in batch suspension culture. Encapsulation of cells in agarose or alginate beads invariably introduces heterogeneity in the cellular microenvironment, a problem that can be overcome by growth in batch culture from which aliquots are isolated for periodic analysis. The goal is to lay the groundwork for performing these measurements non-invasively on human patients who will be monitored in high-field ( $\geq 7\text{ T}$ ) spectrometers before and following treatment

with appropriate therapeutic agents whose choice will be at least partially dictated by metabolic flux analysis of tumors following administration of appropriate  $^{13}\text{C}$ -labeled substrates. Changes in tumor metabolism indicated by these labeling experiments will point to the probable success or failure of drug delivery and will monitor the effect of these agents on tumor metabolism.

Non-Hodgkin's lymphoma tumors have served as models for developing methods for monitoring response to signal-transduction pathway inhibitors (15) as well as response to more conventional drug combinations, such as RCHOP [Rituximab, Cyclophosphamide, doxorubicin hydrochloride (Hydroxydaunomycin), vincristine sulfate (Oncovin), and Prednisone (16, 17)]. In this review, we will focus on studies of mammalian target of rapamycin (mTOR) inhibitors as representative of the former class of targeted therapeutic agents. Drugs that are inhibitors of signal-transduction pathways are generally more cytostatic rather than cytotoxic and usually do not exhibit significant changes in tumor volume except very late in the course of therapy. For these drugs, monitoring their effect on tumor metabolism may prove to be the most efficient approach to detect therapeutic response. Since  $^{13}\text{C}$  metabolomics/isotopolomic studies are expensive and labor intensive, it may prove advantageous to identify surrogate biomarkers of therapeutic response whose metabolism could be followed by more conventional methods, such as lactate imaging by  $^1\text{H}$  MRS or  $^1\text{H}$  chemical exchange of saturation-transfer ( $^1\text{H}$  CEST), hyperpolarized  $^{13}\text{C}$  MRS or PET/CT with FDG or other appropriate metabolic probes. This two-stage approach – utilizing  $^{13}\text{C}$  MRS for initial exploration of overall tumor metabolism and identification of suitable biomarkers for subsequent follow-up by  $^1\text{H}$  MRS or other appropriate method – is a general strategy that we are proposing for monitoring signal-transduction inhibitors. The feasibility of achieving this “personalized medicine dream” or at least the  $^{13}\text{C}$  MRS exploratory phase is already demonstrated through the pioneer work of investigators at the University of Texas Southwestern, who have monitored the metabolism of  $^{13}\text{C}$ -labeled substrates by *ex vivo* analysis of surgical specimens obtained from patients with brain (18) and lung (19) tumors. Studies of human tumor xenografts in mice detected by  $^{13}\text{C}$  MRS (see below) will further demonstrate the potential feasibility of non-invasive monitoring of tumor metabolism. The purpose of this manuscript is to describe the technical details on how  $^{13}\text{C}$  isotope kinetics can be monitored and quantitatively analyzed.

## BACKGROUND

### Types of $^{13}\text{C}$ MRS Experiments

Following administration of  $^{13}\text{C}$ -labeled substrates, one can monitor the time course of distribution of the isotopic label among the various metabolites of the substrate either directly by  $^{13}\text{C}$  MRS or indirectly through  $^1\text{H}$  MRS of the protons directly bonded to the isotopically labeled carbon atoms. These methods have been extensively reviewed by de Graaf et al. (20) and will not be considered further here except to note their key advantages and limitations. Direct detection offers the advantage of simultaneously monitoring all the sites of isotopic substitution, but signal intensity will depend on the detection coil, the method used for proton decoupling as well as on the pulse sequence that is used

**Abbreviations:** AA, amino acids; ASCT2, alanine-serine-cysteine (GLN) transporter 2; BC, Bonded Cumomer; CEST, chemical exchange saturation-transfer; CMR, cellular metabolic rate; CMRatp, ATP production rate; CMRlac, Lactate production rate; FA, fatty acid; GLUT, glucose transporter; h, hours; IDH, isocitrate dehydrogenase; MCT, monocarboxylic acid transporter; MID, mass-isotopomer distribution; MRO<sub>2</sub>, O<sub>2</sub> consumption rate; oxphos, oxidative phosphorylation; PPP, pentose phosphate pathway; P/O, phosphate to oxygen ratio; RC, reductive carboxylation; SGOC, serine glycine one carbon metabolism; TCA cycle, tricarboxylic acid cycle.

for  $^{13}\text{C}$  excitation. Broadband decoupling, the method that we have employed, will simultaneously decouple all the protons and will produce nuclear Overhauser enhancements (NOE) that will depend on relaxation times, the fraction of the relaxation occurring through dipolar mechanisms and the broadband decoupling technique (e.g., MLEV and WALTZ). There will be differences in signal enhancement, and these will have to be calibrated. For *in vivo* applications, the NOEs vary between 1.3 and 2.9 for protonated carbons, and are 1.0 for unprotonated carbons or carbons that relax by non-dipolar mechanisms. Alternatively, one could use dynamic polarization-transfer excitation for direct  $^{13}\text{C}$  excitation (21, 22); this method requires quantum mechanical density matrix or product-operator analysis for quantitative interpretation, which is beyond the scope of this manuscript. In general, the direct excitation methods, delineated as  $^{13}\text{C}-\{^1\text{H}\}$ , are less sensitive than the indirect detection techniques,  $^1\text{H}-\{^{13}\text{C}\}$ , by which the protons directly bonded to the isotopically labeled carbon atoms are monitored with the  $^{13}\text{C}$  magnetization being manipulated either by simple subtraction of multiple experiments, by multiple quantum coherence transfer or by J-difference pulse sequences that depend on spin–spin coupling (20). Another key consideration in these experiments is the issue of power deposition or sample heating, which becomes limiting in the inverse-detection techniques when broadband decoupling of carbon resonances is applied and also depends on coil design and various other factors. While we note the potential signal enhancing possibilities that can be achieved with indirect detection, most investigators, and our group included, utilize simple direct  $^{13}\text{C}-\{^1\text{H}\}$  detection with broadband decoupling at least as a starting point for MRS studies of  $^{13}\text{C}$  isotope exchange kinetics.

## Metabolic Flux-Analysis Models

Metabolic flux-analysis dates back to the classic study published in 1983 by Chance, Seeholtzer, Kobayashi, and Williamson at the University of Pennsylvania and University College London, on flux through the tricarboxylic acid cycle (TCA cycle) in Langendorff perfused rat hearts (1). These investigators sacrificed large numbers of rats, excised their hearts, mounted them in a Langendorff retrograde perfusion apparatus, perfused the hearts with various  $^{13}\text{C}$  enriched substrates ([3- $^{13}\text{C}$ ] pyruvate or [2- $^{13}\text{C}$ ] acetate), freeze clamped the hearts at various time points, extracted the water soluble metabolites with perchloric acid, and analyzed the extracts with direct  $^{13}\text{C}-\{^1\text{H}\}$  MRS to measure the time course of isotopic labeling of glutamate, alanine, and aspartate. The data were fit by least-squares analysis to an idealized TCA cycle model consisting of oxaloacetate in equilibrium with aspartate, citrate,  $\alpha$ -ketoglutarate, and reactions involving glutamate, succinate, and malate. The analysis required about 325 differential equations that were solved with the aid of a Cray supercomputer. The model fit estimates of isotope enrichment of carbon atoms in glutamate and aspartate, and calculated the rate of TCA cycling, but did not attempt to validate this rate. This was accomplished later by Chatham et al. (2), who calculated the metabolic rate of oxygen consumption ( $\text{MRO}_2$ ) from the rate of production of reducing equivalents assuming that the system was at equilibrium. They compared the calculated rate with the experimental rate measured with oxygen electrodes placed at the inlet and outlet

ports of the Langendorff perfusion apparatus; MRS and  $\text{MRO}_2$  data acquisition were performed directly in the magnet on the beating heart, and the mathematical fitting was performed with a simple laptop computer. The results demonstrated that the original model proposed by Chance et al. (1) consistently predicted  $\text{MRO}_2$  values that were significantly below the experimentally measured rates. The error was attributed to the absence of the shuttles in the TCA cycle model; inclusion of the malate-aspartate and glycerophosphate shuttles in the model led to perfect agreement between experimental and model-predicted data. We believe that this was the first validated isotope enrichment model.

In 1994, Sherry and Malloy and coworkers at Dallas Southwestern (23) introduced a considerably more efficient method, isotopomer analysis, which took into account multiple sites of isotope labeling and substantially simplified the mathematics of analysis of the kinetics of isotope labeling. This method was first employed to measure relative rates of anaplerotic vs. TCA cycle flux in the heart and was later extended to monitor more extensive metabolic pathways in various organs, including liver (24–30) and brain (31–42). Comparison of experimental and predicted  $\text{MRO}_2$  values validated the cardiac isotopomer analysis model of Jeffrey et al. (3).

The motivation for developing additional theoretical framework to study the fluxome (13) came from the challenges of modern metabolic flux analysis. The details of flux analysis based on cumomers were introduced in Ref. (43). Alternative cumomer methods, such as elementary metabolite units (44), aim to minimize the dimension of variables space and to reduce the cost of computation.

More recently, Shestov and colleagues introduced bonded cumomer analysis at the University of Minnesota, where research focused primarily on the brain (45), and later at the University of Pennsylvania, where tumors were the central focus of research (14, 46). Cumomer analysis is a more efficient method of generating the various isotopomer equations. Two variants of the cumomer method are still under development, bonded cumomer analysis, which applies to the analysis of  $^{13}\text{C}$  MRS data (14, 46), and fragmented cumomer analysis (47–49) that analyzes LC-MS data. The relative efficiency of the cumomer methods is perhaps best illustrated by the fact that the original study of TCA cycle metabolism of the heart using a model that lacked inclusion of the two shuttles required about 325 differential equations to solve, whereas the current bonded cumomer model describing about 10 pathways of tumor intermediary metabolism including the TCA cycle and the pentose phosphate pathway are accomplished with ~210 differential equations that can be solved virtually in real time with an ordinary laptop computer.

## Types of $^{13}\text{C}$ Metabolic Models

Metabolic isotope kinetic models can be subdivided into steady-state and dynamic models, with the former analyzing measurements of isotope distribution after isotopic steady state has been established and the latter requiring a complete kinetic study. The kinetic analysis is much more demanding and is yet to be achieved in the clinical arena (18, 19). Steady-state measurements can only measure relative rates, normalized to some standard reference rate, such as TCA cycle flux, whereas the true kinetic

measurements yield absolute fluxes through individual metabolic pathways. Steady-state measurements can often be made on surgically excised or biopsy derived specimens, and in the case of MRS measurements, their signal-to-noise ratio can be enhanced by long-term signal averaging, but kinetic measurements have to be performed non-invasively in real time by MRS studies of isolated perfused cells grown in a suitable bioreactor contained in the NMR spectrometer or by non-invasive MRS measurements on living animals or humans. Alternatively, one can perform kinetic experiments by periodically sampling cells or extracts from a living host or from a bioreactor system. Both types of measurements may eventually prove useful in the clinic, but the hope is that high-field MRS will for the first time enable totally non-invasive studies of human subjects. Dynamic nuclear polarization already enables performance of true kinetic measurements in living animals and even in humans, but to date this has not been accomplished at normal *in vivo* concentrations; instead, *ex vivo* injections of much higher concentrations of isotopically labeled hyperpolarized specimens, most often labeled pyruvate have been utilized and monitored within about a minute in real time. The relationship of such studies to actual *in vivo* metabolism is the subject of considerable controversy and debate that requires further investigation. Even if such methods distort *in vivo* metabolism, they might still be useful for clinical diagnosis and monitoring of disease and therapy.

## Mass Spectrometric Studies of Tumor Metabolism

For dynamic isotopic labeling, DB-1 cells were cultured in glutamine-free DMEM containing 2 mM [ $\text{U}-^{13}\text{C}_5, ^{15}\text{N}_2$ ] glutamine supplemented with 10% fetal bovine serum. After 0, 0.5, 1, 2, 4, and 6 h of incubation, medium was aspirated and cells were snap frozen on dry ice. For comparing euglycemic vs. hyperglycemia conditions, cells were labeled with glutamine-free DMEM containing 2 mM [ $\text{U}-^{13}\text{C}_5, ^{15}\text{N}_2$ ] glutamine and 5 mM glucose or 25 mM glucose for 8 h. LC-MS analysis of isotopic labeled metabolites was performed as previously described (47).

## The Metabolic Network Model

We have utilized a novel three-compartment metabolic network model with the bionetwork schematically depicted in **Figure 1** to calculate fluxes through key pathways of tumor energy metabolism from  $^{13}\text{C}$  isotopic labeling data. This model includes the perfusion medium, cytosolic and mitochondrial compartments interconnected by various transporters, carriers, and enzymes that span adjacent compartments. The model is applicable to bioreactor systems and to *in vivo* data. Glucose (GLUT), monocarboxylic acid (MCT), and glutamine (GLN) transporters to the cytosolic compartment are included in the cytosolic membrane. Tumors generally express GLUT1 and GLUT3, but only GLUT1 is currently included in the model; similarly DB-1 contains MCT1 and MCT4 in approximately equal proportions (50), but since the  $K_M$  of MCT1 is approximately one-fifth that of MCT4 (51–53), we have only included MCT1. Because of the critical role of glutamine in tumor energetics and metabolism, we have also included the GLN transporter (ASCT2). This model can readily be extended to incorporate other isoforms of MCT and GLUT as well as transporters for other amino acids (AAs) and metabolites.

The following metabolic pathways are included in the network: glycolysis, TCA cycle,  $\alpha$ -ketoglutarate-glutamate, and oxaloacetate-aspartate exchange through the malate-aspartate shuttle, anaplerosis through (a) pyruvate carboxylase (PC) activity, (b) at the succinyl-CoA level, and (c) glutaminolysis through mitochondrial glutaminase (GLS and GLS2), pyruvate recycling through cytosolic (ME1) and mitochondrial malic enzymes (ME2 + ME3), lactate dehydrogenase (LDH) activity, and transport processes. Oxidative and non-oxidative branches of the pentose phosphate pathway (PPP) fluxes were included in the modeling analysis as well as *de novo* lipogenesis and fatty acid (FA) oxidation.

In order to permit access of pyruvate to the pyruvate dehydrogenase complex (PDH) complex for conversion to acetyl-CoA and incorporation into the TCA cycle, we have included the mitochondrial pyruvate carrier (MPC), which was recently identified in all mammalian cells (54–56). Pyruvate is also linked to the TCA cycle via PC. The cytosolic compartment with direct links through the mitochondria to the TCA cycle also contains citrate, glutamate, and malate. As noted above, the mitochondrial compartment contains the complete TCA cycle with links to the cytosol for citrate and malate.  $\alpha$ -Ketoglutarate is linked to glutamate via glutamate dehydrogenase (GLUD) and two aminotransferases, aspartate aminotransferase (GOT), and alanine aminotransferase (GPT).

In order to fit  $^{13}\text{C}$  time courses of labeled lactate, glutamate and FAs to determine the corresponding metabolic fluxes and the transport parameter for bidirectional lactate transport through the cell membrane, we constructed a BC dynamic model adapted to perfusion bioreactor experiments. In the model, the perfused [1,6- $^{13}\text{C}_2$ ] glucose and glutamine (labeled in some experiments, see below) are transported from the extracellular medium to the DB-1 cells. Reversible non-steady-state Michaelis–Menten facilitative transport kinetics are assumed to occur through glucose (GLUT family) or glutamine (ASCT2) transporters:

$$J_i^{\text{tr}} = \frac{J_{\text{tr}}^{\max} \left( \frac{M_{ei}}{K_{mi}^{\text{tr}}} - \frac{M_i}{K_{mi}^{\text{tr}}} \right)}{1 + \frac{M_{ei}}{K_{mi}^{\text{tr}}} + \frac{M_i}{K_{mi}^{\text{tr}}}}, \quad (1)$$

where  $J_i^{\text{tr}}$  is the net transport flux for boundary species  $i$  between media and cytosol or cytosol and mitochondria;  $M_{ei}$  is the extracellular concentration for species  $i$ ,  $J_{\text{tr}}^{\max}$  is the maximal transport rate, and  $K_{mi}^{\text{tr}}$  is the Michaelis–Menten constant for transport. Labeled lactate from the cell is transported into the medium while obeying Michaelis–Menten kinetics through the monocarboxylic acid transporter (MCT family). Facilitated media-cell transport is assumed for glucose, lactate, and glutamine.

Two types of mass balance equations for chemical and isotope variables were expressed mathematically using the mass balance equation for the total metabolite concentration in the medium, cytosol, and mitochondria:

$$\frac{dM_i}{dt} = J_i^{\text{tr}} + \sum_j v_i^{pj} F_i^{pj} - \sum_k v_i^{uk} F_i^{uk}, \quad (2)$$

where  $M_i$  is the intracellular concentration of the  $i$  species,  $J_i^{\text{tr}}$  is the net transport flux for boundary species  $i$  between media and cytosol or cytosol and mitochondria,  $F_i^{pj}$  and  $F_i^{uk}$  are the normalized reaction fluxes that produce ( $j$ ) or utilize ( $k$ ) cellular species  $i$ ,

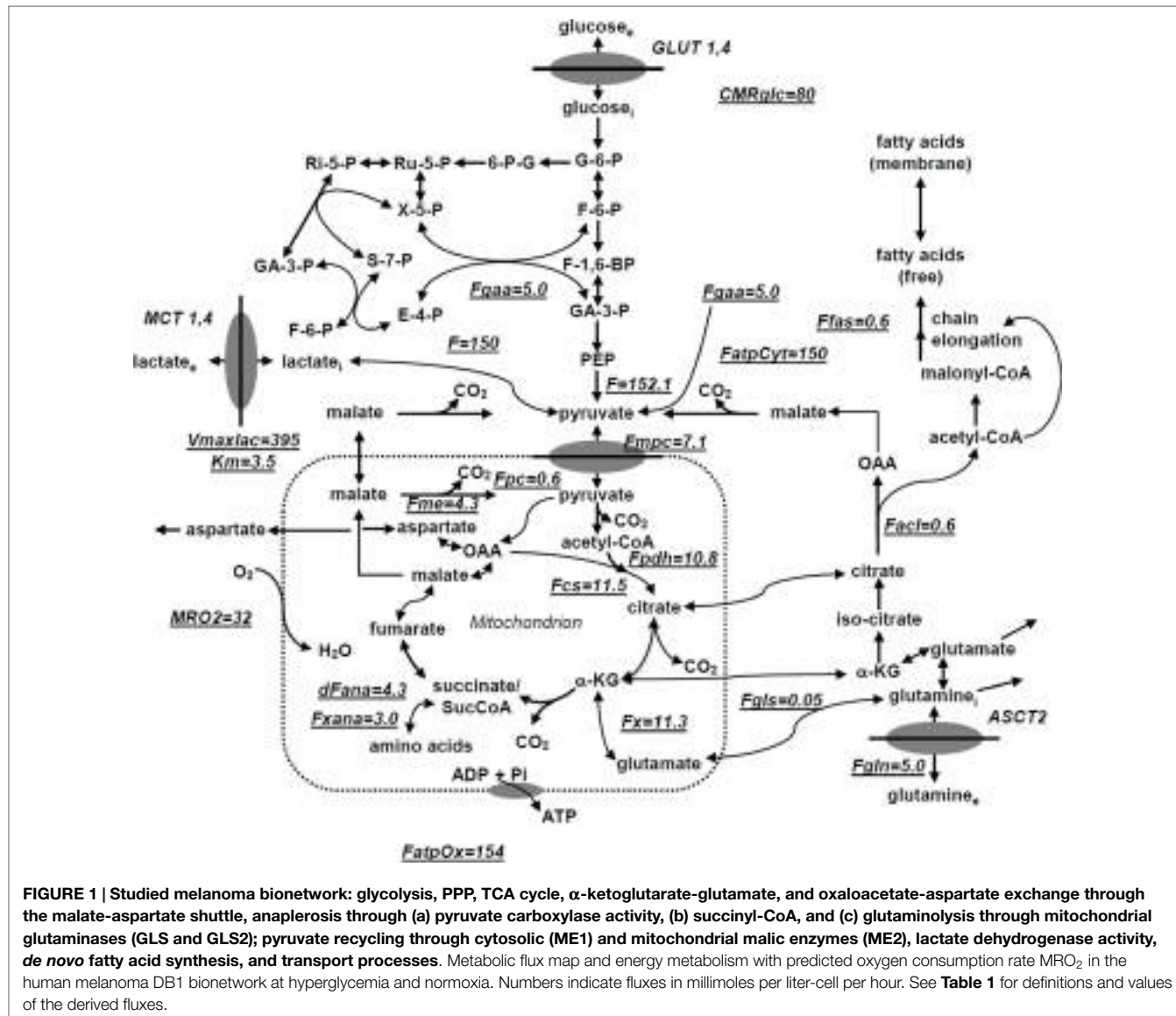


**FIGURE 1 | Studied melanoma bionetwork: glycolysis, PPP, TCA cycle,  $\alpha$ -ketoglutarate-glutamate, and oxaloacetate-aspartate exchange through the malate-aspartate shuttle, anaplerosis through (a) pyruvate carboxylase activity, (b) succinyl-CoA, and (c) glutaminolysis through mitochondrial glutaminases (GLS and GLS2); pyruvate recycling through cytosolic (ME1) and mitochondrial malic enzymes (ME2), lactate dehydrogenase activity, *de novo* fatty acid synthesis, and transport processes. Metabolic flux map and energy metabolism with predicted oxygen consumption rate MRO<sub>2</sub> in the human melanoma DB1 bionetwork at hyperglycemia and normoxia. Numbers indicate fluxes in millimoles per liter-cell per hour. See Table 1 for definitions and values of the derived fluxes.**

and  $v_i^{pj}$  and  $v_i^{uk}$  are the corresponding stoichiometric coefficients. The following general dynamic mass balance equations were used to describe the extracellular boundary metabolites in the medium:

$$\frac{dM_e}{dt} = r_{ie} \times J_i^{\text{tr}}, \quad (3)$$

where extracellular species concentration is  $M_e$ , and  $r_{ie}$  is the ratio of cell volume to media volume. We also included an additional term for the medium flow rate. Note that we do not assume here that media boundary metabolites are at constant concentration.

## Bonded Cumomer Analysis

One can monitor flux through the biochemical network model by measuring changes in isotopic enrichment of individual carbons in a molecule containing N carbon atoms. This yields a total of N-independent time-courses or steady-state values. However, by considering all the different combinations of labeled and

unlabeled carbons, isotopomer models take full advantage of the biochemical information that can be obtained from the NMR spectra, yielding a total of  $2^N - 1$  independent variables for a molecule with N different carbon atoms. Because not all possible isotopomers are detectable by NMR, a model including all possible isotopomers would be unnecessarily complex. The concept of *bonded cumomers* leads to a reduced number of equations as well as a more simple derivation of these equations compared to a model, including all possible isotopomers, while retaining all the NMR measurable isotopomer information.

Let  $M_{\{i\}}$  denote the isotopomer of a metabolite M, where  $\{i\}$  is a set of integers  $i_1, i_2, \dots, i_n$  indicating the positions of all the labeled carbons. We refer to  $m_{\{i\}}$  as the isotopomer fraction  $[M_{\{i\}}]/[M]$  of molecules M labeled exactly at positions  $i_1, i_2, \dots, i_n$ . A cumulative isotopomer fraction (or cumomer fraction), noted as  $p_{M_{\{i\}}}$  is by definition, the sum of isotopomer fractions for all isotopomers labeled at least at positions  $i_1, i_2, \dots, i_n$ , whatever the label at the other positions. We refer to the size n of the set  $\{i\}$  as the order of

the p-function. For example, assuming that M has a total of four carbons, the second order p-function  $p_{M\{1,3\}}$  can be expressed as:

$$p_{M\{1,3\}} = m_{\{1,3\}} + m_{\{1,2,3\}} + m_{\{1,3,4\}} + m_{\{1,2,3,4\}} \quad (4)$$

For example, the cumomer fraction  $p_{M\{1,3\}}$  for cumomer M{1,3} is the probability that both the first and third carbon atoms of this molecule are labeled. Shestov et al. (45) have presented a complete exposition of the bonded cumomer formalism. Here, we will present examples of how this formalism can be utilized to efficiently monitor flux through the various metabolic pathways in **Figure 1** in various types of perfused cells and in xenografts of these tumor cells in immunosuppressed mice. These examples illustrate the type of information that can be obtained from similar dynamic studies performed on human tumors *in situ* or from extracts of biopsy or surgically excised freeze-clamped specimens of these tumors measured at isotopic steady state.

Isotopomer dynamics of this system together with the initial metabolome state vector  $M_0 \in R^N$  and fluxome  $F_0 \in R^M$  (subscript “0” refers to baseline steady-state values and reaction rates) are formulated as an initial value problem for ordinary differential equations (ODE) in terms of Bonded Cumomer fractions as the state variables. Metabolite  $^{13}\text{C}$  cumomer mass balance for parallel monomolecular reactions was expressed in the form:

$$[M] \frac{d\pi_{(i)}}{dt} = \sum_j F_j \pi_{\sigma j(i)} - \left( \sum_k F_k \right) \pi_{(i)}, \quad (5)$$

where metabolite  $M$  with pool size  $[M]$  is downstream of metabolites  $S_j$ . While  $\pi_{(i)}$  and  $\pi_{\sigma j(i)}$  represent the  $i$ th cumomer fraction of metabolite  $M$  and metabolite  $S_j$  ( $i$  Bonded Cumomer), respectively. The total outflux  $\sum F_k$  balances influx  $\sum F_j$ .

Shestov and coworkers (45) have described how isotopomer balance equations have been derived for every metabolite Bonded Cumomer of orders 1, 2, 3 (e.g., glutamate, glutamine, aspartate). This resulted in a set of ~210 differential equations with fine structure multiplets completely described by each metabolite’s Bonded Cumomers of order 1, 2, and 3. Wiechert et al. (43) first proposed the term cumomer, and the concept of cumomer was used by Muzykantov and Shestov (57) in early studies. There are connection matrices between the “Bonded Cumomer”  $\pi$  vectors (which reflect subsets of metabolite isotopomers) and the vectors of “fine structure” multiplets of  $^{13}\text{C}$  NMR spectra (singlets, doublets, triplets, and quartets of  $^{13}\text{C}$ -labeled metabolite). Using matrix connection equations, one derives kinetic equations in the form of fine-structure spectroscopic-defined NMR data.

The fitted time-courses for [1,6- $^{13}\text{C}_2$ ] glucose perfusion were: Glu4Tot (Tot-total), Glu4s, Glu4d34, Glu3Tot, Glu3d, Glu2Tot, Glu2s, Lac3Tot, and acyl methylene  $(-\text{CH}_2)_n-$  resonance, for a total of nine curves from which we determined the following free fluxes: melanoma TCA cycle  $F_{\text{TCA}}$ , PC  $F_{\text{PC}}$ , exchange between glutamate and  $\alpha$ -ketoglutarate  $F_X$ , anaplerotic exchange and net flux at the level of SucCoA,  $F_{\text{ANA}}$ , mitochondrial malic enzyme (ME2 + ME3) activity, *de novo* FA production, glutaminolysis, aspartate efflux, and three other parameters – Michaelis–Menten lactate transport  $V_{\text{max}}^{\text{LAC}}$  and  $K_m^{\text{LAC}}$  and total cellular lactate concentration. Based on flux balance analysis including non-oxidative

glycolytic flux CMRlac and others, we also calculated other fluxes and parameters, including the Warburg parameter (ratio of flux from pyruvate to lactate vs. pyruvate to the MPC). Using the Runge–Kutta fourth-order procedure for stiff systems in terms of Bonded Cumomers, we solved these differential equations to obtain time courses for all possible fine structure  $^{13}\text{C}$  multiplets of glutamate, glutamine, and aspartate. Minimization of the cost function was performed using Broyden–Fletcher–Goldfarb–Shanno or Simplex algorithms. By verifying that goodness-of-fit values were close to expected theoretical values, we confirmed proper mean-square convergence. Monte Carlo simulations with experimental noise levels were used to calculate parameter errors (58). All numerical procedures were carried out in Matlab (Mathworks, Natick, MA, USA).

Liquid chromatography-mass spectrometry data without detailed flux analysis were utilized to compare fluxes under different conditions (e.g., hyperglycemia vs. euglycemia) since no statistically significant change was observed between the different medium glucose concentrations.

## Metabolic Isotopomer Control Analysis for Bonded Cumomer Models

Metabolic control analysis (MCA) was originally proposed to quantify sensitivity – i.e., to measure the effect of changes in any parameter of a system on the other variables in that system. This approach was developed independently by two groups in the 1970s (59, 60) and has been limited to systems at steady state. In this approach, the sensitivity of changes in variables, such as metabolite concentrations due to changes in other parameters is quantified by control coefficients. Metabolic control coefficients are used for comparison of many parameters that span several orders of magnitude. A control coefficient is defined as the relative change in the variable per relative change in the parameter, when infinitesimal changes are introduced:

$$C_p^R = \left( \frac{\partial R/R}{\partial p/p} \right)_{ss} = \left( \frac{\partial \ln R}{\partial \ln p} \right)_{ss}, \quad (6)$$

where  $p$  is varied parameter and  $R$  is a system response, e.g., concentration or flux; the subscript ss indicates steady state. Sensitivity analysis measures the robustness of the metabolic model and network topology to variations in parameter values. The robust parameters with greatest influence on model simulation can help to identify critical fluxes and pathways. These fluxes also have less experimental error. Here, we extend the MCA technique to dynamic metabolic flux analysis in which the behavior of interest occurs in the temporal responses. First, we introduce the dynamic isotopomer control coefficient or the sensitivity function:

$$ICC_k^i = \left( \frac{\partial \pi_{(i)}/\pi_{(i)}}{\partial F_k/F_k} \right), \quad (7)$$

where  $\pi_{(i)}$  represents the  $i$ th cumomer fraction of metabolite  $M$ , and  $F_k$  is a certain parameter, such as a flux. By introducing these variables, isotopomer sensitivity equations can be derived by differentiating dynamic bonded cumomer balance equations (Eq. 5) with respect to identified fluxes or other parameters that yield

the corresponding initial value Cauchy problem for non-linear ODE. The dynamic sensitivity equations determine the time evolution of isotopomer control coefficients. These consist of a large number of equations that must be solved simultaneously with the initial system (1) resulting in double the number of differential equations. These characteristics of the output sensitivity matrix with respect to the flux vector  $F$  and other parameters provide a framework for analysis of isotopomer model robustness. By simulating the dynamic time course of sensitivity functions, one identifies the fluxes most sensitive to a particular bonded cumomer of a metabolite and  $^{13}\text{C}$  fine structure multiplet. **Figure 2A** displays calculated values of those dynamic isotopomer control coefficients (or relative sensitivity functions).

We also computed the sensitivity of the mean squared difference between experimental and corresponding model output (i.e., error) to finite changes in parameter values. The sensitivity to each parameter was calculated as the relative change in mean squared error (MSE) due to 5% change in the given parameter value:

$$S_i = \frac{\max |(E(p_i \pm 0.05p_i) - E(p_i))|}{\frac{0.05p_i}{p_i} * E(p_i)}, \quad (8)$$

where  $E$  represents the minimum mean squared difference between model simulation and experimental data. These sensitivity values represent the degree to which the theoretical curves are sensitive to the value of individual parameters. High values of the sensitivity parameter  $S_i$  indicate that changing a parameter  $p_i$

results in a significant change in the simulated curves and in the MSE  $E$ .

**Figure 2B** shows calculated MSE sensitivities for several free fitted fluxes.

## Applications of Metabolomics to Melanoma and Lymphoma

To illustrate the application of these techniques to studies of human cancer, we will describe studies of human melanoma models grown in culture, as perfused tumor cells grown on solid microcarrier beads and as xenografts in immunosuppressed mice. The cell studies will be utilized to validate the bonded cumomer model and to estimate the contributions of glycolytic metabolism and mitochondrial metabolism to ATP production under hyperglycemic (26 mM) and euglycemic (5 mM) conditions. Effects of euglycemia and hyperglycemia on glutamine metabolism, flux through the pentose shunt and FA metabolic pathways will also be evaluated using both  $^{13}\text{C}$  MRS and bonded cumomer analysis as well as LC-MS and fragmented cumomer analysis.

To demonstrate how  $^{13}\text{C}$  MRS and LC-MS can be used to detect response to signal-transduction inhibitors, we will present data on the effect of rapamycin, a well known inhibitor of the mTOR pathway, on DLCL2 human diffuse large B-cell NHL cells grown in culture as perfused cells immobilized by encasement in agarose beads and as xenografts in immunosuppressed mice. We will

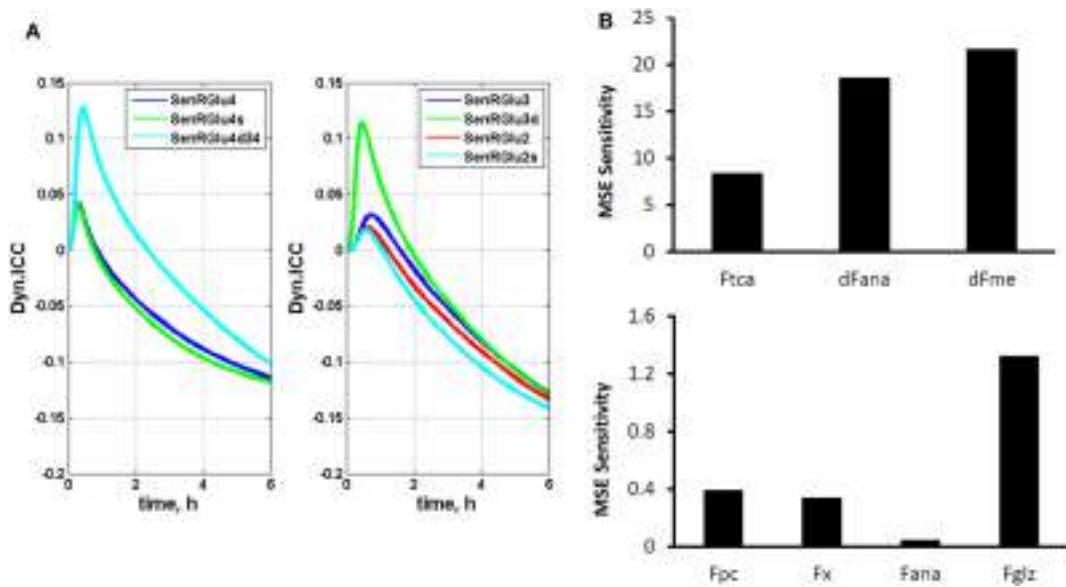


**FIGURE 2 | The dynamic multiplet control coefficients and sensitivity analysis. (A)** In the left panel, the dynamic multiplet control coefficients are shown with respect to glutaminolysis flux for the glutamate-C4 total and doublet C4d34 and singlet C4s multiplets and the glutamate-C3 and glutamate-C2 total and their multiplets (right panel) during perfusion with medium containing [1,6- $^{13}\text{C}_2$ ] glucose and unlabeled glutamine. Data show the time courses of normalized multiplet sensitivities to variation of the glutaminolysis flux. For simulation, the conditions were chosen to optimize extracted fluxes, while glutaminolysis flux was set at 5% of the TCA cycle flux. The glutamate doublet 4d34 is the most sensitive glutamate multiplet to measure glutaminolysis net flux during the first ~1.5 h, and afterwards the 4s singlet becomes more sensitive. The data in the right panel demonstrate the superior sensitivity of the glutamate 3d doublet at the beginning and glutamate 2s singlet after ~1.5 h. **(B)** Total relative mean squared error (MSE) sensitivity function output during perfusion with medium containing [1,6- $^{13}\text{C}_2$ ] glucose and unlabeled glutamine with respect to free fitted fluxes. Upper panel shows the sensitivities to the TCA cycle, anaplerotic net flux at the level of SuccCoA and mitochondrial malic enzyme activities; and lower panel shows MSE sensitivities to the pyruvate carboxylase (pc), exchange flux  $\alpha\text{-Kg} \leftrightarrow \text{glu}$  (x), exchange flux at the level of SuccCoA (ana) and glutaminolysis flux (gls). Note also the significant sensitivities for the fluxes in the upper panel and higher sensitivity for glutaminolysis compared to other fluxes in the lower panel.

demonstrate that response to this inhibitor can also be monitored by  $^1\text{H}$  MRS lactate imaging in cells and in xenografts. Ultimately, the goal will be to translate these methods into the clinic to manage human NHL patients. Preliminary studies leading to this approach have been published (15).

## MATERIALS AND METHODS

### Cell Culture

The human DB-1 melanoma cell line was derived by David Berd from a lymph node metastasis of one of his patients (Thomas Jefferson University Hospital, Philadelphia, PA, USA) before administration of any treatment. Cells were cultured from the tumor and cryopreserved after the 16th passage. Monoclonal antibodies were used to confirm cell surface antigens (61). DB-1 cells were grown as monolayers for routine culture at 37°C in 5% CO<sub>2</sub> in α-MEM medium supplemented with 10% fetal bovine serum, 2 mM glutamine, 26 mM glucose, and 1% (v/v) non-essential AAs and 10 mM HEPES buffer. In tissue culture flasks, the doubling time was 48 h (50). The V600E BRAF mutation is expressed by the DB-1 cells.

### Cell Perfusion and NMR Spectroscopy

For NMR studies of perfused tumor cells, DB-1 cells were cultured in DMEM with 1% non-essential AAs (Invitrogen, Grand Island, NY, USA), 10% fetal bovine serum, 10 mM HEPES, 4 mM glutamine, and 26 mM glucose (complete DMEM). Approximately  $5 \times 10^8$  cells were grown on the surface of non-porous microcarriers that had a mean diameter of 170 microns (Solohill, Ann Arbor, MI, USA). These microcarriers were coated with either collagen or ProNectin® to enhance cell attachment and proliferation and tightly packed inside a 20 mm NMR tube in which they were perfused continuously in the open bioreactor system. Mancuso et al. (62) have published a detailed description of the perfusion system, including flow rates, cell adhesion procedures, etc.

The method of Bental et al. (63) was used to immobilize lymphoma cells (DLCL2) by encapsulation into agarose beads. In brief, we thoroughly mixed 1.5 ml of  $\sim 5 \times 10^8$  cells in culture medium with an equal volume of the low-temperature-gelling agarose at 37°C and magnetically stirred the mixture after addition of 3 ml paraffin oil at 37°C generating the cell-encapsulated spherical beads with 100–200  $\mu\text{m}$  diameters. The beads were cooled by continuous stirring, and the oil was removed by centrifugation. The encapsulated cells were then loaded into a 10 mm NMR tube connected to the perfusion system.

Medium was circulated through the microcarriers or agarose gel at a flow rate of 12 ml/min with a peristaltic pump (Masterflex, Cole Parmer, Chicago, IL, USA). A gas-exchange module consisting of a silicone membrane (thin-wall silicone tubing) was situated before the perfusion chamber along the medium flow path for removal of carbon dioxide and addition of oxygen. The oxygen level was measured continuously with a polarographic oxygen probe (Mettler-Toledo, Columbus, OH, USA) situated at the inlet port to the perfusion chamber and maintained at a steady-state pressure near air saturation. The medium was then warmed to 40°C, and a second polarographic oxygen probe was used to detect the oxygen level of the medium coming out of the NMR

tube permitting the oxygen consumption rate of the culture to be monitored continuously from the decrease in pO<sub>2</sub>. A pH probe (Mettler-Toledo, Columbus, OH, USA) was inserted downstream of the outlet oxygen probe. Adjustment of the level of CO<sub>2</sub> in the gas-exchange module was used to modify/maintain the pH of the medium. The temperature of the medium entering the NMR tube was monitored with a thermocouple at the exit port of the perfusion chamber and was fine-tuned with a microstat-controller and an electrical resistance heater to 37.0 ± 0.2°C. The glucose concentration in the recirculating medium was maintained at a constant level (clamped) by continuously feeding fresh medium typically at a flow rate of 24 ml/h and removing depleted medium from a recirculation bottle while maintaining the total volume of recirculating medium at 120 ml. During  $^{13}\text{C}$  experiments, 32 mM [1,6- $^{13}\text{C}_2$ ] glucose was fed into the system, and the recirculating glucose level was clamped at 26 mM by adjusting the feed rate.

$^{13}\text{C}$  NMR spectra were acquired with standard  $^1\text{H}$  decoupled NOE  $^{13}\text{C}$  acquisition on a 9.4 T/89 mm vertical bore Varian spectrometer (Varian Inc., Palo Alto, CA, USA) with acquisition parameters: 60° pulse angle, 1.2 s repetition rate, 25,000 Hz spectral width, 16,384 points, and 750 transients per spectrum. Free-induction decays were apodized by exponential multiplication (2 Hz) for signal to noise enhancement and peak areas were measured with Nuts NMR (Acorn NMR, Fremont, CA, USA) software. The number of cells in the NMR tube was determined from the total NTP level measured by  $^{31}\text{P}$  NMR as described previously (64) using the following spectral parameters: 60° pulse angle, 1 s repetition rate, 15,000 Hz, 1,200 transients.

Melanoma cells were initially studied under normoxic hyperglycemic (26 mM glucose) conditions to enhance lactic acidosis (65, 66) and subsequently under normoxic euglycemia (5 mM glucose) to more closely simulate *in vivo* conditions. The effect of these changes in glucose concentration on flux through various pathways of tumor metabolism was determined over a ~6 h time course during which the kinetics of labeling of lactate, glutamate and other metabolites was monitored. The estimated TCA cycle flux was compared to the oxygen consumption flux to test the accuracy of the calculations.

### In vivo animal studies

Immunosuppressed mice were used for *in vivo* studies. Tumors were developed by subcutaneous implantation of tumor cells to the flanks of nude mice. NMR studies on mice were performed using a home-built  $^{13}\text{C}/^1\text{H}$  dual-tuned probe at 9.4 T (Varian Inc.). All animal studies were approved by the Institutional Animal Care and Use Committee (IACUC) of the University of Pennsylvania, and performed in accordance with its regulatory standards.

### Statistical Analysis

Student's *t*-test was used to calculate *p*-values. *P*-values <0.05 were considered significant.

## RESULTS AND DISCUSSION

### Melanoma Studies

Determination of the relative levels of glycolytic and oxidative metabolism of specific tumors plays an important role in

development of strategies for treating neoplasms and for choosing appropriate methods to detect tumor response to specific therapies. Development of a non-invasive method for quantifying the fraction of ATP production by tumors that occurs by glycolytic and mitochondrial metabolism would be very useful in the management of cancer patients and tailor-fitting of therapeutic regimens to their individual needs. In addition, various other pathways of tumor metabolism play critical roles in tumor proliferation by providing essential precursors for cell replication. We, therefore, sought to develop a method for quantitating tumor intermediary metabolism in cells with appropriate extension to animal tumor models and eventually to human cancer patients.

## Metabolic Fate of [1,6-<sup>13</sup>C<sub>2</sub>] Glucose in DB-1 Cells

The entire metabolic network that is included in the current analysis is depicted in **Figure 1**. **Figures 3A** and **4** summarized <sup>13</sup>C labeling kinetics of DB-1 melanoma cells grown at a constant glucose level of 26 mM. Dynamic <sup>13</sup>C NMR spectra obtained during the experiment appear in **Figure 3A**. We detected resonances of C3 lactate, C2, C3, and C4 glutamate, C2 and C3 of aspartate, and fatty acyl carbons. Under hyperglycemic conditions (26 mM glucose), lactate labeled at C3 (20.9 ppm) appeared in the spectrum within the first few minutes (**Figures 3A** and **4C**). Levels of this metabolite increased throughout the experiment but did not reach saturation. Lactate resonance intensity was the combined result of the biological rate of lactate formation and the rates of washout of lactate due to the continuous addition of fresh medium and withdrawal of spent medium from the perfusion system. Fifteen minutes after introduction of labeled glucose, isotopic <sup>13</sup>C incorporation in C4 of glutamate (34.3 ppm) was detected; **Figure 4A** shows the full-time course for labeling results for this resonance. The concentration of C4-labeled glutamate increased linearly for ~1 h. Satellites were subsequently detected indicating the presence of <sup>13</sup>C-<sup>13</sup>C coupling between glutamate-C4 and glutamate-C3 (1). The rate of labeling of glutamate exclusively on

C4 (producing a singlet peak) gradually slowed and approached steady state after approximately 6 h. The level of coupled glutamate labeled at both C3 and C4 continued to increase steadily throughout the experiment. Labeling of the glutamate-C3 resonance at 28.8 ppm is displayed in **Figures 4A,B**. <sup>13</sup>C labeling of this carbon increased linearly but did not reach saturation. Approximately, two-thirds of the C3 glutamate carbon was coupled (predominantly to glutamate-C4). Within 1 h, glutamate-C2 labeling was detected (**Figures 4A,B**). However, only a singlet was observed for the first 3 h, unlike glutamate-C3 which exhibited multiplet structure. Subsequently, a doublet appeared due to the presence of glutamate-C2,3 labeling after carbon 1 was removed from glutamate-C3,4 during the third turn of the TCA cycle (1).

Labeling was also observed in long chain FAs at approximately 30 ppm, indicating that DB-1 melanoma cells produce lipid *de novo* from glucose (see **Figure 4D**), consistent with results for other cancer cell lines grown in culture (67). Low levels of labeling of aspartate-C2 and C3 were also observed. Labeling of alanine was not detected, probably due to the low total concentration of this AA; this result is unusual since most cancer cell lines produce <sup>13</sup>C-labeled alanine from glucose (62, 67). Resonances were observed at approximately 65 ppm, a spectral region associated with the glycerol backbone of phospholipids in triglycerides as well as other glycolytic intermediates.

## Quantifying Bionetwork Fluxes

We utilized Bonded Cumomer analysis to fit <sup>13</sup>C NMR DB-1 melanoma data acquired during continuous perfusion of cells with [1,6-<sup>13</sup>C<sub>2</sub>] glucose in the bioreactor system. Isotopomer time course data were converted to <sup>13</sup>C-metabolite concentration curves (**Figure 4**). Only those multiplets with end-point concentrations >0.5 mM were used in the fitting procedure in order to minimize the bias introduced by using multiplets with low signal to noise ratio. Since the noise level of the remaining experimental multiplets was expected to be high (not shown), these resonances were used only as reference points for visually examining the fit predicted for low intensity curves to experimental data but not

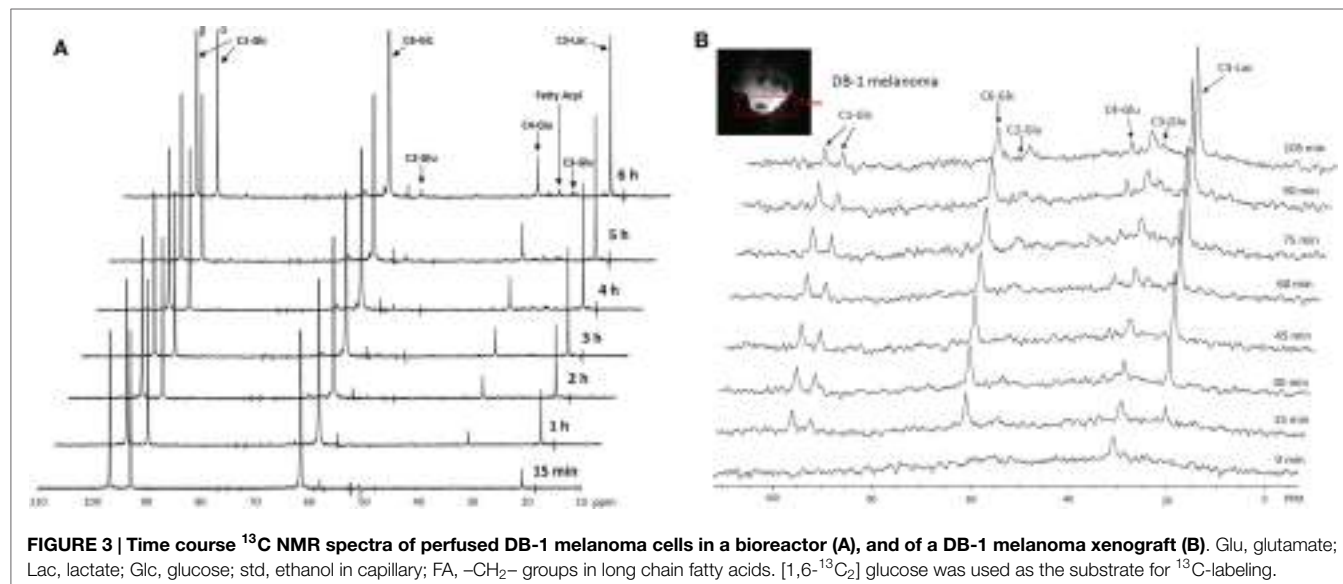
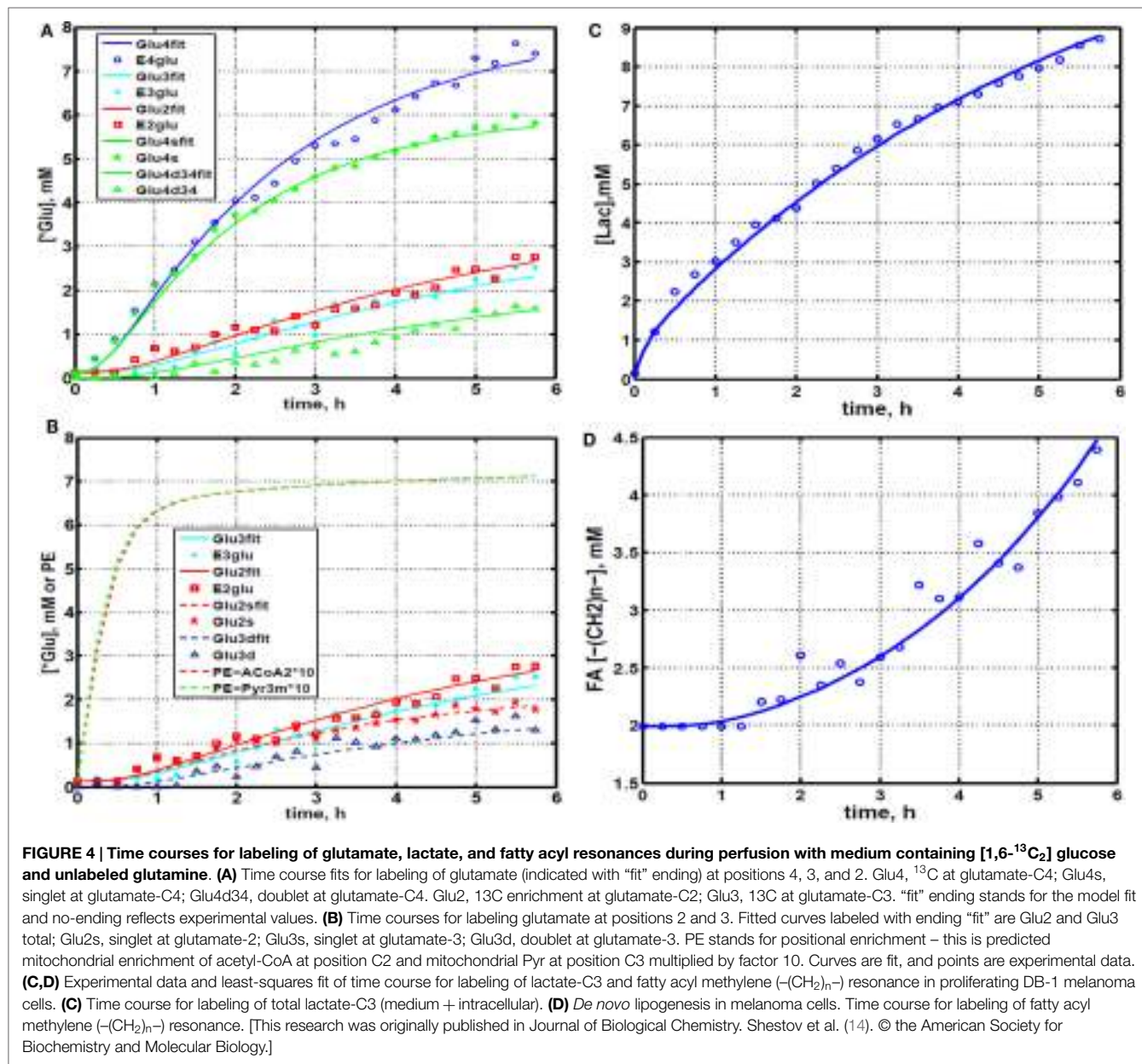


**FIGURE 3 |** Time course <sup>13</sup>C NMR spectra of perfused DB-1 melanoma cells in a bioreactor (A), and of a DB-1 melanoma xenograft (B). Glu, glutamate; Lac, lactate; Glc, glucose; std, ethanol in capillary; FA, -CH<sub>2</sub>- groups in long chain fatty acids. [1,6-<sup>13</sup>C<sub>2</sub>] glucose was used as the substrate for <sup>13</sup>C-labeling.



for calculating the goodness of fit of these metabolite resonances. Four types of measurements were used to quantify tumor central metabolic fluxes: three sets of time courses of (1) glutamate isotopomers (multiplets), (2) total lactate-C3 labeling, (3) acyl groups of FA resonances determined by NMR *in situ*, and (4) steady-state  $^{13}\text{C}$  NMR lactate isotopomers. The following time courses were utilized in the curve-fitting procedure: Glu4Tot (Total: Tot), Glu4s, Glu4d34, Glu3Tot, Glu3d, Glu2Tot, Glu2s, Lac3Tot, and acyl methylene  $(-\text{CH}_2)_n-$  resonance, yielding a total of nine curves. Estimation of the model-free parameters was achieved by fitting labeling patterns of glutamate, lactate, and FAs acyl methylene groups. Table 1 and the flux map in Figure 1 summarized the fluxes determined by the fitting procedure. Monte Carlo simulations were used to estimate errors in parameters included in Table 1.

## Model Validation

To validate the bonded cumomer network model, we compared parameters inferred from the model with experimentally determined values. We measured the  $\text{O}_2$  consumption rate ( $\text{MRO}_2$ ) with polarographic oxygen probes during the perfusion experiment. The fluxes obtained by fitting of dynamic  $^{13}\text{C}$  data produced good agreement between the experimentally observed oxygen consumption rate, 33 mmol/L-cell/h, and the calculated  $\text{MRO}_2$ , 32 mmol/L-cell/h (see Tables 2 and 3). The experimental total glutamate concentration was 8.6 mM that was in good agreement with the calculated glutamate pool size of 9.2 mM. The measured glucose consumption rate ( $\text{MRglc}$ ) was 90 mmol/L-cell/h, that compared favorably with the predicted  $\text{MRglc}$  of 81 mmol/L-cell/h. The measured lactate production flux ( $\text{CMRlac}$ ) was 155 mmol/L-cell/h, whereas the predicted  $\text{CMRlac}$  was

**TABLE 1 | Extracted fluxes using bonded cumomer modeling.**

Reaction	Flux (mmol/L-cell/h) <sup>a</sup>
Pentose phosphate pathway (oxidative branch), net PPP F <sub>pppOx</sub>	3.3 ± 72%
Transketolase 1 (exchange) relative to glycolysis, TK1	21 ± 56%
Transketolase 2 (exchange) relative to glycolysis, TK2	0.5 ± 90%
Transaldolase (exchange) relative to glycolysis, TA	44 ± 64%
Glucogenic amino acids contribution to pyruvate, F <sub>gaa</sub>	5.0 ± 20%
TCA cycle rate, F <sub>tca</sub> (isocitrate → α-Kg)	10.9 ± 8%
Exchange, Mal-Asp shuttle, F <sub>x</sub> (reversible)	11.3 ± 19%
Pyruvate carboxylase Flux, F <sub>pc</sub>	0.6 ± 51%
Anaplerotic exchange flux at SucCoA, F <sub>xana</sub>	3.0 ± 15%
Net Anaplerotic flux to the TCA cycle, dF <sub>ana</sub>	4.3 ± 15%
Flux of ketogenic AA and FA to Acetyl-CoA formation, F <sub>kaa</sub>	0.1 ± 19%
Glutaminolysis Flux, F <sub>gls</sub>	0.05 ± 60%
Pyruvate dehydrogenase Flux, F <sub>pdh</sub>	10.8 ± 16%
Citrate synthase flux, F <sub>cs</sub>	11.5 ± 14%
Net fumarase activity, Fum → Mal, F <sub>fum</sub>	15.3 ± 16%
Fatty acids synthesis, F <sub>fas</sub>	0.59 ± 15%
Mitochondrial pyruvate transport, F <sub>mpc</sub>	7.1 ± 23%
Malic enzyme (mitochondrion), ME2 + ME3, F <sub>mec</sub>	4.3 ± 12%
Malic enzyme (cytosolic), ME1, F <sub>mec</sub>	0.6 ± 15%
Aspartate efflux, dF <sub>xasp</sub>	0.06 ± 45%
Production Flux of ATP, glycolytic, Warburg, F <sub>atpCyt</sub>	150 ± 13%
Production Flux of ATP, mitochondrial, ophos, F <sub>atpOx</sub>	154 ± 12%
Warburg parameter (net LDH/MPC flux ratio)	21 ± 24% (unitless)
Combined glycolysis and PPP flux from G6P to pyruvate	152.1 ± 12%
Glutamine consumption flux (for protein, nucleotides, amino acids, glutathione, etc)	4.9 ± 10% <sup>b</sup>
Net LDH activity, Pyr → Lac, F <sub>ldh</sub>	150 ± 12%
Lactate transport, V <sub>maxlac</sub>	395 ± 12%
Lactate transport, Michaelis–Menten parameter, K <sub>m</sub>	3.5 mM ± 70%

<sup>a</sup>Calculated rates of flux are expressed in millimoles per liter-cell per hour with relative SDs in percent for pathways shown in **Figure 1**. Warburg parameter is the ratio of the net flux through lactate dehydrogenase (LDH) to the mitochondrial pyruvate carrier influx (MPC).

<sup>b</sup>SD was estimated based on experimental measurements of glutamine consumption. This research was originally published in *Journal of Biological Chemistry*. Shestov et al. (14). © The American Society for Biochemistry and Molecular Biology.

150 mmol/L-cell/h. We note that we did not use experimentally measured fluxes as constraints in our Bonded Cumomer metabolic flux analysis.

**Tables 2 and 3** also compare glucose and glutamine uptake under euglycemic (6 mM glucose) and hyperglycemic (23 mM) conditions. Under euglycemic conditions, glutamine influx approximately doubles, whereas glucose consumption remains essentially unchanged.

Finally, we were able to generate a flux map that was included with the bionetwork in **Figure 1**. This figure shows the extracted metabolic fluxes with the predicted oxygen consumption rate MRO<sub>2</sub>. Numbers indicate fluxes in mmol/L-cell/h. See **Table 1** for definitions and values of the derived fluxes; **Table 2** summarizes the predicted and calculated metabolic rates derived from

**TABLE 2 | Experimental data compared to calculated values determined by dynamic bonded cumomer modeling (mmol/L-cell/h).**

Reaction	Exp. Flux (mmol/L-cell/h)	Calculated flux (mmol/L-cell/h)
Oxygen consumption MRO <sub>2</sub>	36	32
Glucose uptake	91.0	85
Pyruvate to lactate	155.0	150
Glutamine uptake	5.0	— <sup>a</sup>
Glutamate concentration	8.6 mM	9.2 mM

<sup>a</sup>The flux was not estimated, as glutamine is consumed in numerous reactions we did not study here. This research was originally published in *Journal of Biological Chemistry*. Shestov et al. (14). © The American Society for Biochemistry and Molecular Biology.

**TABLE 3 | Experimental glucose and glutamine consumption fluxes under euglycemia (6.4 mM) and hyperglycemic conditions (23.2 mM in medium).**

	Glutamine flux	Glucose flux
Euglycemia (6.4 mM)	0.064	0.86
Hyperglycemia (23.2 mM)	0.035	0.79

Glutamine [Gln] = 3.0 mM at low glucose and 3.4 mM at high glucose. F<sub>glc</sub>, glucose consumption flux (mmol/10<sup>9</sup> cells/h) and F<sub>gln</sub>, glutamine consumption (mmol/10<sup>9</sup> cells/h). Flux ratios were F<sub>glc</sub>/F<sub>gln</sub> = 22.4 at high glucose and F<sub>glc</sub>/F<sub>gln</sub> = 13.5 at euglycemia. This research was originally published in *Journal of Biological Chemistry*. Shestov et al. (14). © The American Society for Biochemistry and Molecular Biology.

these data. The excellent agreement between model-predicted and experimental values validates the model.

## Quantifying ATP Production Routes

The predicted fluxes were used to calculate contributions of glycolysis and oxidative phosphorylation (ophos) to ATP production. We assumed that the oxidative phosphorylation P/O ratio equals 1.5 for FADH<sub>2</sub> and 2.5 for NADH oxidation. To assess the contribution of glucose, FAs and glucogenic AAs and glutamine to generating reducing power, we calculated the fluxes for each of these metabolites. For each of the above substrates, we calculated the NADH/FADH<sub>2</sub> reaction flux based on the different labeling patterns that we were able to track both from the labeled and unlabeled C atoms. The combined cytosolic ATP production flux was 150 mmol/L-cell/h, and the mitochondrial compartment produced 154 mmol/L-cell/h due to oxidative phosphorylation. The results are presented in **Table 1**.

Consequently, about 50% of the energy of this tumor model comes from oxidative metabolism, whereas many authors have suggested that tumors derive most of their energy from aerobic glycolysis. The glycolytic contribution will, no doubt, increase *in vivo* where tumors are often located in regions of hypoxia, which produce a Pasteur effect, and, hence, a shift toward glycolytic metabolism; however, it is likely that many tumors like melanomas will be strongly dependent on oxidative metabolism for their energy source, particularly in tumors that express the V600E BRAF mutation, about 50% of human melanomas. (68) High fluxes of pyruvate mitochondrial transport (~70% of the TCA cycle activity) and mitochondrial ATP production are promoted by melanoma associated BRAF mutation. Recent work (69) has demonstrated that BRAF V600E mutated melanoma cells exhibit increased pyruvate entry through the activated PDH. PDH flux (~106% of the TCA flux) is regulated by

phosphorylation/dephosphorylation mediated by PDH kinase (PDK) and PDH phosphatase (PDP). The oncogene BRAF V600E causes concerted activation of PDH complex by downregulation of PDK1 expression and upregulation of PDP2 thereby promoting oxidative pyruvate utilization and leading to increased cellular respiration.

## Pentose Phosphate Pathway

We used the Bonded Cumomer flux model to fit  $^{13}\text{C}$  NMR steady-state data acquired after 8 h incubation of DB-1 cells with [1,2- $^{13}\text{C}_2$ ]glucose tracer. The fitted steady-state data were Lac3Tot, Lac2Tot, Lac3s, Lac3d23, Lac2s, and Lac2d23 multiplets. All the experimental  $^{13}\text{C}$  NMR spectra and the results of fitting are shown in the **Figure 5**. The extracted fluxes relative to glycolytic flux are presented in **Table 1**. Flux SDs were calculated by Monte Carlo calculations. Flux through the oxidative PPP was estimated to be 3.6% of the glycolytic rate. Given the extensive experimental data that have been obtained for the lactate  $^{13}\text{C}$  NMR multiplets, we were also able to estimate non-oxidative exchange fluxes (the smallest rate for reversible reaction) of the classical PPP (**Figure 1**), which are presented in **Table 1**. Transketolase 1 and transaldolase exchange fluxes in the non-Ox PPP branch were consequently relatively high at 21 and 44%, respectively, and transketolase 2 activity was close to 0. The flux SDs (**Table 1**) demonstrate that all fluxes through PPP were resolved with relatively poor resolution when using only  $^{13}\text{C}$  NMR isotopomers of lactate as a reporter molecule. NADPH production flux via the oxidative PPP pathway was estimated to be 6.6 mmol/L-cell/h.

## Quantifying Glutaminolysis Flux

Our recent focus has turned to refinement of the details of glutaminolysis because of its critical role in the metabolism of many malignancies. For example, one glutamine molecule could produce up to 22.5 ATP molecules. Therefore, even a small amount of glutaminolysis can have a major effect on the bioenergetics of cancer cells. In DB-1 melanoma under hyperglycemic conditions, glutamine uptake flux ranged up to 50% of the TCA cycle flux. Under euglycemic conditions, glutamine uptake doubled reaching approximately the same level as TCA cycle flux. Glutamine uptake can lead to protein synthesis, glutathione synthesis, or nucleotide synthesis as well as to ATP production by the glutaminolysis pathway (see below) or to cytosolic reductive carboxylation (RC) driven by glutaminase 1 (GLS; it is considered to be present both in mitochondria and cytosol) or other glutamine-glutamate conversion enzymes in cytosol and isocitrate dehydrogenase 1 (IDH1) (70). It was, therefore, important to refine the metabolic analysis of DB-1 melanoma to accurately assess the contributions of the glutaminolysis pathway in these tumor cells (See **Figure 1**). In order to quantify the glutaminolysis contribution to energy production, we modified the bionetwork simultaneously allowing net glutamine influx into mitochondria through glutaminase 1 and 2 (GLS and GLS2) (**Figure 1**).

“Classical” glutaminolysis includes uptake of glutamine by the cell, transport to mitochondria, conversion to glutamate through mitochondrial glutaminase 1 or 2 (GLS and GLS2), and finally entry into the TCA cycle to  $\alpha$ -ketoglutarate via GLUD1 and GLUD2 or via mitochondrial aminotransferases (GPT2 and

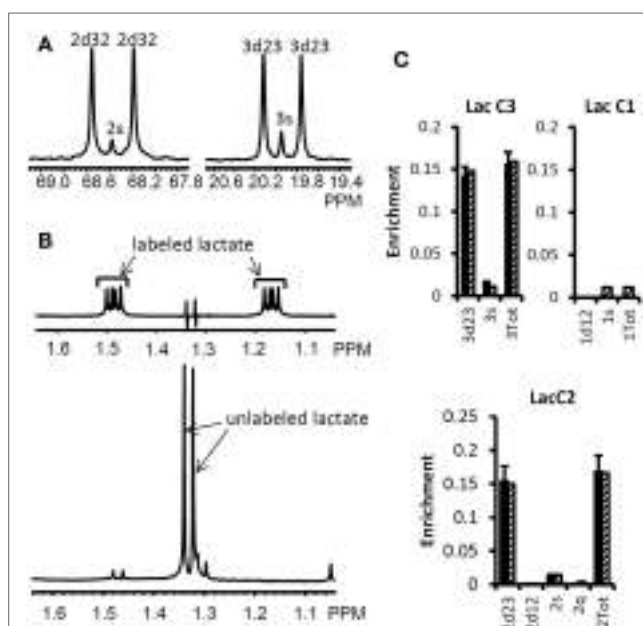


**FIGURE 5 |** High-resolution  $^{13}\text{C}$  and  $^1\text{H}$  NMR spectra of lactate from DB-1 cells incubated with [1,2- $^{13}\text{C}_2$ ] glucose and experimental lactate multiplets vs. fit. **(A)**  $^{13}\text{C}$  NMR spectra. The left panel shows the NMR spectrum at the chemical shifts around lactate C2, and the right panel shows the spectrum around lactate C3. 2s, lactate singlet at C2 position; 2d32, lactate C2 doublet with carbon coupling between the carbon 2 and 3 positions; 3s, lactate singlet from the C3 position; 3d23, lactate C3 doublet with carbon coupling between the carbon 2 and 3 positions. **(B)** Proton-edited carbon-edited (POCE)  $^1\text{H}$  NMR spectra. The upper panel shows the labeled lactate and the lower panel shows the unlabeled lactate. **(C)** Experimental multiplet fraction (left bars, black) vs. fitting (right bars, patterned) for lactate C3 and C2, and the predicted lactate C1 multiplets, based on the evaluated oxidative and non-oxidative branches of the PPP. Error bars indicate SDs. The extracted oxidative PPP flux and the relative exchange fluxes for transketolases and aldolase are presented in **Table 1**. [This research was originally published in Journal of Biological Chemistry. Shestov et al. (14). © the American Society for Biochemistry and Molecular Biology.]

GOT2). Alternatively, glutaminolysis could partially occur in the cytosol by producing glutamate or  $\alpha$ -ketoglutarate from glutamine and eventually by entry of those metabolites into the TCA cycle via  $\alpha$ -ketoglutarate. Further flux in the TCA cycle then moves to malate where malate-pyruvate cycling occurs (**Figure 1**). There are two pathways for pyruvate-malate cycling. One pathway involves conversion of malate via mitochondrial malic enzyme (ME2) to pyruvate; it then returns to oxaloacetate via PC, or it can go from pyruvate to acetyl-CoA leading to citrate. The second pyruvate cycling pathway goes from malate in the mitochondria through a transporter into the cytosol and from there to cytosolic pyruvate via cytosolic malic enzyme (ME1). The cytosolic pyruvate can return to the mitochondria through the MPC or it can be converted to lactate via LDH or to alanine via alanine aminotransferase (GPT1). The BC approach can distinguish between these pyruvate-malate pathways or their combinations under real conditions (**Figure 1**).

We continue the analysis of data of DB-1 melanoma cells treated with [1,6- $^{13}\text{C}_2$ ]glucose as the tracer with respect to sensitivities of the experimental multiplets to glutaminolysis. Dynamic

isotopomer control analysis (ICA) indicates that the curves resulting from fitting of the C4-labeled glutamate multiplets, particularly the glutamate 3,4 doublet-glu4d34 resulting from simultaneous labeling of C3 and C4 (during the second TCA cycle turn) and the singlet resulting from glutamate labeling exclusively at C4 (during the first turn of the TCA cycle) are very sensitive to flux through the glutaminolysis pathway even when only natural abundance medium glutamine has been used. See for example **Figure 2A**, where we display the dynamic multiplet control coefficients with respect to glutaminolysis activity for the glutamate C4 total and the glutamate C4 singlet and 3,4 doublet-4d34, and for the glutamate C3 and C3d doublet and glutamate-C2 and C2s singlet. This figure clearly indicates that glutamate labeling kinetics is sufficiently sensitive to glutaminolysis flux and that there is no need to purchase or synthesize exotically labeled glutamine (with <sup>13</sup>C, <sup>15</sup>N, or <sup>2</sup>H labeling) to evaluate glutaminolysis. Control simulation was based on the optimal set of extracted fluxes, and glutaminolysis flux was set at 5% of the TCA cycle flux. The plotted dynamic glutamate multiplet control coefficients indicate that the glutamate doublet 4d34 is the most sensitive glutamate multiplet with respect to glutaminolysis net flux during the first ~1.5 h when the sensitivity of the RGlu4d34 doublet is positive (positive mode) and afterwards when the RGlu4s singlet 4s becomes most sensitive in the negative operation mode. The data in the right panel of **Figure 2A** demonstrate the superiority of the sensitivity to glutaminolysis flux of the glutamate 3d doubled at the beginning and glutamate 2s singlet during the time course after ~1.5 h.

We then evaluated the contribution of glutaminolysis flux to overall energy production of DB-1 melanoma cells. We found that for this tumor line, glutaminolysis flux through the truncated TCA cycle and via pyruvate–malate cycling by malic enzyme ME2 is essentially 0. This conclusion resulted directly from the ability of the model to detect glutaminolysis flux by fitting of data on the glutamate multiplets (see above). To further confirm this conclusion, we forced the model to accommodate glutaminolysis flux between 5 and 20% of the TCA cycle flux. Invariably, this grossly deteriorated the goodness-of-fit of the isotope kinetic data to the model (results not shown).

Even though glutaminolysis does not contribute substantially to mitochondrial ATP production, there is still substantial mitochondrial malic enzyme flux (combined activities of NADH producing ME2 and NADPH producing ME3), which is equal to approximately 40% of the TCA flux (see **Table 1**).

There has been considerable interest in glutamine metabolism as a key source of tumor energy production linked to c-myc expression (71–75). Our model of tumor metabolism (**Figure 1**) contains a specific glutamine transporter on the cell membrane. The classical model of glutaminolysis includes an additional specific glutamine transporter on the mitochondrial membrane that leads to mitochondrial glutaminase (GLS2 or GLS), which converts glutamine to glutamate, which is then converted to α-ketoglutarate by enzymes, such as GLUD1 and GLUD2. Two additional transaminases can carry out the glutamate to α-ketoglutarate exchange, aspartate aminotransferase, and alanine aminotransferase. The α-ketoglutarate then produces reducing equivalents via the oxidative branch of the TCA cycle leading to ATP production by oxidative phosphorylation. Various pathways, including the malate-aspartate shuttle, PC, malic enzyme,

and phosphoenolpyruvate carboxykinase (PEPCK1 and 2) all contribute to metabolism of the glutamine carbon atoms. As previously noted, glutamine metabolism can lead to production of 22.5 molecules of ATP per glutamine molecule. In the case of DB-1 melanoma cells under hyperglycemic conditions, glutamine influx constituted about 50% of the TCA cycle flux, with about double this level of glutamine uptake under euglycemic conditions (**Tables 2** and **3**). However, the transaminase reactions are reversible and may exhibit high exchange fluxes in both directions with very little net glutamine uptake by the TCA cycle and nearly no energy production from the glutaminolysis pathway in DB-1 cells. It is important to note that because carbon atoms of glutamate originating from glucose will be isotopically labeled (first on C4 position and then on C2 and C3, etc.), whereas carbons coming from glutamine will be unlabeled, it was possible to distinguish the two pools of carbon atoms originating from these two substrates. The data fitting clearly indicated that the net flux from glutamine being metabolized via the TCA cycle was very small.

We also conducted a sensitivity analysis to show that using [1,6-<sup>13</sup>C<sub>2</sub>] glucose tracer alone is enough to reliably calculate glutaminolysis flux in malignant cells and tissues. **Figure 2A** shows that the glutamate-C4 doublets due to C3-C4 coupling (glu4d34) is most sensitive to glutaminolysis and all experimental glutamate multiplets, including total positional enrichments at glutamate C4, C3, and C2 are sensitive to the net flux of unlabeled glutamine entering the TCA cycle. Fitting analysis indicated that there was little net influx from glutamine into the TCA cycle. Note also that this conclusion can also be reached from <sup>13</sup>C NMR data without the use of labeled glutamine.

By contrast, some investigators utilizing mass spectrometry have equated glutamine uptake minus glutamate release with net glutaminolysis flux (76). In the present case, the net influx of glutamine is ~5 mmol/L-cell/h, which, if it were equated with glutaminolysis flux, would have been interpreted as 113 mmol/L-cell/h of ATP per h or about 75% of the glycolytic production of ATP. Under euglycemic conditions, which produce about twice the level of glutamine uptake, such an analysis would have attributed about 50% higher ATP production to glutaminolysis rather than to glycolysis, and most of the tumor energy production would have been attributed to glutaminolysis. This is incorrect in our case; in reality the net glutaminolysis flux under hyperglycemic conditions is ~0.1 mmol/L-cell/h or ~2 mmol ATP/L-cell/h or ~1% of the glycolytic ATP production rate. Bonded Cumomer analysis provides a method for making this crucial distinction. Our labeled LC-MS data for the TCA cycle intermediates with [U-<sup>13</sup>C<sub>5</sub>, U-<sup>15</sup>N<sub>2</sub>] glutamine confirmed that no glutaminolysis occurred under euglycemic conditions vs. hyperglycemia (**Figure 6**). The absence of change in glutaminolysis or RC flux is evident from similar mass-isotopomer distribution (MID) of several key metabolites. Our finding of nearly zero glutaminolysis flux contradicts the view of Scott et al. (77), who, on the basis of glutamine uptake and label appearance in some TCA cycle metabolites, concluded that glutamine was utilized as an anaplerotic substrate of several human melanoma lines. However, these authors failed to conduct a rigorous metabolic modeling analysis to measure flux through the TCA cycle. Consequently, they were unable to distinguish between actual flux through the cycle via glutaminolysis and exchange labeling between

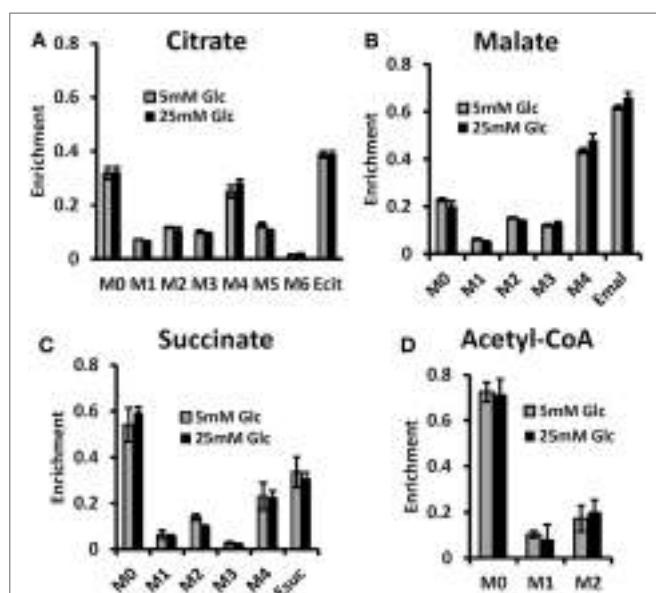


**FIGURE 6 |** Mass-isotopomer distribution (MID) for the TCA cycle intermediate and acetyl-CoA measured at hyperglycemic and euglycemic conditions during [ $U-^{13}\text{C}_5$ ] glutamine labeling. MID of (A) citrate, (B) malate, (C) succinate, and (D) acetyl-CoA. The figure clearly demonstrates that there are no significant differences in labeling patterns of key metabolites ( $p$ -value was always  $>0.05$ ) between 5 mM glucose and 25 mM medium glucose conditions. [This research was originally published in Journal of Biological Chemistry. Shestov et al. (14). © The American Society for Biochemistry and Molecular Biology.]

$\alpha$ -ketoglutarate and glutamate without any net flux. In addition, glutamine could be used for many other metabolic processes besides energy production, e.g., protein and nucleotide synthesis. If the net uptake of glutamine is 5 mmol/L-cell/h with negligible contribution to energy production, glutamine must be contributing primarily to anabolic processes, such as AA, nucleotide, and protein production as well as to *de novo* lipogenesis.

## Effect of Hyperglycemia/Euglycemia on Glutamine and Fatty Acid Metabolism

The MID of several TCA cycle metabolites from [ $U-^{13}\text{C}_5, ^{15}\text{N}_2$ ] glutamine labeling experiments is shown in Figure 6 at different glucose concentrations in the medium – at 5 mM for euglycemia and 25 mM for hyperglycemia. With this tracer, increased glutaminolysis flux resulted in increased abundance of  $M + 4$  mass-isotopomer of citrate, succinate, and malate (70), whereas RC resulted in increased  $M + 3$  for malate,  $M + 4$  for succinate, and  $M + 5$  for citrate. RC and increased glucose contribution to the FAs production also disturbs the acetyl-CoA mass-MID. Figure 6 clearly shows that there are no significant differences in labeling patterns of all four metabolites. Consequently, based on bioreactor data, we can exclude any major change in glutaminolysis flux as well for FA production during hyperglycemia vs. euglycemia.

## Quantifying *De Novo* Lipogenesis Flux in DB-1 Cells

During culturing of DB-1 cells with [ $1,6-^{13}\text{C}_2$ ] glucose, progressive labeling of FAs was observed for multiple resonances

(see Figures 3 and 4D). FA synthesis occurs first by cytosolic citrate production from glucose and through RC in cytosol from glutamine through isocitrate dehydrogenase (IDH1 isoform). By ATP citrate lyase, cytosolic citrate is converted to oxaloacetate and cytosolic acetyl-CoA, which is converted further to malonyl-CoA by the rate-limiting acetyl-CoA carboxylase beta (ACC-beta) and through FAs synthases to elongated precursors via sequential addition of acetyl-CoA, eventually leading to palmitate production. Palmitate is further elongated or desaturated to produce numerous other FAs. To address *de novo* FA flux production, we utilized the BC model with cytosolic FAs and their precursors as well as membrane FAs as the second FA pool. We calculated FA concentrations based on the total FA content of approximately 20% of cell dry weight of 200 mg/ $10^9$  cells ( $5 \times 10^8$  cells = 1 ml). Total FA content referenced to palmitate is at the level of several tens of mmol/L-cell. We iteratively varied the ratio of cytosolic to membrane FA and found the best fit at approximately 10 times more FA in the cytosolic membrane compartment (Figure 4D). The *de novo* flux of conversion of glucose to FA was 0.59 mmol/L-cell/h and NADPH consumption flux in FA biosynthesis was 8.4 mmol/L-cell/h.

While glutamine-derived carbons have been unlabeled, we have monitored lipogenesis by  $^{13}\text{C}$  NMR detecting methylene carbon acyl groups originating from labeled glucose (Figures 3A and 4D). Table 1 indicates that *de novo* lipogenesis corresponds to ~6% of the TCA cycle flux under hyperglycemic conditions. However, this does not include possible direct contributions from unlabeled glutamine (i.e., through cytosolic RC by isocitrate dehydrogenase IDH1 or mitochondrial IDH2) and potentially from cytosolic acetyl-CoA synthetase 2 (ACSS2) reaction, which involve participation of cytosolic acetate or acetate from the medium (78).

This modest flux for *de novo* FA synthesis requires a large contribution of NADPH cofactor production (~8.3 mmol/L-cell/h). NADPH could be produced by the oxidative branch of the PPP, ME, or IDH activities or by serine-glycine one-carbon metabolism (folate metabolism). Our calculated malic enzyme activities in mitochondria (even if all this activity is represented by ME3) would account for 4.3 mmol/L-cell/h and cytosolic NADPH flux (ME1, 0.6 mmol/L-cell/h) would not account for the required high level of NADPH flux. A recent elegant study (79) suggested that in some cancers folate metabolism is the biggest producer of NADPH. Based on these data (48), we estimated that the serine-glycine one-carbon SGOC pathway cannot account for the required NADPH consumption. In light of our  $^{13}\text{C}$  NMR lactate labeling data, the oxidative branch of the PPP is the main producer of NADPH in these cancer cells (6.6 mmol/L-cell/h). This constitutes ~80% in agreement with the NADPH consumption rate during FAs biosynthesis. Thus, the flux through the oxidative PPP appears to be ~80% sufficient to supply all of the NADPH required for FA production and is the main supplier of reducing equivalents in DB-1 melanoma. A 20% difference in the rates of NADPH production and consumption indicates that alternative sources of NADP reduction, considered above, need to be taken into account. We also found that mitochondrial-pyruvate-malate cycling was very high (4.3 mmol/L-cell/h). This could also contribute to defense against reactive oxygen species by producing sufficient NADPH via ME3.

## Lymphoma Studies

### Rapamycin Inhibits mTORC1 Signaling and Lowers Lactate Concentration in B-Cell Lymphoma Cells

The effects of rapamycin on mTORC1 signaling and cell growth were first examined in four B-cell lymphoma cell lines, sub-classified either as germinal-center type DLBCL (DLCL2, Val, and Ly18) or Burkitt (Ramos). As indicated by loss of mTORC1-dependent S6rp phosphorylation, rapamycin suppressed mTORC1 activity in all the cell lines and profoundly inhibited BrdU uptake-detected cell proliferation (15).

We have evaluated the effect of rapamycin on the cellular concentration of lactate in NHL cells by  $^1\text{H}$  MRS (Figures 7A,B) because mTOR has been implicated in various aspects of cell metabolism. To varying extents rapamycin significantly decreased intracellular lactate relative to controls in all four cell lines (15). Significantly, the relative reduction in intracellular lactate concentrations in rapamycin treated cells vs. controls was more pronounced after 48 than 24 h exposure to rapamycin and correlated with the suppression of cell growth indicating that the effect is not directly due to drug–enzyme interaction or direct effects on mTOR signaling but is most likely due to gene translation.

### Kinetics of the Rapamycin-Induced Suppression of Lactate Concentration

To determine how early the rapamycin-induced metabolic changes can be detected, we examined the intracellular lactate concentration at 2, 4, 8, 24, and 48 h in two B-cell lymphoma cell lines (15). While 2 and 4 h exposure to rapamycin did not have a definitive effect, we noted statistically significant differences between vehicle- and rapamycin-treated cells at 8 h in both

cell lines ( $p = 0.002$  and  $0.03$  for DLCL2 and Ramos, respectively;  $n = 3$ ) with increased differences at 24 and 48 h. Changes of lactate and glucose concentrations in the medium indicated diminished glycolysis following rapamycin treatment with corresponding changes in lactate secretion and glucose uptake per cell. Lactate secretion and glucose uptake exhibited maximum differences between vehicle- and rapamycin-treated cell cultures at 24 h in contrast to intracellular lactate that remained approximately unchanged. The amount of secreted lactate per cell was three to four orders of magnitude greater than the intracellular lactate levels, which indicates that most of the lactate generated by cellular metabolism was secreted by the cell. Nonetheless, the level of intracellular lactate was more sensitive than secreted lactate levels for distinguishing metabolic differences between vehicle- and rapamycin-treated cells. This was, in part, due to the intracellular lactate concentration remaining essentially constant after rapamycin treatment.

### Rapamycin Inhibits Expression of Hexokinase II

While inhibition of mTORC1 signaling by rapamycin reaches an optimum within minutes after drug administration (80–82), the drug's effects on the lactate concentration were not detectable until 8 h post-treatment and became more pronounced at 24 and 48 h in cultured cells (15). This marked timing difference indicates that the inhibition of glycolysis does not directly result from inhibition of the mTORC1 signaling but most likely originates from diminished expression of enzymes involved in the glycolytic pathway. To test this assumption, we performed gene expression profiling of the DLCL2 and Ramos cell lines treated with rapamycin or medium alone (Figure 7C). The component of the

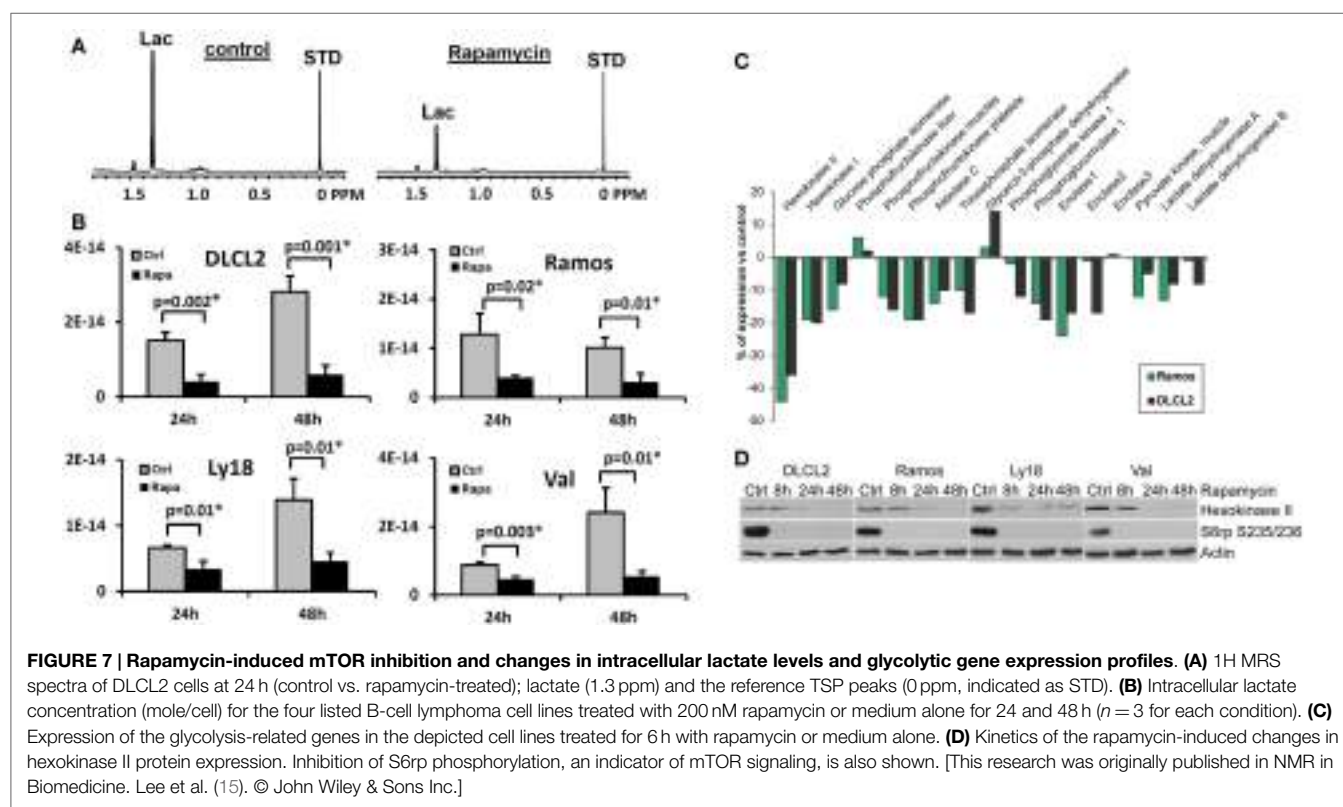


**FIGURE 7 |** Rapamycin-induced mTOR inhibition and changes in intracellular lactate levels and glycolytic gene expression profiles. **(A)**  $^1\text{H}$  MRS spectra of DLCL2 cells at 24 h (control vs. rapamycin-treated); lactate (1.3 ppm) and the reference TSP peaks (0 ppm, indicated as STD). **(B)** Intracellular lactate concentration (mole/cell) for the four listed B-cell lymphoma cell lines treated with 200 nM rapamycin or medium alone for 24 and 48 h ( $n = 3$  for each condition). **(C)** Expression of the glycolysis-related genes in the depicted cell lines treated for 6 h with rapamycin or medium alone. **(D)** Kinetics of the rapamycin-induced changes in hexokinase II protein expression. Inhibition of S6rp phosphorylation, an indicator of mTOR signaling, is also shown. [This research was originally published in NMR in Biomedicine. Lee et al. (15). © John Wiley & Sons Inc.]

glycolytic pathway whose gene expression was most profoundly inhibited by the rapamycin treatment was hexokinase II although some other glycolytic genes showed similar trends. The steady loss of hexokinase II expression was confirmed on the protein level in all the cell lines examined (Figure 7D).

### Rapamycin-Induced Suppression of Lactate Concentration Directly Correlates with Inhibition of Lymphoma Growth *In vivo*

To determine if the rapamycin-induced suppression of lactate concentration can also be detected *in vivo*, we evaluated xenotransplanted lymphoma models (Figure 8), the DLCL2 and Ramos B-cell lines studied in greatest detail *in vitro* as described above. The tumors displayed the appropriate transformed lymphoid cell morphology and human B-cell phenotype confirming that they originated from the implanted lymphoma cell lines.

Administration of rapamycin to mice with DLCL2 and Ramos xenografts inhibited mTORC1 signaling and decreased the proliferative rate of the lymphoma cells as determined by suppression of S6rp phosphorylation and decreased expression of the

cell cycle-associated marker mib1 (15). Western blots confirmed effective and specific mTORC1 inhibition, which revealed greatly diminished S6rp phosphorylation and intact phosphorylation of Akt. Prolonged treatment with rapamycin resulted in tumor growth arrest for the DLCL2 cell line and a marked decrease in tumor volume for the Ramos cell line (Figure 8). It is noteworthy that these effects were preceded by decreases in tumor lactate concentrations measured by *in vivo* MRS. The decrease was already statistically significant at 48 h following initiation of rapamycin treatment and increased at 96 h. At 2 days after initiation of treatment, the effect of rapamycin on tumor volume was not yet noticeable while tumor lactate had already significantly decreased. These observations strongly suggest that *in vivo* measurement of lactate originating from the tumor provides an early marker predictive of effective mTOR inhibition that correlates with substantially later tumor shrinkage.

### Discussion of Rapamycin Data

The above results clearly document that mTOR inhibition can be monitored *in vitro* and *in vivo* by measuring changes in lactate

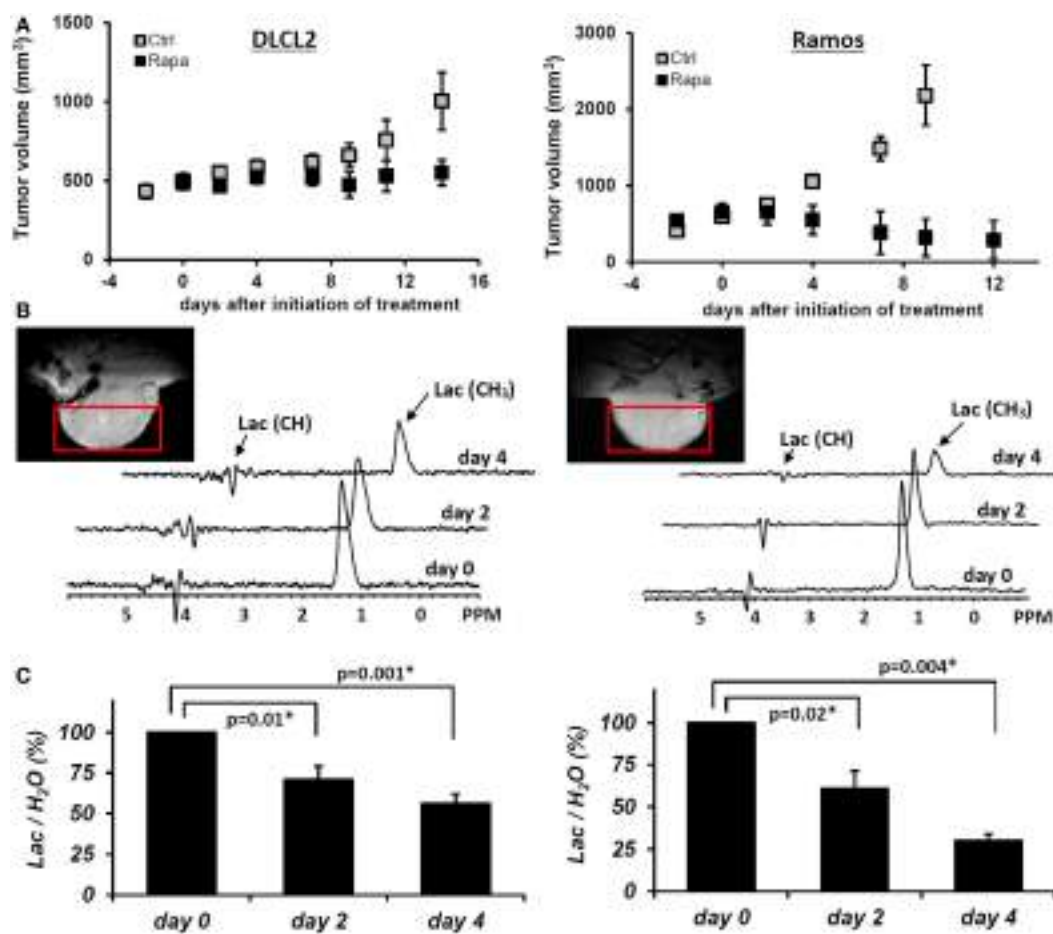


**FIGURE 8 | Rapamycin-induced inhibition of tumor growth and glucose metabolism *in vivo*.** Xenotransplants of DLCL2 cells (left panel) and Ramos cells (right panel). (A) Tumor growth curve. The data are presented as mean  $\pm$  SD ( $n \geq 5$  in each group). (B) Time course *in vivo* localized MRS. (C) Lac/H<sub>2</sub>O ratios normalized to the pretreatment values; mean  $\pm$  SE ( $n = 5$ ). Statistically significant changes in Lac/H<sub>2</sub>O were observed at 48 h and after from initiation of rapamycin treatment in both xenografts while control tumors ( $n = 5$ ) did not have significant changes in Lac/H<sub>2</sub>O until 96 h. [This research was originally published in NMR in Biomedicine. Lee et al. (15). © John Wiley & Sons Inc.]

concentration. Accumulating evidence indicates that mTORC1 can be activated by a variety of cell-surface receptor complexes. While the original studies implicated the activation of receptors for the insulin-family growth factors (83–85), subsequent observations by the Wasik laboratory (80–82) and by others (86–91) demonstrated that a large spectrum of receptors and their ligands triggered mTORC1 activation. These include interleukin-2, anaplastic lymphoma kinase, CD40 ligand, notch, thyroid-stimulating hormone, fibroblast growth factor-9, polycystein-1, and prostaglandin F2a. These diverse ligand–receptor complexes activate mTORC1 through the signaling pathways PI3K/Akt (92–94), MEK/ERK (95), and possibly Syk (96). Therefore, the inhibition of these pathways should also be amenable to detection by monitoring changes in glycolysis. Given that these pathways are frequently deregulated in malignant cells and clinical-grade inhibitors are already available, evaluation of glucose metabolism as a surrogate for monitoring mTOR activity may prove useful in the management of cancer patients treated with a variety of kinase inhibitors. Indeed, inhibition of the oncogenic BCR/ABL tyrosine kinase led to decreased glucose uptake and lactate production (97, 98), all but certainly indicating that mTORC1 signaling was involved (99). Hence, the apparent lack of specificity of lactate actually reflects its versatility. Provided that a single kinase inhibitor is administered, there is no lack in specificity of detecting response to the drug; if multiple kinase inhibitors are used, then lactate still serves as a biomarker for the combination.

### Genomic Analysis of mTOR Inhibition

In view of a recent report (100) that several metabolic pathways were modified in mouse fibroblasts with hyper-activated mTOR, we analyzed changes in expression of metabolic genes in DLCL2 and Ramos cells induced by rapamycin. **Table 4** lists significantly affected (up- and downregulated;  $p < 0.02$ ,  $n = 3$ ) of representative metabolic genes in DLCL2 cells (Ramos data are similar). The anticipated related alterations in the cellular metabolism indicate that in the DLCL2 cells mTOR inhibition diminishes

not only glucose metabolism but also TCA cycle activity, *de novo* FA and sterol biosynthesis, pyruvate cycling activity, and flux through pentose phosphate pathway. Glutaminolysis should also be affected due to novel PPAT gene expression, which is responsible for enzymatic glutamate production from glutamine (see footnote “b” in **Table 4**).

### Cell Perfusion and $^{13}\text{C}$ NMR Spectroscopy

**Figure 9A** shows data obtained from DLCL2 cells immobilized in agarose beads and perfused with normoxic (20%  $\text{O}_2$ , 75%  $\text{N}_2$ , 5%  $\text{CO}_2$ ) media containing 5 mM [1,6- $^{13}\text{C}_2$ ] glucose over a 12-h period in a 10 mm diameter NMR bioreactor. Cells were studied before treatment and 24 and 48 h (not shown) after treatment with rapamycin. Using a two-compartmental enzyme kinetic model, we calculated lactate production rates. The results were 6.9 mM/h (pretreatment) and 1.6 mM/h (post-treatment), which indicate a profound decrease in glycolysis. There is also a decrease in labeling of Glu C4 reflecting a decrease in TCA cycle flux. Alanine and fatty acid labeling are also diminished, and glycogen stores have been completely depleted, probably as a result of decreased energy production by both glycolytic and TCA cycle pathways.

### *In vivo* $^{13}\text{C}$ NMR Studies of DLCL2 Cell Metabolism

**Figure 9B** shows the time course of  $^{13}\text{C}$  MR spectra measured after infusion of [1,6- $^{13}\text{C}_2$ ] glucose into a mouse with a 12 mm DLCL2 xenograft ( $500 \text{ mm}^3$ ) growing on its flank. The inset to this figure shows the MR image of the tumor and the Hadamard voxel that localizes the spectral data in the tumor (i.e., insuring no contributions from external tissues). These studies demonstrate the feasibility of performing  $^{13}\text{C}$  MRS studies non-invasively in these *in vivo* lymphoma tumor models in mice. The spectra show the time course of labeling of tumor metabolites by transfer of  $^{13}\text{C}$  by metabolism of the labeled glucose over 120 min with each spectrum measured in 15 min. The same animal was studied before and 4 days later after seven doses of rapamycin (10 mg/kg) with two doses administered per day (bottom of **Figure 9B**).

**TABLE 4 | Changes in gene expression following treatment of DLCL2 cells with rapamycin.<sup>a</sup>**

Entrez ID	Gene Symbol	Enzyme name	EC number	Fold change	P value	Pathway Affected
<b>Upregulated</b>						
5106	PCK2	Phosphoenolpyruvate carboxykinase 2 (mit)	EC 4.1.1.32	1.51	0.000434	Pyruvate cycling
<b>Downregulated</b>						
3099	HK2	Hexokinase 2	EC 2.7.1.1	-1.78	0.00515	Glycolysis
57546	PDP2	Pyruvate DH phosphatase subunit 2	EC3.1.3.43	-1.54	0.0150	PDH, TCA
3419	IDH3A	Isocitrate DH 3 (NAD+) alpha (mito)	EC1.1.1.41	-1.60	0.000673	TCA Cycle
5471	PPAT	Amidophosphoribosyl transferase	EC2.4.2.14	-1.73	0.0163	Glutaminolysis <sup>b</sup>
31	ACACA	Acetyl-CoA carboxylase alpha	EC6.3.4.14	-1.80	0.00518	Fatty acids
2180	ACSL1	Acyl-CoA synthetase long-chain member 1	EC 6.2.1.3	-1.52	0.0161	Fatty acids
23171	GPD1L	Glycerol-3-phosphate dehydrogenase 1-like	EC 1.1.1.8	-1.56	0.00446	Glycerophospholipid
22934	RPIA	Ribose 5-phosphate isomerase A	EC 5.3.1.6	-1.58	0.00451	Pentose phosphate
1717	DHC7	7-dehydrocholesterol reductase	EC1.3.1.21	-1.72	0.00363	Cholesterol
6307	MSMO1	Methylsterol monooxygenase 1	EC1.14.13.72	-1.74	0.0165	Cholesterol
1723	DHDH	Dihydroorotate dehydrogenase	EC 1.3.5.2	-1.51	0.000190	Pyrimidine metabolism
5198	PFAS	Phosphoribosylformylglycinamide synthase	EC 6.3.5.3	-1.51	0.00120	Purine metabolism

<sup>a</sup>Data were compiled from KEGG database. Gene expression of a large number of enzymes demonstrated statistically significant changes, but only one or two representative enzymes are listed for pathways showing changes greater than 50%.

<sup>b</sup>This is a new link for glutamine to glutamate interconversion through operation of enzyme 5-phospho-β-D-ribosylamine:diphosphate phospho-α-D-ribosyl-transferase (glutamate amidation reaction).

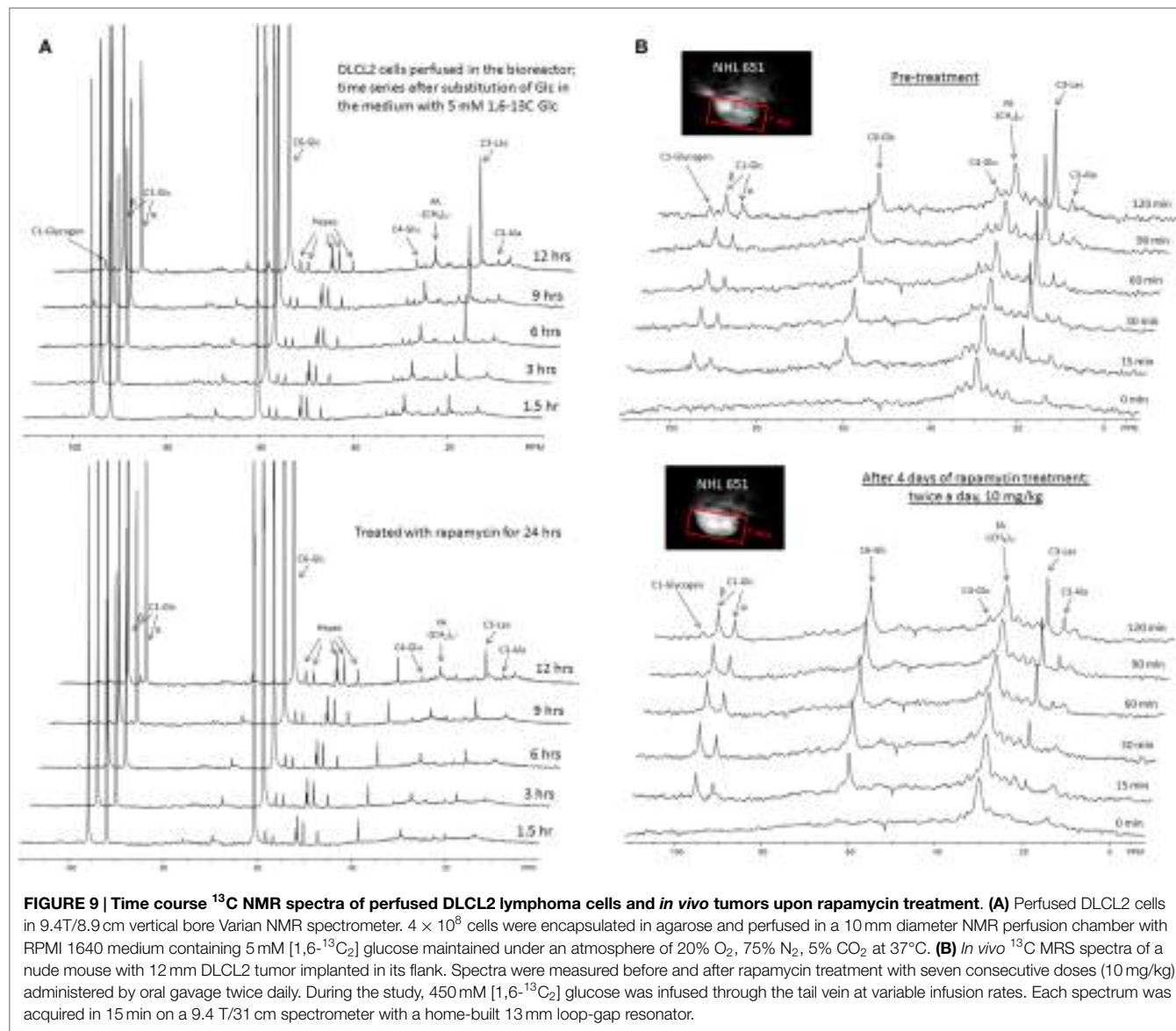


**FIGURE 9 | Time course <sup>13</sup>C NMR spectra of perfused DLCL2 lymphoma cells and *in vivo* tumors upon rapamycin treatment.** (A) Perfused DLCL2 cells in 9.4T/8.9 cm vertical bore Varian NMR spectrometer.  $4 \times 10^8$  cells were encapsulated in agarose and perfused in a 10 mm diameter NMR perfusion chamber with RPMI 1640 medium containing 5 mM [1,6-<sup>13</sup>C] glucose maintained under an atmosphere of 20% O<sub>2</sub>, 75% N<sub>2</sub>, 5% CO<sub>2</sub> at 37°C. (B) *In vivo* <sup>13</sup>C MRS spectra of a nude mouse with 12 mm DLCL2 tumor implanted in its flank. Spectra were measured before and after rapamycin treatment with seven consecutive doses (10 mg/kg) administered by oral gavage twice daily. During the study, 450 mM [1,6-<sup>13</sup>C] glucose was infused through the tail vein at variable infusion rates. Each spectrum was acquired in 15 min on a 9.4 T/31 cm spectrometer with a home-built 13 mm loop-gap resonator.

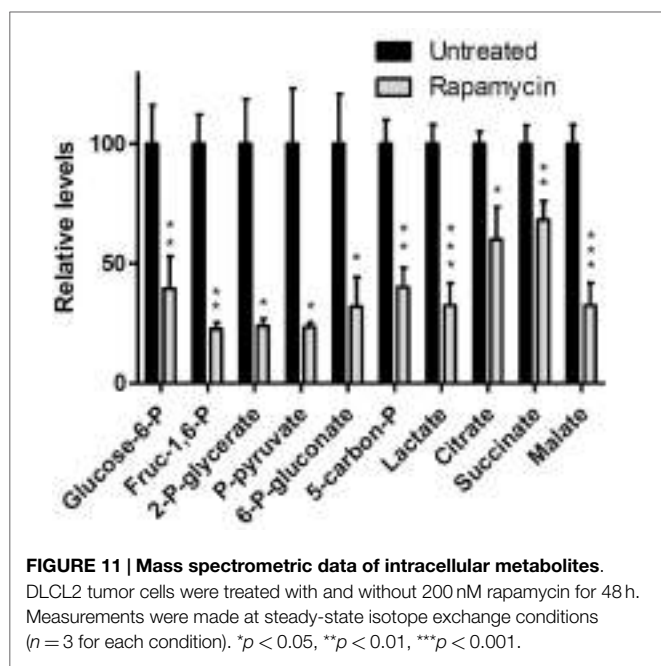
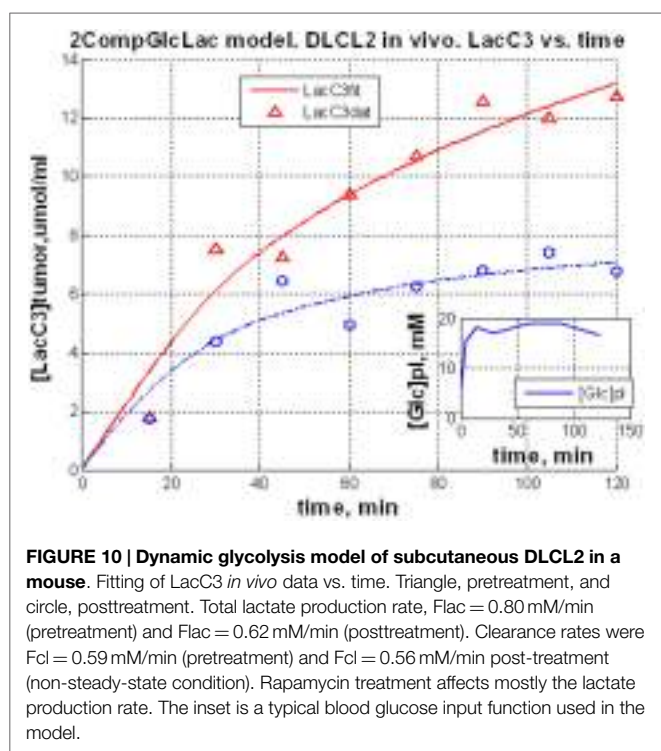
The rate of lactate labeling has decreased, whereas the rate of alanine labeling appears to have increased. Glutamate-C4 was detectable and appears to have decreased after rapamycin treatment, suggesting a decrease in TCA cycle flux. The glycogen peak appears very small in both sets of spectra and seems to have been diminished but not eliminated after treatment. These are among the first *in vivo* spectra we or anyone else we are aware of have reported. We are pursuing a number of strategies for improving the resolution and S/N ratio. Obviously, higher magnetic fields or cryoprobes would increase the sensitivity, but even with the equipment at hand it is clearly feasible to obtain quantitative data *in vivo*.

A computational analysis (**Figure 10**) of the time course *in vivo* data from a mouse to a two-compartment non-steady-state enzyme kinetic model generated total lactate production and clearance rates (indicated in the figure caption). The model included glycolysis, alanine production, and exchange of cytosolic

and vascular/interstitial lactate through MCT1 (the dominant monocarboxylic acid transporter). The calculated fluxes indicate a decrease in glycolytic metabolism caused by treatment with rapamycin. Clearly a more comprehensive analysis, including other metabolic pathways that contribute to lactate production is required, but this demonstrates feasibility of our precise data analysis approach.

#### LC-MS Studies of DLCL2 Tumor Cells

Preliminary studies of DLCL2 cells in suspension culture have been initiated in Dr. Blair's laboratory (**Figure 11**). Cells were grown in batch culture. Harvested cells were spiked with [<sup>13</sup>C] lactate, citrate, and succinate as internal standards. The extracted metabolites were separated by a reverse-phase ion-pairing chromatography and analyzed by MS. Note that these are steady-state measurements, which only provide information about relative fluxes. Kinetic data are required for absolute flux measurements.



Significant changes are evident in levels of glycolytic metabolites (glucose-6P, fructose-1,6-P, 2-phosphoglycerate, pyruvate, and lactate), pentose shunt metabolites (6-phosphogluconate and 5-carbon phosphates), and TCA cycle (citrate, succinate, and malate) (100, 101).

In view of the recent interest in glutamine metabolism of tumors (71), preliminary studies were performed on DLCL2 cells grown in culture with 4 mM [ $\text{U}^{-13}\text{C}$ ] glutamine; after 6 h steady

**TABLE 5 | Pathway activities for DLCL2 cells based on  $^{13}\text{C}$  LC-MS data.<sup>a</sup>**

Pathway name	Control	Rapamycin	P-value
Reductive carboxylation (cytosolic)	$0.29 \pm 0.05$	$0.17 \pm 0.03$	0.0235
Glutaminolysis	$0.27 \pm 0.10$	$0.014 \pm 0.02$	0.0122
Mitochondrial pyruvate carrier	$0.63 \pm 0.06$	$0.90 \pm 0.09$	0.0124
Pyruvate dehydrogenase complex	$0.60 \pm 0.07$	$0.56 \pm 0.05$	0.466
Pyruvate carboxylase (mitochondrial)	$0.075 \pm 0.030$	$0.39 \pm 0.09$	0.0045
De Novo fatty acid production	$0.39 \pm 0.07$	$0.23 \pm 0.05$	0.0322

<sup>a</sup>Presented as real parameter value  $\pm$  error in terms of standard deviation (SD). Errors are based on Monte Carlo simulations assuming Gaussian noise with 0 mean and  $\sigma = 0.01$  for SD; synthetic renormalized steady-state mass-isotopomers fit by fragmented cumomer model using Simplex.

state was achieved. A preliminary analysis fitted the LC-MS isotopomer data (aspartate, glutamate, lactate, malate, succinate, citrate, and  $\alpha$ -ketoglutarate, Mo,  $M_1, \dots, M_n$ ,  $n$  = number of carbons) to all the metabolic pathways included in the fragmented cumomer model (Shestov et al., manuscript in preparation) (13, 48, 49). There was excellent agreement between observed and calculated isotopomer levels (data not shown). The metabolic network includes all the pathways included in the bonded cumomer model (Figure 1). Table 5 summarizes changes in flux through various pathways for which there was adequate significance. Rapamycin produced dramatic changes in RC (41% decrease), glutaminolysis (95% decrease), MPC (50% increase) and PC (520% increase). Clearly, further study of these effects is required, but these data strongly suggest that multiple pathways are affected and, potentially, may serve as key biomarkers of effective mTOR inhibition.

## CONCLUSION AND SUMMARY

We have for the first time formulated and validated a detailed metabolic network model of tumor intermediary metabolism that includes all the key pathways except glycogen and phospholipid metabolism as well as serine–glycine one-carbon metabolism. These pathways can be added in the future. We have demonstrated that glutamine metabolism, while critical to AA and nucleoside/tide production, makes minimal contribution to energy production in DB-1 melanoma. Studies of FA metabolism have been initiated and need to be advanced further. Aerobic glycolysis and oxidative metabolism contribute approximately equally to energy production in this tumor and probably contribute in similar proportions to energy production by many tumors, with relative contributions of glycolysis being modulated by oxygen supply in the local environment of the tumor.

Using NHL as a model and rapamycin as a specific therapeutic agent, we have formulated a general strategy for monitoring therapeutic response of signal transduction. This strategy includes preliminary exploratory non-invasive  $^{13}\text{C}$  MRS studies of tumor *in situ* and *ex vivo*  $^{13}\text{C}$  MRS and LC-MS studies of tumor metabolism to identify key pathways that are modified by treatment of individual patients with specific inhibitors. Because of the intrinsic low sensitivity of  $^{13}\text{C}$  MRS, a key goal of these exploratory studies will be to identify biomarkers of therapeutic response that

can be more readily studied by more sensitive methods, such as <sup>1</sup>H MRS and CEST (102) and PET/CT. In this regard, lactate appears to be a critical metabolite that plays a central role in a number of key metabolic pathways susceptible to modulation by signaling inhibitors. Dynamic nuclear polarization may also play an important role, although the short lifetime of probes, such as <sup>13</sup>C-labeled pyruvate, forces them to be employed at abnormally high concentrations, which may modify the metabolic pathways that are being monitored. Despite its intrinsically low sensitivity, <sup>13</sup>C MRS of glucose, lipids as well as low molecular weight metabolites, such as acetate and glutamine, should not be ignored, especially in view of the increasing availability of high-field instruments, such as 7 Ts, of which more than 60 are already available at leading institutions throughout the world. These are likely to soon gain FDA approval and will become much more useful as body coils and other probes become more available. The recent demonstration of the feasibility of *ex vivo* <sup>13</sup>C MRS and LC-MS analysis of tumor specimens that have been surgically excised (18, 19) in conjunction with the current *in vivo* <sup>13</sup>C MRS study at 9.4 T of human melanoma and lymphoma xenografts in mice point to the feasibility of non-invasive human metabolic studies. Overall, metabolic studies are likely to complement genomic studies of human cancer in the near future.

## REFERENCES

- Chance EM, Seeholzer SH, Kobayashi K, Williamson JR. Mathematical-analysis of isotope labeling in the citric-acid cycle with applications to C-13 NMR-studies in perfused rat hearts. *J Biol Chem* (1983) 258:13785–94.
- Chatham JC, Forder JR, Glickson JD, Chance EM. Calculation of absolute metabolic flux and the elucidation of the pathways of glutamate labeling in perfused rat-heart by C-13 NMR-spectroscopy and nonlinear least-squares analysis. *J Biol Chem* (1995) 270:7999–8008. doi:10.1074/jbc.270.14.7999
- Jeffrey FMH, Reshetov A, Storey CJ, Carvalho RA, Sherry AD, Malloy CR. Use of a single C-13 NMR resonance of glutamate for measuring oxygen consumption in tissue. *Am J Physiol Endocrinol Metab* (1999) 277:E1111–21.
- Malloy CR, Sherry AD, Jeffrey FMH. Carbon flux through citric-acid cycle pathways in perfused heart by C-13 NMR-spectroscopy. *FEBS Lett* (1987) 212:58–62. doi:10.1016/0014-5793(87)81556-9
- Weiss RG, Kalil-Filho R, Herskowitz A, Chacko VP, Litt M, Stern MD, et al. Tricarboxylic-acid cycle activity in postischemic rat hearts. *Circulation* (1993) 87:270–82. doi:10.1161/01.CIR.87.1.270
- Yu X, White LT, Doumen C, Damico LA, LaNoue KF, Alpert NM, et al. Kinetic analysis of dynamic C-13 NMR spectra: metabolic flux, regulation, and compartmentation in hearts. *Biophys J* (1995) 69:2090–102. doi:10.1016/S0006-3495(95)80080-9
- Gruetter R, Seaquist ER, Ugrubil K. A mathematical model of compartmentalized neurotransmitter metabolism in the human brain. *Am J Physiol Endocrinol Metab* (2001) 281:E100–12.
- Mason GF, Gruetter R, Rothman DL, Behar KL, Shulman RG, Novotny EJ. Simultaneous determination of the rates of the TCA cycle, glucose-utilization, alpha-ketoglutarate glutamate exchange, and glutamine synthesis in human brain by NMR. *J Cereb Blood Flow Metab* (1995) 15:12–25. doi:10.1038/jcbfm.1995.2
- Mason GF, Rothman DL, Behar KL, Shulman RG. NMR determination of the TCA cycle rate and alpha-ketoglutarate glutamate exchange-rate in rat-brain. *J Cereb Blood Flow Metab* (1992) 12:434–47. doi:10.1038/jcbfm.1992.61
- Befroy DE, Perry RJ, Jain N, Dufour S, Cline GW, Trimmer JK, et al. Direct assessment of hepatic mitochondrial oxidative and anaplerotic fluxes in humans using dynamic <sup>13</sup>C magnetic resonance spectroscopy. *Nat Med* (2014) 20:98–102. doi:10.1038/nm.3415
- Jones JG, Solomon MA, Cole SM, Sherry AD, Malloy CR. An integrated <sup>2</sup>H and <sup>13</sup>C NMR study of gluconeogenesis and TCA cycle flux in humans. *Am J Physiol Endocrinol Metab* (2001) 281:E848–56.
- Jucker BM, Lee JV, Shulman RG. *In vivo* <sup>13</sup>C NMR measurements of hepatocellular tricarboxylic acid cycle flux. *J Biol Chem* (1998) 273:12187–94. doi:10.1074/jbc.273.20.12187
- Shestov AA, Barker B, Gu Z, Locasale JW. Computational approaches for understanding energy metabolism. *Wiley Interdiscip Rev Syst Biol Med* (2013) 5(6):733–50. doi:10.1002/wsbm.1238
- Shestov AA, Mancuso A, Lee SC, Guo L, Nelson DS, Roman JC, et al. Bonded cumomer analysis of human melanoma metabolism monitored by <sup>13</sup>C NMR spectroscopy of perfused tumor cells. *J Biol Chem* (2016) 291:5157–71. doi:10.1074/jbc.M115.701862
- Lee SC, Marzec M, Liu X, Wehrli S, Kantekure K, Ragunath PN, et al. Decreased lactate concentration and glycolytic enzyme expression reflect inhibition of mTOR signal transduction pathway in B-cell lymphoma. *NMR Biomed* (2013) 26:106–14. doi:10.1002/nbm.2825
- Lee SC, Delikatny EJ, Poptani H, Pickup S, Glickson JD. *In vivo* <sup>1</sup>H MRS of WSU-DLCL2 human non-Hodgkin's lymphoma xenografts: response to rituximab and rituximab plus CHOP. *NMR Biomed* (2009) 22:259–65. doi:10.1002/nbm.1316
- Lee SC, Huang MQ, Nelson DS, Pickup S, Wehrli S, Adegbola O, et al. *In vivo* MRS markers of response to CHOP chemotherapy in the WSU-DLCL2 human diffuse large B-cell lymphoma xenograft. *NMR Biomed* (2008) 21:723–33. doi:10.1002/nbm.1250
- Maher EA, Marin-Valencia I, Bachoo RM, Mashimo T, Raisanen J, Hatanpaa KJ, et al. Metabolism of U-<sup>13</sup>C glucose in human brain tumors *in vivo*. *NMR Biomed* (2012) 25:1234–44. doi:10.1002/nbm.2794
- Hensley CT, DeBerardinis RJ. *In vivo* analysis of lung cancer metabolism: nothing like the real thing. *J Clin Invest* (2015) 125:495–7. doi:10.1172/JCI79188
- de Graaf RA, Rothman DL, Behar KL. State of the art direct C-13 and indirect H-1-C-13 NMR spectroscopy *in vivo*. A practical guide. *NMR Biomed* (2011) 24:958–72. doi:10.1002/nbm.1761
- Brindle KM, Bohndiek SE, Gallagher FA, Kettunen MI. Tumor imaging using hyperpolarized C-13 magnetic resonance. *Magn Reson Med* (2011) 66:505–19. doi:10.1002/mrm.22999

## AUTHOR CONTRIBUTIONS

The study was conceived and coordinated by JG and AS; SL, KN, LG, DN, and JR designed and performed the experiments, and collected the data; AS, SL, KN, LG, IB, and JG analyzed and interpreted the experiments; AS performed computational metabolic analysis; MW and DL provided technical assistance and contributed to the preparation of the manuscript; JG provided conceptual advice; JG, SL, and AS wrote and edited the manuscript with the assistance of all authors.

## ACKNOWLEDGMENTS

These studies were performed at the Small Animal Imaging Facility of the University of Pennsylvania under the management of Dr. Stephen Pickup, whose assistance and guidance is gratefully acknowledged. Authors appreciate Dr. Anthony Mancuso for helpful discussion.

## FUNDING

This work was supported by the National Institute of Health Grants R01 CA129544 (JG) and R01 CA172820 (JG).

22. Park I, Larson PE, Zierhut ML, Hu S, Bok R, Ozawa T, et al. Hyperpolarized C-13 magnetic resonance metabolic imaging: application to brain tumors. *Neuro Oncol* (2010) 12:133–44. doi:10.1093/neuonc/nop043
23. Gavva SR, Wiethoff AJ, Zhao PY, Malloy CR, Sherry AD. A C-13 isotopomer NMR method for monitoring incomplete beta-oxidation of fatty-acids in intact tissue. *Biochem J* (1994) 303:847–53. doi:10.1042/bj3030847
24. Burgess SC, Haasler N, Merritt M, Jeffrey FM, Storey C, Milde A, et al. Impaired tricarboxylic acid cycle activity in mouse livers lacking cytosolic phosphoenolpyruvate carboxykinase. *Journal of Biological Chemistry* (2004) 279:48941–9. doi:10.1074/jbc.M407120200
25. Burgess SC, He T, Yan Z, Lindner J, Sherry AD, Malloy CR, et al. Cytosolic phosphoenolpyruvate carboxykinase does not solely control the rate of hepatic gluconeogenesis in the intact mouse liver. *Cell Metab* (2007) 5:313–20. doi:10.1016/j.cmet.2007.03.004
26. Burgess SC, Leone TC, Wende AR, Croce MA, Chen Z, Sherry AD, et al. Diminished hepatic gluconeogenesis via defects in tricarboxylic acid cycle flux in peroxisome proliferator-activated receptor gamma coactivator-1 alpha (PGC-1 alpha)-deficient mice. *J Biol Chem* (2006) 281:19000–8. doi:10.1074/jbc.M600050200
27. Haasler N, Browning J, Merritt M, Storey C, Milde A, Jeffrey FM, et al. Effects of insulin and cytosolic redox state on glucose production pathways in the isolated perfused mouse liver measured by integrated H-2 and C-13 NMR. *Biochem J* (2006) 394:465–73. doi:10.1042/BJ20051174
28. Jin ES, Jones JG, Merritt M, Burgess SC, Malloy CR, Sherry AD. Glucose production, gluconeogenesis, and hepatic tricarboxylic acid cycle fluxes measured by nuclear magnetic resonance analysis of a single glucose derivative. *Anal Biochem* (2004) 327:149–55. doi:10.1016/j.ab.2003.12.036
29. Jones JG, Naidoo R, Sherry AD, Jeffrey FM, Cottam GL, Malloy CR. Measurement of gluconeogenesis and pyruvate recycling in the rat liver: a simple analysis of glucose and glutamate isotopomers during metabolism of 1,2,3-C-13(3) propionate. *FEBS Lett* (1997) 412:131–7. doi:10.1016/S0014-5793(97)00764-3
30. Sherry AD, Jeffrey FMH, Malloy CR. Analytical solutions for C-13 isotopomer analysis of complex metabolic conditions: substrate oxidation, multiple pyruvate cycles, and gluconeogenesis. *Metab Eng* (2004) 6:12–24. doi:10.1016/j.ymben.2003.10.007
31. Bachelard H. Landmarks in the application of C-13-magnetic resonance spectroscopy to studies of neuronal/glial relationships. *Dev Neurosci* (1998) 20:277–88. doi:10.1159/000017322
32. Dusick JR, Glenn TC, Lee WN, Vespa PM, Kelly DF, Lee SM, et al. Increased pentose phosphate pathway flux after clinical traumatic brain injury: a 1,2-C-13(2) glucose labeling study in humans. *J Cereb Blood Flow Metab* (2007) 27:1593–602. doi:10.1038/sj.jcbfm.9600458
33. Fan TWM, Lane AN. Structure-based profiling of metabolites and isotopomers by NMR. *Prog Nucl Magn Reson Spectrosc* (2008) 52:69–117. doi:10.1016/j.pnmrs.2007.03.002
34. Gruetter R, Novotny EJ, Boulware SD, Mason GF, Rothman DL, Shulman GI, et al. Localized C-13 NMR-spectroscopy in the human brain of amino-acid labeling from D-1-C-13 GLUCOSE. *J Neurochem* (1994) 63:1377–85. doi:10.1046/j.1471-4159.1994.63041377.x
35. Hassel B, Brathe A. Cerebral metabolism of lactate in vivo: evidence for neuronal pyruvate carboxylation. *J Cereb Blood Flow Metab* (2000) 20:327–36. doi:10.1097/00004647-200002000-00014
36. Henry PG, Tkac I, Gruetter R. H-1-localized broadband C-13 NMR spectroscopy of the rat brain in vivo at 9.4 T. *Magn Reson Med* (2003) 50:684–92. doi:10.1002/mrm.10601
37. Kunnecke B, Cerdan S, Seelig J. Cerebral metabolism of 1,2-C-13(2) glucose and U-C-13(4) 3-hydroxybutyrate in rat-brain as detected by C-13 NMR-spectroscopy. *NMR Biomed* (1993) 6:264–77. doi:10.1002/nbm.1940060406
38. Lapidot A, Gopher A. Cerebral metabolic compartmentation – estimation of glucose flux via pyruvate-carboxylase pyruvate-dehydrogenase by C-13 NMR isotopomer analysis of D-U-C-13 glucose metabolites. *J Biol Chem* (1994) 269:27198–208.
39. Mason GF, Rothman DL. Basic principles of metabolic modeling of NMR C-13 isotopic turnover to determine rates of brain metabolism in vivo. *Metab Eng* (2004) 6:75–84. doi:10.1016/j.ymben.2003.10.003
40. Oz G, Berkich DA, Henry PG, Xu Y, LaNoue K, Hutson SM, et al. Neuroglial metabolism in the awake rat brain: CO<sub>2</sub> fixation increases with brain activity. *Journal of Neuroscience* (2004) 24:11273–9. doi:10.1523/JNEUROSCI.3564-04.2004
41. Zwingmann C, Richter-Landsberg C, Brand A, Leibfritz D. NMR spectroscopic study on the metabolic fate of 3-C-13 alanine in astrocytes, neurons, and cocultures: implications for glia-neuron interactions in neurotransmitter metabolism. *Glia* (2000) 32:286–303. doi:10.1002/1098-1136(200012)32:3<286::AID-GLIA80>3.0.CO;2-P
42. Zwingmann C, Richter-Landsberg C, Leibfritz D. C-13 isotopomer analysis of glucose and alanine metabolism reveals cytosolic pyruvate compartmentation as part of energy metabolism in astrocytes. *Glia* (2001) 34:200–12. doi:10.1002/glia.1054
43. Wiechert W, Mollney M, Isermann N, Wurzel M, de Graaf AA. Bidirectional reaction steps in metabolic networks: III. Explicit solution and analysis of isotopomer labeling systems. *Biotechnol Bioeng* (1999) 66:69–85. doi:10.1002/(SICI)1097-0290(1999)66:2<69::AID-BIT1>3.0.CO;2-6
44. Antoniewicz MR, Kelleher JK, Stephanopoulos G. Elementary metabolite units (EMU): a novel framework for modeling isotopic distributions. *Metab Eng* (2007) 9:68–86. doi:10.1016/j.ymben.2006.09.001
45. Shestov AA, Valette J, Deelchand DK, Ugurbil K, Henry PG. Metabolic modeling of dynamic brain C-13 NMR multiplet data: concepts and simulations with a two-compartment neuronal-glial model. *Neurochem Res* (2012) 37:2388–401. doi:10.1007/s11064-012-0782-5
46. Shestov AA, Mancuso A, Leeper DB, Glickson JD. Metabolic network analysis of DB1 melanoma cells: how much energy is derived from aerobic glycolysis? *Adv Exp Med Biol* (2013) 765:265–71. doi:10.1007/978-1-4614-4989-8\_37
47. Guo L, Shestov AA, Worth AJ, Nath K, Nelson DS, Leeper DB, et al. Inhibition of mitochondrial complex II by the anticancer agent lonidamine. *J Biol Chem* (2016) 291:42–57. doi:10.1074/jbc.M115.697516
48. Mehrmohamadi M, Liu XJ, Shestov AA, Locasale JW. Characterization of the usage of the serine metabolic network in human cancer. *Cell Rep* (2014) 9:1507–19. doi:10.1016/j.celrep.2014.10.026
49. Tzika AA, Fontes-Oliveira CC, Shestov AA, Constantinou C, Psychogios N, Righi V, et al. Skeletal muscle mitochondrial uncoupling in a murine cancer cachexia model. *Int J Oncol* (2013) 43:886–94. doi:10.3892/ijo.2013.1998
50. Wahl ML, Owen JA, Burd R, Herlands RA, Nogami SS, Rodeck U, et al. Regulation of intracellular pH in human melanoma: potential therapeutic implications. *Mol Cancer Ther* (2002) 1:617–28.
51. Fox JEM, Meredith D, Halestrap AP. Characterisation of human monocarboxylate transporter 4 substantiates its role in lactic acid efflux from skeletal muscle. *J Physiol* (2000) 529:285–93. doi:10.1111/j.1469-7793.2000.00285.x
52. Nancolas B, Sessions RB, Halestrap AP. Identification of key binding site residues of MCT1 for AR-C155858 reveals the molecular basis of its isoform selectivity. *Biochem J* (2015) 466:177–88. doi:10.1042/BJ20141223
53. Ovens MJ, Davies AJ, Wilson MC, Murray CM, Halestrap AP. AR-C155858 is a potent inhibitor of monocarboxylate transporters MCT1 and MCT2 that binds to an intracellular site involving transmembrane helices 7–10. *Biochem J* (2010) 425:523–30. doi:10.1042/BJ20091515
54. Bricker DK, Taylor EB, Schell JC, Orsak T, Boutron A, Chen YC, et al. A mitochondrial pyruvate carrier required for pyruvate uptake in yeast, *Drosophila*, and humans. *Science* (2012) 337:96–100. doi:10.1126/science.1218099
55. Halestrap AP. The mitochondrial pyruvate carrier: has it been unearthed at last? *Cell Metab* (2012) 16:141–3. doi:10.1016/j.cmet.2012.07.013
56. Herzog S, Raemy E, Montessuit S, Veuthey JL, Zamboni N, Westermann B, et al. Identification and functional expression of the mitochondrial pyruvate carrier. *Science* (2012) 337:93–6. doi:10.1126/science.1218530
57. Muzykantov VS, Shestov AA. Kinetic equations for the redistribution of isotopic molecules due to reversible dissociation. Homoeexchange of methane. *React Kinetics Catal Lett* (1986) 32(2):307–12.
58. Shestov AA, Valette J, Ugurbil K, Henry PG. On the reliability of (13)C metabolic modeling with two-compartment neuronal-glial models. *J Neurosci Res* (2007) 85:3294–303. doi:10.1002/jnr.21269
59. Heinrich R, Rapoport TA. A linear steady-state treatment of enzymatic chains. General properties, control and effector strength. *Eur J Biochem* (1974) 42:89–95. doi:10.1111/j.1432-1033.1974.tb03319.x
60. Kacser H, Burns JA. The control of flux. *Symp Soc Exp Biol* (1973) 27:65–104.

61. Hill LL, Korngold R, Jaworsky C, Murphy G, McCue P, Berd D. Growth and metastasis of fresh human melanoma tissue in mice with severe combined immunodeficiency. *Cancer Res* (1991) 51:4937–41.
62. Mancuso A, Beardsley NJ, Wehrli S, Pickup S, Matschinsky FM, Glickson JD. Real-time detection of <sup>13</sup>C NMR labeling kinetics in perfused EMT6 mouse mammary tumor cells and betaHC9 mouse insulinomas. *Biotechnol Bioeng* (2004) 87:835–48. doi:10.1002/bit.20191
63. Bentel M, Pick U, Avron M, Degani H. Metabolic studies with NMR-spectroscopy of the alga dunalia-salina trapped within agarose beads. *Eur J Biochem* (1990) 188:111–6. doi:10.1111/j.1432-1033.1990.tb15377.x
64. Mancuso A, Fernandez EJ, Blanch HW, Clark DS. A nuclear magnetic resonance technique for determining hybridoma cell concentration in hollow fiber bioreactors. *Biotechnology (N Y)* (1990) 8:1282–5. doi:10.1038/nbt1290-1282
65. Leeper DB, Engin K, Thistlethwaite AJ, Hitchon HD, Dover JD, Li DJ, et al. Human tumor extracellular pH as a function of blood glucose concentration. *Int J Radiat Oncol Biol Phys* (1994) 28:935–43. doi:10.1016/0360-3016(94)90114-7
66. Tannock IF, Rotin D. Acid pH in tumors and its potential for therapeutic exploitation. *Cancer Res* (1989) 49:4373–84.
67. Mancuso A, Zhu A, Beardsley NJ, Glickson JD, Wehrli S, Pickup S. Artificial tumor model suitable for monitoring <sup>31</sup>P and <sup>13</sup>C NMR spectroscopic changes during chemotherapy-induced apoptosis in human glioma cells. *Magn Reson Med* (2005) 54:67–78. doi:10.1002/mrm.20545
68. Ascierto PA, Kirkwood JM, Grob JJ, Simeone E, Grimaldi AM, Maio M, et al. The role of BRAF V600 mutation in melanoma. *J Transl Med* (2012) 10:85. doi:10.1186/1479-5876-10-85
69. Kaplon J, Zheng L, Meissl K, Chaneton B, Selivanov VA, Mackay G, et al. A key role for mitochondrial gatekeeper pyruvate dehydrogenase in oncogene-induced senescence. *Nature* (2013) 498:109–12. doi:10.1038/nature12154
70. Mullen AR, Hu Z, Shi X, Jiang L, Boroughs LK, Kovacs Z, et al. Oxidation of alpha-ketoglutarate is required for reductive carboxylation in cancer cells with mitochondrial defects. *Cell Rep* (2014) 7:1679–90. doi:10.1016/j.celrep.2014.04.037
71. DeBerardinis RJ, Mancuso A, Daikhin E, Nissim I, Yudkoff M, Wehrli S, et al. Beyond aerobic glycolysis: transformed cells can engage in glutamine metabolism that exceeds the requirement for protein and nucleotide synthesis. *Proc Natl Acad Sci U S A* (2007) 104:19345–50. doi:10.1073/pnas.0709747104
72. Wise DR, DeBerardinis RJ, Mancuso A, Sayed N, Zhang XY, Pfeiffer HK, et al. Myc regulates a transcriptional program that stimulates mitochondrial glutaminolysis and leads to glutamine addiction. *Proc Natl Acad Sci U S A* (2008) 105:18782–7. doi:10.1073/pnas.0810199105
73. Rajagopalan KN, DeBerardinis RJ. Role of glutamine in cancer: therapeutic and imaging implications. *J Nucl Med* (2011) 52:1005–8. doi:10.2967/jnumed.110.084244
74. Hensley CT, Wasti AT, DeBerardinis RJ. Glutamine and cancer: cell biology, physiology, and clinical opportunities. *J Clin Invest* (2013) 123:3678–84. doi:10.1172/JCI69600
75. Le A, Dang CV. Studying Myc's role in metabolism regulation. *Methods Mol Biol* (2013) 1012:213–9. doi:10.1007/978-1-62703-429-6\_14
76. Fan J, Kamphorst JJ, Mathew R, Chung MK, White E, Shlomi T, et al. Glutamine-driven oxidative phosphorylation is a major ATP source in transformed mammalian cells in both normoxia and hypoxia. *Mol Syst Biol* (2013) 9:712. doi:10.1038/msb.2013.65
77. Scott DA, Richardson AD, Filipp FV, Knutzen CA, Chiang GG, Ronai ZA, et al. Comparative metabolic flux profiling of melanoma cell lines: beyond the Warburg effect. *J Biol Chem* (2011) 286:42626–34. doi:10.1074/jbc.M111.282046
78. Schug ZT, Peck B, Jones DT, Zhang Q, Grosskurth S, Alam IS, et al. Acetyl-CoA synthetase 2 promotes acetate utilization and maintains cancer cell growth under metabolic stress. *Cancer Cell* (2015) 27:57–71. doi:10.1016/j.ccr.2014.12.002
79. Fan J, Ye J, Kamphorst JJ, Shlomi T, Thompson CB, Rabinowitz JD. Quantitative flux analysis reveals folate-dependent NADPH production. *Nature* (2014) 510:298–302. doi:10.1038/nature13236
80. Marzec M, Kasprzycka M, Liu X, El-Salem M, Halasa K, Raghunath PN, et al. Oncogenic tyrosine kinase NPM/ALK induces activation of the rapamycin-sensitive mTOR signaling pathway. *Oncogene* (2007) 26:5606–14. doi:10.1038/sj.onc.1209843
81. Marzec M, Liu X, Kasprzycka M, Witkiewicz A, Raghunath PN, El-Salem M, et al. IL-2- and IL-15-induced activation of the rapamycin-sensitive mTORC1 pathway in malignant CD4(+) T lymphocytes. *Blood* (2008) 111:2181–9. doi:10.1182/blood-2007-06-095182
82. Włodarski P, Kasprzycka M, Liu X, Marzec M, Robertson ES, Slupianek A, et al. Activation of mammalian target of rapamycin in transformed B lymphocytes is nutrient dependent but independent of Akt, mitogen-activated protein kinase/extracellular signal-regulated kinase kinase, insulin growth factor-1, and serum. *Cancer Res* (2005) 65:7800–8. doi:10.1158/0008-5472.CAN-04-4180
83. Corradetti MN, Guan KL. Upstream of the mammalian target of rapamycin: do all roads pass through mTOR? *Oncogene* (2006) 25:6347–60. doi:10.1038/sj.onc.1209885
84. Petroulakis E, Mamane Y, Le Bacquer O, Shahbazian D, Sonenberg N. mTOR signaling: implications for cancer and anticancer therapy. *Br J Cancer* (2006) 94:195–9. doi:10.1038/sj.bjc.6602902
85. Sabatini DM. mTOR and cancer: insights into a complex relationship. *Nat Rev Cancer* (2006) 6:729–34. doi:10.1038/nrc1974
86. Arvisais EW, Romanelli A, Hou XY, Davis JS. AKT-independent phosphorylation of TSC2 and activation of mTOR and ribosomal protein S6 kinase signaling by prostaglandin F2 alpha. *J Biol Chem* (2006) 281:26904–13. doi:10.1074/jbc.M605371200
87. Chan SM, Weng AP, Tibshirani R, Aster JC, Utz PJ. Notch signals positively regulate activity of the mTOR pathway in T-cell acute lymphoblastic leukemia. *Blood* (2007) 110:278–86. doi:10.1182/blood-2006-08-039883
88. Sakata A, Kuwahara K, Ohmura T, Inui S, Sakaguchi N. Involvement of a rapamycin-sensitive pathway in CD40-mediated activation of murine B cells in vitro. *Immunol Lett* (1999) 68:301–9. doi:10.1016/S0165-2478(99)00053-X
89. Shillingford JM, Murcia NS, Larson CH, Low SH, Hedgepeth R, Brown N, et al. The mTOR pathway is regulated by polycystin-1, and its inhibition reverses renal cystogenesis in polycystic kidney disease. *Proc Natl Acad Sci USA* (2006) 103:5466–71. doi:10.1073/pnas.0509694103
90. Suh JM, Song JH, Kim DW, Kim H, Chung HK, Hwang JH, et al. Regulation of the phosphatidylinositol 3-kinase, Akt/protein kinase B, FRAP/mammalian target of rapamycin, and ribosomal S6 kinase 1 signaling pathways by thyroid-stimulating hormone (TSH) and stimulating type TSH receptor antibodies in the thyroid gland. *Journal of Biological Chemistry* (2003) 278:21960–71. doi:10.1074/jbc.M300805200
91. Wing LYC, Chen HM, Chuang PC, Wu MH, Tsai SJ. The mammalian target of rapamycin-p70 ribosomal S6 kinase but not phosphatidylinositol 3-kinase-Akt signaling is responsible for fibroblast growth factor-9-induced cell proliferation. *J Biol Chem* (2005) 280:19937–47. doi:10.1074/jbc.M411865200
92. Nave BT, Ouwendam DM, Withers DJ, Alessi DR, Shepherd PR. Mammalian target of rapamycin is a direct target for protein kinase B: identification of a convergence point for opposing effects of insulin and amino-acid deficiency on protein translation. *Biochem J* (1999) 344:427–31. doi:10.1042/0264-6021:3440427
93. Sekulić A, Hudson CC, Homme JL, Yin P, Otterness DM, Karrnitz LM, et al. A direct linkage between the phosphoinositide 3-Kinase-AKT signaling pathway and the mammalian target of rapamycin in mitogen-stimulated and transformed cells. *Cancer Res* (2000) 60:3504–13.
94. Tee AR, Anjum R, Blenis J. Inactivation of the tuberous sclerosis complex-1 and -2 gene products occurs by phosphoinositide 3-kinase/Akt-dependent and -independent phosphorylation of tuberin. *J Biol Chem* (2003) 278:37288–96. doi:10.1074/jbc.M303257200
95. Ma L, Chen ZB, Erdjument-Bromage H, Tempst P, Pandolfi PP. Phosphorylation and functional inactivation of TSC2 by Erk: implications for tuberous sclerosis and cancer pathogenesis. *Cell* (2005) 121:179–93. doi:10.1016/j.cell.2005.02.031
96. Leseux L, Hamdi SM, Al Saati T, Capilla F, Recher C, Laurent G, et al. Syk-dependent mTOR activation in follicular lymphoma cells. *Blood* (2006) 108:4156–62. doi:10.1182/blood-2006-05-026203
97. Gottschalk S, Anderson N, Hainz C, Eckhardt SG, Serkova NJ. Imatinib (ST1571)-mediated changes in glucose metabolism in human leukemia BCR-ABL-positive cells. *Clin Cancer Res* (2004) 10:6661–8. doi:10.1158/1078-0432.CCR-04-0039
98. Kominsky DJ, Klawitter J, Brown JL, Boros LG, Melo JV, Eckhardt SG, et al. Abnormalities in glucose uptake and metabolism in imatinib-resistant human BCR-ABL-positive cells. *Clinical Cancer Research* (2009) 15:3442–50. doi:10.1158/1078-0432.CCR-08-3291

99. Carayol N, Katsoulidis E, Sassano A, Altman JK, Druker BJ, Platanias LC. Suppression of programmed cell death 4 (PDCD4) protein expression by BCR-ABL-regulated engagement of the mTOR/p70 S6 kinase pathway. *Journal of Biological Chemistry* (2008) 283:8601–10. doi:10.1074/jbc.M707934200
100. Düvel K, Yecies JL, Menon S, Raman P, Lipovsky AI, Souza AL, et al. Activation of a metabolic gene regulatory network downstream of mTOR complex 1. *Mol Cell* (2010) 39:171–83. doi:10.1016/j.molcel.2010.06.022
101. Nath K, Nelson DS, Ho AM, Lee SC, Darpolar MM, Pickup S, et al. 31P and 1H MRS of DB-1 melanoma xenografts: lonidamine selectively decreases tumor intracellular pH and energy status and sensitizes tumors to melphalan. *NMR Biomed* (2013) 26(1):98–105. doi:10.1002/nbm.2824
102. DeBrosse C, Nanga RP, Bagga P, Nath K, Haris M, Marincola F, et al. Lactate chemical exchange saturation transfer (LATEST) imaging in vivo: a biomarker for LDH activity. *Sci Rep* (2016) 6:19517. doi:10.1038/srep19517

**Conflict of Interest Statement:** The authors declare that the research was conducted in the absence of any commercial or financial relationships that could be construed as a potential conflict of interest.

The reviewer NM and handling Editor declared their shared affiliation and the handling Editor states that the process nevertheless met the standards of a fair and objective review.

Copyright © 2016 Shestov, Lee, Nath, Guo, Nelson, Roman, Leeper, Wasik, Blair and Glickson. This is an open-access article distributed under the terms of the Creative Commons Attribution License (CC BY). The use, distribution or reproduction in other forums is permitted, provided the original author(s) or licensor are credited and that the original publication in this journal is cited, in accordance with accepted academic practice. No use, distribution or reproduction is permitted which does not comply with these terms.



# Molecular Imaging of Metabolic Reprograming in Mutant IDH Cells

Pavithra Viswanath, Myriam M. Chaumeil and Sabrina M. Ronen\*

Department of Radiology and Biomedical Imaging, University of California San Francisco, San Francisco, CA, USA

## OPEN ACCESS

**Edited by:**

Zaver Bhujwalla,  
Johns Hopkins University School of  
Medicine, USA

**Reviewed by:**

Luigi Aloj,  
Istituto Nazionale Tumori Fondazione  
G. Pascale, Italy  
Natalie Julie Serkova,  
University of Colorado, USA  
Tariq Shah,  
Johns Hopkins University, USA

**\*Correspondence:**

Sabrina M. Ronen  
sabrina.ronen@ucsf.edu

**Specialty section:**

This article was submitted to Cancer  
Imaging and Diagnosis,  
a section of the journal  
*Frontiers in Oncology*

**Received:** 07 December 2015

**Accepted:** 28 February 2016

**Published:** 14 March 2016

**Citation:**

Viswanath P, Chaumeil MM and  
Ronan SM (2016) Molecular Imaging of  
Metabolic Reprograming in Mutant  
IDH Cells.  
*Front. Oncol.* 6:60.  
doi: 10.3389/fonc.2016.00060

Mutations in the metabolic enzyme isocitrate dehydrogenase (IDH) have recently been identified as drivers in the development of several tumor types. Most notably, cytosolic IDH1 is mutated in 70–90% of low-grade gliomas and upgraded glioblastomas, and mitochondrial IDH2 is mutated in ~20% of acute myeloid leukemia cases. Wild-type IDH catalyzes the interconversion of isocitrate to  $\alpha$ -ketoglutarate ( $\alpha$ -KG). Mutations in the enzyme lead to loss of wild-type enzymatic activity and a neomorphic activity that converts  $\alpha$ -KG to 2-hydroxyglutarate (2-HG). In turn, 2-HG, which has been termed an “oncometabolite,” inhibits key  $\alpha$ -KG-dependent enzymes, resulting in alterations of the cellular epigenetic profile and, subsequently, inhibition of differentiation and initiation of tumorigenesis. In addition, it is now clear that the IDH mutation also induces a broad metabolic reprogramming that extends beyond 2-HG production, and this reprogramming often differs from what has been previously reported in other cancer types. In this review, we will discuss in detail what is known to date about the metabolic reprogramming of mutant IDH cells, and how this reprogramming has been investigated using molecular metabolic imaging. We will describe how metabolic imaging has helped shed light on the basic biology of mutant IDH cells, and how this information can be leveraged to identify new therapeutic targets and to develop new clinically translatable imaging methods to detect and monitor mutant IDH tumors *in vivo*.

**Keywords:** mutant IDH1, metabolic reprogramming, magnetic resonance spectroscopy, molecular imaging, cancer, 2-hydroxyglutarate, low-grade gliomas

## INTRODUCTION

Altered cellular metabolism is a feature of malignant cancer cells (1–4). In the 1920s, Warburg described the elevated conversion of glucose into lactate, which occurs in tumor cells even under normoxia (Warburg effect) (5). Contrary to Warburg's hypothesis that held defective mitochondrial function responsible for aerobic glycolysis, it is now understood that tumor cells actively reprogram cellular metabolism to support tumor growth and metastasis (6–8). This increased glucose consumption and glycolytic flux contribute to acidification of the microenvironment, likely facilitating metastasis (9). Furthermore, glycolytic intermediates are used for anabolic reactions leading to nucleotide, phospholipid, and amino acid biosynthesis, providing the building blocks required for cell proliferation (7, 8, 10). Additionally, glutaminolysis provides the anaplerotic flux to replenish TCA cycle intermediates depleted for biosynthetic purposes and generates NADPH required for redox homeostasis and lipid synthesis (11–13). Choline metabolism is also modulated to provide precursors for membrane biosynthesis (14).

To date, the emerging paradigm recognizes that oncogene and tumor suppressor signaling pathways are responsible for the deregulation of metabolic pathways in cancer (15–22). Mutations in the PI3K and LKB1–AMPK signaling pathways, Myc and Ras oncogenes, and the tumor suppressor p53 all reprogram metabolism (16, 23–34). However, the discovery of tumors with gain-of-function mutations in metabolic enzymes provides strong evidence that altered metabolism can also result from mutations in metabolic enzymes. This is particularly true for tumors with mutations in the cytosolic or mitochondrial forms of isocitrate dehydrogenase (IDH1 and IDH2, respectively) (19, 35, 36).

Mutations in IDH1 were first described in a whole-genome sequence analysis of glioblastoma patients (37). Subsequent studies confirmed the presence of IDH mutations in 70–90% of low-grade glioma and secondary glioblastoma, in ~20% of acute myeloid leukemia, and in intrahepatic cholangiocarcinoma, chondrosarcoma, and melanoma (36, 38, 39). The IDH1 mutation is one of the earliest known genetic events in low-grade gliomas, and it is thought to be a “driver” mutation for tumorigenesis (40). Discovery of the IDH1 mutation has also led to a molecular (rather than histological) classification of gliomas (41). Presence of the IDH1 mutation in this new classification is associated with a more favorable prognosis compared to tumors with wild-type IDH1 (42). The reasons for this better prognosis remain to be determined, but different cellular metabolism could be a contributing factor.

From a metabolic perspective, mutations in IDH1 and IDH2 lead not only to the loss of wild-type enzyme activity [interconversion of isocitrate to  $\alpha$ -ketoglutarate ( $\alpha$ -KG)] but also to a gain-of-function that results in the conversion of  $\alpha$ -KG to the “oncometabolite” 2-hydroxyglutarate (2-HG) (43). 2-HG is a competitive inhibitor of multiple  $\alpha$ -KG-dependent dioxygenases, such as the prolyl hydroxylases, the Jumonji C family of histone demethylases, and the TET family of DNA hydroxylases (44). As a result, IDH1/2 mutant cells undergo extensive epigenetic modifications that ultimately result in tumorigenesis (45–48).

Among other changes, the IDH mutation leads to alterations in cellular metabolism extending beyond 2-HG production. Interestingly, many of these changes differ from those observed in other, non-IDH mutated, cancer cells. To date, the metabolic characterization of mutant IDH cells has been carried out using either mass spectrometry (MS) or magnetic resonance spectroscopy (MRS) (49). MS has the advantage of exquisite sensitivity (as low as picomolar) yielding a wealth of information on a wide range of cellular metabolites. However, with some exceptions (e.g., acute myeloid leukemia), MS requires the destruction of cell/tissue sample; and hence, clinical translation is limited. MRS can only detect metabolites above 0.1–1 mM and *in vivo* spectra at clinical field strengths cannot resolve closely resonating metabolites. Nonetheless, MRS can be used as a translational, non-invasive modality to detect and quantify metabolites in cells and *in vivo* in animals and patients.  $^1\text{H}$ - and  $^{31}\text{P}$ -MRS can be used to quantify steady-state metabolite levels, whereas  $^{13}\text{C}$ - and hyperpolarized  $^{13}\text{C}$ -MRS can be used to monitor metabolic fluxes (50–55).

In this review, we will discuss what is known about the metabolic reprogramming of mutant IDH cells from a molecular imaging perspective. We will begin by reviewing the various MRS

approaches that have been applied to image 2-HG. This will be followed by a comprehensive discussion of metabolic alterations in mutant IDH tumors and the imaging methods used to investigate these changes. We will describe how molecular imaging has helped shed light on the basic biology of mutant IDH cells and will address how this knowledge could serve to identify new therapeutic targets and novel methods for imaging mutant IDH tumors in the clinic.

## IMAGING 2-HG AND 2-HG PRODUCTION

### *Ex Vivo* Measurement of 2-HG Levels

The most obvious metabolic change in IDH mutant cells is the production of 2-HG (Figure 1). Using MS, Dang et al. reported elevated levels of 2-HG (5–35  $\mu\text{mol/g}$  tissue) in patient glioma tissues (43). Gross et al., again using MS, reported elevated 2-HG levels (~10,000 ng/2  $\times 10^6$  cells) in extracts from patients with IDH1/2 mutant acute myeloid leukemia (38). Elkhaled et al. used  $^1\text{H}$  high-resolution magic-angle spinning spectroscopy (HRMAS) to quantify 2-HG levels in patients with low-grade glioma (56). 2-HG levels correlated with the IDH1 mutation determined by immunohistochemistry with 86% concordance. Interestingly, 2-HG levels across tumor samples of different grades correlated positively with increased cellularity and mitotic density on histopathology, suggesting that the amount of 2-HG per cell remained unchanged during malignant transformation. This finding is consistent with the role of mutant IDH1 as a driver mutation essential for initiating tumorigenesis (40). Kalinina et al. also analyzed tumor biopsy samples from low-grade glioma patients using two-dimensional (2D) correlation spectroscopy (COSY) (57). In a randomized blinded analysis of 45 glioma samples, spectroscopic analysis was successful in quantifying the 2-HG cross-peaks in IDH mutant tissues with 97.8% accuracy.

### *In Vivo* Measurement of 2-HG Levels

Although 2-HG levels are relatively high in IDH1 mutant tumors (5–35 mM), *in vivo* detection using  $^1\text{H}$ -MRS is hampered by the presence of overlapping resonances from glutamate and glutamine in the 2–3 ppm region of the spectrum. Strategies to enable proper 2-HG quantification therefore need to be implemented, either at acquisition or at postprocessing.

Two studies validated a single-voxel  $^1\text{H}$ -MR double-echo Point RESolved Spectroscopy (PRESS) sequence to estimate 2-HG levels in mutant IDH1 tumor patients (58, 59). Pope et al. evaluated 27 patients with glial tumors using a dedicated LC-model postprocessing analysis to measure 2-HG in tumor voxels. They found significantly elevated 2-HG levels in IDH mutant tumors compared to wild-type tumors and correlated the 2-HG levels with values measured by MS (58). Choi et al. examined  $^1\text{H}$ -MRS data from 30 glioma patients in a manner blinded to IDH mutational status (59). In this study, in addition to postprocessing dedicated to fitting the data, the authors also carefully optimized the acquisition echo time to minimize the overlap between 2-HG and glutamate/glutamine resonances. In every case where 2-HG was detected by MRS, the sample showed the presence of an IDH1/2 mutation. Conversely, the absence of a 2-HG signal was

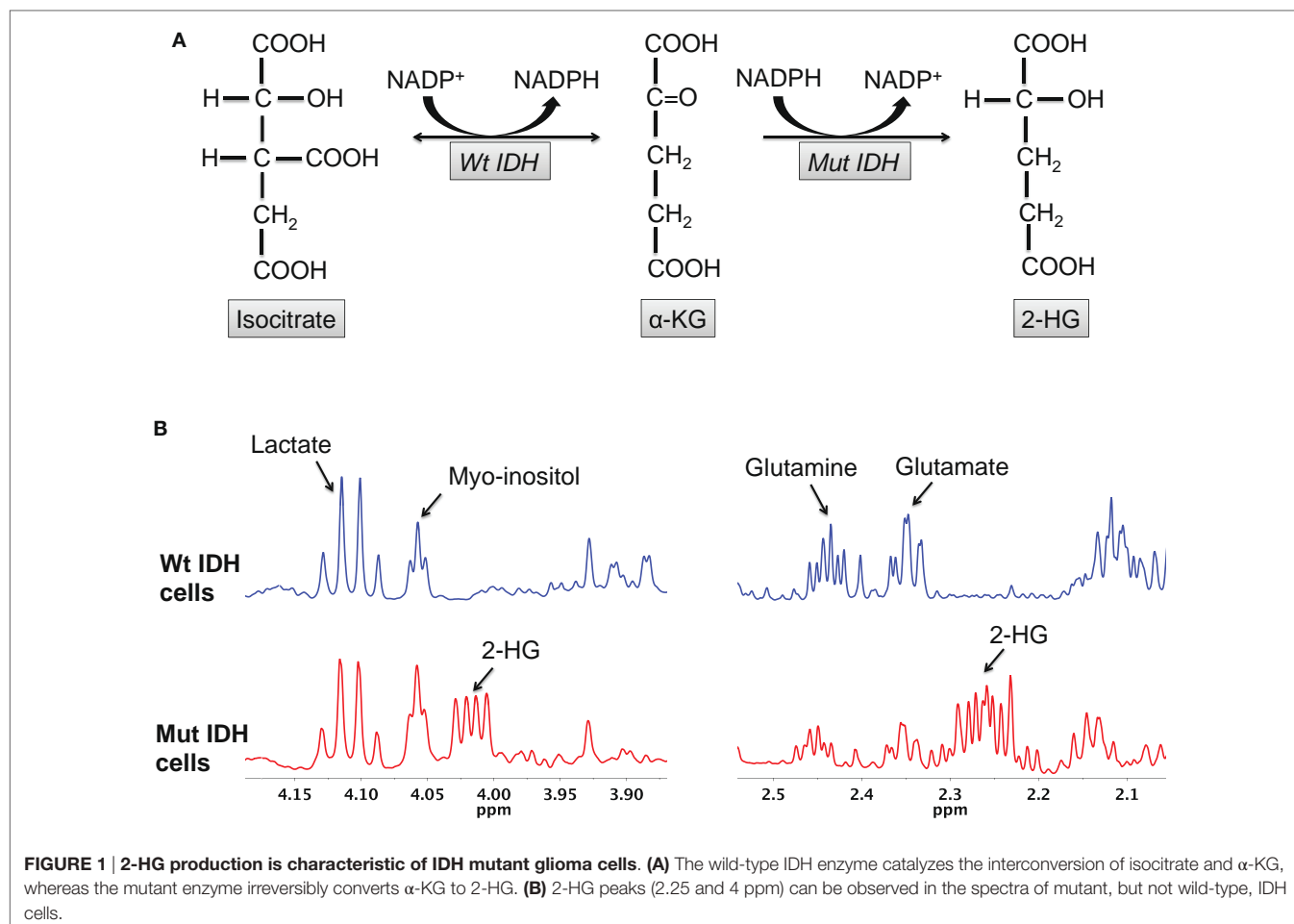


**FIGURE 1 |** 2-HG production is characteristic of IDH mutant glioma cells. **(A)** The wild-type IDH enzyme catalyzes the interconversion of isocitrate and  $\alpha$ -KG, whereas the mutant enzyme irreversibly converts  $\alpha$ -KG to 2-HG. **(B)** 2-HG peaks (2.25 and 4 ppm) can be observed in the spectra of mutant, but not wild-type, IDH cells.

associated with IDH wild-type status. In a third study, Andronesi et al. used a more complex 2D-COSY MRS method to detect 2-HG in mutant IDH1 glioma patients and in *ex vivo* biopsy samples (60). Use of the 2D acquisition method could prevent false-positive detection of 2-HG that might result from improper fitting of 1D MR spectra and the spectral proximity of 2-HG to glutamate/glutamine. However, the acquisition time for 2D data is significantly longer than 1D method and thus potentially more challenging to implement in the clinic.

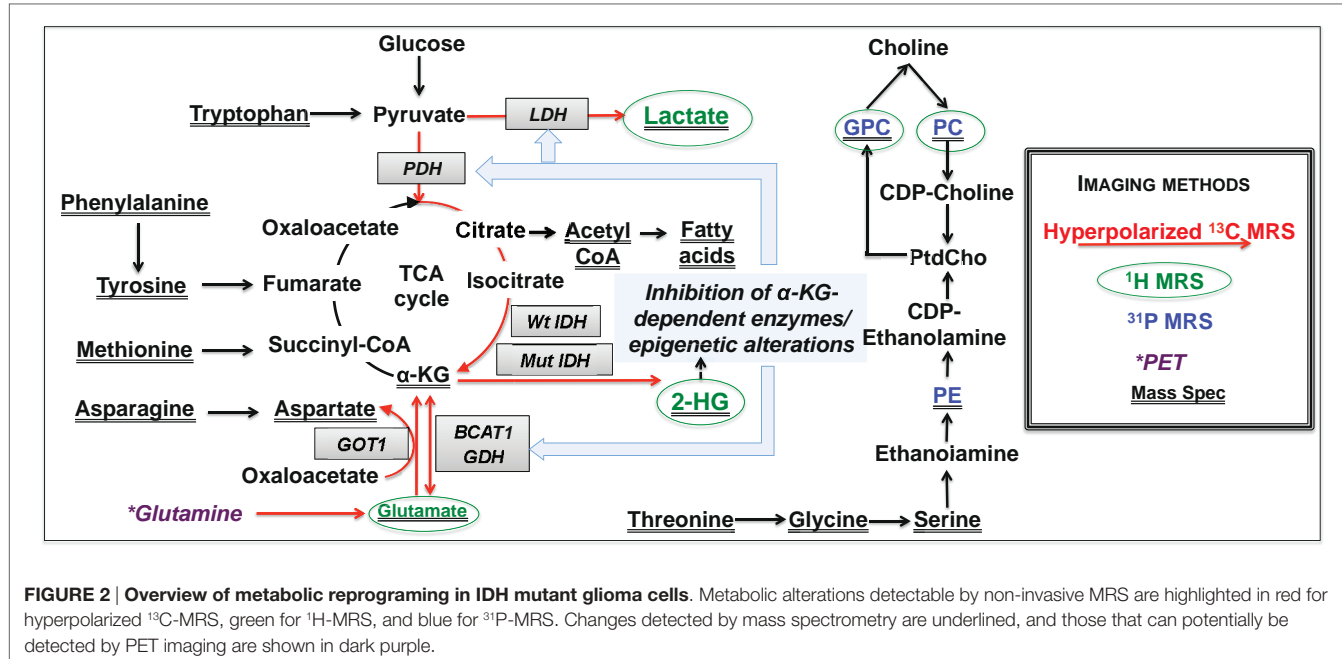
### In Vivo Measurement of 2-HG Production

$^{13}\text{C}$ -MRS has been used extensively, especially in the preclinical arena, to inform on real-time metabolic fluxes by probing the fate of exogenous  $^{13}\text{C}$ -labeled substrates (61). However,  $^{13}\text{C}$ -MRS lacks sensitivity and therefore requires relatively long acquisition times to achieve an adequate signal-to-noise ratio (SNR), limiting its implementation *in vivo*. The recent development of dissolution dynamic nuclear polarization (DNP) can overcome this limitation. Using dissolution DNP,  $^{13}\text{C}$ -labeled compounds can be hyperpolarized, dissolved into solution, injected into the sample (or subject), and be rapidly detected by MRS with a 10,000- to 50,000-fold increase in SNR compared to thermally polarized compounds (62, 63).  $^{13}\text{C}$ -MRS of hyperpolarized

compounds has been used to monitor enzymatic activities in solution, cells, and *in vivo* (51, 64–66). Using this technology, our laboratory designed and validated a new DNP probe, hyperpolarized [ $1\text{-}^{13}\text{C}$ ]- $\alpha$ -KG, for non-invasive  $^{13}\text{C}$ -MRS imaging of 2-HG synthesis. We showed that, following injection of hyperpolarized [ $1\text{-}^{13}\text{C}$ ]- $\alpha$ -KG, the production of hyperpolarized [ $1\text{-}^{13}\text{C}$ ]-2-HG could be detected in lysates and in orthotopic mutant IDH1 tumors in rodents, but not in their wild-type counterparts (Figure 2) (67). By providing dynamic information with regard to the metabolic fate of hyperpolarized [ $1\text{-}^{13}\text{C}$ ]- $\alpha$ -KG, this approach provides complementary information to  $^1\text{H}$ -MRS, which detects steady-state levels of 2-HG. As such, the hyperpolarized method can inform in real-time on the presence of active mutant IDH1 and on potential inhibition of mutant IDH1 by novel therapies.

### Metabolic Precursors of 2-HG

Although thermal equilibrium  $^{13}\text{C}$ -MRS is not readily translatable, it can be used to monitor metabolic fluxes in the preclinical setting and has been used to identify the metabolic precursors of 2-HG. Dang et al. demonstrated that glutamine is the major precursor of 2-HG (43). However, we and others have demonstrated that glucose also contributes to 2-HG synthesis. In a study by Pichumani et al., mutant IDH1 glioma patients received an



infusion of [ $\text{U-}^{13}\text{C}$ ]-glucose during surgical tumor resection (68). *Ex vivo*  $^{13}\text{C}$ -MRS on biopsy extracts revealed  $^{13}\text{C}$ -labeling in 2-HG, indicating that glucose contributes to 2-HG production. In our laboratory, we incubated two IDH1 mutant glioma models with [ $1-^{13}\text{C}$ ]-glucose and [ $3-^{13}\text{C}$ ]-glutamine and analyzed the proportion of  $^{13}\text{C}$ -labeled 2-HG derived from each precursor. We found that ~20% of 2-HG was derived from glucose and ~80% from glutamine (69). These findings have therapeutic implications since inhibiting glutaminase (the enzyme that converts glutamine to glutamate, the precursor of  $\alpha$ -KG and 2-HG) has been explored as a therapeutic target for IDH mutant cells, without considering that glucose could serve as an alternate source of 2-HG (70, 71).

## IMAGING METABOLIC REPROGRAMMING IN IDH MUTANT CELLS

Although the most obvious metabolic change in IDH mutant cells is the production of 2-HG, a number of studies indicate that IDH mutant cells undergo broader metabolic reprogramming. Reitman et al. conducted an MS-based metabolomic analysis of oligodendrogloma cells engineered to express wild-type or mutant IDH1 and IDH2 (72). Mutant IDH1/2 cells showed significantly increased levels of several amino acids, such as glycine, serine, threonine, asparagine, phenylalanine, tyrosine, tryptophan, and methionine (Figure 2). Glycerophosphocholine (GPC) levels were also higher, whereas glutamate, aspartate, and  $N$ -acetylated amino acid levels were reduced in IDH mutant cells compared to wild-type (Figure 2). Ohka et al. also carried out an MS analysis of wild-type or mutant IDH patient glioma tissues and reported a significant decrease in the levels of  $N$ -acetylated amino acids and glutamate (73). Additionally, both studies reported no change in glycolytic or pentose phosphate pathway intermediates in IDH mutant cells. We used high-resolution  $^1\text{H}$ -MRS to

compare the metabolome of U87 cells expressing wild-type or mutant IDH1 and the metabolome of normal human astrocytes (NHA) expressing wild-type or mutant IDH1 (74). In line with MS observations, we found that the  $^1\text{H}$ -MRS-detectable steady-state levels of intracellular lactate, glutamate, and phosphocholine (PC) were significantly reduced in IDH1 mutant cells relative to wild-type, and GPC levels were higher (Figure 2). Collectively, these studies demonstrated that mutant IDH cells broadly reprogram their metabolism and laid the foundation for more in-depth investigations, as reviewed below.

## Aerobic Glycolysis

In our  $^1\text{H}$ -MRS study, we observed a reduction in intracellular lactate levels in IDH1 mutant glioma cells (Figure 2), suggesting that their metabolic reprogramming could differ from other types of cancer cells (74). Chesnelong et al. confirmed this hypothesis and demonstrated that expression of lactate dehydrogenase A (LDHA), which catalyzes the production of lactate from pyruvate, was reduced in IDH mutant patient-derived glioma tissues compared to IDH wild-type glioblastoma that display elevated lactate production (75, 76). Importantly, LDHA silencing was mediated by increased promoter methylation consistent with the hypermethylator phenotype of IDH mutant cells.

In an effort to develop a complementary and clinically relevant imaging method for probing mutant IDH1-associated LDHA silencing, we recently investigated the fate of hyperpolarized [ $1-^{13}\text{C}$ ]-pyruvate in the BT142 patient-derived mutant IDH1 model *in vivo*. We found that hyperpolarized [ $1-^{13}\text{C}$ ]-lactate produced from hyperpolarized [ $1-^{13}\text{C}$ ]-pyruvate was comparable between mutant IDH1 tumors and normal brain in the BT142 model, in contrast to wild-type IDH1 glioma models, wherein hyperpolarized [ $1-^{13}\text{C}$ ]-lactate is significantly higher than in normal brain (77).

## Glutamate Metabolism and TCA Cycle

Glutamate levels are reduced in IDH mutant cells compared to wild-type (72–74). Furthermore, using  $^1\text{H}$ -MRS, Choi et al. showed that mutant IDH1 tumors showed reduced glutamate levels compared to normal brain, indicating that reduced glutamate could serve as a biomarker of mutant IDH1 tumors (78). In an effort to understand and image the metabolic alterations leading to glutamate reduction, several studies have been performed, each investigating a different step in glutamate production.

Branched chain amino acid (BCAA) transferase (BCAT) 1 and 2 catalyze the transfer of an amino group from BCAA to  $\alpha$ -KG, resulting in the production of glutamate and  $\alpha$ -keto acid. Tonjes et al. reported that BCAT1 expression was significantly reduced in IDH mutant cells (79). To image this reprogramming, we expanded on our previous study (67) and used hyperpolarized [ $1\text{-}^{13}\text{C}$ ]- $\alpha$ -KG to monitor hyperpolarized [ $1\text{-}^{13}\text{C}$ ]-glutamate production in mutant IDH1 tumors (80). We showed that conversion of hyperpolarized [ $1\text{-}^{13}\text{C}$ ]- $\alpha$ -KG to glutamate was reduced in mutant IDH1 tumors compared to wild-type, in line with decreased BCAT1. In addition, we observed decreased expression of aspartate transaminase (GOT1) and glutamate dehydrogenase (GDH), two other enzymes catalyzing  $\alpha$ -KG to glutamate metabolism, suggesting additional metabolic reprogramming associated with the IDH1 mutation (Figure 2). BCAT1 and GOT1 promoter methylation is higher in mutant IDH cells, providing a likely mechanistic link between the IDH1 mutations and reduced  $\alpha$ -KG to glutamate conversion (46, 79).

When considering the hyperpolarized approach for imaging glutamate production, our studies monitoring the fate of hyperpolarized [ $1\text{-}^{13}\text{C}$ ]- $\alpha$ -KG used pulse sequences optimized for the detection of only one metabolite: 2-HG or glutamate. However, further optimization of pulse sequences for detection of both 2-HG and glutamate could provide a molecular imaging approach that would simultaneously image IDH mutational status and the metabolic reprogramming specifically associated with the mutation.

In an effort to consider additional metabolic alterations that could lead to a drop in glutamate levels, we used thermal equilibrium  $^{13}\text{C}$ -MRS to probe upstream metabolic precursors of glutamate (69). We found that there was a significant reduction in  $^{13}\text{C}$ -labeled-glutamate derived from [ $1\text{-}^{13}\text{C}$ ]-glucose in IDH mutant cells compared to wild-type resulting from lower PDH activity (69). Further mechanistic studies revealed that PDH activity was reduced due to increased inhibitory phosphorylation mediated by elevated expression of pyruvate dehydrogenase kinase 3 (PDK3), downstream of mutant IDH-driven stabilization of hypoxia inducible factor-1 $\alpha$  (44, 81, 82). Importantly, treatment of IDH mutant cells with the PDH agonist dichloroacetate (DCA), not only reversed the metabolic changes induced by the IDH mutation but also abrogated the clonogenic potential of IDH1 mutant cells (69). This suggests that reprogramming of PDH activity is essential for tumorigenesis of mutant IDH cells and that PDK inhibitors/PDH agonists deserve further investigation as potential therapeutic targets for low-grade gliomas. From an imaging perspective, we also demonstrated that PDH-mediated conversion of hyperpolarized [ $2\text{-}^{13}\text{C}$ ]-pyruvate to hyperpolarized

[ $5\text{-}^{13}\text{C}$ ]-glutamate could be used to monitor the mutant IDH-driven drop in PDH activity in cells (Figure 2) (69), with potential *in vivo* implementation (83).

## Glutamine Metabolism

As with glycolysis, the reprogramming of glutamine metabolism differs in mutant IDH cells compared to other cancer cells. Cancer cells can use a reductive pathway of glutamine metabolism in which wild-type IDH carboxylates  $\alpha$ -KG to isocitrate (84–86). Subsequent conversion of isocitrate to citrate and of citrate to acetyl CoA contributes to fatty acid synthesis (86, 87). However, mutant IDH1 and IDH2 cannot catalyze reductive carboxylation (88), and IDH1 mutant cells show reduced metabolism of glutamine to citrate and acetyl CoA, resulting in altered fatty acid biosynthesis (89, 90). In addition, as mentioned, glutamine is the primary precursor of 2-HG. Imaging the fate of glutamine could therefore provide a useful complement to other metabolic imaging methods for detecting IDH status.

Infusion of human glioma patients with [ $U\text{-}^{13}\text{C}$ ]-glutamine prior to surgery, followed by  $^{13}\text{C}$ -MR analysis of metabolites extracted from tumor tissue has been used to estimate glutamine metabolism in brain tumors (91), but it is challenging to implement *in vivo*.  $^{13}\text{C}$ -MRS for probing the conversion of hyperpolarized [ $5\text{-}^{13}\text{C}$ ]-glutamine to hyperpolarized [ $5\text{-}^{13}\text{C}$ ]-glutamate has been reported in liver and prostate cancer cells (92, 93) and in rat liver tumor *in vivo* (93) and could potentially be used to characterize mutant IDH tumors. Interestingly, Venneti et al. described positron emission tomography (PET) imaging of glutamine metabolism using the glutamine analog  $4\text{-}^{18}\text{F}\text{-}(2\text{S},4\text{R})\text{-fluoroglutamine}$  ( $^{18}\text{F}$ -FGln) in wild-type gliomas (94). They showed uptake of  $^{18}\text{F}$ -FGln in mouse xenografts *in vivo*, reduced  $^{18}\text{F}$ -FGln uptake in response to temozolomide treatment, and clinical translatability to glioma patients. Further research is needed to assess the value of this approach to mutant IDH gliomas.

## Phospholipid Metabolism

Mass spectrometry and  $^1\text{H}$ -MRS studies have shown a drop in PC and increase in GPC in mutant IDH1 cells compared to wild-type (Figure 2). Esmaeili et al. recently used  $^{31}\text{P}$ -MRS to further assess phospholipid metabolism in glioma rodent xenografts and in human biopsy samples (95). They confirmed that IDH mutant tumors showed higher levels of GPC and also found lower levels of phosphoethanolamine (PE) (Figure 2). Furthermore, ratios of GPC:PE, PC:PE, GPC:glycerophosphoethanolamine (GPE), and (PC + PE:GPC + GPE) were higher in IDH mutant tumors relative to wild-type (95). Further studies are needed to understand the significance of these findings and possible correlations between choline-containing metabolites and IDH status. Nonetheless,  $^{31}\text{P}$ -MRS could prove useful for non-invasive imaging of IDH mutant tumors.

## CONCLUSION

Cancer cells actively reprogram their metabolism to sustain and drive increased cell proliferation. At the preclinical level, metabolic imaging allows visualization of biochemical pathways

promoting a better understanding of the physiological mechanisms of tumorigenesis. It also serves to identify new therapeutic targets. Further studies are needed to fully elucidate the wide range of metabolic changes occurring in mutant IDH cells. Nonetheless, the unique features of glucose, glutamine, and lipid metabolism identified to date can already be exploited for molecular imaging of mutant IDH tumors. Clinical deployment of these imaging methods could provide a useful complement to anatomical imaging methods and aid in tumor detection and monitoring of treatment response.

## REFERENCES

- Kroemer G, Pouyssegur J. Tumor cell metabolism: cancer's Achilles' heel. *Cancer Cell* (2008) **13**(6):472–82. doi:10.1016/j.ccr.2008.05.005
- Hammoudi N, Ahmed KB, Garcia-Prieto C, Huang P. Metabolic alterations in cancer cells and therapeutic implications. *Chin J Cancer* (2011) **30**(8):508–25. doi:10.5732/cjc.011.10267
- Hirschey MD, DeBerardinis RJ, Diehl AM, Drew JE, Frezza C, Green MF, et al. Dysregulated metabolism contributes to oncogenesis. *Semin Cancer Biol* (2015) **35**(Suppl):S129–50. doi:10.1016/j.semcaner.2015.10.002
- Sciacovelli M, Gaudé E, Hilvo M, Frezza C. The metabolic alterations of cancer cells. *Methods Enzymol* (2014) **542**:1–23. doi:10.1016/B978-0-12-416618-9.00001-7
- Warburg O, Posener K, Negelein E. Ueber den Stoffwechsel der Tumoren. *Biochem Z* (1924) **152**:319–44.
- Hanahan D, Weinberg RA. Hallmarks of cancer: the next generation. *Cell* (2011) **144**(5):646–74. doi:10.1016/j.cell.2011.02.013
- Vander Heiden MG, Cantley LC, Thompson CB. Understanding the Warburg effect: the metabolic requirements of cell proliferation. *Science* (2009) **324**(5930):1029–33. doi:10.1126/science.1160809
- Lunt SY, Vander Heiden MG. Aerobic glycolysis: meeting the metabolic requirements of cell proliferation. *Annu Rev Cell Dev Biol* (2011) **27**:441–64. doi:10.1146/annurev-cellbio-092910-154237
- Gatenby RA, Gillies RJ. Why do cancers have high aerobic glycolysis? *Nat Rev Cancer* (2004) **4**(11):891–9. doi:10.1038/nrc1478
- Cantor JR, Sabatini DM. Cancer cell metabolism: one hallmark, many faces. *Cancer Discov* (2012) **2**(10):881–98. doi:10.1158/2159-8290.CD-12-0345
- Hensley CT, Wasti AT, DeBerardinis RJ. Glutamine and cancer: cell biology, physiology, and clinical opportunities. *J Clin Invest* (2013) **123**(9):3678–84. doi:10.1172/JCI69600
- DeBerardinis RJ, Mancuso A, Daikhin E, Nissim I, Yudkoff M, Wehrli S, et al. Beyond aerobic glycolysis: transformed cells can engage in glutamine metabolism that exceeds the requirement for protein and nucleotide synthesis. *Proc Natl Acad Sci U S A* (2007) **104**(49):19345–50. doi:10.1073/pnas.0709747104
- Dang CV. Glutaminolysis: supplying carbon or nitrogen or both for cancer cells? *Cell Cycle* (2010) **9**(19):3884–6. doi:10.4161/cc.9.19.13302
- Glunde K, Bhujwalla ZM, Ronen SM. Choline metabolism in malignant transformation. *Nat Rev Cancer* (2011) **11**(12):835–48. doi:10.1038/nrc3162
- Boroughs LK, DeBerardinis RJ. Metabolic pathways promoting cancer cell survival and growth. *Nat Cell Biol* (2015) **17**(4):351–9. doi:10.1038/ncb3124
- DeBerardinis RJ, Lum JJ, Hatzivassiliou G, Thompson CB. The biology of cancer: metabolic reprogramming fuels cell growth and proliferation. *Cell Metab* (2008) **7**(1):11–20. doi:10.1016/j.cmet.2007.10.002
- Levine AJ, Puzio-Kuter AM. The control of the metabolic switch in cancers by oncogenes and tumor suppressor genes. *Science* (2010) **330**(6009):1340–4. doi:10.1126/science.1193494
- Dang CV. Links between metabolism and cancer. *Genes Dev* (2012) **26**(9):877–90. doi:10.1101/gad.189365.112
- Yang M, Soga T, Pollard PJ. Oncometabolites: linking altered metabolism with cancer. *J Clin Invest* (2013) **123**(9):3652–8. doi:10.1172/JCI67228
- Gomes AP, Blenis J. A nexus for cellular homeostasis: the interplay between metabolic and signal transduction pathways. *Curr Opin Biotechnol* (2015) **34**:110–7. doi:10.1016/j.copbio.2014.12.007
- Wishart DS. Is cancer a genetic disease or a metabolic disease? *EBioMedicine* (2015) **2**(6):478–9. doi:10.1016/j.ebiom.2015.05.022
- Mullen AR, DeBerardinis RJ. Genetically-defined metabolic reprogramming in cancer. *Trends Endocrinol Metab* (2012) **23**(11):552–9. doi:10.1016/j.tem.2012.06.009
- Arcaro A, Guerreiro AS. The phosphoinositide 3-kinase pathway in human cancer: genetic alterations and therapeutic implications. *Curr Genomics* (2007) **8**(5):271–306. doi:10.2174/138920207782446160
- Edinger AL, Thompson CB. Akt maintains cell size and survival by increasing mTOR-dependent nutrient uptake. *Mol Biol Cell* (2002) **13**(7):2276–88. doi:10.1091/mbc.01-12-0584
- Kahn BB, Alquier T, Carling D, Hardie DG. AMP-activated protein kinase: ancient energy gauge provides clues to modern understanding of metabolism. *Cell Metab* (2005) **1**(1):15–25. doi:10.1016/j.cmet.2004.12.003
- Dang CV. MYC, metabolism, cell growth, and tumorigenesis. *Cold Spring Harb Perspect Med* (2013) **3**(8):ii:a014217. doi:10.1101/cshperspect.a014217
- Gabay M, Li Y, Felsher DW. MYC activation is a hallmark of cancer initiation and maintenance. *Cold Spring Harb Perspect Med* (2014) **4**(6):ii:a014241. doi:10.1101/cshperspect.a014241
- Morrish F, Isern N, Sadilek M, Jeffrey M, Hockenberry DM. c-Myc activates multiple metabolic networks to generate substrates for cell-cycle entry. *Oncogene* (2009) **28**(27):2485–91. doi:10.1038/onc.2009.112
- Dang CV, Le A, Gao P. MYC-induced cancer cell energy metabolism and therapeutic opportunities. *Clin Cancer Res* (2009) **15**(21):6479–83. doi:10.1158/1078-0432.CCR-09-0889
- Dang CV. MYC on the path to cancer. *Cell* (2012) **149**(1):22–35. doi:10.1016/j.cell.2012.03.003
- Kimmelman AC. Metabolic dependencies in RAS-driven cancers. *Clin Cancer Res* (2015) **21**(8):1828–34. doi:10.1158/1078-0432.CCR-14-2425
- White E. Exploiting the bad eating habits of RAS-driven cancers. *Genes Dev* (2013) **27**(19):2065–71. doi:10.1101/gad.228122.113
- Liu J, Zhang C, Hu W, Feng Z. Tumor suppressor p53 and its mutants in cancer metabolism. *Cancer Lett* (2015) **356**(2 Pt A):197–203. doi:10.1016/j.canlet.2013.12.025
- Vousden KH, Ryan KM. p53 and metabolism. *Nat Rev Cancer* (2009) **9**(10):691–700. doi:10.1038/nrc2715
- Cairns RA, Mak TW. Oncogenic isocitrate dehydrogenase mutations: mechanisms, models, and clinical opportunities. *Cancer Discov* (2013) **3**(7):730–41. doi:10.1158/2159-8290.CD-13-0083
- Waitkus MS, Diplas BH, Yan H. Isocitrate dehydrogenase mutations in gliomas. *Neuro Oncol* (2016) **18**(1):16–26. doi:10.1093/neuonc/nov136
- Parsons DW, Jones S, Zhang X, Lin JC, Leary RJ, Angenendt P, et al. An integrated genomic analysis of human glioblastoma multiforme. *Science* (2008) **321**(5897):1807–12. doi:10.1126/science.1164382
- Gross S, Cairns RA, Minden MD, Driggers EM, Bittinger MA, Jang HG, et al. Cancer-associated metabolite 2-hydroxyglutarate accumulates in acute myelogenous leukemia with isocitrate dehydrogenase 1 and 2 mutations. *J Exp Med* (2010) **207**(2):339–44. doi:10.1084/jem.20092506
- Yang H, Ye D, Guan KL, Xiong Y. IDH1 and IDH2 mutations in tumorigenesis: mechanistic insights and clinical perspectives. *Clin Cancer Res* (2012) **18**(20):5562–71. doi:10.1158/1078-0432.CCR-12-1773
- Suzuki H, Aoki K, Chiba K, Sato Y, Shiozawa Y, Shiraishi Y, et al. Mutational landscape and clonal architecture in grade II and III gliomas. *Nat Genet* (2015) **47**(5):458–68. doi:10.1038/ng.3273

## AUTHOR CONTRIBUTIONS

All authors listed, have made substantial, direct, and intellectual contribution to the work, and approved it for publication.

## FUNDING

This work was supported by NIH R01CA172845 (SR), NIH R01CA154915 (SR), NIH R21CA161545 (SR), and the UCSF Brain Tumor Center Loglio Collective.

41. Huse JT, Phillips HS, Brennan CW. Molecular subclassification of diffuse gliomas: seeing order in the chaos. *Glia* (2011) **59**(8):1190–9. doi:10.1002/glia.21165
42. Brat DJ, Verhaak RG, Aldape KD, Yung WK, Salama SR, Cooper LA, et al. Comprehensive, integrative genomic analysis of diffuse lower-grade gliomas. *N Engl J Med* (2015) **372**(26):2481–98. doi:10.1056/NEJMoa1402121
43. Dang L, White DW, Gross S, Bennett BD, Bittinger MA, Driggers EM, et al. Cancer-associated IDH1 mutations produce 2-hydroxyglutarate. *Nature* (2009) **462**(7274):739–44. doi:10.1038/nature08617
44. Xu W, Yang H, Liu Y, Yang Y, Wang P, Kim SH, et al. Oncometabolite 2-hydroxyglutarate is a competitive inhibitor of alpha-ketoglutarate-dependent dioxygenases. *Cancer Cell* (2011) **19**(1):17–30. doi:10.1016/j.ccr.2010.12.014
45. Lu C, Ward PS, Kapoor GS, Rohle D, Turcan S, Abdel-Wahab O, et al. IDH mutation impairs histone demethylation and results in a block to cell differentiation. *Nature* (2012) **483**(7390):474–8. doi:10.1038/nature10860
46. Turcan S, Rohle D, Goenka A, Walsh LA, Fang F, Yilmaz E, et al. IDH1 mutation is sufficient to establish the glioma hypermethylator phenotype. *Nature* (2012) **483**(7390):479–83. doi:10.1038/nature10866
47. Sasaki M, Knobbe CB, Munger JC, Lind EF, Brenner D, Brustle A, et al. IDH1(R132H) mutation increases murine haematopoietic progenitors and alters epigenetics. *Nature* (2012) **488**(7413):656–9. doi:10.1038/nature11323
48. Duncan CG, Barwick BG, Jin G, Rago C, Kapoor-Vazirani P, Powell DR, et al. A heterozygous IDH1R132H/WT mutation induces genome-wide alterations in DNA methylation. *Genome Res* (2012) **22**(12):2339–55. doi:10.1101/gr.132738.111
49. Fernie AR, Trethewey RN, Krotzky AJ, Willmitzer L. Metabolite profiling: from diagnostics to systems biology. *Nat Rev Mol Cell Biol* (2004) **5**(9):763–9. doi:10.1038/nrm1451
50. James ML, Gambhir SS. A molecular imaging primer: modalities, imaging agents, and applications. *Physiol Rev* (2012) **92**(2):897–965. doi:10.1152/physrev.00049.2010
51. Kurhanewicz J, Vigneron DB, Brindle K, Chekmenev EY, Comment A, Cunningham CH, et al. Analysis of cancer metabolism by imaging hyperpolarized nuclei: prospects for translation to clinical research. *Neoplasia* (2011) **13**(2):81–97. doi:10.1593/neo.101102
52. Horská A, Barker PB. Imaging of brain tumors: MR spectroscopy and metabolic imaging. *Neuroimaging Clin N Am* (2010) **20**(3):293–310. doi:10.1016/j.nic.2010.04.003
53. Glunde K, Bhujwalla ZM. Metabolic tumor imaging using magnetic resonance spectroscopy. *Semin Oncol* (2011) **38**(1):26–41. doi:10.1053/j.seminoncol.2010.11.001
54. De Graaf RA. *In Vivo NMR Spectroscopy: Principles and Techniques*. 2nd ed. Chichester; Hoboken, NJ: John Wiley & Sons (2007). xxi, 570, 8 of lates.
55. Gillies RJ, Morse DL. In vivo magnetic resonance spectroscopy in cancer. *Annu Rev Biomed Eng* (2005) **7**:287–326. doi:10.1146/annurev.bioeng.7.060804.100411
56. Elkhaled A, Jalbert LE, Phillips JJ, Yoshihara HA, Parvataneni R, Srinivasan R, et al. Magnetic resonance of 2-hydroxyglutarate in IDH1-mutated low-grade gliomas. *Sci Transl Med* (2012) **4**(116):116ra5. doi:10.1126/scitranslmed.3002796
57. Kalinina J, Carroll A, Wang L, Yu Q, Mancheno DE, Wu S, et al. Detection of “oncometabolite” 2-hydroxyglutarate by magnetic resonance analysis as a biomarker of IDH1/2 mutations in glioma. *J Mol Med* (2012) **90**(10):1161–71. doi:10.1007/s00109-012-0888-x
58. Pope WB, Prins RM, Albert Thomas M, Nagarajan R, Yen KE, Bittinger MA, et al. Non-invasive detection of 2-hydroxyglutarate and other metabolites in IDH1 mutant glioma patients using magnetic resonance spectroscopy. *J Neurooncol* (2012) **107**(1):197–205. doi:10.1007/s11060-011-0737-8
59. Choi C, Ganji SK, DeBerardinis RJ, Hatanpaa KJ, Rakheja D, Kovacs Z, et al. 2-Hydroxyglutarate detection by magnetic resonance spectroscopy in IDH-mutated patients with gliomas. *Nat Med* (2012) **18**(4):624–9. doi:10.1038/nm.2682
60. Andronesi OC, Kim GS, Gerstner E, Batchelor T, Tzika AA, Fantin VR, et al. Detection of 2-hydroxyglutarate in IDH-mutated glioma patients by in vivo spectral-editing and 2D correlation magnetic resonance spectroscopy. *Sci Transl Med* (2012) **4**(116):116ra4. doi:10.1126/scitranslmed.3002693
61. Morris P, Bachelard H. Reflections on the application of 13C-MRS to research on brain metabolism. *NMR Biomed* (2003) **16**(6–7):303–12. doi:10.1002/nbm.844
62. Ardenkjær-Larsen JH, Fridlund B, Gram A, Hansson G, Hansson L, Lerche MH, et al. Increase in signal-to-noise ratio of >10,000 times in liquid-state NMR. *Proc Natl Acad Sci U S A* (2003) **100**(18):10158–63. doi:10.1073/pnas.1733835100
63. Golman K, in ’t Zandt R, Thaning M. Real-time metabolic imaging. *Proc Natl Acad Sci U S A* (2006) **103**(30):11270–5. doi:10.1073/pnas.0601319103
64. Chaumeil MM, Najac C, Ronen SM. Studies of metabolism using (13)C MRS of hyperpolarized probes. *Methods Enzymol* (2015) **561**:1–71. doi:10.1016/bs.mie.2015.04.001
65. Brindle KM, Bohndiek SE, Gallagher FA, Kettunen MI. Tumor imaging using hyperpolarized 13C magnetic resonance spectroscopy. *Magn Reson Med* (2011) **66**(2):505–19. doi:10.1002/mrm.22999
66. Nelson SJ, Kurhanewicz J, Vigneron DB, Larson PE, Harzstark AL, Ferrone M, et al. Metabolic imaging of patients with prostate cancer using hyperpolarized [1-(13)C]pyruvate. *Sci Transl Med* (2013) **5**(198):198ra08. doi:10.1126/scitranslmed.3006070
67. Chaumeil MM, Larson PE, Yoshihara HA, Danforth OM, Vigneron DB, Nelson SJ, et al. Non-invasive in vivo assessment of IDH1 mutational status in glioma. *Nat Commun* (2013) **4**:2429. doi:10.1038/ncomms3429
68. Pichumani K, Mashimo T, Baek HM, Ratnakar J, Mickey B, DeBerardinis RJ, et al. Conditions for (13)C NMR detection of 2-hydroxyglutarate in tissue extracts from isocitrate dehydrogenase-mutated gliomas. *Anal Biochem* (2015) **481**:4–6. doi:10.1016/j.ab.2015.04.017
69. Izquierdo-García JL, Viswanath P, Eriksson P, Cai L, Radoul M, Chaumeil MM, et al. IDH1 mutation induces reprogramming of pyruvate metabolism. *Cancer Res* (2015) **75**(15):2999–3009. doi:10.1158/0008-5472.CAN-15-0840
70. Seltzer MJ, Bennett BD, Joshi AD, Gao P, Thomas AG, Ferraris DV, et al. Inhibition of glutaminase preferentially slows growth of glioma cells with mutant IDH1. *Cancer Res* (2010) **70**(22):8981–7. doi:10.1158/0008-5472.CAN-10-1666
71. Emadi A, Jun SA, Tsukamoto T, Fathi AT, Minden MD, Dang CV. Inhibition of glutaminase selectively suppresses the growth of primary acute myeloid leukemia cells with IDH mutations. *Exp Hematol* (2014) **42**(4):247–51. doi:10.1016/j.exphem.2013.12.001
72. Reitman ZJ, Jin G, Karoly ED, Spasojevic I, Yang J, Kinzler KW, et al. Profiling the effects of isocitrate dehydrogenase 1 and 2 mutations on the cellular metabolome. *Proc Natl Acad Sci U S A* (2011) **108**(8):3270–5. doi:10.1073/pnas.1019393108
73. Ohka F, Ito M, Ranjit M, Senga T, Motomura A, Motomura K, et al. Quantitative metabolome analysis profiles activation of glutaminolysis in glioma with IDH1 mutation. *Tumour Biol* (2014) **35**(6):5911–20. doi:10.1007/s13277-014-1784-5
74. Izquierdo-García JL, Viswanath P, Eriksson P, Chaumeil MM, Pieper RO, Phillips JJ, et al. Metabolic reprogramming in mutant IDH1 glioma cells. *PLoS One* (2015) **10**(2):e0118781. doi:10.1371/journal.pone.0118781
75. Chesnelong C, Chaumeil MM, Blough MD, Al-Najjar M, Stechishin OD, Chan JA, et al. Lactate dehydrogenase A silencing in IDH mutant gliomas. *Neuro Oncol* (2014) **16**(5):686–95. doi:10.1093/neuonc/not243
76. Poteet E, Choudhury GR, Winters A, Li W, Ryoo MG, Liu R, et al. Reversing the Warburg effect as a treatment for glioblastoma. *J Biol Chem* (2013) **288**(13):9153–64. doi:10.1074/jbc.M112.440354
77. Chaumeil MM, Radoul M, Eriksson P, Blough MD, Cheneslong C, Pieper RO, et al., editors. The tumor exception that proves the rule: hyperpolarized 13C MRS cannot be used to detect the presence of mutant IDH1 glioma or their responses to temozolamide therapy. *International Society for Magnetic Resonance in Medicine 23rd Annual Meeting & Exhibition*. Toronto (2015).
78. Choi C, Ganji S, Hulsey K, Madan A, Kovacs Z, Dimitrov I, et al. A comparative study of short- and long-TE (1)H MRS at 3 T for in vivo detection of 2-hydroxyglutarate in brain tumors. *NMR Biomed* (2013) **26**(10):1242–50. doi:10.1002/nbm.2943
79. Tonjes M, Barbus S, Park YJ, Wang W, Schlatter M, Lindroth AM, et al. BCAT1 promotes cell proliferation through amino acid catabolism in gliomas carrying wild-type IDH1. *Nat Med* (2013) **19**(7):901–8. doi:10.1038/nm.3217
80. Chaumeil MM, Larson PE, Woods SM, Cai L, Eriksson P, Robinson AE, et al. Hyperpolarized [1-13C] glutamate: a metabolic imaging biomarker

- of IDH1 mutational status in glioma. *Cancer Res* (2014) **74**(16):4247–57. doi:10.1158/0008-5472.CAN-14-0680
81. Zhao S, Lin Y, Xu W, Jiang W, Zha Z, Wang P, et al. Glioma-derived mutations in IDH1 dominantly inhibit IDH1 catalytic activity and induce HIF-1alpha. *Science* (2009) **324**(5924):261–5. doi:10.1126/science.1170944
  82. Sasaki M, Knobbe CB, Itsumi M, Elia AJ, Harris IS, Chio II, et al. D-2-hydroxyglutarate produced by mutant IDH1 perturbs collagen maturation and basement membrane function. *Genes Dev* (2012) **26**(18):2038–49. doi:10.1101/gad.198200.112
  83. Park JM, Josan S, Grafendorfer T, Yen Y-F, Hurd RE, Spielman DM, et al. Measuring mitochondrial metabolism in rat brain in vivo using MR Spectroscopy of hyperpolarized [2-13C]pyruvate. *NMR Biomed* (2013) **26**(10):1197–203. doi:10.1002/nbm.2935
  84. Metallo CM, Gameiro PA, Bell EL, Mattaini KR, Yang J, Hiller K, et al. Reductive glutamine metabolism by IDH1 mediates lipogenesis under hypoxia. *Nature* (2011) **481**(7381):380–4. doi:10.1038/nature10602
  85. Fendt SM, Bell EL, Keibler MA, Olenchock BA, Mayers JR, Wasylewko TM, et al. Reductive glutamine metabolism is a function of the alpha-ketoglutarate to citrate ratio in cells. *Nat Commun* (2013) **4**:2236. doi:10.1038/ncomms3236
  86. Wise DR, Ward PS, Shay JE, Cross JR, Gruber JJ, Sachdeva UM, et al. Hypoxia promotes isocitrate dehydrogenase-dependent carboxylation of alpha-keto-glutarate to citrate to support cell growth and viability. *Proc Natl Acad Sci U S A* (2011) **108**(49):19611–6. doi:10.1073/pnas.1117773108
  87. Corbet C, Feron O. Metabolic and mind shifts: from glucose to glutamine and acetate addictions in cancer. *Curr Opin Clin Nutr Metab Care* (2015) **18**(4):346–53. doi:10.1097/MCO.0000000000000178
  88. Leonardi R, Subramanian C, Jackowski S, Rock CO. Cancer-associated isocitrate dehydrogenase mutations inactivate NADPH-dependent reductive carboxylation. *J Biol Chem* (2012) **287**(18):14615–20. doi:10.1074/jbc.C112.353946
  89. Grassian AR, Parker SJ, Davidson SM, Divakaruni AS, Green CR, Zhang X, et al. IDH1 mutations alter citric acid cycle metabolism and increase dependence on oxidative mitochondrial metabolism. *Cancer Res* (2014) **74**(12):3317–31. doi:10.1158/1538-7445.AM2014-LB-139
  90. Reitman ZJ, Duncan CG, Poteet E, Winters A, Yan LJ, Gooden DM, et al. Cancer-associated isocitrate dehydrogenase 1 (IDH1) R132H mutation and d-2-hydroxyglutarate stimulate glutamine metabolism under hypoxia. *J Biol Chem* (2014) **289**(34):23318–28. doi:10.1074/jbc.M114.575183
  91. Marin-Valencia I, Yang C, Mashimo T, Cho S, Baek H, Yang XL, et al. Analysis of tumor metabolism reveals mitochondrial glucose oxidation in genetically diverse human glioblastomas in the mouse brain in vivo. *Cell Metab* (2012) **15**(6):827–37. doi:10.1016/j.cmet.2012.05.001
  92. Gallagher FA, Kettunen MI, Day SE, Lerche M, Brindle KM. 13C MR spectroscopy measurements of glutaminase activity in human hepatocellular carcinoma cells using hyperpolarized 13C-labeled glutamine. *Magn Reson Med* (2008) **60**(2):253–7. doi:10.1002/mrm.21650
  93. Cabella C, Karlsson M, Canape C, Catanzaro G, Colombo Serra S, Miragoli L, et al. In vivo and in vitro liver cancer metabolism observed with hyperpolarized [5-(13)C]glutamine. *J Magn Reson* (2013) **232**:45–52. doi:10.1016/j.jmr.2013.04.010
  94. Venneti S, Dunphy MP, Zhang H, Pitter KL, Zanzonico P, Campos C, et al. Glutamine-based PET imaging facilitates enhanced metabolic evaluation of gliomas in vivo. *Sci Transl Med* (2015) **7**(274):274ra17. doi:10.1126/scitranslmed.aaa1009
  95. Esmaeili M, Hamans BC, Navis AC, van Horssen R, Bathen TF, Gribbestad IS, et al. IDH1 R132H mutation generates a distinct phospholipid metabolite profile in glioma. *Cancer Res* (2014) **74**(17):4898–907. doi:10.1158/0008-5472.CAN-14-0008

**Conflict of Interest Statement:** The authors declare that the research was conducted in the absence of any commercial or financial relationships that could be construed as a potential conflict of interest.

Copyright © 2016 Viswanath, Chaumeil and Ronen. This is an open-access article distributed under the terms of the Creative Commons Attribution License (CC BY). The use, distribution or reproduction in other forums is permitted, provided the original author(s) or licensor are credited and that the original publication in this journal is cited, in accordance with accepted academic practice. No use, distribution or reproduction is permitted which does not comply with these terms.



# Targeting Phospholipid Metabolism in Cancer

**Menglin Cheng<sup>1</sup>, Zaver M. Bhujwalla<sup>1,2</sup> and Kristine Glunde<sup>1,2\*</sup>**

<sup>1</sup>Division of Cancer Imaging Research, Russell H. Morgan Department of Radiology and Radiological Science, Johns Hopkins University School of Medicine, Baltimore, MD, USA, <sup>2</sup>Sidney Kimmel Comprehensive Cancer Center, Johns Hopkins University School of Medicine, Baltimore, MD, USA

## OPEN ACCESS

### Edited by:

Natalie Julie Serkova,  
University of Colorado School of  
Medicine, USA

### Reviewed by:

Aslam Khan,  
University of Missouri, USA  
Ellen Ackerstaff,  
Memorial Sloan Kettering Cancer  
Center, USA

### \*Correspondence:

Kristine Glunde  
kglunde@mri.jhu.edu

### Specialty section:

This article was submitted to  
Cancer Imaging and Diagnosis,  
a section of the journal  
*Frontiers in Oncology*

**Received:** 31 July 2016

**Accepted:** 14 December 2016  
**Published:** 27 December 2016

### Citation:

Cheng M, Bhujwalla ZM and  
Glunde K (2016) Targeting  
Phospholipid Metabolism in Cancer.  
*Front. Oncol.* 6:266.  
doi: 10.3389/fonc.2016.00266

All cancers tested so far display abnormal choline and ethanolamine phospholipid metabolism, which has been detected with numerous magnetic resonance spectroscopy (MRS) approaches in cells, animal models of cancer, as well as the tumors of cancer patients. Since the discovery of this metabolic hallmark of cancer, many studies have been performed to elucidate the molecular origins of deregulated choline metabolism, to identify targets for cancer treatment, and to develop MRS approaches that detect choline and ethanolamine compounds for clinical use in diagnosis and treatment monitoring. Several enzymes in choline, and recently also ethanolamine, phospholipid metabolism have been identified, and their evaluation has shown that they are involved in carcinogenesis and tumor progression. Several already established enzymes as well as a number of emerging enzymes in phospholipid metabolism can be used as treatment targets for anticancer therapy, either alone or in combination with other chemotherapeutic approaches. This review summarizes the current knowledge of established and relatively novel targets in phospholipid metabolism of cancer, covering choline kinase  $\alpha$ , phosphatidylcholine-specific phospholipase D1, phosphatidylcholine-specific phospholipase C, sphingomyelinases, choline transporters, glycerophosphodiesterases, phosphatidylethanolamine N-methyltransferase, and ethanolamine kinase. These enzymes are discussed in terms of their roles in oncogenic transformation, tumor progression, and crucial cancer cell properties such as fast proliferation, migration, and invasion. Their potential as treatment targets are evaluated based on the current literature.

**Keywords:** cancer, target, phospholipid, metabolism, choline, ethanolamine

## INTRODUCTION

Phospholipids, which form the bilayer structures of all cellular membranes, are an essential component of all cells. The phospholipid content was shown to increase with cell transformation and tumor progression (1–4). For example, lipid analyses of samples from breast cancer tissue displayed an increase in phospholipid content as compared to non-cancerous adjacent healthy breast tissue (5). Concentrations of the two major phospholipid components phosphatidylcholine (PtdCho) and phosphatidylethanolamine (PtdEtn) increased with increasing breast cancer tumor grade (6), indicating that the phospholipid synthesis rate increases with oncogenesis and tumor progression as compared to normal tissue.

Metabolic intermediates of PtdCho metabolism were consistently observed to display abnormal levels with magnetic resonance spectroscopy (MRS) (7). An increased total choline (tCho) signal, which consists of signals from phosphocholine (PC), glycerophosphocholine (GPC), and

free choline (Cho), and whose chemical structures are shown in **Figure 1**, has been detected by  $^1\text{H}$  MRS in all cancers tested so far (7). High-resolution  $^1\text{H}$  MRS, which can resolve the signals from the individual components of the tCho signal, confirmed the increase of PC in breast (8–12), prostate (13, 14), ovarian (15), endometrial (16), cervical (15), and brain cancers (17–19). In some cancer cell types such as isolated breast and ovarian cancer cells, a relative decrease of GPC was observed as well, which led to the suggestion to use a higher ratio of PC/GPC as a marker of tumor progression (20, 21). PC was also reported as a useful imaging biomarker of tumor response to several targeted treatments of cancers, enabling  $^1\text{H}$  MRS to be used for monitoring changes in PC as a non-invasive marker of pharmacodynamic treatment response (22–26). A PC decrease and GPC increase was reported after docetaxel treatment in breast cancer cell lines and xenograft models (27).

Magnetic resonance spectroscopy detection of tCho allows for non-invasive and longitudinal monitoring of deep-seated

tumors, and it is currently being evaluated as non-invasive biomarker for cancer diagnosis, monitoring of treatment response, and anticancer drug development. In clinical studies, *in vivo* MRS detection of the tCho signal was proposed as a marker of breast cancer malignancy (8, 28–31). The tCho signal has been used to monitor neoadjuvant chemotherapy of breast tumors in patients (32), and decreased tCho was associated with the pathology-detected tumor response to chemotherapy (10, 12, 33). One limitation of using choline-based  $^1\text{H}$  MRS is the difficulty of resolving the signals of PC and GPC and free choline in the *in vivo*  $^1\text{H}$  MRS setting.

Phosphorus MRS ( $^{31}\text{P}$  MRS) is also able to detect phospholipid metabolites and displays two sets of phospholipid metabolite peaks: phosphomonoesters (PMEs), which are mainly composed of PC and PE (phosphoethanolamine), and diphosphodiester, with GPC and GPE (glycerophosphoethanolamine) as the main components as shown in **Figure 2**. Early  $^{31}\text{P}$  MRS cancer studies, which were not able to separate the individual components of

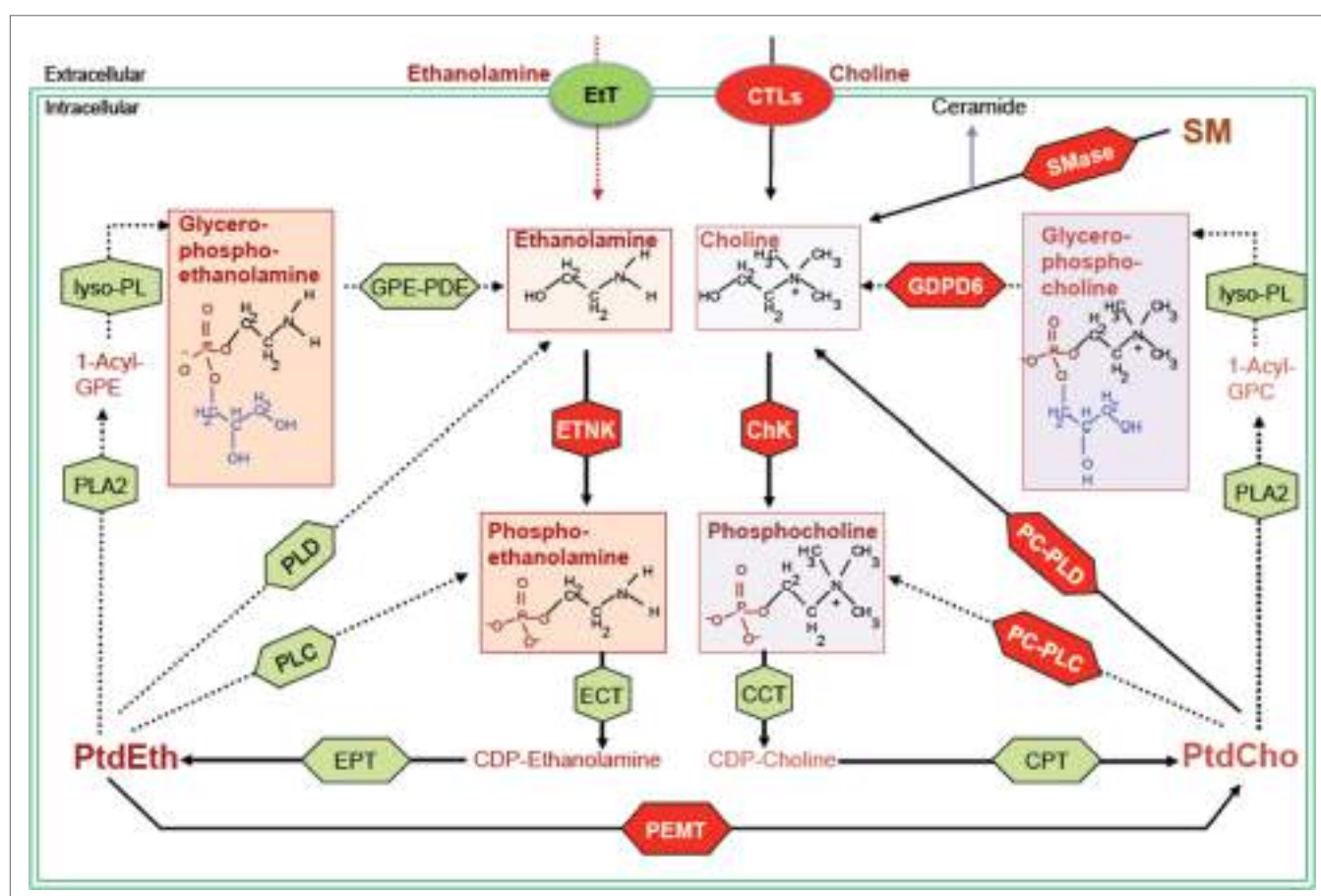


**FIGURE 1 | Biochemical network of ethanolamine and choline phospholipid metabolism showing crosstalk between these two metabolic cycles.** MR detectable metabolites are drawn in boxes. Red shapes show enzymes discussed in this review, and green shapes show other enzymes responsible for the indicated reactions, but not discussed in this review. Metabolite abbreviations: 1-acyl-GPE, 1-acyl-glycerophosphoethanolamine; 1-acyl-GPC, 1-acyl-glycerophosphocholine; PtdCho, phosphatidylcholine; PtdEth, phosphatidylethanolamine; SM, sphingomyelin. Enzyme abbreviations: CCT, phosphocholine cytidylyltransferase; ChK, choline kinase; CPT, diacylglycerol cholinophotransferase; CTL, choline transporter-like protein; EtT, ethanolamine transporter; ECT, phosphoethanolamine cytidylyltransferase; EPT, diacylglycerol ethanolaminophotransferase; ETNK, ethanolamine kinase; GPE-PDE, glycerophosphoethanolamine phosphodiesterase; GPD6, glycerophosphodiester phosphodiesterase domain containing 6; lyso-PL, lysophospholipase; PEMT, phosphatidylethanolamine N-methyltransferase; PLA2, phospholipase A2; PLC, phospholipase C; PLD, phospholipase D.

these two sets of  $^{31}\text{P}$  peaks very well, detected that PMEs were increased in human breast tumors (34–37), neuroblastomas (38), prostate cancers (39), and hepatic lymphomas (40) as compared to corresponding normal tissues. Following chemotherapy or radiotherapy, a PME reduction was observed in human neuroblastoma (38), breast tumors (35, 36), and hepatic lymphoma (40). Recent developments of innovative  $^{31}\text{P}$  MRS approaches that are based on  $^1\text{H}$  to  $^{31}\text{P}$  polarization transfer enable the quantification of *in vivo* levels of PE, PC, GPE, and GPC on small animal and clinical MR scanners (41–44). PE and GPE are the metabolic intermediates of PtdEtn, the second most abundant phospholipid. PE was found to consistently increase in tumors similar to PC (see Figure 2) (45), although its role in cancers is much less explored than PC. The potential of PE and GPE to be monitored is currently being explored along with PC and GPC (41, 44). The changes that occur in tCho, PMEs, and PDEs with oncogenesis and in response to therapy are the result of complex molecular pathways and are therefore not always consistent (8, 37, 46, 47), making it necessary to improve the resolution of clinical *in vivo* MRS applications and to investigate the molecular mechanism underlying these metabolic changes.

Choline uptake and retention can also be imaged using positron emission tomography (PET), mainly with the tracers [ $^{11}\text{C}$ ]-choline, [ $^{18}\text{F}$ ]-fluoromethylcholine, and [ $^{18}\text{F}$ ]-fluoroethylcholine. The use of [ $^{11}\text{C}$ ]-choline PET was approved for clinical use in prostate cancer by the federal drug administration of the United States in 2012 (48). Choline PET/computed tomography (CT) is used in the

clinic as well and has the advantages of providing improved local disease evaluation and staging of prostate cancer as compared to conventional [ $^{18}\text{F}$ ]-FDG PET, giving additional information on nodal staging and suspected metastasis in prostate cancer patients (49).

While choline-based imaging has been explored extensively, discoveries of genes and signaling pathways leading to the changes in choline-containing metabolites are still emerging. The function and regulation of the two enzymes choline kinase  $\alpha$  (ChK $\alpha$ ) and phospholipase D (PLD) has been more widely explored in cancer, but research into other important enzymes in choline metabolism is still at an early stage. These enzymes may provide new targets for cancer therapy. In this review, we will provide a brief update on the established targets in choline phospholipid metabolism and discuss some new anticancer targets in the choline and ethanolamine phospholipid metabolic pathways as highlighted in red in Figure 1.

## CHOLINE KINASE $\alpha$

Choline kinase is the enzyme that phosphorylates free choline and produces PC. There are two genes that encode this enzyme: ChK $\alpha$  and choline kinase beta (ChK $\beta$ ) (50–52). ChK $\alpha$  is well established as an oncogene that promotes tumor initiation and progression (7, 53, 54). Its overexpression and elevated enzyme activity is one of the most established factors that contribute to increased PC and tCho in various tumor tissues including breast

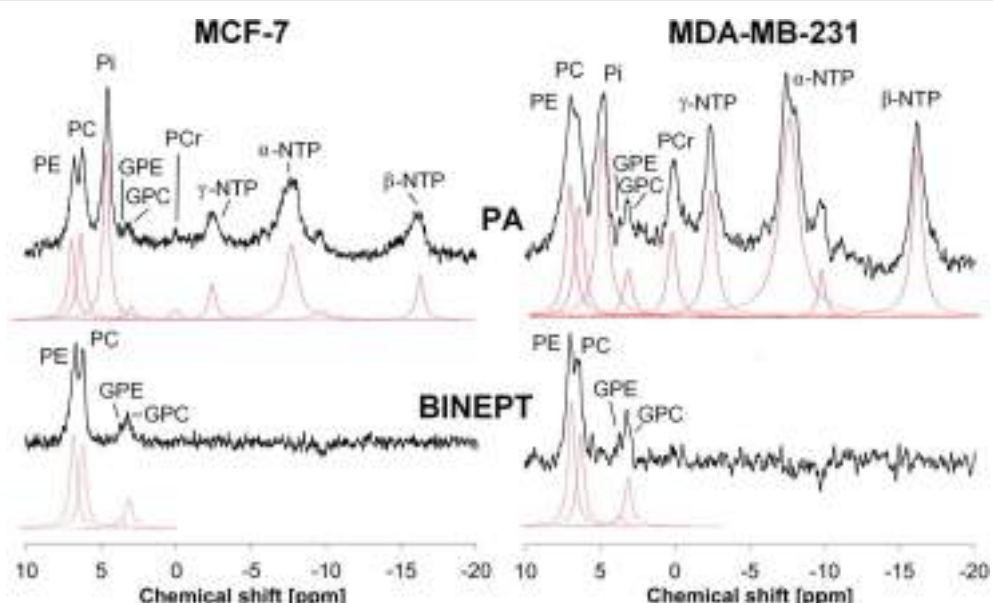


**FIGURE 2 | Example of *in vivo* pulse-acquire (PA, top) and BINEPT (bottom)  $^{31}\text{P}$  MR spectra of a representative MCF-7 (left) and MDA-MB-231 (right) tumor.** Lorentzian lines as fitted by the software jMRUI (<http://www.jmrui.eu/>) are shown below each MR spectrum. All phosphorylated metabolites are visible in the PA spectrum, whereas the BINEPT spectrum only contains signals from phospholipid metabolites with H-P-coupling such as phosphoethanolamine (PE), phosphocholine (PC), glycerophosphoethanolamine (GPE), and glycerophosphocholine (GPC). Note the broad, uneven baseline in the 0–5 ppm region of the PA spectra, where signals from mobile membrane phospholipids are resonating. The signal of  $\beta$ -nucleoside triphosphate (NTP) is formed by  $\beta$ -NTP only. The signal labeled  $\alpha$ -NTP is an overlapping signal from  $\alpha$ -NTP,  $\alpha$ -nucleoside diphosphate ( $\alpha$ -NDP), nicotinamide adenine dinucleotide, and diphosphodiesters. The signal labeled  $\gamma$ -NTP is an overlapping signal from  $\gamma$ -NTP and  $\beta$ -NDP. Typically,  $\beta$ -NTP is the smallest peak of the three NTP signals; however, here,  $\gamma$ -NTP overlaps with a broad baseline signal that makes it appear smaller than  $\beta$ -NTP. Adapted from Wijnen et al. (44).

(55), ovarian (21), colorectal (56), prostate (56), lung (56, 57), endometrial (16), and pancreatic (58) cancer.

In addition to catalyzing the formation of PC in the Kennedy pathway of PtdCho synthesis, ChK $\alpha$  also has other functions in regulating cell signaling pathways. For example, the non-receptor tyrosine kinase c-Src was shown to phosphorylate ChK $\alpha$ , which in turn forms a protein complex with epidermal growth factor receptor to regulate breast cancer cell proliferation and tumorigenesis (59). Downregulation of ChK $\alpha$  decreased the phosphorylation of the mitogen-activated protein kinase (MAPK) signaling pathway protein ERK1/2 to p-ERK1/2 on T202/Y204 (60), and the PI3K/AKT signaling pathway protein AKT to p-AKT on S473 (61). ChK $\alpha$  inhibition induced exacerbated endoplasmic reticulum (ER) stress and triggered apoptosis *via* the CHOP pathway in cancer cells, but not in the non-tumorigenic mammary epithelial cell line MCF-10A (62). CHOP is the major pro-apoptotic transcription factor that is induced by ER stress. Inhibition of ChK $\alpha$  in cancer cells also resulted in an intracellular increase in ceramides, leading to apoptotic cell death, suggesting that ChK $\alpha$  activity disruption may be a highly specific and selective cytotoxic antitumoral strategy. ChK $\alpha$  knockout mice, but not knockout mice with a loss of ChK $\beta$ , are embryonically lethal, implying that ChK $\alpha$  is essential for PtdCho biosynthesis (7, 63, 64).

Several small molecule inhibitors of ChK $\alpha$ - and siRNA-based nanoparticles have been developed to test their potential for MRS-monitored anticancer treatment. Lacal and colleagues have tested several groups of compounds that inhibit ChK $\alpha$  activity, some of which displayed significant levels of antiproliferative activity and led to a reduction of tumor growth (65–67). One of these

inhibitors, TCD-717 (68), is currently being tested in a phase I clinical trial (<https://clinicaltrials.gov/ct2/show/NCT01215864>). Bhujwalla and colleagues have developed siRNA and shRNA strategies (Figure 3) (69, 70), and siRNA-based nanoparticles against ChK $\alpha$  (71) for anticancer therapy. Both methods of therapy can be monitored by detecting ChK $\alpha$  activity with MRS (22, 69, 70, 72). siRNA silencing of ChK $\alpha$  demonstrated synergistic effects with 5-fluorouracil (5-FU) in the treatment of breast cancer cells (73), and ChK $\alpha$  inhibitors showed similar effects in preclinical studies of treating colorectal cancer (74). Overall, ChK $\alpha$  is a well-established antitumor target, with multiple inhibitors and siRNA-based agents against ChK $\alpha$  under development and in initial clinical testing phases. It is possible that ChK $\alpha$  may enter clinical application as stand-alone treatment or in combination with other first-line chemotherapeutic drugs such as 5-FU. MRS monitoring of tumor tCho or PME levels in patients undergoing treatment with ChK $\alpha$ -targeted drugs may facilitate non-invasive assessment of tumor response for more precise treatment monitoring and dynamic adjustment of the treatment plan.

## PtdCho-SPECIFIC PHOSPHOLIPASE D (PLD)

The phospholipase D enzyme hydrolyzes the most abundant phospholipid PtdCho and thereby produces phosphatidic acid (PA) and free choline (75). PA is a second messenger that directly binds to the mammalian target of rapamycin (mTOR) (76). PA can also be converted to other secondary messengers such as

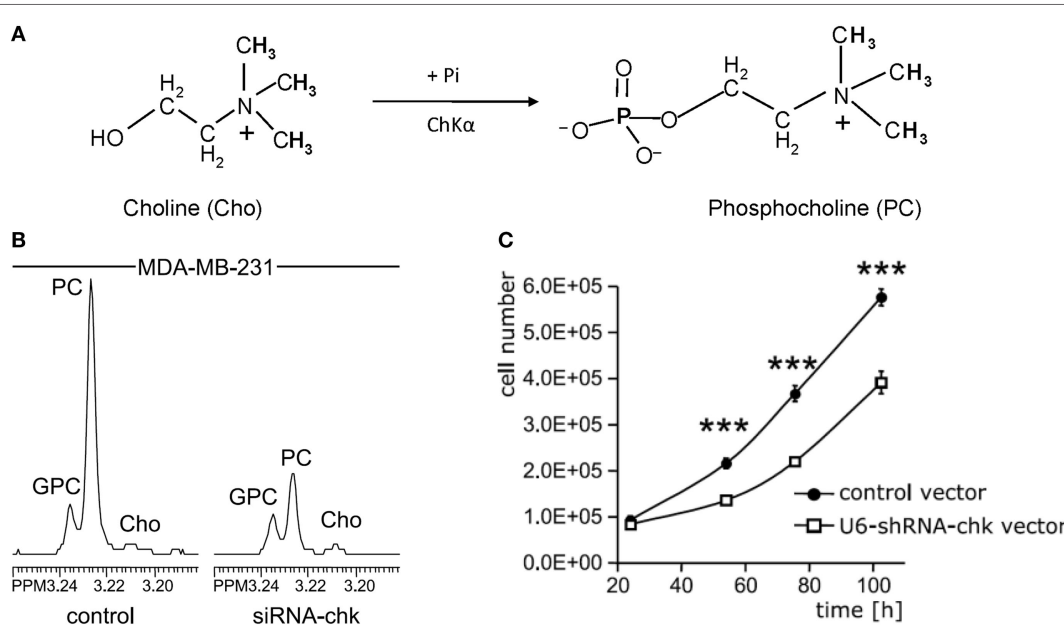


**FIGURE 3 | Choline kinase  $\alpha$  (ChK $\alpha$ ) as target for anticancer treatment. (A)** ChK $\alpha$  converts free choline to phosphocholine (PC). **(B)** Knockdown of ChK $\alpha$  resulted in a dramatic reduction of cellular PC as evident by the decreased PC signal in high-resolution  $^1\text{H}$  MR spectrum obtained from water-soluble metabolites of MDA-MB-231 cells transfected with anti-ChK $\alpha$  siRNA compared to the spectrum from non-target siRNA control. **(C)** Stable knockdown of ChK $\alpha$  with a pSHAG-U6-shRNA vector significantly decreased MDA-MB-231 cell growth rate. Abbreviations: GPC, glycerophosphocholine. \*\*\*represents  $P < 0.001$ , average proliferation rates were calculated from five independent experiments. Adapted from Glunde et al. (69).

diacylglycerol (DAG) by lipid phosphatidate phosphatase, or to lysophosphatidic acid (LPA) by phospholipase A2 (75). There are two isoforms of PLD in the human genome: phospholipase D1 (PLD1) and PLD2, which share 50% amino acid identity and display a similar protein structure (77, 78). PLD1, PLD2, and PA have been reported to interact with several protein partners, forming a molecular network that mediates various cellular functions (79). These cellular functions include vesicle trafficking (endocytosis and exocytosis), trans-Golgi network vesicle formation, cytoskeleton organization, cell migration, cell morphogenesis, autophagy (80), and the regulation of growth, proliferation, survival, and apoptosis (81).

Elevated PtdCho-specific PLD activity and/or increased expression of PLD1 or PLD2 have been observed in many different types of cancer and in transformed cells. A single-nucleotide polymorphism without protein change in PLD1 was reported to increase the risk of small cell lung cancer (82). A polymorphism in PLD2 is associated with the prevalence of colorectal cancer (83). Overexpression of either PLD1 or PLD2 in murine fibroblasts alters their cell growth, confers anchorage-independent growth ability in soft agar, and sarcoma formation in nude mice (84). Genetically enforced overexpression of PLD1 or PLD2 in a human breast cancer xenograft model led to primary tumor initiation and increased metastasis (85). PLD activity was shown to confer rapamycin resistance in human breast cancer cells (86). PLD activity was also demonstrated to couple survival and migration signals in human cancer cells to stress response (87). PLD1 and ChK $\alpha$  are interactive, such that ChK $\alpha$  silencing increases PLD1 expression and PLD1 silencing increases ChK $\alpha$  expression (88). The contributions of PLD to cancer have been summarized by Bruntz et al. as sustaining proliferative signaling, transducing MAPK signaling, regulating mTOR, evading growth suppression, resisting apoptosis- or autophagy-mediated cell death, activating invasion and metastasis, inducing angiogenesis, and deregulating cellular energetics (81).

Targeting PLD for anticancer therapy has been extensively explored. siRNA silencing or genetic ablation of either PLD1 or PLD2 were demonstrated to reduce cell proliferation, cell migration, and/or xenograft growth (85, 89). In ApcMin/+ and azoxymethane/dextran sodium sulfate (AOM/DSS) mouse models, spontaneous and colitis-associated intestinal tumorigenesis was reported to be disrupted by genetic or pharmacological targeting of PLD1, but not PLD2 (90). This was the case because PLD1 inactivation suppressed the self-renewal capacity of colon cancer-initiating cells, which in turn decreased the expression of  $\beta$ -catenin (90). The combination of PLD1 and autophagy inhibition was shown to synergize in inducing tumor cell apoptosis and tumor regression, providing a potential rational target for anticancer therapy (91). In earlier studies, short-chain primary alcohols were used as PLD inhibitor, but concerns were raised about insufficient suppression of PA production and off-target effects (92). Several PLD-specific inhibitors have been screened and evaluated in preclinical studies (81, 92, 93). 5-Fluoro-2-indolyl des-chlorohalopemide (FIPI), a dual inhibitor of PLD1 and PLD2 (93), has shown anticancer potential. Delivering FIPI with an osmotic pump to a xenograft model of breast cancer in mice was able to inhibit primary tumor growth and reduce metastatic growth of nodules in the axillary

lymph nodes and lungs (85). Tumors grew more slowly in FIPI-treated mice and showed a significant decrease in microvessel density as compared to non-treated control mice (94). Later studies have explored the anticancer properties of isoform-selective inhibitors of PLD1 or PLD2 (95). The PLD1 selective inhibitor VU0155069 was shown to attenuate intestinal tumorigenesis in the ApcMin/+ and AOM/DSS mouse models (90). Both PLD1 and PLD2 selective inhibitors were found to enhance the radiosensitivity of breast cancer cells (96).

The generation of PLD1-deficient transgenic mice provided the opportunity of studying the role of PLD1 in the tumor microenvironment. Tumor xenografts growing in *Pld*<sup>−/−</sup>, but not in *Pld*<sup>+/+</sup>, mice were demonstrated to have limited primary tumor growth and reduced lung metastasis as shown in **Figure 4** (94). Further examination showed that vascular endothelial cells

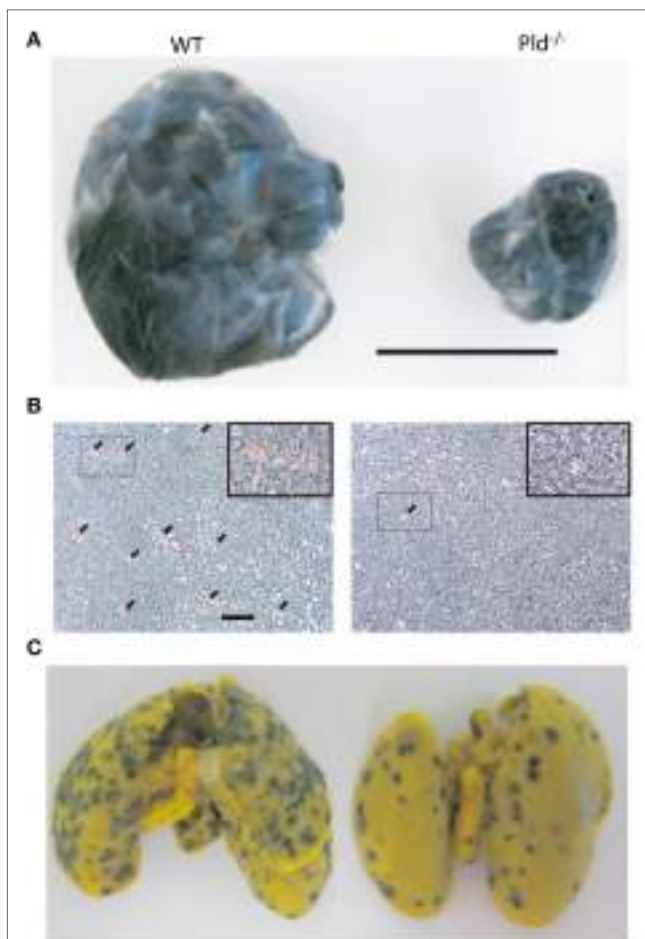


**FIGURE 4 |** Phospholipase D1 activity in the tumor microenvironment is important for tumor growth and metastasis. **(A)** Representative picture showing that melanoma xenografts grown in *Pld*<sup>−/−</sup> mice have limited growth volume compared to that growing in wild-type (WT) mice. Scale bar, 1 cm. **(B)** Melanoma xenografts growing in *Pld*<sup>−/−</sup> mice have fewer blood vessels as compared to those grown in wild-type mice, as evident from H&E stains of the respective tumor sections. Arrowheads in panel **(B)** indicate blood vessels. Scale bar, 50  $\mu$ m. **(C)** For melanoma xenografts, lung metastasis has been significantly lower in lungs of *Pld*<sup>−/−</sup> mice than in lungs of wild-type mice. Adapted from Chen et al. (94).

of PLD1-deficient mice displayed reduced activities in signaling pathways that affect vascular endothelial growth factor as a downstream target (94). These signaling pathways were mediated by reduced phosphorylation of Akt, the MAPK proteins ERK1/2, and P38, leading to decreased integrin-dependent cell adhesion to and migration on extracellular matrices, as well as reduced tumor angiogenesis (**Figure 4B**) (94). Partly mediated by impaired activation of  $\alpha_{IIb}\beta_3$  integrin in platelets, tumor cell–platelet interactions decreased in  $Pld1^{-/-}$  mice, resulting in reduced seeding of tumor cells into the lung parenchyma (**Figure 4C**) (94). Small molecule inhibitors of PLD1 displayed similar effects on tumors as the genetic ablation of PLD1 in the host mice (94).

Both  $Pld1^{-/-}$  and  $Pld2^{-/-}$  mice developed overtly normal (80, 97, 98), indicating that PLD1 inhibitors may have low toxicity. Although the existing small molecule inhibitors against PLD1 only impair cell migration and under-perform in killing cancer cells or reducing the proliferation rate of cancer cells as a stand-alone treatment, they may synergize well with other therapy approaches in combatting cancers, due to PLD1's multiple roles in important cell functions. Moreover, PLD1's role in the tumor microenvironment, which confers the ability to disrupt tumor angiogenesis in some studies (94), makes it an attractive target. Although no PLD1 inhibitors have entered into clinical trials for anticancer therapy yet, promising results emerging from recent preclinical studies may pave the way for PLD1 inhibitors into clinical studies in the near future.

## PHOSPHATIDYLCHOLINE-SPECIFIC PHOSPHOLIPASE C (PtdCho-PLC)

Phosphatidylcholine-specific phospholipase C cleaves the PC moiety from PtdCho, thereby generating and releasing DAG and PC into cytosol. DAG is an important second messenger that activates protein kinase C and induces mitogenic signal transduction. Considering the large abundance of PtdCho, it is possible that PtdCho-PLC hydrolysis of phospholipids can produce a more sustained DAG elevation than phosphatidylinositol-specific PLC cleavage of phosphatidylinositol (99). The sustained mitogenic signal produced by PtdCho-PLC generated DAG may lead to cell transformation. Indeed, NIH3T3 fibroblasts stably transfected with bacterial PtdCho-PLC displayed chronically elevated levels of DAG and PC, and a transformed phenotype that was characterized by anchorage-independent growth in soft agar, formation of transformed foci in tissue culture, and loss of contact inhibition (100). Increased PtdCho-PLC enzyme activity was observed in ovarian cancer cells (101, 102), breast cancer cells (103), and squamous cell carcinoma cells (104) as compared to the corresponding non-malignant, immortalized cells. PtdCho-PLC selectively accumulated in raft domains in the plasma membrane of HER2-overexpressing breast cancer cells, in which it colocalized with HER2 (105).

Since the genes encoding PtdCho-PLC have not yet been cloned from mammalian genomes, it is currently not possible to genetically ablate PtdCho-PLC activity, and mechanistic PtdCho-PLC studies have to rely on small molecule inhibitors of PtdCho-PLC, such as tricyclodecan-9-yl-potassium xanthate (D609).

D609 competitively inhibits PtdCho-PLC activity and was shown to confer antiviral and antitumor effects (106). Inhibition of PtdCho-PLC with D609 reduced the cellular PC content and blocked cell proliferation in human ovarian cancer cells (102). D609 treatment of human MDA-MB-231 breast cancer cells led to a loss of mesenchymal traits, such as decreased Vimentin and N-Cadherin expression, and a changed cell morphology more similar to mature breast epithelial cells, as well as growth arrest and reduced migration and invasion potential (103). PtdCho-PLC inhibition with D609 also resulted in enhanced HER2 internalization and lysosomal degradation, strong retardation of HER2 re-expression on the membrane, and reduced HER2 content in HER2-overexpressing breast cancer cells, suggesting that PtdCho-PLC inhibitors may be potential candidates for the treatment of HER2-amplified or trastuzumab-resistant breast cancers (105). D609 treatment of the two squamous cell carcinoma cell lines A431 and CaSki, which display different stemness potential, led to reduced cell proliferation, decreased sphere-forming efficiency, and down-modulated mRNA levels of stemness-related markers (104). Although the mammalian PtdCho-PLC genes have not yet been identified, it is evident that PtdCho-PLC activity is important in cell transformation and cancer progression, and that inhibiting PtdCho-PLC activity may have potential as an anticancer strategy. Efforts should focus on cloning mammalian PtdCho-PLC gene(s) and identifying compounds that inhibit PtdCho-PLC and are suitable for clinical application.

## SPHINGOMYELINASES (SMAs)

Sphingomyelin is a sphingosine-based phospholipid that exists in cell membranes with a typical mole percentage of around 10–20 (107). Sphingomyelin typically contains a PC or sometimes a PE headgroup similar to glycerol-based phospholipids. SMAs are enzymes that act analogous to phospholipase C, release PC or PE from sphingomyelin, and thereby generate ceramide (108). According to the pH for their optimum enzyme function, they are classified as acidic, neutral, and alkaline SMAs (109).

The importance of acid sphingomyelinase (ASM) function in tumor irradiation has been well established with genetic studies (110). Niemann–Pick patients have an inherited deficiency of ASM activity, which results in their lymphoblasts failing to respond to ionizing radiation with ceramide generation and apoptosis (110). ASM knockout mice also displayed failure of radiation-induced ceramide generation and apoptosis *in vivo* (110). MCA/129 fibrosarcomas and B16F1 melanomas grown in ASM-deficient mice grow much faster than in control mice and showed reduced endothelial apoptosis upon irradiation (111). When these cells were grown in severe combined immunodeficient mice with ASM-deficiency, the xenografts acquired resistance to single-dose radiotherapy (112), implying that ASM-mediated, radiotherapy-induced apoptosis occurs both in cancer cells and in the tumor microenvironment. Production of ceramide after tumor irradiation or treatment with chemotherapeutic agents, including commonly used daunorubicin, doxorubicin, cisplatin, paclitaxel, gemcitabine, among others, is a well-known treatment response (113). The production of ceramide through hydrolysis of sphingomyelin by ASM following chemotherapy is an important

mechanism of cellular ceramide increase which leads to tumor cell apoptosis, as siRNA knockdown of ASM prevents cancer cell death induced by cisplatin (114) or gemcitabine (115, 116).

The molecular mechanism by which ASM promotes cell apoptosis is mainly through its ceramide-producing ability. Moreover, the formation of ceramide-enriched lipid domains can trap and cluster specific membrane receptors such as CD95 and intracellular signaling molecules, and thus, facilitate cellular signal transduction, which leads to apoptosis, autophagic responses, and cell cycle arrest (114, 117, 118). To improve the therapeutic efficacy of ceramide-producing chemotherapy, further increasing the ceramide generation in cancer cells through activation of SMAs may be a worthwhile strategy to enhance anticancer treatment. However, it is generally hard to activate protein function. On the contrary, most rational drug design strategies inhibit rather than activate protein function. Based on this reasoning, ASM does not seem to be a suitable anticancer target at first sight. However, on the other hand, ASM-deficient human patients suffering from Niemann–Pick disease have cells with lysosomal storage disorders and significantly decreased lysosomal stability (119), suggesting that ASM is essential for maintaining normal lysosomal integrity. To escape from apoptosis, tumor cells, especially therapy resistant cancer cells, probably decrease their ASM activity to a critically low level, making them more sensitive than normal cells to ASM inhibition that can lead to lysosomal destabilization (120). Siramesine and several clinically relevant ASM inhibitors were found to trigger cancer-selective lysosomal cell death, displaying great anticancer potential as evident by reducing tumor growth *in vivo*, and reverting multidrug resistance (Figure 5) (121). So the strength of escaping from apoptosis by decreasing ASM levels becomes a weakness of cancers, through which cancer-specific killing agents can be developed especially for malignant and multidrug-resistant cancers (122).

There are several genes in the mammalian genome encoding neutral sphingomyelinases (N-SMase): the nSMase1 gene most likely encodes a lyso-platelet activating factor with phospholipase C activity (123), the nSMase2 and nSMase3 genes encode *bona fide* SMAs (124), and the newly identified MA-nSMase is a mitochondria-associated protein (125). Similar to ASM, N-SMase activity also promotes apoptosis through production of ceramide (124). The antitumoral chemotherapeutic reagents daunorubicine and arabinoside-C activate N-SMase in leukemic cells, resulting in ceramide release, which activates Jun-N-terminal kinases and Lyn protein tyrosine kinase to mediate cell apoptosis (126–128). Doxorubicin also induces nSMase2 mRNA and protein in a dose-dependent manner, and nSMase2 knockdown can prevent doxorubicin-induced growth arrest (129).

Alkaline sphingomyelinase activity is mostly found in the gastrointestinal tract and in human bile (130), and it is associated with colon cancer. Early studies showed that dietary sphingomyelin intake inhibited the formation of colon cancer that was induced with the carcinogen 1,2-dimethylhydrazine in mice (131). Both, human colorectal carcinoma and familial adenomatous polyposis, display a marked reduction in alkaline sphingomyelinase activity (130, 132, 133). Knockout of the alkaline sphingomyelinase encoding gene NPP7 in mice significantly enhanced colonic tumorigenesis as compared to wild-type mice,

after both groups of mice had been treated with a carcinogenic formulation of azoxymethane and dextran sulfate sodium (134). Loss of function mutated NPP7 gene copies were identified in the colon cancer cell line HT-29, the liver cancer cell line HepG2, and in liver tumor tissues (135, 136).

In summary, the family of SMAs generally acts in an anti-cancer role through ceramide release leading to apoptosis. Radiation therapy, chemotherapeutic agents, and some targeted therapy inhibitors exerted their tumor killing ability by activating sphingomyelinase enzyme activity. The functioning of ASM in lysosomal integration has led to the concept of inhibiting ASM to destabilize lysosomes and kill cancer cells (120, 122). The cationic amphiphilic drug siramesine, initially developed as an anti-depression agent which failed for having no effect, may be alternatively developed as an anticancer drug, and may be particularly successful when combined with microtubule-destabilizing antimitotic drugs (137). To date, the effects of sphingomyelinase activation or inhibition on the choline metabolite profile and tCho levels have not yet been studied.

## CHOLINE TRANSPORTERS

The accelerated synthesis of PtdCho to satisfy the need of fast proliferation of cancer cells requires a large quantity of choline as precursor. Cancer cells typically take up free choline from their environment, which in some cases is a rate-limiting step in forming PC and in the Kennedy pathway (138). Free choline, which is an organic cation, cannot cross cell membranes freely, and hence requires active transporters for its import into cells. The human genome has four groups of proteins with choline transport ability: choline transporter 1 (CHT1/SLC5A7), choline transporter-like proteins (CTLs), organic cation transporters (OCTs), and organic cation/carnitine transporters.

A microarray survey of CTL1 revealed that it was expressed in cancers of the central nervous system, ovary, breast, prostate, and leukemia, while highly expressed in melanoma, renal, and colon cancer (139). Functional expression analysis showed that the expression of the CTL family was different across different cancer cell lines, and that cancer cells expressed at least one set of choline transporters to guarantee the import of this essential nutrient. Both the expression of choline transporter genes and the rate of choline uptake in breast cancer cells were shown to be much higher than in the non-malignant human mammary epithelial cell (HMEC) line MCF-10A (140). CHT1 mRNA was only slightly expressed in the neuroblastoma cell lines SH-SY5Y and LA-N-2 (140), while CTL1 was the major choline transporter in these cancer cells (141). CHT1 and OCT2 were upregulated in breast cancer cell lines as compared to HMEC (142), while another study showed that CTL1 and CTL2 were the two genes overexpressed in the breast cancer cell line MCF-7 as compared to the non-malignant mammary epithelial cell line MCF-10A, and CTL2 specifically was detected in human breast cancers by immunohistochemical staining (140). CTL1 was highly overexpressed in human pulmonary adenocarcinoma tissues as compared to matched normal tissues (143). CTL1 was also the major choline transporter that accounts for the enhanced choline uptake in lung adenocarcinoma cell lines, the human HT-29 colon carcinoma

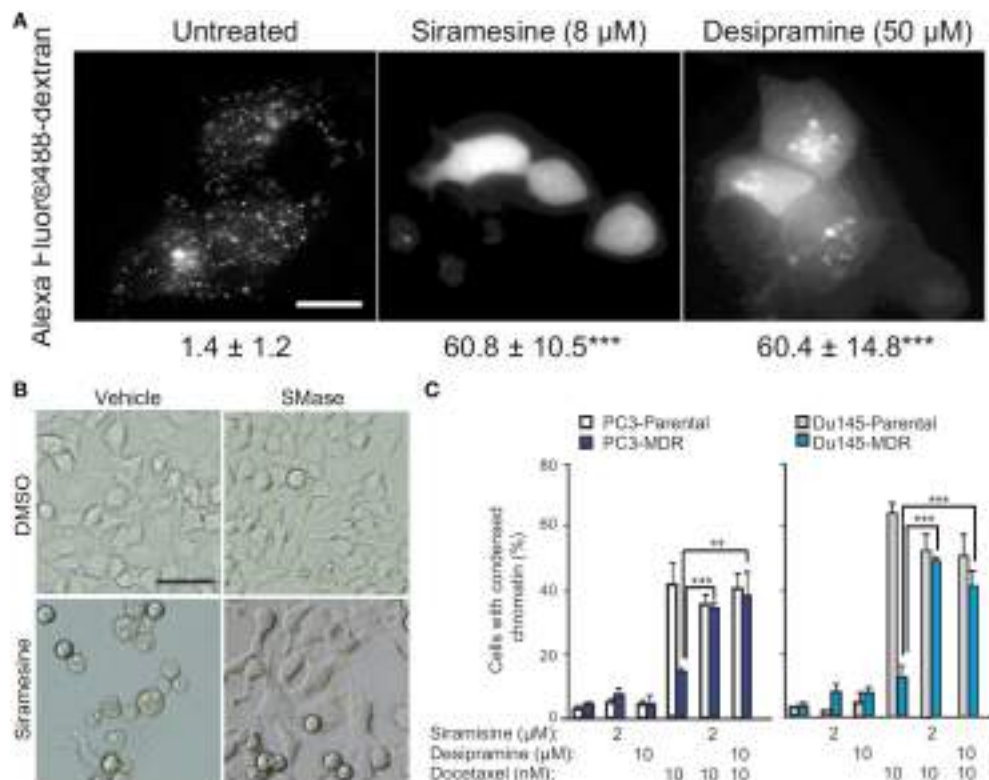


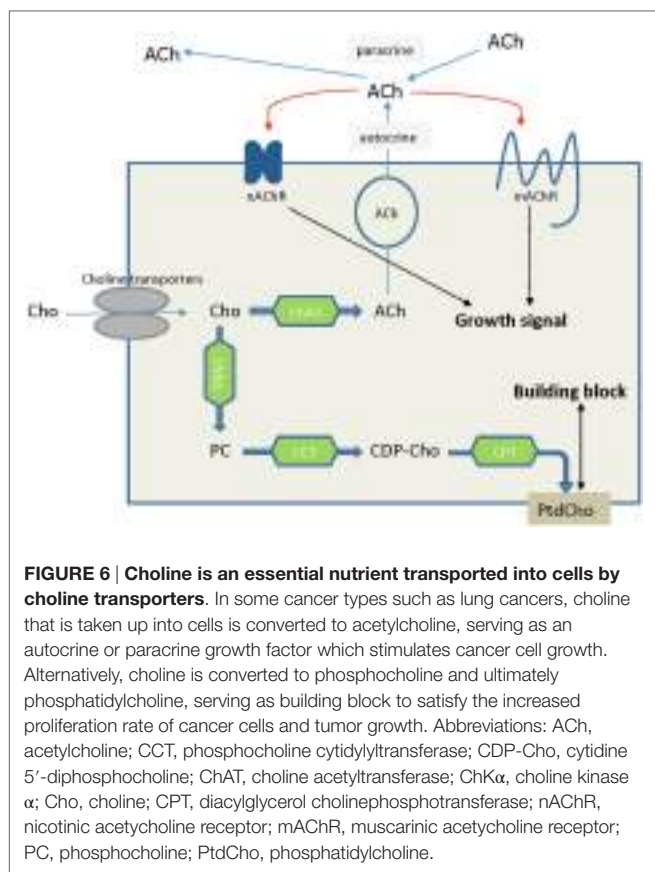
**FIGURE 5 | Targeting acid sphingomyelinases (ASM) is an effective strategy to overcome drug-resistant cancer through lysosome destabilization-mediated cell kill. (A)** Siramesine and Desipramine, two cationic amphiphilic drugs and inhibitors of ASM, cause lysosomal membrane permeabilization in MCF-7 cells. The numbers given underneath each image are the respective percentage of cells with lysosomal membrane permeabilization as indicated by cytosolic Alexa Fluor 488-dextran staining. Scale bar, 20 μm. **(B)** Cell death of transformed NIH 3T3-c-src<sup>Y527F</sup> cells caused by siramesine can be rescued by adding 75 μM ASM from *Bacillus cereus* prior to starting drug treatment. Scale bar, 50 μm. **(C)** ASM inhibition reverts drug resistance of cancer cells. Siramesine and Desipramine treatment of multidrug-resistant (MDR) PC3-MDR or Du145-MDR greatly increased the percentage of cells undergoing apoptotic cell death as evident by condensed chromatin when co-treated with docetaxel. \*\*represents  $P < 0.01$ , \*\*\*represents  $P < 0.001$ . Adapted from Petersen Nikolaj et al. (121).

cell line (144), leukemia cells (140), and human neuroblastoma cells (141).

The requirement for an increased supply of choline implies that cancer cells may be vulnerable to choline transporter inhibition. Organic cation drugs, which likely share the same transporters with choline, might inhibit choline uptake, and thereby reduce cancer cell viability. The choline analog hemicholinium-3 (HC-3) and tetrahexylammonium chloride were reported to inhibit choline uptake and reduce cell proliferation when treating the human colon carcinoma cell line HT-29 (144). The  $\text{Na}^+/\text{H}^+$  exchanger inhibitor dimethylamiloride and various organic cations such as quinine, quinidine, desipramine, imipramine, clomipramine, diphenhydramine, and fluvoxamine, among others were shown to inhibit choline uptake and cell viability in the small cell lung carcinoma cell line NCI-H69 (145). In the same study, HC-3 and CTL1 siRNA were shown to inhibit choline uptake and cell viability as well, along with increasing caspase-3/7 activity (145). CTL1 inhibitors significantly block choline uptake in the lung adenocarcinoma cell lines A549, H1299, and SPC-A-1, and their ability to block uptake was closely associated with their efficacy in reducing cell proliferation (143). HC-3 also significantly

inhibited choline uptake in both HL-60 and Jurkat leukemia cells, thereby leading to increased caspase-3/7 activity and decreased cell viability (140).

The high-affinity choline transporter CHT1 was thought to be unique to cholinergic neurons, in which choline is used to synthesize the neurotransmitter acetylcholine (ACh) (146). However, there is evidence that non-neuronal cholinergic systems exist in lung cancers (147, 148), colon adenocarcinoma (149), and leukemia (140). In these cancers, ACh acts as an autocrine or local paracrine growth factor that stimulates tumor growth, with muscarinic cholinergic receptor subtype M3 or nicotinic cholinergic receptors functioning as its receptors (147, 149, 150), which is indicated in Figure 6. However, the free choline transported into some cells for this non-neuronal ACh synthesis is not dependent on CHT1 transport (150–152). Knockdown of CTL4, but not other genes in the CTL family, in both lung and colon cancer cells significantly decreased ACh secretion and cell growth, suggesting that CTL4 is a reasonable target for certain types of cancer therapy without affecting neuronal ACh synthesis (150, 153). CTL1 was reported to be associated with ACh production in human neuroblastoma cells (141), but negatively associated with



ACh secretion from non-small cell lung carcinoma (154). CTL1 inhibition to reduce ACh production may be an effective way of killing cancer cells in certain types of cancer.

Choline transporters are crucial for cells to import extracellular choline. Inhibition of choline transport would likely lead to choline deficiency and ceramide accumulation, which in turn would trigger apoptosis *via* p53-independent pathway (140, 155, 156). Overall, choline transporters, and in particular CTL1 and CTL4, are interesting targets for anticancer drug development because their inhibition has a great potential to reduce proliferation and induce apoptosis or block the tumor promoting ACh-M3 muscarinic cholinergic receptor system. As CHT1 is necessary for neuronal ACh biogenesis, as evident by the lethal effect of CHT1 knockout in mice (157) and the severe toxicity of its inhibitor hemicholinium-3 (158), developing inhibitors specific to CTLs with low affinity to CHT1 is a must in targeted drug development to avoid possible toxic side effects.

## GLYCEROPHOSPHODIESTERASES

Glycerophosphodiester phosphodiesterases (GDPDs) or glycerophosphodiesterases (GDEs) are enzymes that use glycerophosphodiesters as substrates and break them down into glycerol 3-phosphate and alcohols (see Figure 7A). Although bacterial GDPDs can hydrolyze various glycerophosphodiesters, the mammalian genes display substrate preference, and the

substrates are not limited to glycerophosphodiesters (159). The human genome encodes seven members of the GDE family, and three of them, as well as their close homologs in mice, were reported to hydrolyze glycerophosphodiesters (159). GDE1 displays substrate preference toward glycerophosphoinositol (GPI), while glycerophosphoserine (GPS) and glycerophosphoglycerate (GPG) are direct GDE1 substrates as well, and GPE is able to block the glycerophosphoinositol phosphodiesterase activity of GDE1, but not GPC (160). The two GDPDs: GDPD5 (or GDE2) and GDPD6 (or GDE5, GPCPD1) were reported to display glycerophosphocholine phosphodiesterase (GPC-PDE) activity (161, 162).

GDPD5 was first reported in mice as a GPC-PDE that osmotically regulates GPC levels in renal medullary cells, in which GPC is an abundant and important osmoprotective organic osmolyte (161). Phosphorus MRS measurements of MDA-MB-231 breast cancer xenografts with constitutively silenced GDPD5 in nude mice also displayed an increase in GPC (164). GDPD5 expression was found to correlate with breast cancer malignancy (165). GDPD5, as well as PLD1 and ChK $\alpha$ , were highly expressed in estrogen receptor negative (ER $^-$ ) breast cancers, which also displayed higher PC, tCho, and lower GPC in comparison with ER $^+$  cases (165). High-resolution  $^1\text{H}$  MRS analysis of breast cancer cell lines in which GDPD5 or GDPD6 were silenced demonstrated that GDPD6 has a leading role in regulating the intracellular GPC level in breast cancer cells (Figure 7B) (163). siRNA silencing of GDPD5 reduced the viability (Figure 7C) and migration (Figure 7D) of ER $^+$  MCF-7 breast cancer cells, and decreased the migration and invasion of triple-negative MDA-MB-231 breast cancer cells (163). GDPD5 also has important functions in regulating neuron differentiation through glycosylphosphatidylinositol-anchor cleavage of reversion-inducing cysteine-rich protein with kazal motifs (RECK) (166), which, further downstream, leads to inactivation of the Notch signaling pathway.

GDPD6 was shown to be an Mg $^{2+}$ -dependent GDE that is able to hydrolyze GPC and GPE, but does not show activity with GPG, GPI, and GPS as substrates (167). The role of GDPD6 in cancer was recently identified, demonstrating that GDPD6 expression promotes cancer cell migration and invasion through protein kinase alpha signaling (162). GDPD6 mRNA levels were shown to be increased in metastasizing as compared to non-metastasizing endometrial carcinomas, and GDPD6 expression was negatively associated with relapse-free survival in endometrial and ovarian cancers (162). GDPD6 was overexpressed in endometrial cancers, along with ChK $\alpha$  overexpression, resulting in a 70% increase in PC levels (16). Microarray analysis of GDPD6-silenced MCF-7 and OVCAR-3 cells compared to control samples revealed that the expression of integrin  $\beta 1$  was reduced, which resulted in decreased cell attachment and spreading, while overexpression of GDPD6 had the opposite effect (168). The GDPD6 protein contains two conserved domains, which are a carbohydrate-binding domain and a catalytic domain conferring GDE enzyme activity. GDPD6 was also shown to regulate skeletal muscle development in an enzyme activity-independent domain (167). It is not yet clear whether the choline-releasing enzymatic activity of GDPD6 is important for its function in promoting cancer cell migration and invasion.

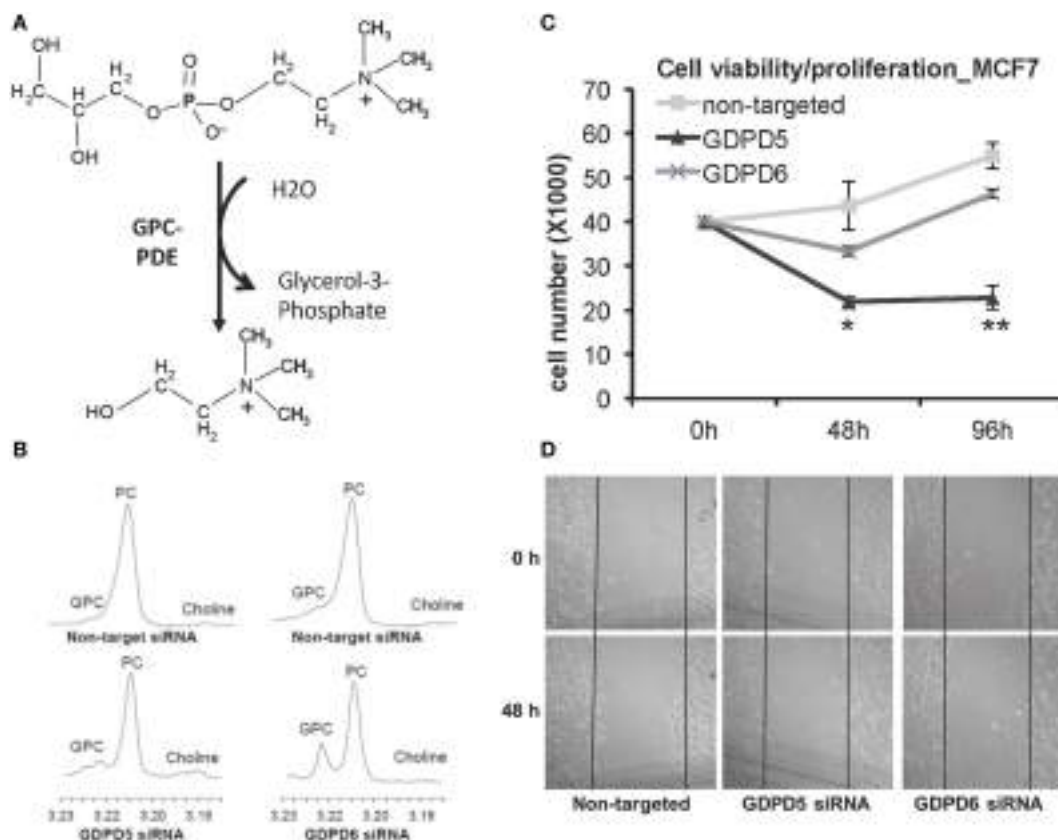


**FIGURE 7 |** GPD5 and GPD6, the two glycerophosphocholine phosphodiesterases (GPC-PDEs) reported to release choline from glycerophosphocholine (GPC), show potential anticancer effects. **(A)** GPC-PDE enzyme activity is defined as cleaving the choline moiety from GPC and thereby generating glycerol-3-phosphate. **(B)** Transient knockdown of GPD5 or GPD6 by siRNA treatment of MDA-MB-231 cells shows that GPD6 silencing leads to a significant elevation of the GPC peak in high-resolution <sup>1</sup>H MR spectra from water-soluble metabolites, while GPD5 silencing marginally increases GPC levels in this cell line. **(C)** GPD5, but not GPD6, siRNA shows cytotoxic effect in MCF-7 breast cancer cells indicated by reduced cell numbers following siRNA treatment of MCF-7 cells. **(D)** Both GPD5 and GPD6 silencing decreased MCF-7 cell migration detected by scratch assay. Abbreviations: PC, phosphocholine. \*represents  $P < 0.05$ , \*\*represents  $P < 0.01$ . Adapted from Cao et al. (163).

Both GPD5 and GPD6 are emerging as potential anticancer targets in choline metabolism. Their differing specific roles in conferring cancer aggressiveness and degrading GPC are at a relatively early stage of investigation and will require additional mechanistic and preclinical studies to evaluate their full potential as possible drug targets for anticancer therapy.

## PHOSPHATIDYLETHANOLAMINE N-METHYLTRANSFERASE (PEMT)

Phosphatidylethanolamine can be directly converted to PtdCho in one step through three methylations of the ethanolamine moiety of PtdEtn, which is catalyzed by the enzyme PEMT. This enzyme was initially isolated from rat liver and was thought to be specific to the liver (169). The first indication that PEMT can suppress cancer was the discovery that the growth of rat hepatoma cells was suppressed by overexpressing the PEMT gene (170). PEMT is highly expressed in normal liver, but its activity was negligible in the two hepatoma cell lines and almost diminished during chemically induced hepatocarcinogenesis (171, 172), and

the induced neoplastic phenotype could be partially reversed by PEMT cDNA transfection (172). When growing hepatoma cells in an animal host, PEMT activity and protein expression were barely detected in the fast proliferation stage, while its mRNA and protein reappeared in stationary growth stages (173). Forced expression of PEMT in McArdle-RH7777 hepatoma cells resulted in cell apoptosis (173).

Most early studies of PEMT function were using non-human hepatoma cells or chemically induced hepatocarcinogenesis models in animals. A later study with clinical samples of human hepatocellular carcinomas (HCC) showed that while the PEMT gene was intact, its mRNA level was reduced or even absent compared to peritumoral normal tissue, which was also observed in parallel for PEMT's enzyme activity (174). PEMT mRNA was found to inversely correlate with HCC histological stage, and the absence of PEMT mRNA in tumor tissue from cancer patients was associated with poor survival (174). While early studies of PEMT's role in cancer were mostly observed in liver cancers, more recent studies indicated that PEMT polymorphism is also related to breast cancer risk (175). In BRCA1-mutated breast

cancer, the PEMT gene undergoes epigenetic repression, and hypermethylation of a specific site in the PEMT promoter is associated with histological grade and estrogen receptor status (176). This finding is consistent with the observation that PtdEtn increased with breast tumor grade (6). Another study in small cell lung cancer indicated that an increase in PEMT expression predicted shorter patient survival time, which is opposite to the observations made in liver and breast cancer (177).

The molecular mechanisms by which PEMT expression suppresses hepatoma growth are not yet fully understood. One study showed that PEMT activity negatively correlated with PtdCho synthesis in the Kennedy pathway (178). When PEMT was overexpressed in McArdle-RH7777 rat hepatoma cells, cellular PtdCho levels did not change even though [<sup>3</sup>H]methionine and [<sup>3</sup>H]ethanolamine were incorporated into PtdCho, suggesting that conversion of PtdEtn to PtdCho occurred (178). Molecular analysis in this study showed that CTP:phosphocholine cytidylyltransferase (CT) activity, which is the rate-limiting step in the Kennedy pathway of PtdCho synthesis, decreased (178). This was most likely the reason for the unchanged PtdCho levels during PEMT overexpression in this study (178). The slowing down of the Kennedy pathway while PEMT activity increased may have contributed to the reduced cell proliferation rate in this study (178). Chemically induced hepatocarcinogenesis and growth of hepatoma cells in host animals also demonstrated opposing activities of PEMT and CT (171, 173). The overexpression of PEMT in CBRH-7919 rat hepatoma cells resulted in a downmodulation of the PI3K/Akt signaling pathway, which was evident by reduced protein levels of c-Met, PDGF receptor, PI3K, Akt, and Bcl-2, in addition to decreased phosphorylation of Akt Thr308, which was accompanied by elevated cell apoptosis (179).

In summary, PEMT, an enzyme that directly converts PtdEtn to PtdCho by sequential methylation, acts as an onco-suppressor. Its function and molecular mechanism of tumor suppression, and its regulation during carcinogenesis are currently starting to emerge and will require more in depth studies.

## ETHANOLAMINE KINASE (ETNK)

The first step in the Kenney pathway toward *de novo* synthesis of PtdEth or PtdCho is the ATP-dependent phosphorylation of free intracellular ethanolamine or free intracellular choline. While ChK $\alpha$  does confer dual choline and ETNK activity with a preference for choline (180), the conversion of free ethanolamine to PE is mainly achieved through ETNK enzyme activity (181, 182). There are two genes encoding ETNK enzymes in the human genome: ETNK1 (or EKI1) and ETNK2 (or EKI2). Forced overexpression of the ETNK1 gene in COS7 cells accelerated the Kennedy pathway of PtdEtn synthesis, but did not result in an accumulation of PtdEtns due to concomitant faster degradation of PtdEtns (183). Interestingly, an ETNK1 recurrent missense mutation was frequently found in systemic mastocytosis with eosinophilia and chronic myelomonocytic leukemia (184, 185). These mutations caused an amino acid change located in the kinase domain, which was predicted to disrupt the enzyme's catalytic activity (184, 185). Metabolite measurements revealed an averaged 5.2-fold decrease in the PtdEtn/PtdCho ratio of

ETNK1-mutated atypical chronic myelomonocytic leukemia samples as compared to ETNK1 wild-type samples (184). In contrast to these findings in leukemia, in different types of human testicular cancers, EKI1 co-amplified with DAD-R and SOX5, all of which reside in close-by chromosomal regions of the short arm of chromosome 12 (12P) (186). The DAD-R gene is thought to be clinically relevant in the malignant transformation of testicular cancers because of elevated DAD-R expression in testicular cancers with 12P amplification, which correlated with invasive growth and a reduced level of apoptosis, as compared to testicular cancers without 12P amplification (186).

While the roles and functions of ETNks in cancer are still at an early stage of investigation, the product of its enzymatic activity, PE, has been known to be elevated in several cancers for decades (45, 187). Moreover, synthetic PE has recently been suggested to have anticancer effects on melanoma (188), Ehrlich ascites tumor (189), and leukemia (190). PE has also been reported to possess anti-angiogenic and anti-metastatic activity in lung cancer (191) and to induce cell cycle arrest and apoptosis in MCF-7 breast cancer cells (192). While the therapeutic effects of PE still need to be verified by additional studies and eventually clinical trials, ETNK may be an additional target for MRS-monitored anticancer treatment and should be the focus of more research studies in the near future. It is also possible that elevated PE levels in several types of cancer could be the result of elevated ChK $\alpha$  expression and activity levels, which is known to also act on free ethanolamine (180). Additional studies are necessary to clarify the involvement of ChK $\alpha$  in the elevated tumoral PE levels.

## THE FUTURE: TARGETING MULTIPLE TARGETS AND METABOLIC NODES

As our molecular understanding of the different roles of choline and ethanolamine phospholipid metabolism enzymes in cancer is growing, it will become important to study the interactions between these enzymes as well. For example, in aggressive ER $+$  breast cancers, GDP5, PLD1, and ChK $\alpha$ , were simultaneously highly expressed, leading to elevated PC and tCho levels (165). Moreover, it was recently shown that by silencing ChK $\alpha$  in breast cancer cells, PtdCho-PLD1 was in turn upregulated and *vice versa* (88). Only silencing of both enzymes simultaneously increased apoptosis in the tested breast cancer cells, supporting the necessity for targeting multiple enzymes in choline phospholipid metabolism as a strategy of choice (88). This is also important as targeting only one choline metabolic enzyme for anticancer treatment may lead to the development of resistance in the treated cancer cells more easily as cancer cells are able to adapt to new growth environments and thereby acquire resistance.

Once the body of knowledge about the regulation of choline and ethanolamine phospholipid enzymes has grown even further, it may be worthwhile pursuing systems biology approaches of network analyses to identify the important nodes in these metabolic pathways that are the most vulnerable for targeting as anticancer treatment strategy. Such types of analyses have already been performed for drug design and development (193) and recently for tissue-specific metabolic networks, including tumors (194).

## CONCLUSION

The aberrant choline and ethanolamine phospholipid metabolism in cancer has recently further been established and solidified as a universal metabolic hallmark of cancer. However, our current knowledge of druggable targets in choline metabolism is still emerging, with only a few enzymes such as ChK $\alpha$  and PLD1 having been explored to a level where a somewhat complete picture of their regulation, oncogenic roles, and interaction networks in cancer are becoming available. For all other enzymes discussed in this review, a lot more basic and translational research is required to evaluate the exact molecular roles of PtdCho-PLC, SMases, choline transporters, GDEs, PEMT, and ETKN in cancer. Metabolic imaging approaches such as MRS and PET are valuable tools to help assess the targeting and regulation outcomes in these studies and to serve later on as monitoring tools in the

clinic to assess the response to treatment. Future studies and computational modeling approaches to evaluate the interaction between choline and ethanolamine metabolic enzymes in cancer will be necessary.

## AUTHOR CONTRIBUTIONS

MC drafted the manuscript and the figures. KG conceived of the manuscript and guided MC through writing it and edited the final manuscript and figures. ZB edited the manuscript.

## FUNDING

The authors gratefully acknowledge support from NIH R01 CA154725 and P50 CA103175.

## REFERENCES

- Dobrzyńska I, Szachowicz-Petelska B, Darewicz B, Figaszewski ZA. Characterization of human bladder cell membrane during cancer transformation. *J Membr Biol* (2015) 248(2):301–7. doi:10.1007/s00232-015-9770-4
- Dobrzynska I, Szachowicz-Petelska B, Sulkowski S, Figaszewski Z. Changes in electric charge and phospholipids composition in human colorectal cancer cells. *Mol Cell Biochem* (2005) 276(1–2):113–9. doi:10.1007/s11007-005-3557-3
- Szachowicz-Petelska B, Dobrzynska I, Skrodzka M, Darewicz B, Figaszewski ZA, Kudelski J. Phospholipid composition and electric charge in healthy and cancerous parts of human kidneys. *J Membr Biol* (2013) 246(5):421–5. doi:10.1007/s00232-013-9554-7
- Sakai K, Okuyama H, Yura J, Takeyama H, Shinagawa N, Tsuruga N, et al. Composition and turnover of phospholipids and neutral lipids in human breast cancer and reference tissues. *Carcinogenesis* (1992) 13(4):579–84. doi:10.1093/carcin/13.4.579
- Hietanen E, Punnonen K, Punnonen R, Auvinen O. Fatty acid composition of phospholipids and neutral lipids and lipid peroxidation in human breast cancer and lipoma tissue. *Carcinogenesis* (1986) 7(12):1965–9. doi:10.1093/carcin/7.12.1965
- Beckonert O, Monnerjahn J, Bonk U, Leibfritz D. Visualizing metabolic changes in breast-cancer tissue using  $^1\text{H}$  NMR spectroscopy and self-organizing maps. *NMR Biomed* (2003) 16(1):1–11. doi:10.1002/nbm.797
- Glunde K, Bhujwalla ZM, Ronen SM. Choline metabolism in malignant transformation. *Nat Rev Cancer* (2011) 11(12):835–48. doi:10.1038/nrc3162
- Bolan PJ. Magnetic resonance spectroscopy of the breast: current status. *Magn Reson Imaging Clin N Am* (2013) 21(3):625–39. doi:10.1016/j.mric.2013.04.008
- Jacobs MA, Barker PB, Bottomley PA, Bhujwalla Z, Bluemke DA. Proton magnetic resonance spectroscopic imaging of human breast cancer: a preliminary study. *J Magn Reson Imaging* (2004) 19(1):68–75. doi:10.1002/jmri.10427
- Meisamy S, Bolan PJ, Baker EH, Bliss RL, Gulbahce E, Everson LI, et al. Neoadjuvant chemotherapy of locally advanced breast cancer: predicting response with *in vivo*  $^1\text{H}$  MR spectroscopy – a pilot study at 4 T. *Radiology* (2004) 233(2):424–31. doi:10.1148/radiol.2332031285
- Manton DJ, Chaturvedi A, Hubbard A, Lind MJ, Lowry M, Maraveyas A, et al. Neoadjuvant chemotherapy in breast cancer: early response prediction with quantitative MR imaging and spectroscopy. *Br J Cancer* (2006) 94(3):427–35. doi:10.1038/sj.bjc.6602948
- Baek HM, Chen JH, Nie K, Yu HJ, Bahri S, Mehta RS, et al. Predicting pathologic response to neoadjuvant chemotherapy in breast cancer by using MR imaging and quantitative  $^1\text{H}$  MR spectroscopy. *Radiology* (2009) 251(3):653–62. doi:10.1148/radiol.2512080553
- Kurhanewicz J, Swanson MG, Nelson SJ, Vigneron DB. Combined magnetic resonance imaging and spectroscopic imaging approach to molecular imaging of prostate cancer. *J Magn Reson Imaging* (2002) 16(4):451–63. doi:10.1002/jmri.10172
- Ackerstaff E, Pflug BR, Nelson JB, Bhujwalla ZM. Detection of increased choline compounds with proton nuclear magnetic resonance spectroscopy subsequent to malignant transformation of human prostatic epithelial cells. *Cancer Res* (2001) 61(9):3599–603.
- Booth SJ, Pickles MD, Turnbull LW. *In vivo* magnetic resonance spectroscopy of gynaecological tumours at 3.0 Tesla. *BJOG* (2009) 116(2):300–3. doi:10.1111/j.1471-0528.2008.02007.x
- Trousil S, Lee P, Pinato DJ, Ellis JK, Dina R, Aboagye EO, et al. Alterations of choline phospholipid metabolism in endometrial cancer are caused by choline kinase alpha overexpression and a hyperactivated deacylation pathway. *Cancer Res* (2014) 74(23):6867–77. doi:10.1158/0008-5472.CAN-13-2409
- Vigneron D, Bollen A, McDermott M, Wald L, Day M, Moyher-Noworolski S, et al. Three-dimensional magnetic resonance spectroscopic imaging of histologically confirmed brain tumors. *Magn Reson Imaging* (2001) 19(1):89–101. doi:10.1016/S0730-725X(01)00225-9
- Einstein DB, Wessels B, Bangert B, Fu P, Nelson AD, Cohen M, et al. Phase II trial of radiosurgery to magnetic resonance spectroscopy-defined high-risk tumor volumes in patients with glioblastoma multiforme. *Int J Radiat Oncol Biol Phys* (2012) 84(3):668–74. doi:10.1016/j.ijrobp.2012.01.020
- Elkhaled A, Jalbert L, Constantin A, Yoshihara HA, Phillips JJ, Molinaro AM, et al. Characterization of metabolites in infiltrating gliomas using *ex vivo*  $^1\text{H}$  high-resolution magic angle spinning spectroscopy. *NMR Biomed* (2014) 27(5):578–93. doi:10.1002/nbm.3097
- Aboagye EO, Bhujwalla ZM. Malignant transformation alters membrane choline phospholipid metabolism of human mammary epithelial cells. *Cancer Res* (1999) 59(1):80–4.
- Iorio E, Mezzanzanica D, Alberti P, Spadaro F, Ramoni C, D'Ascenzo S, et al. Alterations of choline phospholipid metabolism in ovarian tumor progression. *Cancer Res* (2005) 65(20):9369–76. doi:10.1158/0008-5472.CAN-05-1146
- Al-Saffar NM, Troy H, Ramirez de Molina A, Jackson LE, Madhu B, Griffiths JR, et al. Noninvasive magnetic resonance spectroscopic pharmacodynamic markers of the choline kinase inhibitor MN58b in human carcinoma models. *Cancer Res* (2006) 66(1):427–34. doi:10.1158/0008-5472.CAN-05-1338
- Belouche-Babari M, Arunan V, Troy H, te Poel RH, Te Fong A-CW, Jackson LE, et al. Histone deacetylase inhibition increases levels of choline kinase and phosphocholine facilitating noninvasive imaging in human cancers. *Cancer Res* (2012) 72(4):990–1000. doi:10.1158/0008-5472.can-11-2688
- Ward CS, Eriksson P, Izquierdo-Garcia JL, Brandes AH, Ronen SM. HDAC inhibition induces increased choline uptake and elevated phosphocholine levels in MCF7 breast cancer cells. *PLoS One* (2013) 8(4):e62610. doi:10.1371/journal.pone.0062610

25. Belouche-Babari M, Jackson LE, Al-Saffar NMS, Eccles SA, Raynaud FI, Workman P, et al. Identification of magnetic resonance detectable metabolic changes associated with inhibition of phosphoinositide 3-kinase signaling in human breast cancer cells. *Mol Cancer Ther* (2006) 5(1):187–96. doi:10.1158/1535-7163.mct-03-0220
26. Chung Y-L, Troy H, Banerji U, Jackson LE, Walton MI, Stubbs M, et al. Magnetic resonance spectroscopic pharmacodynamic markers of the heat shock protein 90 inhibitor 17-allylaminohydroxygeldanamycin (17AAG) in human colon cancer models. *J Natl Cancer Inst* (2003) 95(21):1624–33. doi:10.1093/jnci/djg084
27. Morse DL, Raghunand N, Sadarangani P, Murthi S, Job C, Day S, et al. Response of choline metabolites to docetaxel therapy is quantified *in vivo* by localized <sup>31</sup>P MRS of human breast cancer xenografts and *in vitro* by high-resolution <sup>31</sup>P NMR spectroscopy of cell extracts. *Magn Reson Med* (2007) 58(2):270–80. doi:10.1002/mrm.21333
28. Roebuck JR, Cecil KM, Schnall MD, Lenkinski RE. Human breast lesions: characterization with proton MR spectroscopy. *Radiology* (1998) 209(1):269–75. doi:10.1148/radiology.209.1.9769842
29. Katz-Bruell R, Lavin PT, Lenkinski RE. Clinical utility of proton magnetic resonance spectroscopy in characterizing breast lesions. *J Natl Cancer Inst* (2002) 94(16):1197–203. doi:10.1093/jnci/94.16.1197
30. Tse GM, Cheung HS, Pang LM, Chu WC, Law BK, Kung FY, et al. Characterization of lesions of the breast with proton MR spectroscopy: comparison of carcinomas, benign lesions, and phyllodes tumors. *AJR Am J Roentgenol* (2003) 181(5):1267–72. doi:10.2214/ajr.181.5.1811267
31. Bartella L, Morris EA, Dershaw DD, Liberman L, Thakur SB, Moskowitz C, et al. Proton MR spectroscopy with choline peak as malignancy marker improves positive predictive value for breast cancer diagnosis: preliminary study. *Radiology* (2006) 239(3):686–92. doi:10.1148/radiol.2393051046
32. Jagannathan NR, Kumar M, Seenu V, Coshic O, Dwivedi SN, Julka PK, et al. Evaluation of total choline from *in vivo* volume localized proton MR spectroscopy and its response to neoadjuvant chemotherapy in locally advanced breast cancer. *Br J Cancer* (2001) 84(8):1016–22. doi:10.1054/bjoc.2000.1711
33. Tozaki M, Sakamoto M, Oyama Y, Maruyama K, Fukuma E. Predicting pathological response to neoadjuvant chemotherapy in breast cancer with quantitative <sup>1</sup>H MR spectroscopy using the external standard method. *J Magn Reson Imaging* (2010) 31(4):895–902. doi:10.1002/jmri.22118
34. Smith TA, Glaholm J, Leach MO, Machin L, Collins DJ, Payne GS, et al. A comparison of *in vivo* and *in vitro* <sup>31</sup>P NMR spectra from human breast tumours: variations in phospholipid metabolism. *Br J Cancer* (1991) 63(4):514–6. doi:10.1038/bjc.1991.122
35. Sijens PE, Wijrdeman HK, Moerland MA, Bakker CJ, Vermeulen JW, Luyten PR. Human breast cancer *in vivo*: <sup>1</sup>H and <sup>31</sup>P MR spectroscopy at 1.5 T. *Radiology* (1988) 169(3):615–20. doi:10.1148/radiology.169.3.2847230
36. Glaholm J, Leach MO, Collins DJ, Mansi J, Sharp JC, Madden A, et al. *In vivo* <sup>31</sup>P magnetic resonance spectroscopy for monitoring treatment response in breast cancer. *Lancet* (1989) 1(8650):1326–7. doi:10.1016/S0140-6736(89)92717-7
37. Leach MO, Verrill M, Glaholm J, Smith TA, Collins DJ, Payne GS, et al. Measurements of human breast cancer using magnetic resonance spectroscopy: a review of clinical measurements and a report of localized <sup>31</sup>P measurements of response to treatment. *NMR Biomed* (1998) 11(7):314–40. doi:10.1002/(SICI)1099-1492(1998110)11:7<314::AID-NBM522>3.0.CO;2-Z
38. Maris JM, Evans AE, McLaughlin AC, D'Angio GJ, Bolinger L, Manos H, et al. <sup>31</sup>P nuclear magnetic resonance spectroscopic investigation of human neuroblastoma *in situ*. *N Engl J Med* (1985) 312(23):1500–5. doi:10.1056/NEJM198506063122307
39. Narayan P, Jajodia P, Kurhanewicz J, Thomas A, MacDonald J, Hubesch B, et al. Characterization of prostate cancer, benign prostatic hyperplasia and normal prostates using transrectal <sup>31</sup>P magnetic resonance spectroscopy: a preliminary report. *J Urol* (1991) 146(1):66–74.
40. Dixon RM, Angus PW, Rajagopalan B, Radda GK. Abnormal phosphomonoester signals in <sup>31</sup>P MR spectra from patients with hepatic lymphoma. A possible marker of liver infiltration and response to chemotherapy. *Br J Cancer* (1991) 63(6):953–8. doi:10.1038/bjc.1991.208
41. Klomp DW, Wijnen JP, Scheenen TW, Heerschap A. Efficient <sup>1</sup>H to <sup>31</sup>P polarization transfer on a clinical 3T MR system. *Magn Reson Med* (2008) 60(6):1298–305. doi:10.1002/mrm.21733
42. van der Kemp WJ, Boer VO, Luijten PR, Wijnen JP, Klomp DW. Increase in SNR for <sup>31</sup>P MR spectroscopy by combining polarization transfer with a direct detection sequence. *Magn Reson Med* (2012) 68(2):353–7. doi:10.1002/mrm.23260
43. Wijnen JP, Scheenen TW, Klomp DW, Heerschap A. <sup>31</sup>P magnetic resonance spectroscopic imaging with polarisation transfer of phosphomono- and diesters at 3 T in the human brain: relation with age and spatial differences. *NMR Biomed* (2010) 23(8):968–76. doi:10.1002/nbm.1523
44. Wijnen JP, Jiang L, Greenwood TR, van der Kemp WJ, Klomp DW, Glunde K. <sup>1</sup>H/<sup>31</sup>P polarization transfer at 9.4 Tesla for improved specificity of detecting phosphomonoesters and phosphodiesters in breast tumor models. *PLoS One* (2014) 9(7):e102256. doi:10.1371/journal.pone.0102256
45. Podo F. Tumour phospholipid metabolism. *NMR Biomed* (1999) 12(7):413–39. doi:10.1002/(SICI)1099-1492(199911)12:7<413::AID-NBM587>3.3.CO;2-L
46. Bathen TF, Heldahl MG, Sitter B, Vettukattil R, Bofin A, Lundgren S, et al. *In vivo* MRS of locally advanced breast cancer: characteristics related to negative or positive choline detection and early monitoring of treatment response. *MAGMA* (2011) 24(6):347–57. doi:10.1007/s10334-011-0280-9
47. Steen RG. Response of solid tumors to chemotherapy monitored by *in vivo* <sup>31</sup>P nuclear magnetic resonance spectroscopy: a review. *Cancer Res* (1989) 49(15):4075–85.
48. U.S. Food and Drug Administration. FDA approves <sup>11</sup>C-choline for PET in prostate cancer. *J Nucl Med* (2012) 53(12):11N.
49. De Bari B, Alongi F, Lestrange L, Giannarilli F. Choline-PET in prostate cancer management: the point of view of the radiation oncologist. *Crit Rev Oncol Hematol* (2014) 91(3):234–47. doi:10.1016/j.critrevonc.2014.04.002
50. Aoyama C, Liao H, Ishidate K. Structure and function of choline kinase isoforms in mammalian cells. *Prog Lipid Res* (2004) 43(3):266–81. doi:10.1016/j.plipres.2004.03.003
51. Gallego-Ortega D, Gomez del Pulgar T, Valdes-Mora F, Cebran A, Lacal JC. Involvement of human choline kinase alpha and beta in carcinogenesis: a different role in lipid metabolism and biological functions. *Adv Enzyme Regul* (2011) 51(1):183–94. doi:10.1016/j.advenzreg.2010.09.010
52. Gallego-Ortega D, Ramirez de Molina A, Ramos MA, Valdes-Mora F, Barderas MG, Sarmentero-Estrada J, et al. Differential role of human choline kinase alpha and beta enzymes in lipid metabolism: implications in cancer onset and treatment. *PLoS One* (2009) 4(11):e7819. doi:10.1371/journal.pone.0007819
53. Ramirez de Molina A, Gallego-Ortega D, Sarmentero J, Banez-Coronel M, Martin-Cantalejo Y, Lacal JC. Choline kinase is a novel oncogene that potentiates RhoA-induced carcinogenesis. *Cancer Res* (2005) 65(13):5647–53. doi:10.1158/0008-5472.CAN-04-4416
54. Lacal JC. Choline kinase: a novel target for antitumor drugs. *IDrugs* (2001) 4(4):419–26.
55. Ramirez de Molina A, Gutierrez R, Ramos MA, Silva JM, Silva J, Bonilla F, et al. Increased choline kinase activity in human breast carcinomas: clinical evidence for a potential novel antitumor strategy. *Oncogene* (2002) 21(27):4317–22. doi:10.1038/sj.onc.1205556
56. Ramirez de Molina A, Rodriguez-Gonzalez A, Gutierrez R, Martinez-Pineiro L, Sanchez J, Bonilla F, et al. Overexpression of choline kinase is a frequent feature in human tumor-derived cell lines and in lung, prostate, and colorectal human cancers. *Biochem Biophys Res Commun* (2002) 296(3):580–3. doi:10.1016/S0006-291X(02)00920-8
57. Ramirez de Molina A, Sarmentero-Estrada J, Belda-Iniesta C, Taron M, Ramirez de Molina V, Cejas P, et al. Expression of choline kinase alpha to predict outcome in patients with early-stage non-small-cell lung cancer: a retrospective study. *Lancet Oncol* (2007) 8(10):889–97. doi:10.1016/S1470-2045(07)70279-6
58. Penet MF, Shah T, Bharti S, Krishnamachary B, Artemov D, Mironchik Y, et al. Metabolic imaging of pancreatic ductal adenocarcinoma detects altered choline metabolism. *Clin Cancer Res* (2015) 21(2):386–95. doi:10.1158/1078-0432.CCR-14-0964
59. Miyake T, Parsons SJ. Functional interactions between choline kinase alpha, epidermal growth factor receptor and c-Src in breast cancer cell proliferation. *Oncogene* (2012) 31(11):1431–41. doi:10.1038/onc.2011.332

60. Clem BF, Clem AL, Yalcin A, Goswami U, Arumugam S, Telang S, et al. A novel small molecule antagonist of choline kinase-alpha that simultaneously suppresses MAPK and PI3K/AKT signaling. *Oncogene* (2011) 30(30):3370–80. doi:10.1038/onc.2011.51
61. Chua BT, Gallego-Ortega D, Ramirez de Molina A, Ullrich A, Lacal JC, Downward J. Regulation of Akt(ser473) phosphorylation by choline kinase in breast carcinoma cells. *Mol Cancer* (2009) 8:131. doi:10.1186/1476-4598-8-131
62. Sanchez-Lopez E, Zimmerman T, Gomez del Pulgar T, Moyer MP, Lacal Sanjuan JC, Cebrian A. Choline kinase inhibition induces exacerbated endoplasmic reticulum stress and triggers apoptosis via CHOP in cancer cells. *Cell Death Dis* (2013) 4:e933. doi:10.1038/cddis.2013.453
63. Sher RB, Aoyama C, Huebsch KA, Ji S, Kerner J, Yang Y, et al. A rostrocaudal muscular dystrophy caused by a defect in choline kinase beta, the first enzyme in phosphatidylcholine biosynthesis. *J Biol Chem* (2006) 281(8):4938–48. doi:10.1074/jbc.M512578200
64. Wu G, Aoyama C, Young SG, Vance DE. Early embryonic lethality caused by disruption of the gene for choline kinase  $\alpha$ , the first enzyme in phosphatidylcholine biosynthesis. *J Biol Chem* (2008) 283(3):1456–62. doi:10.1074/jbc.M708766200
65. Hernandez-Alcoceba R, Fernandez F, Lacal JC. In vivo antitumor activity of choline kinase inhibitors: a novel target for anticancer drug discovery. *Cancer Res* (1999) 59(13):3112–8.
66. Hernandez-Alcoceba R, Saniger L, Campos J, Nunez MC, Khaless F, Gallo MA, et al. Choline kinase inhibitors as a novel approach for anti-proliferative drug design. *Oncogene* (1997) 15(19):2289–301. doi:10.1038/sj.onc.1201414
67. Rodriguez-Gonzalez A, Ramirez de Molina A, Fernandez F, Ramos MA, del Carmen Nunez M, Campos J, et al. Inhibition of choline kinase as a specific cytotoxic strategy in oncogene-transformed cells. *Oncogene* (2003) 22(55):8803–12. doi:10.1038/sj.onc.1207062
68. Lacal JC, Campos JM. Preclinical characterization of RSM-932a, a novel anticancer drug targeting the human choline kinase alpha, an enzyme involved in increased lipid metabolism of cancer cells. *Mol Cancer Ther* (2015) 14(1):31–9. doi:10.1158/1535-7163.MCT-14-0531
69. Glunde K, Raman V, Mori N, Bhujwalla ZM. RNA interference-mediated choline kinase suppression in breast cancer cells induces differentiation and reduces proliferation. *Cancer Res* (2005) 65(23):11034–43. doi:10.1158/0008-5472.CAN-05-1807
70. Krishnamachary B, Glunde K, Wildes F, Mori N, Takagi T, Raman V, et al. Noninvasive detection of lentiviral-mediated choline kinase targeting in a human breast cancer xenograft. *Cancer Res* (2009) 69(8):3464–71. doi:10.1158/0008-5472.CAN-08-4120
71. Li C, Penet MF, Wildes F, Takagi T, Chen Z, Winnard PT, et al. Nanoplex delivery of siRNA and prodrug enzyme for multimodality image-guided molecular pathway targeted cancer therapy. *ACS Nano* (2010) 4(11):6707–16. doi:10.1021/nn102187v
72. Penet MF, Chen Z, Mori N, Krishnamachary B, Bhujwalla ZM. Magnetic resonance spectroscopy of siRNA-based cancer therapy. *Methods Mol Biol* (2016) 1372:37–47. doi:10.1007/978-1-4939-3148-4\_3
73. Mori N, Glunde K, Takagi T, Raman V, Bhujwalla ZM. Choline kinase down-regulation increases the effect of 5-fluorouracil in breast cancer cells. *Cancer Res* (2007) 67(23):11284–90. doi:10.1158/0008-5472.CAN-07-2728
74. de la Cueva A, Ramirez de Molina A, Alvarez-Ayerza N, Ramos MA, Cebrian A, Del Pulgar TG, et al. Combined 5-FU and ChoKalpha inhibitors as a new alternative therapy of colorectal cancer: evidence in human tumor-derived cell lines and mouse xenografts. *PLoS One* (2013) 8(6):e64961. doi:10.1371/journal.pone.0064961
75. McDermott M, Wakelam MJ, Morris AJ. Phospholipase D. *Biochem Cell Biol* (2004) 82(1):225–53. doi:10.1139/o03-079
76. Fang Y, Vilella-Bach M, Bachmann R, Flanigan A, Chen J. Phosphatidic acid-mediated mitogenic activation of mTOR signaling. *Science* (2001) 294(5548):1942–5. doi:10.1126/science.1066015
77. Hammond SM, Altshuller YM, Sung TC, Rudge SA, Rose K, Engebrecht J, et al. Human ADP-ribosylation factor-activated phosphatidylcholine-specific phospholipase D defines a new and highly conserved gene family. *J Biol Chem* (1995) 270(50):29640–3. doi:10.1074/jbc.270.50.29640
78. Hammond SM, Jenco JM, Nakashima S, Cadwallader K, Gu Q, Cook S, et al. Characterization of two alternately spliced forms of phospholipase D1. Activation of the purified enzymes by phosphatidylinositol 4,5-bisphosphate, ADP-ribosylation factor, and rho family monomeric GTP-binding proteins and protein kinase c-alpha. *J Biol Chem* (1997) 272(6):3860–8. doi:10.1074/jbc.272.6.3860
79. Jang J-H, Lee CS, Hwang D, Ryu SH. Understanding of the roles of phospholipase d and phosphatidic acid through their binding partners. *Prog Lipid Res* (2012) 51(2):71–81. doi:10.1016/j.plipres.2011.12.003
80. Dall'Armi C, Hurtado-Lorenzo A, Tian H, Morel E, Nezu A, Chan RB, et al. The phospholipase D1 pathway modulates macroautophagy. *Nat Commun* (2010) 1:142. doi:10.1038/ncomms1144
81. Bruntz RC, Lindsley CW, Brown HA. Phospholipase D signaling pathways and phosphatidic acid as therapeutic targets in cancer. *Pharmacol Rev* (2014) 66(4):1033–79. doi:10.1124/pr.114.009217
82. Ahn MJ, Park SY, Kim WK, Cho JH, Chang BJ, Kim DJ, et al. A single nucleotide polymorphism in the phospholipase D1 gene is associated with risk of non-small cell lung cancer. *Int J Biomed Sci* (2012) 8(2):121–8.
83. Yamada Y, Hamajima N, Kato T, Iwata H, Yamamura Y, Shinoda M, et al. Association of a polymorphism of the phospholipase D2 gene with the prevalence of colorectal cancer. *J Mol Med* (2003) 81(2):126–31. doi:10.1007/s00109-002-0411-x
84. Min DS, Kwon TK, Park WS, Chang JS, Park SK, Ahn BH, et al. Neoplastic transformation and tumorigenesis associated with overexpression of phospholipase D isozymes in cultured murine fibroblasts. *Carcinogenesis* (2001) 22(10):1641–7. doi:10.1093/carcin/22.10.1641
85. Henkels KM, Boivin GP, Dudley ES, Berberich SJ, Gomez-Cambronero J. Phospholipase D (PLD) drives cell invasion, tumor growth and metastasis in a human breast cancer xenograph model. *Oncogene* (2013) 32(49):5551–62. doi:10.1038/onc.2013.207
86. Chen Y, Zheng Y, Foster DA. Phospholipase D confers rapamycin resistance in human breast cancer cells. *Oncogene* (2003) 22(25):3937–42. doi:10.1038/sj.onc.1206565
87. Zheng Y, Rodrik V, Toschi A, Shi M, Hui L, Shen Y, et al. Phospholipase D couples survival and migration signals in stress response of human cancer cells. *J Biol Chem* (2006) 281(23):15862–8. doi:10.1074/jbc.M600660200
88. Gadiya M, Mori N, Cao MD, Mironchik Y, Kakkad S, Gribbestad IS, et al. Phospholipase D1 and choline kinase-alpha are interactive targets in breast cancer. *Cancer Biol Ther* (2014) 15(5):593–601. doi:10.4161/cbt.28165
89. Knoepf SM, Chahal MS, Xie Y, Zhang Z, Brauner DJ, Hallman MA, et al. Effects of active and inactive phospholipase D2 on signal transduction, adhesion, migration, invasion, and metastasis in EL4 lymphoma cells. *Mol Pharmacol* (2008) 74(3):574–84. doi:10.1124/mol.107.040105
90. Kang DW, Choi CY, Cho Y-H, Tian H, Di Paolo G, Choi K-Y, et al. Targeting phospholipase D1 attenuates intestinal tumorigenesis by controlling  $\beta$ -catenin signaling in cancer-initiating cells. *J Exp Med* (2015) 212(8):1219–37. doi:10.1084/jem.20141254
91. Jang YH, Choi KY, Min DS. Phospholipase D-mediated autophagic regulation is a potential target for cancer therapy. *Cell Death Differ* (2014) 21(4):533–46. doi:10.1038/cdd.2013.174
92. Zhang Y, Frohman MA. Cellular and physiological roles for phospholipase D1 in cancer. *J Biol Chem* (2014) 289(33):22567–74. doi:10.1074/jbc.R114.576876
93. Su W, Yeko O, Olepu S, Genna A, Park JS, Ren H, et al. 5-fluoro-2-indolyl des-chlorohalopemide (FIPI), a phospholipase D pharmacological inhibitor that alters cell spreading and inhibits chemotaxis. *Mol Pharmacol* (2009) 75(3):437–46. doi:10.1124/mol.108.053298
94. Chen Q, Hongu T, Sato T, Zhang Y, Ali W, Cavallo J-A, et al. Key roles for the lipid signaling enzyme phospholipase D1 in the tumor microenvironment during tumor angiogenesis and metastasis. *Sci Signal* (2012) 5(249):ra79. doi:10.1126/scisignal.2003257
95. Scott SA, Selvy PE, Buck JR, Cho HP, Criswell TL, Thomas AL, et al. Design of isoform-selective phospholipase D inhibitors that modulate cancer cell invasiveness. *Nat Chem Biol* (2009) 5(2):108–17. doi:10.1038/nchembio.140
96. Cheol Son J, Woo Kang D, Mo Yang K, Choi K-Y, Gen Son T, Min DS. Phospholipase D inhibitor enhances radiosensitivity of breast cancer cells. *Exp Mol Med* (2013) 45:e38. doi:10.1038/emm.2013.75

97. Elvers M, Stegner D, Hagedorn I, Kleinschmitz C, Braun A, Kuijpers MEJ, et al. Impaired  $\alpha$ (IIb) $\beta$ (3) integrin activation and shear-dependent thrombus formation in mice lacking phospholipase D1. *Sci Signal* (2010) 3(103):ra1. doi:10.1126/scisignal.2000551
98. Oliveira TG, Chan RB, Tian H, Laredo M, Shui G, Staniszewski A, et al. Phospholipase D2 ablation ameliorates Alzheimer's disease-linked synaptic dysfunction and cognitive deficits. *J Neurosci* (2010) 30(49):16419–28. doi:10.1523/JNEUROSCI.3317-10.2010
99. Exton JH. Phosphatidylcholine breakdown and signal transduction. *Biochim Biophys Acta* (1994) 1212(1):26–42. doi:10.1016/0005-2760(94)90186-4
100. Johansen T, Bjorkoy G, Overvatn A, Diaz-Meco MT, Traavik T, Moscat J. NIH 3T3 cells stably transfected with the gene encoding phosphatidylcholine-hydrolyzing phospholipase C from *Bacillus cereus* acquire a transformed phenotype. *Mol Cell Biol* (1994) 14(1):646–54. doi:10.1128/MCB.14.1.646
101. Spadaro F, Ramoni C, Mezzanzanica D, Miotti S, Alberti P, Cecchetti S, et al. Phosphatidylcholine-specific phospholipase C activation in epithelial ovarian cancer cells. *Cancer Res* (2008) 68(16):6541–9. doi:10.1158/0008-5472.CAN-07-6763
102. Iorio E, Ricci A, Bagnoli M, Pisanu ME, Castellano G, Di Vito M, et al. Activation of phosphatidylcholine cycle enzymes in human epithelial ovarian cancer cells. *Cancer Res* (2010) 70(5):2126–35. doi:10.1158/0008-5472.CAN-09-3833
103. Abalsamo L, Spadaro F, Bozzuto G, Paris L, Cecchetti S, Lugini L, et al. Inhibition of phosphatidylcholine-specific phospholipase C results in loss of mesenchymal traits in metastatic breast cancer cells. *Breast Cancer Res* (2012) 14(2):R50. doi:10.1186/bcr3151
104. Cecchetti S, Bortolomai I, Ferri R, Mercurio L, Canevari S, Podo F, et al. Inhibition of phosphatidylcholine-specific phospholipase C interferes with proliferation and survival of tumor initiating cells in squamous cell carcinoma. *PLoS One* (2015) 10(9):e0136120. doi:10.1371/journal.pone.0136120
105. Paris L, Cecchetti S, Spadaro F, Abalsamo L, Lugini L, Pisanu ME, et al. Inhibition of phosphatidylcholine-specific phospholipase C downregulates HER2 overexpression on plasma membrane of breast cancer cells. *Breast Cancer Res* (2010) 12(3):R27. doi:10.1186/bcr2575
106. Amtmann E. The antiviral, antitumoural xanthate D609 is a competitive inhibitor of phosphatidylcholine-specific phospholipase C. *Drugs Exp Clin Res* (1996) 22(6):287–94.
107. Voet DJ, Voet JG, Pratt CW. Lipids, bilayers and membranes. *Principles of Biochemistry*. 3rd ed. New York, NY: Wiley (2008).
108. Levade T, Jaffrézou J-P. Signalling sphingomyelinases: which, where, how and why? *Biochim Biophys Acta* (1999) 1438(1):1–17. doi:10.1016/S1388-1981(99)00038-4
109. Henry B, Möller C, Dimanche-Boitrel M-T, Gulbins E, Becker KA. Targeting the ceramide system in cancer. *Cancer Lett* (2013) 332(2):286–94. doi:10.1016/j.canlet.2011.07.010
110. Santana P, Pena LA, Haimovitz-Friedman A, Martin S, Green D, McLoughlin M, et al. Acid sphingomyelinase-deficient human lymphoblasts and mice are defective in radiation-induced apoptosis. *Cell* (1996) 86(2):189–99. doi:10.1016/S0092-8674(00)80091-4
111. Garcia-Barros M, Paris F, Cordon-Cardo C, Lyden D, Rafi S, Haimovitz-Friedman A, et al. Tumor response to radiotherapy regulated by endothelial cell apoptosis. *Science* (2003) 300(5622):1155–9. doi:10.1126/science.1082504
112. Garcia-Barros M, Thin TH, Maj J, Cordon-Cardo C, Haimovitz-Friedman A, Fuks Z, et al. Impact of stromal sensitivity on radiation response of tumors implanted in SCID hosts revisited. *Cancer Res* (2010) 70(20):8179–86. doi:10.1158/0008-5472.CAN-10-1871
113. Senchenkov A, Litvak DA, Cabot MC. Targeting ceramide metabolism—a strategy for overcoming drug resistance. *J Natl Cancer Inst* (2001) 93(5):347–57. doi:10.1093/jnci/93.5.347
114. Lacour S, Hammann A, Grazide S, Lagadic-Gossmann D, Athias A, Sergeant O, et al. Cisplatin-induced CD95 redistribution into membrane lipid rafts of HT29 human colon cancer cells. *Cancer Res* (2004) 64(10):3593–8. doi:10.1158/0008-5472.CAN-03-2787
115. Dumitru CA, Weller M, Gulbins E. Ceramide metabolism determines glioma cell resistance to chemotherapy. *J Cell Physiol* (2009) 221(3):688–95. doi:10.1002/jcp.21907
116. Dumitru CA, Sandacioglu IE, Wagner M, Weller M, Gulbins E. Lysosomal ceramide mediates gemcitabine-induced death of glioma cells. *J Mol Med* (2009) 87(11):1123–32. doi:10.1007/s00109-009-0514-8
117. Morad SA, Cabot MC. Ceramide-orchestrated signalling in cancer cells. *Nat Rev Cancer* (2013) 13(1):51–65. doi:10.1038/nrc3398
118. Grassme H, Cremesti A, Kolesnick R, Gulbins E. Ceramide-mediated clustering is required for CD95-DISC formation. *Oncogene* (2003) 22(35):5457–70. doi:10.1038/sj.onc.1206540
119. Kirkegaard T, Roth AG, Petersen NHT, Mahalka AK, Olsen OD, Moilanen I, et al. Hsp70 stabilizes lysosomes and reverts Niemann-Pick disease-associated lysosomal pathology. *Nature* (2010) 463(7280):549–53. doi:10.1038/nature08710
120. Groth-Pedersen L, Jäättelä M. Combating apoptosis and multidrug resistant cancers by targeting lysosomes. *Cancer Lett* (2013) 332(2):265–74. doi:10.1016/j.canlet.2010.05.021
121. Petersen Nikolaj HT, Olsen Ole D, Groth-Pedersen L, Ellegaard A-M, Bilgin M, Redmer S, et al. Transformation-associated changes in sphingolipid metabolism sensitize cells to lysosomal cell death induced by inhibitors of acid sphingomyelinase. *Cancer Cell* (2013) 24(3):379–93. doi:10.1016/j.ccr.2013.08.003
122. Dobbelstein M, Moll U. Targeting tumour-supportive cellular machineries in anticancer drug development. *Nat Rev Drug Discov* (2014) 13(3):179–96. doi:10.1038/nrd4201
123. Sawai H, Domae N, Nagan N, Hannun YA. Function of the cloned putative neutral sphingomyelinase as lyso-platelet activating factor-phospholipase C. *J Biol Chem* (1999) 274(53):38131–9. doi:10.1074/jbc.274.53.38131
124. Reynolds CP, Maurer BJ, Kolesnick RN. Ceramide synthesis and metabolism as a target for cancer therapy. *Cancer Lett* (2004) 206(2):169–80. doi:10.1016/j.canlet.2003.08.034
125. Wu BX, Rajagopalan V, Roddy PL, Clarke CJ, Hannun YA. Identification and characterization of murine mitochondria-associated neutral sphingomyelinase (MA-nSMase), the mammalian sphingomyelin phosphodiesterase 5. *J Biol Chem* (2010) 285(23):17993–8002. doi:10.1074/jbc.M110.102988
126. Mansat-de Mas V, Bezombes C, Quillet-Mary A, Bettaieb A, D'Orgeix AD, Laurent G, et al. Implication of radical oxygen species in ceramide generation, c-Jun N-terminal kinase activation and apoptosis induced by daunorubicin. *Mol Pharmacol* (1999) 56(5):867–74.
127. Grazide S, Maestre N, Veldman RJ, Bezombes C, Maddens S, Levade T, et al. Ara-C- and daunorubicin-induced recruitment of Lyn in sphingomyelinase-enriched membrane rafts. *FASEB J* (2002) 16(12):1685–7. doi:10.1096/fj.01-0794fje
128. Bezombes C, Plo I, Mansat-De Mas V, Quillet-Mary A, Negre-Salvayre A, Laurent G, et al. Oxidative stress-induced activation of Lyn recruits sphingomyelinase and is requisite for its stimulation by Ara-C. *FASEB J* (2001) 15(9):1583–5.
129. Shamseddine AA, Clarke CJ, Carroll B, Airola MV, Mohammed S, Rella A, et al. P53-dependent upregulation of neutral sphingomyelinase-2: role in doxorubicin-induced growth arrest. *Cell Death Dis* (2015) 6:e1947. doi:10.1038/cddis.2015.268
130. Duan R-D, Cheng Y, Hansen G, Hertervig E, Liu J-J, Syk I, et al. Purification, localization, and expression of human intestinal alkaline sphingomyelinase. *J Lipid Res* (2003) 44(6):1241–50. doi:10.1194/jlr.M300037-JLR200
131. Dillehay DL, Webb SK, Schmelz EM, Merrill AH Jr. Dietary sphingomyelin inhibits 1,2-dimethylhydrazine-induced colon cancer in CF1 mice. *J Nutr* (1994) 124(5):615–20.
132. Hertervig E, Nilsson A, Nyberg L, Duan RD. Alkaline sphingomyelinase activity is decreased in human colorectal carcinoma. *Cancer* (1997) 79(3):448–53. doi:10.1002/(SICI)1097-0142(19970201)79:3<448::AID-CNCR4>3.0.CO;2-E
133. Hertervig E, Nilsson A, Bjork J, Hultkrantz R, Duan RD. Familial adenomatous polyposis is associated with a marked decrease in alkaline sphingomyelinase activity: a key factor to the unrestrained cell proliferation? *Br J Cancer* (1999) 81(2):232–6. doi:10.1038/sj.bjc.6690682
134. Chen Y, Zhang P, Xu SC, Yang L, Voss U, Ekblad E, et al. Enhanced colonic tumorigenesis in alkaline sphingomyelinase (NPP7) knockout mice. *Mol Cancer Ther* (2015) 14(1):259–67. doi:10.1158/1535-7163.MCT-14-0468-T
135. Wu J, Cheng Y, Nilsson A, Duan RD. Identification of one exon deletion of intestinal alkaline sphingomyelinase in colon cancer HT-29 cells and a

- differentiation-related expression of the wild-type enzyme in Caco-2 cells. *Carcinogenesis* (2004) 25(8):1327–33. doi:10.1093/carcin/bgh140
136. Cheng Y, Wu J, Hertervig E, Lindgren S, Duan D, Nilsson A, et al. Identification of aberrant forms of alkaline sphingomyelinase (NPP7) associated with human liver tumorigenesis. *Br J Cancer* (2007) 97(10):1441–8. doi:10.1038/sj.bjc.6604013
137. Groth-Pedersen L, Ostenfeld MS, Hoyer-Hansen M, Nylandsted J, Jäättelä M. Vincristine induces dramatic lysosomal changes and sensitizes cancer cells to lysosome-destabilizing siramesine. *Cancer Res* (2007) 67(5):2217–25. doi:10.1158/0008-5472.can-06-3520
138. Katz-Bruylants R, Degani H. Kinetics of choline transport and phosphorylation in human breast cancer cells; NMR application of the zero trans method. *Anticancer Res* (1996) 16(3B):1375–80.
139. Yuan Z, Tie A, Tarnopolsky M, Bakovic M. Genomic organization, promoter activity, and expression of the human choline transporter-like protein 1. *Physiol Genomics* (2006) 26(1):76–90. doi:10.1152/physiolgenomics.00107.2005
140. Inazu M. Choline transporter-like proteins CTLS/SLC44 family as a novel molecular target for cancer therapy. *Biopharm Drug Dispos* (2014) 35(8):431–49. doi:10.1002/bdd.1892
141. Yamada T, Inazu M, Tajima H, Matsumiya T. Functional expression of choline transporter-like protein 1 (CTL1) in human neuroblastoma cells and its link to acetylcholine synthesis. *Neurochem Int* (2011) 58(3):354–65. doi:10.1016/j.neuint.2010.12.011
142. Eliyahu G, Kreizman T, Degani H. Phosphocholine as a biomarker of breast cancer: molecular and biochemical studies. *Int J Cancer* (2007) 120(8):1721–30. doi:10.1002/ijc.22293
143. Wang T, Li J, Chen F, Zhao Y, He X, Wan D, et al. Choline transporters in human lung adenocarcinoma: expression and functional implications. *Acta Biochim Biophys Sin* (2007) 39(9):668–74. doi:10.1111/j.1745-7270.2007.00323.x
144. Kouji H, Inazu M, Yamada T, Tajima H, Aoki T, Matsumiya T. Molecular and functional characterization of choline transporter in human colon carcinoma HT-29 cells. *Arch Biochem Biophys* (2009) 483(1):90–8. doi:10.1016/j.abb.2008.12.008
145. Inazu M, Yamada T, Kubota N, Yamanaka T. Functional expression of choline transporter-like protein 1 (CTL1) in small cell lung carcinoma cells: a target molecule for lung cancer therapy. *Pharmacol Res* (2013) 76:119–31. doi:10.1016/j.phrs.2013.07.011
146. Okuda T, Haga T, Kanai Y, Endou H, Ishihara T, Katsura I. Identification and characterization of the high-affinity choline transporter. *Nat Neurosci* (2000) 3(2):120–5. doi:10.1038/72059
147. Song P, Sekhon HS, Jia Y, Keller JA, Blusztajn JK, Mark GP, et al. Acetylcholine is synthesized by and acts as an autocrine growth factor for small cell lung carcinoma. *Cancer Res* (2003) 63(1):214–21.
148. Song P, Sekhon HS, Lu A, Arredondo J, Sauer D, Gravett C, et al. M3 muscarinic receptor antagonists inhibit small cell lung carcinoma growth and mitogen-activated protein kinase phosphorylation induced by acetylcholine secretion. *Cancer Res* (2007) 67(8):3936–44. doi:10.1158/0008-5472.CAN-06-2484
149. Cheng K, Samimi R, Xie G, Shant J, Drachenberg C, Wade M, et al. Acetylcholine release by human colon cancer cells mediates autocrine stimulation of cell proliferation. *Am J Physiol Gastrointest Liver Physiol* (2008) 295(3):G591–7. doi:10.1152/ajpgi.00055.2008
150. Song P, Rekow SS, Singleton CA, Sekhon HS, Dissen GA, Zhou M, et al. Choline transporter-like protein 4 (CTL4) links to non-neuronal acetylcholine synthesis. *J Neurochem* (2013) 126(4):451–61. doi:10.1111/jnc.12298
151. Song P, Spindel ER. Basic and clinical aspects of non-neuronal acetylcholine: expression of non-neuronal acetylcholine in lung cancer provides a new target for cancer therapy. *J Pharmacol Sci* (2008) 106(2):180–5. doi:10.1254/jphs.FM0070091
152. Spindel E. Cholinergic targets in lung cancer. *Curr Pharm Des* (2016) 22(14):2152–9. doi:10.2174/1381612822666160127114237
153. Pingfang S, Jia Y, Singleton C, Shane SR, Eliot RS. Choline transporter-like protein 4 (CTL4) is preferentially linked to acetylcholine (ACh) secretion in small cell lung carcinoma. *C66. Molecular Targets for Therapeutic Development in Lung Cancer*. Denver, CO: American Thoracic Society International Conference Abstracts; American Thoracic Society (2011). p. A5079–A.
154. Pingfang S, Mark GP, Spindel ER. Knockdown of choline transporter-like protein 1 (CTL1) increases ACh secretion but decreases choline uptake in small cell lung carcinoma. *B62. Lung Cancer Biomarkers and Therapeutic Response*. New Orleans, LA: American Thoracic Society International Conference Abstracts; American Thoracic Society (2010). p. A3499–A.
155. Albright CD, Liu R, Bethea TC, Da Costa KA, Salganik RI, Zeisel SH. Choline deficiency induces apoptosis in SW40-immortalized CWSV-1 rat hepatocytes in culture. *FASEB J* (1996) 10(4):510–6.
156. Yen C-LE, Mar M-H, Zeisel SH. Choline deficiency-induced apoptosis in PC12 cells is associated with diminished membrane phosphatidylcholine and sphingomyelin, accumulation of ceramide and diacylglycerol, and activation of a caspase. *FASEB J* (1999) 13(1):135–42.
157. Ferguson SM, Bazalakova M, Savchenko V, Tapia JC, Wright J, Blakely RD. Lethal impairment of cholinergic neurotransmission in hemicholinium-3-sensitive choline transporter knockout mice. *Proc Natl Acad Sci U S A* (2004) 101(23):8762–7. doi:10.1073/pnas.0401667101
158. Gardiner JE. The inhibition of acetylcholine synthesis in brain by a hemicholinium. *Biochem J* (1961) 81(2):297–303. doi:10.1042/bj0810297
159. Corda D, Mosca MG, Ohshima N, Grauso L, Yanaka N, Mariggio S. The emerging physiological roles of the glycerophosphodiesterase family. *FEBS J* (2014) 281(4):998–1016. doi:10.1111/febs.12699
160. Zheng B, Berrie CP, Corda D, Farquhar MG. GDE1/MIR16 is a glycerophosphoinositol phosphodiesterase regulated by stimulation of G protein-coupled receptors. *Proc Natl Acad Sci U S A* (2003) 100(4):1745–50. doi:10.1073/pnas.0337605100
161. Gallazzini M, Ferraris JD, Burg MB. GDPD5 is a glycerophosphocholine phosphodiesterase that osmotically regulates the osmoprotective organic osmolyte GPC. *Proc Natl Acad Sci U S A* (2008) 105(31):11026–31. doi:10.1073/pnas.0805496105
162. Stewart JD, Marchan R, Lesjak MS, Lambert J, Hergenroeder R, Ellis JK, et al. Choline-releasing glycerophosphodiesterase EDI3 drives tumor cell migration and metastasis. *Proc Natl Acad Sci U S A* (2012) 109(21):8155–60. doi:10.1073/pnas.1117654109
163. Cao MD, Cheng M, Rizwan A, Jiang L, Krishnamachary B, Bhujwalla ZM, et al. Targeting choline phospholipid metabolism: GDPD5 and GDPD6 silencing decrease breast cancer cell proliferation, migration, and invasion. *NMR Biomed* (2016) 29(8):1098–107. doi:10.1002/nbm.3573
164. Wijnen JP, Jiang L, Greenwood TR, Cheng M, Dopkins M, Cao MD, et al. Silencing of the glycerophosphocholine phosphodiesterase GDPD5 alters the phospholipid metabolite profile in a breast cancer model *in vivo* as monitored by <sup>31</sup>P MRS. *NMR Biomed* (2014) 27(6):692–9. doi:10.1002/nbm.3106
165. Cao MD, Dopkins M, Krishnamachary B, Vesuna F, Gadiya MM, Lonning PE, et al. Glycerophosphodiester phosphodiesterase domain containing 5 (GDPD5) expression correlates with malignant choline phospholipid metabolite profiles in human breast cancer. *NMR Biomed* (2012) 25(9):1033–42. doi:10.1002/nbm.2766
166. Park S, Lee C, Sabharwal P, Zhang M, Meyers CL, Sockanathan S. GDE2 promotes neurogenesis by glycosylphosphatidylinositol-anchor cleavage of RECK. *Science* (2013) 339(6117):324–8. doi:10.1126/science.1231921
167. Okazaki Y, Ohshima N, Yoshizawa I, Kamei Y, Mariggio S, Okamoto K, et al. A novel glycerophosphodiester phosphodiesterase, GDE5, controls skeletal muscle development via a non-enzymatic mechanism. *J Biol Chem* (2010) 285(36):27652–63. doi:10.1074/jbc.M110.106708
168. Lesjak MS, Marchan R, Stewart JD, Rempel E, Rahnenfuhrer J, Hengstler JG. EDI3 links choline metabolism to integrin expression, cell adhesion and spreading. *Cell Adh Migr* (2014) 8(5):499–508. doi:10.4161/cam.29284
169. Vance DE, Ridgway ND. The methylation of phosphatidylethanolamine. *Prog Lipid Res* (1988) 27(1):61–79. doi:10.1016/0163-7827(88)90005-7
170. Cui Z, Houweling M, Vance DE. Suppression of rat hepatoma cell growth by expression of phosphatidylethanolamine N-methyltransferase-2. *J Biol Chem* (1994) 269(40):24531–3.
171. Tessitore L, Dianzani I, Cui Z, Vance DE. Diminished expression of phosphatidylethanolamine N-methyltransferase 2 during hepatocarcinogenesis. *Biochem J* (1999) 337(Pt 1):23–7. doi:10.1042/0264-6021:3370023
172. Tessitore L, Sesca E, Vance DE. Inactivation of phosphatidylethanolamine N-methyltransferase-2 in aflatoxin-induced liver cancer and partial reversion of the neoplastic phenotype by PEMT

- transfection of hepatoma cells. *Int J Cancer* (2000) 86(3):362–7. doi:10.1002/(SICI)1097-0215(20000501)86:3<362::AID-IJC10>3.3.CO;2-1
173. Tessitore L, Sesca E, Bosco M, Vance DE. Expression of phosphatidylethanolamine N-methyltransferase in Yoshida ascites hepatoma cells and the livers of host rats. *Carcinogenesis* (1999) 20(4):561–7. doi:10.1093/carcin/20.4.561
  174. Tessitore L, Marengo B, Vance DE, Papotti M, Mussa A, Daidone MG, et al. Expression of phosphatidylethanolamine N-methyltransferase in human hepatocellular carcinomas. *Oncology* (2003) 65(2):152–8. doi:10.1159/000072341
  175. Xu X, Gammon MD, Zeisel SH, Lee YL, Wetmur JG, Teitelbaum SL, et al. Choline metabolism and risk of breast cancer in a population-based study. *FASEB J* (2008) 22(6):2045–52. doi:10.1096/fj.07-101279
  176. Li D, Bi FF, Chen NN, Cao JM, Sun WP, Zhou YM, et al. Epigenetic repression of phosphatidylethanolamine N-methyltransferase (PEMT) in BRCA1-mutated breast cancer. *Oncotarget* (2014) 5(5):1315–25. doi:10.18632/oncotarget.1800
  177. Zinrajh D, Horl G, Jurgens G, Marc J, Sok M, Cerne D. Increased phosphatidylethanolamine N-methyltransferase gene expression in non-small-cell lung cancer tissue predicts shorter patient survival. *Oncol Lett* (2014) 7(6):2175–9. doi:10.3892/ol.2014.2035
  178. Cui Z, Houweling M, Vance DE. Expression of phosphatidylethanolamine N-methyltransferase-2 in McArdle-RH7777 hepatoma cells inhibits the CDP-choline pathway for phosphatidylcholine biosynthesis via decreased gene expression of CTP:phosphocholine cytidylyltransferase. *Biochem J* (1995) 312(Pt 3):939–45. doi:10.1042/bj3120939
  179. Zou W, Li ZY, Li YL, Ma KL, Tsui ZC. Overexpression of PEMT2 downregulates the PI3K/AKT signaling pathway in rat hepatoma cells. *Biochim Biophys Acta* (2002) 1581(1–2):49–56. doi:10.1016/S1388-1981(02)00120-8
  180. Aoyama C, Nakashima K, Ishidate K. Molecular cloning of mouse choline kinase and choline/ethanolamine kinase: their sequence comparison to the respective rat homologs. *Biochim Biophys Acta* (1998) 1393(1):179–85. doi:10.1016/S0005-2760(98)00062-9
  181. Aoyama C, Ohtani A, Ishidate K. Expression and characterization of the active molecular forms of choline/ethanolamine kinase-alpha and -beta in mouse tissues, including carbon tetrachloride-induced liver. *Biochem J* (2002) 363(Pt 3):777–84. doi:10.1042/0264-6021:3630777
  182. Kersting MC, Choi HS, Carman GM. Regulation of the yeast EKI1-encoded ethanolamine kinase by inositol and choline. *J Biol Chem* (2004) 279(34):35353–9. doi:10.1074/jbc.M405704200
  183. Lykidis A, Wang J, Karim MA, Jackowski S. Overexpression of a mammalian ethanolamine-specific kinase accelerates the CDP-ethanolamine pathway. *J Biol Chem* (2001) 276(3):2174–9. doi:10.1074/jbc.M008794200
  184. Gambacorti-Passerini CB, Donadoni C, Parmiani A, Pirola A, Redaelli S, Signore G, et al. Recurrent ETNK1 mutations in atypical chronic myeloid leukemia. *Blood* (2015) 125(3):499–503. doi:10.1182/blood-2014-06-579466
  185. Lasho TL, Finke CM, Zblewski D, Patnaik M, Ketterling RP, Chen D, et al. Novel recurrent mutations in ethanolamine kinase 1 (ETNK1) gene in systemic mastocytosis with eosinophilia and chronic myelomonocytic leukemia. *Blood Cancer J* (2015) 5:e275. doi:10.1038/bcj.2014.94
  186. Zafarana G, Gillis AJ, van Gurp RJ, Olsson PG, Elstrodt F, Stoop H, et al. Coamplification of DAD-R, SOX5, and EKI1 in human testicular seminomas, with specific overexpression of DAD-R, correlates with reduced levels of apoptosis and earlier clinical manifestation. *Cancer Res* (2002) 62(6):1822–31.
  187. Negendank W. Studies of human tumors by MRS: a review. *NMR Biomed* (1992) 5(5):303–24. doi:10.1002/nbm.1940050518
  188. Ferreira AK, Meneguelo R, Marques FL, Radin A, Filho OM, Neto SC, et al. Synthetic phosphoethanolamine a precursor of membrane phospholipids reduces tumor growth in mice bearing melanoma B16-F10 and *in vitro* induce apoptosis and arrest in G2/M phase. *Biomed Pharmacother* (2012) 66(7):541–8. doi:10.1016/j.biopha.2012.04.008
  189. Ferreira AK, Meneguelo R, Pereira A, Mendonca Filho O, Chierice GO, Maria DA. Anticancer effects of synthetic phosphoethanolamine on Ehrlich ascites tumor: an experimental study. *Anticancer Res* (2012) 32(1):95–104.
  190. Ferreira AK, Santana-Lemos BA, Rego EM, Filho OM, Chierice GO, Maria DA. Synthetic phosphoethanolamine has *in vitro* and *in vivo* anti-leukemia effects. *Br J Cancer* (2013) 109(11):2819–28. doi:10.1038/bjc.2013.510
  191. Ferreira AK, Freitas VM, Levy D, Ruiz JL, Bydlowski SP, Rici RE, et al. Anti-angiogenic and anti-metastatic activity of synthetic phosphoethanolamine. *PLoS One* (2013) 8(3):e57937. doi:10.1371/journal.pone.0057937
  192. Ferreira AK, Meneguelo R, Pereira A, Filho OM, Chierice GO, Maria DA. Synthetic phosphoethanolamine induces cell cycle arrest and apoptosis in human breast cancer MCF-7 cells through the mitochondrial pathway. *Biomed Pharmacother* (2013) 67(6):481–7. doi:10.1016/j.biopha.2013.01.012
  193. Clancy CE, An G, Cannon WR, Liu Y, May EE, Ortleva P, et al. Multiscale modeling in the clinic: drug design and development. *Ann Biomed Eng* (2016) 44(9):2591–610. doi:10.1007/s10439-016-1563-0
  194. Schultz A, Qutub AA. Reconstruction of tissue-specific metabolic networks using CORDA. *PLoS Comput Biol* (2016) 12(3):e1004808. doi:10.1371/journal.pcbi.1004808

**Conflict of Interest Statement:** The authors declare that the research was conducted in the absence of any commercial or financial relationships that could be construed as a potential conflict of interest.

Copyright © 2016 Cheng, Bhujwalla and Glunde. This is an open-access article distributed under the terms of the Creative Commons Attribution License (CC BY). The use, distribution or reproduction in other forums is permitted, provided the original author(s) or licensor are credited and that the original publication in this journal is cited, in accordance with accepted academic practice. No use, distribution or reproduction is permitted which does not comply with these terms.



# The Tumor Microenvironment Modulates Choline and Lipid Metabolism

Noriko Mori<sup>1</sup>, Flonné Wildes<sup>1</sup>, Tomoyo Takagi<sup>1</sup>, Kristine Glunde<sup>1,2</sup> and Zaver M. Bhujwalla<sup>1,2\*</sup>

<sup>1</sup>JHU ICMIC Program, Division of Cancer Imaging Research, The Russell H. Morgan Department of Radiology and Radiological Science, Baltimore, MD, USA, <sup>2</sup>Sidney Kimmel Comprehensive Cancer Center, School of Medicine, The Johns Hopkins University, Baltimore, MD, USA

## OPEN ACCESS

### Edited by:

Cicero Matthew R. Habito,  
Massachusetts General Hospital,  
USA

### Reviewed by:

Meetu Kaushik,  
Yale University, USA

Goutam Chakraborty,  
Memorial Sloan Kettering Cancer  
Center, USA  
Naranamangalam Raghunathan  
Jagannathan,  
All India Institute of Medical Sciences,  
India

\*Correspondence:  
Zaver M. Bhujwalla  
zaver@mri.jhu.edu

### Specialty section:

This article was submitted to  
Cancer Imaging and Diagnosis,  
a section of the journal  
*Frontiers in Oncology*

Received: 23 March 2016

Accepted: 09 December 2016

Published: 22 December 2016

### Citation:

Mori N, Wildes F, Takagi T, Glunde K and Bhujwalla ZM (2016) The Tumor Microenvironment Modulates Choline and Lipid Metabolism. *Front. Oncol.* 6:262.  
doi: 10.3389/fonc.2016.00262

An increase of cellular phosphocholine (PC) and total choline (tCho)-containing compounds as well as alterations in lipids have been consistently observed in cancer cells and tissue. These metabolic changes are closely related to malignant transformation, invasion, and metastasis. The study of cancer cells in culture plays an important role in understanding mechanisms leading to altered choline (Cho) and lipid metabolism in cancer, as it provides a carefully controlled environment. However, a solid tumor is a complex system with a unique tumor microenvironment frequently containing hypoxic and acidic regions and areas of nutrient deprivation and necrosis. Cancer cell–stromal cell interactions and the extracellular matrix may also alter Cho and lipid metabolism. Human tumor xenograft models in mice are useful to mimic the growth of human cancers and provide insights into the influence of *in vivo* conditions on metabolism. Here, we have compared metabolites, obtained with high resolution <sup>1</sup>H MRS of extracts from human breast and prostate cancer cells in a 2-dimensional (2D) monolayer culture and from solid tumor xenografts derived from these cells, as well as the protein expression of enzymes that regulate Cho and lipid metabolism. Our data demonstrate significant differences in Cho and lipid metabolism and protein expression patterns between human breast and prostate cancer cells in culture and in tumors derived from these cells. These data highlight the influence of the tumor microenvironment on Cho and lipid metabolism.

**Keywords:** choline metabolism, lipid metabolism, choline kinase, breast cancer, prostate cancer, cell culture, xenograft model

## INTRODUCTION

A solid tumor is a complex system with a unique microenvironment that frequently contains areas of hypoxia, extracellular acidosis, and necrosis (1). Cancer cell–stromal/endothelial cell interactions and nutrient deprivation are some of the additional factors that influence metabolism in solid tumors

**Abbreviations:** Cho, choline; Chk, choline kinase; GPC, glycerophosphocholine; ER, estrogen receptor; FASN, fatty acid synthase; MRS, magnetic resonance spectroscopy; PC, phosphocholine; PL, phospholipase; PR, progesterone receptor; PtdCho, phosphatidylcholine; PtdE, phosphatidylethanolamine; tCho, total choline; TMS, tetramethylsilane; TSP, 3-(trimethylsilyl) propionic 2,2,3,3-d<sub>4</sub> acid.

(1–3). Although investigating cancer cell metabolism using cells in culture has the advantages of rapid use and lower costs, it is important to validate these results with tumor studies because of the complexities of solid tumor microenvironments that may alter metabolism and gene expression profiles compared to cells in culture. This is important in the development of biomarkers and in identifying targets for cancer treatment.

Cancer cells display aberrant choline (Cho) and lipid metabolism. Phosphatidylcholine (PtdCho), the most abundant phospholipid in eukaryotic cell membranes, contributes to proliferative growth and programmed cell death (4). High levels of cellular phosphocholine (PC) and total choline-containing compounds [tCho: the sum of Cho, PC, and glycerophosphocholine (GPC)] have been consistently observed in cancer cells and tumor tissue and are closely related to malignant transformation, invasion, and metastasis (5–12).

Among the enzymes that regulate Cho metabolism, overexpression of choline kinase (Chk), the enzyme that catalyzes the phosphorylation of Cho to yield PC in the first step of PtdCho biosynthesis (Kennedy pathway) (13, 14), is a major cause of increased PC and tCho observed in cancers (8, 11, 15). The elevated tCho level detected by <sup>1</sup>H magnetic resonance spectroscopy (MRS) is being evaluated as a specific biomarker of prostate cancer, and high tCho is associated with aggressiveness in breast cancer (11, 16). Downregulation of Chk- $\alpha$  has been shown to significantly reduce proliferation in breast cancer cells (17, 18) and tumors (9). Enzymes that control the catabolism of PtdCho include phospholipase A (PLA), PLC, and PLD. These enzymes maintain PtdCho levels. Cytosolic phospholipase A<sub>2</sub> (cPLA<sub>2</sub> $\alpha$ ) has significantly different expression levels in basal-like and luminal-like breast cancer xenografts (19). PLD<sub>1</sub> is upregulated in various human cancers, including breast (20, 21), uterine (22), and endometrial (23) cancers. An association between PLD<sub>1</sub> and Chk- $\alpha$  expression with breast cancer malignancy was recently observed (21). Deregulated Cho phospholipid metabolism is emerging as a metabolic hallmark of oncogenesis and tumor progression.

Lipids function as energy storage molecules, structural components of cell membranes, and signaling molecules involved in cell growth, inflammation, and immunity (24, 25). Increased lipid biosynthesis is a characteristic feature of cancer. Elevated *de novo* fatty acid synthesis is necessary for rapidly proliferating tumor cells to continually provide lipids, such as phospholipids, for membrane production. Proton spectroscopy of lipid-soluble cancer cell and tumor extracts detects signals from fatty acids, cholesterol, and phospholipids. Fatty acid synthase (FASN) is an important lipogenic enzyme required for fatty acid synthesis. FASN overexpression has been reported in several human cancers including breast, prostate, colon, and ovary and has been associated with poor prognosis (26–32).

Here, we obtained high resolution <sup>1</sup>H MR spectra of extracts from cancer cells, and the corresponding tumor xenografts derived from these cells, to identify differences in Cho and lipid metabolism between cells and tumors. We selected two human prostate (DU-145 and PC-3) and two human breast (MCF-7 and MDA-MB-231) cancer cell lines with different aggressiveness for these studies. Expression of Chk- $\alpha$ , cPLA<sub>2</sub>, PLD<sub>1</sub>, and FASN was

characterized in cells and tumors to understand the molecular mechanisms underlying the differences in Cho and lipid metabolism observed between cells and tumors. Significant differences in Cho metabolites, especially PC and tCho, were observed between cells and tumors that were reflected in the differences in enzyme expression. These results underline the importance of the tumor microenvironment and conditions that exist *in vivo*, in modulating the Cho and lipid metabolism of cells in tumors, and provide new insights into the regulation of these metabolic pathways.

## MATERIALS AND METHODS

### Cell Culture

Two prostate and two breast cancer cell lines were used in this study. PC-3 and DU-145 prostate cancer cells are both androgen independent, but PC-3 is more invasive and metastatic than DU-145 prostate cancer cells (33). MDA-MB-231 is a triple negative metastatic human breast cancer cell line, and MCF-7 is an estrogen receptor/progesterone receptor-positive poorly metastatic human breast cancer cell line (33). All cell lines were obtained from American Type Culture Collection (Manassas, VA, USA) and were maintained in a humidified atmosphere with 5% CO<sub>2</sub> in air, at 37°C. The cell lines were grown in RPMI-1640 medium supplemented with 10% fetal bovine serum (Sigma-Aldrich, St. Louis, MO, USA) and 100 units/ml penicillin and 100 µg/ml streptomycin (Life Technologies Ltd., Grand Island, NY, USA).

### Generation of Tumor Xenografts

Approximately 2 × 10<sup>6</sup> cells in 50 µL Hanks' balanced salt solution (Sigma-Aldrich, St. Louis, MO, USA) were inoculated in the mammary fat pad (breast cancer cells) or the flank (prostate cancer cells) of severe combined immunodeficient mice. For MCF-7 tumors, a 17 β-estradiol pellet (0.18 mg 90-day release pellet, Innovative Research of America, Sarasota, FL, USA) was implanted subcutaneously 2 days prior to cancer cell inoculation. Mice were fed with Teklad global 18% protein extruded rodent diet (Harlan, Madison, WI, USA) that includes 1,200 mg/kg of Cho, 0.9% total saturated fatty acids, and 4.7% of total unsaturated fatty acids with minerals, amino acids, vitamins, and no cholesterol.

### Dual-Phase Extraction of Cells and Tumors

Cells were cultured to about 80% confluence, and medium was changed 3 h prior to cell collection to avoid any lack of nutrition. Adherent cells were collected by trypsinization and counted using a hemocytometer after staining dead cells with trypan blue. Approximately 4–5 × 10<sup>7</sup> cells were harvested for cell extraction. Solid tumors were excised at volumes of ~200–500 mm<sup>3</sup> (~0.2–0.4 g) and immediately freeze-clamped in liquid N<sub>2</sub>. The time from cell inoculation to tumor excision was approximately 50 days for DU-145, 30 days for PC-3, 40 days for MCF-7, and 60 days for MDA-MB-231 tumors.

Both lipid- and water-soluble extract fractions were obtained using a dual-phase extraction method as described previously

(17). Briefly, pelleted cells were mixed with 4 mL of ice-cold methanol and vigorously vortexed. For tumor samples, ground tumors in liquid N<sub>2</sub> were mixed with 4 mL of ice-cold methanol and homogenized. After keeping samples on ice for 15 min, 4 mL of chloroform were added, vortexed vigorously, and kept on ice for 10 min. Finally, 4 mL of water were added and shaken well. All operations were performed on ice, and samples were stored at 4°C overnight for phase separation and later centrifuged at 15,000 g at 4°C for 30 min. The water/methanol phase containing water-soluble cellular metabolites such as Cho, PC, and GPC were treated with ~100 mg of chelex beads (Sigma-Aldrich, St. Louis, MO, USA) to remove any divalent cations. After removing the beads, methanol was evaporated using a rotary evaporator. The remaining water phase was lyophilized. The chloroform phase (lipid-soluble phase) was collected in the tube, and chloroform was evaporated using nitrogen gas. Both phases of the extracts were stored at -20°C until use.

## Magnetic Resonance Spectroscopy

Water-soluble extracts from cells and tumors were resuspended in 0.6 mL of deuterated water (D<sub>2</sub>O) containing 2.4 × 10<sup>-7</sup> mol of 3-(trimethylsilyl)propionic 2,2,3,3-d<sub>4</sub> acid (TSP; Sigma-Aldrich, St. Louis, MO, USA) as an internal standard for MR spectral analysis. Lipid-soluble extracts were resuspended in 0.4 mL of chloroform-D and 0.2 mL of methanol-D4 with 0.05 v/v tetramethylsilane (TMS) (Cambridge Isotope Laboratories, Inc., Tewksbury, MA, USA) as an internal standard. Fully relaxed <sup>1</sup>H MR spectra of water-soluble extracts and lipid-soluble extracts were acquired on a Bruker Avance 11.7 T spectrometer (Bruker BioSpin Corp., Billerica, MA, USA) with flip angle = 30°, sweep width = 10,000 Hz, repetition time = 11.2 s, block size = 32 K, and scans = 128. MR spectra were analyzed using Bruker XWIN-NMR 3.5 software (Bruker BioSpin) as previously described (34). Signal integrals of -N<sup>+</sup>(CH<sub>3</sub>)<sub>3</sub> resonances of PC at ~3.226 ppm, GPC at ~3.235 ppm, and free Cho at ~3.208 ppm in water-soluble extracts were determined and normalized to cell number and cell volume and compared to the TSP standard. To determine concentrations of cell samples, peak integration (*I*<sub>met</sub>) from <sup>1</sup>H spectra of PC, GPC, and Cho were compared to that of the internal standard TSP (*I*<sub>TSP</sub>) according to the equation:

$$[\text{metabolite}_{\text{cell}}] = A_{\text{TSP}} \cdot \frac{I_{\text{met}} / H}{(I_{\text{TSP}} / H) \cdot N_{\text{cell}} \cdot V_{\text{cell}}} \quad (1)$$

$$[\text{metabolite}_{\text{tumor}}] = A_{\text{TSP}} \cdot \frac{I_{\text{met}} / H}{(I_{\text{TSP}} / H) \cdot V_{\text{tumor}}} \quad (2)$$

In these equations, [metabolite]<sub>cell</sub> represents the intracellular concentration of the metabolite of interest expressed as mole per liter (M), *A*<sub>TSP</sub> is the number of moles of TSP (2.4 × 10<sup>-7</sup> mol) in the sample, *H* is the number of protons contributing to the signal, *N*<sub>cell</sub> is the cell number, and *V*<sub>cell</sub> is the cell volume. To determine the cell volume, cell size was determined by trypsinizing the cells and measuring the diameter (d) of 100 randomly selected cells using an optical microscope and calculated as [(4π/3) × (d/2)<sup>3</sup>]. The cell volumes used for calculation are

MDA-MB-231: 2,050 μm<sup>3</sup>, MCF-7: 3,128 μm<sup>3</sup>, PC-3: 3,120 μm<sup>3</sup>, and DU-145: 3,630 μm<sup>3</sup> (7).

Tumor metabolite concentration [metabolite]<sub>tumor</sub> was calculated in mole per liter (M), *V*<sub>tumor</sub> is the tumor volume in liter (assuming 1 g = 1 mL).

In lipid phase samples, chemical shifts were referenced to the internal standard TMS resonance at 0 ppm using published data (35–38). To determine the arbitrary unit (A.U.) of metabolites from lipid phase samples, signal integrals (*I*<sub>met</sub>) of methyl groups assigned to C<sub>18</sub> of cholesterol (C<sub>18</sub>) at ~0.7 ppm, methyl groups (-CH<sub>3</sub>) at ~0.9 ppm, methylene groups -(CH<sub>2</sub>)<sub>n</sub>- at ~1.3 ppm, and ethylene groups (-CH = CH-) at ~5.4 ppm in acyl chains of lipids, -CH<sub>2</sub>-N in phosphatidylethanolamine (PtdE) at ~3.1 ppm, the Cho group (-N<sup>+</sup>(CH<sub>3</sub>)<sub>3</sub>) primarily from PtdCho at ~3.2 ppm peaks were determined and compared to that of TMS (*I*<sub>TMS</sub>). A.U. values were standardized by cell number (*N*<sub>cell</sub>) or tumor weight (g) (*W*<sub>tumor</sub>). For the comparison of cells and tumors, ratios of A.U. values were used.

$$\text{A.U./cell} = \frac{I_{\text{met}} \cdot 10^9}{I_{\text{TMS}} \cdot N_{\text{cell}}} \quad (3)$$

$$\text{A.U./g} = \frac{I_{\text{met}} \cdot 10}{I_{\text{TMS}} \cdot W_{\text{tumor}}} \quad (4)$$

## Immunoblot Analysis

Cells were grown in culture medium and scraped into RIPA buffer [50 mM Tris, pH 7.4, 150 mM NaCl, 1 mM EDTA, 1% Triton-100, 1% sodium deoxycholate, 1 mM phenylmethylsulfonyl fluoride, 0.1% SDS, and a protease inhibitor cocktail at 1:200 dilution (Sigma-Aldrich, St. Louis, MO, USA)], and cell lysates were incubated on ice for 30 min. Protein samples from tumors were prepared after grinding freeze-clamped tumors in liquid N<sub>2</sub> and sonicating in Hepes buffer with a protease inhibitor cocktail. Cell and tumor lysates were spun down at 16,000 g (refrigerated centrifuge 5415 R, Eppendorf, Westbury, NY, USA) and 4°C twice. Protein concentrations were estimated using the Bio-Rad DC assay (Bio-Rad, Hercules, CA, USA). Equal amounts of total protein (40 or 50 μg) from cells or tumors were resolved on one-dimensional 7.5% SDS-PAGE gels and transferred to a nitrocellulose membrane (Bio-Rad). After blocking in 5% milk-TBST (TBS Tween), the membrane was separately probed with a custom-made polyclonal Chk-α antibody (Proteintech Group, Inc., Chicago, IL, USA) (17), cPLA<sub>2</sub> antibody (Santa Cruz Biotechnology, Inc. Dallas, TX, USA), FASN antibody (Santa Cruz Biotechnology), and PLD<sub>1</sub> antibody (Abcam, Cambridge, MA, USA). Anti-GAPDH antibody (Molecular Probes, Eugene, OR, USA) was used for equal loading assessment. Secondary antibodies were horseradish peroxidase conjugated anti-mouse or anti-rabbit IgG (Vector Laboratories, Burlingame, CA, USA). Reactions were recorded on Blue Bio film (Denville Scientific, Metuchen, NJ, USA) following use of Super Signal West Pico Substrate (Pierce Biotech, Rockford, IL, USA).

## Statistical Analysis

Data were expressed as mean ± SD. The statistical significance was evaluated using a two-tailed unpaired Student's *t*-test. *P* values of

less than 0.05 were considered to be significant unless otherwise stated. Four or more samples were used for cell culture data and tumor data.

## RESULTS

### Levels of Cho Metabolites in Water-Soluble Extracts Determined by MRS

Representative  $^1\text{H}$  MR spectra of water-soluble metabolites obtained from PC-3 cells and a tumor extract are shown in **Figure 1**. Expanded Cho metabolite regions of water-soluble cell and tumor extract spectra from DU-145, PC-3, MCF-7, and MDA-MB-231 cell lines are shown in **Figure 2** to demonstrate the differences in the pattern of Cho metabolites between the cell and tumor pairs. Data averaged over four cell studies and six tumors

showed a consistent decrease of PC in tumors compared to cells in all four cell lines (**Figure 3A**). The two most aggressive cell lines (PC-3 and MDA-MB-231) showed the strongest decline of PC in tumors compared to cells. GPC tended to increase in tumors compared to cells in PC-3 and MDA-MB-231 with the exception of DU-145 cells where there was a significant decrease in tumors. The several fold decrease of PC overshadowed the small increase of GPC in tumors compared to cells, resulting in a significant decrease of tCho in PC-3, and MDA-MB-231 tumors compared to the cells. In DU-145 tumors, the decrease of both PC and GPC resulted in a significant decrease of tCho in tumors compared to the cells.

The PC/GPC ratio was higher in cells than in tumors (**Figure 3B**), and the differences were larger in the more malignant cell lines (PC-3 and MDA-MB-231) compared to the less malignant cell lines (DU-145 and MCF-7). Interestingly, the higher PC/GPC ratio observed in the more aggressive cell lines

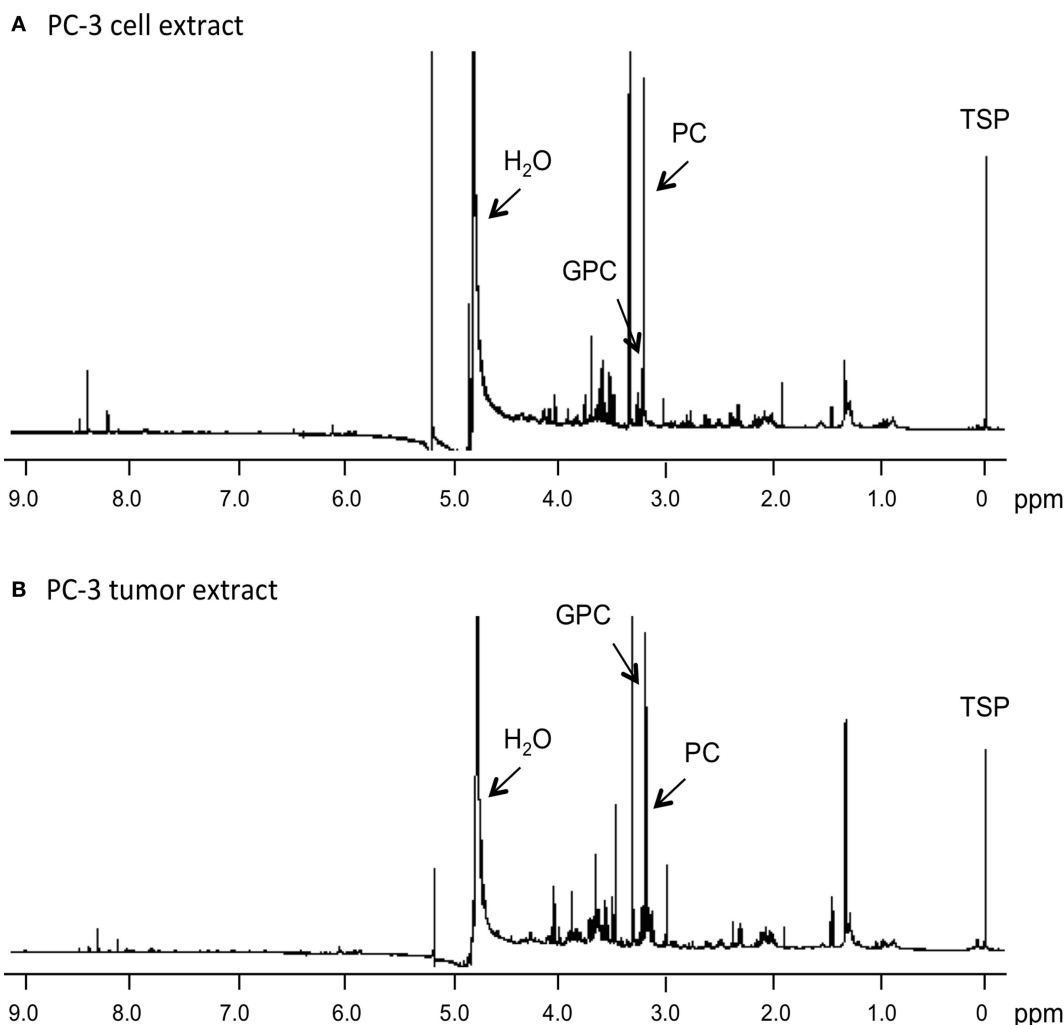


**FIGURE 1 |** Representative  $^1\text{H}$  MR spectra obtained from water-soluble extracts of (A) PC-3 cells ( $4 \times 10^7$  cells) and (B) PC-3 tumor xenograft (0.4 g). Spectra were acquired on a Bruker Avance 11.7 T spectrometer with a  $30^\circ$  flip angle, 10,000 Hz sweep width, 11.2 s repetition time, 32 K block size, and 128 scans. TSP, 3-(trimethylsilyl)propionic 2,2,3,3-d<sub>3</sub> acid, an internal standard at 0 ppm; PC, phosphocholine; GPC, glycerophosphocholine;  $\text{H}_2\text{O}$ , water signal.

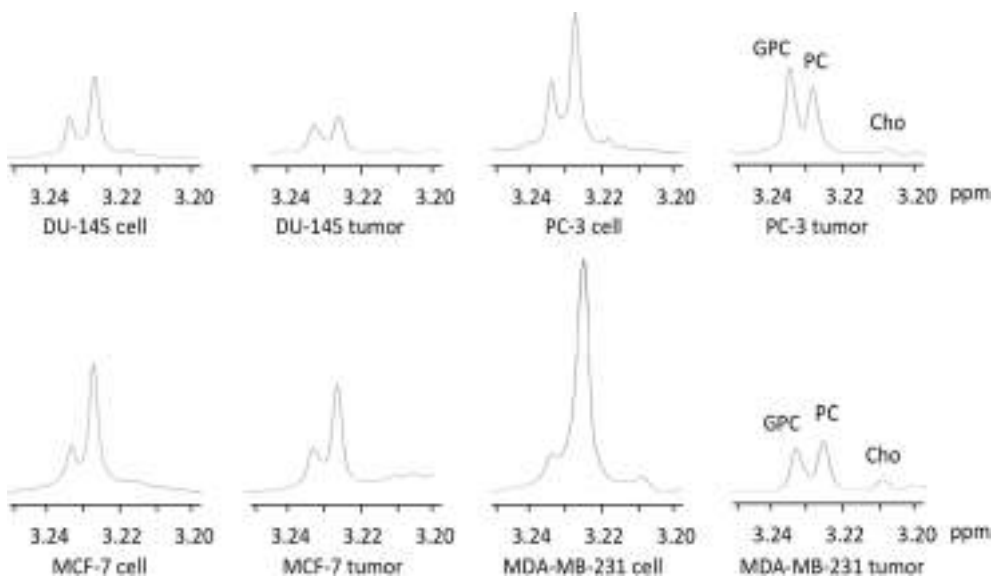


**FIGURE 2 | Representative choline metabolite regions of  $^1\text{H}$  MR spectra obtained from water-soluble extracts of DU-145, PC-3, MCF-7, and MDA-MB-231 cells and the corresponding tumor xenografts.** Spectra are expanded to display signals from 3.20 to 3.25 ppm. Peak assignments are: free Cho at ~3.208 ppm, PC at ~3.226 ppm, and GPC at ~3.235 ppm.

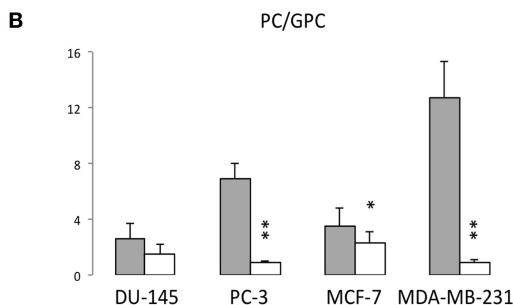
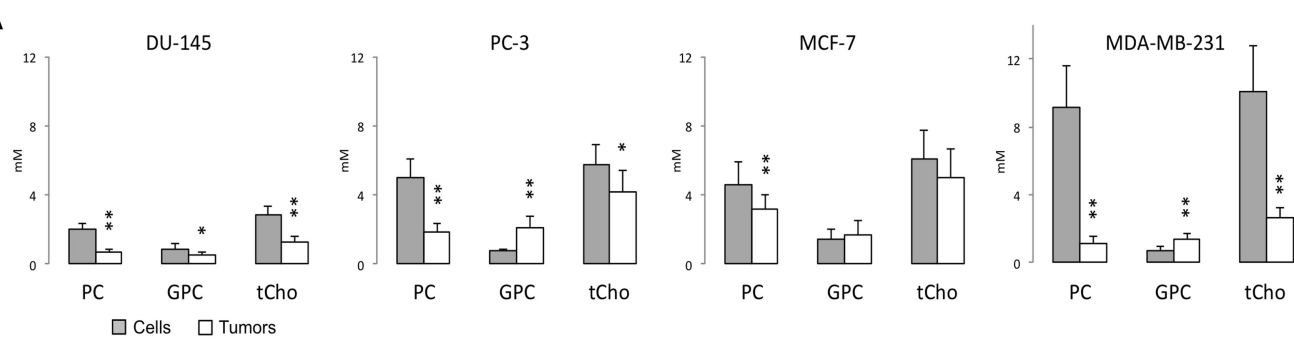


**FIGURE 3 | (A)** PC, GPC, and total choline (tCho) (PC + GPC + Cho) levels, and **(B)** PC/GPC in water-soluble extracts obtained from  $^1\text{H}$  MR spectra of DU-145, PC-3, MCF-7, and MDA-MB-231 cells (gray bar) or the corresponding tumor xenografts (white bar). Average cell number used for water-soluble extracts are DU-145:  $4.09 \pm 1.00 \times 10^7$  ( $n = 7$ ), PC-3:  $3.85 \pm 0.40 \times 10^7$  ( $n = 6$ ), MCF-7:  $4.84 \pm 0.99 \times 10^7$  ( $n = 10$ ), and MDA-MB-231:  $4.55 \pm 0.93 \times 10^7$  ( $n = 4$ ). Average tumor weights in gram used for water-soluble extracts are DU-145:  $0.31 \pm 0.07$  ( $n = 8$ ), PC-3:  $0.34 \pm 0.08$  ( $n = 7$ ), MCF-7:  $0.28 \pm 0.09$  ( $n = 11$ ), and MDA-MB-231:  $0.31 \pm 0.05$  ( $n = 7$ ). Data represent mean  $\pm$  SD. \*\* $P < 0.01$ , \* $P < 0.05$  between cells and tumors.

(PC-3 and MDA-MB-231) compared to the less aggressive cell lines (DU-145 and MCF-7) was not observed in tumor extracts.

## Levels of Lipid Metabolites in Lipid-Soluble Extracts Determined by MRS

<sup>1</sup>H MRS was used to compare lipid-soluble metabolites from cells and tumors. Representative <sup>1</sup>H MR spectra from MCF-7 cells are shown in Figure 4. Data summarized over multiple cell and

tumor samples are presented as A.U./cell from cells in culture (Figure 5A) and A.U./g from tumors (Figure 5B). Data from the methyl groups assigned to C<sub>18</sub> of cholesterol (C<sub>18</sub>), the methyl groups (−CH<sub>3</sub>), the methylene groups (−(CH<sub>2</sub>)n−), and ethylene groups (−CH=CH−) in acyl chains of lipids, −CH<sub>2</sub>−N in PtdE, the Cho group (−N<sup>+</sup>(CH<sub>3</sub>)<sub>3</sub>) primarily from PtdCho are presented. To compare cells and tumors within the same cell lines, metabolite integrals were normalized to the −CH<sub>3</sub> signal to obtain ratios of C<sub>18</sub>/−CH<sub>3</sub>, −(CH<sub>2</sub>)n−/−CH<sub>3</sub>, PtdE/−CH<sub>3</sub>, −N<sup>+</sup>(CH<sub>3</sub>)<sub>3</sub>/−CH<sub>3</sub>, −CH=CH−/−CH<sub>3</sub>. Additional analysis was performed to obtain

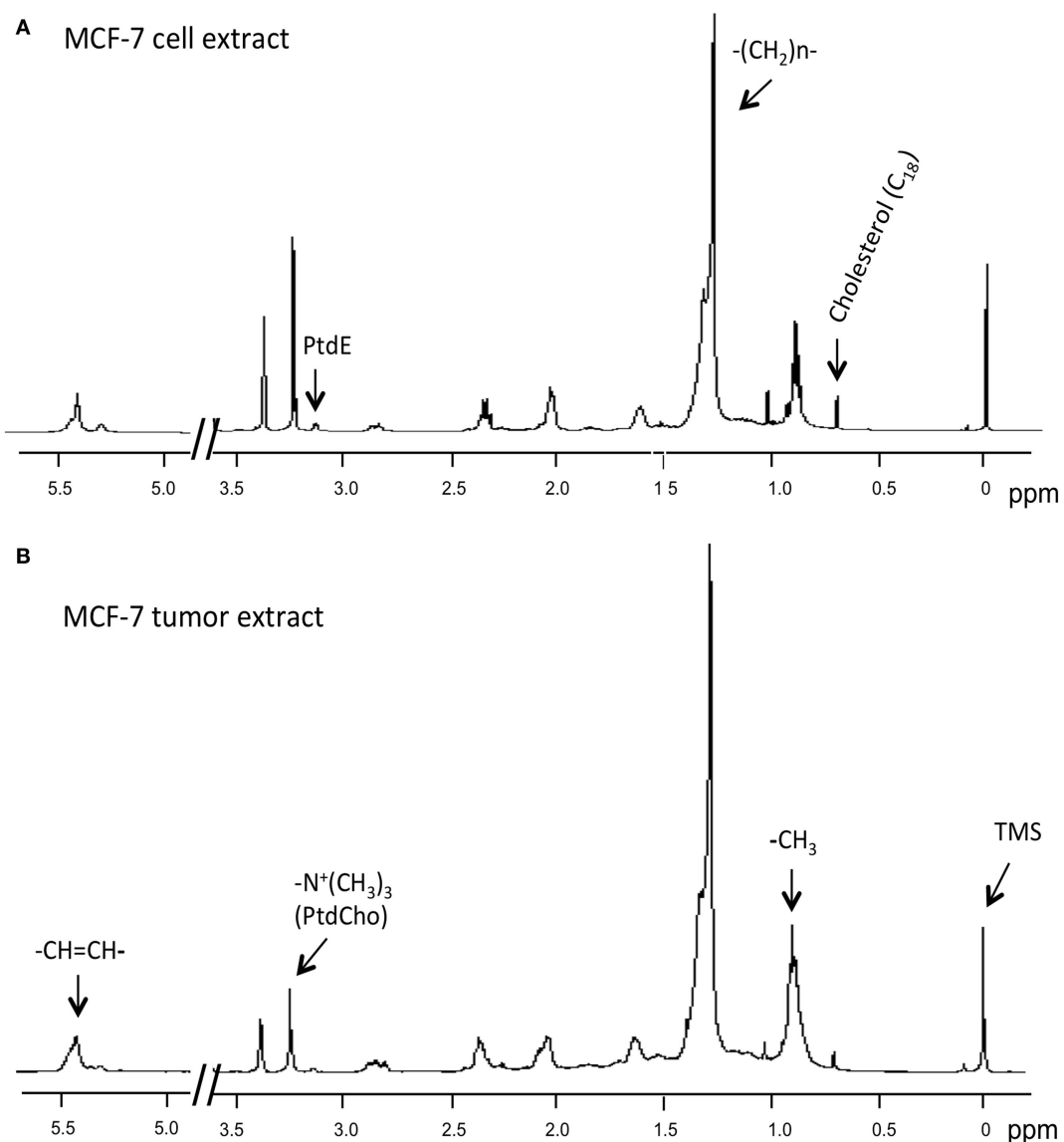


**FIGURE 4 | Representative <sup>1</sup>H MR spectra obtained from lipid-soluble extracts of (A) MCF-7 cells and (B) MCF-7 tumor xenograft.** Spectra were acquired on a Bruker Avance 11.7 T spectrometer and are expanded to display signals from 0 to 5.5 ppm (except for 3.7–4.8 ppm). Lipid spectra were acquired with a 30° flip angle, 10,000 Hz sweep width, 11.2 s repetition time, 32 K block size, and 128 scans. Peak assignments are: TMS, tetramethylsilane (internal standard) at 0 ppm, methyl groups assigned to C<sub>18</sub> of cholesterol (C<sub>18</sub>) at ~0.7 ppm, the methyl groups (−CH<sub>3</sub>) at ~0.9 ppm, methylene groups (−(CH<sub>2</sub>)n−) at ~1.3 ppm, and ethylene groups (−CH=CH−) at ~5.4 ppm in acyl chains of lipids, −CH<sub>2</sub>−N in phosphatidylethanolamine at ~3.1 ppm, and the choline group (−N<sup>+</sup>(CH<sub>3</sub>)<sub>3</sub>) primarily from phosphatidylcholine at ~3.2 ppm.

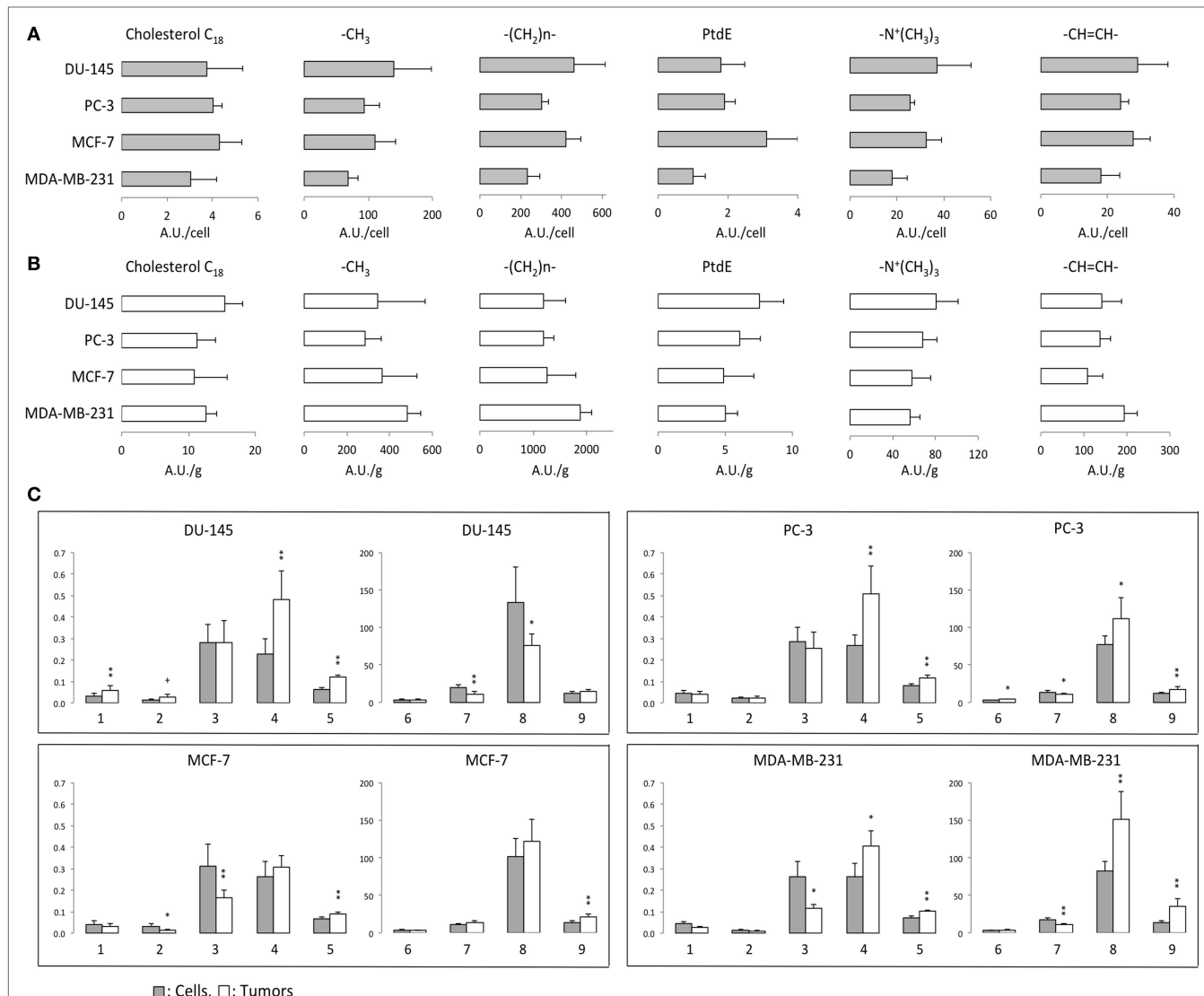


**FIGURE 5 | (A)** Lipid metabolites in arbitrary unit (A.U.)/cell from <sup>1</sup>H MR spectra obtained from lipid-soluble extracts of DU-145, PC-3, MCF-7, and MDA-MB-231 cells. **(B)** Lipid metabolites in A.U./g from <sup>1</sup>H MR spectra obtained from lipid-soluble extracts of DU-145, PC-3, MCF-7, and MDA-MB-231 xenograft models. **(C)** Ratios of lipid resonances from cells (gray bar) and solid tumors (white bar). 1: C<sub>18</sub>/-CH<sub>3</sub>, 2: phosphatidylethanolamine (PtdE)/-CH<sub>3</sub>, 3: -N<sup>+</sup>(CH<sub>3</sub>)<sub>3</sub>/-CH<sub>3</sub>, 4: -CH=CH-/-(CH<sub>2</sub>)n-, 5: -(CH<sub>2</sub>)n-/CH<sub>3</sub>, 6: -N<sup>+</sup>(CH<sub>3</sub>)<sub>3</sub>/PtdE, 8: -(CH<sub>2</sub>)n-/C<sub>18</sub>, 9: -(CH<sub>2</sub>)n-/N<sup>+</sup>(CH<sub>3</sub>)<sub>3</sub>. Average cell number used for lipid extracts are DU-145:  $4.30 \pm 0.96 \times 10^7$  ( $n = 6$ ), PC-3:  $3.85 \pm 0.40 \times 10^7$  ( $n = 6$ ), MCF-7:  $5.07 \pm 0.92 \times 10^7$  ( $n = 7$ ), and MDA-MB-231:  $4.55 \pm 0.93 \times 10^7$  ( $n = 4$ ). Average tumor weights in gram used for lipid extracts are DU-145:  $0.33 \pm 0.07$  ( $n = 6$ ), PC-3:  $0.34 \pm 0.08$  ( $n = 7$ ), MCF-7:  $0.27 \pm 0.09$  ( $n = 9$ ), and MDA-MB-231:  $0.30 \pm 0.05$  ( $n = 6$ ). Data represent mean  $\pm$  SD. \*\* $P < 0.01$ , \* $P < 0.05$ , + $P < 0.06$  between cells and tumors.

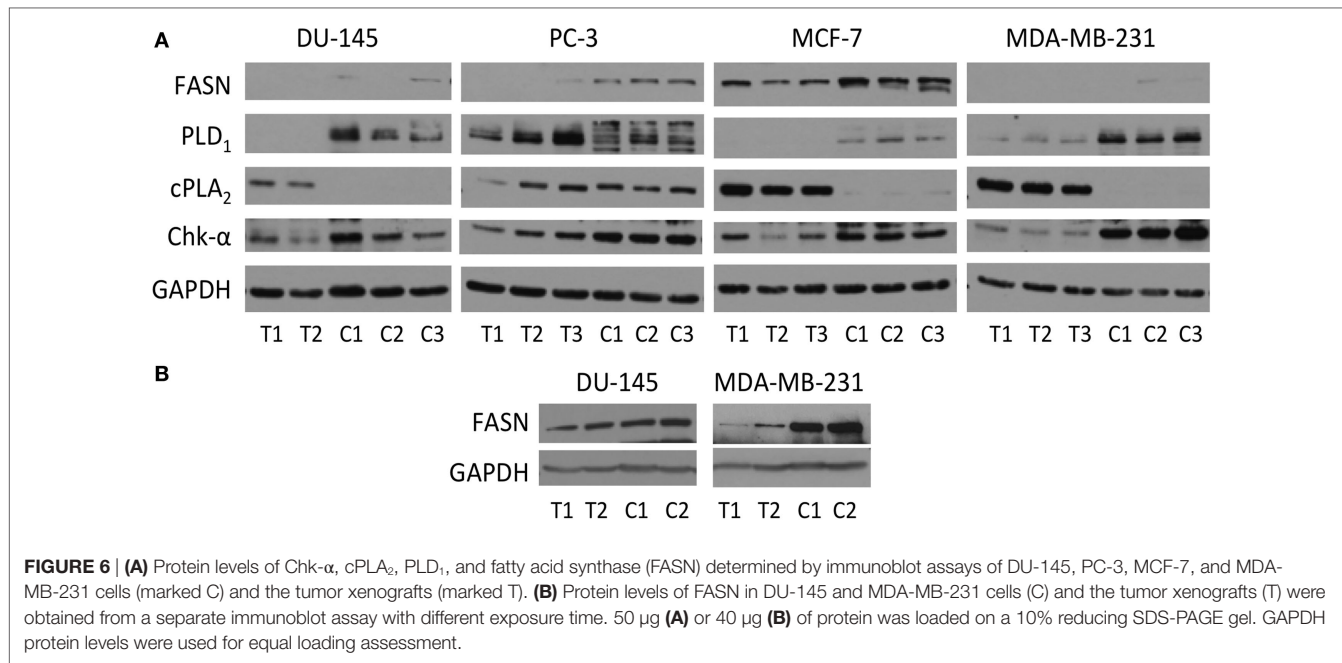
ratios of -CH=CH-/-(CH<sub>2</sub>)n-, -N<sup>+</sup>(CH<sub>3</sub>)<sub>3</sub>/PtdE, -(CH<sub>2</sub>)n-/C<sub>18</sub>, and -(CH<sub>2</sub>)n-/N<sup>+</sup>(CH<sub>3</sub>)<sub>3</sub> (Figure 5C).

The degree of lipid unsaturation estimated from -CH=CH-/CH<sub>3</sub> or -CH=CH-/-(CH<sub>2</sub>)n- was significantly and consistently higher in tumors than in cells, in all the cell lines (Figure 5C). The ratio of -(CH<sub>2</sub>)n-/CH<sub>3</sub>, which is related to the length of fatty acids, was significantly higher in PC-3 tumors than in cells. Ratios of PtdCho (-N<sup>+</sup>(CH<sub>3</sub>)<sub>3</sub>) to -CH<sub>3</sub> were higher in cells than in tumors in the breast cancer cell lines. The -N<sup>+</sup>(CH<sub>3</sub>)<sub>3</sub>/PtdE ratios were higher in cells than in tumors in the prostate cancer cell lines and the MDA-MB-231 breast cancer cell line but not in MCF-7 cells. Ratios of -(CH<sub>2</sub>)n-/C<sub>18</sub> and -(CH<sub>2</sub>)n-/N<sup>+</sup>(CH<sub>3</sub>)<sub>3</sub>

were higher in tumors than in cells from more malignant PC-3 and MDA-MB-231 cell lines. C<sub>18</sub>/-CH<sub>3</sub> and -(CH<sub>2</sub>)n-/C<sub>18</sub> results showed DU-145 tumors had higher ratio of cholesterol in lipids. Both aggressive PC-3 and MDA-MB-231 cell lines showed similar lipid metabolite changes in cells and tumors.

## Levels of Protein That Are Related to Cholesterol Phospholipid Metabolism and Lipid Metabolism

Immunoblot assays of Chk- $\alpha$ , cPLA<sub>2</sub>, PLD<sub>1</sub>, and FASN antibodies are shown in Figure 6A. A consistently higher expression of



Chk- $\alpha$  was observed in cells compared to solid tumors that was most pronounced in MDA-MB-231 cells.

Higher expression of cPLA<sub>2</sub> was observed in DU-145, MDA-MB-231, and MCF-7 tumors compared to the corresponding cells. Like Chk- $\alpha$ , PLD<sub>1</sub> was higher in cells than in corresponding tumors with the exception of PC-3 cells.

Overall, levels of FASN were higher in cells than in tumors. The levels of FASN were higher in PC-3 and MCF-7 cells than in the corresponding tumors (**Figure 6A**). Since levels of FASN in DU-145 and MDA-MB-231 were lower than in the other prostate or breast cancer cell lines, these were not detectable on the same gel (**Figure 6A**). Therefore, samples from DU-145 and MDA-MB-231 cells and tumors were loaded separately and run with different exposure time (**Figure 6B**). MDA-MB-231 had higher level of FASN protein in cells than in tumors, and DU-145 had slightly higher or comparable level of FASN in cells than in tumors.

## DISCUSSION

Here, for the first time, we have compared Cho and lipid metabolites in cells maintained in 2-dimensional (2D) monolayer cell culture to the corresponding tumor xenografts and have performed molecular characterization of some of the major enzymes that regulate Cho and lipid metabolism in these cells and tumors. We observed significant differences in metabolite and enzyme expression patterns between cells and tumors confirming the importance of the tumor microenvironment in modulating metabolism. A compendium of factors including vascularization that control substrate delivery and hypoxia, acidic extracellular pH (pHe), and areas of cell death can influence the enzymes and the metabolites measured in high resolution spectra of tumor extracts.

One common difference to emerge across all the cell lines was a significant decrease of PC and tCho in tumors compared to cells

that was consistent with the decrease of Chk- $\alpha$  observed in the tumors compared to the cells. This uniform difference across cell lines is surprising given the differences in vascularization (33), necrosis, hypoxia, and acidosis that have been observed in these tumor models and implicates the high cellular density in tumors, compared to cells in culture, as one mechanism underlying the difference. Additional mechanisms causing the decrease of PC, tCho, and Chk- $\alpha$  in tumors may be related to cancer cell-stromal cell and cancer cell-extracellular matrix (ECM) interactions that are intrinsic to tumor growth *in vivo*.

The second common difference that emerged from the comparison was a decrease of FASN in tumors compared to cells. Again the uniformity of this observation across the cell lines suggests that the reduction of FASN in tumors was cell density, stromal cell, or ECM related. Given that mechanical stress can create significant changes in cell function (39), it is possible that cancer cells growing within an ECM may demonstrate differences in enzyme expression and consequently metabolism. The uniform decrease of FASN observed in the tumors may also explain the higher unsaturated fatty acids observed in tumors compared to cells, in all the cell lines. Although endogenous and exogenous fatty acids are utilized similarly by MDA-MB-231 and MCF-7 cells in culture (40), mouse diet contains higher unsaturated fat (4.7%) than saturated fat (0.9%), which may also contribute to increased unsaturated fatty acids observed in tumors compared to cells.

Another interesting observation that emerged from these studies was that the high PC/GPC ratio associated with aggressive breast and prostate cancer cells in culture (6, 41) was not replicated in tumors. This was primarily because of the significant decrease of PC in tumors compared to cells as well as an increase of GPC in tumors compared to cells. Acidic pHe that is frequently observed in tumors (42) has been shown to decrease PC and increase GPC in cells (43). Further characterization, in the future,

of GPC phosphodiesterase, the enzyme that converts GPC into Cho and glycerol-3-phosphate (44, 45) and lysophospholipase, the enzyme that converts lyso-PtdCho to GPC (15), may provide further insights into the differences in GPC between cells and tumors observed here. Increased cell density has also been observed to increase GPC levels (46). We have previously studied PC-3, DU-145, and MDA-MB-231 cells in a cell perfusion system where multilayered cells grow on 3D beads and have observed similar metabolic profiles as observed in 2D culture, especially in PC-3 (47) and MDA-MB-231 cells (48). Although we cannot rule out differences between 2D and 3D culture contributing to the metabolic differences, the differences observed here are more likely due to the tumor microenvironment including cancer cell-stromal cell and ECM interactions.

With the exception of the PC-3 cell line, PLD<sub>1</sub> was higher in cells compared to tumors, and cPLA<sub>2</sub> was higher in tumors compared to cells. In our experience (33), PC-3 tumors are the least vascularized in the four models studied here. The absence of a difference in PLD<sub>1</sub> and cPLA<sub>2</sub> between the PC-3 cell line compared to the remaining three cell lines may be related to the poor vascularization in PC-3 tumors and the resultant reduction of paracrine signaling from vascular molecules.

Additional characterization, in future studies, of metabolites and cytokines in the tumor interstitial fluid, necrosis, pH, and oxygenation as well as an expanded characterization of the enzymes in Cho and lipid metabolism in culture and in tumors will provide further insights into the mechanisms underlying the differences between cells and tumors observed here. Investigation of metabolite differences between primary tumors and metastatic growth will also provide important insights. Such insights will provide further understanding of the functioning of tumors that

## REFERENCES

- Gillies RJ, Raghunand N, Karczmar GS, Bhujwalla ZM. MRI of the tumor microenvironment. *J Magn Reson Imaging* (2002) 16(4):430–50. doi:10.1002/jmri.10181
- Mori N, Natarajan K, Chacko VP, Artemov D, Bhujwalla ZM. Choline phospholipid metabolites of human vascular endothelial cells altered by cyclooxygenase inhibition, growth factor depletion, and paracrine factors secreted by cancer cells. *Mol Imaging* (2003) 2(2):124–30. doi:10.1162/153535003322332000
- Criscitiello C, Esposito A, Curigliano G. Tumor-stroma crosstalk: targeting stroma in breast cancer. *Curr Opin Oncol* (2014) 26(6):551–5. doi:10.1097/CCO.0000000000000122
- Ridgway ND. The role of phosphatidylcholine and choline metabolites to cell proliferation and survival. *Crit Rev Biochem Mol Biol* (2013) 48(1):20–38. doi:10.3109/10409238.2012.735643
- Gribbestad IS, Singstad TE, Nilsen G, Fjosne HE, Engan T, Haugen OA, et al. In vivo <sup>1</sup>H MRS of normal breast and breast tumors using a dedicated double breast coil. *J Magn Reson Imaging* (1998) 8(6):1191–7. doi:10.1002/jmri.1880080602
- Aboagye EO, Bhujwalla ZM. Malignant transformation alters membrane choline phospholipid metabolism of human mammary epithelial cells. *Cancer Res* (1999) 59(1):80–4.
- Ackerstaff E, Pflug BR, Nelson JB, Bhujwalla ZM. Detection of increased choline compounds with proton nuclear magnetic resonance spectroscopy subsequent to malignant transformation of human prostatic epithelial cells. *Cancer Res* (2001) 61(9):3599–603.
- Ramirez de Molina A, Gutierrez R, Ramos MA, Silva JM, Silva J, Bonilla F, et al. Increased choline kinase activity in human breast carcinomas: clinical evidence for a potential novel antitumor strategy. *Oncogene* (2002) 21(27):4317–22. doi:10.1038/sj.onc.1205556
- Krishnamachary B, Glunde K, Wildes F, Mori N, Takagi T, Raman V, et al. Noninvasive detection of lentiviral-mediated choline kinase targeting in a human breast cancer xenograft. *Cancer Res* (2009) 69(8):3464–71. doi:10.1158/0008-5472.CAN-08-4120
- Iorio E, Ricci A, Bagnoli M, Pisani ME, Castellano G, Di Vito M, et al. Activation of phosphatidylcholine cycle enzymes in human epithelial ovarian cancer cells. *Cancer Res* (2010) 70(5):2126–35. doi:10.1158/0008-5472.CAN-09-3833
- Glunde K, Bhujwalla ZM, Ronen SM. Choline metabolism in malignant transformation. *Nat Rev Cancer* (2011) 11(12):835–48. doi:10.1038/nrc3162
- Podo F, Canevari S, Canese R, Pisani ME, Ricci A, Iorio E. MR evaluation of response to targeted treatment in cancer cells. *NMR Biomed* (2011) 24(6):648–72. doi:10.1002/nbm.1658
- Kennedy EP. Metabolism of lipides. *Annu Rev Biochem* (1957) 26:119–48. doi:10.1146/annurev.bi.26.070157.001003
- Aoyama C, Liao H, Ishidate K. Structure and function of choline kinase isoforms in mammalian cells. *Prog Lipid Res* (2004) 43(3):266–81. doi:10.1016/j.plipres.2003.12.001
- Glunde K, Jie C, Bhujwalla ZM. Molecular causes of the aberrant choline phospholipid metabolism in breast cancer. *Cancer Res* (2004) 64(12):4270–6. doi:10.1158/0008-5472.CAN-03-3829
- Chen JH, Mehta RS, Baek HM, Nie K, Liu H, Lin MQ, et al. Clinical characteristics and biomarkers of breast cancer associated with choline concentration measured by <sup>1</sup>H MRS. *NMR Biomed* (2011) 24(3):316–24. doi:10.1002/nbm.1595
- Glunde K, Raman V, Mori N, Bhujwalla ZM. RNA interference-mediated choline kinase suppression in breast cancer cells induces differentiation and

is critical to developing biomarkers and treatment strategies targeting metabolism.

## ETHICS STATEMENT

All surgical procedures and animal handling were performed in accordance with protocols approved by the Johns Hopkins University Institutional Animal Care and Use Committee and conformed to the Guide for the Care and Use of Laboratory Animals published by the NIH.

## AUTHOR CONTRIBUTIONS

NM; design of the work, the acquisition, analysis, and interpretation of data for the work; drafting the work; final approval of the version to be published; agreement to be accountable for all aspects of the work. FW and TT; the acquisition, analysis, and interpretation of data for the work; revising it critically for important intellectual content; final approval of the version to be published; agreement to be accountable for all aspects of the work. KG and ZB; design of the work; revising it critically for important intellectual content; final approval of the version to be published; agreement to be accountable for all aspects of the work.

## ACKNOWLEDGMENTS

We thank Dr. V. P. Chacko and Dr. J. Zhang for technical support for the MRS experiments, and Mr. G. Cromwell for assistance with the animal studies. This work was supported by NIH R01 CA73850, R01 CA82337, R01 CA136576, R01 CA138515, and P50 CA103175.

- reduces proliferation. *Cancer Res* (2005) 65(23):11034–43. doi:10.1158/0008-5472.CAN-05-1807
18. Mori N, Glunde K, Takagi T, Raman V, Bhujwalla ZM. Choline kinase down-regulation increases the effect of 5-fluorouracil in breast cancer cells. *Cancer Res* (2007) 67(23):11284–90. doi:10.1158/0008-5472.CAN-07-2728
  19. Moestue SA, Borgen E, Huuse EM, Lindholm EM, Sitter B, Borresen-Dale AL, et al. Distinct choline metabolic profiles are associated with differences in gene expression for basal-like and luminal-like breast cancer xenograft models. *BMC Cancer* (2010) 10:433. doi:10.1186/1471-2407-10-433
  20. Noh DY, Ahn SJ, Lee RA, Park IA, Kim JH, Suh PG, et al. Overexpression of phospholipase D1 in human breast cancer tissues. *Cancer Lett* (2000) 161(2):207–14. doi:10.1016/S0304-3835(00)00612-1
  21. Gadiya M, Mori N, Cao MD, Mironchik Y, Kakkad S, Gribbestad IS, et al. Phospholipase D1 and choline kinase-alpha are interactive targets in breast cancer. *Cancer Biol Ther* (2014) 15(5). doi:10.4161/cbt.28165
  22. Dhingra S, Rodriguez ME, Shen Q, Duan X, Stanton ML, Chen L, et al. Constitutive activation with overexpression of the mTORC2-phospholipase D1 pathway in uterine leiomyosarcoma and STUMP: morphoproteomic analysis with therapeutic implications. *Int J Clin Exp Pathol* (2011) 4(2):134–46.
  23. Shen Q, Stanton ML, Feng W, Rodriguez ME, Ramondetta L, Chen L, et al. Morphoproteomic analysis reveals an overexpressed and constitutively activated phospholipase D1-mTORC2 pathway in endometrial carcinoma. *Int J Clin Exp Pathol* (2010) 4(1):13–21.
  24. Eyster KM. The membrane and lipids as integral participants in signal transduction: lipid signal transduction for the non-lipid biochemist. *Adv Physiol Educ* (2007) 31(1):5–16. doi:10.1152/advan.00088.2006
  25. Varga T, Nagy L. Nuclear receptors, transcription factors linking lipid metabolism and immunity: the case of peroxisome proliferator-activated receptor gamma. *Eur J Clin Invest* (2008) 38(10):695–707. doi:10.1111/j.1365-2362.2008.02022.x
  26. Shurbaji MS, Kalbfleisch JH, Thurmond TS. Immunohistochemical detection of a fatty acid synthase (OA-519) as a predictor of progression of prostate cancer. *Hum Pathol* (1996) 27(9):917–21. doi:10.1016/S0046-8177(96)90218-X
  27. Gansler TS, Hardman W III, Hunt DA, Schaffel S, Hennigar RA. Increased expression of fatty acid synthase (OA-519) in ovarian neoplasms predicts shorter survival. *Hum Pathol* (1997) 28(6):686–92. doi:10.1016/S0046-8177(97)90177-5
  28. Milgraum LZ, Witters LA, Pasternack GR, Kuhajda FP. Enzymes of the fatty acid synthesis pathway are highly expressed in situ breast carcinoma. *Clin Cancer Res* (1997) 3(11):2115–20.
  29. Rashid A, Pizer ES, Moga M, Milgraum LZ, Zahurak M, Pasternack GR, et al. Elevated expression of fatty acid synthase and fatty acid synthetic activity in colorectal neoplasia. *Am J Pathol* (1997) 150(1):201–8.
  30. Wang Y, Kuhajda FP, Li JN, Pizer ES, Han WF, Sokoll LJ, et al. Fatty acid synthase (FAS) expression in human breast cancer cell culture supernatants and in breast cancer patients. *Cancer Lett* (2001) 167(1):99–104. doi:10.1016/S0304-3835(01)00464-5
  31. Menendez JA, Lupu R. Fatty acid synthase and the lipogenic phenotype in cancer pathogenesis. *Nat Rev Cancer* (2007) 7(10):763–77. doi:10.1038/nrc2222
  32. Mashima T, Seimiya H, Tsuruo T. De novo fatty-acid synthesis and related pathways as molecular targets for cancer therapy. *Br J Cancer* (2009) 100(9):1369–72. doi:10.1038/sj.bjc.6605007
  33. Bhujwalla ZM, Artemov D, Natarajan K, Ackerstaff E, Solaiyappan M. Vascular differences detected by MRI for metastatic versus nonmetastatic breast and prostate cancer xenografts. *Neoplasia* (2001) 3(2):143–53. doi:10.1038/sj.neo.7900129
  34. Mori N, Gadiya M, Wildes F, Krishnamachary B, Glunde K, Bhujwalla ZM. Characterization of choline kinase in human endothelial cells. *NMR Biomed* (2013) 26(11):1501–7. doi:10.1002/nbm.2983
  35. Sze DY, Jardetzky O. Characterization of lipid composition in stimulated human lymphocytes by 1H-NMR. *Biochim Biophys Acta* (1990) 1054(2):198–206. doi:10.1016/0167-4889(90)90241-5
  36. Casu M, Anderson GJ, Choi G, Gibbons WA. Nmr lipid profiles of cells, tissues and body-fluids 0.1. 1d and 2d proton Nmr of lipids from rat-liver. *Magn Reson Chem* (1991) 29(6):594–602. doi:10.1002/mrc.1260290610
  37. Pollesello P, Eriksson O, Kvam BJ, Paoletti S, Saris NE. 1H-NMR studies of lipid extracts of rat liver mitochondria. *Biochem Biophys Res Commun* (1991) 179(2):904–11. doi:10.1016/0006-291X(91)91904-Q
  38. Le Moyec L, Legrand O, Larue V, Kawakami M, Marie JP, Calvo F, et al. Magnetic resonance spectroscopy of cellular lipid extracts from sensitive, resistant and reverting K562 cells and flow cytometry for investigating the P-glycoprotein function in resistance reversion. *NMR Biomed* (2000) 13(2):92–101. doi:10.1002/(SICI)1099-1492(200004)13:2<92::AID-NBM615>3.0.CO;2-R
  39. Yoon AR, Stasinopoulos I, Kim JH, Yong HM, Kilic O, Wirtz D, et al. COX-2 dependent regulation of mechanotransduction in human breast cancer cells. *Cancer Biol Ther* (2015) 16(3):430–7. doi:10.1080/15384047.2014.1003004
  40. Hopperton KE, Duncan RE, Bazinet RP, Archer MC. Fatty acid synthase plays a role in cancer metabolism beyond providing fatty acids for phospholipid synthesis or sustaining elevations in glycolytic activity. *Exp Cell Res* (2014) 320(2):302–10. doi:10.1016/j.yexcr.2013.10.016
  41. Iorio E, Mezzanotte D, Alberti P, Spadaro F, Ramoni C, D'Ascenzo S, et al. Alterations of choline phospholipid metabolism in ovarian tumor progression. *Cancer Res* (2005) 65(20):9369–76. doi:10.1158/0008-5472.CAN-05-1146
  42. Gillies RJ, Bhujwalla ZM, Evelhoch J, Garwood M, Neeman M, Robinson SP, et al. Applications of magnetic resonance in model systems: tumor biology and physiology. *Neoplasia* (2000) 2(1–2):139–51. doi:10.1038/sj.neo.7900076
  43. Galons JP, Job C, Gillies RJ. Increase of GPC levels in cultured mammalian cells during acidosis. A 31P MR spectroscopy study using a continuous bioreactor system. *Magn Reson Med* (1995) 33(3):422–6. doi:10.1002/mrm.1910330317
  44. Cao MD, Dopkens M, Krishnamachary B, Vesuna F, Gadiya MM, Lonning PE, et al. Glycerophosphodiester phosphodiesterase domain containing 5 (GDPD5) expression correlates with malignant choline phospholipid metabolite profiles in human breast cancer. *NMR Biomed* (2012) 25(9):1033–42. doi:10.1002/nbm.2766
  45. Stewart JD, Marchan R, Lesjak MS, Lambert J, Hergenroeder R, Ellis JK, et al. Choline-releasing glycerophosphodiesterase EDI3 drives tumor cell migration and metastasis. *Proc Natl Acad Sci U S A* (2012) 109(21):8155–60. doi:10.1073/pnas.1117654109
  46. Lyng H, Sitter B, Bathen TF, Jensen LR, Sundfor K, Kristensen GB, et al. Metabolic mapping by use of high-resolution magic angle spinning 1H MR spectroscopy for assessment of apoptosis in cervical carcinomas. *BMC Cancer* (2007) 7:11. doi:10.1186/1471-2407-7-11
  47. Shah T, Wildes F, Kakkad S, Artemov D, Bhujwalla ZM. Lymphatic endothelial cells actively regulate prostate cancer cell invasion. *NMR Biomed* (2016) 29(7):904–11. doi:10.1002/nbm.3543
  48. Glunde K, Ackerstaff E, Natarajan K, Artemov D, Bhujwalla ZM. Real-time changes in 1H and 31P NMR spectra of malignant human mammary epithelial cells during treatment with the anti-inflammatory agent indomethacin. *Magn Reson Med* (2002) 48(5):819–25. doi:10.1002/mrm.10295

**Conflict of Interest Statement:** The authors declare that the research was conducted in the absence of any commercial or financial relationships that could be construed as a potential conflict of interest.

Copyright © 2016 Mori, Wildes, Takagi, Glunde and Bhujwalla. This is an open-access article distributed under the terms of the Creative Commons Attribution License (CC BY). The use, distribution or reproduction in other forums is permitted, provided the original author(s) or licensor are credited and that the original publication in this journal is cited, in accordance with accepted academic practice. No use, distribution or reproduction is permitted which does not comply with these terms.



# Characterization of the Tumor Microenvironment and Tumor–Stroma Interaction by Non-invasive Preclinical Imaging

Nirilanto Ramamonjisoa and Ellen Ackerstaff\*

Department of Medical Physics, Memorial Sloan Kettering Cancer Center, New York, NY, USA

## OPEN ACCESS

### Edited by:

Franca Podo,  
Istituto Superiore di Sanità, Italy

### Reviewed by:

Piotr Kozlowski,  
University of British Columbia,  
Canada  
Silvana Canevari,  
Istituto Nazionale dei Tumori (IRCCS),  
Italy

### \*Correspondence:

Ellen Ackerstaff  
ackerste@mskcc.org

### Specialty section:

This article was submitted to  
Cancer Imaging and Diagnosis,  
a section of the journal  
*Frontiers in Oncology*

Received: 21 October 2016

Accepted: 05 January 2017

Published: 31 January 2017

### Citation:

Ramamonjisoa N and Ackerstaff E (2017) Characterization of the Tumor Microenvironment and Tumor–Stroma Interaction by Non-invasive Preclinical Imaging. *Front. Oncol.* 7:3.  
doi: 10.3389/fonc.2017.00003

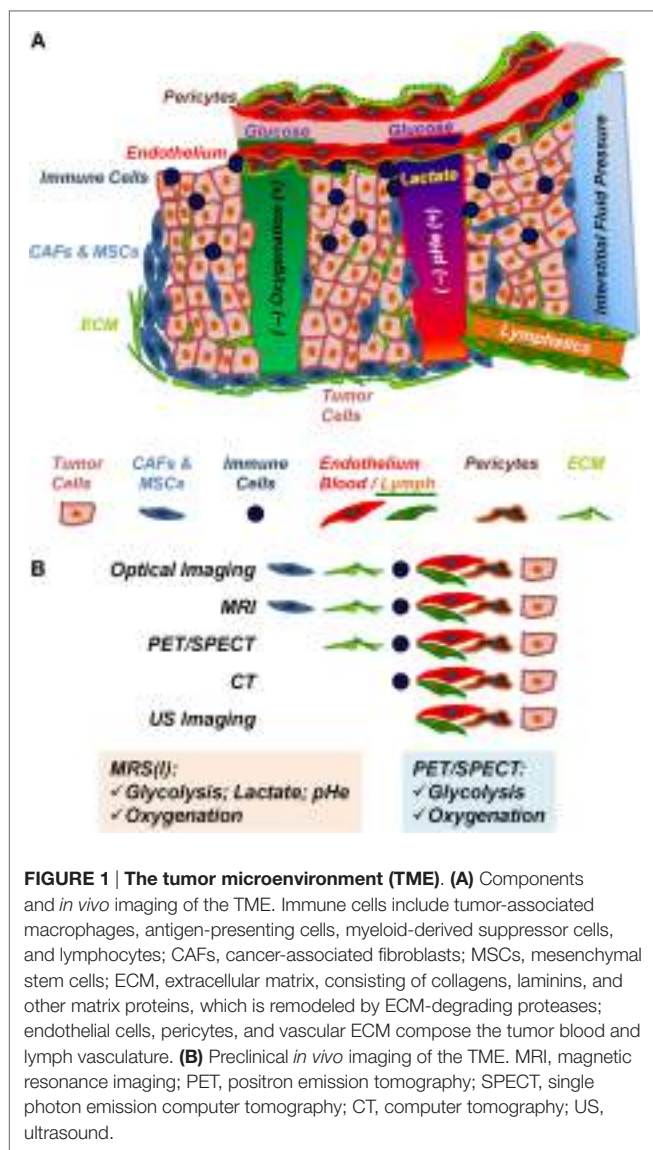
Tumors are often characterized by hypoxia, vascular abnormalities, low extracellular pH, increased interstitial fluid pressure, altered choline-phospholipid metabolism, and aerobic glycolysis (Warburg effect). The impact of these tumor characteristics has been investigated extensively in the context of tumor development, progression, and treatment response, resulting in a number of non-invasive imaging biomarkers. More recent evidence suggests that cancer cells undergo metabolic reprogramming, beyond aerobic glycolysis, in the course of tumor development and progression. The resulting altered metabolic content in tumors has the ability to affect cell signaling and block cellular differentiation. Additional emerging evidence reveals that the interaction between tumor and stroma cells can alter tumor metabolism (leading to metabolic reprogramming) as well as tumor growth and vascular features. This review will summarize previous and current preclinical, non-invasive, multimodal imaging efforts to characterize the tumor microenvironment, including its stromal components and understand tumor–stroma interaction in cancer development, progression, and treatment response.

**Keywords:** cancer, microenvironment, stroma, metabolic cooperation, tumor–stroma interaction, preclinical multimodal imaging

## INTRODUCTION—THE TUMOR MICROENVIRONMENT (TME)

The TME (**Figure 1A**), composed of tumor cells and stroma, is often characterized by hypoxia, vascular abnormalities, low extracellular pH (pHe), increased interstitial fluid pressure (1–7), increased aerobic glycolysis (Warburg effect) (8, 9), glutamine addiction (10–13), and altered choline-phospholipid metabolism (14–19). Recent evidence suggests that metabolic reprogramming in the course of tumor development and progression increases in more aggressive cancer cells/tumors the ability to easily adapt metabolism to the most advantageous pathways, beyond the Warburg effect, in order to ensure their growth and survival in response to varying environmental stimuli, such as hypoxia or limited nutrient supply (20–24). Altered metabolic content in tumors may affect cell signaling and degree of cellular differentiation (11, 25–27).

While previous research focused extensively on the tumor cells, over the last two decades or so, further evidence emerged that the tumor stroma is altered during tumor development/progression and that the tumor–stroma interaction plays an essential role in tumor metabolism (**Figure 2**), development, progression, and treatment response (2, 22, 23, 26, 28–37).



The stroma in solid tumors consists of extracellular matrix (ECM), and stromal cells, including fibroblasts, endothelial cells, pericytes, and various immune cells, such as macrophages, neutrophils, mast cells, myeloid progenitors, and lymphocytes (**Figure 1A**), with cancer cells playing an active role in the recruitment and metabolic reprogramming of stromal cells (**Figure 2**) (22, 26, 40) and the dynamic remodeling of ECM by tumor and stromal cells promoting tumor progression (41–44).

Multiple preclinical imaging techniques (**Table 1**; **Figure 1B**) have been developed to visualize and quantify specific characteristics of the TME (5, 45, 46). This review summarizes the efforts to image and characterize non-invasively the TME (**Figure 1**), including its stromal components, and tumor-stroma interaction (**Figures 2–7**) in preclinical cancer. Stromal components and their imaging are described in the context of preclinical cancer in Section “The Tumor Stroma and Its Imaging.” Section “Non-invasive Multimodal Imaging of Tumor–Stroma Interaction” focuses on the more recent attempts to assess the interaction of stromal components with cancer cells by non- or minimally invasive preclinical multimodal imaging.

## THE TUMOR STROMA AND ITS IMAGING

In this chapter, we describe briefly the stromal components and their imaging with its strengths and limitations.

### The ECM

The ECM, a complex structure composed of laminins, collagens, proteoglycans, fibronectin, elastin, etc. (71), changes its composition during cancer progression (41, 72, 73). Many of its components are regulated by matrix metalloproteinases (MMPs) which are involved in growth signaling [by proteolytic activation of the transforming growth factor- $\beta$  (TGF- $\beta$ ) pathway], apoptosis, and angiogenesis (73–76).

Available imaging methods focus on targeting the ECM component itself or the enzymes that degrade it, typically, by using activatable imaging probes (**Figure 1B**; **Table 1**). Imaging of cell–matrix adhesion can elucidate the dynamic interplay of

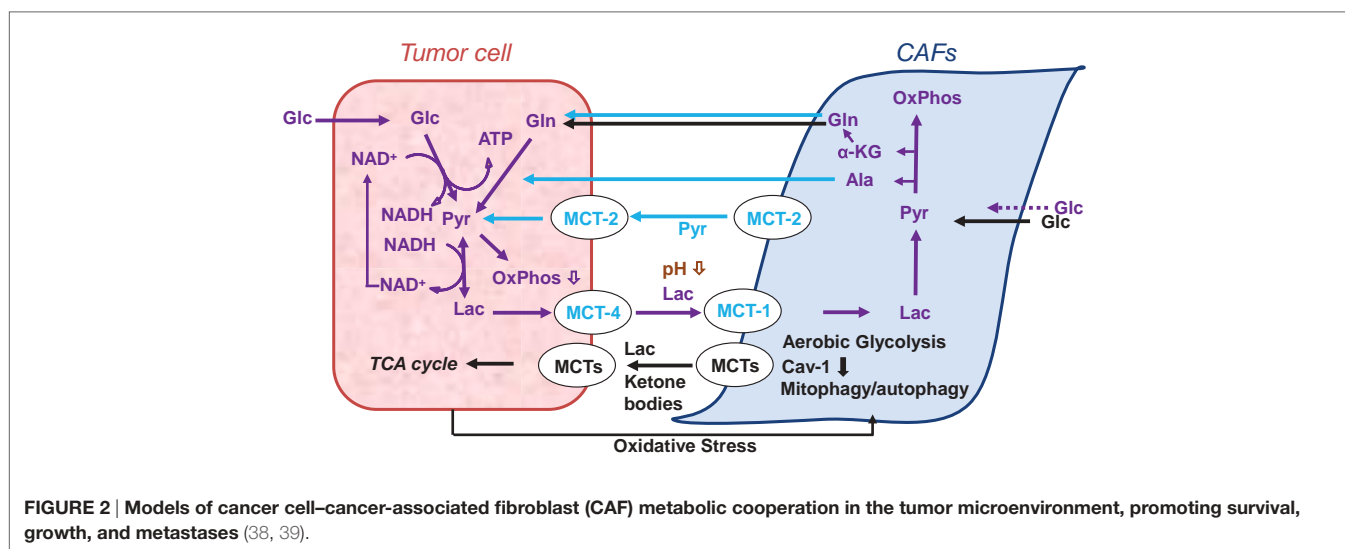


**TABLE 1 | Summary of modalities for *in vivo* imaging of the tumor microenvironment in preclinical (small animal) tumor models.**

Imaging modality			Resolution			Contrast agent
			In-plane	Coverage/depths	Temporal per frame	
Optical	Bioluminescence imaging (47, 48)	BLI	>3–5 µm	1–2 cm	>1 s to min	Reporter genes
	Fluorescence imaging (47, 48)	FLI	2–3 µm	<1 cm	>1 s to min	Fluorophores, fluorescent nanoparticles
	Fluorescence lifetime microscopy (49)	FLIM	nm range	~1,000 µm	>1 s to min	Fluorophores, fluorescent nanoparticles
	Fluorescence micro-lymphangiography (50)	FML	50 µm	200 µm	Video rates	FITC-dextran
	Fluorescence molecular tomography (51, 52)	FMT	<1 mm	1–2 mm	>1 s to min	NIRF dyes, quantum dots, reporter genes
	Fourier transform infrared imaging (53–56)	FTIR	>~3–5 µm	<20 µm	>1 ms to min	Endogenous
	Near-infrared fluorescence imaging (50)	NIRF	~200 µm	<3–4 cm	50–800 ms	NIRF dyes, quantum dots, reporter genes
	Optical coherence tomography (57)	OCT	<7.5 µm	2–3 mm	<1 s	Endogenous
	Photoacoustic imaging (tomography) (52, 58–60)	PAI (PAT)	100 µm	<5–6 cm	>1 s to min	Fluorophores, nanoparticles, quantum dots
	Second-harmonic generation microscopy (61, 62)	SHG	<1 µm	≤1 mm	>10 s	Endogenous
	Third-harmonic generation microscopy (61)	THG	<1 µm	≤1 mm	>10 s	Endogenous
X-rays	Computer tomography (47, 48, 50, 52)	CT	~50–200 µm	Whole body	>20 s	Water-soluble, iodinated probes
Magnetic resonance	Magnetic resonance imaging (47, 48, 50, 52, 63)	MRI	~25–100 µm	Whole body	>2 min	Label-free
			0.1–0.3 mm	Whole body	min to h	Gd- or iron-oxide-based probes; dendrimer-based macromolecules
	Magnetic resonance spectroscopic imaging (64)	MRSI	mm range	Whole body	min to h	Endogenous; injected marker or metabolic substrates
Nuclear	Electron paramagnetic resonance imaging (65)	EPR	>0.5 mm	cm	min to h	Injected tracer
	Positron emission tomography (47, 48, 52)	PET	1–2 mm	Whole body	>10 s to min	Radiolabeled substrates (nutrients, antibodies, antibody fragments), activatable probes
	Single photon emission computer tomography (47, 52)	SPECT	1–2 mm	Whole body	min	Radiolabeled antibodies, antibody fragments, and antigens
Ultrasound	Ultrasound imaging (47, 52)	US	50–500 µm	mm to cm	>1 s to min	Endogenous; targeted microbubbles

Imaging modalities are color-coded separating optical, X-ray, magnetic resonance-, nuclear-(radioactivity-), and ultrasound-based imaging methods.

cells and surrounding tissue during ECM remodeling, immune cell recruitment, wound healing, and cancer metastasis (77).

### Collagen Imaging

Methods, such as colorimetry (78), weight measurements (79), atomic force microscopy (80–82), and immunostaining (83–85), to image collagen structures risk their destruction and are limited by their *in vivo* translatability. The dorsal skinfold (window) chamber setup allows optical measurements by replacing skin with glass but may lead to collagen structural changes due to inflammation and mechanotransduction by the glass (86). The advances in ultrafast optics significantly improved the ability to image fibrillar collagen (the predominant structural protein in mammalian ECM and mostly type I) by second-harmonic generation (SHG) or third-harmonic generation (61) microscopy *in vivo* and *ex vivo* (87–91). The strength of SHG imaging is its specificity to fibrillar collagen (62, 87, 89, 92) and that it can be fairly easily combined with other optical imaging methods, *in vivo* (**Figures 3–5A**) and *ex vivo* (49, 90, 93–95). Ability for clinical

translation has been demonstrated in breast cancer patients by combining SHG and bright-field high-resolution microscopy with large field of view to design a semi-automated technique to predict survival based on collagen fiber classifications (93). Recently, confocal microscopy has been used *in vivo* to detect collagen turnover after introduction of fluorescent fibrillar collagen into the dermis of live mice (96). However, all optical imaging methods suffer from their limited imaging depth, rendering them often an invasive tool and limiting their clinical translation (49, 57). Thus, the diagnosis and treatment of pathologies related to collagen remodeling has benefited greatly from the development of collagen-binding or hybridizing peptides, bearing an imaging contrast agent (CA) for, e.g., magnetic resonance imaging (MRI) or fluorescence imaging, or theranostic agents, to image triple-helical, intact, and/or unfolded, denatured collagen and treatment response (97). Other imaging modalities [e.g., ultrasound (US) (98, 99), optical coherence tomography (OCT) (100, 101), Fourier transform infrared spectroscopic imaging (53), or multispectral photoacoustic imaging (PAI) (102)], and various

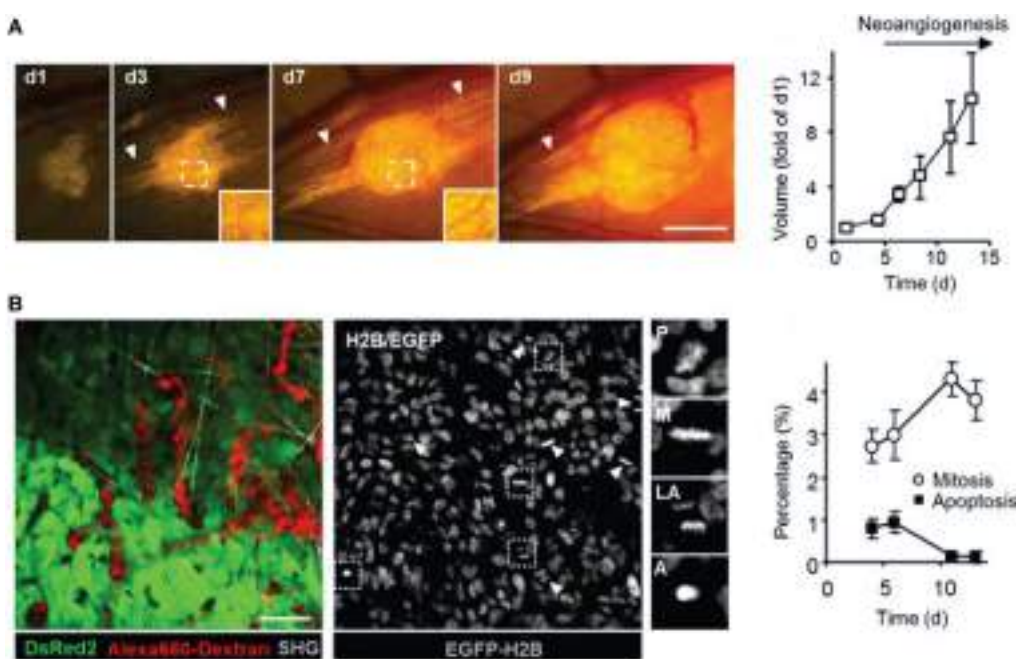


**FIGURE 3 | Intravital microscopy of the tumor microenvironment.** **(A)** Epifluorescence microscopy was used to monitor and quantify tumor growth in a human fibrosarcoma xenograft model. The invasion of tumor into the surrounding tissue during growth can be visualized (white arrowheads). Bar 50  $\mu$ m. Adapted with permission from Ref. (66). **(B)** Tumor morphology, vascularization, proliferation, and apoptosis in a human fibrosarcoma xenograft, as detected by intravital microscopy: tumor cells express cytoplasmic DsRed2 and nuclear histone 2B (H2B)-EGFP. Collagen fibers are detected by second-harmonic generation. Non-disrupted vessels are detected from the fluorescence signal of i.v.-administered Alexa660-Dextran. Bar 50  $\mu$ m. Nuclear morphology including mitotic (white arrowheads) and apoptotic figures (black arrowhead) can be derived and quantified from imaging H2B-EGFP and DsRed2. Insets show prophase (P), metaphase (M), late anaphase (LA), and apoptosis (A). Bar 50  $\mu$ m. Adapted with permission from Ref. (66).

collagen-targeted agents, e.g., quantum dots (84, 85, 103, 104) or collagen-mimetic peptide-based imaging agents (105, 106) are being developed/applied to improve collagen imaging and to measure collagen turnover during tissue remodeling.

### MMP Imaging

The key role that various MMPs play during cancer initiation and progression, with clear links to tumor invasion and metastasis (107), make them desirable treatment and cancer imaging targets (108). Targeted probes to image MMPs *in vivo* by optical imaging (fluorescence and bioluminescence), positron emission tomography (PET), single photon emission computer tomography (SPECT), and MRI have been developed (108–110), with a “broad-spectrum” MMP-activatable fluorescence probe available commercially (MMPSense, PerkinElmer, Akron, OH, USA). Each modality and imaging probe displays strengths and weaknesses in effectively imaging MMP activity (108, 110). However, optical imaging has limited penetration depth (108) and, while tomography is possible, anatomical information is lacking. Targeted, inhibitor-based PET and SPECT probes harness the excellent sensitivity of radioactive tracers and may be theranostic, but their synthesis may be difficult and, so far, it has not been possible to quantify proteolytic activity *in vivo* due to non-specific binding (108, 109, 111). Recently, an  $^{18}\text{F}$ -labeled MMP-activatable PET probe has been developed to overcome the lack of specificity of inhibitor-based probes (112). Photoacoustic

tomography (PAT or PAI) (58, 113, 114) combines ultrasonic resolution with electromagnetic-enhanced contrast to obtain quantitative information on tissue structure, blood flow, and perfusion, and, through targeted probes (59), on receptor status or enzyme activity. For example, a photoacoustic probe activated by MMP-2 and MMP-9 demonstrated sensing of MMP-2/-9 activity in a follicular thyroid carcinoma model (115). With an imaging depth of >30 mm, depending on setup and desired spatial resolution (58), PAT expands on the tissue penetration of up to 20 mm typical for optical imaging (51, 108) and is thus suitable to monitor non-invasively tumor characteristics in orthotopic preclinical cancer models. The lack of anatomical/morphological information inherent to optical imaging, PAT/PAI, and PET/SPECT can be overcome by multimodal imaging. Using fluorescence molecular tomography (FMT) (51) coregistered with MRI, Salaun et al. (116) found increasing MMP-13 levels as lung tumors progressed. In skin squamous cell carcinoma xenografts, MMP-2, -3, -7, -9, -12, and -13 activities correlated with degree of angiogenesis and tumor invasion, as imaged by FMT combined with  $\mu$ CT (117). PAT/PAI, combined with US and OCT, can provide non-invasively morphological and functional tumor characteristics (60). Molecular MRI to measure MMP activity using protease-modulated CAs is still emerging and is hampered by its insensitivity, requiring long acquisition times but is potentially quantitative, and anatomical information can be obtained in the same setting (108, 109). Of

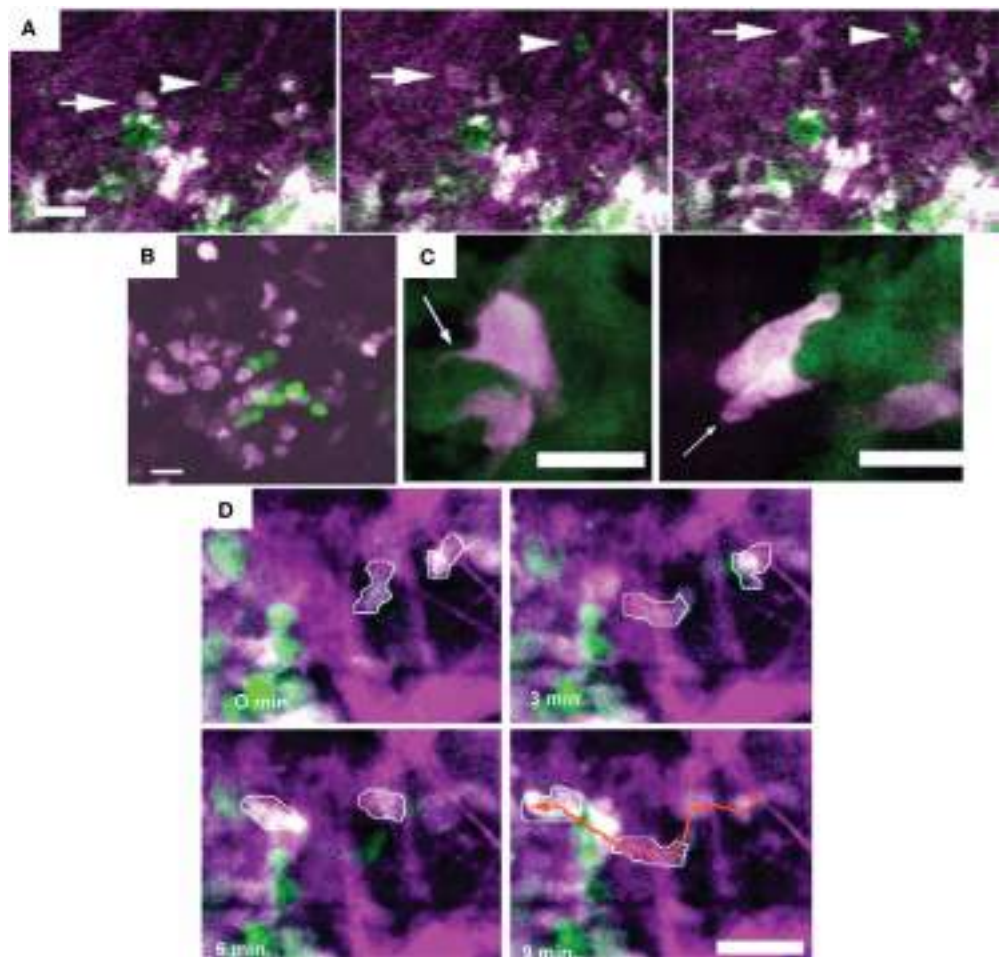


**FIGURE 4 |** Different motility and invasion of low-metastatic, GFP-expressing (green) and high-metastatic, CFP-expressing (white) mammary tumor cells within the collagen network (purple) was imaged by *in vivo* intravital microscopy with FL and second-harmonic generation. Bars 25  $\mu$ m. **(A)** Time series demonstrating the migration of GFP-expressing (arrow head) and CFP-expressing (arrow) tumor cells along collagen fibers. **(B)** Metastatic growth of color-coded cells in the lung. **(C)** Protruding filopod (arrow, left) and lamellapod (arrow, right) of CFP-expressing cell near GFP-expressing cells. **(D)** Overall, the high-metastatic cells (outlined in white) move more frequently (see orange arrow path) than the low-metastatic cells (green). Adapted with permission from Ref. (67).

note is that the interpretation of MMP images obtained with the typically broad-spectrum probes (110) is further complicated by the function of MMPs in biological processes beyond ECM remodeling (111).

### Proteoglycan (Hyaluronan) Imaging

Another major ECM constituent, the proteoglycan hyaluronan [hyaluronic acid (HA), hyaluronate] is a high molecular weight glycosaminoglycan with a significant role in tumor growth and metastasis (118, 119), acting as tumor suppressor or promoter depending on its molecular weight (120).

It is degraded by hyaluronidases (Hyals), with hyaluronidase-1, -2 (Hyal1, Hyal2) currently being the most studied in cancer (119). Hyal1 overexpression has been associated with more aggressive tumors in a variety of epithelial cancers (e.g., bladder, colorectal, breast, and ovary), while Hyal2 may function as a tumor suppressor or promoter (119). The development of various HA probes to image HA turnover and clearance and of

theranostic HA probes where encapsulated drugs are released in response to Hyal activity (119, 121, 122) has expanded greatly in recent years, and a detailed review is beyond the scope of this paper. HA probes often exploit the high specificity of HA for the CD44 receptor, a transmembrane receptor overexpressed in many tumor cell types (120, 121, 123–134). Single moiety, HA-based CAs have been used to image Hyals activity by MRI (135) and NIRF (124). Fluorescence correlation spectroscopy and Forster resonance energy transfer of HA-conjugated probes have shown promise in quantitative bladder cancer staging by detecting shedded Hyals in urine samples (119). Also, fluorescent HA probes may be used in an intraoperative to assess Hyal activity or drug delivery of theranostic probes (119). Often, HA probes contain more than one CA moiety to harness the strength of multimodal imaging, such as MRI/optical imaging (123, 136), MRI/computer tomography (CT) (137), NIRF/CT (138), or NIRF/PA imaging (139–141) to improve diagnostic capability and monitoring of therapeutic efficacy (121, 142).

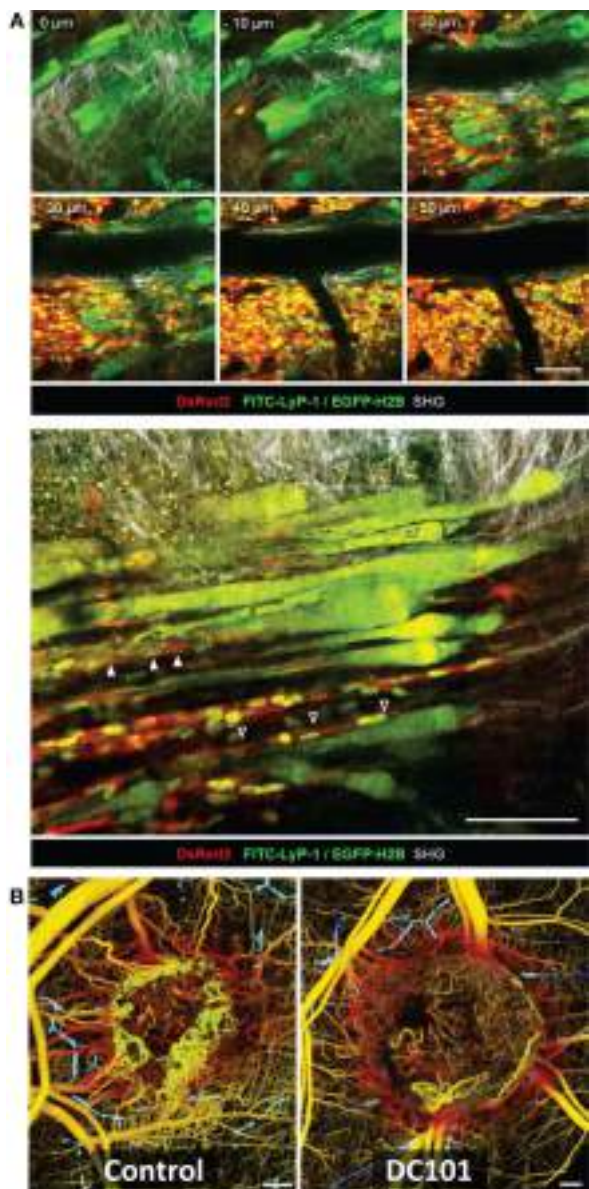


**FIGURE 5 |** Intravital microscopy of the tumor blood vessels, lymph vasculature, and vascular response to treatment. **(A)** Top: Z-stack of lymphatics detected by near-infrared fluorescence (NIRF) multiphoton microscopy of FITC-tagged LyP-1 peptide (green), collagen fibers detected by second-harmonic generation, and tumor cells imaged by epifluorescence of cytoplasmic DsRed2 (red) and nuclear histone 2B (H2B)-EGFP (green) shows lymph vessels at the tumor margin. Bottom: intralymphatic (white arrowheads) and perilymphatic (black arrowheads) invasion of fibrosarcoma cells expressing cytoplasmic DsRed2 (red) and H2B-EGFP (green). Bars 100  $\mu$ m. Adapted with permission from Ref. (66). **(B)** In vivo optical frequency domain imaging of blood [depth denoted from red (up to 2 mm deep) to yellow (superficial)] and lymph (blue) vessels in control and DC101-treated tumors, depicting the antivascular effect of VEGFR-2 inhibition. Adapted with permission from Ref. (68).

## Other ECM Constituents

Only a few studies report the *in vivo* imaging of other ECM constituents, such as fibronectin or laminins, in cancer. Fibronectin,

whose expression increases with epithelial–mesenchymal transition, is typically targeted to image tumor-associated angiogenesis (143, 144). Laminins are a family of glycoproteins which interact with other ECM proteins, assuring the ECM organization, and are involved in cellular signal transduction pathways (145), cell adhesion, migration, and proliferation (146) and thus affect in cancer, tumor invasion, angiogenesis, and metastasis (145, 147). While laminins and their function have been studied extensively *in vitro* or *ex vivo* (29, 148–150), *in vivo* studies directly imaging laminins have been limited. Cuesta et al. developed a fluorescent trimerbody recognizing an angiogenesis-associated laminin epitope, accumulating in tumors (151). Other studies have used imaging agents targeting laminin cell surface receptors directly or indirectly to detect or treat tumors (152–154).

## Mesenchymal Stromal (Stem) Cells (MSCs), Cancer-Associated Fibroblasts (CAFs), and Immune Cells

By tumor cells recruited adult, multipotent, non-hematopoietic stem cells (mesenchymal stromal (stem) cells, MSCs), typically derived from adipose tissue and bone marrow, have been found to differentiate into osteoblasts, CAFs, and pericytes among other cell types (155). In tumors, MSCs may contribute to tumor initiation, progression, angiogenesis, and metastasis, while also impacting immune function (155).

Cancer-associated fibroblasts are fibroblasts that reside within the tumor or tumor margins (156). They promote tumorigenic features, such as drug resistance, ECM modulation, chronic inflammation, and invasiveness (156). They may originate from normal fibroblasts or smooth muscle cells (altered by tumor cells), bone marrow-derived stem cells (mesenchymal stromal (stem) cells, MSCs), recruited and altered by tumor cells, or epithelial cells through transdifferentiation to myofibroblasts, or endothelial cells through endothelial-to-mesenchymal transition (156–158).

The TME (Figure 1) includes various immune cells: innate [tumor-associated macrophages (TAMs)], neutrophils, mast cells, myeloid-derived suppressor, dendritic, and natural killer cells, and adaptive (T and B lymphocytes), with TAMs and T cells the most prevalent cell types (159). Immune cells may enhance tumor growth and metastasis or exhibit antitumor immunity by modulating the immune and inflammatory milieu in the TME through paracrine and autocrine cell interactions, and thus, affecting the production of pro-angiogenic and growth factors, proteases, recruitment of other hematopoietic cells, or release of reactive oxygen or nitrogen species (159, 160). Immunotherapy aims at enhancing the antitumor activity of tumor-associated immune cells (161).

## MSC Imaging

In preclinical cancer models, the preferential homing of *ex vivo* cultured MSCs to tumor tissue and metastasis has been imaged non-invasively *in vivo* after intravenous/arterial injection of MSCs, pre-(multi-)labeled with bioluminescence (162–167), fluorescence (168), MRI (169–171), PET (170–173), or SPECT (171, 174) imaging probes (175). The tumor effects and/or

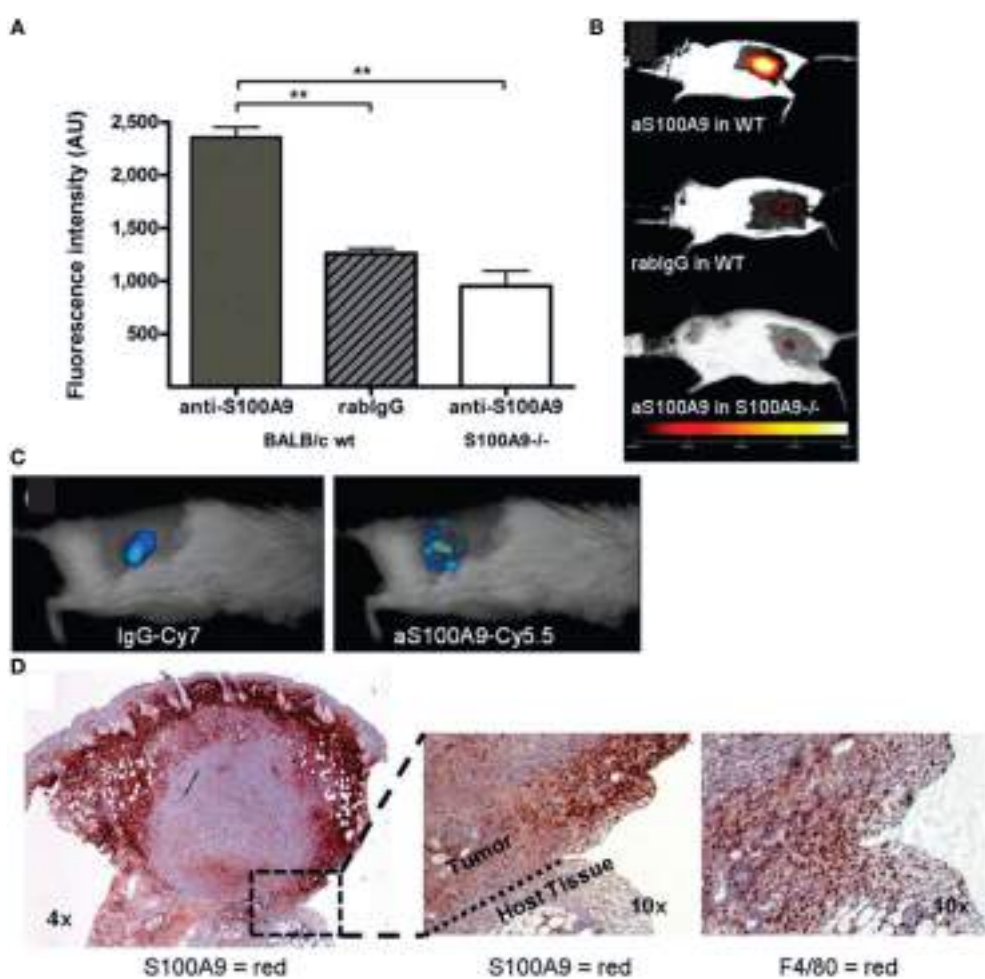


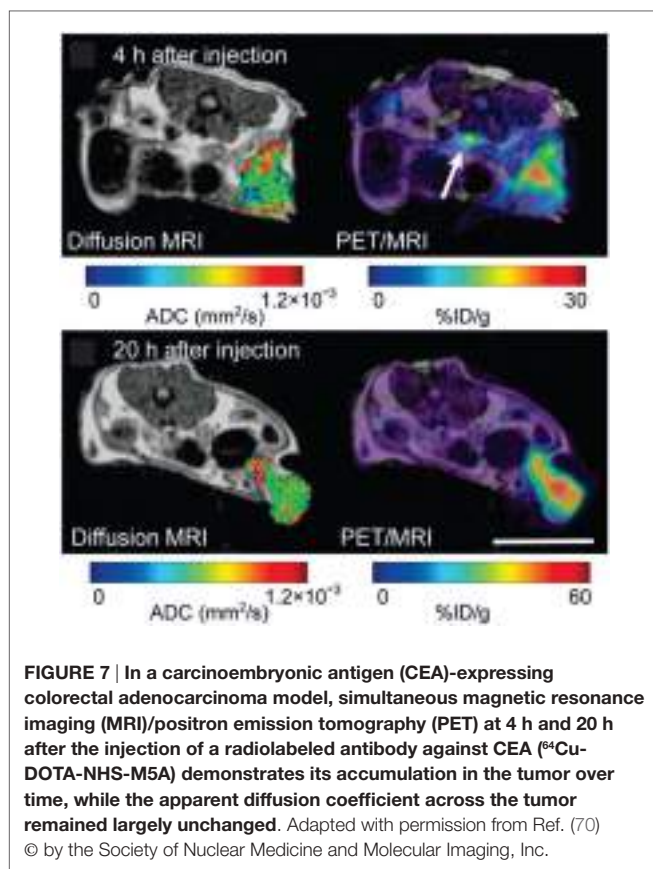
**FIGURE 6 | In vivo immune cell imaging.** **(A,B)** Specificity of *in vivo* imaging of immune cells in 4T1 mammary breast tumors by fluorescence-reflectance imaging with a Cy5.5-labeled polyclonal antibody against murine S100A9 (aS100A9-C5.5). **(C)** Fluorescence molecular tomography of coinjected rabIgG-Cy7 and aS100A9-C5.5 demonstrates homogeneous perfusion (left) and immune cell distribution (right), respectively. **(D)** *Ex vivo* validation shows S100A9<sup>+</sup> cells in the tumor periphery corresponding to F4/80<sup>+</sup> TAMs. Adapted with permission from Ref. (69) © by the Society of Nuclear Medicine and Molecular Imaging, Inc.

localization of MSCs, pre-labeled with an imaging probe and coinjected with tumor cells, have been monitored *in vivo* with MRI (176) and bioluminescence (177–180) imaging. The preferential accumulation of MSCs at sites of inflammation and tumors makes them an ideal vehicle for treatment delivery (155, 181, 182), and combined treatment/imaging MSC moieties are being developed for cell tracking and treatment monitoring (175, 177, 178, 183). While overall safe clinically (175, 184), *ex vivo* culture and pre-labeling of MSCs may lead to secondary tumors (185) and/or impact functionality (186). Using fluorescent, transgenic mice (187), potentially avoids *ex vivo* culture and pre-labeling of MSCs, with the disadvantage that typically all cell types express the imaging marker, limiting the *in vivo* identification of different stromal cell types, unless pre-labeled.

### CAF Imaging

Various markers, such as  $\alpha$ -smooth muscle actin ( $\alpha$ -SMA), vimentin, and fibroblast-activation protein  $\alpha$  (FAP), have been

used to identify CAFs (188). In preclinical models, CAFs have been shown to promote breast tumor growth and metastasis by enhancing the recruitment of immune suppressor cells and TAMs (189) and to mediate collagen remodeling (190). The high expression of FAP in CAFs (191, 192) makes it a desirable target for diagnostic and therapeutic imaging, although it may also be expressed in some other tissues and tumor cells (192–194). One difficulty for the development of FAP-targeted *in vivo* imaging probes is that FAP shares peptide substrates with other post-prolyl peptidases, resulting in non-specific binding *in vivo* (192). Thus to track CAFs *in vivo* by MRI or NIRF imaging, Granot et al. took advantage of caveolae-mediated endocytosis in fibroblasts by pre-labeling CAFs *in vitro* with the CAs biotin-bovine serum albumin-gadolinium diethylenetriaminepentaacetic acid, Feridex, or 1,1'-dioctadecyl-3,3,3-tetramethylindotricarbocyanine iodide (195, 196). Recently developed FAP-specific, activatable NIR fluorescence probes (193, 194) show promise in *in vivo* imaging of FAP-expressing tumors. And novel cancer treatments



based on the depletion of FAP-expressing stromal cells would greatly benefit from monitoring response *in vivo* with improved multimodal imaging probes (197).

### Immune Cell Imaging and Monitoring of Immunotherapy

Multiple recent reviews summarize the imaging techniques applied to track various immune cell types *in vivo* and to monitor immunotherapy response, including the ability to optimize administration route of therapeutic immune cells (45, 47, 61, 63, 198–202).

To visualize immune cells *in vivo*, cells may be labeled *ex vivo* with paramagnetic, fluorescent, or radiochemical probes for MRI, FLI, or PET/SPECT respectively or transfected with reporter genes for PET, SPECT, bioluminescence imaging (BLI), and/or FLI (or FMT) before injection into the host (45, 198, 201, 203–206). Tumor-infiltrating lymphocytes, dendritic cells (DCs), or TAMs can be imaged by FLI or PET/SPECT, using fluorescently labeled (Figure 6) or radiolabeled antibodies or antibody fragments targeting cell-type specific surface receptors (198, 199, 201). Delivery of full-size antibodies may be affected by vascular dysfunction in tumors, thus, potentially affecting image quality and interpretation [false positives, reduced specificity (50)]. Targeted US microbubbles have been used to track B7-H3 expressing TAMs and tumor cells (198). The high endocytic activity of TAMs facilitates their imaging by MRI, PET, and to a lesser extent by CT, FLI, US, Raman imaging, or PAI, using nanoparticles,

either uncoated (e.g., ultra-small superparamagnetic iron-oxide nanoparticles for MRI) or coated to increase macrophage affinity (199, 200). Nanoparticle uptake may vary across different macrophage populations and may be detected also in other cell types (e.g., tumor cells) to a variable degree, confounding potentially macrophage tracking, but has been used successfully in clinical lymph node cancer staging by MRI (200). Cellular MRI of DC migration using CAs (iron oxide-based nanoparticles, perfluorocarbon emulsions) permits repeated monitoring (a limitation in PET/SPECT) and does not require pre-labeling with reporter genes, as in BLI or FLI, but has lower sensitivity (63). Intravital microscopy of stroma–tumor cell dynamics (207) has been an essential tool in assessing lymphocytic interactions in tumors and draining lymph nodes by optical imaging (208). The clinical translatability of these imaging methods has been reviewed previously (202, 209), with optical methods currently limited to intraoperative imaging (50).

### Tumor Vasculature and Lymphatics—Endothelial Cells and Pericytes

Endothelial cells line the inside of tumor blood vessels and lymphatics and interact with pericytes and vascular smooth muscle cells in the vessel wall (Figure 1) (210–212). Cancer-associated endothelial cells often display an enhanced angiogenic potential (211), due to proangiogenic factors secreted from cancer cells and/or tumor-stroma cells, forming heterogeneous neovasculature of enhanced permeability (6). The role of pericytes in tumor vascular development is still largely unexplored (212).

Tumors outgrowing their vascular supply lead to constant vascular remodeling, acute and permanent hypoxic tumor areas, and nutrient deprivation (23, 45, 213), increasing treatment resistance (due to, e.g., reduced radical formation in hypoxic tumor areas affecting radiotherapy and limiting drug delivery of chemotherapeutics) (214–216).

### Imaging of Tumor Vascularity

Vascular function and distribution has been assessed *in vivo* non-invasively by MRI (45, 217–226), CT ( $\mu$ CT) (45, 52, 227, 228),  $H_2^{15}O$  or  $^{11}C$  PET (45, 217), US (45, 52, 229) [clinical (230)], PAI (45, 58, 114), and intravital optical imaging methods (231), such as FLI (48), second-generation OCT [optical frequency domain imaging (OFDI)] (45, 48, 52, 68), and FMT (45).

In vascular MRI, five acquisition methods are used to measure the enhancement of exogenous (i, ii) or endogenous (iii–v) contrast dynamically: (i) Dynamic contrast-enhanced (DCE)-MRI, which exploits the shortening of the  $T_1$  relaxation time of water protons near a CA, typically Gd-based and low molecular weight (223, 229), (ii) dynamic susceptibility contrast (DSC)-MRI, which measures the effect of the CA (e.g., Gd-based CA or superparamagnetic iron oxide particles) on the  $T_2$  and  $T_{2}^*$  relaxation time of nearby water protons (218, 222), (iii) arterial spin labeling (ASL)-MRI, where the dynamic measurement of the in- and out-flow of magnetically labeled water protons, which serve as endogenous “CA,” characterizes the vasculature in a region of interest (223, 232), (iv) blood oxygen level dependent MRI (BOLD-MRI) where oxyhemoglobin confers diamagnetic

and deoxyhemoglobin paramagnetic contrast, respectively (223), and (v) diffusion-weighted MRI (DW-MRI), where intravoxel incoherent motion (IVIM) reflects vascular perfusion (64, 224, 229, 233, 234).

In DCE- and DSC-MRI, the first pass of the exogenous CA uptake is characterized by the venous or arterial input function (219, 220, 222, 235–237), after which the CA distributes throughout the vasculature, extravasates at sites of leaky blood vessels into the interstitium, and is ultimately cleared from the body. Rate and path (e.g., liver and kidney) of tissue and vascular clearance are dependent on the specific CA (e.g., size and type of CA) used (223, 225, 238). Hemodynamic parameters, such as vessel density, vascular permeability, vascular perfusion, extravascular space, vessel size and plasma volume, etc., are either derived from semiquantitative measures of signal enhancement (220, 239–241) or from pharmacokinetic modeling of signal-*versus*-time curves (222, 242) with the underlying principle based on standard tracer-kinetic theory of linear and stationary systems (221, 243) and the model adjusted to account for variations of CA characteristics, e.g., low versus high molecular weight (impacting the ability of the CA to extravasate), receptor targeted (e.g.,  $\alpha,\beta_3$ -integrin), extra- or intracellular or both, with exchange (218, 223, 235, 244). More recently vascular feature-based analyses have been developed to assess intratumor vascular heterogeneity (245, 246).

Hemodynamic parameters conferred from ASL- and BOLD-MRI are tissue blood flow and volume (223, 232). Tissue perfusion and diffusivity are obtained from IVIM DW-MRI by fitting data with a bi-exponential model (224).

Similarly to DCE-MRI, DCE-CT has been used clinically to obtain blood flow, blood volume, and permeability with the disadvantage of radioactivity limiting serial monitoring and often worse spatial resolution than DCE-MRI (227, 228). In preclinical models, the relatively high radiation dose of  $\mu$ CT limits its *in vivo* use (45), and vascular networks have been assessed *ex vivo* (247). Viscosity of CA for DCE-CT may also result in complications, such as vessel rupture, and DCE- $\mu$ CT still suffers from artifacts generated from, e.g., bones or large vessels (52). Generally, functional vascular parameters similar to DCE-MRI can be extracted from DCE- $\mu$ CT data (52, 248).

While  $\text{H}_2^{15}\text{O}$  PET measures specifically tissue perfusion (217), the short half-life of  $^{15}\text{O}$  limits the applicability of vascular perfusion measurements by PET (45). Vascular permeability can be obtained from dynamic PET using the macromolecular CAs  $^{68}\text{Gd}$ -DOTA-albumin (45),  $^{11}\text{C}$ -methylalbumin (limited by the 20.4 min short half-life of  $^{11}\text{C}$ ), or  $^{68}\text{Ga}$ -transferrin (217). However, lack of accompanying anatomical information and ionizing radiation limits (especially serial) vascularity measurements by PET, despite its potential higher sensitivity than DCE-MRI and its ability to directly measure tissue perfusion.

Tumor angiogenesis, i.e., perfusion and vascular density have been successfully measured in small animals by Doppler or contrast-enhanced US with microbubbles (non-targeted and targeted to, e.g., VEGFR2 (249),  $\alpha,\beta_3$ -integrin, or endoglin) with a spatial resolution of ~50–100  $\mu\text{m}$  (45, 52, 229). One advantage of the combining contrast-enhanced and non-contrast-enhanced high-frequency volumetric power Doppler US is the ability to distinguish mature and immature vessels (52). While US is cheaper

than DCE-MRI, it is not suitable for whole-body imaging, has limited soft tissue contrast, and is to some extent user dependent, limiting its applicability, especially for monitoring of antiangiogenic treatments (52).

In PAI of tumor angiogenesis, the intrinsic contrast from hemoglobin permits visualization of microvasculature and quantification of blood oxygen saturation (45, 52), with its usefulness recently extended to flow imaging (114). Submillimeter resolution is achieved, albeit restricted to depth of a few centimeters (58). Reporter genes or endogenous targeted CAs extend the ability to visualize and quantify tumor angiogenesis *in vivo* (52). The hemodynamic response to external stimuli or treatment is quantified from contrast changes after image reconstruction (52, 58, 114).

Blood vessel diameter, surface area, and branching pattern have been assessed with intravital optical imaging methods during tumor growth and/or treatment (Figure 5) (45, 48, 52, 68, 231).

### Imaging of Lymphatic Tumor Vasculature

Imaging of the lymphatic system is here summarized only briefly, as is has been reviewed in detail previously (50, 250). The lymphatic system (Figure 1) drains lymph fluid from interstitial space to the venous circulation, thus, maintaining tissue fluid homoeostasis, transports immune cells to lymphoid organs, and plays a role in lipid absorption (50, 250). While the lymphatic vasculature near tumors provides a route for metastatic dissemination of cancer cells, its role has only been explored by non-invasive imaging methods over the past decade (50, 250). Lymphangiography traces the drainage of a CA for X-ray, CT, MRI, US, PAI, or optical imaging but is lacking specificity, requiring direct injection into a lymph vessel (difficult to perform in preclinical models) or intradermal injection near sites draining into the dermal capillary plexus (50, 250). Identifying sentinel lymph nodes containing cancer cells has been achieved with intravenously injected CAs that identify blocked drainage or directly target cancer cells (50). *In vivo* OCT (or OFDI) and laser speckle imaging permit CA-free visualization of lymphatics (Figure 5) (68, 250). The most specific imaging approach to identify and characterize the lymphatic system is to use CAs, targeted to lymphatic vascular-specific molecules, i.e., vascular endothelial growth factor receptor-3 (VEGFR-3), lymphatic vessel hyaluronan receptor-1 (LYVE-1), podoplanin, or prospero-related homeodomain transcription factor PROX1, with LYVE-1 the most widely used lymphatic endothelial cell marker (250). LYVE-1-targeted CAs have been developed for PET (251) and optical imaging (252). Preclinically, fluorescent or bioluminescent gene reporters in transgenic mouse models have been also been used to visualize lymphatics, typically by intravital imaging methods (50).

### Metabolic Imaging

Metabolic reprogramming during tumor development and progression leads to a characteristic *in vivo* tumor metabolic phenotype (see Section “Introduction—The Tumor Microenvironment”).

### Choline-Phospholipid Metabolism

Changes in choline-phospholipid metabolism have typically been assessed preclinically (and clinically) by non-invasive  $^{31}\text{P}$  and  $^1\text{H}$

magnetic resonance spectroscopy or spectroscopic imaging (MRS or MRSI) (14–16, 18, 253). Choline uptake and metabolic conversion have also been assessed with high sensitivity by <sup>18</sup>F-fluoro-, <sup>3</sup>H-, or <sup>11</sup>C-choline PET and successfully translated to the clinic (254–257). As with any PET tracer though, radiolabeled choline PET does not discriminate between different metabolites (256), limiting its value for pathway studies.

### Hypoxia

Tumor hypoxia has been imaged non-invasively and visualized directly by hypoxia markers accumulating in hypoxic cells using PET, electron paramagnetic resonance (EPR), or <sup>19</sup>F MRS (65, 248, 258–266). Delivery of a specific hypoxia marker to less vascularized regions, which are typically associated with hypoxia, may impact the intensity of the accumulating hypoxia marker (246, 267). Since evolution of chronic or acute hypoxia in tissue is linked to the vascular delivery of oxygen, several indirect MRI methods based on vascular features associated with tumor hypoxia, such as BOLD, TOLD, or DCE-MRI, have been developed to identify hypoxic areas or hypoxia changes in tumors (64, 246, 268–271). Tissue oxygen tensions have been mapped by <sup>19</sup>F MRI oxymetry using perfluorocarbons; as with any exogenous tracer, these measurements are vascular delivery dependent, and thus, potentially biased toward well-perfused tumor regions (271). While carbonic anhydrase-IX (CA-IX) has been proposed as an intrinsic hypoxia marker in tumors, CA-IX expression, measured by immunohistochemistry, correlated to hypoxia in some and not in other studies (260). Nevertheless, attempts are underway to image CA-IX expression *in vivo* by PET (272), NIRF (273), and SPECT (274).

### Glycolysis and Lactate

Tumor glycolysis is typically assessed by *in vivo* PET using the cellular entrapment of <sup>18</sup>F-FDG, after uptake of <sup>18</sup>F-FDG by glucose transporters (GLUT-1, GLUT-3; often overexpressed in cancer) and subsequent phosphorylation by hexokinase II (256, 275). While it is quite insensitive, <sup>13</sup>C MRS has been applied preclinically to evaluate glycolysis and the <sup>13</sup>C labeling of downstream metabolites (275–277). Detection sensitivity of <sup>13</sup>C MRS can be significantly improved by magnetization transfer techniques or indirect inverse detection (276, 277). Hyperpolarization of <sup>13</sup>C-labeled substrates increases detection sensitivity up to 10,000-fold, with the caveats that the hyperpolarization is short lived and currently limited to few substrates, including glucose (64, 275, 276, 278, 279). Compressed sensing can further improve acquisition speed and spatial resolution in hyperpolarized (HP) <sup>13</sup>C MRSI (280). Lactate production from precursors, such as <sup>13</sup>C-labeled pyruvate or glucose, can be rapidly assessed globally and localized by HP <sup>13</sup>C MRSI (278, 279). Steady state levels of tumor lactate have been assessed by <sup>1</sup>H MRS and MRSI, using spectral editing methods to suppress the high lipid signal overlapping lactate (64, 275, 281–285).

### pH

Measuring tumor tissue pH non-invasively is challenging, and various methods have been and are being developed to measure

preclinically extracellular and/or intracellular pH (pHe or pHi) (64, 286).

Tumor pHe and pHi distributions can be obtained by <sup>31</sup>P MRS/MRSI using 3-aminopropylphosphonate (287, 288). However, insensitivity of <sup>31</sup>P MRSI limits its spatial resolution and restricts broad applicability. Thus, <sup>1</sup>H MRSI pHe markers have been developed to improve detection sensitivity (288–291). To shorten acquisition times and improve sensitivity further, with potential for clinical translation, HP <sup>13</sup>C MRSI of injected bicarbonate has been proposed for pH imaging, with pH (predominantly pHi, though it does not distinguish between pHi and pHe) calculated from the signal intensity ratio of hyperpolarized  $\text{H}^{13}\text{CO}_3^-$  to  $\text{CO}_2$  (292, 293). However, the reaction is dependent on CA-IX activity in the tissue, thus, calibration has to be performed for each tissue type separately, restricting its applicability (294). Chemical exchange saturation transfer (CEST) MRI detects the pH-dependent chemical exchange between an amide proton and surrounding water molecules (291, 295). In acidCEST, the pH dependence of the CEST effect ratio of a CEST agent with two amide protons, generating two CEST effects, is used to measure pHe (295–297). Challenges to measure pH by acidCEST include its low sensitivity, requiring optimization of experimental parameters (295), and it may not always be a given that the CEST effect is solely visible for the amide protons of the selected CEST agent and only affected by pH (291).

Recently, the pH-dependency of cellular membrane insertion of radiolabeled pH (low) insertion peptides has been used to image tumor pH (at the intra-/extracellular interface) preclinically with PET (298–301).

Other non-invasive imaging modalities assessing pH *in vivo* include optical imaging with pH-sensitive dyes (302–304) or a pH-sensitive reporter gene (305), ratiometric PAI with pH-sensitive nanoprobe (306, 307), MRI using a CA with pH-sensitive (and concentration-dependent) relaxivity, with the difficulty of measuring *in vivo* the CA concentration (291), and EPR spectroscopy (308, 309).

Additionally, pH-sensitive probes are being developed as theranostic agents, combining treatment with diagnostic and monitoring ability (310–314). Of note is that all exogenous pH markers are delivery dependent and may not be clinically translatable, adding further challenges to pHe/pHi imaging.

## NON-INVASIVE MULTIMODAL IMAGING OF TUMOR-STROMA INTERACTION

Here, after a brief overview and some examples of recently recognized tumor-stroma interactions (see Section “Tumor-Stroma Interactions”), ongoing efforts to apply directly non-invasive multimodal imaging to characterize and understand tumor-stroma interaction in the context of tumor development, progression, and treatment will be summarized (see Section “Non-invasive *In Vivo* Imaging of Tumor-Stroma Interactions”). As is evident from the comparably fewer studies (see Section “Non-invasive *In Vivo* Imaging of Tumor-Stroma Interactions”), it is much more challenging to image directly and non-invasively the tumor-stroma interaction in *in vivo* cancer animal models (237, 315) and to confirm *in vitro* and *ex vivo* findings.

## Tumor–Stroma Interactions

Tumor stroma interactions focus on the complex crosstalk between cancer and stromal cells and cell interactions with the ECM (316–320). These interactions are mediated by chemokines, soluble factors from enzymes, growth factors, extracellular vesicles (e.g., exosomes) and/or microRNAs, etc., and regulate enzymes activities, expression of genes and proteins, and metabolic pathways involved in tumor growth, metastases, survival, and drug resistance (37, 188, 211, 319–325). In this section, we present selected examples of *in vitro*, *ex vivo*, and *in vivo* tumor growth studies that highlight tumor–stroma interactions by using preclinical models that attempt to incorporate/simulate microenvironmental conditions of ultimately clinical relevance.

Various *in vitro* models mimicking the TME, such as cocultures between stromal and tumor cells or CAF-derived exosomes and cancer cells (326), 3D culture systems (327), bioreactors for live cell studies (20, 277, 328–330) have been developed to understand the nature and mechanisms behind tumor–stroma interactions by, e.g., gene expression microarrays from cocultures (331).

For example, in *in vitro* 2D and 3D cultures of the two breast cancer cell lines MDA-MB-231 and MCF-7 cocultured with CAFs or control fibroblasts, CAFs promoted invasion and proliferation in both MDA-MB-231 and MCF-7, and the more invasive MDA-MB-231 increased  $\alpha$ -smooth muscle actin ( $\alpha$ -SMA, a marker of fibroblast-to-myofibroblast transition) expression of CAFs contrary to the non-invasive MCF-7 (332), demonstrating reciprocal interaction. In cocultures of the cervical cancer cell line CSCC7 with CAFs or control fibroblasts, increased CSCC7 migration was associated with a CAF-induced decrease and partial replacement of fibrillar ECM components with laminin-1 (148). In 3D cocultures of oral tongue squamous cancer cells and CAFs in matrigel, CAFs (and CAF-conditioned medium) promoted growth, proliferation, migration, and epithelial-to-mesenchymal transition of the cancer cells (333). As observed by OCT, 3D cocultures of breast cancer cells and immortalized fibroblasts induced larger and more spherical acini with increased lumen size than cocultures using immortalized breast cells (101). Besides CAFs, the presence of TAMs has been shown also to affect ECM remodeling (334). For example, excretion of MMPs into the supernatant increased significantly in coculture of two breast cancer cell lines and macrophages, enhancing tumor cell invasiveness, and not in the benign breast cell line/macrophage coculture (335).

Tumor cells and CAFs also interact metabolically (Figure 2). As shown *in vitro*, CAFs take up and metabolize extracellular lactate (38) and export pyruvate which is taken up and metabolized by cancer cells (336) (Figure 2). Other research implies that epithelial cancer cells use metabolites, such as lactate, ketone bodies, and glutamine, excreted by CAFs in response to cancer cell-induced oxidative stress (39, 334, 337) (Figures 1 and 2). Glycolysis and glutamine-dependent reductive carboxylation increased in cancer cells following oxidative phosphorylation (OXPHOS) inhibition induced by exposure to CAF-derived exosomes (326). Additionally, immune cells and adipocytes may further impact the metabolic tumor phenotype

(334). Closer to the *in vivo* scenario, *ex vivo* tumor/stroma immunostaining, molecular profiling from tissue microarrays of excised tumors (338), or multiplexed staining and *in situ* transcriptome profiling techniques (339) improve further our understanding of tumor–stroma interaction. For example, Choi et al. (338) classified breast cancer subtypes of patient tumors into four subgroups defined by the *ex vivo* expression of the glycolysis markers Glut-1 and/or CA-IX in the tumor and stroma, respectively: Warburg type (tumor: GLUT-1 and/or CA-IX positive; stroma: Glut-1 and CAIX negative), reverse Warburg type (tumor: Glut-1 and CAIX negative; stroma: GLUT-1 and/or CA-IX positive), mixed type (tumor and stroma: GLUT-1 and/or CA-IX positive), and null type (tumor and stroma: Glut-1 and CAIX negative). The Warburg and mixed type were predominantly associated with triple-negative breast cancer, while the reverse Warburg and null-types predominantly associated with luminal breast cancer (338).

These data/models of metabolic interaction between cancer cells and CAFs or other stromal cells highlight the complexities of metabolic crosstalk and the need for further research to understand how metabolic plasticity of tumor and stromal cells benefit tumor progression and evasion of treatment.

While MSCs can dedifferentiate into various stromal cells after recruitment to tumors, many questions about the mechanisms of MSC homing and MSC–cancer cell interaction are still topics for future research (155). In a recent study, MSCs promoted *in vivo* growth of subcutaneous colorectal tumor models by a  $\beta$ 1-integrin-dependent interaction of MSCs and cancer cells (340). Coinjection of breast or prostate cancer cells with either normal fibroblasts or CAFs into animal models showed that, compared to normal fibroblasts, the presence of CAFs enhanced tumor growth (341, 342) and, as shown for the breast model, increased angiogenesis through elevated stromal cell-derived factor 1 *via* recruitment of endothelial progenitor cells (341). As demonstrated by *in vivo* fluorescence imaging and caliper tumor volume measurements, coinjection of human endometrial cancer cells with CAFs into nude mice increased tumor growth compared to tumor initiation without coinjection of CAFs (343). It was shown that the proliferation of endometrial cancer cells was increased in the presence of CAFs through the activation of JAK/STAT3/c-myc pathway (343).

Tumor–stroma interactions may sensitize tumors to treatment or be a source of treatment resistance across a wide range of therapeutics (320). And targeting tumor–stroma interactions by targeting its mediators, such as chemokines, may improve treatment response. For example, as observed with BLI, treatment of a prostate cancer model with the CXCR4-specific inhibitor AMD3100 in combination with docetaxel significantly reduced tumor growth compared to docetaxel alone (344). As a high-throughput alternative to *in vivo* models, an *in vitro* tumor cell-specific bioluminescence imaging (CS-BLI) assay for tumor–stroma cell cocultures has been proposed (345). Using this assay, it was shown that multiple myeloma cells exhibited chemoresistance to dexamethasone and doxorubicin when cocultured with bone marrow stromal cells, while effectiveness of reversine was enhanced by the presence of stromal cells (345).

Novel treatments, targeting tumor–stroma interaction by therapeutic targeting of adhesion, proteolysis, and/or signaling pathways, may improve on current treatment regimens and overcome treatment resistance (2, 346).

## Non-Invasive *In Vivo* Imaging of Tumor–Stroma Interactions

Studying tumor–stroma interactions *in vivo* enables the comprehensive characterization of the TME and its impact on treatment efficacy, potentially leading to improved diagnosis, to the identification of new treatment targets, and closing further the gap between preclinical and clinical studies (320). While single imaging methods have been used to image different aspects of the TME, only recently multimodal imaging has become more frequent. One major challenge of imaging the TME is that tumor and stromal cells use common pathways (286), necessitating cell-type-specific labeling and ideally imaging with cellular resolution. Localized, high-resolution imaging or combining multiple imaging modalities may to some extent overcome this inherent challenge. Intravital microscopy (66), which is considered a minimally invasive imaging modality, provides high-resolution imaging, including imaging of cellular processes (86, 208, 347), and has been to date the method of choice to study cancer cell interaction with the TME (**Figures 3–5**).

By using transgenic mice expressing green fluorescent protein (GFP) in all cells or in specific organs or driven by a cell marker and tumor cells expressing red fluorescent protein (RFP) (237, 348) or GFP in the nucleus and RFP in the cytoplasm (349), whole-body fluorescence imaging has been used to study tumor–TME interactions. While morphology and location of cells may help to identify what type of stromal cell may be involved in a specific biological process (237), specificity is lacking as all cell types of the host express the same fluorescence and *ex vivo* studies are needed for confirmation (349). By *ex vivo* validation of cell types, it was confirmed in a GFP-expressing mammary tumor model and a host with GFP-expressing macrophages, that both, cancer cells and macrophages migrated into microneedles filled with EGF, TGF-alpha, and CSF-1, as detected by multiphoton intravital microscopy (350). Using these techniques, it has been shown that paracrine loops associated with macrophage and tumor cell interaction impact tumor cell migration, intravasation, and dissemination (351).

Using intravital microscopy with multiphoton laser scanning microscopy (LSM) and SHG imaging of a human soft tissue sarcoma in VEGF-GFP mice, increased ECM remodeling by CAFs after exposure to relaxin has been imaged *in vivo*, with the involvement of CAFs confirmed by *ex vivo* cell typing (352). Using human, DsRed2- and nuclear histone 2B (H2B)-EGFP-expressing fibrosarcoma cells implanted into deep dermis of nude mice, tumor growth and tumor cell invasion into the surrounding tissue could be imaged by epifluorescence microscopy (**Figure 3A**) (66). In the same tumors, morphology (including collagen fibers), neoangiogenesis, cancer cell mitosis, and apoptosis were assessed *in vivo* during tumor growth by intravital microscopy with FLI and SHG (**Figure 3B**) (66). Multiphoton LSM combined with collagen (SHG) imaging of murine mammary tumors grown from a mix of a low-metastatic cell line expressing GFP and a high-metastatic

subline transfected expressing CFP (cyan fluorescence protein) in the cytoplasm has been used to track and visualize cell shape, subcellular structures, and behavior *in vivo* (67) (**Figure 4**). The motility of the cells with the larger metastatic potential was about 4.5-fold higher than in the cells with low-metastatic potential with migration along collagen fibers (67).

Beyond migration and imaging of vasculature and collagen structures, the redox ratio based on endogenous NADH/(FAD + NADH) had been imaged by intravital microscopy with multiphoton fluorescence lifetime microscopy (FLIM), and redox ratio changes have been found to relate to changes observed by <sup>18</sup>F-FDG PET, and, in ovarian cancer, were related to disease risk (49). As fluorescence lifetime changes with binding state and TME of metabolic enzymes (49), multiphoton FLIM, combined with other imaging modalities and intravital microscopy, is uniquely qualified to observe such changes *in vivo*, with the limitation of imaging depth.

Tumor vascularization, lymph vasculature, and vascular response to treatment have also been evaluated by intravital microscopy within the context of tumor growth and collagen structures (**Figure 5**) (66, 68, 86). Alexander et al. (66) imaged the intra- and perilymphatic invasion of fluorescent fibrosarcoma cells, indicative of a potential route of metastatic dissemination *via* the lymph vasculature located at the tumor margin (**Figure 5A**). Using intrinsic contrast, Vakoc et al. (68) imaged the antivascular effect of an antiangiogenic agent inhibiting VEGFR-2 on the tumor vasculature *in vivo* at the microscopic level, depicting lymph and blood vessels (**Figure 5B**). They found in response to VEGFR-2 blockade that intratumor vessel length and mean vessel diameter decreased, as tumor growth was delayed (68).

Nakasone et al. (353, 354) showed by intravital microscopy with a microlensed spinning-disk confocal microscope (355) of tumors in MMTV-PyMT mice expressing ACTB-ECFP in all host cells and c-fms-EGFP in myeloid cells, respectively, that vascular permeability and innate immune cell infiltration impact response to doxorubicin. The accumulation of macrophages with tumor growth as well as increased macrophage infiltration with increased metastatic ability have been imaged non-invasively in breast cancer models by fluorescence-reflectance imaging using a fluorescently labeled specific probe for alarmin S100A9, a calcium-binding protein secreted by monocytes/macrophages with the protein complex S100A8/A9 acting as mediator between tumor and immune cells (69) (**Figure 6**).

The fairly recent development of MRI/PET instrumentation permits the simultaneous imaging of metabolic, anatomical, and dynamic information, including cell tracking using appropriate labeled probes, during tumor progression and in response to treatment (70, 356–358) (**Figure 7**). The ability to effectively observe intratumoral function and heterogeneity over time by simultaneous MRI/PET has been demonstrated in a carcinogenic antigen-expressing colorectal adenocarcinoma model (**Figure 7**) (70). A recent study showed that microvessel volume and density index (determined from MRI) were significantly lower for glioblastoma tumors treated with bevacizumab and the PI3K/mTOR inhibitor BEZ235 combined than for tumors treated with bevacizumab alone, while <sup>18</sup>F-FET (O-(2-[<sup>18</sup>F]Fluoroethyl)-L-tyrosine) uptake, a PET tracer to assess vessel amino acid

transport, remained unchanged between the two treatments (359). Further, tumor growth, as determined from MRI, and cell proliferation, as determined from <sup>18</sup>F-FLT PET, were the same for the bevacizumab/BEZ235 combination therapy and the bevacizumab alone treatment groups (359). The *in vivo* results were validated by *ex vivo* studies (359).

While still significant more research needs to be done, these studies show the potential of harnessing the strengths of different imaging modalities to image tumor-stroma interaction within the TME *in vivo*, and thus, enhancing our understanding of its impact on tumor growth and treatment response.

## CONCLUSION

The strengths of optical imaging are its high sensitivity for CAs, ability to use a wide range of probes, including activatable probes and reporter genes, and compared to other imaging modalities, such as MRI and PET, low cost. However, optical imaging is typically semiquantitative, limited by penetration depth, small field of view, and, depending on method, high background signals and lack of tomographic information. Some of these limitations are overcome by PAI, which permits real-time quantitative imaging but is hampered by the range of available CAs. Ultrasound imaging is a low cost, rapid, real-time imaging modality with high temporal and spatial resolution, but has a limited field of view with low soft tissue contrast, and is typically semiquantitative and user dependent. Computer tomography is rapid, permits whole-body imaging, has high spatial resolution, is user independent, and mostly low cost, but is limited by its low sensitivity to CAs, lack of endogenous soft tissue contrast and exposure to radiation. Scanners for MRI (MRSI), PET, and SPECT are high in cost with the distinct advantage of whole-body imaging capabilities. While MRI has excellent soft tissue contrast, high spatial resolution, and has a wide range of methods available for tissue imaging and vessel characterization, it is limited by its low sensitivity and the fairly long acquisitions, the latter particularly prominent in spectroscopic imaging. To overcome these challenges, new methods, such as hyperpolarized <sup>13</sup>C MRSI, are being actively developed. The high sensitivity of PET and SPECT, respectively, is offset by their low resolution (1–2 mm), lack of morphological information and radiation exposure from the radioactive tracers, whose half-lives range from 75 s (Rb-82) to 4.18 days (I-124) for PET radioisotopes and from 6 h (Tc-99m) to 59 days (I-125) for SPECT tracers. With the advancement of MRI/PET, the power of various MRS and MRI

methods beyond anatomy and DCE-MRI, such as MRS(I), can be harnessed for future studies, distinguishing itself from PET/CT with reduced radiation exposure, the latter making MRI/PET a powerful tool for serial monitoring.

While CT, MRI (MRSI), PET, SPECT, and US are already standard imaging tools in the clinic, for localized applications, e.g., detecting cancer cells at tumor margins during surgery (360), optical imaging is being assiduously developed. Aside from physical parameters specific to each imaging modality, clinical imaging of tumor-stroma interaction will also be in part defined by the successful development of safe tracers/CAs.

In the majority of preclinical studies, specific aspects of the TME and its stromal components have been investigated separately (a few aspects at a time), selecting the non-invasive preclinical imaging modality best suited for the task. However, recent strong evidence pointing to the importance of the interaction between tumor cells and multiple components of the TME in tumor development, growth, metastases, and treatment response, including drug resistance, has generated a strong interest to further develop imaging technologies to investigate tumor-stroma interactions non-invasively *in vivo*. Despite recent research efforts, the comprehensive characterization (including serial monitoring) of the TME and tumor-stroma interactions non-invasively *in vivo* requires further advancement and to take advantage of the strengths of multimodal imaging tools for preclinical studies, and ultimately for clinical translation.

## AUTHOR CONTRIBUTIONS

EA and NR: conception, design, and writing of review article.

## ACKNOWLEDGMENTS

The authors would like to thank Dr. Radka Stoyanova and Dr. Avigdor Leftin for their helpful reading of the manuscript.

## FUNDING

We acknowledge salary support for Dr. N. Ramamonjisoa from a Cycle for Sarcoma grant and an Imaging and Radiation Sciences grant from MSKCC, as well as salary support for Dr. E. Ackerstaff from grants R01 CA172846 (NIH), R01 CA163980 (NIH), P50 CA092629 (NIH), and PC120233 (DOD). We also acknowledge the Memorial Sloan Kettering Cancer Center support grant P30 CA008748

## REFERENCES

1. Vaupel P, Kallinowski F, Okunieff P. Blood flow, oxygen and nutrient supply, and metabolic microenvironment of human tumors: a review. *Cancer Res* (1989) 49(23):6449–65.
2. Liotta LA, Kohn EC. The microenvironment of the tumour-host interface. *Nature* (2001) 411(6835):375–9. doi:10.1038/35077241
3. Swietach P, Vaughan-Jones RD, Harris AL. Regulation of tumor pH and the role of carbonic anhydrase 9. *Cancer Metastasis Rev* (2007) 26(2):299–310. doi:10.1007/s10555-007-9064-0
4. Pathak AP, Artemov D, Ward BD, Jackson DG, Neeman M, Bhujwalla ZM. Characterizing extravascular fluid transport of macromolecules in the tumor interstitium by magnetic resonance imaging. *Cancer Res* (2005) 65(4):1425–32. doi:10.1158/0008-5472.CAN-04-3682
5. LeBleu VS. Imaging the tumor microenvironment. *Cancer J* (2015) 21(3):174–8. doi:10.1097/PPO.0000000000000118
6. Payne SJ, Jones L. Influence of the tumor microenvironment on angiogenesis. *Future Oncol* (2011) 7(3):395–408. doi:10.2217/fon.11.13
7. Pouyssegur J, Dayan F, Mazure NM. Hypoxia signalling in cancer and approaches to enforce tumour regression. *Nature* (2006) 441(7092):437–43. doi:10.1038/nature04871
8. Warburg O. On respiratory impairment in cancer cells. *Science* (1956) 124(3215):269–70.
9. Warburg O, Wind F, Negelein E. The metabolism of tumors in the body. *J Gen Physiol* (1927) 8(6):519–30. doi:10.1085/jgp.8.6.519

10. Daye D, Wollen KE. Metabolic reprogramming in cancer: unraveling the role of glutamine in tumorigenesis. *Semin Cell Dev Biol* (2012) 23(4):362–9. doi:10.1016/j.semcd.2012.02.002
11. De Vitto H, Perez-Valencia J, Radosevich JA. Glutamine at focus: versatile roles in cancer. *Tumour Biol* (2016) 37(2):1541–58. doi:10.1007/s13277-015-4671-9
12. Wise DR, Thompson CB. Glutamine addiction: a new therapeutic target in cancer. *Trends Biochem Sci* (2010) 35(8):427–33. doi:10.1016/j.tibs.2010.05.003
13. DeBerardinis RJ, Mancuso A, Daikhin E, Nissim I, Yudkoff M, Wehrli S, et al. Beyond aerobic glycolysis: transformed cells can engage in glutamine metabolism that exceeds the requirement for protein and nucleotide synthesis. *Proc Natl Acad Sci U S A* (2007) 104(49):19345–50. doi:10.1073/pnas.0709747104
14. Ackerstaff E, Glunde K, Bhujwalla ZM. Choline phospholipid metabolism: a target in cancer cells? *J Cell Biochem* (2003) 90(3):525–33. doi:10.1002/jcb.10659
15. Glunde K, Ackerstaff E, Mori N, Jacobs MA, Bhujwalla ZM. Choline phospholipid metabolism in cancer: consequences for molecular pharmaceutical interventions. *Mol Pharm* (2006) 3(5):496–506. doi:10.1021/mp060067e
16. Podo F. Tumour phospholipid metabolism. *NMR Biomed* (1999) 12(7):413–39. doi:10.1002/(SICI)1099-1492(199911)12:7<413::AID-NBM587>3.3.CO;2-L
17. Ridgway ND. The role of phosphatidylcholine and choline metabolites to cell proliferation and survival. *Crit Rev Biochem Mol Biol* (2013) 48(1):20–38. doi:10.3109/10409238.2012.735643
18. Glunde K, Bhujwalla ZM, Ronen SM. Choline metabolism in malignant transformation. *Nat Rev Cancer* (2011) 11(12):835–48. doi:10.1038/nrc3162
19. Awwad HM, Geisel J, Obeid R. The role of choline in prostate cancer. *Clin Biochem* (2012) 45(18):1548–53. doi:10.1016/j.clinbiochem.2012.08.012
20. Simoes RV, Serganova IS, Kruchevsky N, Leftin A, Shestov AA, Thaler HT, et al. Metabolic plasticity of metastatic breast cancer cells: adaptation to changes in the microenvironment. *Neoplasia* (2015) 17(8):671–84. doi:10.1016/j.neo.2015.08.005
21. Yoshida GJ. Metabolic reprogramming: the emerging concept and associated therapeutic strategies. *J Exp Clin Cancer Res* (2015) 34:111. doi:10.1186/s13046-015-0221-y
22. Xing Y, Zhao S, Zhou BP, Mi J. Metabolic reprogramming of the tumour microenvironment. *FEBS J* (2015) 282(20):3892–8. doi:10.1111/febs.13402
23. Polet F, Feron O. Endothelial cell metabolism and tumour angiogenesis: glucose and glutamine as essential fuels and lactate as the driving force. *J Intern Med* (2013) 273(2):156–65. doi:10.1111/joim.12016
24. DeBerardinis RJ, Lum JJ, Hatzivassiliou G, Thompson CB. The biology of cancer: metabolic reprogramming fuels cell growth and proliferation. *Cell Metab* (2008) 7(1):11–20. doi:10.1016/j.cmet.2007.10.002
25. Marchiq I, Pouyssegur J. Hypoxia, cancer metabolism and the therapeutic benefit of targeting lactate/H(+) symporters. *J Mol Med (Berl)* (2016) 94(2):155–71. doi:10.1007/s00109-015-1307-x
26. Hanahan D, Weinberg RA. Hallmarks of cancer: the next generation. *Cell* (2011) 144(5):646–74. doi:10.1016/j.cell.2011.02.013
27. Romero-Garcia S, Moreno-Altamirano MM, Prado-Garcia H, Sanchez-Garcia FJ. Lactate contribution to the tumor microenvironment: mechanisms, effects on immune cells and therapeutic relevance. *Front Immunol* (2016) 7:52. doi:10.3389/fimmu.2016.00052
28. Park CC, Bissell MJ, Barcellos-Hoff MH. The influence of the microenvironment on the malignant phenotype. *Mol Med Today* (2000) 6(8):324–9. doi:10.1016/S1357-4310(00)01756-1
29. Mahadevan D, Von Hoff DD. Tumor-stroma interactions in pancreatic ductal adenocarcinoma. *Mol Cancer Ther* (2007) 6(4):1186–97. doi:10.1158/1535-7163.MCT-06-0686
30. Kopfstein L, Christofori G. Metastasis: cell-autonomous mechanisms versus contributions by the tumor microenvironment. *Cell Mol Life Sci* (2006) 63(4):449–68. doi:10.1007/s00018-005-5296-8
31. Jodele S, Blavier L, Yoon JM, DeClerck YA. Modifying the soil to affect the seed: role of stromal-derived matrix metalloproteinases in cancer progression. *Cancer Metastasis Rev* (2006) 25(1):35–43. doi:10.1007/s10555-006-7887-8
32. Farnsworth WE. Prostate stroma: physiology. *Prostate* (1999) 38(1):60–72. doi:10.1002/(SICI)1097-0045(19990101)38:1<60::AID-PROS8>3.0.CO;2-3
33. Romero IL, Mukherjee A, Kenny HA, Litchfield LM, Lengyel E. Molecular pathways: trafficking of metabolic resources in the tumor microenvironment. *Clin Cancer Res* (2015) 21(4):680–6. doi:10.1158/1078-0432.CCR-14-2198
34. Martinez-Outschoorn UE, Pavlides S, Howell A, Pestell RG, Tanowitz HB, Sotgia F, et al. Stromal–epithelial metabolic coupling in cancer: integrating autophagy and metabolism in the tumor microenvironment. *Int J Biochem Cell Biol* (2011) 43(7):1045–51. doi:10.1016/j.biocel.2011.01.023
35. Ratnikov B, Jeon YJ, Smith JW, Ronai ZA. Right on TARGET: glutamine metabolism in cancer. *Oncoscience* (2015) 2(8):681–3. doi:10.18632/oncoscience.205
36. Lisanti MP, Martinez-Outschoorn UE, Sotgia F. Oncogenes induce the cancer-associated fibroblast phenotype: metabolic symbiosis and “fibroblast addiction” are new therapeutic targets for drug discovery. *Cell Cycle* (2013) 12(17):2723–32. doi:10.4161/cc.25695
37. Correia AL, Bissell MJ. The tumor microenvironment is a dominant force in multidrug resistance. *Drug Resist Updat* (2012) 15(1–2):39–49. doi:10.1016/j.drup.2012.01.006
38. Rattigan YI, Patel BB, Ackerstaff E, Sukenick G, Koutcher JA, Glod JW, et al. Lactate is a mediator of metabolic cooperation between stromal carcinoma associated fibroblasts and glycolytic tumor cells in the tumor microenvironment. *Exp Cell Res* (2012) 318(4):326–35. doi:10.1016/j.yexcr.2011.11.014
39. Pavlides S, Vera I, Gandara R, Sneddon S, Pestell RG, Mercier I, et al. Warburg meets autophagy: cancer-associated fibroblasts accelerate tumor growth and metastasis via oxidative stress, mitophagy, and aerobic glycolysis. *Antioxid Redox Signal* (2012) 16(11):1264–84. doi:10.1089/ars.2011.4243
40. Hanahan D, Coussens LM. Accessories to the crime: functions of cells recruited to the tumor microenvironment. *Cancer Cell* (2012) 21(3):309–22. doi:10.1016/j.ccr.2012.02.022
41. Pickup MW, Mouw JK, Weaver VM. The extracellular matrix modulates the hallmarks of cancer. *EMBO Rep* (2014) 15(12):1243–53. doi:10.15252/embr.201439246
42. Hagedorn HG, Bachmeier BE, Nerlich AG. Synthesis and degradation of basement membranes and extracellular matrix and their regulation by TGF-beta in invasive carcinomas (Review). *Int J Oncol* (2001) 18(4):669–81. doi:10.3892/ijo.18.4.669
43. Turley SJ, Cremasco V, Astarita JL. Immunological hallmarks of stromal cells in the tumour microenvironment. *Nat Rev Immunol* (2015) 15(11):669–82. doi:10.1038/nri3902
44. Friedl P, Brocker EB. The biology of cell locomotion within three-dimensional extracellular matrix. *Cell Mol Life Sci* (2000) 57(1):41–64. doi:10.1007/s00180050498
45. Narunsky L, Oren R, Bochner F, Neeman M. Imaging aspects of the tumor stroma with therapeutic implications. *Pharmacol Ther* (2014) 141(2):192–208. doi:10.1016/j.pharmthera.2013.10.003
46. Kobayashi H, Longmire MR, Ogawa M, Choyke PL. Rational chemical design of the next generation of molecular imaging probes based on physics and biology: mixing modalities, colors and signals. *Chem Soc Rev* (2011) 40(9):4626–48. doi:10.1039/c1cs15077d
47. Youn H, Hong KJ. *In vivo* non invasive molecular imaging for immune cell tracking in small animals. *Immune Netw* (2012) 12(6):223–9. doi:10.4110/in.2012.12.6.223
48. Zhou ZN, Boimel PJ, Segall JE. Tumor-stroma: *in vivo* assays and intravital imaging to study cell migration and metastasis. *Drug Discov Today Dis Models* (2011) 8(2–3):95–112. doi:10.1016/j.ddmod.2011.07.003
49. Provenzano PP, Eliceiri KW, Keely PJ. Multiphoton microscopy and fluorescence lifetime imaging microscopy (FLIM) to monitor metastasis and the tumor microenvironment. *Clin Exp Metastasis* (2009) 26(4):357–70. doi:10.1007/s10585-008-9204-0
50. Sevick-Muraca EM, Kwon S, Rasmussen JC. Emerging lymphatic imaging technologies for mouse and man. *J Clin Invest* (2014) 124(3):905–14. doi:10.1172/JCI71612
51. Stuker F, Ripoll J, Rudin M. Fluorescence molecular tomography: principles and potential for pharmaceutical research. *Pharmaceutics* (2011) 3(2):229–74. doi:10.3390/pharmaceutics3020229
52. Ehling J, Lammers T, Kiessling F. Non-invasive imaging for studying anti-angiogenic therapy effects. *Thromb Haemost* (2013) 109(3):375–90. doi:10.1160/TH12-10-0721

53. Noreen R, Chien CC, Chen HH, Bobroff V, Moenner M, Javerzat S, et al. FTIR spectro-imaging of collagen scaffold formation during glioma tumor development. *Anal Bioanal Chem* (2013) 405(27):8729–36. doi:10.1007/s00216-013-7337-8
54. Bhargava R. Infrared spectroscopic imaging: the next generation. *Appl Spectrosc* (2012) 66(10):1091–120. doi:10.1366/12-06801
55. Bellisola G, Sorio C. Infrared spectroscopy and microscopy in cancer research and diagnosis. *Am J Cancer Res* (2012) 2(1):1–21.
56. Lasch P, Naumann D. Spatial resolution in infrared microspectroscopic imaging of tissues. *Biochim Biophys Acta* (2006) 1758(7):814–29. doi:10.1016/j.bbamem.2006.06.008
57. Dhawan AP, D'Alessandro B, Fu X. Optical imaging modalities for biomedical applications. *IEEE Rev Biomed Eng* (2010) 3:69–92. doi:10.1109/RBME.2010.2081975
58. Xu MH, Wang LHV. Photoacoustic imaging in biomedicine. *Rev Sci Instrum* (2006) 77(4). doi:10.1063/1.2195024
59. Wu D, Huang L, Jiang MS, Jiang H. Contrast agents for photoacoustic and thermoacoustic imaging: a review. *Int J Mol Sci* (2014) 15(12):23616–39. doi:10.3390/ijms151223616
60. Mallidi S, Luke GP, Emelianov S. Photoacoustic imaging in cancer detection, diagnosis, and treatment guidance. *Trends Biotechnol* (2011) 29(5):213–21. doi:10.1016/j.tibtech.2011.01.006
61. Weigelin B, Bakker GJ, Friedl P. Third harmonic generation microscopy of cells and tissue organization. *J Cell Sci* (2016) 129(2):245–55. doi:10.1242/jcs.152272
62. Strupler M, Pena AM, Hernest M, Tharaux PL, Martin JL, Beaurepaire E, et al. Second harmonic imaging and scoring of collagen in fibrotic tissues. *Opt Express* (2007) 15(7):4054–65. doi:10.1364/OE.15.004054
63. Dekaban GA, Hamilton AM, Fink CA, Au B, de Chickera SN, Ribot EJ, et al. Tracking and evaluation of dendritic cell migration by cellular magnetic resonance imaging. *Wiley Interdiscip Rev Nanomed Nanobiotechnol* (2013) 5(5):469–83. doi:10.1002/wnnan.1227
64. Bokacheva L, Ackerstaff E, LeKaye HC, Zakian K, Koutcher JA. High-field small animal magnetic resonance oncology studies. *Phys Med Biol* (2014) 59(2):R65–127. doi:10.1088/0031-9155/59/2/R65
65. Vikram DS, Zweier JL, Kuppusamy P. Methods for noninvasive imaging of tissue hypoxia. *Antioxid Redox Signal* (2007) 9(10):1745–56. doi:10.1089/ars.2007.1717
66. Alexander S, Koehl GE, Hirschberg M, Geissler EK, Friedl P. Dynamic imaging of cancer growth and invasion: a modified skin-fold chamber model. *Histochem Cell Biol* (2008) 130(6):1147–54. doi:10.1007/s00418-008-0529-1
67. Sahai E, Wyckoff J, Philippur U, Segall JE, Gertler F, Condeelis J. Simultaneous imaging of GFP, CFP and collagen in tumors *in vivo* using multiphoton microscopy. *BMC Biotechnol* (2005) 5:14. doi:10.1186/1472-6750-5-14
68. Vakoc BJ, Lanning RM, Tyrrell JA, Padera TP, Bartlett LA, Stylianopoulos T, et al. Three-dimensional microscopy of the tumor microenvironment *in vivo* using optical frequency domain imaging. *Nat Med* (2009) 15(10):1219–23. doi:10.1038/nm.1971
69. Becker A, Grosse Hokamp N, Zenker S, Flores-Borja F, Barczyk K, Varga G, et al. Optical *in vivo* imaging of the alarmin S100A9 in tumor lesions allows for estimation of the individual malignant potential by evaluation of tumor-host cell interaction. *J Nucl Med* (2015) 56(3):450–6. doi:10.2967/jnumed.114.146688
70. Ng TS, Bading JR, Park R, Sohi H, Procissi D, Colcher D, et al. Quantitative, simultaneous PET/MRI for intratumoral imaging with an MRI-compatible PET scanner. *J Nucl Med* (2012) 53(7):1102–9. doi:10.2967/jnumed.111.099861
71. Mecham RP. Overview of extracellular matrix. *Curr Protoc Cell Biol* (2012) Chapter 10:Unit 10.1. doi:10.1002/0471143030.cb1001s57
72. Lu P, Weaver VM, Werb Z. The extracellular matrix: a dynamic niche in cancer progression. *J Cell Biol* (2012) 196(4):395–406. doi:10.1083/jcb.201102147
73. Lu P, Takai K, Weaver VM, Werb Z. Extracellular matrix degradation and remodeling in development and disease. *Cold Spring Harb Perspect Biol* (2011) 3(12):a005058. doi:10.1101/cshperspect.a005058
74. Kessenbrock K, Plaks V, Werb Z. Matrix metalloproteinases: regulators of the tumor microenvironment. *Cell* (2010) 141(1):52–67. doi:10.1016/j.cell.2010.03.015
75. Verma RP, Hansch C. Matrix metalloproteinases (MMPs): chemical-biological functions and (Q)SARs. *Bioorg Med Chem* (2007) 15(6):2223–68. doi:10.1016/j.bmc.2007.01.011
76. Page-McCaw A, Ewald AJ, Werb Z. Matrix metalloproteinases and the regulation of tissue remodelling. *Nat Rev Mol Cell Biol* (2007) 8(3):221–33. doi:10.1038/nrm2125
77. Worth DC, Parsons M. Advances in imaging cell-matrix adhesions. *J Cell Sci* (2010) 123(Pt 21):3629–38. doi:10.1242/jcs.064485
78. Valderrama R, Navarro S, Campo E, Camps J, Gimenez A, Pares A, et al. Quantitative measurement of fibrosis in pancreatic tissue. Evaluation of a colorimetric method. *Int J Pancreatol* (1991) 10(1):23–9.
79. Taskiran D, Taskiran E, Yercan H, Kutay FZ. Quantification of total collagen in rabbit tendon by the sirius red method. *Tr J Med Sci* (1999) 29:7–9.
80. Plodinec M, Loparic M, Aebi U. Imaging collagen II using atomic force microscopy (AFM). *Cold Spring Harb Protoc* (2010) 2010(10):db.rot5501. doi:10.1101/pdb.prot5501
81. Maller O, Hansen KC, Lyons TR, Acerbi I, Weaver VM, Prekeris R, et al. Collagen architecture in pregnancy-induced protection from breast cancer. *J Cell Sci* (2013) 126(Pt 18):4108–10. doi:10.1242/jcs.121590
82. Stamat DR, Stock E, Franz CM, Jahnke T, Haschke H. Imaging collagen type I fibrillogenesis with high spatiotemporal resolution. *Ultramicroscopy* (2015) 149:86–94. doi:10.1016/j.ultramic.2014.10.003
83. Dang TT, Prechtel AM, Pearson GW. Breast cancer subtype-specific interactions with the microenvironment dictate mechanisms of invasion. *Cancer Res* (2011) 71(21):6857–66. doi:10.1158/0008-5472.CAN-11-1818
84. Peng CW, Liu XL, Chen C, Liu X, Yang XQ, Pang DW, et al. Patterns of cancer invasion revealed by QDs-based quantitative multiplexed imaging of tumor microenvironment. *Biomaterials* (2011) 32(11):2907–17. doi:10.1016/j.biomaterials.2010.12.053
85. Fang M, Peng CW, Yuan JP, Zhang ZL, Pang DW, Li Y. Coevolution of the tumor microenvironment revealed by quantum dot-based multiplexed imaging of hepatocellular carcinoma. *Future Oncol* (2013) 9(7):1029–37. doi:10.2217/fon.13.63
86. Alexander S, Weigelin B, Winkler F, Friedl P. Preclinical intravital microscopy of the tumour-stroma interface: invasion, metastasis, and therapy response. *Curr Opin Cell Biol* (2013) 25(5):659–71. doi:10.1016/j.ceb.2013.07.001
87. Wu PC, Hsieh TY, Tsai ZU, Liu TM. *In vivo* quantification of the structural changes of collagens in a melanoma microenvironment with second and third harmonic generation microscopy. *Sci Rep* (2015) 5:8879. doi:10.1038/srep08879
88. Williams RM, Zipfel WR, Webb WW. Multiphoton microscopy in biological research. *Curr Opin Chem Biol* (2001) 5(5):603–8. doi:10.1016/S1367-5931(00)00241-6
89. Zoumi A, Yeh A, Tromberg BJ. Imaging cells and extracellular matrix *in vivo* by using second-harmonic generation and two-photon excited fluorescence. *Proc Natl Acad Sci U S A* (2002) 99(17):11014–9. doi:10.1073/pnas.172368799
90. Keikhosravi A, Bredfeldt JS, Sagar AK, Eliceiri KW. Second-harmonic generation imaging of cancer. *Methods Cell Biol* (2014) 123:531–46. doi:10.1016/B978-0-12-420138-5.00028-8
91. Raja AM, Xu S, Sun W, Zhou J, Tai DC, Chen CS, et al. Pulse-modulated second harmonic imaging microscope quantitatively demonstrates marked increase of collagen in tumor after chemotherapy. *J Biomed Opt* (2010) 15(5):056016. doi:10.1117/1.3497565
92. Drifka CR, Tod J, Loeffler AG, Liu Y, Thomas GJ, Eliceiri KW, et al. Periductal stromal collagen topology of pancreatic ductal adenocarcinoma differs from that of normal and chronic pancreatitis. *Mod Pathol* (2015) 28(11):1470–80. doi:10.1038/modpathol.2015.97
93. Bredfeldt JS, Liu Y, Conklin MW, Keely PJ, Mackie TR, Eliceiri KW. Automated quantification of aligned collagen for human breast carcinoma prognosis. *J Pathol Inform* (2014) 5:28. doi:10.4103/2153-3539.139707
94. Kirkpatrick ND, Andreou S, Hoying JB, Utzinger U. Live imaging of collagen remodeling during angiogenesis. *Am J Physiol Heart Circ Physiol* (2007) 292(6):H3198–206. doi:10.1152/ajpheart.01234.2006
95. Pfeffer CP, Olsen BR, Ganikhanov F, Legare F. Multimodal nonlinear optical imaging of collagen arrays. *J Struct Biol* (2008) 164(1):140–5. doi:10.1016/j.jsb.2008.07.002

96. Madsen DH, Bugge TH. Imaging collagen degradation *in vivo* highlights a key role for M2-polarized macrophages in extracellular matrix degradation. *Oncotarget* (2013) 2(12):e27127. doi:10.4161/onci.27127
97. Wahyudi H, Reynolds AA, Li Y, Owen SC, Yu SM. Targeting collagen for diagnostic imaging and therapeutic delivery. *J Control Release* (2016) 240:323–31. doi:10.1016/j.jconrel.2016.01.007
98. Mercado KP, Helguera M, Hocking DC, Dalecki D. Noninvasive quantitative imaging of collagen microstructure in three-dimensional hydrogels using high-frequency ultrasound. *Tissue Eng Part C Methods* (2015) 21(7):671–82. doi:10.1089/ten.TEC.2014.0527
99. Riggan CN, Sarver JJ, Freedman BR, Thomas SJ, Soslowsky LJ. Analysis of collagen organization in mouse Achilles tendon using high-frequency ultrasound imaging. *J Biomech Eng* (2014) 136(2):021029. doi:10.1115/1.4026285
100. Ring HC, Mogensen M, Hussain AA, Steadman N, Banzhaf C, Themstrup L, et al. Imaging of collagen deposition disorders using optical coherence tomography. *J Eur Acad Dermatol Venereol* (2015) 29(5):890–8. doi:10.1111/jdv.12708
101. Chhetri RK, Phillips ZF, Troester MA, Oldenburg AL. Longitudinal study of mammary epithelial and fibroblast co-cultures using optical coherence tomography reveals morphological hallmarks of pre-malignancy. *PLoS One* (2012) 7(11):e49148. doi:10.1371/journal.pone.0049148
102. Wang P, Wang P, Wang HW, Cheng JX. Mapping lipid and collagen by multispectral photoacoustic imaging of chemical bond vibration. *J Biomed Opt* (2012) 17(9):96010–1. doi:10.1117/1.JBO.17.9.96010
103. Fang M, Yuan JB, Peng CW, Pang DW, Li Y. Quantum dots-based *in situ* molecular imaging of dynamic changes of collagen IV during cancer invasion. *Biomaterials* (2013) 34(34):8708–17. doi:10.1016/j.biomaterials.2013.07.069
104. Zheng HM, Chen C, Wu XH, Chen J, Sun S, Sun JZ, et al. Quantum dot-based *in situ* simultaneous molecular imaging and quantitative analysis of EGFR and collagen IV and identification of their prognostic value in triple-negative breast cancer. *Tumour Biol* (2016) 37(2):2509–18. doi:10.1007/s13277-015-4079-6
105. Jin HE, Farr R, Lee SW. Collagen mimetic peptide engineered M13 bacteriophage for collagen targeting and imaging in cancer. *Biomaterials* (2014) 35(33):9236–45. doi:10.1016/j.biomaterials.2014.07.044
106. Li Y, Foss CA, Pomper MG, Yu SM. Imaging denatured collagen strands *in vivo* and *ex vivo* via photo-triggered hybridization of caged collagen mimetic peptides. *J Vis Exp* (2014) 83:e51052. doi:10.3791/51052
107. Brown GT, Murray GI. Current mechanistic insights into the roles of matrix metalloproteinases in tumour invasion and metastasis. *J Pathol* (2015) 237(3):273–81. doi:10.1002/path.4586
108. Scherer RL, McIntyre JO, Matrisian LM. Imaging matrix metalloproteinases in cancer. *Cancer Metastasis Rev* (2008) 27(4):679–90. doi:10.1007/s10555-008-9152-9
109. Yang Y, Hong H, Zhang Y, Cai W. Molecular imaging of proteases in cancer. *Cancer Growth Metastasis* (2009) 2:13–27.
110. Lebel R, Lepage M. A comprehensive review on controls in molecular imaging: lessons from MMP-2 imaging. *Contrast Media Mol Imaging* (2014) 9(3):187–210. doi:10.1002/cmmi.1555
111. Shay G, Lynch CC, Fingleton B. Moving targets: emerging roles for MMPs in cancer progression and metastasis. *Matrix Biol* (2015) 44:46–200–6. doi:10.1016/j.matbio.2015.01.019
112. Chuang CH, Chuang KH, Wang HE, Roffler SR, Shiea JT, Tzou SC, et al. *In vivo* positron emission tomography imaging of protease activity by generation of a hydrophobic product from a noninhibitory protease substrate. *Clin Cancer Res* (2012) 18(1):238–47. doi:10.1158/1078-0432.CCR-11-0608
113. Cox B, Laufer JG, Arridge SR, Beard PC. Quantitative spectroscopic photo-acoustic imaging: a review. *J Biomed Opt* (2012) 17(6):061202. doi:10.1117/1.JBO.17.6.061202
114. van den Berg PJ, Daoudi K, Steenbergen W. Review of photoacoustic flow imaging: its current state and its promises. *Photoacoustics* (2015) 3(3):89–99. doi:10.1016/j.pacs.2015.08.001
115. Levi J, Kothapalli SR, Bohndiek S, Yoon JK, Dragulescu-Andrasi A, Nielsen C, et al. Molecular photoacoustic imaging of follicular thyroid carcinoma. *Clin Cancer Res* (2013) 19(6):1494–502. doi:10.1158/1078-0432.CCR-12-3061
116. Salaun M, Peng J, Hensley HH, Roder N, Flieder DB, Houelle-Crepin S, et al. MMP-13 *in-vivo* molecular imaging reveals early expression in lung adenocarcinoma. *PLoS One* (2015) 10(7):e0132960. doi:10.1371/journal.pone.0132960
117. Al Rawashdeh W, Arns S, Gremse F, Ehling J, Knuchel-Clarke R, Kray S, et al. Optical tomography of MMP activity allows a sensitive noninvasive characterization of the invasiveness and angiogenesis of SCC xeno-grafts. *Neoplasia* (2014) 16(3):235–46,246.e1. doi:10.1016/j.neo.2014.03.005
118. Toole BP. Hyaluronan promotes the malignant phenotype. *Glycobiology* (2002) 12(3):37R–42R. doi:10.1093/glycob/12.3.37R
119. McAtee CO, Barycki JJ, Simpson MA. Emerging roles for hyaluronidase in cancer metastasis and therapy. *Adv Cancer Res* (2014) 123:1–34. doi:10.1016/B978-0-12-800092-2.00001-0
120. Choi KY, Saravanan Kumar G, Park JH, Park K. Hyaluronic acid-based nanocarriers for intracellular targeting: interfacial interactions with proteins in cancer. *Colloids Surf B Biointerfaces* (2012) 99:82–94. doi:10.1016/j.colsurfb.2011.10.029
121. Tripodo G, Trapani A, Torre ML, Giannonna G, Trapani G, Mandracchia D. Hyaluronic acid and its derivatives in drug delivery and imaging: recent advances and challenges. *Eur J Pharm Biopharm* (2015) 97(Pt B):400–16. doi:10.1016/j.ejpb.2015.03.032
122. Veiseh M, Turley EA. Hyaluronan metabolism in remodeling extracellular matrix: probes for imaging and therapy of breast cancer. *Integr Biol (Camb)* (2011) 3(4):304–15. doi:10.1039/c0ib00096e
123. Cho HJ, Yoon HY, Koo H, Ko SH, Shim JS, Cho JH, et al. Hyaluronic acid-ceramide-based optical/MR dual imaging nanoprobe for cancer diagnosis. *J Control Release* (2012) 162(1):111–8. doi:10.1016/j.jconrel.2012.06.011
124. Swierczewska M, Choi KY, Mertz EL, Huang X, Zhang F, Zhu L, et al. A facile, one-step nanocarbon functionalization for biomedical applications. *Nano Lett* (2012) 12(7):3613–20. doi:10.1021/nl301309g
125. Park J, Ku M, Kim E, Park Y, Hong Y, Haam S, et al. CD44-specific supramolecular hydrogels for fluorescence molecular imaging of stem-like gastric cancer cells. *Integr Biol (Camb)* (2013) 5(4):669–72. doi:10.1039/c3ib20203h
126. Park JH, Cho HJ, Yoon HY, Yoon IS, Ko SH, Shim JS, et al. Hyaluronic acid derivative-coated nano-hybrid liposomes for cancer imaging and drug delivery. *J Control Release* (2014) 174:98–108. doi:10.1016/j.jconrel.2013.11.016
127. Lim EK, Kim HO, Jang E, Park J, Lee K, Suh JS, et al. Hyaluronan-modified magnetic nanoclusters for detection of CD44-overexpressing breast cancer by MR imaging. *Biomaterials* (2011) 32(31):7941–50. doi:10.1016/j.biomaterials.2011.06.077
128. Li J, He Y, Sun W, Luo Y, Cai H, Pan Y, et al. Hyaluronic acid-modified hydrothermally synthesized iron oxide nanoparticles for targeted tumor MR imaging. *Biomaterials* (2014) 35(11):3666–77. doi:10.1016/j.biomaterials.2014.01.011
129. Yoon HY, Koo H, Choi KY, Lee SJ, Kim K, Kwon IC, et al. Tumor-targeting hyaluronic acid nanoparticles for photodynamic imaging and therapy. *Biomaterials* (2012) 33(15):3980–9. doi:10.1016/j.biomaterials.2012.02.016
130. Yoon HY, Koo H, Choi KY, Chan Kwon I, Choi K, Park JH, et al. Photo-crosslinked hyaluronic acid nanoparticles with improved stability for *in vivo* tumor-targeted drug delivery. *Biomaterials* (2013) 34(21):5273–80. doi:10.1016/j.biomaterials.2013.03.050
131. Thomas RG, Moon MJ, Lee H, Sasikala AR, Kim CS, Park IK, et al. Hyaluronic acid conjugated superparamagnetic iron oxide nanoparticle for cancer diagnosis and hyperthermia therapy. *Carbohydr Polym* (2015) 131:439–46. doi:10.1016/j.carbpol.2015.06.010
132. Ravar F, Saadat E, Gholami M, Dehghankelishadi P, Mahdavi M, Azami S, et al. Hyaluronic acid-coated liposomes for targeted delivery of paclitaxel, *in-vitro* characterization and *in-vivo* evaluation. *J Control Release* (2016) 229:10–22. doi:10.1016/j.jconrel.2016.03.012
133. Yang RM, Fu CP, Li NN, Wang L, Xu XD, Yang DY, et al. Glycosaminoglycan-targeted iron oxide nanoparticles for magnetic resonance imaging of liver carcinoma. *Mater Sci Eng C Mater Biol Appl* (2014) 45:556–63. doi:10.1016/j.msec.2014.09.038
134. Song S, Qi H, Xu J, Guo P, Chen F, Li F, et al. Hyaluronan-based nanocarriers with CD44-overexpressed cancer cell targeting. *Pharm Res* (2014) 31(11):2988–3005. doi:10.1007/s11095-014-1393-4
135. Shiftan L, Israely T, Cohen M, Frydman V, Dafni H, Stern R, et al. Magnetic resonance imaging visualization of hyaluronidase in ovarian carcinoma. *Cancer Res* (2005) 65(22):10316–23. doi:10.1158/0008-5472.CAN-04-3947

136. Hou L, Yang X, Ren J, Wang Y, Zhang H, Feng Q, et al. A novel redox-sensitive system based on single-walled carbon nanotubes for chemo-photothermal therapy and magnetic resonance imaging. *Int J Nanomedicine* (2016) 11:607–24. doi:10.2147/IJN.S98476
137. Li J, Hu Y, Yang J, Wei P, Sun W, Shen M, et al. Hyaluronic acid-modified Fe<sub>3</sub>O<sub>4</sub>@Au core/shell nanostars for multimodal imaging and photothermal therapy of tumors. *Biomaterials* (2015) 38:10–21. doi:10.1016/j.biomaterials.2014.10.065
138. Jin Y, Ma X, Feng S, Liang X, Dai Z, Tian J, et al. Hyaluronic acid modified tantalum oxide nanoparticles conjugating doxorubicin for targeted cancer theranostics. *Bioconjug Chem* (2015) 26(12):2530–41. doi:10.1021/acs.bioconjchem.5b00551
139. Li W, Zheng C, Pan Z, Chen C, Hu D, Gao G, et al. Smart hyaluronidase-activated theranostic micelles for dual-modal imaging guided photodynamic therapy. *Biomaterials* (2016) 101:10–9. doi:10.1016/j.biomaterials.2016.05.019
140. Feng Q, Zhang Y, Zhang W, Shan X, Yuan Y, Zhang H, et al. Tumor-targeted and multi-stimuli responsive drug delivery system for near-infrared light induced chemo-phototherapy and photoacoustic tomography. *Acta Biomater* (2016) 38:129–42. doi:10.1016/j.actbio.2016.04.024
141. Uthaman S, Bom JS, Kim HS, John JV, Bom HS, Kim SJ, et al. Tumor homing indocyanine green encapsulated micelles for near infrared and photoacoustic imaging of tumors. *J Biomed Mater Res B Appl Biomater* (2016) 104(4):825–34. doi:10.1002/jbm.b.33607
142. Swierczewska M, Han HS, Kim K, Park JH, Lee S. Polysaccharide-based nanoparticles for theranostic nanomedicine. *Adv Drug Deliv Rev* (2016) 99(Pt A):70–84. doi:10.1016/j.addr.2015.11.015
143. Sollini M, Boni R, Traino AC, Lazzeri E, Pasqualetti F, Modeo L, et al. New approaches for imaging and therapy of solid cancer. *Q J Nucl Med Mol Imaging* (2015) 59(2):168–83.
144. Abou-Elkacem L, Wilson KE, Johnson SM, Chowdhury SM, Bachawal S, Hackel BJ, et al. Ultrasound molecular imaging of the breast cancer neovasculature using engineered fibronectin scaffold ligands: a novel class of targeted contrast ultrasound agent. *Theranostics* (2016) 6(11):1740–52. doi:10.7150/thno.15169
145. Givant-Horwitz V, Davidson B, Reich R. Laminin-induced signaling in tumor cells. *Cancer Lett* (2005) 223(1):1–10. doi:10.1016/j.canlet.2004.08.030
146. Aumailley M. The laminin family. *Cell Adh Migr* (2013) 7(1):48–55. doi:10.4161/cam.22826
147. Patarroyo M, Tryggvason K, Virtanen I. Laminin isoforms in tumor invasion, angiogenesis and metastasis. *Semin Cancer Biol* (2002) 12(3):197–207. doi:10.1016/S1044-579X(02)00023-8
148. Fullar A, Dudas J, Olah L, Hollosi P, Papp Z, Sobel G, et al. Remodeling of extracellular matrix by normal and tumor-associated fibroblasts promotes cervical cancer progression. *BMC Cancer* (2015) 15:256. doi:10.1186/s12885-015-1273-3
149. Mazzocca A, Coppari R, De Franco R, Cho JY, Libermann TA, Pinzani M, et al. A secreted form of ADAM9 promotes carcinoma invasion through tumor-stromal interactions. *Cancer Res* (2005) 65(11):4728–38. doi:10.1158/0008-5472.CAN-04-4449
150. Moilanen JM, Kokkonen N, Loffek S, Vayrynen JP, Syvaniemi E, Hurskainen T, et al. Collagen XVII expression correlates with the invasion and metastasis of colorectal cancer. *Hum Pathol* (2015) 46(3):434–42. doi:10.1016/j.humpath.2014.11.020
151. Cuesta AM, Sanchez-Martin D, Sanz L, Bonet J, Compte M, Kremer L, et al. *In vivo* tumor targeting and imaging with engineered trivalent antibody fragments containing collagen-derived sequences. *PLoS One* (2009) 4(4):e5381. doi:10.1371/journal.pone.0005381
152. Koliakos G, Trontzos C, Kouzi-Koliakos K, Kanellaki M, Grammaticos P. Lung carcinoma imaging using a synthetic laminin derivative radioiodinated peptide YIGSR. *J Nucl Med* (1997) 38(12):1940–4.
153. Fujita M, Lee BS, Khazenzon NM, Penichet ML, Wawrowsky KA, Patil R, et al. Brain tumor tandem targeting using a combination of monoclonal antibodies attached to biopoly(beta-L-malic acid). *J Control Release* (2007) 122(3):356–63. doi:10.1016/j.jconrel.2007.05.032
154. Stelter L, Tseng JC, Torosjan A, Levin B, Longo VA, Pillarssetty N, et al. Tumor-specific targeting with modified Sindbis viral vectors: evaluation with optical imaging and positron emission tomography *in vivo*. *Mol Imaging Biol* (2013) 15(2):166–74. doi:10.1007/s11307-012-0585-8
155. Droujinine IA, Eckert MA, Zhao W. To grab the stroma by the horns: from biology to cancer therapy with mesenchymal stem cells. *Oncotarget* (2013) 4(5):651–64. doi:10.18632/oncotarget.1040
156. Madar S, Goldstein I, Rotter V. ‘Cancer associated fibroblasts’ – more than meets the eye. *Trends Mol Med* (2013) 19(8):447–53. doi:10.1016/j.molmed.2013.05.004
157. Xing F, Saidou J, Watabe K. Cancer associated fibroblasts (CAFs) in tumor microenvironment. *Front Biosci (Landmark Ed)* (2010) 15:166–79. doi:10.2741/3613
158. Shiga K, Hara M, Nagasaki T, Sato T, Takahashi H, Takeyama H. Cancer-associated fibroblasts: their characteristics and their roles in tumor growth. *Cancers (Basel)* (2015) 7(4):2443–58. doi:10.3390/cancers7040902
159. Grivennikov SI, Greten FR, Karin M. Immunity, inflammation, and cancer. *Cell* (2010) 140(6):883–99. doi:10.1016/j.cell.2010.01.025
160. Pollard JW. Tumour-educated macrophages promote tumour progression and metastasis. *Nat Rev Cancer* (2004) 4(1):71–8. doi:10.1038/nrc1256
161. Coussens LM, Zitvogel L, Palucka AK. Neutralizing tumor-promoting chronic inflammation: a magic bullet? *Science* (2013) 339(6117):286–91. doi:10.1126/science.1232227
162. Kidd S, Spaeth E, Dembinski JL, Dietrich M, Watson K, Klopp A, et al. Direct evidence of mesenchymal stem cell tropism for tumor and wounding microenvironments using *in vivo* bioluminescent imaging. *Stem Cells* (2009) 27(10):2614–23. doi:10.1002/stem.187
163. Klopp AH, Spaeth EL, Dembinski JL, Woodward WA, Munshi A, Meyn RE, et al. Tumor irradiation increases the recruitment of circulating mesenchymal stem cells into the tumor microenvironment. *Cancer Res* (2007) 67(24):11687–95. doi:10.1158/0008-5472.CAN-07-1406
164. Compte M, Cuesta AM, Sanchez-Martin D, Alonso-Camino V, Vicario JL, Sanz L, et al. Tumor immunotherapy using gene-modified human mesenchymal stem cells loaded into synthetic extracellular matrix scaffolds. *Stem Cells* (2009) 27(3):753–60. doi:10.1634/stemcells.2008-0831
165. Xiang J, Tang J, Song C, Yang Z, Hirst DG, Zheng QJ, et al. Mesenchymal stem cells as a gene therapy carrier for treatment of fibrosarcoma. *Cytotherapy* (2009) 11(5):516–26. doi:10.1080/14653240902960429
166. Kidd S, Caldwell L, Dietrich M, Samudio I, Spaeth EL, Watson K, et al. Mesenchymal stromal cells alone or expressing interferon-beta suppress pancreatic tumors *in vivo*, an effect countered by anti-inflammatory treatment. *Cytotherapy* (2010) 12(5):615–25. doi:10.3109/14653241003631815
167. Doucette T, Rao G, Yang Y, Gumin J, Shinohima N, Bekele BN, et al. Mesenchymal stem cells display tumor-specific tropism in an RCAS/Ntv-a glioma model. *Neoplasia* (2011) 13(8):716–25. doi:10.1593/neo.101680
168. Ke CC, Liu RS, Suetsugu A, Kimura H, Ho JH, Lee OK, et al. *In vivo* fluorescence imaging reveals the promotion of mammary tumorigenesis by mesenchymal stromal cells. *PLoS One* (2013) 8(7):e69658. doi:10.1371/journal.pone.0069658
169. Wu X, Hu J, Zhou L, Mao Y, Yang B, Gao L, et al. *In vivo* tracking of superparamagnetic iron oxide nanoparticle-labeled mesenchymal stem cell tropism to malignant gliomas using magnetic resonance imaging. *Laboratory investigation. J Neurosurg* (2008) 108(2):320–9. doi:10.3171/JNS/2008/108/2/0320
170. Huang X, Zhang F, Wang H, Niu G, Choi KY, Swierczewska M, et al. Mesenchymal stem cell-based cell engineering with multifunctional mesoporous silica nanoparticles for tumor delivery. *Biomaterials* (2013) 34(7):1772–80. doi:10.1016/j.biomaterials.2012.11.032
171. Belmar-Lopez C, Mendoza G, Oberg D, Burnet J, Simon C, Cervello I, et al. Tissue-derived mesenchymal stromal cells used as vehicles for anti-tumor therapy exert different *in vivo* effects on migration capacity and tumor growth. *BMC Med* (2013) 11:139. doi:10.1186/1741-7015-11-139
172. Hung SC, Deng WP, Yang WK, Liu RS, Lee CC, Su TC, et al. Mesenchymal stem cell targeting of microscopic tumors and tumor stroma development monitored by noninvasive *in vivo* positron emission tomography imaging. *Clin Cancer Res* (2005) 11(21):7749–56. doi:10.1158/1078-0432.CCR-05-0876
173. Knoop K, Kolokythas M, Klutz K, Willhauck MJ, Wunderlich N, Draganovici D, et al. Image-guided, tumor stroma-targeted 131I therapy of hepatocellular cancer after systemic mesenchymal stem cell-mediated NIS gene delivery. *Mol Ther* (2011) 19(9):1704–13. doi:10.1038/mtn.2011.93

174. Dwyer RM, Ryan J, Havelin RJ, Morris JC, Miller BW, Liu Z, et al. Mesenchymal stem cell-mediated delivery of the sodium iodide symporter supports radionuclide imaging and treatment of breast cancer. *Stem Cells* (2011) 29(7):1149–57. doi:10.1002/stem.665
175. Shah K. Mesenchymal stem cells engineered for cancer therapy. *Adv Drug Deliv Rev* (2012) 64(8):739–48. doi:10.1016/j.addr.2011.06.010
176. Loebinger MR, Kyrtatos PG, Turmaine M, Price AN, Pankhurst Q, Lythgoe MF, et al. Magnetic resonance imaging of mesenchymal stem cells homing to pulmonary metastases using biocompatible magnetic nanoparticles. *Cancer Res* (2009) 69(23):8862–7. doi:10.1158/0008-5472.CAN-09-1912
177. Sasportas LS, Kasmieh R, Wakimoto H, Hinggen S, van de Water JA, Mohapatra G, et al. Assessment of therapeutic efficacy and fate of engineered human mesenchymal stem cells for cancer therapy. *Proc Natl Acad Sci U S A* (2009) 106(12):4822–7. doi:10.1073/pnas.0806647106
178. Uchibori R, Okada T, Ito T, Urabe M, Mizukami H, Kume A, et al. Retroviral vector-producing mesenchymal stem cells for targeted suicide cancer gene therapy. *J Gene Med* (2009) 11(5):373–81. doi:10.1002/jgm.1313
179. Jia XH, Du Y, Mao D, Wang ZL, He ZQ, Qiu JD, et al. Zoledronic acid prevents the tumor-promoting effects of mesenchymal stem cells via MCP-1 dependent recruitment of macrophages. *Oncotarget* (2015) 6(28):26018–28. doi:10.18632/oncotarget.4658
180. Meleshina AV, Cherkasova EI, Shirmanova MV, Klementieva NV, Kiseleva EV, Snopova LB, et al. Influence of mesenchymal stem cells on metastasis development in mice *in vivo*. *Stem Cell Res Ther* (2015) 6:15. doi:10.1186/s13287-015-0003-7
181. Ozawa K, Sato K, Oh I, Ozaki K, Uchibori R, Obara Y, et al. Cell and gene therapy using mesenchymal stem cells (MSCs). *J Autoimmun* (2008) 30(3):121–7. doi:10.1016/j.jaut.2007.12.008
182. Caimi PF, Reese J, Lee Z, Lazarus HM. Emerging therapeutic approaches for multipotent mesenchymal stromal cells. *Curr Opin Hematol* (2010) 17(6):505–13. doi:10.1097/MOH.0b013e32833e5b18
183. Mader EK, Maeyama Y, Lin Y, Butler GW, Russell HM, Galanis E, et al. Mesenchymal stem cell carriers protect oncolytic measles viruses from antibody neutralization in an orthotopic ovarian cancer therapy model. *Clin Cancer Res* (2009) 15(23):7246–55. doi:10.1158/1078-0432.CCR-09-1292
184. Centeno CJ, Schultz JR, Cheever M, Robinson B, Freeman M, Marasco W. Safety and complications reporting on the re-implantation of culture-expanded mesenchymal stem cells using autologous platelet lysate technique. *Curr Stem Cell Res Ther* (2010) 5(1):81–93. doi:10.2174/157488810790442796
185. Tolar J, Nauta AJ, Osborn MJ, Panoskaltsis Mortari A, McElmurry RT, Bell S, et al. Sarcoma derived from cultured mesenchymal stem cells. *Stem Cells* (2007) 25(2):371–9. doi:10.1634/stemcells.2005-0620
186. Boddington SE, Sutton EJ, Henning TD, Nedopil AJ, Sennino B, Kim A, et al. Labeling human mesenchymal stem cells with fluorescent contrast agents: the biological impact. *Mol Imaging Biol* (2011) 13(1):3–9. doi:10.1007/s11307-010-0322-0
187. Myers JT, Petrosiute A, Huang AY. Utilization of multiphoton imaging for real-time fate determination of mesenchymal stem cells in an immunocompetent mouse model. *J Stem Cell Res Ther* (2014) 4(7):1000217. doi:10.4172/2157-7633.1000217
188. Orimo A, Weinberg RA. Heterogeneity of stromal fibroblasts in tumors. *Cancer Biol Ther* (2007) 6(4):618–9. doi:10.4161/cbt.6.4.4255
189. Liao D, Luo Y, Markowitz D, Xiang R, Reisfeld RA. Cancer associated fibroblasts promote tumor growth and metastasis by modulating the tumor immune microenvironment in a 4T1 murine breast cancer model. *PLoS One* (2009) 4(11):e7965. doi:10.1371/journal.pone.0007965
190. Hanley CJ, Noble F, Ward M, Bullock M, Drifka C, Mellone M, et al. A subset of myofibroblastic cancer-associated fibroblasts regulate collagen fiber elongation, which is prognostic in multiple cancers. *Oncotarget* (2016) 7(5):6159–74. doi:10.18632/oncotarget.6740
191. Koczorowska MM, Tholen S, Bucher F, Lutz L, Kizhakkedathu JN, De Wever O, et al. Fibroblast activation protein-alpha, a stromal cell surface protease, shapes key features of cancer associated fibroblasts through proteome and degradome alterations. *Mol Oncol* (2016) 10(1):40–58. doi:10.1016/j.molonc.2015.08.001
192. Brennen WN, Isaacs JT, Denmeade SR. Rationale behind targeting fibroblast activation protein-expressing carcinoma-associated fibroblasts as a novel chemotherapeutic strategy. *Mol Cancer Ther* (2012) 11(2):257–66. doi:10.1158/1535-7163.MCT-11-0340
193. Li J, Chen K, Liu H, Cheng K, Yang M, Zhang J, et al. Activatable near-infrared fluorescent probe for *in vivo* imaging of fibroblast activation protein-alpha. *Bioconjug Chem* (2012) 23(8):1704–11. doi:10.1021/bc300278r
194. Ruger R, Tansi FL, Rabenhold M, Steiniger F, Kontermann RE, Fahr A, et al. *In vivo* near-infrared fluorescence imaging of FAP-expressing tumors with activatable FAP-targeted, single-chain Fv-immunoliposomes. *J Control Release* (2014) 186:1–10. doi:10.1016/j.jconrel.2014.04.050
195. Granot D, Addadi Y, Kalchenko V, Harmelin A, Kunz-Schughart LA, Neeman M. *In vivo* imaging of the systemic recruitment of fibroblasts to the angiogenic rim of ovarian carcinoma tumors. *Cancer Res* (2007) 67(19):9180–9. doi:10.1158/0008-5472.CAN-07-0684
196. Granot D, Kunz-Schughart LA, Neeman M. Labeling fibroblasts with biotin-BSA-GdDTPA-FAM for tracking of tumor-associated stroma by fluorescence and MR imaging. *Magn Reson Med* (2005) 54(4):789–97. doi:10.1002/mrm.20628
197. Lo A, Wang LC, Scholler J, Monslow J, Avery D, Newick K, et al. Tumor-promoting desmoplasia is disrupted by depleting FAP-expressing stromal cells. *Cancer Res* (2015) 75(14):2800–10. doi:10.1158/0008-5472.CAN-14-3041
198. Juergens RA, Zukotynski KA, Singnurkar A, Snider DP, Valliant JF, Gulenchyn KY. Imaging biomarkers in immunotherapy. *Biomark Cancer* (2016) 8(Suppl 2):1–13. doi:10.4137/BIC.S31805
199. Freise AC, Wu AM. *In vivo* imaging with antibodies and engineered fragments. *Mol Immunol* (2015) 67(2 Pt A):142–52. doi:10.1016/j.molimm.2015.04.001
200. Weissleder R, Nahrendorf M, Pittet MJ. Imaging macrophages with nanoparticles. *Nat Mater* (2014) 13(2):125–38. doi:10.1038/nmat3780
201. Malviya G, Galli F, Sonni I, Signore A. Imaging T-lymphocytes in inflammatory diseases: a nuclear medicine approach. *Q J Nucl Med Mol Imaging* (2014) 58(3):237–57.
202. Aarntzen EH, Srinivas M, Radu CG, Punt CJ, Boerman OC, Fidgor CG, et al. *In vivo* imaging of therapy-induced anti-cancer immune responses in humans. *Cell Mol Life Sci* (2013) 70(13):2237–57. doi:10.1007/s00018-012-1159-2
203. Ottobrini L, Martelli C, Trabattoni DL, Clerici M, Lucignani G. *In vivo* imaging of immune cell trafficking in cancer. *Eur J Nucl Med Mol Imaging* (2011) 38(5):949–68. doi:10.1007/s00259-010-1687-7
204. Dubey P. Reporter gene imaging of immune responses to cancer: progress and challenges. *Theranostics* (2012) 2(4):355–62. doi:10.7150/thno.3903
205. Singh AS, Radu CG, Ribas A. PET imaging of the immune system: immune monitoring at the whole body level. *Q J Nucl Med Mol Imaging* (2010) 54(3):281–90.
206. Jha P, Golovko D, Bains S, Hostetter D, Meier R, Wendland MF, et al. Monitoring of natural killer cell immunotherapy using noninvasive imaging modalities. *Cancer Res* (2010) 70(15):6109–13. doi:10.1158/0008-5472.CAN-09-3774
207. Lohela M, Werb Z. Intravital imaging of stromal cell dynamics in tumors. *Curr Opin Genet Dev* (2010) 20(1):72–8. doi:10.1016/j.gde.2009.10.011
208. Zal T, Chodaczek G. Intravital imaging of anti-tumor immune response and the tumor microenvironment. *Semin Immunopathol* (2010) 32(3):305–17. doi:10.1007/s00281-010-0217-9
209. Srinivas M, Aarntzen EH, Bulte JW, Oyen WJ, Heerschap A, de Vries IJ, et al. Imaging of cellular therapies. *Adv Drug Deliv Rev* (2010) 62(11):1080–93. doi:10.1016/j.addr.2010.08.009
210. Armulik A, Abramsson A, Betsholtz C. Endothelial/pericyte interactions. *Circ Res* (2005) 97(6):512–23. doi:10.1161/01.RES.0000182903.16652.d7
211. Kohlhapp FJ, Mitra AK, Lengyel E, Peter ME. MicroRNAs as mediators and communicators between cancer cells and the tumor microenvironment. *Oncogene* (2015) 34(48):5857–68. doi:10.1038/onc.2015.89
212. Armulik A, Genove G, Betsholtz C. Pericytes: developmental, physiological, and pathological perspectives, problems, and promises. *Dev Cell* (2011) 21(2):193–215. doi:10.1016/j.devcel.2011.07.001
213. Casazza A, Di Conza G, Wenes M, Finisguerra V, Deschoemaeker S, Mazzone M. Tumor stroma: a complexity dictated by the hypoxic tumor microenvironment. *Oncogene* (2014) 33(14):1743–54. doi:10.1038/onc.2013.121

214. Varlotto J, Stevenson MA. Anemia, tumor hypoxemia, and the cancer patient. *Int J Radiat Oncol Biol Phys* (2005) 63(1):25–36. doi:10.1016/j.ijrobp.2005.04.049
215. Vaupel P, Mayer A. Hypoxia in cancer: significance and impact on clinical outcome. *Cancer Metastasis Rev* (2007) 26(2):225–39. doi:10.1007/s10555-007-9055-1
216. Rafat M, Ali R, Graves EE. Imaging radiation response in tumor and normal tissue. *Am J Nucl Med Mol Imaging* (2015) 5(4):317–32.
217. de Langen AJ, van den Boogaart VE, Marcus JT, Lubberink M. Use of H2(15) O-PET and DCE-MRI to measure tumor blood flow. *Oncologist* (2008) 13(6):631–44. doi:10.1634/theoncologist.2007-0235
218. Willats L, Calamante F. The 39 steps: evading error and deciphering the secrets for accurate dynamic susceptibility contrast MRI. *NMR Biomed* (2013) 26(8):913–31. doi:10.1002/nbm.2833
219. Loveless ME, Halliday J, Liess C, Xu L, Dortch RD, Whisenant J, et al. A quantitative comparison of the influence of individual versus population-derived vascular input functions on dynamic contrast enhanced-MRI in small animals. *Magn Reson Med* (2012) 67(1):226–36. doi:10.1002/mrm.22988
220. Barnes SL, Whisenant JG, Loveless ME, Yankelev TE. Practical dynamic contrast enhanced MRI in small animal models of cancer: data acquisition, data analysis, and interpretation. *Pharmaceutics* (2012) 4(3):442–78. doi:10.3390/pharmaceutics4030442
221. Koh TS, Bisdas S, Koh DM, Thng CH. Fundamentals of tracer kinetics for dynamic contrast-enhanced MRI. *J Magn Reson Imaging* (2011) 34(6):1262–76. doi:10.1002/jmri.22795
222. Calamante F. Perfusion MRI using dynamic-susceptibility contrast MRI: quantification issues in patient studies. *Top Magn Reson Imaging* (2010) 21(2):75–85. doi:10.1097/RMR.0b013e31821e53f5
223. Barrett T, Brechbiel M, Bernardo M, Choyke PL. MRI of tumor angiogenesis. *J Magn Reson Imaging* (2007) 26(2):235–49. doi:10.1002/jmri.20991
224. Le Bihan D, Poupon C, Amadon A, Lethimonnier F. Artifacts and pitfalls in diffusion MRI. *J Magn Reson Imaging* (2006) 24(3):478–88. doi:10.1002/jmri.20083
225. Barrett T, Kobayashi H, Brechbiel M, Choyke PL. Macromolecular MRI contrast agents for imaging tumor angiogenesis. *Eur J Radiol* (2006) 60(3):353–66. doi:10.1016/j.ejrad.2006.06.025
226. Neeman M, Gilad AA, Dafni H, Cohen B. Molecular imaging of angiogenesis. *J Magn Reson Imaging* (2007) 25(1):1–12. doi:10.1002/jmri.20774
227. Kidwell CS, Hsia AW. Imaging of the brain and cerebral vasculature in patients with suspected stroke: advantages and disadvantages of CT and MRI. *Curr Neurol Neurosci Rep* (2006) 6(1):9–16. doi:10.1007/s11910-996-0003-1
228. van Elmpt W, Das M, Hullner M, Sharifi H, Zegers CM, Reymen B, et al. Characterization of tumor heterogeneity using dynamic contrast enhanced CT and FDG-PET in non-small cell lung cancer. *Radiother Oncol* (2013) 109(1):65–70. doi:10.1016/j.radonc.2013.08.032
229. Cyran CC, Paprottka PM, Eisenblatter M, Clevert DA, Rist C, Nikolaou K, et al. Visualization, imaging and new preclinical diagnostics in radiation oncology. *Radiat Oncol* (2014) 9:3. doi:10.1186/1748-717X-9-3
230. Chen M, Wang WP, Jia WR, Tang L, Wang Y, Zhan WW, et al. Three-dimensional contrast-enhanced sonography in the assessment of breast tumor angiogenesis: correlation with microvessel density and vascular endothelial growth factor expression. *J Ultrasound Med* (2014) 33(5):835–46. doi:10.7863/ultra.33.5.835
231. Koehl GE, Gaumann A, Geissler EK. Intravital microscopy of tumor angiogenesis and regression in the dorsal skin fold chamber: mechanistic insights and preclinical testing of therapeutic strategies. *Clin Exp Metastasis* (2009) 26(4):329–44. doi:10.1007/s10585-008-9234-7
232. Detre JA, Zhang W, Roberts DA, Silva AC, Williams DS, Grandis DJ, et al. Tissue specific perfusion imaging using arterial spin labeling. *NMR Biomed* (1994) 7(1–2):75–82. doi:10.1002/nbm.1940070112
233. Le Bihan D, Breton E, Lallemand D, Aubin ML, Vignaud J, Laval-Jeantet M. Separation of diffusion and perfusion in intravoxel incoherent motion MR imaging. *Radiology* (1988) 168(2):497–505. doi:10.1148/radiology.168.2.3393671
234. Garcia-Figueiras R, Padhani AR, Baleato-Gonzalez S. Therapy monitoring with functional and molecular MR imaging. *Magn Reson Imaging Clin N Am* (2016) 24(1):261–88. doi:10.1016/j.mric.2015.08.003
235. Ingrisch M, Sourbron S. Tracer-kinetic modeling of dynamic contrast-enhanced MRI and CT: a primer. *J Pharmacokinet Pharmacodyn* (2013) 40(3):281–300. doi:10.1007/s10928-013-9315-3
236. Pathak AP, Gimi B, Glunde K, Ackerstaff E, Artemov D, Bhujwalla ZM. Molecular and functional imaging of cancer: advances in MRI and MRS. *Methods Enzymol* (2004) 386:3–60. doi:10.1016/S0076-6879(04)86001-4
237. Yang M, Li L, Jiang P, Moossa AR, Penman S, Hoffman RM. Dual-color fluorescence imaging distinguishes tumor cells from induced host angiogenic vessels and stromal cells. *Proc Natl Acad Sci U S A* (2003) 100(24):14259–62. doi:10.1073/pnas.2436101100
238. Geraldes CF, Laurent S. Classification and basic properties of contrast agents for magnetic resonance imaging. *Contrast Media Mol Imaging* (2009) 4(1):1–23. doi:10.1002/cmmi.265
239. Leach MO, Brindle KM, Evelhoch JL, Griffiths JR, Horsman MR, Jackson A, et al. The assessment of antiangiogenic and antivascular therapies in early-stage clinical trials using magnetic resonance imaging: issues and recommendations. *Br J Cancer* (2005) 92(9):1599–610. doi:10.1038/sj.bjc.6602550
240. Bradley DP, Tessier JJ, Ashton SE, Waterton JC, Wilson Z, Worthington PL, et al. Correlation of MRI biomarkers with tumor necrosis in Hras5 tumor xenograft in athymic rats. *Neoplasia* (2007) 9(5):382–91. doi:10.1593/neo.07145
241. Hsu YH, Ferl GZ, Ng CM. GPU-accelerated nonparametric kinetic analysis of DCE-MRI data from glioblastoma patients treated with bevacizumab. *Magn Reson Imaging* (2013) 31(4):618–23. doi:10.1016/j.mri.2012.09.007
242. Brix G, Lucht R, Griebel J. Tracer kinetic analysis of signal time series from dynamic contrast-enhanced MR imaging. *Biomed Tech (Berl)* (2006) 51(5–6):325–30. doi:10.1515/BMT.2006.065
243. Sourbron SP, Buckley DL. Tracer kinetic modelling in MRI: estimating perfusion and capillary permeability. *Phys Med Biol* (2012) 57(2):R1–33. doi:10.1088/0031-9155/57/2/R1
244. Sourbron SP, Buckley DL. Classic models for dynamic contrast-enhanced MRI. *NMR Biomed* (2013) 26(8):1004–27. doi:10.1002/nbm.2940
245. O'Connor JP, Rose CJ, Waterton JC, Carano RA, Parker GJ, Jackson A. Imaging intratumor heterogeneity: role in therapy response, resistance, and clinical outcome. *Clin Cancer Res* (2015) 21(2):249–57. doi:10.1158/1078-0432.CCR-14-0990
246. Stoyanova R, Huang K, Sandler K, Cho H, Carlin S, Zanzonico PB, et al. Mapping tumor hypoxia *in vivo* using pattern recognition of dynamic contrast-enhanced MRI data. *Transl Oncol* (2012) 5(6):437–47. doi:10.1593/tlo.12319
247. Fritz V, Noel D, Bouquet C, Opolon P, Voide R, Apparailly F, et al. Antitumoral activity and osteogenic potential of mesenchymal stem cells expressing the urokinase-type plasminogen antagonist amino-terminal fragment in a murine model of osteolytic tumor. *Stem Cells* (2008) 26(11):2981–90. doi:10.1634/stemcells.2008-0139
248. Koyasu S, Tsuji Y, Harada H, Nakamoto Y, Nobashi T, Kimura H, et al. Evaluation of tumor-associated stroma and its relationship with tumor hypoxia using dynamic contrast-enhanced CT and <sup>18</sup>F misonidazole PET in murine tumor models. *Radiology* (2015) 278(3):734–41. doi:10.1148/radiol.2015150416
249. Mancini M, Greco A, Salvatore G, Liuzzi R, Di Maro G, Vergara E, et al. Imaging of thyroid tumor angiogenesis with microbubbles targeted to vascular endothelial growth factor receptor type 2 in mice. *BMC Med Imaging* (2013) 13:31. doi:10.1186/1471-2342-13-31
250. Yousefi S, Zhi Z, Wang RK. Label-free optical imaging of lymphatic vessels within tissue beds. *IEEE J Sel Top Quantum Electron* (2014) 20(2):6800510. doi:10.1109/JSTQE.2013.2278073
251. Mumprecht V, Honer M, Vigl B, Proulx ST, Trachsel E, Kaspar M, et al. *In vivo* imaging of inflammation- and tumor-induced lymph node lymphangiogenesis by immuno-positron emission tomography. *Cancer Res* (2010) 70(21):8842–51. doi:10.1158/0008-5472.CAN-10-0896
252. Bhang SH, Won N, Lee TJ, Jin H, Nam J, Park J, et al. Hyaluronic acid-quantum dot conjugates for *in vivo* lymphatic vessel imaging. *ACS Nano* (2009) 3(6):1389–98. doi:10.1021/nm900138d
253. Podo F, Caneveri S, Canese R, Pisani ME, Ricci A, Iorio E. MR evaluation of response to targeted treatment in cancer cells. *NMR Biomed* (2011) 24(6):648–72. doi:10.1002/nbm.1658

254. Challapalli A, Aboagye EO. Positron emission tomography imaging of tumor cell metabolism and application to therapy response monitoring. *Front Oncol* (2016) 6:44. doi:10.3389/fonc.2016.00044
255. Cuccurullo V, Di Stasio GD, Evangelista L, Castoria G, Mansi L. Biochemical and pathophysiological premises to positron emission tomography with choline radiotracers. *J Cell Physiol* (2017) 232(2):270–5. doi:10.1002/jcp.25478
256. Haberkorn U, Markert A, Mier W, Askoxylakis V, Altmann A. Molecular imaging of tumor metabolism and apoptosis. *Oncogene* (2011) 30(40):4141–51. doi:10.1038/onc.2011.169
257. Zhu A, Marcus DM, Shu HK, Shim H. Application of metabolic PET imaging in radiation oncology. *Radiat Res* (2012) 177(4):436–48. doi:10.1667/RR2702.1
258. Ljungkvist AS, Bussink J, Kaanders JH, van der Kogel AJ. Dynamics of tumor hypoxia measured with bioreductive hypoxic cell markers. *Radiat Res* (2007) 167(2):127–45. doi:10.1667/RR0719.1
259. Robinson SP, Griffiths JR. Current issues in the utility of <sup>19</sup>F nuclear magnetic resonance methodologies for the assessment of tumour hypoxia. *Philos Trans R Soc Lond B Biol Sci* (2004) 359(1446):987–96. doi:10.1098/rstb.2003.1376
260. Tatum JL, Kelloff GJ, Gillies RJ, Arbeit JM, Brown JM, Chao KS, et al. Hypoxia: importance in tumor biology, noninvasive measurement by imaging, and value of its measurement in the management of cancer therapy. *Int J Radiat Biol* (2006) 82(10):699–757. doi:10.1080/09553000601002324
261. Thorwarth D, Eschmann SM, Paulsen F, Alber M. A kinetic model for dynamic [<sup>18</sup>F]-Fmiso PET data to analyse tumour hypoxia. *Phys Med Biol* (2005) 50(10):2209–24. doi:10.1088/0031-9155/50/10/002
262. Zanzonico P, O'Donoghue J, Chapman JD, Schneider R, Cai S, Larson S, et al. Iodine-124-labeled iodo-azomycin-galactoside imaging of tumor hypoxia in mice with serial microPET scanning. *Eur J Nucl Med Mol Imaging* (2004) 31(1):117–28. doi:10.1007/s00259-003-1322-y
263. Rajendran JG, Krohn KA. F-18 fluoromisonidazole for imaging tumor hypoxia: imaging the microenvironment for personalized cancer therapy. *Semin Nucl Med* (2015) 45(2):151–62. doi:10.1053/j.semnuclmed.2014.10.006
264. Ackerstaff E, Suehiro M, Kruchevsky N, Carlin S, Rosenfeld EH, Burgman P, et al., editors. Trifluoromisonidazole detects hypoxia – an *in vivo* and *in vitro* multimodality study. *ISMRM 19th Annual Meeting & Exhibition*. Montreal, Canada (2011).
265. Serganova I, Humm J, Ling C, Blasberg R. Tumor hypoxia imaging. *Clin Cancer Res* (2006) 12(18):5260–4. doi:10.1158/1078-0432.CCR-06-0517
266. Penet MF, Krishnamachary B, Chen Z, Jin J, Bhujwalla ZM. Molecular imaging of the tumor microenvironment for precision medicine and theranostics. *Adv Cancer Res* (2014) 124:235–56. doi:10.1016/B978-0-12-411638-2.00007-0
267. Gulliksrød K, Vestvik IK, Galappathi K, Mathiesen B, Rofstad EK. Detection of different hypoxic cell subpopulations in human melanoma xenografts by pimonidazole immunohistochemistry. *Radiat Res* (2008) 170(5):638–50. doi:10.1667/RR1400.1
268. White DA, Zhang Z, Li L, Gerberich J, Stojadinovic S, Peschke P, et al. Developing oxygen-enhanced magnetic resonance imaging as a prognostic biomarker of radiation response. *Cancer Lett* (2016) 380(1):69–77. doi:10.1016/j.canlet.2016.06.003
269. Zhao D, Pacheco-Torres J, Hallac RR, White D, Peschke P, Cerdan S, et al. Dynamic oxygen challenge evaluated by NMR T<sub>1</sub> and T<sub>2</sub>\* – insights into tumor oxygenation. *NMR Biomed* (2015) 28(8):937–47. doi:10.1002/nbm.3325
270. Hallac RR, Zhou H, Pidikiti R, Song K, Stojadinovic S, Zhao D, et al. Correlations of noninvasive BOLD and TOLD MRI with pO<sub>2</sub> and relevance to tumor radiation response. *Magn Reson Med* (2014) 71(5):1863–73. doi:10.1002/mrm.24846
271. Mason RP, Zhao D, Pacheco-Torres J, Cui W, Kodibagkar VD, Gulaka PK, et al. Multimodality imaging of hypoxia in preclinical settings. *Q J Nucl Med Mol Imaging* (2010) 54(3):259–80.
272. Lau J, Zhang Z, Jenni S, Kuo HT, Liu Z, Vullo D, et al. PET imaging of carbonic anhydrase IX expression of HT-29 tumor xenograft mice with (<sup>68</sup>Ga)-labeled benzene-sulfonamides. *Mol Pharm* (2016) 13(3):1137–46. doi:10.1021/acs.molpharmaceut.5b00934
273. Lv PC, Roy J, Putt KS, Low PS. Evaluation of a carbonic anhydrase IX-targeted near-infrared dye for fluorescence-guided surgery of hypoxic tumors. *Mol Pharm* (2016) 13(5):1618–25. doi:10.1021/acs.molpharmaceut.6b00065
274. Lv PC, Putt KS, Low PS. Evaluation of nonpeptidic ligand conjugates for SPECT imaging of hypoxic and carbonic anhydrase IX-expressing cancers. *Bioconjug Chem* (2016) 27(7):1762–9. doi:10.1021/acs.bioconjchem.6b00271
275. Di Gialleonardo V, Wilson DM, Keshari KR. The potential of metabolic imaging. *Semin Nucl Med* (2016) 46(1):28–39. doi:10.1053/j.semnuclmed.2015.09.004
276. Glunde K, Bhujwalla ZM. Metabolic tumor imaging using magnetic resonance spectroscopy. *Semin Oncol* (2011) 38(1):26–41. doi:10.1053/j.seminoncol.2010.11.001
277. Valette J, Tiret B, Boumezeur F. Experimental strategies for *in vivo* <sup>13</sup>C NMR spectroscopy. *Anal Biochem* (2016). doi:10.1016/j.ab.2016.08.003
278. Dafni H, Ronen SM. Dynamic nuclear polarization in metabolic imaging of metastasis: common sense, hypersense and compressed sensing. *Cancer Biomark* (2010) 7(4):189–99. doi:10.3233/CBM-2010-0185
279. Chen AP, Tropp J, Hurd RE, Van Criekinge M, Carvajal LG, Xu D, et al. *In vivo* hyperpolarized <sup>13</sup>C MR spectroscopic imaging with 1H decoupling. *J Magn Reson* (2009) 197(1):100–6. doi:10.1016/j.jmr.2008.12.004
280. Hu S, Lustig M, Balakrishnan A, Larson PE, Bok R, Kurhanewicz J, et al. 3D compressed sensing for highly accelerated hyperpolarized (<sup>13</sup>C) MRSI with *in vivo* applications to transgenic mouse models of cancer. *Magn Reson Med* (2010) 63(2):312–21. doi:10.1002/mrm.22233
281. He Q, Xu RZ, Shkarin P, Pizzorno G, Lee-French CH, Rothman DL, et al. Magnetic resonance spectroscopic imaging of tumor metabolic markers for cancer diagnosis, metabolic phenotyping, and characterization of tumor microenvironment. *Dis Markers* (2003) 19(2–3):69–94. doi:10.1155/2004/424395
282. Hetherington HP, Avison MJ, Shulman RG. 1H homonuclear editing of rat brain using semiselective pulses. *Proc Natl Acad Sci U S A* (1985) 82(10):3115–8. doi:10.1073/pnas.82.10.3115
283. Lee SC, Huang MQ, Nelson DS, Pickup S, Wehrli S, Adegbola O, et al. *In vivo* MRS markers of response to CHOP chemotherapy in the WSU-DLCL2 human diffuse large B-cell lymphoma xenograft. *NMR Biomed* (2008) 21(7):723–33. doi:10.1002/nbm.1250
284. Lee SC, Poptani H, Pickup S, Jenkins WT, Kim S, Koch CJ, et al. Early detection of radiation therapy response in non-Hodgkin's lymphoma xenografts by *in vivo* <sup>1</sup>H magnetic resonance spectroscopy and imaging. *NMR Biomed* (2010) 23(6):624–32. doi:10.1002/nbm.1505
285. Muruganandham M, Koutcher JA, Pizzorno G, He Q. *In vivo* tumor lactate relaxation measurements by selective multiple-quantum-coherence (Sel-MQC) transfer. *Magn Reson Med* (2004) 52(4):902–6. doi:10.1002/mrm.20206
286. Del Vecchio S, Zannetti A, Iommelli F, Lettieri A, Brunetti A, Salvatore M. Molecular imaging of tumor microenvironment: challenges and perspectives. *Q J Nucl Med Mol Imaging* (2010) 54(3):249–58.
287. Gillies RJ, Liu Z, Bhujwalla Z. <sup>31</sup>P-MRS measurements of extracellular pH of tumors using 3-aminopropylphosphonate. *Am J Physiol* (1994) 267(1 Pt 1):C195–203.
288. Raghunand N. Tissue pH measurement by magnetic resonance spectroscopy and imaging. *Methods Mol Med* (2006) 124:347–64. doi:10.1385/1-59745-010-3:347
289. van Sluis R, Bhujwalla ZM, Raghunand N, Ballesteros P, Alvarez J, Cerdan S, et al. *In vivo* imaging of extracellular pH using <sup>1</sup>H MRSI. *Magn Reson Med* (1999) 41(4):743–50. doi:10.1002/(SICI)1522-2594(199904)41:4<743::AID-MRM13>3.3.CO;2-Q
290. Provent P, Benito M, Hiba B, Farion R, Lopez-Larrubia P, Ballesteros P, et al. Serial *in vivo* spectroscopic nuclear magnetic resonance imaging of lactate and extracellular pH in rat gliomas shows redistribution of protons away from sites of glycolysis. *Cancer Res* (2007) 67(16):7638–45. doi:10.1158/0008-5472.CAN-06-3459
291. Perez-Mayoral E, Negri V, Soler-Padros J, Cerdan S, Ballesteros P. Chemistry of paramagnetic and diamagnetic contrast agents for magnetic resonance imaging and spectroscopy pH responsive contrast agents. *Eur J Radiol* (2008) 67(3):453–8. doi:10.1016/j.ejrad.2008.02.048
292. Gallagher FA, Kettunen MI, Brindle KM. Imaging pH with hyperpolarized <sup>13</sup>C. *NMR Biomed* (2011) 24(8):1006–15. doi:10.1002/nbm.1742

293. Gallagher FA, Kettunen MI, Day SE, Hu DE, Ardenkjær-Larsen JH, Zandt R, et al. Magnetic resonance imaging of pH *in vivo* using hyperpolarized <sup>13</sup>C-labelled bicarbonate. *Nature* (2008) 453(7197):940–3. doi:10.1038/nature07017
294. Gallagher FA, Sladen H, Kettunen MI, Serrao EM, Rodrigues TB, Wright A, et al. Carbonic anhydrase activity monitored *in vivo* by hyperpolarized <sup>13</sup>C-magnetic resonance spectroscopy demonstrates its importance for pH regulation in tumors. *Cancer Res* (2015) 75(19):4109–18. doi:10.1158/0008-5472.CAN-15-0857
295. Moon BF, Jones KM, Chen LQ, Liu P, Randtke EA, Howison CM, et al. A comparison of iopromide and iopamidol, two acidOCEST MRI contrast media that measure tumor extracellular pH. *Contrast Media Mol Imaging* (2015) 10(6):446–55. doi:10.1002/cmmi.1647
296. Chen LQ, Randtke EA, Jones KM, Moon BF, Howison CM, Pagel MD. Evaluations of tumor acidosis within *in vivo* tumor models using parametric maps generated with acidO CEST MRI. *Mol Imaging Biol* (2015) 17(4):488–96. doi:10.1007/s11307-014-0816-2
297. Randtke EA, Granados JC, Howison CM, Pagel MD, Cardenas-Rodriguez J. Multislice CEST MRI improves the spatial assessment of tumor pH. *Magn Reson Med* (2016). doi:10.1002/mrm.26348
298. Vavere AL, Biddlecombe GB, Spees WM, Garbow JR, Wijesinghe D, Andreev OA, et al. A novel technology for the imaging of acidic prostate tumors by positron emission tomography. *Cancer Res* (2009) 69(10):4510–6. doi:10.1158/0008-5472.CAN-08-3781
299. Demoin DW, Wyatt LC, Edwards KJ, Abdel-Atti D, Sarparanta M, Pourat J, et al. PET imaging of extracellular pH in tumors with (64)Cu- and (18)F-labeled pHLIP peptides: a structure-activity optimization study. *Bioconjug Chem* (2016) 27(9):2014–23. doi:10.1021/acs.bioconjchem.6b00306
300. Viola-Villegas NT, Carlin SD, Ackerstaff E, Sevak KK, Divilov V, Serganova I, et al. Understanding the pharmacological properties of a metabolic PET tracer in prostate cancer. *Proc Natl Acad Sci U S A* (2014) 111(20):7254–9. doi:10.1073/pnas.1405240111
301. Macholl S, Morrison MS, Iveson P, Arbo BE, Andreev OA, Reshetnyak YK, et al. *In vivo* pH imaging with (99m)Tc-pHLIP. *Mol Imaging Biol* (2012) 14(6):725–34. doi:10.1007/s11307-012-0549-z
302. Martin GR, Jain RK. Noninvasive measurement of interstitial pH profiles in normal and neoplastic tissue using fluorescence ratio imaging microscopy. *Cancer Res* (1994) 54(21):5670–4.
303. Schrem S, Meier RJ, Wolfbeis OS, Landthaler M, Szeimies RM, Babilas P. 2D luminescence imaging of pH *in vivo*. *Proc Natl Acad Sci U S A* (2011) 108(6):2432–7. doi:10.1073/pnas.1006945108
304. Wang L, Fan Z, Zhang J, Changyi Y, Huang C, Gu Y, et al. Evaluating tumor metastatic potential by imaging intratumoral acidosis via pH-activatable near-infrared fluorescent probe. *Int J Cancer* (2015) 136(4):E107–16. doi:10.1002/ijc.29153
305. Shirmanova MV, Druzhkova IN, Lukina MM, Matlashov ME, Belousov VV, Snopova LB, et al. Intracellular pH imaging in cancer cells *in vitro* and tumors *in vivo* using the new genetically encoded sensor SypHer2. *Biochim Biophys Acta* (2015) 1850(9):1905–11. doi:10.1016/j.bbagen.2015.05.001
306. Chen Q, Liu X, Chen J, Zeng J, Cheng Z, Liu Z. A self-assembled albumin-based nanoprobe for *in vivo* ratiometric photoacoustic pH imaging. *Adv Mater* (2015) 27(43):6820–7. doi:10.1002/adma.201503194
307. Song J, Kim J, Hwang S, Jeon M, Jeong S, Kim C, et al. “Smart” gold nanoparticles for photoacoustic imaging: an imaging contrast agent responsive to the cancer microenvironment and signal amplification via pH-induced aggregation. *Chem Commun (Camb)* (2016) 52(53):8287–90. doi:10.1039/c6cc03100e
308. Khrantsov VV, Grigor'ev IA, Foster MA, Lurie DJ, Nicholson I. Biological applications of spin pH probes. *Cell Mol Biol (Noisy-le-grand)* (2000) 46(8):1361–74.
309. Samoilov A, Efimova OV, Bobko AA, Sun Z, Petryakov S, Eubank TD, et al. *In vivo* proton-electron double-resonance imaging of extracellular tumor pH using an advanced nitroxide probe. *Anal Chem* (2014) 86(2):1045–52. doi:10.1021/ac402230h
310. Chen Y, Ai K, Liu J, Sun G, Yin Q, Lu L. Multifunctional envelope-type mesoporous silica nanoparticles for pH-responsive drug delivery and magnetic resonance imaging. *Biomaterials* (2015) 60:111–20. doi:10.1016/j.biomaterials.2015.05.003
311. Zhang S, Qian X, Zhang L, Peng W, Chen Y. Composition-property relationships in multifunctional hollow mesoporous carbon nanosystems for pH-responsive magnetic resonance imaging and on-demand drug release. *Nanoscale* (2015) 7(17):7632–43. doi:10.1039/c5nr00451a
312. Min KH, Min HS, Lee HJ, Park DJ, Yhee JY, Kim K, et al. pH-controlled gas-generating mineralized nanoparticles: a theranostic agent for ultrasound imaging and therapy of cancers. *ACS Nano* (2015) 9(1):134–45. doi:10.1021/nn506210a
313. Lv R, Yang P, He F, Gai S, Yang G, Dai Y, et al. An imaging-guided platform for synergistic photodynamic/photothermal/chemo-therapy with pH/temperature-responsive drug release. *Biomaterials* (2015) 63:115–27. doi:10.1016/j.biomaterials.2015.05.016
314. Yu Q, Liu Y, Cao C, Le F, Qin X, Sun D, et al. The use of pH-sensitive functional selenium nanoparticles shows enhanced *in vivo* VEGF-siRNA silencing and fluorescence imaging. *Nanoscale* (2014) 6(15):9279–92. doi:10.1039/c4nr02423k
315. Bougnaud S, Golebiewska A, Oudin A, Keunen O, Harter PN, Mader L, et al. Molecular crosstalk between tumour and brain parenchyma instructs histopathological features in glioblastoma. *Oncotarget* (2016) 7(22):31955–71. doi:10.18632/oncotarget.7454
316. Ungefroren H, Sebens S, Seidl D, Lehnert H, Hass R. Interaction of tumor cells with the microenvironment. *Cell Commun Signal* (2011) 9:18. doi:10.1186/1478-811X-9-18
317. Langley RR, Fidler IJ. The seed and soil hypothesis revisited – the role of tumor-stroma interactions in metastasis to different organs. *Int J Cancer* (2011) 128(11):2527–35. doi:10.1002/ijc.26031
318. Witz IP. Tumor-microenvironment interactions: dangerous liaisons. *Adv Cancer Res* (2008) 100:203–29. doi:10.1016/S0006-230X(08)00007-9
319. Pietras K, Ostman A. Hallmarks of cancer: interactions with the tumor stroma. *Exp Cell Res* (2010) 316(8):1324–31. doi:10.1016/j.yexcr.2010.02.045
320. McMillin DW, Negri JM, Mitsiadis CS. The role of tumour-stromal interactions in modifying drug response: challenges and opportunities. *Nat Rev Drug Discov* (2013) 12(3):217–28. doi:10.1038/nrd3870
321. Bhowmick NA, Moses HL. Tumor-stroma interactions. *Curr Opin Genet Dev* (2005) 15(1):97–101. doi:10.1016/j.gde.2004.12.003
322. Bruno S, Collino F, Iavello A, Camussi G. Effects of mesenchymal stromal cell-derived extracellular vesicles on tumor growth. *Front Immunol* (2014) 5:382. doi:10.3389/fimmu.2014.00382
323. Lee J, Condello S, Yakubov B, Emerson R, Caperell-Grant A, Hitomi K, et al. Tissue transglutaminase mediated tumor-stroma interaction promotes pancreatic cancer progression. *Clin Cancer Res* (2015) 21(19):4482–93. doi:10.1158/1078-0432.CCR-15-0226
324. Gangadhara S, Barrett-Lee P, Nicholson RI, Hiscox S. Pro-metastatic tumor-stroma interactions in breast cancer. *Future Oncol* (2012) 8(11):1427–42. doi:10.2217/fon.12.134
325. Luga V, Wrana JL. Tumor-stroma interaction: revealing fibroblast-secreted exosomes as potent regulators of Wnt-planar cell polarity signaling in cancer metastasis. *Cancer Res* (2013) 73(23):6843–7. doi:10.1158/0008-5472.CAN-13-1791
326. Zhao H, Yang L, Baddour J, Achreja A, Bernard V, Moss T, et al. Tumor microenvironment derived exosomes pleiotropically modulate cancer cell metabolism. *Elife* (2016) 5:e10250. doi:10.7554/elife.10250
327. Holton SE, Bergamaschi A, Katzenellenbogen BS, Bhargava R. Integration of molecular profiling and chemical imaging to elucidate fibroblast-microenvironment impact on cancer cell phenotype and endocrine resistance in breast cancer. *PLoS One* (2014) 9(5):e96878. doi:10.1371/journal.pone.0096878
328. Ackerstaff E, Artemov D, Gillies RJ, Bhujwalla ZM. Hypoxia and the presence of human vascular endothelial cells affect prostate cancer cell invasion and metabolism. *Neoplasia* (2007) 9(12):1138–51. doi:10.1593/neop.07568
329. Gillies RJ, Galons JP, McGovern KA, Scherer PG, Lien YH, Job C, et al. Design and application of NMR-compatible bioreactor circuits for extended perfusion of high-density mammalian cell cultures. *NMR Biomed* (1993) 6(1):95–104. doi:10.1002/nbm.1940060115
330. Peng X, Recchia FA, Byrne BJ, Wittstein IS, Ziegelstein RC, Kass DA. *In vitro* system to study realistic pulsatile flow and stretch signaling in cultured vascular cells. *Am J Physiol Cell Physiol* (2000) 279(3):C797–805.

331. Casbas-Hernandez P, Fleming JM, Troester MA. Gene expression analysis of *in vitro* cocultures to study interactions between breast epithelium and stroma. *J Biomed Biotechnol* (2011) 2011:520987. doi:10.1155/2011/520987
332. Angelucci C, Maulucci G, Lama G, Proietti G, Colabianchi A, Papi M, et al. Epithelial-stromal interactions in human breast cancer: effects on adhesion, plasma membrane fluidity and migration speed and directness. *PLoS One* (2012) 7(12):e50804. doi:10.1371/journal.pone.0050804
333. Li H, Zhang J, Chen SW, Liu LL, Li L, Gao F, et al. Cancer-associated fibroblasts provide a suitable microenvironment for tumor development and progression in oral tongue squamous cancer. *J Transl Med* (2015) 13:198. doi:10.1186/s12967-015-0551-8
334. Icard P, Kafara P, Steyaert JM, Schwartz L, Lincet H. The metabolic cooperation between cells in solid cancer tumors. *Biochim Biophys Acta* (2014) 1846(1):216–25. doi:10.1016/j.bbcan.2014.06.002
335. Hagemann T, Robinson SC, Schulz M, Trumper L, Balkwill FR, Binder C. Enhanced invasiveness of breast cancer cell lines upon co-cultivation with macrophages is due to TNF-alpha dependent up-regulation of matrix metalloproteases. *Carcinogenesis* (2004) 25(8):1543–9. doi:10.1093/carcin/bgh146
336. Giatromanolaki A, Koukourakis MI, Koutsopoulos A, Mendrinos S, Sivridis E. The metabolic interactions between tumor cells and tumor-associated stroma (TAS) in prostatic cancer. *Cancer Biol Ther* (2012) 13(13):1284–9. doi:10.4161/cbt.21785
337. Morandi A, Chiarugi P. Metabolic implication of tumor:stroma crosstalk in breast cancer. *J Mol Med (Berl)* (2014) 92(2):117–26. doi:10.1007/s00109-014-1124-7
338. Choi J, Kim DH, Jung WH, Koo JS. Metabolic interaction between cancer cells and stromal cells according to breast cancer molecular subtype. *Breast Cancer Res* (2013) 15(5):R78. doi:10.1186/bcr3472
339. Guldner IH, Zhang S. A journey to uncharted territory: new technical frontiers in studying tumor-stromal cell interactions. *Integr Biol (Camb)* (2015) 7(2):153–61. doi:10.1039/c4ib00192c
340. Widder M, Lutzkendorf J, Caysa H, Unverzagt S, Wickenhauser C, Benndorf RA, et al. Multipotent mesenchymal stromal cells promote tumor growth in distinct colorectal cancer cells by a beta1-integrin-dependent mechanism. *Int J Cancer* (2015) 138(4):964–75. doi:10.1002/ijc.29844
341. Orimo A, Gupta PB, Sgroi DC, Arenzana-Seisdedos F, Delaunay T, Naeem R, et al. Stromal fibroblasts present in invasive human breast carcinomas promote tumor growth and angiogenesis through elevated SDF-1/CXCL12 secretion. *Cell* (2005) 121(3):335–48. doi:10.1016/j.cell.2005.02.034
342. Olumi AF, Grossfeld GD, Hayward SW, Carroll PR, Tlsty TD, Cunha GR. Carcinoma-associated fibroblasts direct tumor progression of initiated human prostate epithelium. *Cancer Res* (1999) 59(19):5002–11. doi:10.1371/journal.pone.0068923
343. Subramaniam KS, Omar IS, Kwong SC, Mohamed Z, Woo YL, Mat Adenan NA, et al. Cancer-associated fibroblasts promote endometrial cancer growth via activation of interleukin-6/STAT-3/c-Myc pathway. *Am J Cancer Res* (2016) 6(2):200–13.
344. Domanska UM, Timmer-Bosscha H, Nagengast WB, Oude Munnink TH, Kruizinga RC, Ananias HJ, et al. CXCR4 inhibition with AMD3100 sensitizes prostate cancer to docetaxel chemotherapy. *Neoplasia* (2012) 14(8):709–18. doi:10.1593/neo.12324
345. McMillin DW, Delmore J, Weisberg E, Negri JM, Geer DC, Klipfel S, et al. Tumor cell-specific bioluminescence platform to identify stroma-induced changes to anticancer drug activity. *Nat Med* (2010) 16(4):483–9. doi:10.1038/nm.2112
346. Sebens S, Schafer H. The tumor stroma as mediator of drug resistance – a potential target to improve cancer therapy? *Curr Pharm Biotechnol* (2012) 13(11):2259–72. doi:10.2174/138920112802501999
347. Maeda A, Kubatski I, DaCosta RS. Emerging applications for optically enabled intravital microscopic imaging in radiobiology. *Mol Imaging* (2015) 14(9):452–74.
348. Hoffman RM. Imaging tumor angiogenesis with fluorescent proteins. *APMIS* (2004) 112(7–8):441–9. doi:10.1111/j.1600-0463.2004.apm11207-0806.x
349. Yang M, Jiang P, Hoffman RM. Whole-body subcellular multicolor imaging of tumor-host interaction and drug response in real time. *Cancer Res* (2007) 67(11):5195–200. doi:10.1158/0008-5472.CAN-06-4590
350. Wyckoff J, Wang W, Lin EY, Wang Y, Pixley F, Stanley ER, et al. A paracrine loop between tumor cells and macrophages is required for tumor cell migration in mammary tumors. *Cancer Res* (2004) 64(19):7022–9. doi:10.1158/0008-5472.CAN-04-1449
351. Dovas A, Patsialou A, Harney AS, Condeelis J, Cox D. Imaging interactions between macrophages and tumour cells that are involved in metastasis *in vivo* and *in vitro*. *J Microsc* (2013) 251(3):261–9. doi:10.1111/j.1365-2818.2012.03667.x
352. Perentes JY, McKee TD, Ley CD, Mathew H, Dawson M, Padera TP, et al. *In vivo* imaging of extracellular matrix remodeling by tumor-associated fibroblasts. *Nat Methods* (2009) 6(2):143–5. doi:10.1038/nmeth.1295
353. Nakasone ES, Askautrud HA, Kees T, Park JH, Plaks V, Ewald AJ, et al. Imaging tumor-stroma interactions during chemotherapy reveals contributions of the microenvironment to resistance. *Cancer Cell* (2012) 21(4):488–503. doi:10.1016/j.ccr.2012.02.017
354. Nakasone ES, Askautrud HA, Egeblad M. Live imaging of drug responses in the tumor microenvironment in mouse models of breast cancer. *J Vis Exp* (2013) 73:e50088. doi:10.3791/50088
355. Ewald AJ, Werb Z, Egeblad M. Dynamic, long-term *in vivo* imaging of tumor-stroma interactions in mouse models of breast cancer using spinning-disk confocal microscopy. *Cold Spring Harb Protoc* (2011) 2011(2):db.2011. doi:10.1101/pdb.top97
356. Cherry SR. The 2006 Henry N. Wagner lecture: of mice and men (and positrons) – advances in PET imaging technology. *J Nucl Med* (2006) 47(11):1735–45.
357. Judenhofer MS, Catana C, Swann BK, Siegel SB, Jung WI, Nutt RE, et al. PET/MR images acquired with a compact MR-compatible PET detector in a 7-T magnet. *Radiology* (2007) 244(3):807–14. doi:10.1148/radiol.2443061756
358. Catana C, Wu Y, Judenhofer MS, Qi J, Pichler BJ, Cherry SR. Simultaneous acquisition of multislice PET and MR images: initial results with a MR-compatible PET scanner. *J Nucl Med* (2006) 47(12):1968–76.
359. O'Halloran PJ, Viel T, Murray DW, Wachsmuth L, Schwegmann K, Wagner S, et al. Mechanistic interrogation of combination bevacizumab/dual PI3K/mTOR inhibitor response in glioblastoma implementing novel MR and PET imaging biomarkers. *Eur J Nucl Med Mol Imaging* (2016) 43(9):1673–83. doi:10.1007/s00259-016-3343-3
360. Garland M, Yim JJ, Bogyo M. A bright future for precision medicine: advances in fluorescent chemical probe design and their clinical application. *Cell Chem Biol* (2016) 23(1):122–36. doi:10.1016/j.chembiol.2015.12.003

**Conflict of Interest Statement:** The authors declare that the research was conducted in the absence of any commercial or financial relationships that could be construed as a potential conflict of interest.

Copyright © 2017 Ramamonjisoa and Ackerstaff. This is an open-access article distributed under the terms of the Creative Commons Attribution License (CC BY). The use, distribution or reproduction in other forums is permitted, provided the original author(s) or licensor are credited and that the original publication in this journal is cited, in accordance with accepted academic practice. No use, distribution or reproduction is permitted which does not comply with these terms.



# Potential of Induced Metabolic Bioluminescence Imaging to Uncover Metabolic Effects of Antiangiogenic Therapy in Tumors

Stefano Indraccolo<sup>1\*</sup> and Wolfgang Mueller-Klieser<sup>2</sup>

<sup>1</sup> Immunology and Molecular Oncology Unit, Istituto Oncologico Veneto – IRCCS, Padova, Italy, <sup>2</sup> University Medical Center of the Johannes Gutenberg University, Institute of Pathophysiology, Mainz, Germany

## OPEN ACCESS

**Edited by:**

Zaver Bhujwalla,  
Johns Hopkins University  
School of Medicine, USA

**Reviewed by:**

Paul Thomas Winnard Jr.,  
Johns Hopkins University  
School of Medicine, USA  
Pierre Danhier,  
Université Catholique de Louvain,  
Belgium

**\*Correspondence:**

Stefano Indraccolo  
stefano.indraccolo@unipd.it

**Specialty section:**

This article was submitted to Cancer Imaging and Diagnosis, a section of the journal Frontiers in Oncology

**Received:** 13 November 2015

**Accepted:** 14 January 2016

**Published:** 01 February 2016

**Citation:**

Indraccolo S and Mueller-Klieser W (2016) Potential of Induced Metabolic Bioluminescence Imaging to Uncover Metabolic Effects of Antiangiogenic Therapy in Tumors. *Front. Oncol.* 6:15.  
doi: 10.3389/fonc.2016.00015

Tumor heterogeneity at the genetic level has been illustrated by a multitude of studies on the genomics of cancer, but whether tumors can be heterogeneous at the metabolic level is an issue that has been less systematically investigated so far. A burning-related question is whether the metabolic features of tumors can change either following natural tumor progression (i.e., in primary tumors versus metastasis) or therapeutic interventions. In this regard, recent findings by independent teams indicate that antiangiogenic drugs cause metabolic perturbations in tumors as well as metabolic adaptations associated with increased malignancy. Induced metabolic bioluminescence imaging (imBI) is an imaging technique that enables detection of key metabolites associated with glycolysis, including lactate, glucose, pyruvate, and ATP in tumor sections. Signals captured by imBI can be used to visualize the topographic distribution of these metabolites and quantify their absolute amount. imBI can be very useful for metabolic classification of tumors as well as to track metabolic changes in the glycolytic pathway associated with certain therapies. Imaging of the metabolic changes induced by antiangiogenic drugs in tumors by imBI or other emerging technologies is a valuable tool to uncover molecular sensors engaged by metabolic stress and offers an opportunity to understand how metabolism-based approaches could improve cancer therapy.

**Keywords:** angiogenesis, metabolism, imaging, glycolysis, cancer, mouse models

## INTRODUCTION

Malignant tumors are endowed with distinct metabolic features that distinguish them from the normal cells of the tissue where they arise. Major metabolic alterations in tumors include enhanced glucose uptake and lactate production, increased glutamine utilization and *de novo* fatty acid synthesis, as well as aberrant choline and serine metabolism (1, 2). Tumor heterogeneity – best known at the genetic level – has recently been illustrated also at the metabolic level by a number of different approaches (3, 4). Still largely unknown is whether metabolic features of tumors are stable

**Abbreviations:** H&E, hematoxylin and eosin; HIF, hypoxia inducible factor; imBI, induced metabolic bioluminescence imaging; NMR, nuclear magnetic resonance; PET, positron emission tomography; VEGF, vascular endothelial growth factor.

or can change either following natural tumor progression (i.e., in primary tumors versus metastasis) or therapeutic interventions.

Antiangiogenic therapy is a consolidated approach to treat cancer. By targeting the tumor-associated microvasculature, antiangiogenic drugs – especially blocking signaling downstream of vascular endothelial growth factor (VEGF)/VEGF receptors – cause vessel pruning, which is followed by hypoxia and reduced supply of other nutrients (5–8). Since antiangiogenic drugs do not have, in general, direct effects of tumor cells; the therapeutic activity of these drugs is almost entirely dependent on modulation of the supportive functions of the tumor microenvironment. Albeit still hypothetical, it is quite possible that the ability of tumor cells to adapt to the starving effects of antiangiogenic therapy – i.e., its metabolic effects – could be important to determine the therapeutic activity of these drugs.

Imaging techniques are extremely valuable both to perform metabolic profiling of tumors and to uncover metabolic fluctuations caused by drugs. With regard to antiangiogenic therapy, some of these techniques have been used to measure uptake of selected metabolites in tumors, such as positron emission tomography (PET) (9), whereas others, including hyperpolarized  $^{13}\text{C}$  spectroscopy (10) and proton nuclear magnetic resonance (NMR) (11), enabled quantitative assessment of certain metabolites in experimental tumors.

We were the first to exploit a technique termed induced metabolic bioluminescence imaging (imBI) to investigate metabolic perturbations associated with anti-VEGF therapy (9, 12). Notably, although somewhat limited by the small number of metabolites that can be analyzed, imBI provides an accurate representation of the steady-state levels of the metabolites, matching them to the histology of the tumor section. The rest of this chapter is devoted to the methodologic description of this valuable imaging technique and its applications in the field of tumor angiogenesis.

## THE TECHNIQUE FOR INDUCED METABOLIC BIOLUMINESCENCE IMAGING

### Specific Detection of Tissue Metabolites

The imBI technique was developed in the laboratory at the University of Mainz for the detection of metabolites in cryosections from snap-frozen tissue *in situ* (13–15). Self-made kits containing definite exogenous enzymes and cofactors are used to achieve high specificity and sensitivity. Endogenous enzyme activities in the tissue sections of interest are heat-inactivated immediately before imBI measurement to avoid interference with exogenous enzymes within the kit. To prevent the reactions from substrate saturation, all components of the kit are provided in excess. The enzymatic activity induced by the metabolite of interest in the target tissue is biochemically coupled to luciferases leading to light emission, i.e., to bioluminescence. This coupling, which involves the NAD(P)H $\text{+H}^+$  redox system, induces low level light emission with an intensity that is proportional to the respective metabolite. The biochemistry for the detection of ATP, glucose, pyruvate, and lactate *via* imBI is illustrated diagrammatically in Figure S1 in Supplementary Material. Since a specific enzyme

mixture has to be prepared for each metabolite of interest, the imBI technique allows for the detection of only one metabolite per section. On the other hand, section thickness is adjusted in most cases to values in the range of 10–20  $\mu\text{m}$ , and thus different metabolites can be determined in serial sections at a quasi-identical location within a tissue.

For processing of the tissue specimens, the frozen biopsy is embedded in Tissue-Tek® (O.C.T.™ Compound; Sakura Finetek Europe B.V., Alphen aan den Rijn, Netherlands) on a sample holder of a cryomicrotome (SLEE cryostat, Type MEV; SLEE, Mainz, Germany). Serial sectioning is then performed precisely at a temperature between  $-20$  and  $-12^\circ\text{C}$  depending on the tissue composition of the specimen. As indicated in the upper panel of **Figure 1A**, two parallel channels are driven into each biopsy by a specially designed “micro-fork.” Sectioning perpendicular to these channels leads to two holes in each section. These holes make it possible to precisely overlay sequential sections and, thus, to colocalize different parameter values in different adjacent sections.

### Localization of Tissue Metabolites

The spatial resolution of imBI is generated by a sandwich technique providing a homogeneous contact between enzyme cocktail and tissue section (**Figure 1A**). An excess volume of enzyme solution is pipetted into a casting mold within a metal slide. A cover glass with a tissue section adhered is laid upside-down onto the enzyme solution within the casting mold. This provides complete contact between tissue and enzyme solution, which has been kept in a liquid state at the measuring temperature. The contact between substrate and enzyme mixture then initiates the bioluminescence reaction. The sandwich is put on the thermostated stage of a microscope (Axiohot, Zeiss, Oberkochen, Germany) within a light-impervious chamber. An ultrasensitive back-illuminated EM-CCD camera (iXonEM<sup>+</sup> DU-888; Andor Technology PLC, Belfast, UK) connected to the microscope enables the registration of the low light bioluminescence intensity with the optics focused on the tissue section plane. The image signal is transferred to a computer for image analysis. By integrating the light emission intensities over a selected time interval, a two-dimensional density profile is obtained representing the two-dimensional metabolite distribution across the tissue section.

### Quantification of Tissue Metabolites

Using appropriate standards, which are handled in exactly the same way as the tissue of interest, bioluminescence intensities can be transformed into absolute tissue concentrations of the respective metabolite, e.g., in micromoles per gram of tissue, which corresponds approximately to millimolar in solution. Routine standards are obtained by mixing cryo-embedding medium (Tissue-Tek®) with defined amounts of substrate. The frozen medium is then cryosectioned and processed in the same way as the tissue of interest.

The calibration allows for the illustration of the two-dimensional substrate distribution in a color-coded manner, as indicated in **Figure 1A** (lower panel). This procedure is applicable to all metabolites specified above.

It is obvious that the light intensity is also influenced by the microscopic magnification, since pixel density per unit image area

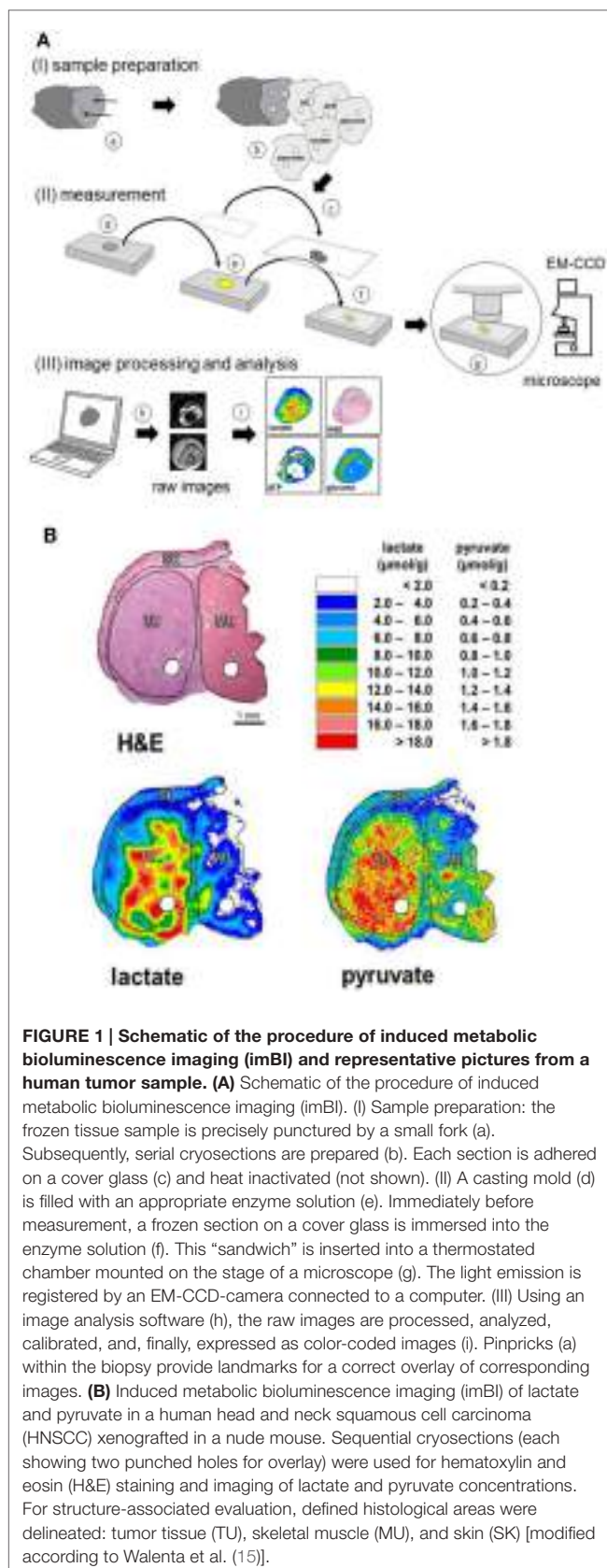


**FIGURE 1 | Schematic of the procedure of induced metabolic bioluminescence imaging (imBI) and representative pictures from a human tumor sample. (A)** Schematic of the procedure of induced metabolic bioluminescence imaging (imBI). (I) Sample preparation: the frozen tissue sample is precisely punctured by a small fork (a). Subsequently, serial cryosections are prepared (b). Each section is adhered on a cover glass (c) and heat inactivated (not shown). (II) A casting mold (d) is filled with an appropriate enzyme solution (e). Immediately before measurement, a frozen section on a cover glass is immersed into the enzyme solution (f). This "sandwich" is inserted into a thermostated chamber mounted on the stage of a microscope (g). The light emission is registered by an EM-CCD-camera connected to a computer. (III) Using an image analysis software (h), the raw images are processed, analyzed, calibrated, and, finally, expressed as color-coded images (i). Pinpricks (a) within the biopsy provide landmarks for a correct overlay of corresponding images. **(B)** Induced metabolic bioluminescence imaging (imBI) of lactate and pyruvate in a human head and neck squamous cell carcinoma (HNSCC) xenografted in a nude mouse. Sequential cryosections (each showing two punched holes for overlay) were used for hematoxylin and eosin (H&E) staining and imaging of lactate and pyruvate concentrations. For structure-associated evaluation, defined histological areas were delineated: tumor tissue (TU), skeletal muscle (MU), and skin (SK) [modified according to Walenta et al. (15)].

and, hence, light intensity is much lower at a high magnification and *vice versa*. Other factors with impact on light intensity are the viscosity of the enzyme solution, the measuring temperature, the light integration interval, or the quantum efficiency of the bioluminescence reaction itself. And all these factors are mutually related and not at all independent of each other. In essence, the concert of these factors determines the sensitivity of the technique being on the micromolar level.

## Combined Quantification and Localization of Metabolites

High sensitivity and high spatial resolution are contradicting demands, but the advantage of imBI is its versatility in adjusting the measuring conditions toward either resolution or sensitivity depending on the requirements of an actual experiment. Spatial resolution is restricted at a low viscosity and high temperature of the enzyme solution and at long light integration interval. Such conditions favor lateral diffusion of metabolites and enzymes resulting in a "smearing out" the gradients in the metabolic profiles.

For most measurements in tumor biopsies, experimental settings are chosen in a way that the minimum detectable substrate concentration is around 100 µmol/g with a spatial linear resolution of around 100 µm. Keeping the former sensitivity of detection, the spatial resolution can be adjusted to 20 µm in imaging metabolic gradients in multicellular spheroids adjusting an appropriate registration temperature and viscosity of the enzyme solution.

In our routine technology, as described above, the minimum detectable substrate concentration is around 100 µmol/g of viable tissue. Taking a given thickness of the cryosection used of 10 µm and a section area of 1 cm<sup>2</sup>, this corresponds to a minimum detectable absolute amount of substrate (i.e., the substrate content of one cryosection) of around 10 pg. By reducing the section thickness, increasing the enzyme components in the detection cocktails and optimizing the photon registration technique, it is possible to detect minimum substrate concentrations in the nanomolar per gram range.

## Structure-Associated Metabolite Detection and Colocalization

Using serial sections, a section can be stained for the histological structure, e.g., with hematoxylin and eosin (H&E) followed by sections stained for the various metabolites. As outlined above, the "two holes technique" allows for an exact, computer-assisted overlay between the sections. Such an overlay makes it possible to detect the bioluminescence signals in a structure-associated way, i.e., within selected histological areas, such as viable tumor regions, stromal areas, or necrosis. The strategy is exemplified in Figure 1B.

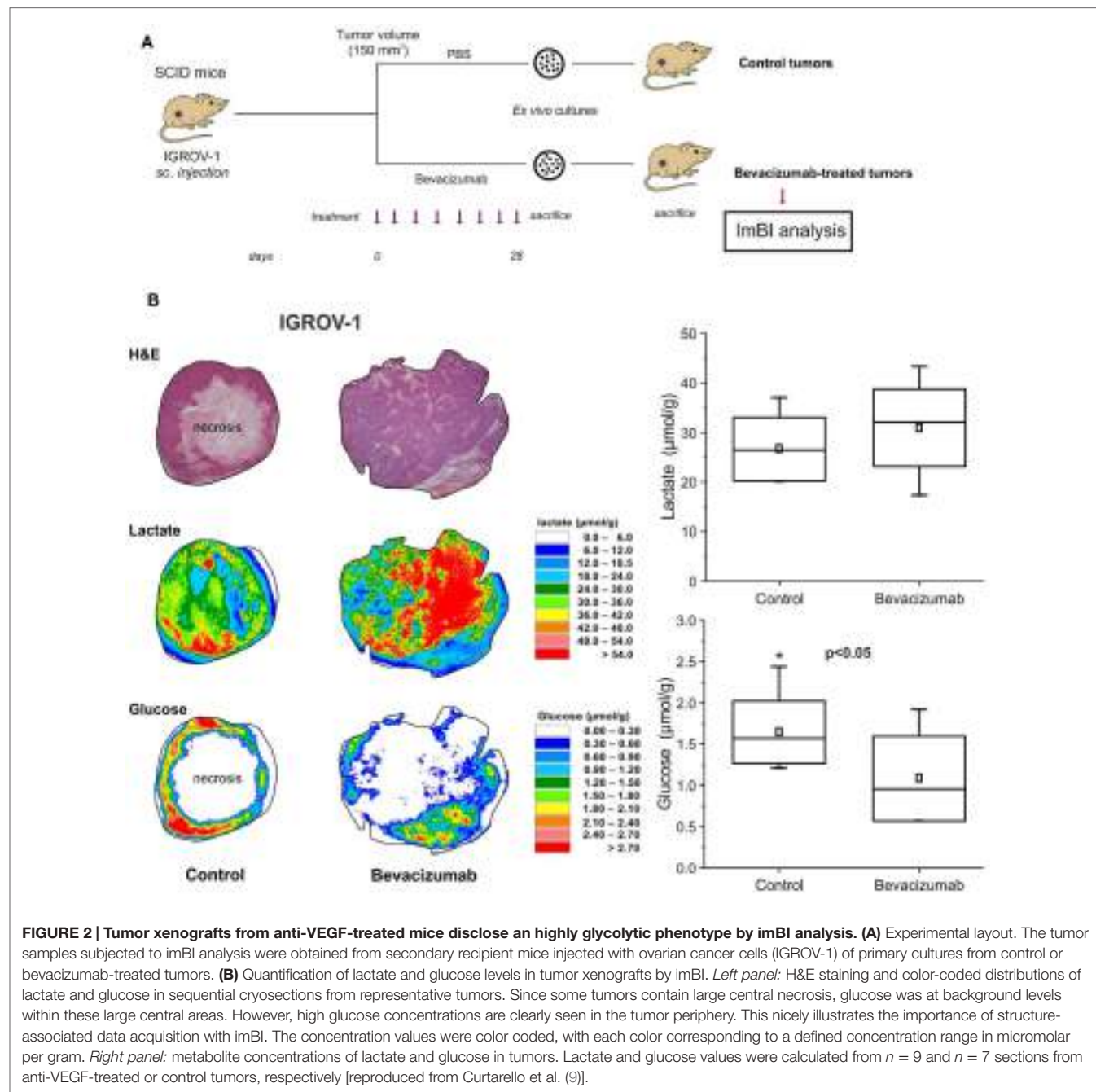
Colocalization studies can be extended to virtually all parameters that can be visualized in cryosections, e.g., mRNAs detected by *in situ* hybridization, proteins assessed by immunostaining or functional parameters, such as blood perfusion imaged by fluorescent stains or hypoxic cells identified by pimonidazole (16).

## APPLICATIONS OF imBI IN THE FIELD OF TUMOR ANGIOGENESIS

Induced metabolic bioluminescence imaging proved to be an extremely useful technique to investigate modulations in the concentration of metabolites in tumors treated with antiangiogenic drugs (Figure 2). In tumor xenografts, we observed a dramatic reduction in glucose and ATP levels in the tumor microenvironment following anti-VEGF therapy (12). Such changes led us to speculate that glucose-addicted tumors could be particularly vulnerable to the effects of VEGF blockade. In fact, the amount

of necrotic area in the highly glycolytic tumors was much larger compared with values found in poorly glycolytic tumors, thus connecting a metabolic trait of tumor cells to an histological pattern of response to VEGF neutralization.

It is currently unknown whether this intriguing observation might hold true also in the case of other angiogenesis inhibitors acting downstream of the VEGF receptor, such as tyrosine kinase inhibitors, nor whether the findings can be generalized to tumors grown in different organs/tissues, as tissue-specific features of the microvasculature could also impact on the outcome of VEGF blockade. Despite these limitations, it should be acknowledged



that imBI was key to enable us to formulate the initial hypothesis. To further validate it in translational studies, it will probably be necessary to replace assessment of the tumor glycolytic phenotype by imBI – which requires frozen tissues – with an appropriate *in situ* marker of glycolysis, such as monocarboxylate transporter 4 (MCT4), which could be assessed by routine immunohistochemistry staining in hundreds of formalin-fixed paraffin-embedded (FFPE) tumor samples.

In addition, imBI could be used to perform metabolic classification of tumors and compare *in vitro* and *in vivo* assessment of metabolic features, as we recently showed (17). Given the adequate spatial resolution of this technique (~100 µm), and the possibility of matching metabolic parameters with histology, it can be anticipated that imBI could be utilized to describe both inter-tumor and intra-tumor metabolic heterogeneity, as first step of an in-depth characterization of tumor regions with different abundance of lactate or other measurable metabolites.

In summary, imBI has a clear role in preclinical studies of tumor angiogenesis in that it can (I) be utilized to investigate metabolic modulations associated with antiangiogenic therapy and (II) can enable metabolic classification of tumors and detect metabolic heterogeneity.

## CONCLUDING REMARKS

A more comprehensive understanding of metabolic perturbations caused by antiangiogenic drugs in tumors might represent a first step toward improvement of therapeutic efficacy, which is currently blunted by adaptive resistance (18, 19). Along this line, recent studies reported perturbations in lipid metabolism under hypoxic conditions. Bensaad et al. described increased fatty acids uptake and accumulation of lipid droplets in the cytoplasm of tumor cells incubated under hypoxic conditions or in tumors treated with bevacizumab (20); this phenomenon was associated with hypoxia inducible factor (HIF)-1α-driven expression of fatty acids binding proteins 3 and 7 in tumor cells. Moreover, Huang et al. observed that hypoxic stress regulates lipid metabolism in hepatocellular carcinoma cells. Specifically, these authors reported that HIF-1-mediated suppression of medium and long-chain acyl-CoA dehydrogenases and fatty acid oxidation leads to fatty acids accumulation and is critical for cancer progression (21). As antiangiogenic therapy generally increases tumor hypoxia, in future studies, it will be important to further investigate whether anti-VEGF therapy causes perturbations in lipids.

In the long-term, metabolic changes caused by anti-VEGF therapy could indeed represent an opportunity for new

metabolism-targeting drugs. In this regard, our previous studies (9, 12) showed that tumor xenografts formed by different tumor cell lines have marked metabolic differences, which would likely convey limited therapeutic response to glycolysis inhibitors (Figure 2). In contrast, after antiangiogenic therapy tumors become homogeneously highly glycolytic and glucose addicted, which could render them more responsive to glycolysis-targeting drugs. In a related study, Sounni et al. demonstrated that breast tumors treated with antiangiogenic tyrosine kinase inhibitors (sunitinib) in the post-treatment time undergo a metabolic shift involving increased lipid synthesis and have improved response to the lipogenesis inhibitor orlistat (22). Altogether, these observations suggest that sequential combination of antiangiogenic drugs and certain metabolism-targeting drugs might represent a new therapeutic concept for cancer.

With regard to imBI, its successful application in the field of glucose metabolism should encourage set-up of new protocols for the detection of additional metabolites, such as amino acids and fatty acids. The imBI technique is indeed appropriate for the detection of any metabolite that can be enzymatically linked to the NAD(P)H<sup>+</sup>H<sup>+</sup> redox system. This offers the opportunity to analyze a broad spectrum of metabolic pathways beyond glycolysis. For example, lipid metabolism may be investigated by quantifying L-3-hydroxyacyl-CoA with imBI using hydroxyacyl-CoA-dehydrogenase as an enzymatic link. Similarly, ketogenesis may be studied by the detection of acetoacetate using beta-hydroxybutyrate dehydrogenase.

In conclusion, in the near future, it will be feasible to use imBI to achieve an integrated view on serial tumor sections of the metabolic pathways active in individual tumors and their variations following targeted therapies.

## AUTHOR CONTRIBUTIONS

SI and WM-K wrote and edited the text.

## FUNDING

This work was supported by grants from AIRC (IG grant 14295), the Deutsche Forschungsgemeinschaft (Mu 576/15-1, 15-2), and by the German Federal Ministry of Education and Research (“ISIMEP”; 02NUK016A).

## SUPPLEMENTARY MATERIAL

The Supplementary Material for this article can be found online at <http://journal.frontiersin.org//article/10.3389/fonc.2016.00015>

## REFERENCES

- DeBerardinis RJ, Lum JJ, Hatzivassiliou G, Thompson CB. The biology of cancer: metabolic reprogramming fuels cell growth and proliferation. *Cell Metab* (2008) 7:11–20. doi:10.1016/j.cmet.2007.10.002
- Dang CV. Links between metabolism and cancer. *Genes Dev* (2012) 26:877–90. doi:10.1101/gad.189365.112
- Cantor JR, Sabatini DM. Cancer cell metabolism: one hallmark, many faces. *Cancer Discov* (2012) 2:881–98. doi:10.1158/2159-8290.CD-12-0345
- Pribluda A, de la Cruz CC, Jackson EL. Intratumoral heterogeneity: from diversity comes resistance. *Clin Cancer Res* (2015) 21:2916–23. doi:10.1158/1078-0432.CCR-14-1213
- Grothey A, Galanis E. Targeting angiogenesis: progress with anti-VEGF treatment with large molecules. *Nat Rev Clin Oncol* (2009) 6:507–18. doi:10.1038/nrclinonc.2009.110
- Heath VL, Bicknell R. Anticancer strategies involving the vasculature. *Nat Rev Clin Oncol* (2009) 6:395–404. doi:10.1038/nrclinonc.2009.52

7. Carmeliet P, Jain RK. Principles and mechanisms of vessel normalization for cancer and other angiogenic diseases. *Nat Rev Drug Discov* (2011) **10**:417–27. doi:10.1038/nrd3455
8. Jayson GC, Hicklin DJ, Ellis LM. Antiangiogenic therapy – evolving view based on clinical trial results. *Nat Rev Clin Oncol* (2012) **9**:297–303. doi:10.1038/nrclinonc.2012.8
9. Curtarello M, Zulato E, Nardo G, Valtorta S, Guzzo G, Rossi E, et al. VEGF-targeted therapy stably modulates the glycolytic phenotype of tumor cells. *Cancer Res* (2015) **75**:120–33. doi:10.1158/0008-5472.CAN-13-2037
10. Bohndiek SE, Kettunen MI, Hu DE, Brindle KM. Hyperpolarized (13)C spectroscopy detects early changes in tumor vasculature and metabolism after VEGF neutralization. *Cancer Res* (2012) **72**:854–64. doi:10.1158/0008-5472
11. Keunen O, Johansson M, Oudin A, Sanzey M, Rahim SA, Fack F, et al. Anti-VEGF treatment reduces blood supply and increases tumor cell invasion in glioblastoma. *Proc Natl Acad Sci U S A* (2011) **108**:3749–54. doi:10.1073/pnas.1014480108
12. Nardo G, Favaro E, Curtarello M, Moserle L, Zulato E, Persano L, et al. Glycolytic phenotype and AMP kinase modify the pathologic response of tumor xenografts to VEGF neutralization. *Cancer Res* (2011) **71**:4214–25. doi:10.1158/0008-5472.CAN-11-0242
13. Walenta S, Mueller-Klieser WF. Lactate: mirror and motor of tumor malignancy. *Semin Radiat Oncol* (2004) **14**:267–74. doi:10.1016/j.semradonc.2004.04.004
14. Walenta S, Schroeder T, Mueller-Klieser W. Lactate in solid malignant tumors: potential basis of a metabolic classification in clinical oncology. *Curr Med Chem* (2004) **11**:2195–204. doi:10.2174/0929867043364711
15. Walenta S, Voelken NF, Sattler UGA, Mueller-Klieser W. Localizing and quantifying metabolites in situ with luminometry: induced metabolic bioluminescence imaging (imBI). In: Hirrlinger WH, editor. *Brain Energy Metabolism*. New York: Humana Press (Springer) (2014). p. 195–216.
16. Yaromina A, Quennet V, Zips D, Meyer S, Shakirin G, Walenta S, et al. Co-localisation of hypoxia and perfusion markers with parameters of glucose metabolism in human squamous cell carcinoma (hSCC) xenografts. *Int J Radiat Biol* (2009) **85**:972–80. doi:10.3109/09553000903232868
17. Fabian C, Koetz L, Favaro E, Indraccolo S, Mueller-Klieser W, Sattler UG. Protein profiles in human ovarian cancer cell lines correspond to their metabolic activity and to metabolic profiles of respective tumor xenografts. *FEBS J* (2012) **279**:882–91. doi:10.1111/j.1742-4658.2012.08479.x
18. Bergers G, Hanahan D. Modes of resistance to anti-angiogenic therapy. *Nat Rev Cancer* (2008) **8**:592–603. doi:10.1038/nrc2442
19. Bottsford-Miller JN, Coleman RL, Sood AK. Resistance and escape from antiangiogenesis therapy: clinical implications and future strategies. *J Clin Oncol* (2012) **30**:4026–34. doi:10.1200/JCO.2012.41.9242
20. Bensaad K, Favaro E, Lewis CA, Peck B, Lord S, Collins JM, et al. Fatty acid uptake and lipid storage induced by HIF-1alpha contribute to cell growth and survival after hypoxia-reoxygenation. *Cell Rep* (2014) **9**:349–65. doi:10.1016/j.celrep.2014.08.056
21. Huang D, Li T, Li X, Zhang L, Sun L, He X, et al. HIF-1-mediated suppression of acyl-CoA dehydrogenases and fatty acid oxidation is critical for cancer progression. *Cell Rep* (2014) **8**:1930–42. doi:10.1016/j.celrep.2014.08.028
22. Sounni NE, Cimino J, Blacher S, Primac I, Truong A, Mazzucchelli G, et al. Blocking lipid synthesis overcomes tumor regrowth and metastasis after antiangiogenic therapy withdrawal. *Cell Metab* (2014) **20**:280–94. doi:10.1016/j.cmet.2014.05.022

**Conflict of Interest Statement:** The authors declare that the research was conducted in the absence of any commercial or financial relationships that could be construed as a potential conflict of interest.

Copyright © 2016 Indraccolo and Mueller-Klieser. This is an open-access article distributed under the terms of the Creative Commons Attribution License (CC BY). The use, distribution or reproduction in other forums is permitted, provided the original author(s) or licensor are credited and that the original publication in this journal is cited, in accordance with accepted academic practice. No use, distribution or reproduction is permitted which does not comply with these terms.



# Activation of Phosphatidylcholine-Specific Phospholipase C in Breast and Ovarian Cancer: Impact on MRS-Detected Choline Metabolic Profile and Perspectives for Targeted Therapy

Franca Podo<sup>1\*</sup>, Luisa Paris<sup>1</sup>, Serena Cecchetti<sup>1</sup>, Francesca Spadaro<sup>1</sup>, Laura Abalsamo<sup>1</sup>, Carlo Ramoni<sup>1</sup>, Alessandro Ricci<sup>1</sup>, Maria Elena Pisani<sup>1</sup>, Francesco Sardanelli<sup>2</sup>, Rossella Canese<sup>1</sup> and Egidio Iorio<sup>1</sup>

## OPEN ACCESS

### Edited by:

Cicero Matthew R. Habito,  
Harvard Medical School, USA

### Reviewed by:

Orazio Schillaci,  
University of Rome Tor Vergata, Italy

Goutam Chakraborty,  
Memorial Sloan-Kettering  
Cancer Center, USA

### \*Correspondence:

Franca Podo  
franca.podo@iss.it,  
franca.podo@alice.it

### Specialty section:

This article was submitted to  
Cancer Imaging and Diagnosis,  
a section of the journal  
*Frontiers in Oncology*

**Received:** 16 March 2016

**Accepted:** 05 July 2016

**Published:** 02 August 2016

### Citation:

Podo F, Paris L, Cecchetti S,  
Spadaro F, Abalsamo L, Ramoni C,  
Ricci A, Pisani ME, Sardanelli F,  
Canese R and Iorio E (2016)  
Activation of Phosphatidylcholine-Specific Phospholipase C in Breast and Ovarian Cancer: Impact on MRS-Detected Choline Metabolic Profile and Perspectives for Targeted Therapy.  
*Front. Oncol.* 6:171.  
doi: 10.3389/fonc.2016.00171

<sup>1</sup> Molecular and Cellular Imaging Unit, Department of Cell Biology and Neurosciences, Istituto Superiore di Sanità, Rome, Italy, <sup>2</sup> Department of Biomedical Sciences for Health, Università degli Studi di Milano, Research Hospital Policlinico San Donato, Milan, Italy

Elucidation of molecular mechanisms underlying the aberrant phosphatidylcholine cycle in cancer cells plays in favor of the use of metabolic imaging in oncology and opens the way for designing new targeted therapies. The anomalous choline metabolic profile detected in cancer by magnetic resonance spectroscopy and spectroscopic imaging provides molecular signatures of tumor progression and response to therapy. The increased level of intracellular phosphocholine (PCho) typically detected in cancer cells is mainly attributed to upregulation of choline kinase, responsible for choline phosphorylation in the biosynthetic Kennedy pathway, but can also be partly produced by activation of phosphatidylcholine-specific phospholipase C (PC-PLC). This hydrolytic enzyme, known for implications in bacterial infection and in plant survival to hostile environmental conditions, is reported to be activated in mitogen- and oncogene-induced phosphatidylcholine cycles in mammalian cells, with effects on cell signaling, cell cycle regulation, and cell proliferation. Recent investigations showed that PC-PLC activation could account for 20–50% of the intracellular PCho production in ovarian and breast cancer cells of different subtypes. Enzyme activation was associated with PC-PLC protein overexpression and subcellular redistribution in these cancer cells compared with non-tumoral counterparts. Moreover, PC-PLC coimmunoprecipitated with the human epidermal growth factor receptor-2 (HER2) and EGFR in HER2-overexpressing breast and ovarian cancer cells, while pharmacological PC-PLC inhibition resulted into long-lasting HER2 downregulation, retarded receptor re-expression on plasma membrane and antiproliferative effects. This body of evidence points to PC-PLC as a potential target for newly designed therapies, whose effects can be preclinically and clinically monitored by metabolic imaging methods.

**Keywords:** choline metabolism, phosphatidylcholine phospholipase C, choline kinase, breast cancer, ovarian cancer, magnetic resonance spectroscopy, targeted therapy

## PHOSPHATIDYLCHOLINE-SPECIFIC PHOSPHOLIPASE C IN LIVING SYSTEMS

Phosphatidylcholine-specific phospholipase C (EC 3.1.4.3, here abbreviated as PC-PLC) is responsible for hydrolysis of this glycerophospholipid into phosphocholine (PCho) and 1,2-diacylglycerols (DAG).

Phospholipases of this class are known to be important secreted pathogenicity factors in some bacteria, parasites, and fungi (1, 2) in which they act as lytic agents against eukaryotic cells and interfere with the host immune defense. Some bacterial PC-PLCs are also involved in lipid remodeling in response to phosphate-limiting conditions. Amino acid sequences and encoding genes have been identified for various toxic and non-toxic PC-PLCs produced by Gram-positive and Gram-negative bacteria. Since some PC-PLCs play important roles in the pathogenesis of diseases, they could also form components of vaccines.

Phospholipases C endowed with a broader substrate specificity (collectively called NPC, as an acronym for “non-specific phospholipases C”) were discovered, sequenced, and cloned in plants as a novel family of phospholipid-cleaving enzymes homologous to bacterial PC-PLCs and responsible for lipid conversion under phosphate-limiting conditions (3). Notably, phosphatidylcholine-hydrolyzing members of the NPC family in *Arabidopsis* were implicated in stress response to phytohormones, root development, and tolerance to adverse environmental conditions (3).

Phosphatidylcholine-specific phospholipase C activity is reported to be an essential source of phospholipid-derived signaling in animal cells (4, 5) in which this phospholipase can be implicated in various intracellular regulatory mechanisms, including long-term cell response to mitogens (6–9); cell cycle regulation and cell proliferation (8, 10, 11); programmed cell death (12, 13); activation of cells of the immune system (14–22); cell transformation (23, 24); oncogene-driven cell signaling and tumor progression (25–28); and cell differentiation of tumoral and non-tumoral cells (29–34).

Phosphatidylcholine-specific phospholipase C isoforms of varying molecular weights have been isolated from mammalian sources (35–37). However, differently from phosphatidylinositol-bis-phosphate specific PLCs (PIP<sub>2</sub>-PLCs), well-recognized key regulatory enzymes of cell growth, development, and stress responses in living organisms, a slower progress has been so far achieved in the molecular characterization of PC-PLCs in animal cells, in which these phospholipases have not yet been sequenced and cloned. For these reasons, the role of PC-PLCs in mammalian cells has remained elusive until recently. Despite these limitations, the PC-PLC protein expression could be effectively investigated in mammalian cells using cross-reacting polyclonal antibodies raised in rabbits against bacterial PC-PLCs, as first described by Clark et al. (37). Using these antibodies, a 66-kDa PC-PLC isoform has been detected in various mammalian cell systems, such as mouse NIH-3T3 fibroblasts (8, 38), synaptic endings (39, 40), epithelial ovarian cancer (EOC) cells and surgical specimens (26, 27), breast cancer (BC) (28) and hepatoma cells (11, 30, 41). Furthermore, near-infrared probes capable to non-invasively detect PC-PLC in experimental animals have been developed and their utility tested for *in vivo* cancer imaging (42).

An increasing interest in filling the existing gaps in the molecular and genomic characterization of mammalian PC-PLCs arises from accruing evidence that protein overexpression, subcellular redistribution, and activation of this enzyme in tumor cells represent relevant features of the aberrant choline phospholipid metabolism in cancer (43). In addition, evidence for a physical interaction of PC-PLC with the human epidermal growth factor receptor-2 (HER2) and EGFR is provided by coimmunoprecipitation tests on HER2-overexpressing BC (28) and EOC cells.<sup>1</sup> Pharmacological PC-PLC inhibition is associated in these cells with long-lasting HER2 downmodulation and induction of antiproliferative effects, suggesting a role for PC-PLC activity in controlling HER2-driven tumorigenicity. Furthermore, inhibition of PC-PLC is associated with loss of mesenchymal traits in the highly metastatic triple-negative MDA-MB-231 cells and with decreased *in vitro* cell migration and invasion capabilities, suggesting a pivotal role for PC-PLC in BC cell differentiation (34).

This article provides a brief overview on metabolic and functional features of PC-PLC in BC and EOC cells and outlines some perspectives offered by further elucidation of the impact of this phospholipase on cancer cell biology and therapy targeting.

## PC-PLC IN BREAST AND OVARIAN CANCER CELLS

### PC-PLC Activation and Contribution to Elevated Phosphocholine Production

Phosphatidylcholine, the most abundant phospholipid of eukaryotic cells, plays the double role of basic structural component of cell membranes and precursor of agonist-induced signaling lipids (44) through a network of enzymatic reactions known as the phosphatidylcholine cycle (45) (scheme in Figure 1). The agonist-induced production and utilization within this cycle of signaling lipids, such as DAG, phosphatidate, lysophosphatidylcholine, and arachidonic acid, are associated with changes in the fluxes and steady-state levels of water-soluble phosphatidylcholine metabolites, such as PCho, glycerophosphocholine (GPCho), and free choline (Cho), main components of the so-called total choline (tCho) metabolic profile.

Magnetic resonance spectroscopy (MRS) and spectroscopic imaging (MRSI) represent powerful means to detect changes induced in the tCho pool by oncogene-driven activation of phosphatidylcholine cycle enzymes in cancer and to evaluate the response of the tCho profile to agents targeted against selected enzymes (43, 46–48). Figure 1 shows examples of (i) the <sup>1</sup>H-MRS tCho profile in aqueous extracts of normal ovarian surface epithelial cells (OSE, Figure 1A) compared with the EOC cell line SKOV3 and its *in vivo*-passaged cell variant SKOV3.ip, characterized by higher HER2 overexpression (Figure 1B) and enhanced *in vivo* tumorigenicity (25, 27, 49, 50); (ii) the effects induced on the SKOV3.ip tCho profile by cell exposure to D609, a competitive PC-PLC inhibitor (Figure 1C);

<sup>1</sup>Paris L, Podo F, Spadaro F, Abalsamo L, Pisanu ME, Ricci A, et al. Phosphatidylcholine-specific phospholipase C inhibition reduces HER2-overexpression and tumor growth in a highly tumorigenic ovarian cancer model. Manuscript in preparation (2016).

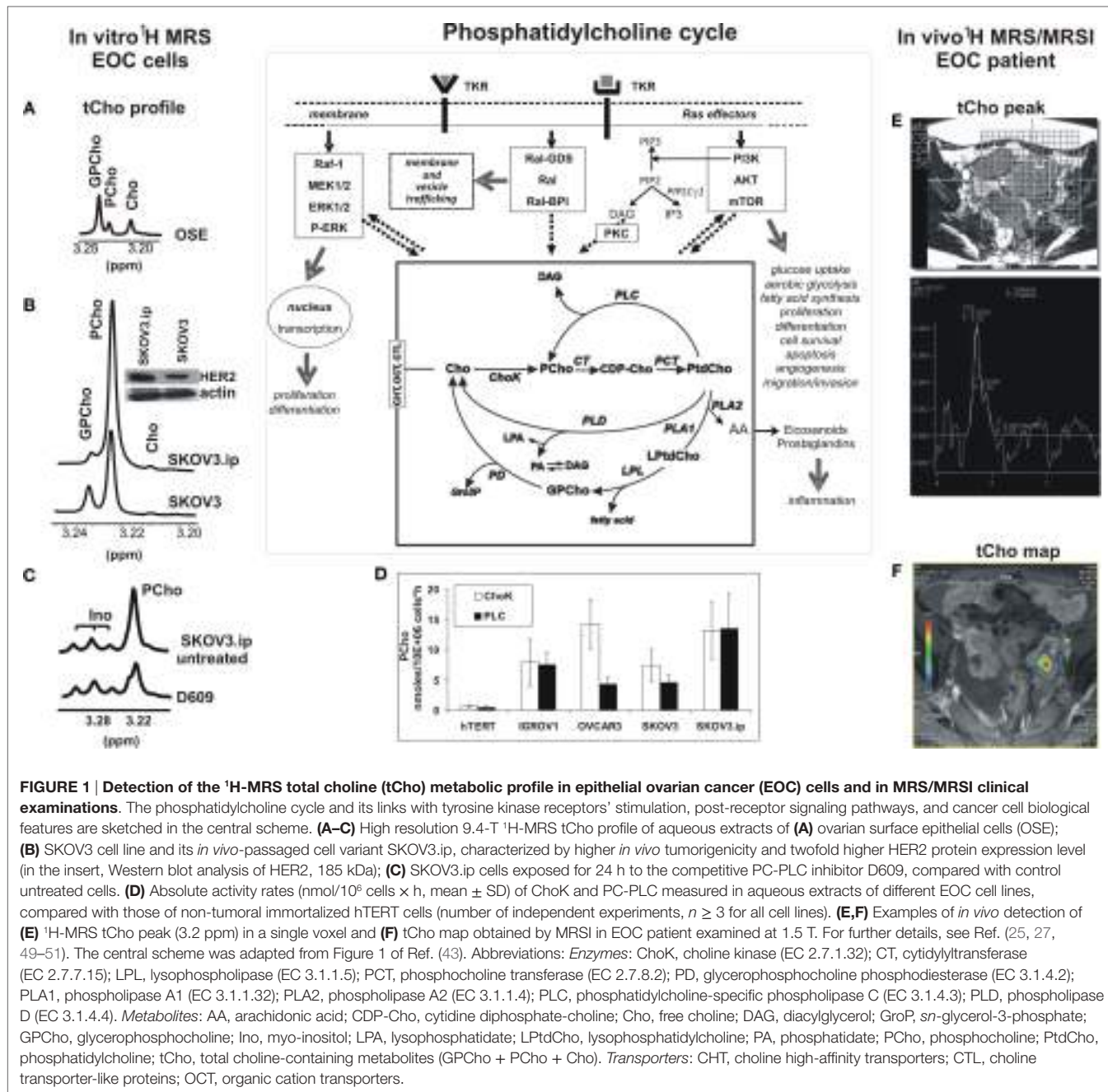


**FIGURE 1 | Detection of the <sup>1</sup>H-MRS total choline (tCho) metabolic profile in epithelial ovarian cancer (EOC) cells and in MRS/MRSI clinical examinations.** The phosphatidylcholine cycle and its links with tyrosine kinase receptors' stimulation, post-receptor signaling pathways, and cancer cell biological features are sketched in the central scheme. **(A–C)** High resolution 9.4-T <sup>1</sup>H-MRS tCho profile of aqueous extracts of **(A)** ovarian surface epithelial cells (OSE); **(B)** SKOV3 cell line and its *in vivo*-passaged cell variant SKOV3.ip, characterized by higher *in vivo* tumorigenicity and twofold higher HER2 protein expression level (in the insert, Western blot analysis of HER2, 185 kDa); **(C)** SKOV3.ip cells exposed for 24 h to the competitive PC-PLC inhibitor D609, compared with control untreated cells. **(D)** Absolute activity rates (nmol/10<sup>6</sup> cells × h, mean ± SD) of ChoK and PC-PLC measured in aqueous extracts of different EOC cell lines, compared with those of non-tumoral immortalized hTERT cells (number of independent experiments, *n* ≥ 3 for all cell lines). **(E,F)** Examples of *in vivo* detection of **(E)** <sup>1</sup>H-MRS tCho peak (3.2 ppm) in a single voxel and **(F)** tCho map obtained by MRSI in EOC patient examined at 1.5 T. For further details, see Ref. (25, 27, 49–51). The central scheme was adapted from Figure 1 of Ref. (43). Abbreviations: Enzymes: ChoK, choline kinase (EC 2.7.1.32); CT, cytidylyltransferase (EC 2.7.7.15); LPL, lysophospholipase (EC 3.1.1.5); PCT, phosphocholine transferase (EC 2.7.8.2); PD, glycerophosphocholine phosphodiesterase (EC 3.1.4.2); PLA1, phospholipase A1 (EC 3.1.1.32); PLA2, phospholipase A2 (EC 3.1.1.4); PLC, phosphatidylcholine-specific phospholipase C (EC 3.1.4.3); PLD, phospholipase D (EC 3.1.4.4). Metabolites: AA, arachidonic acid; CDP-Cho, cytidine diphosphate-choline; Cho, free choline; DAG, diacylglycerol; GroP, *sn*-glycerol-3-phosphate; GPCho, glycerophosphocholine; Ino, myo-inositol; LPA, lysophosphatidate; LPtdCho, lysophosphatidylcholine; PA, phosphatidate; PCho, phosphocholine; PtdCho, phosphatidylcholine; tCho, total choline-containing metabolites (GPCho + PCho + Cho). Transporters: CHT, choline high-affinity transporters; CTL, choline transporter-like proteins; OCT, organic cation transporters.

(iii) the simultaneous activation of ChoK and PC-PLC in different EOC cell lines versus hTERT, a non-tumoral immortalized ovarian cell line (**Figure 1D**); and (iv) examples of *in vivo* detection of the <sup>1</sup>H-MRS tCho peak (3.2 ppm) in a selected voxel (**Figure 1E**) and a tCho map obtained by 3D-MRSI in a EOC patient (**Figure 1F**) (51).

The <sup>1</sup>H-MRS PCho signal increased 3.6- to 6.5-fold in the investigated EOC cell lines compared with non-tumoral counterparts (25, 27, 50). Notably, the 2-fold higher HER2 expression of SKOV3.ip versus SKOV3 cells was associated with a 1.7-fold higher PCho content (50). An elevated PCho level was the principal cause of the higher tCho pool detected in these cancer cells, in

agreement with the general view that an increased tCho represents a metabolic signature of malignancy (43, 46–48, 52, 53). The enhanced PCho production in cancer cells is currently attributed to the upregulation of choline kinase (43, 46), the enzyme committed to choline phosphorylation in the biosynthetic Kennedy pathway. This enzyme (notably the ChoK-alpha isoform) has been proposed as a new target for cancer therapy (54, 55). A substantial contribution to the production of the intracellular PCho pool in cancer cells may, however, also derive from PC-PLC activation (see scheme in **Figure 1**). The question therefore arises on the relative contributions possibly given by PC-PLC activation to PCho production in different EOC cells. Measurements in

our laboratory (**Figure 1D**) showed that a mean 12- to 24-fold activation of ChoK was paralleled by a 10- to 30-fold activation of PC-PLC in four EOC cell lines (IGROV1, OVCAR3, SKOV3, and SKOV3.ip) versus the non-tumoral hTERT cell line (in which both enzymes had a basal activity of about  $0.5 \text{ nmol}/10^6 \text{ cells} \times \text{h}$ ). In some EOC cell lines (IGROV1, SKOV3.ip), ChoK and PC-PLC showed very similar activity rates, suggesting about equal contributions of the two enzymes to the PCho production. Accordingly, there was a 40–50% decrease of the PCho signal in SKOV3.ip cells following 24-h exposure to the competitive PC-PLC inhibitor D609 (example in **Figure 1C**). In another cell line (OVCAR3), the mean activity rate of ChoK was instead fourfold higher than that of PC-PLC. Overall, these data showed that the contribution of PC-PLC to the PCho production could vary, according to the cell line, between 20% and 50%, in substantial agreement with the effects of D609 or si-RNA ChoK silencing on the PCho levels measured in different EOC cells [**Figure 1C**; (27, 56)].

This body of evidence supports the conclusion that PC-PLC can contribute to a substantial extent to the accumulation of PCho in EOC cells. This evidence may allow a better interpretation of changes occurring in the *in vivo* MRS- and MRSI-detected tCho peak in preclinical EOC models (57) and in EOC clinical lesions (examples in **Figures 1E,F**) during tumor progression, response to treatment, or relapse.

Regarding human BC cells, a significant 2- to 5.5-fold ChoK activation was detected by Eliyahu and colleagues in cell lines of different subtypes (58), such as luminal-A MCF-7, HER2-positive SKBr3, and basal-like EGFR-positive MDA-MB-231 (respective activity rates  $21 \pm 3$ ,  $43 \pm 6$ , and  $17 \pm 2 \text{ nmol/mg protein} \times \text{h}$ ), versus mammary epithelial cells ( $8.0 \pm 2.0 \text{ nmol/mg protein} \times \text{h}$ ). Enzymatic assays in our laboratory (34) showed threefold to sixfold higher PC-PLC activity rates (ranging between  $12 \pm 2$  and  $22 \pm 4 \text{ nmol/mg protein} \times \text{h}$ ) in these BC cells versus the fibrocystic MCF-10 cell line (**Figure 2A**). Overall, these data suggest that the contribution of PC-PLC to the intracellular PCho production also varied in these BC cells between 20% and 50%, as reported above for EOC cell lines.

## PC-PLC Overexpression and Subcellular Redistribution

Western blot analyses showed that the reported threefold to sixfold activation of PC-PLC in BC cell lines was associated with a threefold to sixfold elevated PC-PLC protein expression (34), the highest value being detected in the triple-negative MDA-MB-231 cells. Confocal laser scanning microscopy (CLSM) of fixed and permeabilized cancer cells (**Figure 2B**, top panels) showed that the enzyme was localized both in nuclear and cytoplasmic compartments. Only a few PC-PLC-positive granules, mainly localized in perinuclear areas and absent in the nuclear matrix, were instead detected in the non-tumoral MCF-10A cells. CLSM of unfixed cells showed that PC-PLC massively accumulated on plasma membrane of the HER2-positive SKBr3 cells, but not on that of cells with basal HER2 expression (**Figure 2B**, bottom panels). PC-PLC extensively colocalized with HER2 in raft domains of plasma membrane of SKBr3 cells [**Figure 2C**; (28)], in which coimmunoprecipitation tests showed a physical association of PC-PLC with HER2 and with other members of the ErbB family, such as EGFR and HER3.

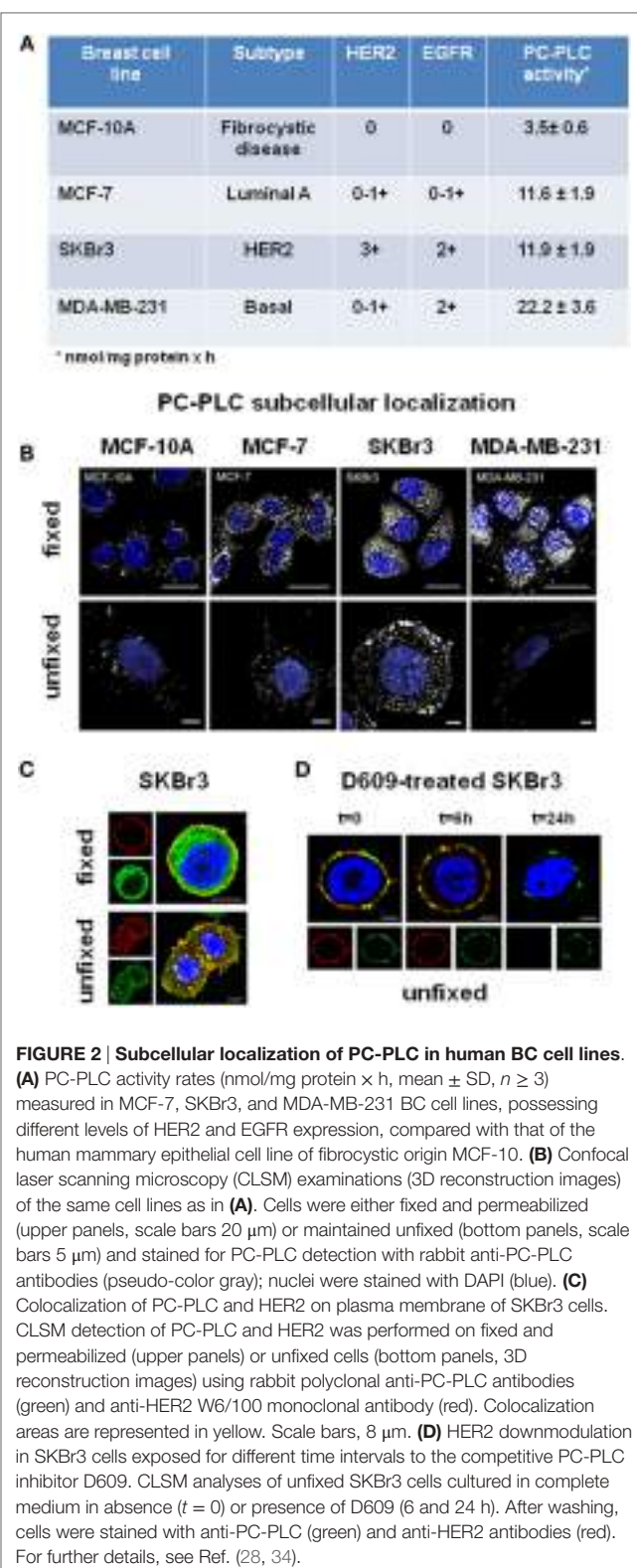


**FIGURE 2 |** Subcellular localization of PC-PLC in human BC cell lines.

**(A)** PC-PLC activity rates (nmol/mg protein  $\times$  h, mean  $\pm$  SD,  $n \geq 3$ ) measured in MCF-7, SKBr3, and MDA-MB-231 BC cell lines, possessing different levels of HER2 and EGFR expression, compared with that of the human mammary epithelial cell line of fibrocystic origin MCF-10. **(B)** Confocal laser scanning microscopy (CLSM) examinations (3D reconstruction images) of the same cell lines as in **(A)**. Cells were either fixed and permeabilized (upper panels, scale bars  $20 \mu\text{m}$ ) or maintained unfixed (bottom panels, scale bars  $5 \mu\text{m}$ ) and stained for PC-PLC detection with rabbit anti-PC-PLC antibodies (pseudo-color gray); nuclei were stained with DAPI (blue). **(C)** Colocalization of PC-PLC and HER2 on plasma membrane of SKBr3 cells. CLSM detection of PC-PLC and HER2 was performed on fixed and permeabilized (upper panels) or unfixed cells (bottom panels, 3D reconstruction images) using rabbit polyclonal anti-PC-PLC antibodies (green) and anti-HER2 W6/100 monoclonal antibody (red). Colocalization areas are represented in yellow. Scale bars,  $8 \mu\text{m}$ . **(D)** HER2 downmodulation in SKBr3 cells exposed for different time intervals to the competitive PC-PLC inhibitor D609. CLSM analyses of unfixed SKBr3 cells cultured in complete medium in absence ( $t = 0$ ) or presence of D609 (6 and 24 h). After washing, cells were stained with anti-PC-PLC (green) and anti-HER2 antibodies (red). For further details, see Ref. (28, 34).

Regarding PC-PLC distribution in EOC cells, a massive accumulation of this phospholipase was detected by CLSM on plasma membrane of all investigated cell lines and on that of cancer cells isolated from patient peritoneal exudate, but not on OSE cells (26).

The enzyme extensively colocalized with  $\beta 1$ -integrin in non-raft domains of EOC cells (26). The extent of colocalization of the two proteins substantially decreased on membrane of serum-deprived cancer cells, but returned to the original level upon cell restimulation by platelet-derived growth factor. These data warrant further investigations on the functional role of the interaction between PC-PLC and  $\beta 1$ -integrin, an adhesion protein well-known for its involvement in metastatic spread (59). Furthermore, CLSM and coimmunoprecipitation experiments showed an extensive colocalization and physical association of PC-PLC with HER2 on plasma membrane of SKOV3 and SKOV3.ip cells, confirming the interest of further investigating the role of this phospholipase in regulating HER2 overexpression in ovarian cancer.

## Effects of PC-PLC Inhibition

Exposure of BC cell lines to D609 led to cell proliferation arrest, changes in cell morphology, and formation of lipid bodies typical of BC cell differentiation (34). Moreover, in the poorly differentiated MDA-MB-231 cells, PC-PLC inhibition was associated with progressive decreases of mesenchymal traits, such as vimentin and N-cadherin expression, reduced galectin-3 and milk fat globule EGF-factor 8 levels,  $\beta$ -casein formation, and decrease of *in vitro* cell migration and invasion (34). We therefore proposed that the inhibition of this phospholipase can be envisaged as a means to promote differentiation of metastatic BC cells, with potential therapeutic effects.

Besides inducing cell differentiation, exposure of SKBr3 cells to D609 resulted in a progressive downmodulation of both HER2 and PC-PLC on plasma membrane, an effect already evident at 6 h and almost complete at 24 h (Figure 2D). This effect was associated with HER2 internalization and lysosomal degradation, long-lasting retardation of re-expression of this receptor on membrane, and an about 50% decrease in the overall protein expression (28). Notably, no substantial influence on HER2 externalization is known to be exerted in these cells using Trastuzumab (60), the anti-HER2 humanized monoclonal antibody mostly used at the clinical level, whose *in vivo* therapeutic efficacy is mainly attributed to antibody-mediated cytotoxicity. This body of evidence suggests that PC-PLC inhibition may be envisaged as a potential alternative approach to counteract the tumorigenic effects of HER2, especially in cases of resistance (or contraindication) to current anti-HER2 treatment.

Long-standing decreases of HER2 and phospho-HER2 contents, reduced HER2 mRNA expression, and cell cycle arrest were also detected in the highly tumorigenic SKOV3.ip EOC cells exposed to a non-apoptotic dose of D609<sup>1</sup>. Furthermore, reduced tumor growth and decrease in HER2 and Ki67 immunostaining were detected in SKOV3.ip xenografts upon *in vivo* treatment with D609, pointing to the interest of further evaluating the potential role of PC-PLC as a therapy target in preclinical HER2-overexpressing EOC models.

## FUTURE RESEARCH DIRECTIONS

In summary, PC-PLC is overexpressed and activated in BC and EOC cells, and pharmacological PC-PLC inhibition can lead to downregulation of HER2 and induction of antiproliferative

effects. Furthermore, cell differentiation and decreases in cell migration and invasion were induced in the highly metastatic MDA-MB-231 BC cell line exposed to the PC-PLC inhibitor. These findings point to PC-PLC as a potential target (or cotarget) for anticancer therapy, especially in cases of resistance or contraindications to currently adopted treatments. In this context, the following issues appear worth of further elucidation:

## Molecular Mechanisms Responsible for Oncogene-Driven PC-PLC Activation and Impact on Molecular Imaging

The 1.7-fold increase in PC-PLC activity in a SKOV3 cell variant (SKOV3.ip) endowed with a 2-fold higher HER2 overexpression (50) and the over 3-fold increase in PC-PLC activity in the HER2-positive SKBr3 cells (34) warrant further investigations on the molecular mechanisms linking PC-PLC activation with HER2 overexpression and oncogenic effects of HER2 and HER2-EGFR heterodimers. Interestingly, the PC-PLC inhibitor D609, but not Trastuzumab, induced decreases of HER2 expression and cell proliferation in the Trastuzumab-resistant SKBr3 cell line. Conversely D609, either alone or in combination with Trastuzumab, induced in the Trastuzumab-sensitive BT-474 cells a decrease in cell proliferation comparable to that induced using Trastuzumab alone (28).

The sixfold activation of PC-PLC in MDA-MB-231 BC cells and its strong nuclear localization (Figures 2A,B) warrant investigations on the relationships between PC-PLC and EGFR overexpression in triple-negative BC cells and their metastatic derivatives.

Overexpression of EGFR and c-Src in BC cells has been reported to synergistically increase ChoK-alpha protein expression and activity levels (61). Further elucidation of EGFR-driven mechanisms responsible for the activation of both ChoK-alpha or PC-PLC in BC cells may lead to novel multi-targeted anticancer therapies, whose effects could be preclinically and clinically monitored by MRS-based and optical metabolic imaging methods.

Integration of MRS with <sup>11</sup>C or <sup>18</sup>F choline-based positron emission tomography (PET) may allow discrimination of the contributions to PCho production, provided by the biosynthetic and catabolic pathways, respectively. In fact, while both ChoK and PC-PLC can contribute to the MRS-detected PCho signal, the choline-PET standardized uptake value (SUV) mainly reflects choline transport and phosphorylation in the Kennedy pathway, with negligible contributions from products of radiolabeled phosphatidylcholine catabolism in a time window of about 1 h (the duration of a typical choline-PET examination) (43).

## Molecular and Functional Characterization of the Interaction between PC-PLC and Receptors of the ErbB Family

The interaction of an activated PC-PLC isoform with HER2, detected by coimmunoprecipitation tests, appears essential to the functional localization of this receptor in BC cells, since PC-PLC inhibition induces a long-lasting HER2 downmodulation (28). The association of these effects with reduced cell proliferation, induction of cell differentiation, and decrease in cell migration

and invasion suggests that an activated PC-PLC may act as a sort of chaperone for HER2. A local overproduction of DAG by enhanced PC-PLC-mediated phosphatidylcholine hydrolysis could mediate this action. A local accumulation of DAG can, in fact, perturb the phospholipid bilayer, alter protein-lipid interactions, and influence the formation of microdomains, thus modifying the exposure of surface membrane receptors and affecting their recycling between membrane and inner cell compartments (62, 63). Interestingly, ChoK-alpha has also been proposed to act as a chaperone for the androgen receptor, a ligand-inducible transcription factor of the nuclear hormone receptor superfamily, critically involved in prostate cancer progression (64). The newly suggested role of ChoK and PC-PLC as regulators of expression for oncogenes and growth factor receptors may lead to new targeted or multi-targeted anticancer therapies.

## Structural and Genomic Characterization of PC-PLC Isoforms Active in Cancer Cells

This body of evidence points to the need for overcoming the current limitations deriving from (a) the scarce attention so far devoted to the genomic and structural characterization of mammalian PC-PLC isoforms and (b) the availability until now of only one PC-PLC inhibitor, D609, a synthetic tricyclic compound having a xanthate group, possessing antiviral, anti-tumor, anti-inflammatory, and anti-apoptosis properties and used as a lipid-related enzyme inhibitor for the past three decades (65).

Steps forward in translational oncology may be expected from:

- investigating the role of PC-PLC expression and the effects of PC-PLC inhibition in BC and EOC stem cells, to identify potential ways to reinforce therapeutic strategies aimed to eradicate malignancies (66, 67);
- exploring in preclinical models the correlation between PC-PLC activity and disease progression or response to therapy, as a ground for evaluating the impact of PC-PLC activation on clinical outcome.

## CONCLUSION

Recent evidence shows protein overexpression and enzymatic activation of PC-PLC in BC and EOC cells compared with non-tumoral counterparts.

## REFERENCES

1. Titball RW. Bacterial phospholipases C. *Microbiol Rev* (1993) 57:347–66.
2. Ghannoum MA. Potential role of phospholipases in virulence and fungal pathogenesis. *Clin Microbiol Rev* (2000) 13:122–43. doi:10.1128/CMR.13.1.122-143.2000
3. Pokotylo I, Pejchar P, Potocky M, Kokourková D, Krcková Z, Ruelland E, et al. The plant non-specific phospholipase C gene family. Novel competitors in lipid signaling. *Prog Lipid Res* (2013) 52:62–79. doi:10.1016/j.plipres.2012.09.001
4. Billah MM, Antes JC. The regulation and cellular functions of phosphatidylcholine hydrolysis (review). *Biochem J* (1990) 269:281–91. doi:10.1042/bj2690281
5. Exton JH. Phosphatidylcholine breakdown and signal transduction. *Biochim Biophys Acta* (1994) 1212:26–42. doi:10.1016/0005-2760(94)90186-4
6. Larrodera P, Cornet ME, Diaz-Meco MT, Lopez-Barahona M, Diaz-Laviada I, Guddal PH, et al. Phospholipase C-mediated hydrolysis of phosphatidylcholine is an important step in PDGF-stimulated DNA synthesis. *Cell* (1990) 61:1113–20. doi:10.1016/0092-8674(90)90074-O
7. Van Dijck MCM, Muriana FJG, De Widt J, Hilmann H, Van Blitterswijk WJ. Involvement of phosphatidylcholine-specific phospholipase C in platelet-derived growth factor-induced activation of the mitogen-activated protein kinase pathway in rat-1 fibroblasts. *J Biol Chem* (1997) 272:11011–6. doi:10.1074/jbc.272.17.11011
8. Ramoni C, Spadaro F, Barletta B, Dupuis ML, Podo F. Phosphatidylcholine-specific phospholipase C in mitogen-stimulated fibroblasts. *Exp Cell Res* (2004) 299:370–82. doi:10.1016/j.yexcr.2004.05.037
9. Li F, Wu N, Su R-B, Zheng JQ, Xu B, Lu XQ, et al. Involvement of phosphatidylcholine-selective phospholipases C in activation of mitogen-activated protein-kinase pathways in imidazoline receptor antisera selected protein. *J Cell Biochem* (2006) 98:1615–28. doi:10.1002/jcb.20806
10. Plo I, Lautier D, Levade T, Sekouri H, Jaffrézou JP, Laurent G, et al. Phosphatidylcholine-specific phospholipase C and phospholipase D are

The activation of PC-PLC can contribute to 20–50% of the production of intracellular PCCho in BC and EOC cells.

Phosphatidylcholine-specific phospholipase C activation is associated in these cancer cells with its protein overexpression and subcellular redistribution, the underlying molecular mechanisms deserving further elucidation.

Phosphatidylcholine-specific phospholipase C interacts with HER2 and EGFR in HER2-overexpressing BC and EOC cells, while its pharmacologic inhibition may play a pivotal role in HER2 downmodulation, reduction of cell proliferation, and cancer cell differentiation.

Overall, this body of evidence supports the interest of evaluating the possible role of this phospholipase as a key metabolic target for anticancer therapy.

## ETHICS STATEMENT

The study on patients mentioned in this Perspective article (**Figures 1E,F**) was approved by the Institutional Review Board of the Research Hospital Policlinico San Donato Milanese, Italy. Written informed consent was obtained from all patients. Between July 2007 and April 2009, the study prospectively enrolled a series of patients with already known ovarian masses, who were consecutively referred to the Radiology Unit of Policlinico San Donato Milanese for presurgical staging. Exclusion criteria were the lack of informed consent and general contraindications to MRI or to the intravenous administration of contrast material. All patients underwent surgery with removal of the mass and histopathological examination. Further details are given in Ref. (51).

## AUTHOR CONTRIBUTIONS

The manuscript was written by FP; revised by EI, SC, FSp, RC, FSa, and FP; read and approved by all coauthors.

## FUNDING

The group at the Istituto Superiore di Sanità (ISS, Rome) acknowledges partial support by the Associazione Italiana per la Ricerca sul Cancro (AIRC) Research Program 2007–2009, IG-4251 (PI: FP) and Ministero della Salute, Integrated Oncology Program RO 065/ISS No. Q09 and Special Research Program Onc. Ord, 37/07/ISS No. 70CF/4 (PI:FP).

- respectively implicated in mitogen-activated protein kinase and nuclear factor  $\kappa$ B activation in tumor-necrosis-factor- $\alpha$ -treated immature acute-myeloid-leukaemia cells. *Biochem J* (2000) 351:459–67. doi:10.1042/0264-6021:3510459
11. Fu D, Ma Y, Wu W, Zhu X, Jia C, Zao Q, et al. Cell-cycle dependent PC-PLC regulation by APC/C<sup>Cdc20</sup>-mediated ubiquitin-proteasome pathway. *J Cell Biochem* (2009) 107:686–96. doi:10.1002/jcb.22163
  12. Cifone MG, Rocaioli P, De Maria R, Camarda G, Santoni A, Ruberti G, et al. Multiple pathways originated at Fas/Apo-1 (CD95) receptor: sequential involvement of phosphatidylcholine-specific phospholipase C and acidic sphingomyelinase in the propagation of the apoptotic signal. *EMBO J* (1995) 14:5859–68.
  13. Liu X, Zhao Q, Araki S, Zhang S, Miao J. Contrasting effects of phosphatidylinositol- and phosphatidylcholine-specific phospholipase C on apoptosis in cultured endothelial cells. *Endothelium* (2006) 13:205–11. doi:10.1080/10623320600760423
  14. Ramoni C, Spadaro F, Menegon M, Podo F. Cellular localization and functional role of phosphatidylcholine-specific phospholipase C in NK cells. *J Immunol* (2001) 167:2642–50. doi:10.4049/jimmunol.167.5.2642
  15. Andrei C, Margiocco P, Poggi A, Lotti LV, Torrisi MR, Rubartelli A. Phospholipases C and A2 control lysosome-mediated IL- $\beta$  secretion: implications for inflammatory processes. *Proc Natl Acad Sci U S A* (2004) 101:9745–50. doi:10.1073/pnas.0308558101
  16. Moreno-Garcia ME, Lopez-Bojorguez LN, Zentella A, Humphries LA, Rawlings DJ, Santos-Arqumedo L. CD38 signaling regulates B lymphocyte activation via a phospholipase C (PLC)-gamma 2-independent, protein kinase C, phosphatidylcholine-PLC, and phospholipase D-dependent signaling cascade. *J Immunol* (2005) 174:2687–95. doi:10.4049/jimmunol.174.5.2687
  17. von Knethen A, Brune B. PKC $\alpha$  depletion in RAW264.7 macrophages following microbial/IFN $\gamma$  stimulation is PC-PLC-mediated. *Antioxid Redox Signal* (2005) 7:1217–22. doi:10.1089/ars.2005.7.1217
  18. Luft T, Rodionova E, Maraskovsky E, Kirsch M, Hess M, Buchholtz C, et al. Adaptive functional differentiation of dendritic cells: integrating the network of extra- and intracellular signals. *Blood* (2006) 107:4763–9. doi:10.1182/blood-2005-04-1501
  19. Cuschieri J, Billgren J, Maier RV. Phosphatidylcholine-specific phospholipase C (PC-PLC) is required for LPS-mediated macrophage activation through CD14. *J Leukoc Biol* (2006) 80:407–14. doi:10.1189/jlb.1105622
  20. Spadaro F, Cecchetti S, Sanchez M, Podo F, Ramoni C. Expression and role of phosphatidylcholine-specific phospholipase C in human NK and T-lymphocyte subsets. *Eur J Immunol* (2006) 36:3277–87. doi:10.1002/eji.200635927
  21. Cecchetti S, Spadaro F, Lugini L, Podo F, Ramoni C. Functional role of phosphatidylcholine-specific phospholipase C in regulating CD16 membrane expression in natural killer cells. *Eur J Immunol* (2007) 37:2912–22. doi:10.1002/eji.200737266
  22. Fantuzzi L, Spadaro F, Purificato C, Cecchetti S, Podo F, Belardelli F, et al. Phosphatidylcholine-specific phospholipase C activation is required for CCR5-dependent, NF- $\kappa$ B-driven CCL2 secretion elicited in response to HIV-1 gp120 in human primary macrophages. *Blood* (2008) 111:3355–63. doi:10.1182/blood-2007-08-104901
  23. Johansen T, Bjørkøy G, Øvervatn A, Diaz-Meco MT, Traaik T, Moscat J. NIH-3T3 cells stably transfected with the gene encoding phosphatidylcholine-hydrolyzing phospholipase C from *Bacillus cereus* acquire a transformed phenotype. *Mol Cell Biol* (1994) 14:646–54. doi:10.1128/MCB.14.1.646
  24. Halstead J, Kemp K, Ignotz RA. Evidence for involvement of phosphatidylcholine-phospholipase C and protein kinase C in transforming growth factor- $\beta$  signaling. *J Biol Chem* (1995) 270:13600–3. doi:10.1074/jbc.270.23.13600
  25. Iorio E, Mezzanzanica D, Alberti P, Spadaro F, Ramoni C, D'Ascreno S, et al. Alterations of choline phospholipid metabolism in ovarian tumor progression. *Cancer Res* (2005) 65:9369–76. doi:10.1158/0008-5472.CAN-05-1146
  26. Spadaro F, Ramoni C, Mezzanzanica D, Miotti S, Alberti P, Cecchetti S, et al. Phosphatidylcholine-specific phospholipase C activation in epithelial ovarian cancer cells. *Cancer Res* (2008) 68:6541–9. doi:10.1158/0008-5472.CAN-07-6763
  27. Iorio E, Ricci A, Bagnoli M, Pisani ME, Castellano G, Di Vito M, et al. Activation of phosphatidylcholine cycle enzymes in human epithelial ovarian cancer cells. *Cancer Res* (2010) 70:2126–35. doi:10.1158/0008-5472.CAN-09-3833
  28. Paris L, Cecchetti S, Spadaro F, Abalsamo L, Lugini L, Pisani ME, et al. Inhibition of phosphatidylcholine-specific phospholipase C downregulates HER2 overexpression on plasma membrane of breast cancer cells. *Breast Cancer Res* (2010) 12:R27. doi:10.1186/bcr2575
  29. Ferretti A, Podo F, Carpinelli GC, Chen LL, Borghi P, Masella R. Detection of neutral active phosphatidylcholine-specific phospholipase C in Friend leukemia cells before and after erythroid differentiation. *Anticancer Res* (1993) 13:2309–18.
  30. Wu XZ, Lu H, Zhou L, Huang Y, Chen H. Changes of phosphatidylcholine-specific phospholipase C in hepatocarcinogenesis and in the proliferation and differentiation of rat liver cancer cells. *Cell Biol Int* (1997) 21:375–81. doi:10.1006/cbir.1997.0148
  31. Kahle PJ, Shooter EM, Johnson RM, Verity AN. Phosphatidylcholine-specific phospholipase inhibitor D609 differentially affects MAP kinases and immediate-early genes in PC12 cells. *Cell Signal* (1998) 10:321–30. doi:10.1016/S0898-6568(98)00010-2
  32. Zhao J, Zhao B, Wang W, Huang B, Zhang S, Miao J. Phosphatidylcholine-specific phospholipases C and ROS were involved in chicken blastodisc differentiation to vascular endothelial cell. *J Cell Biochem* (2007) 102:421–8. doi:10.1002/jcb.21301
  33. Wang N, Sun C, Huo S, Zhang Y, Zhao J, Zhang S, et al. Cooperation of phosphatidylcholine-specific phospholipase C and basic fibroblast growth factor in the neural differentiation of mesenchymal stem cells in vitro. *Int J Biochem Cell Biol* (2008) 40:294–306. doi:10.1016/j.biocel.2007.08.003
  34. Abalsamo L, Spadaro F, Bozzuto G, Paris L, Cecchetti S, Lugini L, et al. Inhibition of phosphatidylcholine-specific phospholipase C results in loss of mesenchymal traits in metastatic breast cancer cells. *Breast Cancer Res* (2012) 14:R50. doi:10.1186/bcr3151
  35. Wolf RA, Gross RW. Identification of neutral active phospholipase C which hydrolyses choline glycerolipids and plasmalogen selective phospholipase A2 in canine myocardium. *J Biol Chem* (1985) 260:7295–303.
  36. Sheikhnejad RG, Srivastava PN. Isolation and properties of a phosphatidylcholine-specific phospholipase C from bull seminal plasma. *J Biol Chem* (1986) 261:7544–9.
  37. Clark MA, Shorr RGL, Bomalaski JS. Antibodies prepared to *Bacillus cereus* phospholipase C crossreact with a phosphatidylcholine-prefering phospholipase C in mammalian cells. *Biochim Biophys Res Commun* (1986) 140:114–9. doi:10.1016/0006-291X(86)91065-X
  38. Podo F, Ferretti A, Knijn A, Zhang P, Ramoni C, Barletta B, et al. Detection of phosphatidylcholine-specific phospholipase C in NIH-3T3 fibroblasts and their H-ras transformants: NMR and immunochemical studies. *Anticancer Res* (1996) 16:1399–412.
  39. Mateos VM, Uranga RM, Salvador GA, Giusto NM. Activation of phosphatidylcholine signalling during oxidative stress in synaptic endings. *Neurochem Int* (2008) 53:199–206. doi:10.1016/j.neuint.2008.07.005
  40. Mateos VM, Salvador GA, Giusto NM. Selective localization of phosphatidylcholine-derived signaling in detergent-resistant membranes from synaptic endings. *Biochim Biophys Acta* (2010) 1798:624–36. doi:10.1016/j.bbamem.2009.12.008
  41. Wu XZ, Lu H. Correlation of calcium-independent phosphatidylcholine-specific phospholipase C and gamma-GT in hepatoma cells. *Acta Biochim Biophys Sin* (1998) 30:104–6.
  42. Mawn TM, Popov AV, Beardsley NJ, Stefflova K, Milkewitch M, Zheng G, et al. In vivo detection of phospholipase C by enzyme-activated near-infrared probes. *Bioconjug Chem* (2011) 22:2434–43. doi:10.1021/bc200242v
  43. Podo F, Canevari S, Canese R, Pisani ME, Ricci A, Iorio E. MR evaluation of response to targeted treatment in cancer cells. *NMR Biomed* (2011) 24:648–72. doi:10.1002/nbm.1658
  44. Li Z, Vance DE. Phosphatidylcholine and choline homeostasis. *J Lipid Res* (2008) 49:1187–94. doi:10.1194/jlr.R700019-JLR200
  45. Pelech SL, Vance DE. Signal transduction via phosphatidylcholine cycles. *Trends Biochem Sci* (1989) 14:28–30. doi:10.1016/0968-0004(89)90086-8

46. Glunde K, Bhujwalla ZM, Ronen SM. Choline metabolism in malignant transformation. *Nat Rev Cancer* (2011) 11:835–48. doi:10.1038/nrc3162
47. Podo F, Sardanelli F, Iorio E, Canese R, Carpinelli G, Fausto A, et al. Abnormal choline phospholipid metabolism in breast and ovarian cancer: molecular bases for noninvasive imaging approaches. *Curr Med Imaging Rev* (2007) 3:123–37. doi:10.2174/157340507780619160
48. Podo F. Tumour phospholipid metabolism. *NMR Biomed* (1999) 12:413–39. doi:10.1002/(SICI)1099-1492(199911)12:7<413::AID-NBM587>3.0.CO;2-U
49. Canese R, Pisani ME, Mezzanzanica D, Ricci A, Paris L, Bagnoli M, et al. Characterization of in vivo ovarian cancer models by quantitative <sup>1</sup>H magnetic resonance spectroscopy and diffusion-weighted imaging. *NMR Biomed* (2012) 25:632–42. doi:10.1002/nbm.1779
50. Pisani ME, Ricci A, Paris L, Surrentino E, Liliac L, Bagnoli M, et al. Monitoring response to cytostatic cisplatin in a HER2(+) ovarian cancer model by MRI and in vitro and in vivo MR spectroscopy. *Br J Cancer* (2014) 110:625–35. doi:10.1038/bjc.2013.758
51. Esseridou A, Di Leo G, Sconfienza LM, Caldiera V, Raspagliesi F, Grijuelo B, et al. In vivo detection of choline in ovarian tumors using 3D magnetic resonance spectroscopy. *Invest Radiol* (2011) 46:377–82. doi:10.1097/RLI.0b013e31821690ef
52. Katz-Büll R, Lavin PT, Lenkinski RE. Clinical utility of proton magnetic resonance spectroscopy in characterizing breast lesions. *J Natl Cancer Inst* (2002) 94:1197–202. doi:10.1093/jnci/94.16.1197
53. Sardanelli F, Fausto A, Di Leo G, de Nijs R, Vorbuchner M, Podo F. In vivo proton MR spectroscopy of the breast using the total peak integral as a marker of malignancy. *AJR Am J Roentgenol* (2009) 192:1608–17. doi:10.2214/AJR.07.3521
54. Gadiya M, Mori N, Cao MD, Mironchik Y, Kakkad S, Gribbestad IS, et al. Phospholipase D1 and choline kinase- $\alpha$  are interactive targets in breast cancer. *Cancer Biol Ther* (2014) 15:593–601. doi:10.4161/cbt.28165
55. Kumar M, Arlauckas SP, Saksena S, Verma G, Ittyerah R, Pickup S, et al. Magnetic resonance spectroscopy for detection of choline kinase inhibition in the treatment of brain tumors. *Mol Cancer Ther* (2015) 14:899–908. doi:10.1158/1535-7163.MCT-14-0775
56. Granata A, Nicoletti R, Perego P, Iorio E, Krishnamachary B, Benigni F, et al. Global metabolic profile identifies choline kinase alpha as a key regulator of glutathione-dependent antioxidant cell defense in ovarian carcinoma. *Oncotarget* (2015) 6:11216–30. doi:10.18632/oncotarget.3589
57. Canese R, Mezzanzanica D, Bagnoli M, Indraccolo S, Canevari S, Podo F, et al. In vivo magnetic resonance metabolic and morphofunctional fingerprints in experimental models of human ovarian cancer. *Front Oncol* (2016) 6:164. doi:10.3389/fonc.2016.00164
58. Eliyahu G, Kreizman T, Degani H. Phosphocholine as a biomarker of breast cancer: molecular and biochemical studies. *Int J Cancer* (2007) 120:1721–30. doi:10.1002/ijc.22293
59. Chen MB, Lamar JM, Li R, Hynes RO, Kamm RD. Elucidation of the roles of tumor integrin  $\beta$ 1 in the extravasation stage of the metastasis cascade. *Cancer Res* (2016) 76:2513–24. doi:10.1158/0008-5472.CAN-15-1325
60. Longva KE, Pedersen NM, Haslekås C, Stang E, Madshus IH. Herceptin-induced inhibition of ErbB2 signaling involves reduced phosphorylation of Akt but not endocytic down-regulation of ErbB2. *Int J Cancer* (2005) 116:659–67. doi:10.1002/ijc.21015
61. Miyake T, Parsons SJ. Functional interactions between ChoK-alpha, epidermal growth factor receptor and c-Src in breast cancer cell proliferation. *Oncogene* (2012) 31:1431–41. doi:10.1038/onc.2011.332
62. Carrasco S, Mérida I. Diacylglycerol, when simplicity becomes complex. *Trends Biochem Sci* (2007) 32:27–36. doi:10.1016/j.tibs.2006.11.004
63. Haucke V, Di Paolo G. Lipids and lipid modifications in the regulation of membrane traffic. *Curr Opin Cell Biol* (2007) 19:426–35. doi:10.1016/j.ceb.2007.06.003
64. Asim M, Massie CE, Orafidiya F, Pérez-Gomes N, Warren AY, Esmaeli M, et al. Choline kinase alpha as an androgen receptor chaperone and prostate cancer therapeutic target. *J Natl Cancer Inst* (2016) 108:dvj371. doi:10.1093/jnci/dvj371
65. Kato M, Hammam MAS, Taniguchi T, Suga Y, Mond K. What is the true structure of D609, a widely used lipid related enzyme inhibitor? *Org Lett* (2016) 18:768–71. doi:10.1021/acs.orglett.6b00025
66. Frank NY, Schatton T, Frank MH. The therapeutic promise of the cancer stem cell concept. *J Clin Invest* (2010) 120:41–50. doi:10.1172/JCI41004
67. Cecchetti S, Bortolomai I, Ferri R, Mercurio L, Canevari S, Podo F, et al. Inhibition of phosphatidylcholine-specific phospholipase C interferes with proliferation and survival of tumor initiating cells in squamous cell carcinoma. *PLoS One* (2015) 10:e0136120. doi:10.1371/journal.pone.0136120

**Conflict of Interest Statement:** The authors declare that the research was conducted in the absence of any commercial or financial relationships that could be construed as a potential conflict of interest.

Copyright © 2016 Podo, Paris, Cecchetti, Spadaro, Abalsamo, Ramoni, Ricci, Pisani, Sardanelli, Canese and Iorio. This is an open-access article distributed under the terms of the Creative Commons Attribution License (CC BY). The use, distribution or reproduction in other forums is permitted, provided the original author(s) or licensor are credited and that the original publication in this journal is cited, in accordance with accepted academic practice. No use, distribution or reproduction is permitted which does not comply with these terms.



# Metabolic Imaging to Assess Treatment Response to Cytotoxic and Cytostatic Agents

Natalie J. Serkova<sup>1,2\*</sup> and S. Gail Eckhardt<sup>2,3</sup>

<sup>1</sup>Department of Anesthesiology, University of Colorado Comprehensive Cancer Center, Aurora, CO, USA, <sup>2</sup>Developmental Therapeutics Program, University of Colorado Comprehensive Cancer Center, Aurora, CO, USA, <sup>3</sup>Division of Medical Oncology, Anschutz Medical Center, University of Colorado Denver, Aurora, CO, USA

## OPEN ACCESS

**Edited by:**

Zaver Bhujwalla,  
Johns Hopkins University School of  
Medicine, USA

**Reviewed by:**

Balaji Krishnamachary,  
Johns Hopkins University, USA  
Marie-France Penet,  
Johns Hopkins University School of  
Medicine, USA  
Kristine Glunde,  
Johns Hopkins University School of  
Medicine, USA

**\*Correspondence:**

Natalie J. Serkova  
natalie.serkova@ucdenver.edu

**Specialty section:**

This article was submitted to  
Cancer Imaging and Diagnosis,  
a section of the journal  
*Frontiers in Oncology*

**Received:** 05 April 2016

**Accepted:** 07 June 2016

**Published:** 15 July 2016

**Citation:**

Serkova NJ and Eckhardt SG (2016)  
Metabolic Imaging to Assess  
Treatment Response to Cytotoxic  
and Cytostatic Agents.  
*Front. Oncol.* 6:152.  
doi: 10.3389/fonc.2016.00152

For several decades, cytotoxic chemotherapeutic agents were considered the basis of anticancer treatment for patients with metastatic tumors. A decrease in tumor burden, assessed by volumetric computed tomography and magnetic resonance imaging, according to the response evaluation criteria in solid tumors (RECIST), was considered as a radiological response to cytotoxic chemotherapies. In addition to RECIST-based dimensional measurements, a metabolic response to cytotoxic drugs can be assessed by positron emission tomography (PET) using <sup>18</sup>F-fluoro-thymidine (FLT) as a radioactive tracer for drug-disrupted DNA synthesis. The decreased <sup>18</sup>FLT-PET uptake is often seen concurrently with increased apparent diffusion coefficients by diffusion-weighted imaging due to chemotherapy-induced changes in tumor cellularity. Recently, the discovery of molecular origins of tumorigenesis led to the introduction of novel signal transduction inhibitors (STIs). STIs are targeted cytostatic agents; their effect is based on a specific biological inhibition with no immediate cell death. As such, tumor size is not anymore a sensitive end point for a treatment response to STIs; novel physiological imaging end points are desirable. For receptor tyrosine kinase inhibitors as well as modulators of the downstream signaling pathways, an almost immediate inhibition in glycolytic activity (the Warburg effect) and phospholipid turnover (the Kennedy pathway) has been seen by metabolic imaging in the first 24 h of treatment. The quantitative imaging end points by magnetic resonance spectroscopy and metabolic PET (including <sup>18</sup>F-fluoro-deoxyglucose, FDG, and total choline) provide an early treatment response to targeted STIs, before a reduction in tumor burden can be seen.

**Keywords:** chemotherapeutics, signal transduction inhibitors, magnetic resonance spectroscopy, positron emission tomography, RECIST

## INTRODUCTION

The field of medical oncology has emerged in the 1950s when various chemotherapeutic drugs were used to control cancer cell growth by interfering with the cell cycle and DNA replication. Later, in the 1960s and 1970s, drugs were combined to combat the cancer at different points of the cell cycle. For several decades, cytotoxic chemotherapeutic agents were considered the basis of anticancer treatment for patients with solid tumors and metastatic (systemic) disease. A decrease in tumor burden (tumor size and metastasis size/numbers), assessed by dimensional/volumetric magnetic resonance

imaging (MRI) or computed tomography (CT), was considered as a radiological response to a cytotoxic treatment regimen (1, 2).

Recently, the discovery of molecular origins of tumorigenesis led to the introduction of novel targeted agents, the so-called signal transduction inhibitors (STIs), and their translation into the clinic (3–5). By focusing on molecular abnormalities, which are specific to the cancer cell, targeted cancer therapies have a potential to be more effective against cancer and less harmful to normal cells than “standard” chemotherapeutics. STIs are considered a cytostatic (rather than cytotoxic) treatment alternative based on a specific biological inhibition (rather than immediate cell death) (Figure 1). As such, tumor size is not a sensitive end point for the treatment response to STIs; novel physiological imaging end points are desirable (6).

Anticancer therapies are currently undergoing enormous changes. Unfortunately, this biological revolution in cancer treatment comes at a great expense; the aggregate cost of cancer care rose 60% since 2003 (8, 9). In 2014, the price for each new approved cancer drug exceeded \$120,000/year of use. Therefore, the National Cancer Institute (NCI) has currently acknowledged that “there is a tremendous need to incentivize development of validated and accepted diagnostics in order to keep pace with the explosion of new, targeted drugs that are in the pipeline” (10). Advances in oncologic imaging pave the way for rapid optimization of personalized anticancer therapies through the non-invasive assessment of the mechanism of actions, efficacy and resistance development that improve clinical decision making for novel targeted agents beyond the traditional endpoints

of morbidity and mortality. Among other radiological platforms, metabolic imaging – based on positron emission tomography (PET) and magnetic resonance spectroscopy (MRS) – is particularly suited for monitoring the treatment response to cytostatic STIs since the signal transduction pathways are directly linked to the aberrant metabolic phenotype exhibited in human malignancies (11–16). Introduced in 1977, <sup>18</sup>F-fluoro-deoxy-glucose (FDG)-PET remains the main metabolic imaging technique for the non-invasive assessment of glucose consumption and the Warburg effect (17, 18). The use of PET has been expanded by the introduction of other radiolabeled ligands, such as amino acids and nucleosides. While tracer uptake studies represent the main strength of metabolic PET, <sup>1</sup>H-MRS provides complementary metabolic information on major endogenous metabolites (19–21). In the past 10 years, advances in hyperpolarized <sup>13</sup>C-MRS allowed for non-invasive assessment of metabolic activities in glucose, lipid, and amino acid metabolism in tumor-bearing animals and humans (22, 23).

## ANTICANCER TREATMENT STRATEGIES

### Cytotoxic Drugs

Herbal and other preparations have been used for cancer treatment already in the Ancient World. The very first attempt to treat leukemia with a chemical agent (potassium arsenite) took place in 1865 by Heinrich Lissauer. Then, a treatment benefit of estrogen in prostate cancer was shown in the early 1940s.

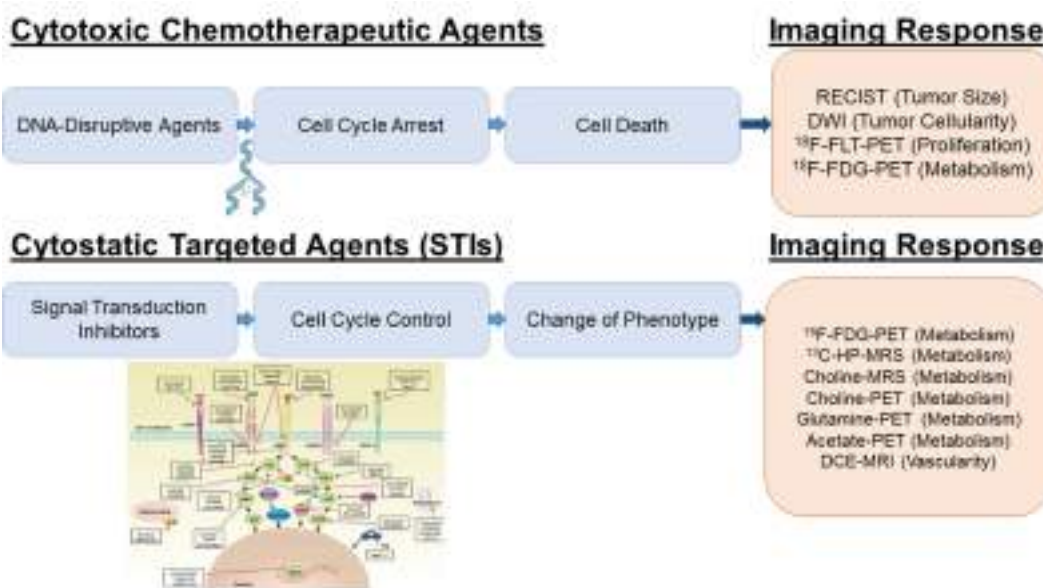


**FIGURE 1 | Imaging platforms for treatment response to cytotoxic and cytostatic agents.** For DNA disrupting agents (“Cytotoxic Chemotherapeutic Agents”), increased ADC values by DWI and decreased FLT and FDG uptake by PET reflect a cytotoxic treatment response due to the decreased in tumor cellularity, DNA synthesis and metabolism. For receptor tyrosine kinase inhibitors and PI3K/AKT/mTOR inhibition (“STIs”), a specific early decrease in glycolytic activity has been reported; therefore, glucose imaging using hyperpolarized <sup>13</sup>C-pyruvate MRSI or FDG-PET is most sensitive. Inhibition of the Kennedy pathway as monitored by decreased total choline MRSI or <sup>1</sup>C-/<sup>18</sup>F-choline PET is a putative marker for the treatment response of Ras/Raf/MEK/MAPK inhibitors. Glutamine and acetate imaging can be useful for c-myc and FASN inhibitors, respectively. For antiangiogenic agents (VEGF/VEGFR2 inhibitors), DCE-MRI is the technique of choice to assess decreased perfusion and vascularity. The picture was partially adapted from Munagala et al. (7).

Shortly after, nitrogen mustard (mustine), now considered as truly the first chemotherapeutic agent, was discovered and applied for the treatment of lymphomas and other solid tumors. Later, with the elucidation of the double-helical structure of DNA in 1953, it was shown that nitrogen mustard chemically reacts with DNA (24). This discovery had revolutionized the treatment of various cancers and resulted in a rapid development of several cytotoxic chemotherapeutics, which affect the integrity of the cell's genetic material (25). As such, most of classic chemotherapeutic drugs act in a cytotoxic manner, kill cells that divide rapidly, which includes *cancer cells*, immune cells, gastrointestinal (GI) tract, hair follicles, and result in a wide range of serious side effects to normal cells with high replication rate, including myelosuppression, GI toxicity, and alopecia (26–28).

Most of the cytotoxic chemotherapeutic drugs affect DNA synthesis or cell division and are commonly divided into four major classes (29–33): (i) mitotic poisons (preventing microtubule functions), (ii) DNA-reacting drugs (chemically modifying DNA as alkylating agents), (iii) inhibitors of DNA replications (acting as antimetabolites for pyrimidine, pyrimidine, and thymine synthesis), and (iv) agents that change DNA topology (topoisomerase inhibitors and cytotoxic antibiotics) (**Table 1**).

## Cytostatic Targeted Agents

The discovery of molecular targets has enabled the development of new and potentially more effective treatments for metastatic disease with considerably low toxic side effects (28). Due to our improved understanding of cancer biology and specific

onco-pathways that lead to uncontrolled cell proliferation, the main focus of anticancer treatment strategies has shifted from cytotoxic chemotherapies (which lead to cell death) to cytostatic targeted STIs. This has resulted in new requirements for pharmacodynamic markers (including imaging-based end points) for therapy response and resistance development to STIs (34). Oncologic imaging represents an ideal technology to answer these questions non-invasively and in real time (35–37).

Most of the targeted agents interfere with proteins that are involved in signal transduction processes. Progressive disease, the process of tumor growth, angiogenesis, invasion, and metastasis, is largely regulated by circulating growth factors and their binding to receptor tyrosine kinases (38, 39). Inhibition of these signaling pathways as a therapeutic approach has gained a lot of attention and current strategies include: antigrowth factor antibodies, receptor antagonists, anti-receptor monoclonal antibodies, and small-molecule tyrosine kinase inhibitors (24, 40). The use of molecularly targeted anticancer drugs began with the introduction of trastuzumab and imatinib, which target HER2/neu [*human epidermal growth factor (EGF) receptor 2*] and BCR-ABL [*from Philadelphia chromosome*]/PDGFR [*platelet-derived growth factor receptor*]/c-Kit [*stem cell growth factor receptor*], for the treatment of breast cancer and chronic myeloid leukemia, respectively (41–43). Some of the signal transduction pathways commonly altered in the malignant phenotype include various the upstream receptor tyrosine kinases, such as vascular endothelial growth factor (VEGF), EGF, insulin-like growth factor (IGF1), and PDGF, as well as downstream signaling kinases, specifically, PI3K/AKT/mTOR and Ras/Raf/MEK/MAPK pathways (38, 44–48) (**Table 2**).

**TABLE 1 | Major classes of cytotoxic agents.**

Cytotoxic chemotherapeutics			
Mitotic poisons	DNA-reactive drugs	Inhibitors of DNA replication	Modulators of DNA topology
Vincristine (1960)	N <sub>2</sub> -Mustard (1950)	Methotrexate (1955)	Doxorubicin (1975)
Vinblastine (1960)	Cyclophosphamide (1960)	5-Fluorouracil (1960)	Amsacrine (1985)
Paclitaxel (1990)	Alkylating agents (1965)	Gemcitabine (1995)	Topotecan (1995)
Docetaxel (1995)	Mitomycin (1970)		Irinotecan (2000)
	Bleomycin (1975)		
	Cisplatin (1980)		
	Carboplatin (1985)		

**TABLE 2 | Major classes of cytostatic agents.**

Cytostatic signal transduction inhibitors					
Receptor tyrosine kinase inhibitors	PI3K/AKT/mTOR inhibitors	Ras/Raf/MEK/MAPK inhibitors	Antiangiogenic (VEGF/VEGFR2)	Hormone therapy (estrogen/androgen)	Immune checkpoint inhibitors
- Imatinib (PDGFR)	- Everolimus (mTOR)	- Sorafenib (Raf)	- Bevacizumab (VEGF)	- Estrogen receptor	Nivolumab (anti-PD-1)
- Trastuzumab (Her2)	- Temsirolimus (mTOR)	- Dabrafenib (BRAF)	- - Tamoxifen	-	Pembrolizumab
- Lapatinib (Her2)	- Enzastaurin (PI3K)	- Trametinib (MEK)	- - Toremifene	-	(anti-PD-1)
- Pertuzumab (Her2)	- Afuresertib (AKT)	- Selumetinib (MEK)	- - Fulvestrant	-	Pidilizumab (anti-PD-1)
- Gefitinib (EGFR)		- Binimetinib (MEK)	- - Androgen receptor	-	MPDL3280A
- Erlotinib (EGFR)			- - Milutamide	-	(anti-PD-L1)
- Cetuximab (EGFR)			- - Finasteride	-	BMS-936559 (anti-PD-L1)
- Panitumumab (EGFR)					MEDI4736 (anti-PD-L1)
- Picropodophyllin (IGF-1R)					
- Linsitinib (IGF-1R)					
- Pazopanib (multi)					

## IMAGING TREATMENT RESPONSE

### Response Evaluation Criteria in Solid Tumors

In the past, anatomical imaging using plain radiographs, CT, MRI, and ultrasound (US) has been applied to assess the efficacy of cytotoxic chemotherapeutics based on lesion numbers and tumor size. Response evaluation criteria in solid tumors (RECIST) to measure lesion diameters have been the “gold standard” end point for cytotoxic agents for decades (49–51). Once target lesions are measured using single linear summation (lesion diameter by RECIST) or the bilinear volumetric approach [World Health Organization (WHO)], the treatment response is usually assigned as complete response (CR), partial response (PR, >30% linear decrease), stable disease (SD), or progressive disease (PD, >20% linear increase) (52). Since the introduction of the most recent version (RECIST 1.1) in 2009, several weakness areas have been identified, including the absence of potential early indicators of response, such as functional imaging, the scarceness of validation in rare tumors, and the lack of validation for novel targeted agents. As such, attempts to optimize the RECIST criteria are still needed to accurately evaluate tumor responses.

### Advanced Imaging of Cytotoxic Response

Introduction of diffusion-weighted imaging (DWI) to assess tumor cellularity was the next step in bringing imaging endpoints from a simple volumetric measurement to a functional assessment of therapy response. Tissues with high cellularity have restricted water diffusion, which can be quantitatively assessed by calculation of water apparent diffusion coefficients (ADC) from DWI, which are considerably low in fast proliferating tumors (53–56). Aggressive tumor and metastatic lesions are repeatedly reported to have ADC values below  $1.2 \times 10^{-3} \text{ mm}^2/\text{s}$ . A decrease in tumor cellularity and induction of cell death by cytotoxic chemotherapeutics results in increased ADC values, and increased ADC values have been reported as imaging biomarkers for chemotherapy response (57–60). For example, in breast cancer patients, an increase in ADC values in responders (as early as one cycle of neoadjuvant chemotherapy) is a good predictor for the later decrease in MRI tumor diameters (59).

Alternative imaging platforms for cytotoxic response are based on metabolic PET. Malignant tissues are chiefly composed of rapidly dividing cells, which exhibit highly upregulated DNA synthesis.  $^{18}\text{F}$ -fluoro-3-deoxy-thymidine ( $^{18}\text{FLT}$ ) is a PET tracer for tumor cell proliferation (based on the high thymidine uptake by proliferating cells in the pyrimidine salvage pathway during S-phase). Although not highly specific (61, 62), a decreased signal intensity in  $^{18}\text{FLT}$ -PET can be observed when DNA synthesis is disrupted by chemotherapeutic agents, often simultaneously with a profound DWI response by MRI (63–65). Another PET application is based on the fact that cancer cells use large amounts of glucose as a direct source of energy to permit the exaggerated utilization of amino acids and nucleosides in the synthesis of DNA. The radioactive glucose analog FDG is the most widely used tracer in oncologic PET/CT to

assess metabolic cancer aggressiveness based on high glucose uptake and metabolism through high GLUT-1 transporters and hexokinase expression/activity (66). It has been shown that in patients with lung, breast, head-and-neck, esophageal, colorectal cancers, and lymphoma, the standardized uptake values of FDG decrease in responding tumors after one cycle of chemotherapy (18, 67).

### Imaging in Radiation Oncology

Radiation therapy is used as part of cancer treatment, mostly in combination with systemic chemotherapy, in roughly 50% of all cancer cases. It is especially effective in head-and-neck, breast, prostate, cervical, and skin cancer, while colorectal cancer, soft tissue sarcomas, and high-grade gliomas usually show only a limited response rate. The posttreatment effects of radiotherapy are attributed to tumor inflammation, cell necrosis and often increased angiogenesis (68, 69). Clinically, FDG-PET/CT is frequently acquired at the baseline for radiation treatment planning since high metabolic activity is regarded as a positive predictive factor for treatment response (70). A profound metabolic response, as detected by decreased FDG uptake values on postradiation PET/CT scans, has correlated with high progression-free survival rates in almost all types of cancer (71–73). Hyperpolarized MRS using [ $1\text{-}^{13}\text{C}$ ]-pyruvate also showed a significant decrease in lactate production as early as 96 h after irradiation in orthotopic rat glioma models (74) and colorectal flank xenografts (75).

### Metabolic Imaging of Signal Transduction Inhibition

Changes in tumor size, the “gold-standard” of tumor response for cytotoxic chemotherapeutic agents, are often not useful in monitoring therapy response in the first cycles of STI-based therapy. Humanized monoclonal antibodies and small-molecule receptor tyrosine kinase inhibitors have been developed to target epidermal growth factor receptors (EGFR), platelet-derived growth factor receptor (PDGFR), and insulin-like growth factor receptor (IGF-1R), which are overexpressed in a significant number of human malignancies. These inhibitors of the receptor activity include gefitinib, erlotinib, imatinib, cetuximab, and trastuzumab and have the most profound metabolic effects by inhibiting both glucose and choline metabolism, which are two main metabolic hallmarks of cancer (76–78). Therefore, the imaging response to receptor inhibitors has been successfully monitored – both preclinically and clinically – using glucose-based (FDG-PET and hyperpolarized  $^{13}\text{C}$ -MRS) (79–89) and choline-based ( $^{1}\text{H}$ -/ $^{31}\text{P}$ -MRS and choline-PET) metabolic imaging (90–92). The metabolic response on FDG-PET was seen as early as 8 days after initiation of treatment (93).

Upstream receptor upregulation leads to the downstream activation of two main intracellular onco-pathways: the GTPase Ras/Raf/MEK/MAPK and the lipid kinase PI3K/AKT/mTOR pathways. It has been convincingly shown that the PI3K/AKT/mTOR pathway directly downregulates glucose metabolism: a significant decrease in glucose uptake, lactate production, and glycolytic enzyme expression has been seen with several mTOR (94–97) and PI3K inhibitors (98, 99).  $^{13}\text{C}$ -MRSI measurements

of the conversion of hyperpolarized [1-<sup>13</sup>C]-pyruvate into lactate have been used to image the decrease in tumor LDH activity due to the inhibition of the PI3K/AKT/mTOR pathway. Confirming these MRS data, the decreased FDG uptake was seen on PET scans upon mTOR/PI3K inhibition (97, 100, 101). Most recently, the US Centers for Medicare and Medicaid Services (CMS) have approved the coverages of FDG-PET/CT for treatment response in most solid tumors, especially for the treatment strategies based on receptor tyrosine kinase inhibitors and PI3K/AKT/mTOR mediated pathways (88). FDG-PET is intrinsically a quantitative imaging technique for early STI treatment response based on calculations of the standardized uptake value (SUV) of FDG uptake (77, 97). An improved quantification of treatment response based on decreased SUVs has been introduced as the PET response criteria in solid tumors (PERCIST 1.0) (102).

In contrast, MEK inhibitors, with MEK being the main therapeutic target from the Ras/Raf/MEK/MAPK pathway, do not exhibit a considerable glycolytic effect as revealed by FDG-PET and hyperpolarized MRS (64, 103, 104), but significantly reduce choline metabolism (104–106). Choline is a precursor of phosphatidylcholine, the major cell membrane phospholipid. Ras/Raf/MEK/MAPK pathway inhibition leads to the decrease in choline transporters and might also influence the activity of choline kinase (CHK $\alpha$ ) leading to a significant decrease of the total choline peak detected by MRS. <sup>11</sup>C- or <sup>18</sup>F-choline PET/CT can be used to detect a significant decrease in tracer uptake following treatment with various targeted STIs, especially those from the Ras/Raf/MEK/MAPK pathway (107).

While the PI3K/AKT/mTOR pathway is considered to be “glucose-dependent,” recent studies have shown that the MYC oncogene, which encodes a master transcription factor c-Myc, regulates glutamine catabolism to fuel growth and proliferation of cancer cells through upregulating glutaminase (GLS) (108–110). The first success in imaging glutaminase activity by MRS was achieved using hyperpolarized <sup>13</sup>C-glutamine (111). Recently, <sup>11</sup>C- and <sup>18</sup>F-labeled glutamine has been synthesized and successfully utilized for non-invasive PET detection of c-Myc tumors in rodent models (112, 113). In addition, recent *in vitro* MRS studies with c-Myc overexpressed breast cancer cells showed a significant suppression of glutaminolysis when treated with aminoxyacetate, an inhibitor of aminotransferases involved in amino acid metabolism (114, 115). Several c-Myc inhibitors are now in preclinical testing, and glutamine-PET will be an obvious technique of choice for monitoring metabolic treatment response.

Positron emission tomography measurements of the uptake and trapping of <sup>11</sup>C-acetate, due to the increased expression of fatty acid synthase (FASN), have been used to detect prostate cancer and hepatocellular carcinoma – two cancers where FDG-PET evaluations have proven to be challenging or non-effective (116–118). The use of <sup>11</sup>C-acetate PET/CT can be useful while assessing treatment response to FASN and fat oxidation inhibitors, such as orlistat and etomoxir, in prostate cancer (119, 120).

Finally, the therapeutic efficacy of antiangiogenic agents targeting the VEGF/VEGFR2 pathway can be monitored using dynamic contrast-enhanced (DCE)-MRI (121–123). The time-dependent

signal enhancement on dynamic T1-weighted MRI reflects intratumoral contrast delivery after an intravenous injection of gadolinium contrast and is proportional to tumor perfusion and vascularity. A dramatic decrease in T1-enhancement, calculated as decreased gadolinium transfer constant,  $K^{trans}$ , or the decreased area under the enhancement curve, AUC, was seen after tumor treatment with VEGF antibodies, such as bevacizumab, or VEGFR2 tyrosine kinase inhibitors.

## Imaging of Hormone- and Immune-Based Therapies

In addition to cytotoxic DNA-interfering agents and cytostatic STIs, other classes of anticancer drugs have been developed. The most promising are hormones and hormone antagonists for breast, prostate, and endocrine tumors. <sup>18</sup>F-labeled PET tracers for androgen and estrogen receptor imaging have been developed and tested in animal models (124, 125); <sup>18</sup>F-fluoroestradiol (FES) is undergoing clinical trials to monitor early treatment response to aromatase inhibitors, such as tamoxifen and fulvestrant, in ER+ breast cancer patients (126, 127). Finally, the most exciting area in anticancer treatment lies in cancer immunotherapy and novel immunomodulatory targeted agents (128). The inhibitors of the programmed cell death receptor PD-1 and its ligands PDL-1, such as nivolumab and pembrolizumab, have recently shown a promising antitumor activity in melanoma and lung cancers and, to some degree, in triple-negative breast cancers (129–131). The most recent report from the phase Ib on pembrolizumab in patients with advanced melanoma clearly demonstrated that conventional RECIST criteria are not appropriate for the adequate assessment of immune response and might underestimate the benefit of the immune checkpoint blockade in 15% of treated patients leading to premature cessation of treatment (132). However, the metabolic aspects of this activated antitumor immune response are still to be elucidated.

## CONCLUSION

For “classic” chemotherapeutic agents, increased ADC values by DWI reflect an early cytotoxic treatment response due to decreased tumor cellularity and are an attractive alternative to volumetric imaging. For novel STIs, physiological and metabolic imaging protocols should be carefully chosen based on a particular signal transduction pathway involved. For receptor tyrosine kinase inhibitors and PI3K/AKT/mTOR inhibition, a specific decrease in glycolytic activity has been reported; therefore, glucose imaging using hyperpolarized <sup>13</sup>C-pyruvate MRSI or FDG-PET is most sensitive. Inhibition of the Kennedy pathway as monitored by decreased total choline MRSI or <sup>11</sup>C-/ <sup>18</sup>F-choline PET is a putative marker for the treatment response of Ras/Raf/MEK/MAPK inhibitors. For antiangiogenic agents (VEGF/VEGFR2 inhibitors), DCE-MRI is the technique of choice to assess decreased perfusion and vascularity.

Introduction of novel targeted STIs, including immune checkpoint inhibitors, requires a robust validation of novel quantitative imaging end points from PET, MRS, and other

supporting imaging platforms that characterize early physiological and metabolic treatment response before a reduction in tumor burden can be seen (6). Using medical imaging to distinguish responders versus non-responders at early time points can contribute to improved tailoring of therapy in individual cancer patients. The new term, *radiogenomics*, has recently been introduced to link quantitative physiological imaging end points with molecular markers of signal transduction pathway inhibition (133).

## REFERENCES

- Curran SD, Muellner AU, Schwartz LH. Imaging response assessment in oncology. *Cancer Imaging* (2006) 6:S126–30. doi:10.1102/1470-7330.2006.9039
- Marcus CD, Ladam-Marcus V, Cucu C, Bouche O, Lucas L, Hoeffel C. Imaging techniques to evaluate the response to treatment in oncology: current standards and perspectives. *Crit Rev Oncol Hematol* (2009) 72(3):217–38. doi:10.1016/j.critrevonc.2008.07.012
- Druker B. Signal transduction inhibition: results from phase I clinical trials in chronic myeloid leukemia. *Semin Hematol* (2001) 38(3 Suppl 8):9–14. doi:10.1016/S0037-1963(01)90112-X
- Kelly CM, Power DG, Lichtman SM. Targeted therapy in older patients with solid tumors. *J Clin Oncol* (2014) 32(24):2635–46. doi:10.1200/JCO.2014.55.4246
- Alvarez RH, Valero V, Hortobagyi GN. Emerging targeted therapies for breast cancer. *J Clin Oncol* (2010) 28(20):3366–79. doi:10.1200/JCO.2009.25.4011
- Brindle K. New approaches for imaging tumour responses to treatment. *Nat Rev Cancer* (2008) 8(2):94–107. doi:10.1038/nrc2289
- Munagala R, Aqil F, Gupta RC. Promising molecular targeted therapies in breast cancer. *Indian J Pharmacol* (2011) 43(3):236–45. doi:10.4103/0253-7613.81497
- Kantarjian H, Rajkumar SV. Why are cancer drugs so expensive in the United States, and what are the solutions? *Mayo Clin Proc* (2015) 90(4):500–4. doi:10.1016/j.mayocp.2015.01.014
- Tefferi A, Kantarjian H, Rajkumar SV, Baker LH, Abkowitz JL, Adamson JW, et al. In support of a patient-driven initiative and petition to lower the high price of cancer drugs. *Mayo Clin Proc* (2015) 90(8):996–1000. doi:10.1016/j.mayocp.2015.06.001
- Sawyers CL, van't Veer LJ. Reliable and effective diagnostics are keys to accelerating personalized cancer medicine and transforming cancer care: a policy statement from the American Association for Cancer Research. *Clin Cancer Res* (2014) 20(19):4978–81. doi:10.1158/1078-0432.CCR-14-2295
- Memmott RM, Dennis PA. Akt-dependent and -independent mechanisms of mTOR regulation in cancer. *Cell Signal* (2009) 21(5):656–64. doi:10.1016/j.cellsig.2009.01.004
- Flavin R, Zadra G, Loda M. Metabolic alterations and targeted therapies in prostate cancer. *J Pathol* (2011) 223(2):283–94. doi:10.1002/path.2809
- Vander Heiden MG. Targeting cancer metabolism: a therapeutic window opens. *Nat Rev Drug Discov* (2011) 10(9):671–84. doi:10.1038/nrd3504
- Shen L, Sun X, Fu Z, Yang G, Li J, Yao L. The fundamental role of the p53 pathway in tumor metabolism and its implication in tumor therapy. *Clin Cancer Res* (2012) 18(6):1561–7. doi:10.1158/1078-0432.CCR-11-3040
- Kimmelman AC. Metabolic dependencies in RAS-driven cancers. *Clin Cancer Res* (2015) 21(8):1828–34. doi:10.1158/1078-0432.CCR-14-2425
- White E, Mehnert JM, Chan CS. Autophagy, metabolism, and cancer. *Clin Cancer Res* (2015) 21(22):5037–46. doi:10.1158/1078-0432.CCR-15-0490
- Herholz K, Coop D, Jackson A. Metabolic and molecular imaging in neuro-oncology. *Lancet Neurol* (2007) 6(8):711–24. doi:10.1016/S1474-4422(07)70192-8
- Juwaid ME, Cheson BD. Positron-emission tomography and assessment of cancer therapy. *N Engl J Med* (2006) 354(5):496–507. doi:10.1056/NEJMra050276
- Bolan PJ, Nelson MT, Yee D, Garwood M. Imaging in breast cancer: magnetic resonance spectroscopy. *Breast Cancer Res* (2005) 7(4):149–52. doi:10.1186/bcr1202
- Sardanelli F, Fausto A, Di Leo G, de Nijs R, Vorbuchner M, Podo F. In vivo proton MR spectroscopy of the breast using the total choline peak integral as a marker of malignancy. *AJR Am J Roentgenol* (2009) 192(6):1608–17. doi:10.2214/AJR.07.3521
- Glunde K, Ackerstaff E, Mori N, Jacobs MA, Bhujwalla ZM. Choline phospholipid metabolism in cancer: consequences for molecular pharmaceutical interventions. *Mol Pharm* (2006) 3(5):496–506. doi:10.1021/mp060067e
- Day SE, Kettunen MI, Gallagher FA, Hu DE, Lerche M, Wolber J, et al. Detecting tumor response to treatment using hyperpolarized <sup>13</sup>C magnetic resonance imaging and spectroscopy. *Nat Med* (2007) 13(11):1382–7. doi:10.1038/nm1650
- Albers MJ, Bok R, Chen AP, Cunningham CH, Zierhut ML, Zhang VY, et al. Hyperpolarized <sup>13</sup>C lactate, pyruvate, and alanine: noninvasive biomarkers for prostate cancer detection and grading. *Cancer Res* (2008) 68(20):8607–15. doi:10.1158/0008-5472.CAN-08-0749
- Bates SE, Amiri-Kordestani L, Giaccone G. Drug development: portals of discovery. *Clin Cancer Res* (2012) 18(1):23–32. doi:10.1158/1078-0432.CCR-11-1001
- Nygren P; SBU-Group Swedish Council on Technology Assessment in Health Care. What is cancer chemotherapy? *Acta Oncol* (2001) 40(2–3):166–74. doi:10.1080/02841860151116204
- Awada A. New cytotoxic agents and molecular-targeted therapies in the treatment of metastatic breast cancer. *Forum (Genova)* (2002) 12(1):4–15.
- Esteva FJ, Valero V, Pusztai L, Boehnke-Michaud L, Buzdar AU, Hortobagyi GN. Chemotherapy of metastatic breast cancer: what to expect in 2001 and beyond. *Oncologist* (2001) 6(2):133–46. doi:10.1634/theoncologist.6-2-133
- Tol J, Koopman M, Cats A, Rodenburg CJ, Creemers GJ, Schrama JG, et al. Chemotherapy, bevacizumab, and cetuximab in metastatic colorectal cancer. *N Engl J Med* (2009) 360(6):563–72. doi:10.1056/NEJMoa080268
- Crown J, O'Leary M. The taxanes: an update. *Lancet* (2000) 355(9210):1176–8. doi:10.1016/S0140-6736(00)02074-2
- Cunningham D, Starling N, Rao S, Iveson T, Nicolson M, Coxon F, et al. Capecitabine and oxaliplatin for advanced esophagogastric cancer. *N Engl J Med* (2008) 358(1):36–46. doi:10.1056/NEJMoa073149
- Gianni L, Norton L, Wolmark N, Suter TM, Bonadonna G, Hortobagyi GN. Role of anthracyclines in the treatment of early breast cancer. *J Clin Oncol* (2009) 27(28):4798–808. doi:10.1200/JCO.2008.21.4791
- Rivera E, Valero V, Syrewicz L, Rahman Z, Esteva FJ, Theriault RL, et al. Phase I study of stealth liposomal doxorubicin in combination with gemcitabine in the treatment of patients with metastatic breast cancer. *J Clin Oncol* (2001) 19(6):1716–22.
- Gokduman K. Strategies targeting DNA topoisomerase I in cancer chemotherapy: camptothecins, nanocarriers for camptothecins, organic non-camptothecin compounds and metal complexes. *Curr Drug Targets* (2016).
- Booth CM, Ohorodnyk P, Eisenhauer EA. Call for clarity in the reporting of benefit associated with anticancer therapies. *J Clin Oncol* (2009) 27(33):e213–4. doi:10.1200/JCO.2009.24.8542
- Serkova NJ, Garg K, Bradshaw-Pierce EL. Oncologic imaging end-points for the assessment of therapy response. *Recent Pat Anticancer Drug Discov* (2009) 4(1):36–53. doi:10.2174/157489209787002434
- El-Deiry WS, Siganian CC, Kelloff GJ. Imaging and oncologic drug development. *J Clin Oncol* (2006) 24(20):3261–73. doi:10.1200/JCO.2006.06.5623
- Padhani AR, Miles KA. Multiparametric imaging of tumor response to therapy. *Radiology* (2010) 256(2):348–64. doi:10.1148/radiol.10091760
- Mendelsohn J, Baselga J. Epidermal growth factor receptor targeting in cancer. *Semin Oncol* (2006) 33(4):369–85. doi:10.1053/j.seminoncol.2006.04.003

## AUTHOR CONTRIBUTIONS

Both the authors listed, have made substantial, direct, and intellectual contribution to the work, and approved it for publication.

## FUNDING

This work was supported by the NIH 1UM1 CA186688, P30 CA046934, UL1 TR001082, and R21 CA194477 grants.

39. Baselga J. Targeting tyrosine kinases in cancer: the second wave. *Science* (2006) 312(5777):1175–8. doi:10.1126/science.1125951
40. Benavent M, de Miguel MJ, Garcia-Carbonero R. New targeted agents in gastroenteropancreatic neuroendocrine tumors. *Target Oncol* (2012) 7(2):99–106. doi:10.1007/s11523-012-0218-9
41. Leyland-Jones B. Trastuzumab: hopes and realities. *Lancet Oncol* (2002) 3(3):137–44. doi:10.1016/S1470-2045(02)00676-9
42. Druker BJ. Perspectives on the development of imatinib and the future of cancer research. *Nat Med* (2009) 15(10):1149–52. doi:10.1038/nm1009-1149
43. Druker B. Imatinib (Gleevec) as a paradigm of targeted cancer therapies. *Keio J Med* (2010) 59(1):1–3. doi:10.2302/kjm.59.1
44. Ellis LM. Antiangiogenic therapy: more promise and, yet again, more questions. *J Clin Oncol* (2003) 21(21):3897–9. doi:10.1200/JCO.2003.07.977
45. Hegi ME, Rajakannu P, Weller M. Epidermal growth factor receptor: a re-emerging target in glioblastoma. *Curr Opin Neurol* (2012) 25(6):774–9. doi:10.1097/WCO.0b013e328359b0bc
46. Hirakawa T, Yashiro M, Murata A, Hirata K, Kimura K, Amano R, et al. IGF-1 receptor and IGF binding protein-3 might predict prognosis of patients with resectable pancreatic cancer. *BMC Cancer* (2013) 13:392. doi:10.1186/1471-2407-13-392
47. Shaw RJ, Cantley LC. Ras, PI(3)K and mTOR signalling controls tumour cell growth. *Nature* (2006) 441(7092):424–30. doi:10.1038/nature04869
48. Early Breast Cancer Trialists' Collaborative Group. Effects of chemotherapy and hormonal therapy for early breast cancer on recurrence and 15-year survival: an overview of the randomised trials. *Lancet* (2005) 365(9472):1687–717. doi:10.1016/S0140-6736(05)66544-0
49. Jaffe CC. Measures of response: RECIST, WHO, and new alternatives. *J Clin Oncol* (2006) 24(20):3245–51. doi:10.1200/JCO.2006.06.5599
50. Jaffe CC. Response assessment in clinical trials: implications for sarcoma clinical trial design. *Oncologist* (2008) 13(Suppl 2):14–8. doi:10.1634/theoncologist.13-S2-14
51. Eisenhauer EA, Therasse P, Bogaerts J, Schwartz LH, Sargent D, Ford R, et al. New response evaluation criteria in solid tumours: revised RECIST guideline (version 1.1). *Eur J Cancer* (2009) 45(2):228–47. doi:10.1016/j.ejca.2008.10.026
52. Chia S, Dent S, Ellard S, Ellis PM, Vandenberg T, Gelmon K, et al. Phase II trial of OGX-011 in combination with docetaxel in metastatic breast cancer. *Clin Cancer Res* (2009) 15(2):708–13. doi:10.1158/1078-0432.CCR-08-1159
53. Hamstra DA, Rehemtulla A, Ross BD. Diffusion magnetic resonance imaging: a biomarker for treatment response in oncology. *J Clin Oncol* (2007) 25(26):4104–9. doi:10.1200/JCO.2007.11.9610
54. Padhani AR, Koh DM, Collins DJ. Whole-body diffusion-weighted MR imaging in cancer: current status and research directions. *Radiology* (2011) 261(3):700–18. doi:10.1148/radiol.11110474
55. Partridge SC, Mullins CD, Kurland BF, Allain MD, DeMartini WB, Eby PR, et al. Apparent diffusion coefficient values for discriminating benign and malignant breast MRI lesions: effects of lesion type and size. *AJR Am J Roentgenol* (2010) 194(6):1664–73. doi:10.2214/AJR.09.3534
56. Eiber M, Holzapfel K, Ganter C, Apple K, Metz S, Geinitz H, et al. Whole-body MRI including diffusion-weighted imaging (DWI) for patients with recurring prostate cancer: technical feasibility and assessment of lesion conspicuity in DWI. *J Magn Reson Imaging* (2011) 33(5):1160–70. doi:10.1002/jmri.22542
57. Lee KC, Hamstra DA, Bhojani MS, Khan AP, Ross BD, Rehemtulla A. Noninvasive molecular imaging sheds light on the synergy between 5-fluorouracil and TRAIL/Apo2L for cancer therapy. *Clin Cancer Res* (2007) 13(6):1839–46. doi:10.1158/1078-0432.CCR-06-1657
58. Padhani AR, Khan AA. Diffusion-weighted (DW) and dynamic contrast-enhanced (DCE) magnetic resonance imaging (MRI) for monitoring anticancer therapy. *Target Oncol* (2010) 5(1):39–52. doi:10.1007/s11523-010-0135-8
59. Jensen LR, Garzon B, Heldahl MG, Bathen TF, Lundgren S, Gribbestad IS. Diffusion-weighted and dynamic contrast-enhanced MRI in evaluation of early treatment effects during neoadjuvant chemotherapy in breast cancer patients. *J Magn Reson Imaging* (2011) 34(5):1099–109. doi:10.1002/jmri.22726
60. Ng TS, Wert D, Sohi H, Procissi D, Colcher D, Raubitschek AA, et al. Serial diffusion MRI to monitor and model treatment response of the targeted nanotherapy CRLX101. *Clin Cancer Res* (2013) 19(9):2518–27. doi:10.1158/1078-0432.CCR-12-2738
61. Zhang CC, Yan Z, Li W, Kuszpit K, Painter CL, Zhang Q, et al. [(18)F]FLT-PET imaging does not always “light up” proliferating tumor cells. *Clin Cancer Res* (2012) 18(5):1303–12. doi:10.1158/1078-0432.CCR-11-1433
62. Shields AF. PET imaging of tumor growth: not as easy as it looks. *Clin Cancer Res* (2012) 18(5):1189–91. doi:10.1158/1078-0432.CCR-11-3198
63. Weber WA. Monitoring tumor response to therapy with 18F-FLT PET. *J Nucl Med* (2010) 51(6):841–4. doi:10.2967/jnumed.109.071217
64. Honndorf VS, Schmidt H, Wiehr S, Wehr HF, Quintanilla-Martinez L, Stahlschmidt A, et al. The synergistic effect of selumetinib/docetaxel combination therapy monitored by [(18) F]FDG/[(18) F]FLT PET and diffusion-weighted magnetic resonance imaging in a colorectal tumor xenograft model. *Mol Imaging Biol* (2016) 18(2):249–57. doi:10.1007/s11307-015-0881-1
65. Leyton J, Latigo JR, Perumal M, Dhaliwal H, He Q, Aboagye EO. Early detection of tumor response to chemotherapy by 3'-deoxy-3'-[18F] fluorothymidine positron emission tomography: the effect of cisplatin on a fibrosarcoma tumor model in vivo. *Cancer Res* (2005) 65(10):4202–10. doi:10.1158/0008-5472.CAN-04-4008
66. Kaira K, Endo M, Abe M, Nakagawa K, Ohde Y, Okumura T, et al. Biologic correlation of 2-[18F]-fluoro-2-deoxy-D-glucose uptake on positron emission tomography in thymic epithelial tumors. *J Clin Oncol* (2010) 28(23):3746–53. doi:10.1200/JCO.2009.27.4662
67. Shankar LK, Hoffman JM, Bacharach S, Graham MM, Karp J, Lammertsma AA, et al. Consensus recommendations for the use of 18F-FDG PET as an indicator of therapeutic response in patients in National Cancer Institute Trials. *J Nucl Med* (2006) 47(6):1059–66.
68. Bonner JA, Harari PM, Giralt J, Azarnia N, Shin DM, Cohen RB, et al. Radiotherapy plus cetuximab for squamous-cell carcinoma of the head and neck. *N Engl J Med* (2006) 354(6):567–78. doi:10.1056/NEJMoa053422
69. Dirix P, Vandecaveye V, De Keyzer F, Stroobants S, Hermans R, Nyuyts S. Dose painting in radiotherapy for head and neck squamous cell carcinoma: value of repeated functional imaging with (18)F-FDG PET, (18)F-fluoromisonidazole PET, diffusion-weighted MRI, and dynamic contrast-enhanced MRI. *J Nucl Med* (2009) 50(7):1020–7. doi:10.2967/jnumed.109.062638
70. Herrera FG, Breunaval T, Prior JO, Bourhis J, Ozsahin M. [(18)F]FDG-PET/CT metabolic parameters as useful prognostic factors in cervical cancer patients treated with chemo-radiotherapy. *Radiat Oncol* (2016) 11(1):43. doi:10.1186/s13014-016-0614-x
71. Schwarz JK, Siegel BA, Dehdashti F, Myerson RJ, Fleshman JW, Grigsby PW. Tumor response and survival predicted by post-therapy FDG-PET/CT in anal cancer. *Int J Radiat Oncol Biol Phys* (2008) 71(1):180–6. doi:10.1016/j.ijrobp.2007.09.005
72. Krause BJ, Herrmann K, Wieder H, zum Buschenfelde CM. 18F-FDG PET and 18F-FDG PET/CT for assessing response to therapy in esophageal cancer. *J Nucl Med* (2009) 50(Suppl 1):89S–96S. doi:10.2967/jnumed.108.057232
73. Schoder H, Fury M, Lee N, Kraus D. PET monitoring of therapy response in head and neck squamous cell carcinoma. *J Nucl Med* (2009) 50(Suppl 1):74S–88S. doi:10.2967/jnumed.108.057208
74. Day SE, Kettunen MI, Cherukuri MK, Mitchell JB, Lizak MJ, Morris HD, et al. Detecting response of rat C6 glioma tumors to radiotherapy using hyperpolarized [1-13C]pyruvate and 13C magnetic resonance spectroscopic imaging. *Magn Reson Med* (2011) 65(2):557–63. doi:10.1002/mrm.22698
75. Saito K, Matsumoto S, Takakusagi Y, Matsuo M, Morris HD, Lizak MJ, et al. 13C-MR spectroscopic imaging with hyperpolarized [1-13C]pyruvate detects early response to radiotherapy in SCC tumors and HT-29 tumors. *Clin Cancer Res* (2015) 21(22):5073–81. doi:10.1158/1078-0432.CCR-14-1717
76. Podo F, Canevari S, Canese R, Pisano ME, Ricci A, Iorio E. MR evaluation of response to targeted treatment in cancer cells. *NMR Biomed* (2011) 24(6):648–72. doi:10.1002/nbm.1658
77. Contractor KB, Aboagye EO. Monitoring predominantly cytostatic treatment response with 18F-FDG PET. *J Nucl Med* (2009) 50(Suppl 1):97S–105S. doi:10.2967/jnumed.108.057273
78. Moestue SA, Engebraaten O, Gribbestad IS. Metabolic effects of signal transduction inhibition in cancer assessed by magnetic resonance spectroscopy. *Mol Oncol* (2011) 5(3):224–41. doi:10.1016/j.molonc.2011.04.001
79. Na II, Byun BH, Kang HJ, Cheon GJ, Koh JS, Kim CH, et al. 18F-fluorodeoxy-glucose uptake predicts clinical outcome in patients with

- gefitinib-treated non-small cell lung cancer. *Clin Cancer Res* (2008) 14(7):2036–41. doi:10.1158/1078-0432.CCR-07-4074
80. Aukema TS, Kappers I, Olmos RA, Codrington HE, van Tinteren H, van Pel R, et al. Is 18F-FDG PET/CT useful for the early prediction of histopathologic response to neoadjuvant erlotinib in patients with non-small cell lung cancer? *J Nucl Med* (2010) 51(9):1344–8. doi:10.2967/jnumed.110.076224
  81. van Gool MH, Aukema TS, Hartemink KJ, Valdes Olmos RA, van Tinteren H, Klomp HM. FDG-PET/CT response evaluation during EGFR-TKI treatment in patients with NSCLC. *World J Radiol* (2014) 6(7):392–8. doi:10.4329/wjr.v6.i7.392
  82. van Gool MH, Aukema TS, Schaake EE, Rijna H, Valdes Olmos RA, van Pel R, et al. Timing of metabolic response monitoring during erlotinib treatment in non-small cell lung cancer. *J Nucl Med* (2014) 55(7):1081–6. doi:10.2967/jnumed.113.130674
  83. Cheyne RW, Trembleau L, McLaughlin A, Smith TA. Changes in 2-fluoro-2-deoxy-D-glucose incorporation, hexokinase activity and lactate production by breast cancer cells responding to treatment with the anti-HER-2 antibody trastuzumab. *Nucl Med Biol* (2011) 38(3):339–46. doi:10.1016/j.nucmedbio.2010.09.005
  84. Krystal GW, Alesi E, Tatum JL. Early FDG/PET scanning as a pharmacodynamic marker of anti-EGFR antibody activity in colorectal cancer. *Mol Cancer Ther* (2012) 11(7):1385–8. doi:10.1158/1535-7163.MCT-12-0011
  85. Su H, Bodenstein C, Dumont RA, Seimbille Y, Dubinett S, Phelps ME, et al. Monitoring tumor glucose utilization by positron emission tomography for the prediction of treatment response to epidermal growth factor receptor kinase inhibitors. *Clin Cancer Res* (2006) 12(19):5659–67. doi:10.1158/1078-0432.CCR-06-0368
  86. Soundararajan A, Abraham J, Nelom LD, Prajapati SI, Zarzabal LA, Michalek JE, et al. 18F-FDG microPET imaging detects early transient response to an IGF1R inhibitor in genetically engineered rhabdomyosarcoma models. *Pediatr Blood Cancer* (2012) 59(3):485–92. doi:10.1002/pbc.24075
  87. Ekman S, Frodin JE, Harmenberg J, Bergman A, Hedlund A, Dahg P, et al. Clinical phase I study with an insulin-like growth factor-1 receptor inhibitor: experiences in patients with squamous non-small cell lung carcinoma. *Acta Oncol* (2011) 50(3):441–7. doi:10.3109/0284186X.2010.499370
  88. McKinley ET, Bugaj JE, Zhao P, Guleryuz S, Mantis C, Gokhale PC, et al. 18FDG-PET predicts pharmacodynamic response to OSI-906, a dual IGF-1R/IR inhibitor, in preclinical mouse models of lung cancer. *Clin Cancer Res* (2011) 17(10):3332–40. doi:10.1158/1078-0432.CCR-10-2274
  89. Kominsky DJ, Klawitter J, Brown JL, Boros LG, Melo JV, Eckhardt SG, et al. Abnormalities in glucose uptake and metabolism in imatinib-resistant human BCR-ABL-positive cells. *Clin Cancer Res* (2009) 15(10):3442–50. doi:10.1158/1078-0432.CCR-08-3291
  90. Klawitter J, Kominsky DJ, Brown JL, Klawitter J, Christians U, Leibfritz D, et al. Metabolic characteristics of imatinib resistance in chronic myeloid leukaemia cells. *Br J Pharmacol* (2009) 158(2):588–600. doi:10.1111/j.1476-5381.2009.00345.x
  91. Klawitter J, Anderson N, Klawitter J, Christians U, Leibfritz D, Eckhardt SG, et al. Time-dependent effects of imatinib in human leukaemia cells: a kinetic NMR-profiling study. *Br J Cancer* (2009) 100(6):923–31. doi:10.1038/sj.bjc.6604946
  92. Glunde K, Serkova NJ. Therapeutic targets and biomarkers identified in cancer choline phospholipid metabolism. *Pharmacogenomics* (2006) 7(7):1109–23. doi:10.2217/14622416.7.7.1109
  93. Stroobants S, Goeminne J, Seegers M, Dimitrijevic S, Dupont P, Nuyts J, et al. 18FDG-Positron emission tomography for the early prediction of response in advanced soft tissue sarcoma treated with imatinib mesylate (Glivec). *Eur J Cancer* (2003) 39(14):2012–20. doi:10.1016/S0959-8049(03)00073-X
  94. Lee SC, Marzec M, Liu X, Wehrli S, Kantekure K, Ragunath PN, et al. Decreased lactate concentration and glycolytic enzyme expression reflect inhibition of mTOR signal transduction pathway in B-cell lymphoma. *NMR Biomed* (2013) 26(1):106–14.
  95. Chaumeil MM, Ozawa T, Park I, Scott K, James CD, Nelson SJ, et al. Hyperpolarized 13C MR spectroscopic imaging can be used to monitor everolimus treatment in vivo in an orthotopic rodent model of glioblastoma. *Neuroimage* (2012) 59(1):193–201. doi:10.1016/j.neuroimage.2011.07.034
  96. Wei LH, Si H, Hildebrandt IJ, Phelps ME, Czernin J, Weber WA. Changes in tumor metabolism as readout for mammalian target of rapamycin kinase inhibition by rapamycin in glioblastoma. *Clin Cancer Res* (2008) 14(11):3416–26. doi:10.1158/1078-0432.CCR-07-1824
  97. Ma WW, Jacene H, Song D, Vilardell F, Messersmith WA, Laheru D, et al. [18F]fluorodeoxyglucose positron emission tomography correlates with Akt pathway activity but is not predictive of clinical outcome during mTOR inhibitor therapy. *J Clin Oncol* (2009) 27(16):2697–704. doi:10.1200/JCO.2008.18.8383
  98. Ward CS, Venkatesh HS, Chaumeil MM, Brandes AH, Vancrikings M, Dafni H, et al. Noninvasive detection of target modulation following phosphatidylinositol 3-kinase inhibition using hyperpolarized 13C magnetic resonance spectroscopy. *Cancer Res* (2010) 70(4):1296–305. doi:10.1158/0008-5472.CAN-09-2251
  99. Lodi A, Ronen SM. Magnetic resonance spectroscopy detectable metabolomic fingerprint of response to antineoplastic treatment. *PLoS One* (2011) 6(10):e26155. doi:10.1371/journal.pone.0026155
  100. Nogova L, Boellaard R, Kobe C, Hoetjes N, Zander T, Gross SH, et al. Downregulation of 18F-FDG uptake in PET as an early pharmacodynamic effect in treatment of non-small cell lung cancer with the mTOR inhibitor everolimus. *J Nucl Med* (2009) 50(11):1815–9. doi:10.2967/jnumed.109.065367
  101. Maynard J, Ricketts SA, Gendrin C, Dudley P, Davies BR. 2-Deoxy-2-[18F] fluoro-D-glucose positron emission tomography demonstrates target inhibition with the AKT inhibitor AZD5363. *Mol Imaging Biol* (2013) 15(4):476–85. doi:10.1007/s11307-013-0613-3
  102. Wahl RL, Jacene H, Kasamon Y, Lodge MA. From RECIST to PERCIST: evolving considerations for PET response criteria in solid tumors. *J Nucl Med* (2009) 50(Suppl 1):122S–50S. doi:10.2967/jnumed.108.057307
  103. Lodi A, Woods SM, Ronen SM. MR-detectable metabolic consequences of mitogen-activated protein kinase kinase (MEK) inhibition. *NMR Biomed* (2014) 27(6):700–8. doi:10.1002/nbm.3109
  104. Lodi A, Woods SM, Ronen SM. Treatment with the MEK inhibitor U0126 induces decreased hyperpolarized pyruvate to lactate conversion in breast, but not prostate, cancer cells. *NMR Biomed* (2013) 26(3):299–306. doi:10.1002/nbm.2848
  105. Beloueche-Babari M, Jackson LE, Al-Saffar NM, Workman P, Leach MO, Ronen SM. Magnetic resonance spectroscopy monitoring of mitogen-activated protein kinase signaling inhibition. *Cancer Res* (2005) 65(8):3356–63.
  106. Morelli MP, Tentler JJ, Kulikowski GN, Tan AC, Bradshaw-Pierce EL, Pitts TM, et al. Preclinical activity of the rational combination of selumetinib (AZD6244) in combination with vorinostat in KRAS-mutant colorectal cancer models. *Clin Cancer Res* (2012) 18(4):1051–62. doi:10.1158/1078-0432.CCR-11-1507
  107. Larson SM, Schoder H. New PET tracers for evaluation of solid tumor response to therapy. *Q J Nucl Med Mol Imaging* (2009) 53(2):158–66.
  108. Gao P, Tchernyshyov I, Chang TC, Lee YS, Kita K, Ochi T, et al. c-Myc suppression of miR-23a/b enhances mitochondrial glutaminase expression and glutamine metabolism. *Nature* (2009) 458(7239):762–5. doi:10.1038/nature07823
  109. Dang CV. Rethinking the Warburg effect with Myc micromanaging glutamine metabolism. *Cancer Res* (2010) 70(3):859–62. doi:10.1158/0008-5472.CAN-09-3556
  110. Liu W, Le A, Hancock C, Lane AN, Dang CV, Fan TW, et al. Reprogramming of proline and glutamine metabolism contributes to the proliferative and metabolic responses regulated by oncogenic transcription factor c-MYC. *Proc Natl Acad Sci U S A* (2012) 109(23):8983–8. doi:10.1073/pnas.1203244109
  111. Gallagher FA, Kettunen MI, Day SE, Lerche M, Brindle KM. 13C MR spectroscopy measurements of glutaminase activity in human hepatocellular carcinoma cells using hyperpolarized 13C-labeled glutamine. *Magn Reson Med* (2008) 60(2):253–7. doi:10.1002/mrm.21650
  112. Qu W, Oya S, Lieberman BP, Ploessl K, Wang L, Wise DR, et al. Preparation and characterization of L-[5-11C]-glutamine for metabolic imaging of tumors. *J Nucl Med* (2012) 53(1):98–105. doi:10.2967/jnumed.111.093831
  113. Wu Z, Zha Z, Li G, Lieberman BP, Choi SR, Ploessl K, et al. [(18)F](2S,4S)-4-(3-fluoropropyl)glutamine as a tumor imaging agent. *Mol Pharm* (2014) 11(11):3852–66. doi:10.1021/mp500236y
  114. Korangath P, Teo WW, Sadiq H, Han L, Mori N, Huijts CM, et al. Targeting glutamine metabolism in breast cancer with aminoxyacetate. *Clin Cancer Res* (2015) 21(14):3263–73. doi:10.1158/1078-0432.CCR-14-1200

115. Chakrabarti G, Moore ZR, Luo X, Ilcheva M, Ali A, Padanad M, et al. Targeting glutamine metabolism sensitizes pancreatic cancer to PARP-driven metabolic catastrophe induced by ss-lapachone. *Cancer Metabol* (2015) 3:12. doi:10.1186/s40170-015-0137-1
116. Leisser A, Pruscha K, Ubl P, Wadsak W, Mayerhofer M, Mitterhauser M, et al. Evaluation of fatty acid synthase in prostate cancer recurrence: SUV of [(11)C]acetate PET as a prognostic marker. *Prostate* (2015) 75(15):1760–7. doi:10.1002/pros.23061
117. Cheung TT, Ho CL, Lo CM, Chen S, Chan SC, Chok KS, et al. 11C-acetate and 18F-FDG PET/CT for clinical staging and selection of patients with hepatocellular carcinoma for liver transplantation on the basis of Milan criteria: surgeon's perspective. *J Nucl Med* (2013) 54(2):192–200. doi:10.2967/jnumed.112.107516
118. Liu DD, Khong PL, Gao Y, Mahmood U, Quinn B, Germain JS, et al. Radiation dosimetry of whole-body dual tracer 18F-FDG and 11C-acetate PET/CT for hepatocellular carcinoma. *J Nucl Med* (2016) 57(6):907–12. doi:10.2967/jnumed.115.165944
119. Schlaepfer IR, Glode LM, Hitz CA, Pac CT, Boyle KE, Maroni P, et al. Inhibition of lipid oxidation increases glucose metabolism and enhances 2-deoxy-2-[(18)F]fluoro-D-glucose uptake in prostate cancer mouse xenografts. *Mol Imaging Biol* (2015) 17(4):529–38. doi:10.1007/s11307-014-0814-4
120. Sankaranarayananpillai M, Zhang N, Baggerly KA, Gelovani JG. Metabolic shifts induced by fatty acid synthase inhibitor orlistat in non-small cell lung carcinoma cells provide novel pharmacodynamic biomarkers for positron emission tomography and magnetic resonance spectroscopy. *Mol Imaging Biol* (2013) 15(2):136–47. doi:10.1007/s11307-012-0587-6
121. Troiani T, Serkova NJ, Gustafson DL, Henthorn TK, Lockerbie O, Merz A, et al. Investigation of two dosing schedules of vandetanib (ZD6474), an inhibitor of vascular endothelial growth factor receptor and epidermal growth factor receptor signaling, in combination with irinotecan in a human colon cancer xenograft model. *Clin Cancer Res* (2007) 13(21):6450–8. doi:10.1158/1078-0432.CCR-07-1094
122. Yap TA, Arkenau HT, Camidge DR, George S, Serkova NJ, Gwyther SJ, et al. First-in-human phase I trial of two schedules of OSI-930, a novel multikinase inhibitor, incorporating translational proof-of-mechanism studies. *Clin Cancer Res* (2013) 19(4):909–19. doi:10.1158/1078-0432.CCR-12-2258
123. O'Connor JP, Jackson A, Parker GJ, Roberts C, Jayson GC. Dynamic contrast-enhanced MRI in clinical trials of antivascular therapies. *Nat Rev Clin Oncol* (2012) 9(3):167–77. doi:10.1038/nrclinonc.2012.2
124. Khayum MA, Doorduin J, Antunes IF, Kwizera C, Zijlma R, den Boer JA, et al. In vivo imaging of brain androgen receptors in rats: a [(18)F]FDHT PET study. *Nucl Med Biol* (2015) 42(6):561–9. doi:10.1016/j.nucmedbio.2015.02.003
125. Fowler AM, Chan SR, Sharp TL, Fettig NM, Zhou D, Dence CS, et al. Small-animal PET of steroid hormone receptors predicts tumor response to endocrine therapy using a preclinical model of breast cancer. *J Nucl Med* (2012) 53(7):1119–26. doi:10.2967/jnumed.112.103465
126. Linden HM, Kurland BF, Peterson LM, Schubert EK, Gralow JR, Specht JM, et al. Fluoroestradiol positron emission tomography reveals differences in pharmacodynamics of aromatase inhibitors, tamoxifen, and fulvestrant in patients with metastatic breast cancer. *Clin Cancer Res* (2011) 17(14):4799–805. doi:10.1158/1078-0432.CCR-10-3321
127. Peterson LM, Kurland BF, Schubert EK, Link JM, Gadi VK, Specht JM, et al. A phase 2 study of 16alpha-[(18)F]-fluoro-17beta-estradiol positron emission tomography (FES-PET) as a marker of hormone sensitivity in metastatic breast cancer (MBC). *Mol Imaging Biol* (2014) 16(3):431–40. doi:10.1007/s11307-013-0699-7
128. Mahoney KM, Rennert PD, Freeman GJ. Combination cancer immunotherapy and new immunomodulatory targets. *Nat Rev Drug Discov* (2015) 14(8):561–84. doi:10.1038/nrd4591
129. Ribas A, Hamid O, Daud A, Hodis FS, Wolchok JD, Kefford R, et al. Association of pembrolizumab with tumor response and survival among patients with advanced melanoma. *JAMA* (2016) 315(15):1600–9. doi:10.1001/jama.2016.4059
130. Sunshine J, Taube JM. PD-1/PD-L1 inhibitors. *Curr Opin Pharmacol* (2015) 23:32–8. doi:10.1016/j.coph.2015.05.011
131. Swaika A, Hammond WA, Joseph RW. Current state of anti-PD-L1 and anti-PD-1 agents in cancer therapy. *Mol Immunol* (2015) 67(2 Pt A):4–17. doi:10.1016/j.molimm.2015.02.009
132. Hodis FS, Hwu WJ, Kefford R, Weber JS, Daud A, Hamid O, et al. Evaluation of immune-related response criteria and RECIST v1.1 in patients with advanced melanoma treated with pembrolizumab. *J Clin Oncol* (2016) 34(13):1510–7. doi:10.1200/JCO.2015.64.0391
133. Gevaert O, Mitchell LA, Achrol AS, Xu J, Echegaray S, Steinberg GK, et al. Glioblastoma multiforme: exploratory radiogenomic analysis by using quantitative image features. *Radiology* (2014) 273(1):168–74. doi:10.1148/radiol.14131731

**Conflict of Interest Statement:** The authors declare that the research was conducted in the absence of any commercial or financial relationships that could be construed as a potential conflict of interest.

The reviewers M-FP, KG, and BK and handling Editor declared their shared affiliation, and the handling Editor/Specialty Chief Editor states that the process nevertheless met the standards of a fair and objective review..

Copyright © 2016 Serkova and Eckhardt. This is an open-access article distributed under the terms of the Creative Commons Attribution License (CC BY). The use, distribution or reproduction in other forums is permitted, provided the original author(s) or licensor are credited and that the original publication in this journal is cited, in accordance with accepted academic practice. No use, distribution or reproduction is permitted which does not comply with these terms.

# Estrogen Receptor-Targeted Contrast Agents for Molecular Magnetic Resonance Imaging of Breast Cancer Hormonal Status

Adi Pais<sup>†</sup> and Hadassa Degani<sup>\*</sup>

Department of Biological Regulation, Weizmann Institute of Science, Rehovot, Israel

## OPEN ACCESS

**Edited by:**

Franca Podo,  
Istituto Superiore di Sanità, Italy

**Reviewed by:**

Zaver Bhujwalla,  
Johns Hopkins University School of  
Medicine, USA  
Naranamangalam Raghunathan  
Jagannathan,  
All India Institute of Medical Sciences,  
India

**\*Correspondence:**

Hadassa Degani  
hadassa.degani@weizmann.ac.il

**†Present address:**

Adi Pais,  
Neuroimaging Unit, Edmond and Lily  
Safra Center for Brain Sciences, The  
Hebrew University of Jerusalem,  
Jerusalem, Israel

**Specialty section:**

This article was submitted to Cancer  
Imaging and Diagnosis,  
a section of the journal  
*Frontiers in Oncology*

**Received:** 31 December 2015

**Accepted:** 11 April 2016

**Published:** 27 April 2016

**Citation:**

Pais A and Degani H (2016) Estrogen Receptor-Targeted Contrast Agents for Molecular Magnetic Resonance Imaging of Breast Cancer Hormonal Status.  
*Front. Oncol.* 6:100.  
doi: 10.3389/fonc.2016.00100

The estrogen receptor (ER)  $\alpha$  is overexpressed in most breast cancers, and its level serves as a major prognostic factor. It is important to develop quantitative molecular imaging methods that specifically detect ER *in vivo* and assess its function throughout the entire primary breast cancer and in metastatic breast cancer lesions. This study presents the biochemical and molecular features, as well as the magnetic resonance imaging (MRI) effects of two novel ER-targeted contrast agents (CAs), based on pyridine-tetra-acetate-Gd(III) chelate conjugated to  $17\beta$ -estradiol (EPTA-Gd) or to tamoxifen (TPTA-Gd). The experiments were conducted in solution, in human breast cancer cells, and in severe combined immunodeficient mice implanted with transfected ER-positive and ER-negative MDA-MB-231 human breast cancer xenografts. Binding studies with ER in solution and in human breast cancer cells indicated affinities in the micromolar range of both CAs. Biochemical and molecular studies in breast cancer cell cultures showed that both CAs exhibit estrogen-like agonistic activity, enhancing cell proliferation, as well as upregulating cMyc oncogene and downregulating ER expression levels. The MRI longitudinal relaxivity was significantly augmented by EPTA-Gd in ER-positive cells as compared to ER-negative cells. Dynamic contrast-enhanced studies with EPTA-Gd *in vivo* indicated specific augmentation of the MRI water signal in the ER-positive versus ER-negative xenografts, confirming EPTA-Gd-specific interaction with ER. In contrast, TPTA-Gd did not show increased enhancement in ER-positive tumors and did not appear to interact *in vivo* with the tumors' ER. However, TPTA-Gd was found to interact strongly with muscle tissue, enhancing muscle signal intensity in a mechanism independent of the presence of ER. The specificity of EPTA-Gd interaction with ER *in vivo* was further verified by acute and chronic competition with tamoxifen. The chronic tamoxifen treatment also revealed that this drug increases the microvascular permeability of breast cancer xenograft in an ER-independent manner. In conclusion, EPTA-Gd has been shown to serve as an efficient molecular imaging probe for specific assessment of breast cancer ER *in vivo*.

**Keywords:** estrogen receptor-targeted probes, contrast agents for MRI, breast cancer, estrogen receptor, molecular imaging

## INTRODUCTION

Breast cancer is the most common malignancy in women and the second leading cause of cancer death among women (1). The overexpression of the estrogen receptor (ER) (2) is currently an established molecular feature for assessing breast cancer prognosis and predicting response to endocrine therapies [Ref. (3) and references cited therein]. The critical importance of ER measurements in managing breast cancer treatment was recently emphasized in the results of a meta-analysis of randomized trials showing that ER status of the primary tumor was the only patient or tumor characteristic that strongly predicted tamoxifen efficacy, whereas the progesterone receptor measurement did not seem to be importantly predictive of efficacy (4).

Estrogen receptor status is predominantly evaluated today by immunohistochemistry staining of ER, which is a semi-quantitative method and, therefore, may lack reproducibility and standardization across different laboratories (5–8). In addition, this method requires fresh randomly selected tumor tissue, not always available, particularly in metastatic breast disease.

Part of the above described limitations can be overcome by developing molecular imaging techniques that will detect and map ER level over the entire tumor tissue in a quantitative manner. Thus, ER imaging has become an important target for future development (9). Today, molecular imaging of ER is primarily based on the application of radiolabeling selective estrogen receptor modulators (SERMs) that can be detected by single photon emission computed tomography (SPECT) or positron emission tomography (PET) (10). The most clinically advanced ER imaging method today uses 16- $\alpha$ -[f-18]-fluoro-17- $\beta$ -estradiol (FES) and PET (11). These methods provided quantitative imaging ER expression *in vivo* in animal models and in breast cancer patients (12–14), but it is not applicable yet as a routine imaging technique for the workup of breast cancer patients.

Currently, magnetic resonance imaging (MRI) methods demonstrated excellent efficiency for breast cancer detection and diagnosis [Ref. (15) and references cited therein]. The challenge of molecular MRI to evaluate ER expression can provide a direct critical prognostic factor at the stage of diagnosis. Therefore, we embarked on developing novel contrast agents (CAs) targeted to the ER that should be detected by MRI. To that end, we have synthesized two new CAs targeted to the ER, which are composed of Gadolinium chelate of pyridine-tetra-acetate (PTA-Gd) conjugated with the native ligand 17 $\beta$ -estradiol (EPTA-Gd) or with the antiestrogen tamoxifen (TPTA-Gd), and evaluated their MRI properties in solution, in breast cancer cells and in breast cancer xenografts in animal models (16–18). In addition, direct structural information on the crystal structure of the ligand-binding domain of ER bound to the europium chelate of EPTA (EPTA-Eu) was obtained using X-ray crystallography (19). This paper presents characterization of the binding capacity and the hormonal/molecular effects of EPTA-Gd and TPTA-Gd in human breast cancer cells, as well as restates and expands the data evaluation of the MRI properties of these CAs in cell cultures and animal models of breast cancer. We have focused on investigating the interaction and binding affinity with ER, the hormonal-induced changes in cell proliferation, and the up or downregulation of

estrogen-induced genes. Furthermore, investigation of the ER-specific and non-specific interactions of these probes in breast cancer cells and tumors and in muscle tissue, as well as the competition with tamoxifen emphasized the advantage of EPTA-Gd over TPTA-Gd as an ER-targeted CA *in vivo*.

## MATERIALS AND METHODS

### Solution-Binding Affinity to ER

The binding affinities were measured by a radioactive inhibitory competitive assay in solution, using recombinant hER $\alpha$  (1.76 nM) (PanVera, Inc., Madison, WI, USA), tritiated 17 $\beta$ -estradiol ( $^3\text{HE}2=2.0\text{--}3.5\text{ nM}$ , 140 Ci/mmol) (NEN, Boston, MA, USA), and EPTA-Gd and TPTA-Gd as the competing ligands. Experiments were done in duplicates. The concentration of competing ligand required to replace half of the tritiated 17 $\beta$ -estradiol that would be bound to the hER $\alpha$ , IC<sub>50</sub>, was derived by non-linear regression analysis of the experimental data to the following equation:

$$Y = \text{Non-Specific Binding} + (\text{Total Binding} - \text{Specific Binding}) / (1 + 10^{\log X - \log IC_{50}})$$

with Y, the observed data and X, the inhibitor concentration; non-specific binding of  $^3\text{HE}2$  is measured by competition with excess of 1  $\mu\text{M}$  cold E2 and total-specific binding is maximal binding of  $^3\text{HE}2$  measured without competition. The absolute inhibition constant, Ki, was determined according to the Cheng–Prusoff equation:

$$Ki = IC_{50} / [1 + (^3\text{HE}2 / Kd)]$$

using Kd = 0.2 nM of 17 $\beta$ -estradiol.

### Cells

T47D (clone 11) and MDA-MB-231 human breast cancer cells were cultured in RPMI 1640 medium supplemented with 10% FCS (Biological Industries, Israel), 4 mM L-glutamine, and 0.1% combined antibiotics (Bio-Lab, Israel). In addition, T47D medium included insulin (0.8 ml/l) and MDA medium included pyruvate (1 mM). MCF7 human breast cancer cells were cultured in DMEM medium supplemented with 6% FCS (Biological Industries, Israel), 4 mM L-glutamine, and 0.1% combined antibiotics (Bio-Lab, Israel).

Estrogen receptor-positive MDA-MB-231 cells were obtained by stably transfecting the wild type (WT) MDA-MB-231 cells with a plasmid encoding tetracycline repressor (TR) protein pcDNA6/TR (T-REX™ System, Invitrogen, USA) and with a plasmid encoding ER $\alpha$  pcDNA4/ER, as previously described (20). The expression of ER $\alpha$  in these cells was induced by adding doxycycline (1  $\mu\text{g/ml}$ ) (doxycycline hydrate, Sigma-Aldrich, MO, USA) to the growth medium for at least 3 days.

### Cell Proliferation Assay

Cells were grown in phenol red-free medium supplemented with 10% dextran-coated charcoal stripped fetal bovine serum – DCC-FBS (Biological industries, Beit Haemek, Israel) for a minimum of 5 days and were then seeded in a 96-well plate ( $3.5 \times 10^3$  cells/

well) and cultured in the same medium with the various treatments administered to the medium. The number of cells was determined by the cell viability MTT (3-(4,5-dimethylthiazol-2-yl)-2,5-diphenyl tetrazolium bromide) assay (21). Each data point presents an average of six replicate wells in a single experiment; experiments were repeated several times as indicated in the text.

## Western Blotting

Estrogen receptor  $\alpha$ , cMyc, and  $\alpha$ -tubulin protein levels were determined using immunoblotting with mouse anti-human ER $\alpha$  antibody (clone 6F11, Novocastra Laboratories, UK), mouse anti-human cMyc antibody (9e10, Abcam, MA, USA), and mouse anti-human  $\alpha$ -tubulin antibody (clone DM-1A, Sigma-Aldrich, MO, USA), respectively. Goat anti-mouse horseradish peroxidase and alkaline phosphatase were used as secondary antibodies (Jackson ImmunoResearch Laboratories, PA, USA). Densitometric analyses were performed using Quantity One 4.6 (Bio-Rad Laboratories, CA, USA). The changes in the expression due to treatment with the ER-targeted probes were performed in cells grown in phenol red-free medium for a minimum of 5 days prior to the treatment. The expression of ER in the different human breast cancer cell lines was quantified by normalizing the intensity of the bands to those of standard, known concentrations of recombinant hER $\alpha$  protein (PanVera, Inc., Madison, WI, USA).

## MRI- and Fluorescence-Binding Studies

The interaction of the ER-targeted probes with ER-positive and ER-negative MDA-MB-231 cells were investigated by T1-relaxation measurements and by a fluorescence assay using the Eu-chelate of EPTA, EPTA-Eu. Studies were also performed on cells cultivated on microspheres. The cells,  $\sim 3 \times 10^6$ , were seeded on 0.5 ml microspheres (Biosilon polystyrene microspheres, NUNC, 160–300  $\mu\text{m}$  diameter) placed in non-adherent bacterial Petri dishes using FCS-supplemented DMEM medium. After 4 days, the medium was replaced by phenol red-free medium supplemented with DCC-FBS for additional 3 days. On day 7, the medium was replaced by serum-free medium containing either EPTA-Gd or TPTA-Gd for 60 min incubation and placed in wells (0.5 ml/well) (Microtest 96-well plate, BD Falcon, NJ, USA). Proton T1-relaxation rates were measured at 23°C with a 4.7-T Bruker Biospec spectrometer (Bruker, Karlsruhe, Germany) by applying a 2D spin-echo pulse sequence, field of view (FOV) 8 cm  $\times$  8 cm, matrix of 256  $\times$  192, slice thickness of 3 mm, echo time (TE) = 16 ms, and six different repetition times (TRs). T1-relaxation times per pixel were calculated by non-linear least-squares fitting (using simplex algorithm Matlab R2009b, MathWorks, Natick, MA, USA) of the MRI signal intensity, SI, to the equation  $SI = So[1 - \exp(-TR/T1)]$  with two free parameters So and T1.

T1- and T2-relaxation rate measurements were also conducted in ER-positive and ER-negative cells cultured on microspheres and perfused during the experiments under sterile conditions with oxygenated, phenol red-free, and serum-free medium at  $36 \pm 1^\circ\text{C}$ , as previously described (22). The measurements were conducted in a 9.4-T NMR spectrometer (DMX-400, Bruker, Karlsruhe, Germany). EPTA-Gd and TPTA-Gd were gradually

added at various concentrations (range 0.1–7.5  $\mu\text{M}$ ) to the perfusion medium reservoir and at the end of the experiments, the CA was washed out by fresh medium. Proton T1-relaxation rates (R1) and T2-relaxation rates (R2) were measured by MRS of the water signal using standard inversion recovery pulse sequence and a Carr-Purcell-Meiboom-Gill sequence, respectively.  $\Delta R1$  and  $\Delta R2$  were defined as the difference between R1 (or R2) of cells perfused with medium containing the CA and the contrast-free medium. T1 relaxivity,  $r_1$ , in  $\text{mM}^{-1} \text{s}^{-1}$ , was calculated from the slope of a linear fit of  $\Delta R1$  as a function of the CA concentration.

For the fluorescence-binding assay, both ER-positive and ER-negative cells were seeded and grown on polystyrene Biosilon beads, as described above, placed in glass Petri dishes covered with silicone (Sigmacote, Sigma-Aldrich, MO, USA) to minimize non-specific binding. On day 7, the medium was replaced with fresh serum-free medium containing EPTA-Eu at concentrations ranging from 0.1 to 0.5  $\mu\text{M}$  for 60 min at 37°C. Then, the cells were washed three times with 10 ml of the fresh medium, and DELFIA enhancement solution (1244-105, PerkinElmer, MA, USA) was added (4–5 ml/plate) and stirred in the dark for 15 min at room temperature. The solution was then transferred into a 48-well plate (300  $\mu\text{l}$ /well in quadruplicate) and scanned on a Wallac Victor3 instrument, using the standard europium time resolved fluorescence measurement (340 nm excitation, 400  $\mu\text{s}$  delay, and emission collection for 400  $\mu\text{s}$  at 615 nm). The specific binding to ER was calculated by subtracting the non-specific fluorescence of ER-negative cells from the fluorescence of ER-positive cells. The fluorescence optical density (OD) intensities were converted to molar units by using a calibration curve obtained from OD values of known EPTA-Eu concentrations. The final concentration data points reflecting specific binding in the cells to ER were fitted to a one-site binding equation  $Y = B_{\max} \times X / (K_d + X)$ , where Y is the measured OD converted to molar units and X is the administrated concentration of EPTA-Eu using non-linear least-squares Levenberg-Marquardt algorithm (origin version 6.1) yielding the dissociation constant Kd, which is the inverse of the association constant Ka and maximal-binding capacity (Bmax) of EPTA-Eu to ER.

## MRI of Breast Cancer Xenografts in Mice

All experimental protocols were reviewed and approved by the Institutional Animal Care and Use Committee of the Weizmann Institute of Science. Female CB-17 severe combined immunodeficient (SCID) mice (Harlan Biotech Israel Ltd., Israel), 6–7 weeks old, were ovariectomized. About a week later, WT human MDA-MB-231 breast cancer cells and stable ER-transfected MDA-MB-231 cells were inoculated ( $2.5 \times 10^6$  cells in 0.1 ml phosphate-buffered saline) into the left and right mammary fat pad, respectively. One week later, ER expression in the implanted cells was induced by supplementing the drinking water with 0.2 mg/ml doxycycline (44577 doxycycline hydiate, Sigma-Aldrich, MO, USA) in 3% sucrose. The size of the xenografts was measured by caliper, estimating the volume by assuming a hemiellipsoid shape according to volume =  $(\text{length}/2 \times \text{width}/2 \times \text{height}/2) \times 4\pi/3$ .

*In vivo* MRI experiments were conducted 2–4 weeks after cell implantation. During the MRI scanning, mice were anesthetized

with isoflurane (Medeva Pharmaceuticals, Inc., Bethlehem, PA, USA) (3% for induction and 1–2% for maintenance) mixed with compressed air (1 l/min) and delivered through a nasal mask. Once anesthetized, the animals were placed in a head-holder to assure reproducible positioning inside the magnet. Respiration rate was monitored and kept throughout the scanning period around 60–80 breaths per minute.

All *in vivo* MR images were acquired on a 9.4-T Biospec AVANCE II spectrometer (Bruker, Karlsruhe, Germany). The protocol included a multi-slice T2-weighted sequence and a dynamic contrast-enhanced (DCE) 3D gradient-echo pulse sequence with TE/TR 2.5/15 ms and flip angle 40°, four averages (1.5 min). The latter images alternated between images of the tumors recorded in the axial direction with a spatial resolution of 0.156 mm × 0.156 mm × 1.2 mm and images of the descending aorta and muscle tissue in coronal direction with spatial resolution of 0.234 mm × 0.156 mm × 1 mm.

Each ER-targeted probe was injected as a bolus into the tail vein of the mice. The dose of EPTA-Gd was 0.03 mmol/kg ( $n = 4$ ) or 0.075 mmol ( $n = 5$ ). The dose of TPTA-Gd was 0.075 mmol/kg ( $n = 4$ ).

Competition of EPTA-Gd with tamoxifen was tested *in vivo* using two modes of tamoxifen treatment, acute (1 h) and chronic (3 days). In the acute treatment, tamoxifen citrate salt – TAM (T9262, Sigma-Aldrich, St. Louis, MO, USA) dissolved in sterile sunflower oil (4 mg/ml) or 4-hydroxytamoxifen – OHT (H7904, Sigma-Aldrich) dissolved in sterile sunflower oil containing 20% ethanol were stirred overnight at 37°C and administered by intraperitoneal injection at a final dose of 0.07 mmol/kg TAM ( $n = 3$ ) or 0.1 mmol/kg OHT ( $n = 1$ ). One hour later, EPTA-Gd was injected into the tail vein at a dose of 0.075 mmol/kg. In the chronic treatment, tamoxifen pellets (5 mg/pellet, 4w-release time; Innovative Research of America, Sarasota, FL, USA) were implanted subcutaneously in the back of the mouse and 3 days later EPTA-Gd was administered ( $n = 4$ ). The MRI protocol was the same as described above for the direct, non-competitive, contrast-enhanced experiments.

Changes in signal intensity were calculated per pixel yielding enhancement datasets defined as  $[I(t) - I(0)]/I(0)$ , where  $I(0)$  and  $I(t)$  are the signal intensities pre- and post-contrast, respectively. Enhancement maps at pixel resolution were calculated in regions of interest (ROI) in all slices including tumors' tissue. ROIs were delineated on the anatomical T2-weighted images and transferred to the corresponding DCE images.  $I(0)$  per pixel was calculated as a mean intensity of the four pre-contrast images.

## Histology

The tumors were removed, fixed in 4% formaldehyde, sectioned to 4 µm histological slices and stained with hematoxylin and eosin (H&E), as well as immune-stained for nuclear ERα. The immunostaining was performed using rabbit monoclonal anti-ER antibody (ER-SP1, Ventana Medical System, AZ, USA) and an automated slide staining BenchMark XT system operated, according to the manufacturer's instructions (Ventana Medical System, AZ, USA). An experienced breast pathologist evaluated the extent of intensity of staining [absent ( $i = 0$ ), weak ( $i = +1$ ), moderate ( $i = +2$ ), or strong ( $i = +3$ )], and the percentage of

ER-stained cell nuclei. These two evaluations were used for calculating a specific intensity index defined as:  $\Sigma I(i) \times \text{fraction of cells stained with } (i)$ .

## Statistics

Student's two-tailed paired *t*-tests (GraphPad Software, Inc., QuickCalcs Web site <http://www.graphpad.com/quickcalcs/ttest1.cfm>) were applied to evaluate the effect of each treatment on the measured cellular parameter relative to control non-treated cells or to control ER-negative cells undergoing the same treatment. This test was also applied to evaluate the differences between the size and EPTA-Gd-induced enhancement in the ER-positive and ER-negative xenografts. A level at  $p < 0.05$  was considered significant.

## RESULTS

### Binding to ER in Solution and in Cells

The chemical structures of the two gadolinium chelate of pyridine-tetra-acetate (PTA-Gd) conjugated with the native ligand 17β-estradiol (EPTA-Gd) or with the antiestrogen tamoxifen (TPTA-Gd) are presented in **Figure 1A**. The binding affinities of EPTA-Gd and TPTA-Gd to an isolated hERα were determined in reference to tamoxifen by a competitive radioactive-binding assay with <sup>3</sup>HE2 as described in Section "Materials and Methods" (**Figure 1B**). Non-linear least-squares fitting of the experimental data yielded inhibitory dissociation constants  $K_{i,\text{EPTA-Gd}} = 0.97 \pm 0.07 \mu\text{M}$  and  $K_{i,\text{TPTA-Gd}} = 0.13 \pm 0.006 \mu\text{M}$  as compared to  $K_{i,\text{Tamoxifen}} = 0.005 \pm 0.001 \mu\text{M}$ .

Specific binding of these agents to ER in human breast cancer cells was demonstrated by augmentation in the T1-relaxation rate in ER-positive cells as compared to ER-negative cells cultivated on microspheres. The change in T1-relaxation rate in the ER-positive cells in the presence of EPTA-Gd (6 µM), measured in eight independent experiments, yielded a mean  $\pm$  SD of  $74 \pm 20 \text{ ms}^{-1}$ . This change in T1-relaxation rate was significantly higher than that in ER-negative cells of  $46 \pm 20 \text{ ms}^{-1}$  ( $p = 0.02$ ,  $n = 8$ ). Nine independent experiments with TPTA-Gd (5 µM) augmented the T1-relaxation rate in ER-positive cells by a mean  $\pm$  SD of  $72 \pm 6 \text{ ms}^{-1}$  and in ER-negative cells by  $64 \pm 10 \text{ ms}^{-1}$  with a borderline significant difference between the cells ( $p = 0.07$ ,  $n = 9$ ).

Concentration-dependent studies of the T1-relaxation rates ( $R_1$ ) of ER-positive and ER-negative breast cancer cells cultivated on microspheres and perfused during the experiments with increasing concentrations of each CA indicated an increase in T1 relaxivity due to binding to ER (**Figures 2A,B**). The concentration dependence of  $\Delta R_1$  (the difference between  $R_1$  of cells perfused with medium containing the CA and the same cells perfused with contrast-free medium) showed that EPTA-Gd and TPTA-Gd augment the T1 relaxivity in ER-positive cells as compared to ER-negative cells by 45 and 22%, respectively. After washing out EPTA-Gd (7.5 µM) or TPTA-Gd (7.5 µM) from the perfusion system with fresh medium, both  $\Delta R_1$  and  $\Delta R_2$  remained significantly higher in ER-positive cells as compared to ER-negative cells. Generally, gadolinium-based

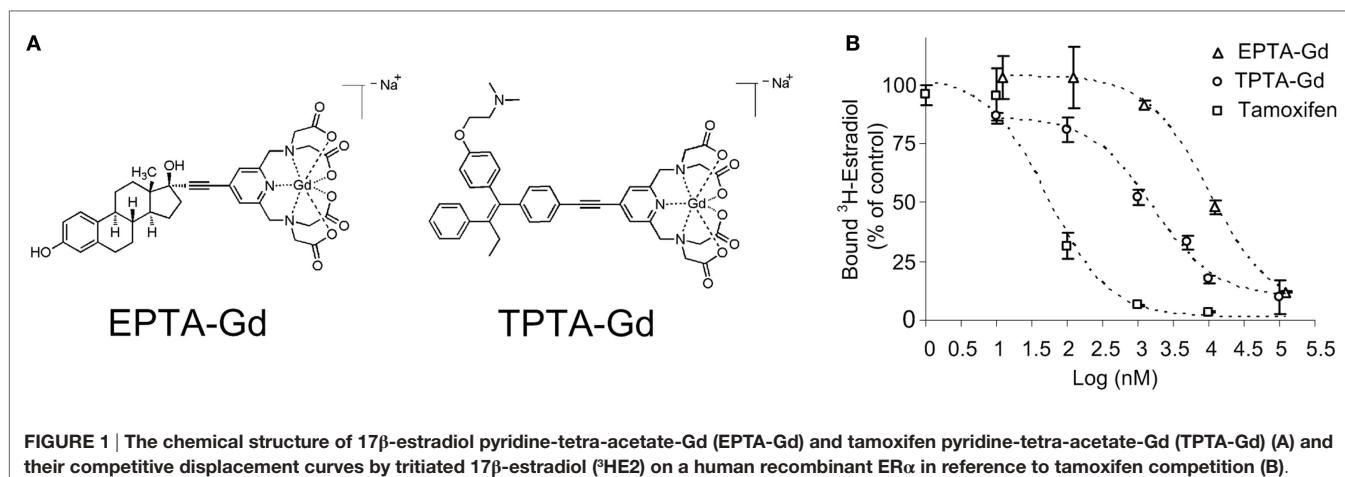


**FIGURE 1 |** The chemical structure of 17 $\beta$ -estradiol pyridine-tetra-acetate-Gd (EPTA-Gd) (A) and tamoxifen pyridine-tetra-acetate-Gd (TPTA-Gd) (A) and their competitive displacement curves by tritiated 17 $\beta$ -estradiol ( $^3\text{H}$ E2) on a human recombinant ER $\alpha$  in reference to tamoxifen competition (B).

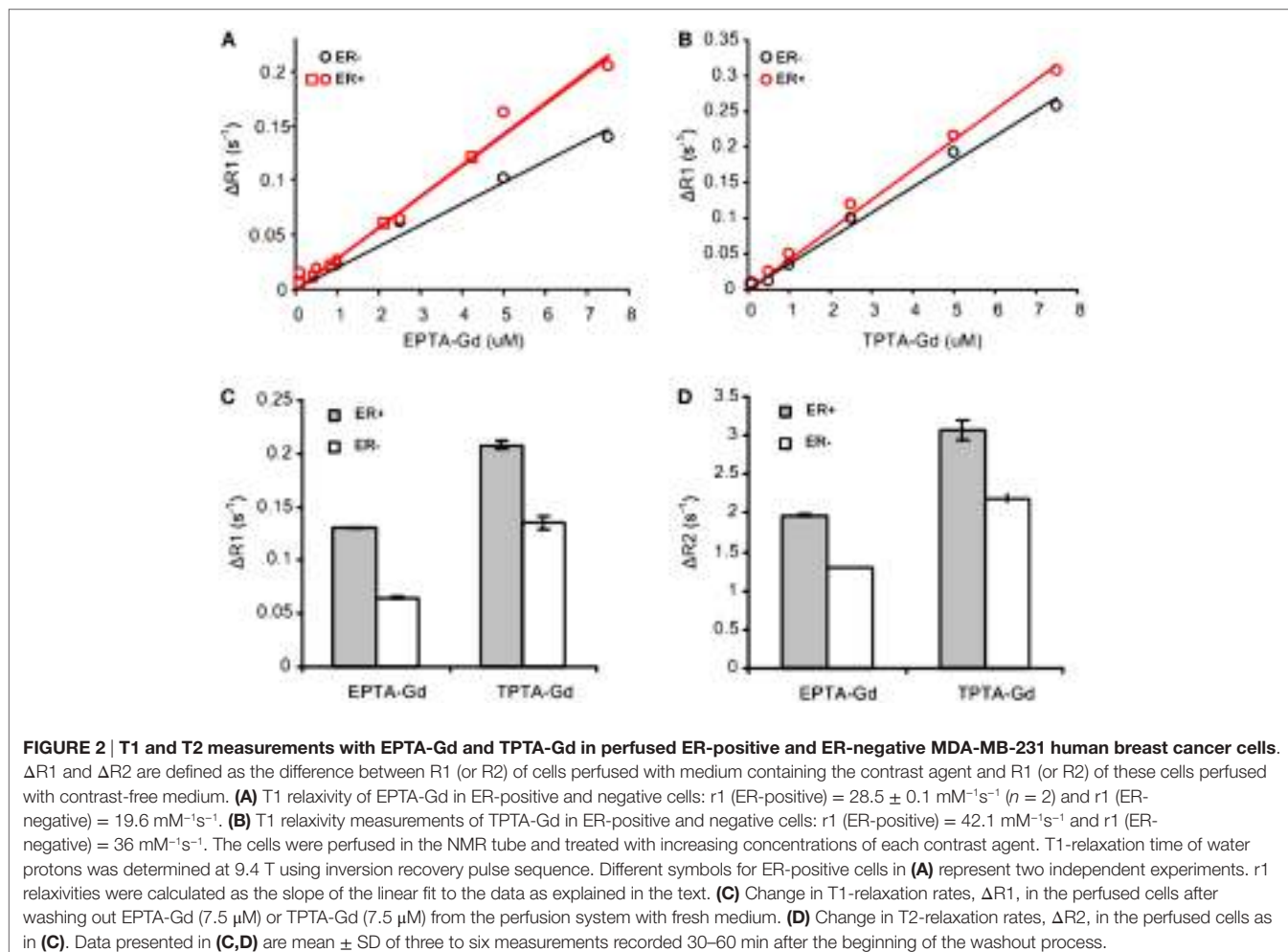


**FIGURE 2 |** T1 and T2 measurements with EPTA-Gd and TPTA-Gd in perfused ER-positive and ER-negative MDA-MB-231 human breast cancer cells.  $\Delta R_1$  and  $\Delta R_2$  are defined as the difference between  $R_1$  (or  $R_2$ ) of cells perfused with medium containing the contrast agent and  $R_1$  (or  $R_2$ ) of these cells perfused with contrast-free medium. (A) T1 relaxivity of EPTA-Gd in ER-positive and negative cells:  $r_1$  (ER-positive) =  $28.5 \pm 0.1 \text{ mM}^{-1}\text{s}^{-1}$  ( $n = 2$ ) and  $r_1$  (ER-negative) =  $19.6 \text{ mM}^{-1}\text{s}^{-1}$ . (B) T1 relaxivity measurements of TPTA-Gd in ER-positive and negative cells:  $r_1$  (ER-positive) =  $42.1 \text{ mM}^{-1}\text{s}^{-1}$  and  $r_1$  (ER-negative) =  $36 \text{ mM}^{-1}\text{s}^{-1}$ . The cells were perfused in the NMR tube and treated with increasing concentrations of each contrast agent. T1-relaxation time of water protons was determined at 9.4 T using inversion recovery pulse sequence. Different symbols for ER-positive cells in (A) represent two independent experiments.  $r_1$  relaxivities were calculated as the slope of the linear fit to the data as explained in the text. (C) Change in T1-relaxation rates,  $\Delta R_1$ , in the perfused cells after washing out EPTA-Gd (7.5  $\mu\text{M}$ ) or TPTA-Gd (7.5  $\mu\text{M}$ ) from the perfusion system with fresh medium. (D) Change in T2-relaxation rates,  $\Delta R_2$ , in the perfused cells as in (C). Data presented in (C,D) are mean  $\pm$  SD of three to six measurements recorded 30–60 min after the beginning of the washout process.

CA will affect both T1- and T2-relaxation rates and thus the results above confirm specific binding of these agents to ER (Figures 2C,D).

Further verification of the binding to ER was performed by direct measurement of the binding affinity of cellular ER to the

european complex of EPTA-Eu, using a dissociation-enhanced lanthanide fluorescence assay. Specific binding to ER was obtained by subtracting the non-specific binding in ER-negative cells from the total binding in ER-positive cells (Figure 3). The specific binding curve (Figure 3B) yielded an association constant in the

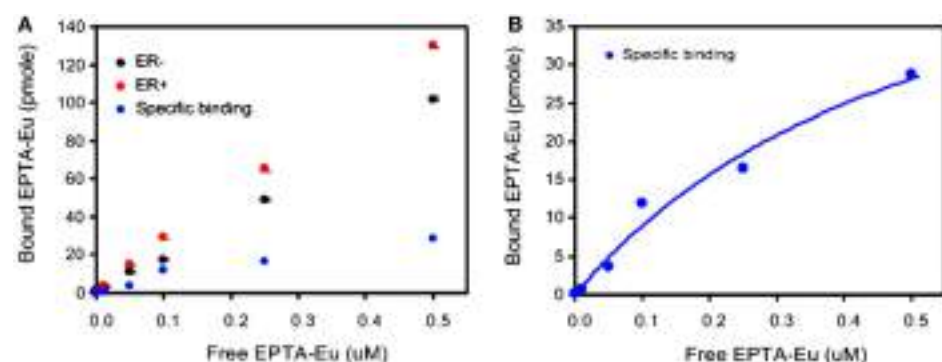


**FIGURE 3 | Binding affinity of EPTA-Eu to ER in human breast cancer cells.** ER-positive and ER-negative MDA-MB-231 human breast cancer cells, grown on microspheres, were incubated in the presence of the indicated concentrations of EPTA-Eu for 1 h at 37°C and subjected to DELFIA assay. **(A)** Total binding (red) was determined in ER-positive cells and non-specific binding (black) was determined in ER-negative cells. Specific binding (blue) was calculated by subtracting non-specific from total binding. **(B)** Saturation-binding curve. Data points of specific binding were fitted to one-site binding equation yielding  $K_d = 0.56 \mu\text{M}$ ,  $B_{\text{MAX}} = 60.9 \text{ pmole}$ , and  $R^2 = 0.97$ . Data of OD scale were converted to molar units by comparing to OD values of known EPTA-Eu concentrations.

cells,  $K_a_{\text{EPTA-Eu}}$  of  $1.75 \pm 0.2 \mu\text{M}$  and maximal-binding capacity  $B_{\text{MAX}} = 3.53 \pm 0.17 \text{ pmole per } 10^6 \text{ cells}$  ( $n = 3$ ).

## Hormonal-Induced Bioactivities of EPTA-Gd and TPTA-Gd in Human Breast Cancer Cells

The protein level of ER $\alpha$  in the various human breast cancer cells examined in this study were determined by western blotting, calibrating the levels using a calibration curve of commercial hER $\alpha$  protein (Figure 4). The level of ER in the estrogen responsive cells T47D and MCF7 was  $1,802 \pm 842$  and  $10,377 \pm 1,044 \text{ fmol/mg protein}$ , respectively. The WT MDA-MB-231 cells had a null level, and the ER-transfected MDA-MB-231 cells had a high level of  $14,800 \pm 980 \text{ fmol/mg protein}$ . The expression levels in T47D, MCF7, and WT MDA-MB231 cells are in accord with previously published values for these cells (20, 23, 24).

Both EPTA-Gd and TPTA-Gd stimulated the proliferation of T47D and MCF7 cells in a dose- and time-dependent manner, but did not affect the proliferation rate of ER-negative MDA-MB-231 cells (Figure 5). Statistical analysis of the proliferation rate of MCF7 and T47D cells induced by 1–2  $\mu\text{M}$  EPTA-Gd showed a reproducible and significant stimulation of approximately two-fold ( $p < 0.02$ ,  $n = 5$ , two-tail paired  $t$ -test).

Unlike tamoxifen, competition of TPTA-Gd with E2 did not affect the proliferation of T47D and MCF7 cells ( $p > 0.3$ , two-tailed paired  $t$ -test,  $n = 7$ ). Thus, both ER-targeted probes exerted mild agonistic effect on the proliferation of estrogen responsive cells and were neither cytotoxic nor cytostatic to these cells.

The ability of the two targeted probes to regulate specific estrogen-induced molecular changes was investigated in MCF7 cells. EPTA-Gd treatment induced a marked effect on cMyc and ER $\alpha$  expression level upregulating the level of cMyc by ~250% within 2 h and reducing ER level to 25% of its initial value at 4 h. Figure 6A shows the time course of the changes in cMyc and ER $\alpha$  expression induced by EPTA-Gd, obtained from two independent experiments. This time course is very similar to that reported

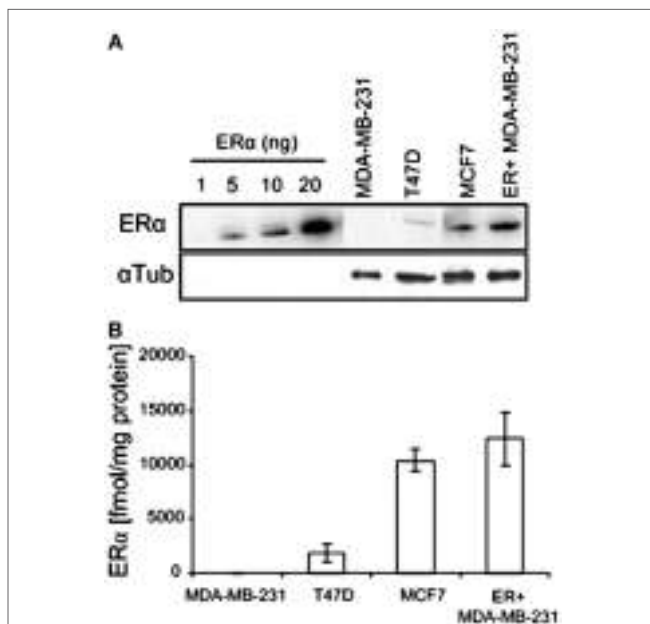
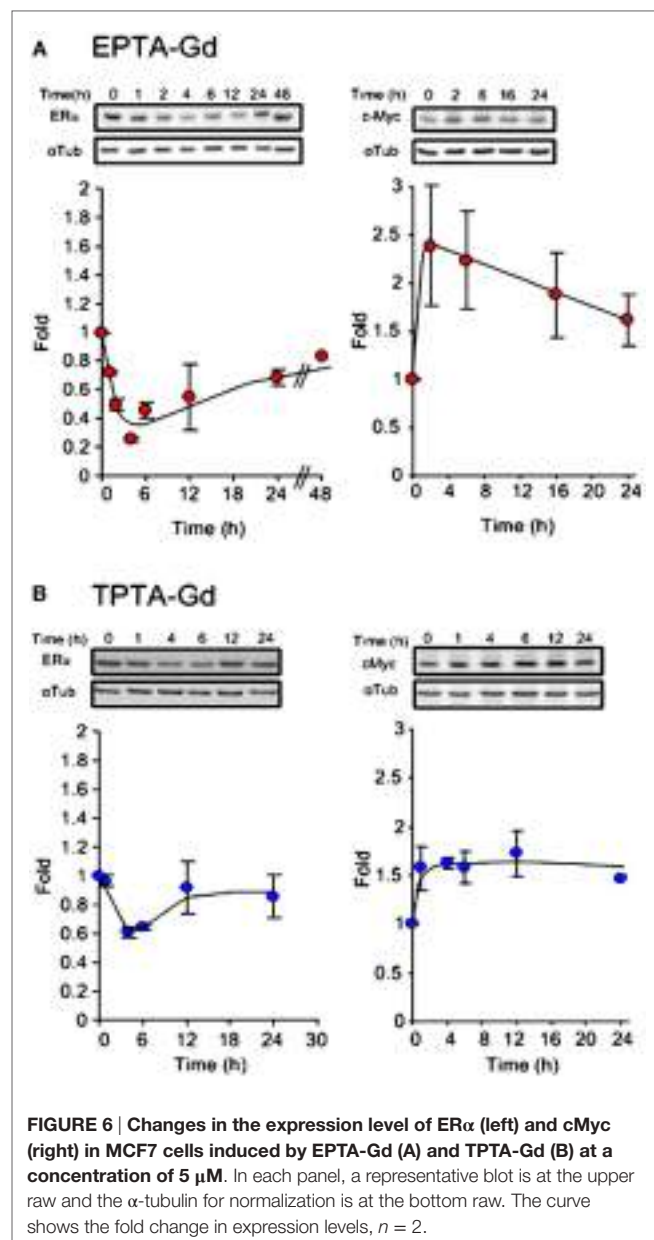
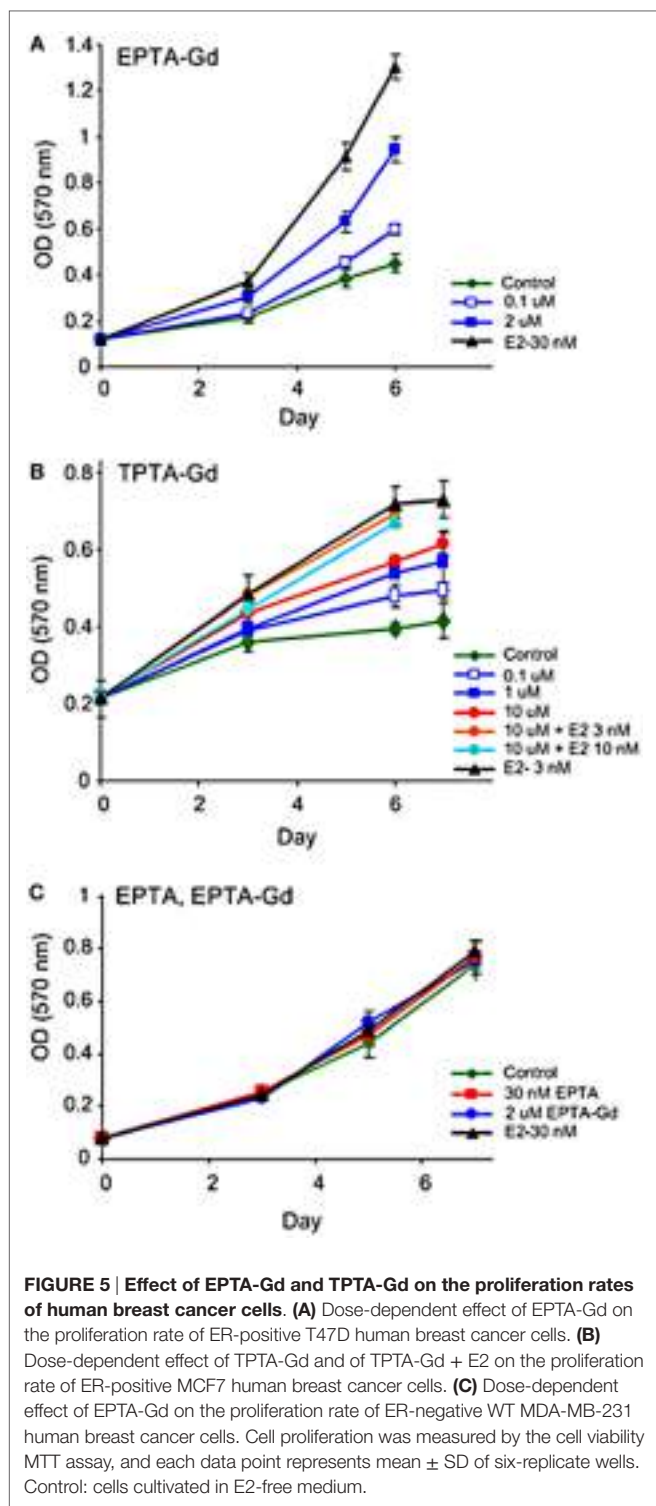


**FIGURE 4 | ER $\alpha$  expression in various human breast cancer cell lines.** **(A)** Western blots of recombinant hER $\alpha$  and of ER $\alpha$  in human breast cancer cell extracts. **(B)** Quantification of western blot experiments ( $n = 2$ ).

for  $17\beta$ -estradiol in the same type of cells (21). TPTA-Gd showed less pronounced effects than EPTA-Gd, yet cMyc expression increased to ~150% of its initial level and ER level decreased to 60% of its initial level (Figure 6B, two independent experiments). These specific induced activities demonstrated the agonistic activity of EPTA-Gd and TPTA-Gd in a mechanism similar to  $17\beta$ -estradiol.

## In Vivo Interaction with ER

The *in vivo* interaction of EPTA-Gd and TPTA-Gd with ER was investigated in orthotopic breast cancer xenografts of ER-positive



and ER-negative cells implanted in the same SCID mouse and were partly described in earlier publications (17, 18). Solid palpable tumors developed within a week after the implantation of cells into the mammary fat pad of the SCID mice. Both the ER-positive and ER-negative xenografts grew at a similar rate with no significant difference in their volume size during 22 days

of growth ( $n = 10$ , paired  $t$ -test:  $p \geq 0.9$  in days 8, 11, 16, 18, and 22 after implantation of the cells), reaching at 22 days a mean size of  $220 \pm 65 \text{ mm}^3$ .

Immunostaining of the ER-positive xenografts showed high nuclear ER staining in viable regions, whereas in the ER-negative xenografts the staining was very low (Figure 7A). Quantitative analysis showed that the percentage of ER-stained cells in the ER-positive xenografts was more than 10-fold higher ( $71.0 \pm 0.05\%$ ,  $n = 11$ ) than in the ER-negative xenografts ( $2.12 \pm 0.01\%$ ,  $n = 11$ ). Similarly, the specific intensity index in the ER-positive xenografts was 10-fold higher ( $2.12 \pm 0.01$ ) than in the ER-negative xenografts ( $0.02 \pm 0.08$ ).

Administration of EPTA-Gd and TPTA-Gd into the blood circulation caused enhancement of the water signal with different

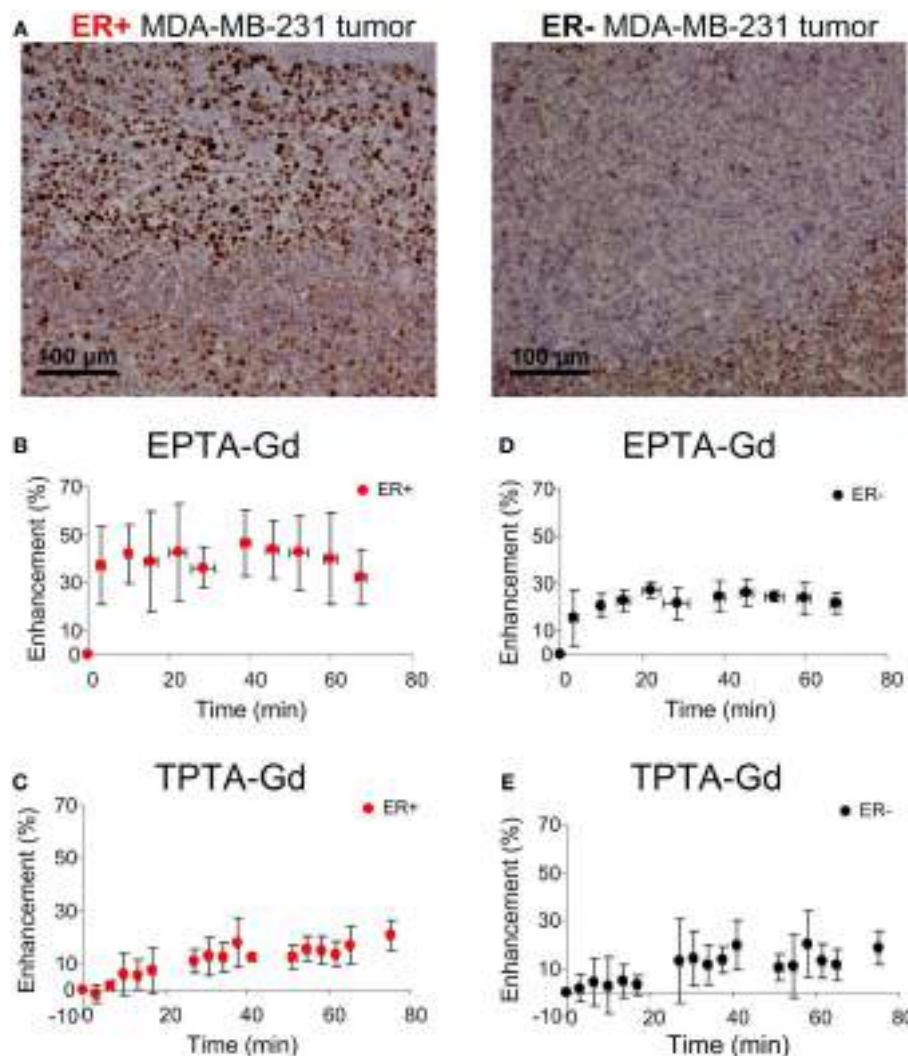


**FIGURE 7 |** Immunohistology staining of ER $\alpha$  (A) and MRI signal enhancement patterns induced by EPTA-Gd (B,D) and by TPTA-Gd (C,E) in ER-positive and ER-negative MDA-MB-231 human breast cancer xenografts. The injected dose of EPTA-Gd and TPTA-Gd was 0.075 mmol/kg. The curves in (B,D) show mean  $\pm$  SD of EPTA-Gd-induced enhancement ( $n = 5$ ). The curves in (C,E) show mean  $\pm$  SD of TPTA-Gd-induced enhancement ( $n = 4$ ).

kinetic profiles for the ER-positive and ER-negative tumors, as shown in the time courses of the mean  $\pm$  SD enhancement curves in Figures 7B–E. The EPTA-Gd enhancement profile in the tumors indicated fast wash-in followed by a plateau, with the enhancement in the ER-positive xenografts (reaching  $43 \pm 20\%$  at 40 min postinjection) significantly higher than in the ER-negative xenografts (reaching  $25 \pm 5\%$  at 40 min postinjection;  $p = 0.005$ ,  $n = 9$ ). In contrast, TPTA-Gd caused a low enhancement of  $13 \pm 2\%$  at 40 min postinjection, which did not differ significantly from the enhancement in the ER-negative cells ( $p = 0.21$ ,  $n = 4$ ). As a reference to ER-negative tissue, we also monitored the enhancement induced by each agent in muscle tissues (Figure 8). The enhancement induced by EPTA-Gd in the muscle was low  $15 \pm 3\%$  at 40 min postinjection ( $n = 9$ ), with a wash-in followed by a marked washout phase (Figure 8C). In contrast, TPTA-Gd induced an appreciable enhancement in the muscle

tissue ( $28 \pm 5\%$  at 40 min postinjection,  $n = 4$ ), with no washout during the 140 min of the entire experiment (Figure 8D). These results indicated that the enhancement induced by EPTA-Gd in ER-positive tumors is significantly higher than in ER-negative tumors and in muscle tissue, however, TPTA-Gd exhibited similar and low enhancement in ER-positive and negative tumors and a specific interaction with muscle component(s). Since the PTA-part is identical in both EPTA-Gd and TPTA-Gd, the accumulation of TPTA-Gd in the muscle is most likely due to the interaction of a muscle component with the tamoxifen moiety.

### Competition Studies of EPTA-Gd with Tamoxifen

Investigation of the time course and extent of EPTA-Gd-induced enhancement showed that shortly after tamoxifen treatment (1 h), a similar enhancement of  $\sim 30\%$  at 40 min postinjection was

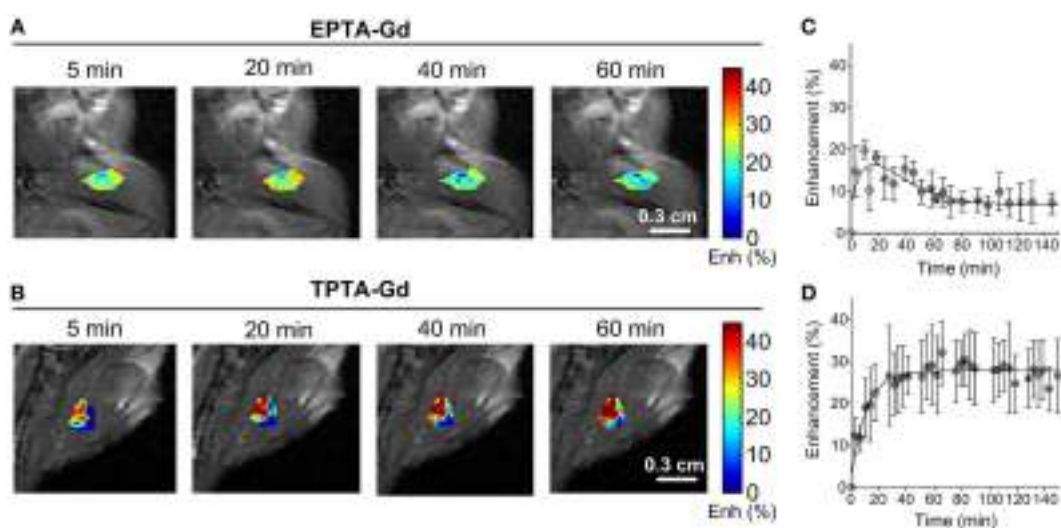


**FIGURE 8 |** Enhancement maps in muscle tissue 20 min after bolus injection of EPTA-Gd (A) and TPTA-Gd (B) into the tail vein of the mice and mean  $\pm$  SD enhancement curves induced by EPTA-Gd [(C),  $n = 5$ ] and TPTA-Gd [(D),  $n = 4$ ]. The injected dose of EPTA-Gd and TPTA-Gd was 0.075 mmol/kg. The enhancement maps are overlaid on the corresponding T1-weighted images.

detected in ER-positive and ER-negative xenografts ( $p = 0.93$ ,  $n = 4$ ), as well as in muscle tissue ( $p = 0.43$ ,  $n = 4$ ) (Figures 9A,C). These results confirmed the binding of tamoxifen to ER and complete blocking of the interaction of EPTA-Gd to the ER.

Chronic treatment with tamoxifen for 3 days also caused the enhancement to be similar in ER-positive and ER-negative xenografts ( $p = 0.36$ ,  $n = 4$ ), confirming tamoxifen blockage of ER and inhibition of EPTA-Gd binding. However, the extent of maximum enhancement in the chronic treated xenografts was significantly higher ( $77 \pm 16\%$ ) than that reached after acute, 1 h treatment with tamoxifen ( $28 \pm 7\%$ ;  $p = 0.003$ ,  $n = 4$ ) (Figures 9B,D). This unexpected result indicated an effect of tamoxifen chronic treatment on tumors' vascular function, increasing the microvascular transcapillary transfer rates in both ER-positive and ER-negative tumors by an hormonal independent mechanism.

## DISCUSSION

The ER is a major prognostic biomarker in breast cancer and a valuable predictor of response to hormonal therapy. New molecular imaging techniques that will enable to detect ER presence and distribution *in vivo*, in both primary and metastatic cancer lesions, could improve accuracy and reproducibility of prognostic assessment and therapy management of breast cancer patients. In this study, we describe the interactions, biological activity, and imaging efficiency of two new paramagnetic ER-targeted CAs in human breast cancer cells and human breast cancer xenografts.

We first measured the ER binding of EPTA-Gd and TPTA-Gd in solution and then monitored the interaction of these probes with ER in human breast cancer cells. In solution, despite the bulky organometallic moiety at the 17 $\alpha$ -position of 17 $\beta$ -estradiol or *trans* 4-position of tamoxifen (occupied by an hydroxyl group in 4-hydroxy tamoxifen), the binding affinity to the receptor was

at the micromolar range, as was also shown previously for other organometallic-labeled estradiol derivatives (25–27). Although the affinity of both ER-targeted probes was two orders of magnitude lower than that of tamoxifen, it appeared to be sufficiently high for interacting and binding to ER in breast cancer cells and xenografts using micromolar concentrations. The MRI relaxation studies and fluorescence binding confirmed the binding inside the cells, most likely to nuclear ER. MRI T1-relaxation studies in ER-positive and negative cells of the same origin showed augmentation of the T1-relaxation rate and the T1 relaxivity in the ER-positive cells as compared to ER-negative cells, indicating entrance to the cells and nuclei and binding to the receptor. Measurements of T1 and T2 in breast cancer cells perfused with medium containing varying concentrations of the ER-targeted probes further confirmed interaction with ER. Generally, Gadolinium-based CAs will affect both T1- and T2-relaxation rates. However, in *in vivo* studies of DCE MRI, due to time limitations, gradient-echo relaxation weighted sequences are applied. The effect of the CA on the signal intensity in T1-weighted images is positive, namely, increase in signal, whereas in T2-weighted images it is negative, namely, signal reduction. An increase in the signal intensity can be detected more efficiently and accurately than the decrease in a T2-weighted image, particularly for a CA that is diffusing into the tissue and when the pre-contrast signal to noise ratio is low, as usually is the situation *in vivo*. Therefore, we predominantly concentrated on T1 measurements using a gradient-echo T1-weighted sequence in the *in vivo* studies.

Fluorescence-binding studies of the analogous paramagnetic agent EPTA-Eu provided a direct measure of the binding affinity in ER-positive cells and confirmed the capability of this agent to enter the cells and to bind to ER as in solution, with a micromolar-binding affinity. It should be noted that relaxation and fluorescence studies in ER-negative cells indicated the presence of non-specific

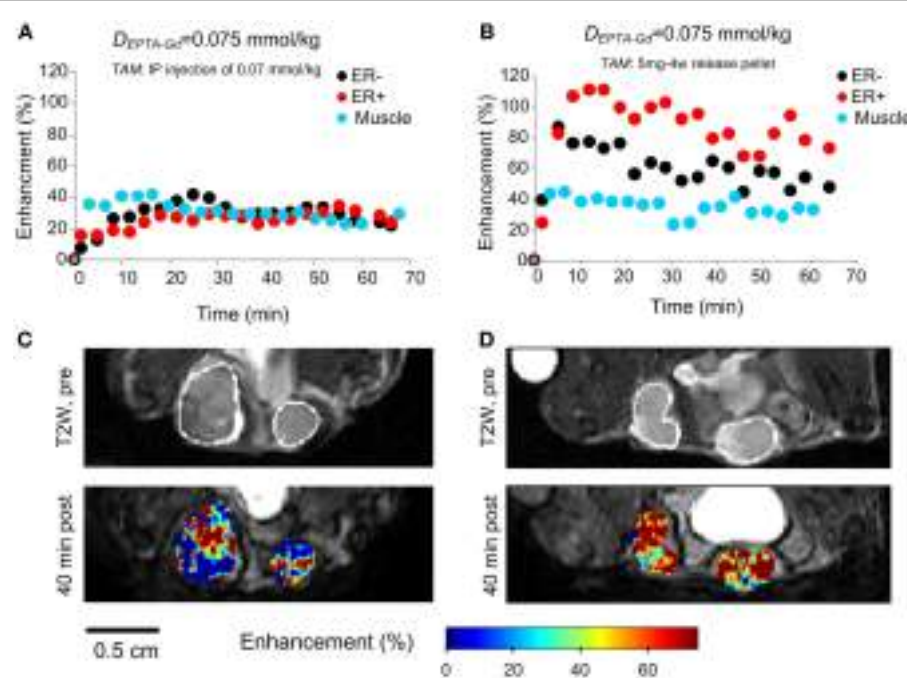


**FIGURE 9 |** EPTA-Gd induced enhancement patterns (A,B) and enhancement maps at 40 min (C,D) in ER-positive and ER-negative MDA-MB-231 xenografts treated with acute (1 h) and chronic (3 days) tamoxifen. The anatomy of the xenografts is demonstrated in the T2-weighted images (C,D). The enhancement maps are overlaid on the corresponding T1-weighted images.

interactions with cell components, but these interactions did not mask the binding and interaction in the ER-positive cells. The ER non-specific interactions of TPTA-Gd appeared to be higher than those of EPTA-Gd, making this agent less favorable as a targeted probe. It was not possible to predict in advance whether the binding of the new probes to ER in cells will modulate gene expression in a similar manner to that of 17 $\beta$ -estradiol or of tamoxifen. It was expected that the 17 $\beta$ -estradiol moiety of EPTA-Gd will induce agonistic activity upon binding to ER, whereas the tamoxifen moiety may exhibit antagonistic activity like tamoxifen. Testing the SERM activity of EPTA-Gd and TPTA-Gd was therefore performed in well-established ER responsive human breast cancer cell lines, MCF7 and T47D, in reference to the ER-negative MDA-MB-231 human breast cancer cells. We have investigated typical estrogen-modulated processes that are known to be inhibited by tamoxifen, such as cell proliferation, the expression level of cMyc, and the ER-expression level [Ref. (28–31) and references cited therein]. EPTA-Gd and TPTA-Gd exhibited estrogen-like agonistic effects, with EPTA-Gd mimicking closely estradiol activity and TPTA-Gd showing mild agonistic effects. Both new agents stimulated cell proliferation at a dose-dependent manner. This stimulation was specific to the presence of ER in the cells, as there was no effect on the growth of ER-negative MDA-MB-231 human breast cancer cells. They also induced the upregulation of cMyc and downregulation of ER, due to ER-enhanced degradation. The ability of these two new agents to induce typical estrogen-like activities clearly indicated their capability to enter the cells and nuclei and interact with the receptor to trigger specific estrogen-mediated responses. Furthermore, the E2-like

activities demonstrated that the conjugated pyridine-Gd complex of EPTA-Gd did not alter the function of the 17 $\beta$ -estradiol moiety in inducing estrogenic agonistic-like activity on breast cancer cell, whereas the conjugated pyridine-Gd complex in TPTA-Gd modified the antagonistic function of the tamoxifen moiety yielding a mild agonistic activity.

The ability of EPTA-Gd to act agonistically was strongly supported by the X-ray crystallographic structure of the complex of EPTA-Eu with the ligand-binding domain of ER (19). Because of the chirality of C17 in the 17 $\beta$ -estradiol moiety and due to the rigid triple bond linking it with the PTA-Eu moiety, the orientation of the organometallic moiety is fixed within the ligand-binding cavity, being almost perpendicular to the flat face of 17 $\beta$ -estradiol and pointing toward helix 7 in an opposite direction to helix 12. Consequently, the conformation of the 17 $\beta$ -estradiol moiety of EPTA-Gd in the ER-binding cavity is almost equivalent to that of free 17 $\beta$ -estradiol and the paramagnetic PTA-Gd moiety causes uncoiling of helices 7 and 8, but does not perturb the agonistic activity determined by helix 12 conformation.

As TPTA-Gd is based on a tamoxifen moiety, it was not clear which conformation it will adopt in the ER-binding cavity and how it will modulate the activity. If the 4-[2-(dimethyl amino) ethoxy] group of the tamoxifen moiety would have been aligned in the ligand-binding cavity as tamoxifen, it could change helix 12 conformation in a similar manner to the change induced by 4-hydroxy tamoxifen (32), leading to antiestrogen activity. However, the rigid triple bond in the 4-position and the flexibility of tamoxifen structure could lead to an enlargement and distortion of the binding cavity in a similar way to that obtained with EPTA-Gd directing

the PTA-Gd moiety toward helices 7 and 8 and accommodating the dimethylamino ethoxy group in a conformation, which does not perturb significantly helix 12 conformation. This hypothesis is in accord with recent X-ray studies suggesting that the flexibility and plasticity of the entire ligand-binding cavity of ER allows expanding of the cavity space in different directions, depending on the chemical nature of the bound ligand (33–35). The well-defined structure by X-ray crystallography provides direct evidence on the ability of a ligand to interact with ER in the solid state and induce agonistic or antagonistic activity. However, it should be noted that conformational changes of ER in the tissue environment, specifically in the nucleus, may alter the interaction between the ligand and the receptor and modify the induced activity.

The main purpose of the *in vivo* studies was to evaluate the ability of the two ER-targeted CAs to demonstrate augmented enhancement upon binding to ER, thereby detecting ER-positive tumors. Indeed, EPTA-Gd interacted with ER as expected from the cell culture studies and specifically augmented significantly the MRI signal in the ER-positive xenografts as compared to the ER-negative xenografts and to muscle tissue. The muscle enhancement was low and also decayed after ~20 min as expected for molecules that do not show specific interaction with extracellular or intracellular components and are cleared out through the kidneys (17). Furthermore, the inability of EPTA-Gd to induce enhancement when ER was blocked by tamoxifen served to prove its selective binding to free ER. In contrast, the interaction and enhancement patterns induced by TPTA-Gd could not be predicted from the breast cancer cell culture studies, as this probe strongly enhanced *in vivo* muscle tissues, demonstrating a dominant non-ER-specific binding to muscle components. This non-specific interaction is most likely determined by the tamoxifen moiety as the paramagnetic moiety is the same in EPTA-Gd and TPTA-Gd. It was previously shown that in addition to its high-affinity binding to the ER, tamoxifen binds with high affinity to microsomal antiestrogen-binding site (AEBS) and inhibits with a micromolar efficiency, protein kinase C (PKC), calmodulin (CaM)-dependent enzymes, and Acyl coenzyme A: cholesterol acyltransferase (ACAT) (36–38).

An additional ER-independent effect of tamoxifen was revealed in the competition studies of EPTA-Gd and tamoxifen. Acute tamoxifen treatment for 1 h did not affect the vascular function of the ER-positive and negative xenografts. However, chronic treatment for 3 days caused in both types of xenografts a higher transcapillary transfer and augmented enhancement suggesting specific tamoxifen-induced interaction with tumor endothelial cells that change the vascular permeability. It was previously demonstrated that chronic tamoxifen treatment for several days increased the transcapillary transfer of MCF7 xenografts in nude mice (39). It was also shown by Blackwell et al. (40) that tamoxifen exerts significant inhibition of angiogenesis in an ER-independent mechanism. The effects on the vascular function during chronic treatment with tamoxifen could be indirect, such as increased hypoxia and consequently upregulation of VEGF expression level, but we cannot exclude direct interaction with endothelial cells.

Of specific interest was the effect of EPTA-Gd on ER level. The amount of ER in cells is controlled by a balance between its

synthesis and degradation and is influenced by the nature of the bound ligand. Like estrogen treatment (21), EPTA-Gd induced a marked decrease in ER within few hours, which slowly returned to steady state level at 48 h posttreatment. This temporal change in ER level are directly associated with the functional response of ER and reflects estrogen responsiveness in general. Further studies are required for extending the use of EPTA-Gd to monitor temporal changes in ER level and characterize ER functional activity. Moreover, it was recently indicated that the shape of an estrogenic ligand programs the conformation of the ER complex, which, in turn, can modulate the activity of estrogen-induced apoptosis (41). The mechanism of estrogen-induced apoptosis has been associated with the positive response to treatment with estradiol, or with partial ER agonists of ER-positive breast cancers resistant to long-term estrogen deprivation (for example, by tamoxifen) (42, 43).

The ability of partial ER agonists to induce apoptosis in ER-positive cells suggests that the clinical application of EPTA-Gd may not cause any harm to breast cancer patients with ER-positive tumors and could even be effective by inducing apoptosis. Further studies investigating whether EPTA-Gd can induce apoptosis may lead to its development as a dual-targeted ER probe for imaging and treatment, particularly of tamoxifen-resistant ER-positive cancers. Clearly, although EPTA-Gd was found to be non-toxic to mice, at the doses administered in this study, and to be cleared out into the urine, any future clinical utilization will require controlled toxicity studies in humans. Thus far, new MRI probes targeted to the progesterone receptor were also synthesized, demonstrating specific enhancement in progesterone – positive cancer cells and animal model tumors (44–47). Currently, however, the only imaging approach for visual assessment and quantitative measurement of steroid hormone receptors in humans have focused predominately on <sup>18</sup>F-based radiopharmaceuticals and PET, in combination with computed tomography (48).

In summary, EPTA-Gd and TPTA-Gd were found to act as SERMs with partial agonistic activities, inducing proliferation of estrogen responsive cells and modulating gene expression levels of ER and cMyc. Both agents entered the cells and augmenting the T1-relaxation rate of the water in their surrounding through binding to ER. However, only EPTA-Gd was found to be an adequate ER-targeted probe *in vivo* as TPTA-Gd exhibited non-specific interaction with cell components other than ER, particularly in muscle tissue, that dominated its ability to induce MRI contrast in ER-positive tumors.

## AUTHOR CONTRIBUTIONS

AP performed the entire acquisition, analysis, and interpretation of the data in this work, worked on drafting this manuscript and preparing the illustrations, including approval of the final version, and accounting for all aspects of the work in ensuring that questions related to the accuracy or integrity of any part of the work are appropriately investigated and resolved. HD is responsible for the conception of the work and for the design of the experiments and the interpretation of the data, revising the manuscript and adding content of intellectual importance

including approving the final version, and accounting for all aspects of the work in ensuring that questions related to the accuracy or integrity of any part of the work are appropriately investigated and resolved.

## ACKNOWLEDGMENTS

We thank Dr. C. Gunanathan and Prof. D. Milstein for the chemical synthesis and analysis of the ER-targeted contrast agents, Dr. D. Seger and T. Kreizman for their assistance with

## REFERENCES

- Jemal A, Siegel R, Xu J, Ward E. Cancer statistics, 2010. *CA Cancer J Clin* (2010) **60**:277–300. doi:10.3322/caac.20073
- Jensen EV, Jacobson HI, Walf AA, Frye CA. Estrogen action: a historic perspective on the implications of considering alternative approaches. *Physiol Behav* (2010) **99**:151–62. doi:10.1016/j.physbeh.2009.08.013
- Weigel MT, Dowsett M. Current and emerging biomarkers in breast cancer: prognosis and prediction. *Endocr Relat Cancer* (2010) **17**:R245–62. doi:10.1677/ERC-10-0136
- Davies C, Godwin J, Gray R, Clarke M, Cutter D, Darby S, et al. Relevance of breast cancer hormone receptors and other factors to the efficacy of adjuvant tamoxifen: patient-level meta-analysis of randomised trials. *Lancet* (2011) **378**:771–84. doi:10.1016/S0140-6736(11)60993-8
- Barnes DM, Millis RR, Bees LV, Thorpe SM, Leake RE. Increased use of immunohistochemistry for oestrogen receptor measurement in mammary carcinoma: the need for quality assurance. *Eur J Cancer* (1998) **34**:1677–82. doi:10.1016/S0959-8049(98)00149-X
- Harvey JM, Clark GM, Osborne CK, Allred DC. Estrogen receptor status by immunohistochemistry is superior to the ligand-binding assay for predicting response to adjuvant endocrine therapy in breast cancer. *J Clin Oncol* (1999) **17**:1474–81.
- Gown AM. Current issues in ER and HER2 testing by IHC in breast cancer. *Mod Pathol* (2008) **21**(Suppl 2):S8–15. doi:10.1038/modpathol.2008.34
- Fitzgibbons PL, Murphy DA, Hammond MEH, Allred DC, Valenstein PN. Recommendations for validating estrogen and progesterone receptor immunohistochemistry assays. *Arch Pathol Lab Med* (2010) **134**:930–5. doi:10.1043/1543-2165-134.6.930
- Katzenellenbogen JA, Coleman RE, Hawkins RA, Krohn KA, Larson SM, Mendelsohn J, et al. Tumor receptor imaging: proceedings of the National Cancer Institute workshop, review of current work, and prospective for further investigations. *Clin Cancer Res* (1995) **1**:921–32.
- Katzenellenbogen JA. The 2010 Philip S. Portoghese Medicinal Chemistry Lectureship: addressing the “core issue” in the design of estrogen receptor ligands. *J Med Chem* (2011) **54**:5271–82. doi:10.1021/jm200801h
- Mintun MA, Welch MJ, Siegel BA, Mathias CJ, Brodack JW, McGuire AH, et al. Breast cancer: PET imaging of estrogen receptors. *Radiology* (1988) **169**:45–8. doi:10.1148/radiology.169.1.3262228
- de Vries EFJ, Rots MG, Hospers GAP. Nuclear imaging of hormonal receptor status in breast cancer: a tool for guiding endocrine treatment and drug development. *Curr Cancer Drug Targets* (2007) **7**:510–9. doi:10.2174/156800907781662301
- Peterson LM, Mankoff DA, Lawton T, Yagle K, Schubert EK, Stekhova S, et al. Quantitative imaging of estrogen receptor expression in breast cancer with PET and 18F-fluoroestradiol. *J Nucl Med* (2008) **49**:367–74. doi:10.2967/jnumed.107.047506
- Peterson LM, Kurland BF, Link JM, Schubert EK, Stekhova S, Linden HM, et al. Factors influencing the uptake of 18F-fluoroestradiol in patients with estrogen receptor positive breast cancer. *Nucl Med Biol* (2011) **38**:969–78. doi:10.1016/j.nucmedbio.2011.03.002
- DeMartini W, Lehman C, Partridge S. Breast MRI for cancer detection and characterization: a review of evidence-based clinical applications. *Acad Radiol* (2008) **15**:408–16. doi:10.1016/j.acra.2007.11.006
- the molecular biology studies, R. Margalit for the support in the animal studies, Dr. I. Biton for supporting the MRI studies, and Dr. E. Furman-Haran for the valuable discussions. HD holds the Fred and Andrea Fallek Chair for Breast Cancer Research.
- Gunanathan C, Pais A, Furman-Haran E, Seger D, Eyal E, Mukhopadhyay S, et al. Water-soluble contrast agents targeted at the estrogen receptor for molecular magnetic resonance imaging. *Bioconjug Chem* (2007) **18**:1361–5. doi:10.1021/bc700230m
- Pais A, Gunanathan C, Margalit R, Biton IE, Yosepovich A, Milstein D, et al. In vivo magnetic resonance imaging of the estrogen receptor in an orthotopic model of human breast cancer. *Cancer Res* (2011) **71**:7387–97. doi:10.1158/0008-5472.CAN-11-1226
- Pais A, Biton IE, Margalit R, Degani H. Characterization of estrogen-receptor-targeted contrast agents in solution, breast cancer cells, and tumors in vivo. *Magn Reson Med* (2013) **70**:193–206. doi:10.1002/mrm.24442
- Li M-J, Greenblatt HM, Dym O, Albeck S, Pais A, Gunanathan C, et al. Structure of estradiol metal chelate and estrogen receptor complex: the basis for designing a new class of selective estrogen receptor modulators. *J Med Chem* (2011) **54**:3575–80. doi:10.1021/jm200192y
- Legros N, Jin L, Leclercq G. Tamoxifen-induced estrogen receptor up-regulation in mammary tumor cells is not related to growth inhibition. *Cancer Chemother Pharmacol* (1997) **39**:380–2. doi:10.1007/s002800050587
- Dadiani M, Seger D, Kreizman T, Badikhi D, Margalit R, Eilam R, et al. Estrogen regulation of vascular endothelial growth factor in breast cancer in vitro and in vivo: the role of estrogen receptor alpha and c-Myc. *Endocr Relat Cancer* (2009) **16**:819–34. doi:10.1677/ERC-08-0249
- Degani H, Ronen SM, Furman-Haran E. Breast cancer: spectroscopy and imaging of cells and tumors. In: Gillies R, editor. *NMR in Physiology and Biomedicine*. San Diego, CA: Academic Press (1994). p. 329–51.
- Miller MA, Katzenellenbogen BS. Characterization and quantitation of antiestrogen binding sites in estrogen receptor-positive and -negative human breast cancer cell lines. *Cancer Res* (1983) **43**:3094–100.
- Nawata H, Bronzert D, Lippman ME. Isolation and characterization of a tamoxifen-resistant cell line derived from MCF-7 human breast cancer cells. *J Biol Chem* (1981) **256**:5016–21.
- el Amouri H, Vessières A, Vichard D, Top S, Gruselle M, Jaouen G. Syntheses and affinities of novel organometallic-labeled estradiol derivatives: a structure-affinity relationship. *J Med Chem* (1992) **35**:3130–5. doi:10.1021/jm00095a006
- Jackson A, Davis J, Pither RJ, Rodger A, Hannon MJ. Estrogen-derived steroidal metal complexes: agents for cellular delivery of metal centers to estrogen receptor-positive cells. *Inorg Chem* (2001) **40**:3964–73. doi:10.1021/ic010152a
- Gabano E, Cassino C, Bonetti S, Prandi C, Colangelo D, Ghiglia A, et al. Synthesis and characterisation of estrogenic carriers for cytotoxic Pt(II) fragments: biological activity of the resulting complexes. *Org Biomol Chem* (2005) **3**:3531–9. doi:10.1039/b507716h
- Musgrove EA, Sergio CM, Loi S, Inman CK, Anderson LR, Alles MC, et al. Identification of functional networks of estrogen- and c-Myc-responsive genes and their relationship to response to tamoxifen therapy in breast cancer. *PLoS One* (2008) **3**:e2987. doi:10.1371/journal.pone.0002987
- Xu J, Chen Y, Olopade OI. MYC and breast cancer. *Genes Cancer* (2010) **1**:629–40. doi:10.1177/1947601910378691
- Nawaz Z, Lonard DM, Dennis AP, Smith CL, O’Malley BW. Proteasome-dependent degradation of the human estrogen receptor. *Proc Natl Acad Sci U S A* (1999) **96**:1858–62. doi:10.1073/pnas.96.5.1858
- Kocanova S, Mazaheri M, Caze-Sobra S, Bystricky K. Ligands specify estrogen receptor alpha nuclear localization and degradation. *BMC Cell Biol* (2010) **11**:98. doi:10.1186/1471-2121-11-98

32. Shiu AK, Barstad D, Loria PM, Cheng L, Kushner PJ, Agard DA, et al. The structural basis of estrogen receptor/coactivator recognition and the antagonism of this interaction by tamoxifen. *Cell* (1998) **95**:927–37. doi:10.1016/S0092-8674(00)81717-1
33. Egner U, Heinrich N, Ruff M, Gangloff M, Mueller-Fahrnow A, Wurtz JM. Different ligands-different receptor conformations: modeling of the hER alpha LBD in complex with agonists and antagonists. *Med Res Rev* (2001) **21**:523–39. doi:10.1002/med.1024
34. Nettles KW, Bruning JB, Gil G, O'Neill EE, Nowak J, Guo Y, et al. Structural plasticity in the oestrogen receptor ligand-binding domain. *EMBO Rep* (2007) **8**:563–8. doi:10.1038/sj.emboj.7400963
35. Maximov PY, Myers CB, Curpan RF, Lewis-Wambi JS, Jordan VC. Structure-function relationships of estrogenic triphenylethylenes related to endoxifen and 4-hydroxytamoxifen. *J Med Chem* (2010) **53**:3273–83. doi:10.1021/jm901907u
36. Sutherland RL, Murphy LC, San Foo M, Green MD, Whybourne AM, Krozowski ZS. High-affinity anti-oestrogen binding site distinct from the oestrogen receptor. *Nature* (1980) **288**:273–5. doi:10.1038/288273a0
37. de Medina P, Favre G, Poirot M. Multiple targeting by the antitumor drug tamoxifen: a structure-activity study. *Curr Med Chem Anticancer Agents* (2004) **4**:491–508. doi:10.2174/1568011043352696
38. Lopes MC, Vale MG, Carvalho AP. Ca2(+)-dependent binding of tamoxifen to calmodulin isolated from bovine brain. *Cancer Res* (1990) **50**:2753–8.
39. Furman-Haran E, Margalit R, Maretzek AF, Degani H. Angiogenic response of MCF7 human breast cancer to hormonal treatment: assessment by dynamic GdDTPA-enhanced MRI at high spatial resolution. *J Magn Reson Imaging* (1996) **6**:195–202. doi:10.1002/jmri.1880060135
40. Blackwell KL, Haroon ZA, Shan S, Saito W, Broadwater G, Greenberg CS, et al. Tamoxifen inhibits angiogenesis in estrogen receptor-negative animal models. *Clin Cancer Res* (2000) **6**:4359–64.
41. Jordan VC. The new biology of estrogen-induced apoptosis applied to treat and prevent breast cancer. *Endocr Relat Cancer* (2015) **22**:R1–31. doi:10.1530/ERC-14-0448
42. Obiorah IE, Fan P, Sengupta S, Jordan VC. Selective estrogen-induced apoptosis in breast cancer. *Steroids* (2014) **90**:60–70. doi:10.1016/j.steroids.2014.06.003
43. Xiong R, Patel HK, Gutgesell LM, Zhao J, Delgado-Rivera L, Pham TND, et al. Selective human estrogen receptor partial agonists (ShERPA)s for tamoxifen-resistant breast cancer. *J Med Chem* (2016) **59**:219–36. doi:10.1021/acs.jmedchem.5b01276
44. Lee J, Burdette JE, MacRenaris KW, Mustafi D, Woodruff TK, Meade TJ. Rational design, synthesis, and biological evaluation of progesterone-modified MRI contrast agents. *Chem Biol* (2007) **14**:824–34. doi:10.1016/j.chembiol.2007.06.006
45. Sukerkar PA, MacRenaris KW, Townsend TR, Ahmed RA, Burdette JE, Meade TJ. Synthesis and biological evaluation of water-soluble progesterone-conjugated probes for magnetic resonance imaging of hormone related cancers. *Bioconjug Chem* (2011) **22**(11):2304–16. doi:10.1021/bc2003555
46. Sukerkar PA, MacRenaris KW, Meade TJ, Burdette JE. A steroid-conjugated magnetic resonance probe enhances contrast in progesterone receptor expressing organs and tumors in vivo. *Mol Pharm* (2011) **8**(4):1390–400. doi:10.1021/mp200219e
47. Townsend TR, Moyle-Heyrman G, Sukerkar PA, MacRenaris KW, Burdette JE, Meade TJ. Progesterone-targeted magnetic resonance imaging probes. *Bioconjug Chem* (2014) **25**(8):1428–37. doi:10.1021/bc500265h
48. Fowler AM, Clark AS, Katzenellenbogen JA, Linden HM, Dehdashti F. Imaging diagnostic and therapeutic targets: steroid receptors in breast cancer. *J Nucl Med* (2016) **57**(Suppl 1):75S–80S. doi:10.2967/jnumed.115.157933

**Conflict of Interest Statement:** The research was conducted in the absence of any commercial or financial relationships that could be construed as a potential conflict of interest.

Copyright © 2016 Pais and Degani. This is an open-access article distributed under the terms of the Creative Commons Attribution License (CC BY). The use, distribution or reproduction in other forums is permitted, provided the original author(s) or licensor are credited and that the original publication in this journal is cited, in accordance with accepted academic practice. No use, distribution or reproduction is permitted which does not comply with these terms.



# Key Players in Choline Metabolic Reprograming in Triple-Negative Breast Cancer

Egidio Iorio<sup>1\*</sup>, Maria José Caramujo<sup>1†</sup>, Serena Cecchetti<sup>1</sup>, Francesca Spadaro<sup>2</sup>, Giulia Carpinelli<sup>1</sup>, Rossella Canese<sup>1</sup> and Franca Podo<sup>1</sup>

<sup>1</sup>Department of Cell Biology and Neurosciences, Istituto Superiore di Sanità, Rome, Italy, <sup>2</sup>Department of Hematology, Oncology and Molecular Medicine, Istituto Superiore di Sanità, Rome, Italy

## OPEN ACCESS

### Edited by:

Kristine Glunde,  
Johns Hopkins School of Medicine,  
USA

### Reviewed by:

Hadassa Degani,  
Weizmann Institute of Science, Israel  
Balaji Krishnamachary,  
Johns Hopkins University, USA  
Jerry David Glickson,  
University of Pennsylvania, USA

### \*Correspondence:

Egidio Iorio  
egidio.iorio@iss.it

### †Present address:

Maria José Caramujo,  
Faculdade de Ciências,  
Centre for Ecology, Evolution  
and Environmental Changes  
(CE3C), Universidade de Lisboa,  
Lisboa, Portugal

### Specialty section:

This article was submitted  
to Cancer Imaging and  
Diagnosis, a section of the  
journal Frontiers in Oncology

Received: 02 April 2016

Accepted: 12 September 2016

Published: 30 September 2016

### Citation:

Iorio E, Caramujo MJ, Cecchetti S, Spadaro F, Carpinelli G, Canese R and Podo F (2016) Key Players in Choline Metabolic Reprograming in Triple-Negative Breast Cancer. *Front. Oncol.* 6:205.  
doi: 10.3389/fonc.2016.00205

Triple-negative breast cancer (TNBC), defined as lack of estrogen and progesterone receptors in the absence of protein overexpression/gene amplification of human epidermal growth factor receptor 2, is still a clinical challenge despite progress in breast cancer care. <sup>1</sup>H magnetic resonance spectroscopy allows identification and non-invasive monitoring of TNBC metabolic aberrations and elucidation of some key mechanisms underlying tumor progression. Thus, it has the potential to improve *in vivo* diagnosis and follow-up and also to identify new targets for treatment. Several studies have shown an altered phosphatidylcholine (PtdCho) metabolism in TNBCs, both in patients and in experimental models. Upregulation of choline kinase-alpha, an enzyme of the Kennedy pathway that phosphorylates free choline (Cho) to phosphocholine (PCho), is a major contributor to the increased PCho content detected in TNBCs. Phospholipase-mediated PtdCho headgroup hydrolysis also contributes to the build-up of a PCho pool in TNBC cells. The oncogene-driven PtdCho cycle appears to be fine tuned in TNBC cells in at least three ways: by modulating the choline import, by regulating the activity or expression of specific metabolic enzymes, and by contributing to the rewiring of the entire metabolic network. Thus, only by thoroughly dissecting these mechanisms, it will be possible to effectively translate this basic knowledge into further development and implementation of Cho-based imaging techniques and novel classes of therapeutics.

**Keywords:** triple-negative breast cancer, phosphatidylcholine metabolism, metabolic reprogramming, phospholipase, choline kinase

## INTRODUCTION

Classification of breast cancer (BC) has been historically based on both analysis of tumor morphology and histological detection of three marker proteins: the estrogen receptor (ER), the progesterone receptor (PR), and the human epidermal growth factor (EGF) receptor tyrosine kinase 2 (ErbB2 or HER2). Tumors which express none of these three markers are collectively referred to as triple-negative breast cancer (TNBC; ER<sup>-</sup>, PR<sup>-</sup>, HER2<sup>-</sup>) and still pose a clinical challenge. More recently, gene expression analyses showed that BC is a more heterogeneous disease than previously assumed and the BC histotypes based on ER/PR/HER2 classification were expanded to include five major transcriptional subtypes: basal-like, HER2-enriched, luminal A, luminal B, and normal breast-like (1, 2). The majority (70–80%) of TNBCs are defined as basal-like by gene expression (3) and

share other molecular features with this BC subtype. According to most epidemiological studies, TNBCs represent 10–20% of all BCs, although a higher proportion can be found in some ethnic groups and among BRCA1 mutation carriers. TNBCs are typically poorly differentiated, frequently have high histological grade and mitotic index, and often present early onset and shorter disease-free and overall survival (4, 5). Recent large-scale gene expression and genome-based studies have shown that TNBC is a heterogeneous disease (**Figure 1A**) comprising at least four to six definable molecular subtypes that express elements of distinct oncogenic signaling pathways (6, 7). Interestingly, 50–70% of all TNBCs overexpress the EGF receptor tyrosine kinase 1 (ErbB1, EGFR, or HER1). EGFR is one of the major regulators of survival, proliferation, and migration (8), leading to activation of the phosphoinositide 3-kinase (PI3K) and ERK pathways, which in turn stimulate other receptor-activated signaling cascades associated with cancer onset and progression (**Figure 1B**) (9).

The aggressiveness of TNBC and the lack of targeted therapies specifically recommended for TNBC patients highlight the need to explore additional molecular mechanisms beyond genomic and proteomic changes to better elucidate the metabolic pathways required for TNBC growth and survival (10, 11).

## METABOLIC REPROGRAMMING IN TNBC CELLS

Molecular genomic and proteomic studies have been carried out to understand the complexity of TNBC and identify markers that can be therapeutically targeted. However, little is known about the metabolic alterations that distinguish TNBC from non-triple-negative subtypes and characterize TNBC progression. Previous studies have shown that proteins that are involved in glycolysis, glutaminolysis, and glycine or serine metabolism are differentially expressed among different BC subtypes in tissue microarray sections and in a large series of invasive BC specimens (12–14). In particular, several observations reported that TNBC have elevated glucose uptake and a glycolytic gene/protein expression signature (12, 14). A recent study reported a novel mechanism, whereby the transcription factor c-Myc drives glucose metabolism in TNBC MDA-MB-157 cells by direct repression of thioredoxin-interacting protein (TXNIP), a potent negative regulator of glucose uptake, aerobic glycolysis, and glycolytic gene expression. A Myc<sup>high</sup>/TXNIP<sup>low</sup> gene signature correlates with decreased overall patient survival and decreased metastasis-free survival in BC. The correlation between the Myc<sup>high</sup>/TXNIP<sup>low</sup> gene signature and poor clinical outcome is evident only in TNBC, not in other BC subclasses. Furthermore, mutation in p53 (TP53), found in the majority of TNBCs, enhances the correlation between the Myc<sup>high</sup>/TXNIP<sup>low</sup> gene signature and death from BC (15). Finally, an increase of glycolysis was found in a panel of five TNBC cells and accumulation of fructose-1,6-bisphosphate (F1,6BP), a glycolytic intermediate that directly binds to and enhances the activity of EGFR, was detected in MDA-MB-468 cells, with enhanced lactate excretion, tumor growth, and immune escape (16). TNBC cell lines, such as MDA-MB-468, MDA-MB-231, MDA-MB-436, and BT20,

exhibit function defects in multiple respiratory complexes with a reduction in expression of complex I and complex III proteins of the mitochondrial respiratory chain relative to receptor-positive cell lines (17). The increased glycolytic activity in TNBCs could be responsible for the increased <sup>18</sup>F-fluorodeoxyglucose (FDG) uptake generally reported in PET examinations of these patients, beyond a large variability in the maximum and mean standardized uptake values and in metabolic volumes (18–21).

Lipid metabolism activation in BC cells is recognized as a hallmark of carcinogenesis (22, 23). Increased fatty acid (FA) synthesis due to increased levels of fatty acid synthase (FAS) has been observed in various cancers and is correlated with a poor prognosis in many instances (23). FAS could, in principle, be an appealing therapeutic target because most cancer cells depend on FAS-mediated *de novo* FA synthesis, whereas most healthy cells prefer to incorporate exogenous FAs (24). However, reports on the overexpression of FAS across BC subtypes, and in TNBC in particular, are still contradictory (25–27), and further studies are needed before considering this enzyme as a strong therapeutic target.

The concerted activation of an assembly of molecular complexes in cancer cells cooperates to sustain an oncogene-induced cell signaling through multiple postreceptor pathways involved in phospholipid biosynthesis and breakdown. Among these, phosphatidylinositol 4-phosphate 5-kinase Igamma (PIP $\kappa$ I $\gamma$ ) is overexpressed in TNBC cells, in which the loss of this enzyme impairs PI3K/Akt activation (28). Furthermore, two major enzymes involved in the agonist-induced phosphatidylcholine (PtdCho) cycle, such as choline kinase (ChoK) and PtdCho-specific phospholipase C (PC-PLC), are overexpressed and activated in various BC subtypes, including TNBC cells, with the implications on expression and oncogenic function of EGF receptors' family members (29–33).

The present evidence points to the existence of multiple links between enzymes involved in the glycolytic gene/protein signature and those responsible for enhanced carbon fluxes through the oncogene-driven PtdCho biosynthesis and catabolism in BC cells (**Figure 2**). This biochemical interplay may also serve as a key regulator of tumor progression in TNBCs.

## PtdCho METABOLISM IN TNBC

The introduction of magnetic resonance spectroscopy (MRS) in cancer biology allowed the detection of abnormal profiles of aqueous total choline-containing metabolites (tCho) of the PtdCho cycle in cancer cells and tissues, both at preclinical and clinical level (9, 34–37). Substantially modified <sup>1</sup>H MRS tCho spectral profiles have been reported on malignant transformation of human mammary (38–40) and prostate epithelial cells (41) and in ovarian cancers (42–44). These modifications occur in the 3.20–3.24 ppm <sup>1</sup>H MRS spectral region and are typical of the trimethylammonium headgroups of PtdCho precursors and catabolites, such as phosphocholine (PCho), glycerophosphocholine (GPCho), and free choline (Cho).

Phospholipids play the dual role of being basic structural components of membranes and acting as substrates of reactions involved in key regulatory functions in mammalian cells (45, 46).

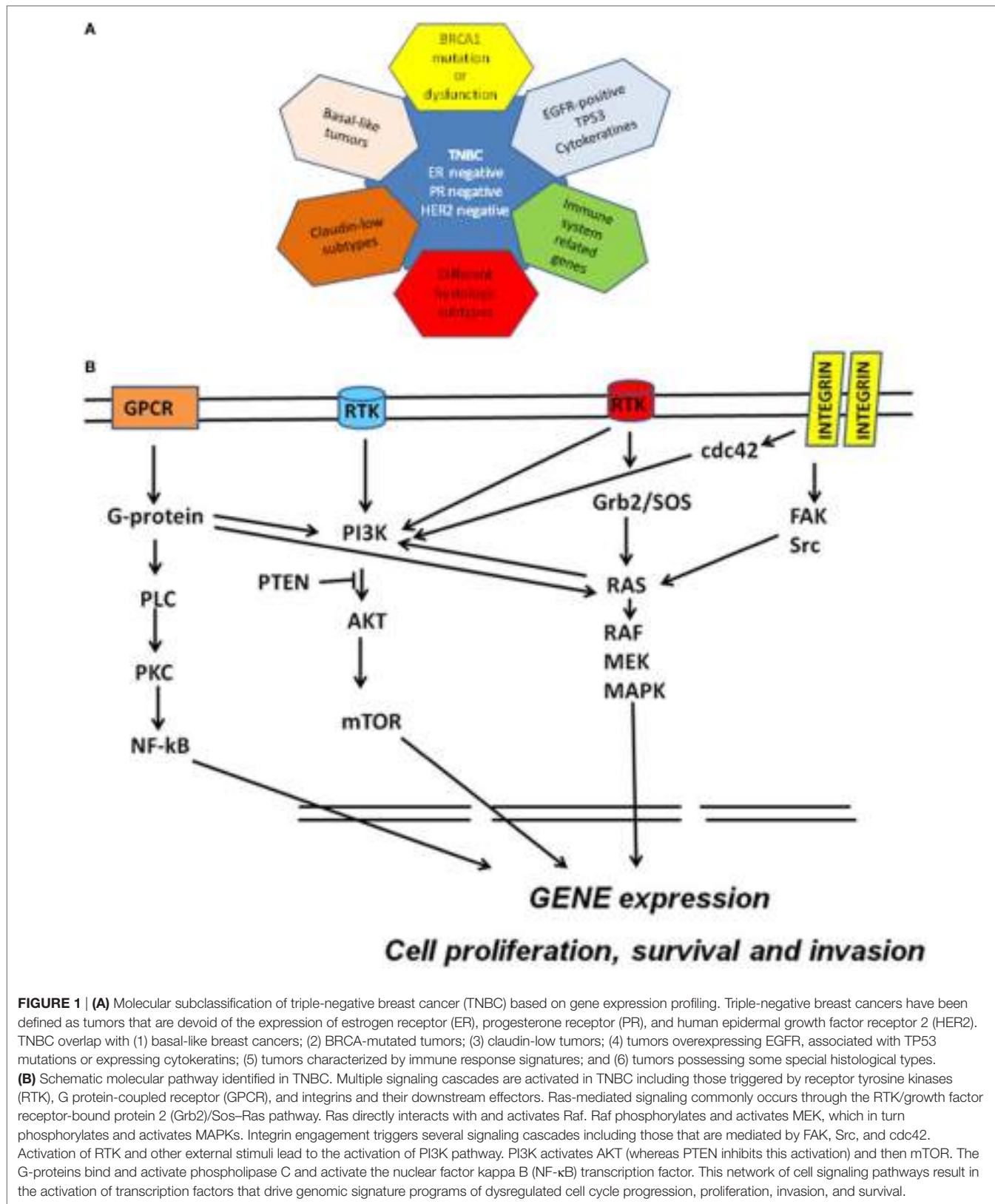


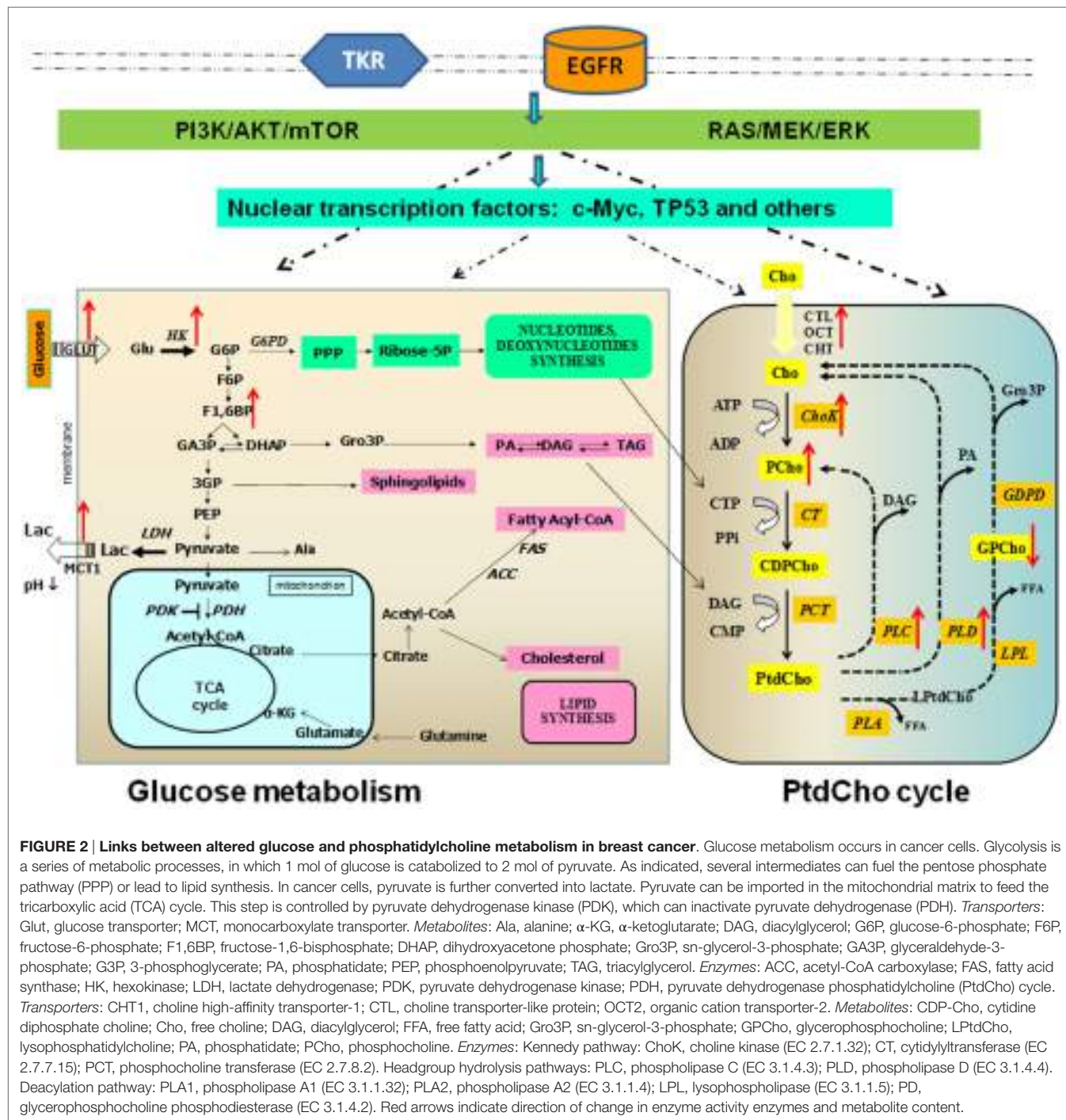
**FIGURE 1 | (A)** Molecular subclassification of triple-negative breast cancer (TNBC) based on gene expression profiling. Triple-negative breast cancers have been defined as tumors that are devoid of the expression of estrogen receptor (ER), progesterone receptor (PR), and human epidermal growth factor receptor 2 (HER2). TNBC overlap with (1) basal-like breast cancers; (2) BRCA-mutated tumors; (3) claudin-low tumors; (4) tumors overexpressing EGFR, associated with TP53 mutations or expressing cytokeratins; (5) tumors characterized by immune response signatures; and (6) tumors possessing some special histological types. **(B)** Schematic molecular pathway identified in TNBC. Multiple signaling cascades are activated in TNBC including those triggered by receptor tyrosine kinases (RTK), G protein-coupled receptor (GPCR), and integrins and their downstream effectors. Ras-mediated signaling commonly occurs through the RTK/growth factor receptor-bound protein 2 (Grb2)/Sos-Ras pathway. Ras directly interacts with and activates Raf. Raf phosphorylates and activates MEK, which in turn phosphorylates and activates MAPKs. Integrin engagement triggers several signaling cascades including those that are mediated by FAK, Src, and cdc42. Activation of RTK and other external stimuli lead to the activation of PI3K pathway. PI3K activates AKT (whereas PTEN inhibits this activation) and then mTOR. The G-proteins bind and activate phospholipase C and activate the nuclear factor kappa B (NF- $\kappa$ B) transcription factor. This network of cell signaling pathways result in the activation of transcription factors that drive genomic signature programs of dysregulated cell cycle progression, proliferation, invasion, and survival.

Hydrolysis of PtdCho, the most abundant phospholipid in eukaryotic cell membranes, can generate second messengers, such as diacylglycerol (DAG), phosphatidic acid (PA), lysophosphatidic

acid (LPA), arachidonic acid (AA), and lysophosphatidylcholine (LPtdCho). These PtdCho metabolites are produced through three major catabolic pathways, respectively, mediated by specific

phospholipases of type C (PC-PLC) and D (PLD), which act at the two distinct phosphodiester bonds of the PtdCho headgroup, and by phospholipases of type A2 and A1 (PLA2 and PLA1), which act in the deacylation reaction cascade (**Figure 2**). PCho accumulation either produced by ChoK in the first reaction of the three-step Kennedy biosynthetic pathway or by PLC-mediated PtdCho catabolism is associated with tumor growth and progression (9, 33–36).

This accumulated evidence supports the inclusion of an altered phospholipid metabolism as a novel candidate hallmark for cancer and as a key regulator in the overall cancer metabolic reprogramming. An aberrant PtdCho metabolism associated with increases in the intracellular total choline-containing PtdCho metabolites (tCho) and phosphocholine (PCho) contents (femtomoles per cubic micrometer cell) were initially observed in BC cells as they progressed from normal to malignant phenotypes,



i.e., from non-tumoral immortalized MCF-12A to the highly metastatic TNBC MDA-MB-231 and MDA-MB-435 cell lines (38). The high intracellular content of PCho seemed unrelated to the demand for cell membrane biosynthesis in the investigated BC cells characterized by different doubling time values (38). Notably, a different rate of increase was observed for PCho ( $6\times$ ) and PtdCho ( $1.5\times$ ) in MDA-MB-231 BC cells compared with the non-malignant MCF12A cells (40). An integration of MRS with gene microarray analysis revealed that a combination of upregulated ChoK and PLD and/or an increased PC-PLC expression/activity caused PCho accumulation in MDA-MB-231 cells, while lower levels of GPCho were consistent with underexpression of cytosolic calcium-dependent PLA2 group IVA and lysophospholipase 1 (40). Elevated levels of ChoK $\alpha$  and PLD1 isoforms were found in both the ER $^-$  MDA-MB-231 BC cell line and in patient-derived ER $^-$  BC specimens, as compared with the corresponding non-metastatic ER $^+$  MCF-7 BC cell line and ER $^+$  patient-derived BC samples (47). Downregulation of ChoK $\alpha$  by RNA silencing increased PLD1 expression, and downregulation of PLD1 increased ChoK $\alpha$  expression, indicating a close relationship between ChoK and PLD enzymes (47). Additionally, ChoK $\alpha$  silencing resulted in increased PC-PLC protein expression (e.g., twofold in MDA-MB-231) suggesting that BC cells could compensate for the loss of ChoK $\alpha$  protein levels with PC-PLC upregulation, thus maintaining an intracellular PCho pool size markedly higher than that of non-tumoral breast epithelial cells (48, 49).

Although the role of PLAs in BC cells remains unknown, very low expression of secreted PLA2 (sPLA2) was found in basal-like breast tumor biopsies and cultured cells (50). As noted by the authors, the mRNA expression of sPLA2s belonging to IIA, III, and X groups is regulated by DNA methylation and histone deacetylation, and all three genes are significantly silenced in aggressive TNBC cells due to both mechanisms. It may be interesting to investigate a possible relationship with the regulation of cytosolic PLA2s underexpressed in TNBC apparently linked to low levels of GPCho in this BC subtype (40).

A study by Eliyahu and colleagues (39) confirmed an altered PtdCho metabolism in different molecular BC subtypes relative to human mammary epithelial cells (HMECs), although the MDA-MB-231 TNBC cells exhibited the lowest PCho/NTP ratio among the investigated BC cell lines. Interestingly, under the adopted experimental conditions, the PCho level in HMEC and BC cells was found to correlate with Cho transport into the cells, mainly due to the organic cation transporter-2 (OCT2) and the choline high-affinity transporter-1 (CHT1), but not with ChoK activity, suggesting that this step is fast and not rate limiting, although its induction ensures increased PCho levels. The upregulation of choline transporters and ChoK may be related to a cascade of genetic changes that are associated with the multistep process of carcinogenesis (51).

Enzymatic assays showed a twofold to sixfold activation of PC-PLC in BC of different subtypes compared with a non-tumoral counterpart (MCF-10A cell line) (32). The activity rate measured in the TNBC MDA-MB-231 cell line was about twofold higher than that of HER2-enriched and ER-positive cell lines. Metabolic analysis of MDA-MB-231 cells identified a characteristic

biochemical signature of these cells relative to the non-tumoral MCF-10A counterpart, consisting of higher contents of PCho and succinate, elevated proportion of monounsaturated FAs and increased ChoK and PC-PLC protein expression (52). The importance of the cell membrane lipid profile to discriminate BC subtypes is receiving increasing attention, and the results suggest possible links between altered metabolic pathways in BC and membrane molecular rearrangement. He and colleagues (53) could discriminate BC cell lines from MCF-10A cells on the basis of phospholipid species composition and expression of five lipogenesis-related enzymes. The authors suggested that elevated expression levels of fatty acid synthase 1 (FAS1), stearoyl-CoA desaturases 1 and 5 (SCD1 and SCD5), and ChoK $\alpha$  may be closely related to enhanced levels of saturated and monounsaturated lipids in BC cell lines. Most interestingly, it was possible to distinguish adequately between MDA-MB-231 cells based on the highest level of PtdCho (36:1) and PtdCho (36:2) and ChoK $\alpha$  expression compared with other BC subtypes (53).

Differences in phospholipid and lipid metabolism between cells in culture and in solid tumors have been detected by *in vivo* MRS in the MDA-MB-231 model. These differences may be ascribed to characteristic conditions of solid tumor microenvironment such as depletion of nutrients and oxygen, changes in pH, and interactions between cancer and stromal/endothelial cells (54, 55). A higher concentration of tCho (mainly due to PCho) was found in hypoxic regions of heterogeneous orthotopic MDA-MB-231 tumor xenografts using three-dimensional multimodal molecular imaging platforms (56, 57). The high tCho content of tumor cells was associated with enriched levels of proteins involved in glucose metabolism, PI3K-Akt/Ras/FAS signaling pathway, protein processing in endoplasmic reticulum, apoptosis, and telomere stress-induced senescence (56). A stable silencing of glycerophosphodiester phosphodiesterase domain containing 5 (GDPD5), which is upregulated in TNBC cells and tumors, induced an increase in the levels of GPCho and phosphoethanolamine in MDA-MB-231 BC cells and in their orthotopic tumor xenografts compared with controls (58, 59) suggesting a close networking between choline and ethanolamine phospholipid cycles. A larger variation in the PCho/GPCho ratio was observed for the basal-like BC subtype of patient-derived xenograft models relative to luminal B subtype xenografts (60, 61). These differences could be explained by lower mRNA expression of ChoK ( $\alpha$  and  $\beta$ ) and higher expression of PLA group 4A in basal tumor xenografts (61). In another experimental subcutaneous model expressing basaloid TNBC markers (HCC1806), phosphomonoesters (which include PCho) and lactate levels were modulated by tumor size (62).

The metabolic characterization of TNBC human biopsies is far from being well established, although different studies reported a higher overall tCho content in TBNCs with respect to non-tumoral tissues. A significantly higher tCho level, either quantified in millimoles per kilogram or expressed as peak integral normalized to the volume of interest and the signal-to-noise ratio, was reported in TNBC compared with non-triple-negative tumors using *in vivo* MRS (63, 64). A quantitative study on *in vivo* MRS examinations of 29 patients indicated that TNBCs exhibited increased tCho levels ranging from 0.4 to 4.9 mmol/kg (65).

TNBCs are more likely to have high tCho than other BC subtypes, although the situation may be reversed in young age patients (range 28–39 years) (66). The high tCho levels were well correlated with the standardized FDG uptake value obtained using PET/CT and with the histological prognostic parameters (19). A recent paper (67) reported that intact TNBC biopsies could be discriminated by HR-MAS analyses from triple-positive BCs based on their content in free Cho and GPCo, which were significantly higher in TNBC relative to triple-positive BC. In this paper (67), the analyzed TNBC biopsies contained lower levels of glutamine and higher levels of glutamate compared with tumors with positive receptor statuses which might result from increased glutaminolysis metabolism and suggests dependence on glutamine to support cell growth. This issue warrants measurements of metabolic fluxes using suitable isotopomeric models, such as bonded cumomer analysis by MRS or fragmented cumomer analysis by mass spectrometry (68, 69).

## TARGETING PtdCho METABOLISM IN TNBC

The role of PtdCho cycle enzymes as potential new molecular targets in TNBC can be investigated using molecular depletion approaches and/or pharmacological inhibitors. However, there are no studies that allowed discrimination of specific effects of targeting PtdCho-cycle enzymes on TNBC versus other BC subtypes, and most of studies were performed using only one or two TNBC cell lines. Although a reduction of 85% of *in vivo* tumor growth was obtained in subcutaneous MDA-MB-231 tumors treated with the ChoK inhibitor Mn58b (70), this result needs further evaluation in different TNBC models. The downregulation of ChoK in MDA-MB-231 cells cultured *in vitro* induced profound alterations in cell proliferation and promoted differentiation, as detected by cytosolic lipid droplet formation and modified expression of galectin-3 (71). These changes were associated with alterations of 33 proliferation-related genes and 9 DNA repair-related genes (72). Interestingly, in MDA-MB-231 cells, a combination of ChoK silencing with a conventional treatment using 5-fluorouracil resulted in higher cell death rate relative to that obtained when each treatment was applied individually (72) confirming a key role for the ChoK enzyme in *in vitro* cell proliferation and survival. Furthermore, *in vivo* targeting of ChoK by either lentiviral gene silencing (73) or by ChoK $\alpha$  depletion using specific short-hairpin RNA (shRNA) (74), respectively, induced a growth delay or strongly repressed tumor growth in MDA-MB-231 xenograft bearing mice.

Additionally, there is mounting evidence from studies on experimental TNBC models that the reduction/destabilization of ChoK protein levels rather than inhibition of the activity of this enzyme is more effective in inhibiting tumor growth. In fact, direct or indirect pharmacological inhibitors that were able to reduce the activity of ChoK (and consequently the levels of tCho and PCho) did not reduce cell viability as long as ChoK $\alpha$  protein expression and PtdCho levels were not reduced in TNBC cells grown *in vitro* (75).

The potential of using PtdCho catabolic pathways as important cotargets for TNBC therapy is gaining relevance. A multi-targeting strategy such as simultaneous silencing of PLD1 and ChoK $\alpha$  in MDA-MB-231 cells increased apoptosis (detected by the TUNEL assay) as compared with individual treatments (47). Exposure of MDA-MB-231 cells to D609 which is an inhibitor of a PC-PLC resulted in 60–80% PC-PLC inhibition associated with tumor cell differentiation, detected by a progressive decrease of mesenchymal traits such as vimentin and N-cadherin expression, reduced galectin-3 and milk fat globule EGF-factor 8 levels,  $\beta$ -casein formation and decreased *in vitro* cell migration and invasion (32). These results, obtained from a single tumor model of TNBC, warrant further investigations on a large data set of human TNBCs that can be fully genotyped and metabolically characterized.

## FUTURE DIRECTIONS

Although evidence of specific metabolic alterations in TNBC is accruing, there is a clear need for extending preclinical investigations to a larger number of TNBC models. On the other hand, clinical investigations have to better elucidate the impact of the heterogeneous nature of TNBC lesions on the metabolic profiles and their changes in tumor progression. It may also prove relevant to assess the links between the tCho profile and molecular features such as EGFR overexpression, p53 status, and other specific biological TNBC characteristics. We hypothesize that the PtdCho cycle may represent a good focus point for personalized/precision medicine, offering markers that may be used as diagnosis tools for assessment of cancer prognosis and response to therapy.

The identification of a role for PtdCho metabolism in TNBC progression supports the view that some enzymes of this cycle may act as key regulators of molecular mechanisms leading to cancer onset, invasion, and metastasis, thus representing a new source of potential targets to counteract cancer growth and metastasis.

## AUTHOR CONTRIBUTIONS

The manuscript was written by EI; revised by FP, MJC, RC, SC, FS, GC, and EI; read and approved by all coauthors.

## FUNDING

We acknowledge partial support by Associazione Italiana per la Ricerca sul Cancro (AIRC) 2007–2010; Integrated Oncology Program RO 06.5/N.ISS/Q0, Oncology Program OncOrd 37/07/N. ISS/70CF/4 and Special Program Alleanza Contro il Cancro 2006, ACC3-AC5/D, Ministry of Health, Italy; Accordo di Collaborazione Italia-USA ISS/530F/0F29; AIRC 2009–2011, IG N. 9147, and AIRC IG 12976 2012 and Programma Oncotecnologico ISS/13ONC/5. MJC was funded by TRAIN programme, Italy (Cofunded by Marie Curie Actions, 7th Framework Programme), Incoming Grant no. 246549.

## REFERENCES

- Perou CM, Sorlie T, Eisen MB, van de Rijn M, Jeffrey SS, Rees CA, et al. Molecular portraits of human breast tumours. *Nature* (2000) 406(6797):747–52. doi:10.1038/35021093
- Sorlie T, Tibshirani R, Parker J, Hastie T, Marron JS, Nobel A, et al. Repeated observation of breast tumor subtypes in independent gene expression data sets. *Proc Natl Acad Sci USA* (2003) 100(14):8418–23. doi:10.1073/pnas.0932692100
- Prat A, Adamo B, Cheang MC, Anders CK, Carey LA, Perou CM. Molecular characterization of basal-like and non-basal-like triple-negative breast cancer. *Oncologist* (2013) 18(2):123–33. doi:10.1634/theoncologist.2012-0397
- Foulkes WD, Smith IE, Reis-Filho JS. Triple-negative breast cancer. *N Engl J Med* (2010) 363(20):1938–48. doi:10.1056/NEJMra1001389
- Podo F, Buydens LM, Degani H, Hilhorst R, Klipp E, Gribbestad IS, et al. Triple-negative breast cancer: present challenges and new perspectives. *Mol Oncol* (2010) 4(3):209–29. doi:10.1016/j.molonc.2010.04.006
- Burstein MD, Tsimelzon A, Poage GM, Covington KR, Contreras A, Fuqua SA, et al. Comprehensive genomic analysis identifies novel subtypes and targets of triple-negative breast cancer. *Clin Cancer Res* (2015) 21(7):1688–98. doi:10.1158/1078-0432.CCR-14-0432
- Price JT, Tiganis T, Agarwal A, Djakiew D, Thompson EW. Epidermal growth factor promotes MDA-MB-231 breast cancer cell migration through a phosphatidylinositol 3'-kinase and phospholipase C-dependent mechanism. *Cancer Res* (1999) 59(21):5475–8.
- Corkery B, Crown J, Clynes M, O'Donovan N. Epidermal growth factor receptor as a potential therapeutic target in triple-negative breast cancer. *Ann Oncol* (2009) 20(5):862–7. doi:10.1093/annonc/mdn710
- Podo F, Canevari S, Canese R, Pisanu ME, Ricci A, Iorio E. MR evaluation of response to targeted treatment in cancer cells. *NMR Biomed* (2011) 24(6):648–72. doi:10.1002/nbm.1658
- Tyanova S, Albrechtsen R, Kronqvist P, Cox J, Mann M, Geiger T. Proteomic maps of breast cancer subtypes. *Nat Commun* (2016) 7:10259. doi:10.1038/ncomms10259
- Xu H, Eirew P, Mullally SC, Aparicio S. The omics of triple-negative breast cancers. *Clin Chem* (2014) 60(1):122–33. doi:10.1373/clinchem.2013.207167
- Choi J, Kim do H, Jung WH, Koo JS. Metabolic interaction between cancer cells and stromal cells according to breast cancer molecular subtype. *Breast Cancer Res* (2013) 15(5):R78. doi:10.1186/bcr3472
- Kanaan YM, Sampey BP, Beyene D, Esnakula AK, Naab TJ, Ricks-Santi LJ, et al. Metabolic profile of triple-negative breast cancer in African-American women reveals potential biomarkers of aggressive disease. *Cancer Genomics Proteomics* (2014) 11(6):279–94.
- Pinheiro C, Sousa B, Albergaria A, Paredes J, Duflot R, Vieira D, et al. GLUT1 and CAIX expression profiles in breast cancer correlate with adverse prognostic factors and MCT1 overexpression. *Histol Histopathol* (2011) 26(10):1279–86.
- Shen L, O'Shea JM, Kaadige MR, Cunha S, Wilde BR, Cohen AL, et al. Metabolic reprogramming in triple-negative breast cancer through Myc suppression of TXNIP. *Proc Natl Acad Sci U S A* (2015) 112(17):5425–30. doi:10.1073/pnas.1501555112
- Lim SO, Li CW, Xia W, Lee HH, Chang SS, Shen J, et al. EGFR signaling enhances aerobic glycolysis in triple-negative breast cancer cells to promote tumor growth and immune escape. *Cancer Res* (2016) 76(5):1284–96. doi:10.1158/0008-5472.CAN-15-2478
- Pelicano H, Zhang W, Liu J, Hammoudi N, Dai J, Xu RH, et al. Mitochondrial dysfunction in some triple-negative breast cancer cell lines: role of mTOR pathway and therapeutic potential. *Breast Cancer Res* (2014) 16(5):434. doi:10.1186/s13058-014-0434-6
- Chiacchio S, Evangelista L, AlSharif A, Manca G, Di Martino F, Negri A, et al. Association between semiquantitative Pet parameters and molecular subtypes of breast invasive ductal carcinoma. *Q J Nucl Med Mol Imaging* (2015).
- Koo HR, Park JS, Kang KW, Cho N, Chang JM, Bae MS, et al. 18F-FDG uptake in breast cancer correlates with immunohistochemically defined subtypes. *Eur Radiol* (2014) 24(3):610–8. doi:10.1007/s00330-013-3037-1
- Tozaki M, Hoshi K. 1H MR spectroscopy of invasive ductal carcinoma: correlations with FDG PET and histologic prognostic factors. *AJR Am J Roentgenol* (2010) 194(5):1384–90. doi:10.2214/AJR.09.3431
- Yue Y, Cui X, Bose S, Audeh W, Zhang X, Fraass B. Stratifying triple-negative breast cancer prognosis using 18F-FDG-PET/CT imaging. *Breast Cancer Res Treat* (2015) 153(3):607–16. doi:10.1007/s10549-015-3558-1
- Hilvo M, Denkert C, Lehtinen L, Muller B, Brockmoller S, Seppanen-Laakso T, et al. Novel theranostic opportunities offered by characterization of altered membrane lipid metabolism in breast cancer progression. *Cancer Res* (2011) 71(9):3236–45. doi:10.1158/0008-5472.CAN-10-3894
- Menendez JA, Lupu R. Fatty acid synthase and the lipogenic phenotype in cancer pathogenesis. *Nat Rev Cancer* (2007) 7(10):763–77. doi:10.1038/nrc2222
- Currie E, Schulze A, Zechner R, Walther TC, Farese RV Jr. Cellular fatty acid metabolism and cancer. *Cell Metab* (2013) 18(2):153–61. doi:10.1016/j.cmet.2013.05.017
- Flores FH, Viñas G, Oliveras G, Giro-Perafita A, Perez-Bueno F, Roque A, et al. Triple negative breast cancer: clinicopathologic characteristics and fatty acid synthase (FASN) expression as a potential target. *Ann Oncol* (2014) 25(4 Suppl):iv58–84. doi:10.1093/annonc/mdu326
- Viñas G, Oliveras G, Perez-Bueno F, Giro A, Blancafort A, Puig-Vives M, et al. Fatty acid synthase (FASN) expression in triple-negative breast cancer. *Cancer Res* (2012) 72(24 Suppl):P4-09-11. doi:10.1158/0008-5472.sabcs12-p4-09-11
- Kim S, Lee Y, Koo JS. Differential expression of lipid metabolism-related proteins in different breast cancer subtypes. *PLoS One* (2015) 10(3):e0119473. doi:10.1371/journal.pone.0119473
- Thapa N, Choi S, Tan X, Wise T, Anderson RA. Phosphatidylinositol phosphate 5-kinase igamma and phosphoinositide 3-kinase/Akt signaling couple to promote oncogenic growth. *J Biol Chem* (2015) 290(30):18843–54. doi:10.1074/jbc.M114.596742
- Pisterzi P, Mercurio L, Caramujo MJ, Iorio E, Podo F, Cecchetti S. Phosphatidylcholine-specific phospholipase C inhibition as a new therapeutic approach to control triple-negative breast cancer cells proliferation. *Proceedings of the Special Conference EACR-AACR-SIC*. Florence (2015).
- Paris L, Cecchetti S, Spadaro F, Abalsamo L, Lugini L, Pisanu ME, et al. Inhibition of phosphatidylcholine-specific phospholipase C downregulates HER2 overexpression on plasma membrane of breast cancer cells. *Breast Cancer Res* (2010) 12(3):R27. doi:10.1186/bcr2575
- Miyake T, Parsons SJ. Functional interactions between choline kinase alpha, epidermal growth factor receptor and c-Src in breast cancer cell proliferation. *Oncogene* (2012) 31(11):1431–41. doi:10.1038/onc.2011.332
- Abalsamo L, Spadaro F, Bozzuto G, Paris L, Cecchetti S, Lugini L, et al. Inhibition of phosphatidylcholine-specific phospholipase C results in loss of mesenchymal traits in metastatic breast cancer cells. *Breast Cancer Res* (2012) 14(2):R50. doi:10.1186/bcr3151
- Podo F, Paris L, Cecchetti S, Spadaro F, Abalsamo L, Ramoni C, et al. Activation of phosphatidylcholine-specific phospholipase C in breast and ovarian cancer: impact on MRS-detected choline metabolic profile and perspectives for targeted therapy. *Front Oncol* (2016) 6:171. doi:10.3389/fonc.2016.00171
- Beloueche-Babari M, Chung YL, Al-Saffar NM, Falck-Miniotis M, Leach MO. Metabolic assessment of the action of targeted cancer therapeutics using magnetic resonance spectroscopy. *Br J Cancer* (2010) 102(1):1–7. doi:10.1038/sj.bjc.6605457
- Glunde K, Bhujwalla ZM, Ronen SM. Choline metabolism in malignant transformation. *Nat Rev Cancer* (2011) 11(12):835–48. doi:10.1038/nrc3162
- Podo F. Tumour phospholipid metabolism. *NMR Biomed* (1999) 12(7):413–39. doi:10.1002/(SICI)1099-1492(199911)12:7<413::AID-NBM587>3.0.CO;2-U
- Sardanelli F, Fausto A, Di Leo G, de Nijs R, Vorbuchner M, Podo F. In vivo proton MR spectroscopy of the breast using the total choline peak integral as a marker of malignancy. *AJR Am J Roentgenol* (2009) 192(6):1608–17. doi:10.2214/AJR.07.3521
- Aboagye EO, Bhujwalla ZM. Malignant transformation alters membrane choline phospholipid metabolism of human mammary epithelial cells. *Cancer Res* (1999) 59(1):80–4.
- Eliyahu G, Kreizman T, Degani H. Phosphocholine as a biomarker of breast cancer: molecular and biochemical studies. *Int J Cancer* (2007) 120(8):1721–30. doi:10.1002/ijc.22293
- Glunde K, Jie C, Bhujwalla ZM. Molecular causes of the aberrant choline phospholipid metabolism in breast cancer. *Cancer Res* (2004) 64(12):4270–6. doi:10.1158/0008-5472.CAN-03-3829
- Ackerstaff E, Pflug BR, Nelson JB, Bhujwalla ZM. Detection of increased choline compounds with proton nuclear magnetic resonance spectroscopy subsequent to malignant transformation of human prostatic epithelial cells. *Cancer Res* (2001) 61(9):3599–603.
- Canese R, Pisanu ME, Mezzananza D, Ricci A, Paris L, Bagnoli M, et al. Characterisation of in vivo ovarian cancer models by quantitative 1H

- magnetic resonance spectroscopy and diffusion-weighted imaging. *NMR Biomed* (2012) 25(4):632–42. doi:10.1002/nbm.1779
43. Iorio E, Mezzanica D, Alberti P, Spadaro F, Ramoni C, D'Ascenzo S, et al. Alterations of choline phospholipid metabolism in ovarian tumor progression. *Cancer Res* (2005) 65(20):9369–76. doi:10.1158/0008-5472.CAN-05-1146
  44. Iorio E, Ricci A, Bagnoli M, Pisano ME, Castellano G, Di Vito M, et al. Activation of phosphatidylcholine cycle enzymes in human epithelial ovarian cancer cells. *Cancer Res* (2010) 70(5):2126–35. doi:10.1158/0008-5472.CAN-09-3833
  45. Fagone P, Jackowski S. Phosphatidylcholine and the CDP-choline cycle. *Biochim Biophys Acta* (2013) 1831(3):523–32. doi:10.1016/j.bbaply.2012.09.009
  46. Vance JE, Vance DE. Phospholipid biosynthesis in mammalian cells. *Biochem Cell Biol* (2004) 82(1):113–28. doi:10.1139/o03-073
  47. Gadiya M, Mori N, Cao MD, Mironchik Y, Kakkad S, Gribbestad IS, et al. Phospholipase D1 and choline kinase-alpha are interactive targets in breast cancer. *Cancer Biol Ther* (2014) 15(5):593–601. doi:10.4161/cbt.28165
  48. Glunde K, Mori N, Takagi T, Cecchetti S, Ramoni C, Iorio E, et al. Choline kinase silencing in breast cancer cells results in compensatory upregulation of phosphatidylcholine-specific phospholipase C. *Proc Int Soc Mag Reson Med* (2008) 16:244.
  49. Podo F, Glunde K, Cecchetti S, Krishnamachary B, Mori N, Paris L, et al. Cross-talk between enzymes responsible for the elevated 1H MRS phosphocholine signal in breast cancer cells. *Proc of the Sixth Annual World Molecular Imaging Congress (WMIC)*. Savannah, GA (2013).
  50. Brgez V, Pucar A, Pungercar J, Lambreau G, Petan T. Secreted phospholipases A(2) are differentially expressed and epigenetically silenced in human breast cancer cells. *Biochem Biophys Res Commun* (2014) 445(1):230–5. doi:10.1016/j.bbrc.2014.01.182
  51. Beckmann MW, Niederacher D, Schnurch HG, Gusterson BA, Bender HG. Multistep carcinogenesis of breast cancer and tumour heterogeneity. *J Mol Med (Berl)* (1997) 75(6):429–39. doi:10.1007/s001090050128
  52. Caramujo MJ, Cecchetti S, Pisterzi P, de Carvalho CCCR, Podo F, Iorio E. Metabolic assessment of breast cancer cells offers evidence of altered phospholipid metabolism. *Magn Reson Mater Phy* (2015) 28(S1):S458. doi:10.1007/s10334-015-0490-7
  53. He M, Guo S, Li Z. In situ characterizing membrane lipid phenotype of breast cancer cells using mass spectrometry profiling. *Sci Rep* (2015) 5:11298. doi:10.1038/srep11298
  54. Mori N, Glunde K, Takagi T, Bhujwalla ZM. The choline phospholipid metabolism detected by comparing cancer cells with tumors. *Proc Int Soc Magn Reson Med* (2008) 16:2800.
  55. Mori N, Wildes F, Takagi T, Glunde K, Bhujwalla ZM. Differences in phospholipid and lipid metabolism between cancer cells in culture and in solid tumors. *Proc Int Soc Magn Reson Med* (2015) 23:1126.
  56. Jiang L, Chughtai K, Purvine SO, Bhujwalla ZM, Raman V, Pasa-Tolic L, et al. MALDI-mass spectrometric imaging revealing hypoxia-driven lipids and proteins in a breast tumor model. *Anal Chem* (2015) 87(12):5947–56. doi:10.1021/ac504503x
  57. Jiang L, Greenwood TR, Artemov D, Raman V, Winnard PT Jr, Heeren RM, et al. Localized hypoxia results in spatially heterogeneous metabolic signatures in breast tumor models. *Neoplasia* (2012) 14(8):732–41. doi:10.1593/neop.12858
  58. Cao MD, Dopkens M, Krishnamachary B, Vesuna F, Gadiya MM, Lonning PE, et al. Glycerophosphodiester phosphodiesterase domain containing 5 (GDPD5) expression correlates with malignant choline phospholipid metabolite profiles in human breast cancer. *NMR Biomed* (2012) 25(9):1033–42. doi:10.1002/nbm.2766
  59. Wijnen JP, Jiang L, Greenwood TR, Cheng M, Dopkens M, Cao MD, et al. Silencing of the glycerophosphocholine phosphodiesterase GDPD5 alters the phospholipid metabolite profile in a breast cancer model *in vivo* as monitored by (31) P MRS. *NMR Biomed* (2014) 27(6):692–9. doi:10.1002/nbm.3106
  60. Grinde MT, Skrbo N, Moestue SA, Rodland EA, Borgan E, Kristian A, et al. Interplay of choline metabolites and genes in patient-derived breast cancer xenografts. *Breast Cancer Res* (2014) 16(1):R5. doi:10.1186/bcr3597
  61. Moestue SA, Borgan E, Huuse EM, Lindholm EM, Sitter B, Borresen-Dale AL, et al. Distinct choline metabolic profiles are associated with differences in gene expression for basal-like and luminal-like breast cancer xenograft models. *BMC Cancer* (2010) 10:433. doi:10.1186/1471-2407-10-433
  62. Liu T, Nath K, Liu W, Zhou R, Chen IW. A study of the relationship of metabolic MR parameters to estrogen dependence in breast cancer xenografts. *NMR Biomed* (2015) 28(9):1087–96. doi:10.1002/nbm.3342
  63. Chen JH, Mehta RS, Baek HM, Nie K, Liu H, Lin MQ, et al. Clinical characteristics and biomarkers of breast cancer associated with choline concentration measured by 1H MRS. *NMR Biomed* (2011) 24(3):316–24. doi:10.1002/nbm.1595
  64. Shin HJ, Baek HM, Cha JH, Kim HH. Evaluation of breast cancer using proton MR spectroscopy: total choline peak integral and signal-to-noise ratio as prognostic indicators. *AJR Am J Roentgenol* (2012) 198(5):W488–97. doi:10.2214/AJR.11.7292
  65. Chen JH, Agrawal G, Feig B, Baek HM, Carpenter PM, Mehta RS, et al. Triple-negative breast cancer: MRI features in 29 patients. *Ann Oncol* (2007) 18(12):2042–3. doi:10.1093/annonc/mdm504
  66. Sah RG, Sharma U, Parshad R, Seenu V, Mathur SR, Jagannathan NR. Association of estrogen receptor, progesterone receptor, and human epidermal growth factor receptor 2 status with total choline concentration and tumor volume in breast cancer patients: an MRI and *in vivo* proton MRS study. *Magn Reson Med* (2012) 68(4):1039–47. doi:10.1002/mrm.24117
  67. Cao MD, Lamichhane S, Lundgren S, Bofin A, Fjosne H, Giskeodegard GF, et al. Metabolic characterization of triple negative breast cancer. *BMC Cancer* (2014) 14:941. doi:10.1186/1471-2407-14-941
  68. Shestov AA, Mancuso A, Lee SC, Guo L, Nelson DS, Roman JC, et al. Bonded cumomer analysis of human melanoma metabolism monitored by 13C NMR spectroscopy of perfused tumor cells. *J Biol Chem* (2016) 291(10):5157–71. doi:10.1074/jbc.M115.701862
  69. Shestov AA, Lee SC, Nath K, Guo L, Nelson DS, Roman JC, et al. (13)C MRS and LC-MS flux analysis of tumor intermediary metabolism. *Front Oncol* (2016) 6:135. doi:10.3389/fonc.2016.00135
  70. Ramirez de Molina A, Banez-Coronel M, Gutierrez R, Rodriguez-Gonzalez A, Olmeda D, Megias D, et al. Choline kinase activation is a critical requirement for the proliferation of primary human mammary epithelial cells and breast tumor progression. *Cancer Res* (2004) 64(18):6732–9. doi:10.1158/0008-5472.CAN-04-0489
  71. Glunde K, Raman V, Mori N, Bhujwalla ZM. RNA interference-mediated choline kinase suppression in breast cancer cells induces differentiation and reduces proliferation. *Cancer Res* (2005) 65(23):11034–43. doi:10.1158/0008-5472.CAN-05-1807
  72. Mori N, Glunde K, Takagi T, Raman V, Bhujwalla ZM. Choline kinase down-regulation increases the effect of 5-fluorouracil in breast cancer cells. *Cancer Res* (2007) 67(23):11284–90. doi:10.1158/0008-5472.CAN-07-2728
  73. Krishnamachary B, Glunde K, Wildes F, Mori N, Takagi T, Raman V, et al. Noninvasive detection of lentiviral-mediated choline kinase targeting in a human breast cancer xenograft. *Cancer Res* (2009) 69(8):3464–71. doi:10.1158/0008-5472.CAN-08-4120
  74. Mignion L, Danhier P, Magat J, Porporato PE, Masquelier J, Gregoire V, et al. Non-invasive *in vivo* imaging of early metabolic tumor response to therapies targeting choline metabolism. *Int J Cancer* (2016) 138(8):2043–9. doi:10.1002/ijc.29932
  75. Mori N, Wildes F, Kakkad S, Jacob D, Solaiyappan M, Glunde K, et al. Choline kinase-alpha protein and phosphatidylcholine but not phosphocholine are required for breast cancer cell survival. *NMR Biomed* (2015) 28(12):1697–706. doi:10.1002/nbm.3429

**Conflict of Interest Statement:** The authors declare that the research was conducted in the absence of any commercial or financial relationships that could be construed as a potential conflict of interest.

The reviewer BK and handling editor declared their shared affiliation, and the handling editor states that the process nevertheless met the standards of a fair and objective review.

Copyright © 2016 Iorio, Caramujo, Cecchetti, Spadaro, Carpinelli, Canese and Podo. This is an open-access article distributed under the terms of the Creative Commons Attribution License (CC BY). The use, distribution or reproduction in other forums is permitted, provided the original author(s) or licensor are credited and that the original publication in this journal is cited, in accordance with accepted academic practice. No use, distribution or reproduction is permitted which does not comply with these terms.



# Impact of Freezing Delay Time on Tissue Samples for Metabolomic Studies

Tonje H. Haukaas<sup>1,2†</sup>, Siver A. Moestue<sup>1,3†</sup>, Riyas Vettukattil<sup>1</sup>, Beathe Sitter<sup>4</sup>, Santosh Lamichhane<sup>1,5</sup>, Remedios Segura<sup>6</sup>, Guro F. Giskeodegård<sup>1,3</sup> and Tone F. Bathen<sup>1,2\*</sup>

<sup>1</sup> Department of Circulation and Medical Imaging, Norwegian University of Science and Technology, Trondheim, Norway

<sup>2</sup> Faculty of Medicine, K. G. Jebsen Center for Breast Cancer Research, Institute of Clinical Medicine, University of Oslo, Oslo, Norway, <sup>3</sup> St. Olavs Hospital, Trondheim University Hospital, Trondheim, Norway, <sup>4</sup> Department of Health Science, Faculty of Health and Social Science, Sør-Trøndelag University College, Trondheim, Norway, <sup>5</sup> Department of Food Science, Faculty of Science and Technology, Aarhus University, Årslev, Denmark, <sup>6</sup> Metabolomic and Molecular Image Laboratory, Health Research Institute INCLIVA, Valencia, Spain

## OPEN ACCESS

### Edited by:

Franca Podo,  
Istituto Superiore di Sanità, Italy

### Reviewed by:

Egidio Iorio,  
Istituto Superiore di Sanità, Italy  
Claudio Luchinat,  
University of Florence, Italy

### \*Correspondence:

Tone F. Bathen  
tone.f.bathen@ntnu.no

<sup>†</sup>Shared first authorship;  
Tonje H. Haukaas and  
Siver A. Moestue contributed equally  
to this work.

### Specialty section:

This article was submitted to  
Cancer Imaging and Diagnosis,  
a section of the journal  
Frontiers in Oncology

Received: 18 November 2015

Accepted: 16 January 2016

Published: 28 January 2016

### Citation:

Haukaas TH, Moestue SA,  
Vettukattil R, Sitter B, Lamichhane S,  
Segura R, Giskeodegård GF and  
Bathen TF (2016) Impact of Freezing  
Delay Time on Tissue Samples for  
Metabolomic Studies.  
*Front. Oncol.* 6:17.  
doi: 10.3389/fonc.2016.00017

**Introduction:** Metabolic profiling of intact tumor tissue by high-resolution magic angle spinning (HR MAS) MR spectroscopy (MRS) provides important biological information possibly useful for clinical diagnosis and development of novel treatment strategies. However, generation of high-quality data requires that sample handling from surgical resection until analysis is performed using systematically validated procedures. In this study, we investigated the effect of postsurgical freezing delay time on global metabolic profiles and stability of individual metabolites in intact tumor tissue.

**Materials and methods:** Tumor tissue samples collected from two patient-derived breast cancer xenograft models ( $n = 3$  for each model) were divided into pieces that were snap-frozen in liquid nitrogen at 0, 15, 30, 60, 90, and 120 min after surgical removal. In addition, one sample was analyzed immediately, representing the metabolic profile of fresh tissue exposed neither to liquid nitrogen nor to room temperature. We also evaluated the metabolic effect of prolonged spinning during the HR MAS experiments in biopsies from breast cancer patients ( $n = 14$ ). All samples were analyzed by proton HR MAS MRS on a Bruker Avance DRX600 spectrometer, and changes in metabolic profiles were evaluated using multivariate analysis and linear mixed modeling.

**Results:** Multivariate analysis showed that the metabolic differences between the two breast cancer models were more prominent than variation caused by freezing delay time. No significant changes in levels of individual metabolites were observed in samples frozen within 30 min of resection. After this time point, levels of choline increased, whereas ascorbate, creatine, and glutathione (GS) levels decreased. Freezing had a significant effect on several metabolites but is an essential procedure for research and biobank purposes. Furthermore, four metabolites (glucose, glycine, glycerophosphocholine, and choline) were affected by prolonged HR MAS experiment time possibly caused by physical release of metabolites caused by spinning or due to structural degradation processes.

**Conclusion:** The MR metabolic profiles of tumor samples are reproducible and robust to variation in postsurgical freezing delay up to 30 min.

**Keywords:** cancer, freezing time delay, HR MAS, metabolic profile, MR spectroscopy, metabolomics, snap-freezing, degradation

## INTRODUCTION

The field of metabolomics has the potential to fill important gaps within the knowledge of cancer biology (1). Within this field, molecular pathways and interactions are studied through the expression of small molecular compounds called metabolites. These compounds are intermediates or end products of ongoing biochemical processes, and the overall metabolic profile represents a unique fingerprint of the cellular state at a specific time point. Metabolites constitute the final level in the -omics cascade, downstream to genomics, transcriptomics, and proteomics, reflecting the combined effect of all the upstream molecular levels (2). However, the metabolic snapshot obtained from a tumor tissue specimen depends on additional factors, such as the tumor microenvironment and the polyclonality frequently observed in cancer, which introduces additional complexity for the interpretation of the metabolic information. Nevertheless, metabolic profiling of intact fresh frozen tissue is gaining popularity in clinical research, as it potentially can identify novel prognostic or predictive metabolic biomarkers or explore the abnormal biochemical activity aiming to identify novel therapeutic approaches.

Metabolomic studies using high-resolution magic angle spinning MR spectroscopy (HR MAS MRS) enables investigation of tumor tissue with minimal sample preparation, thus limiting loss of information through tissue extraction and maintaining high reproducibility (3). HR MAS MRS is also a non-destructive technique (4) shown to retain histopathological characteristics (5) and high RNA quality (6) of analyzed tissue. This technology has been used to discriminate between tumor and normal tissues in several cancers (7), but is increasingly used to explore the role of metabolomics in patient stratification for personalized oncology (8–10). In these studies, biobanks have been established after collecting tumor tissue from large patient cohorts and the association between metabolic characteristics and disease outcome has been investigated. The quality of data from such studies requires a high degree of analytical accuracy and precision, as well as highly standardized and validated protocols for sample collection, storage, and handling prior to analysis.

One of the critical points during sample collection, especially in a clinical setting, is the time period from blood supply cutoff during surgical resection until the sample is frozen for storage (freezing delay time). This interval may vary depending on the difficulty of the surgical procedure and the required tissue processing procedures, while cellular enzymatic and chemical reactions will take place and potentially cause alterations in the tissue metabolomic profile. Therefore, it is important to assess the susceptibility of these profiles to systematic variability resulting from sample handling and analysis. The main objective of this study was to investigate the metabolic effects of freezing delay time, aiming to validate the sample collection protocols normally used in biobanking for MR metabolomics studies. To minimize the impact of inter- and intratumor variability, tumor tissue was obtained from two well-characterized breast cancer xenograft models (11, 12). Furthermore, we describe the metabolic effects of snap-freezing tumor samples and the degradation pattern caused by prolonged HR MAS MRS acquisitions using human

breast cancer samples. Finally, sample collection and handling procedures that ensure optimal data quality in metabolomic studies of cancer tissue are suggested.

## MATERIALS AND METHODS

### Tissue Samples

#### Animal Model

The two orthotopic xenograft models MAS98.12 and MAS98.06 were established by direct transplantation of biopsy tissue from primary mammary carcinomas in immunodeficient SCID mice and thereafter passaged as previously described (11). These models have been characterized by unsupervised hierarchical clustering of intrinsic genes (13, 14) to represent basal-like (poor prognosis) and luminal-like (better prognosis) breast cancer phenotype respectively (11), and they also have distinct metabolic profiles (12, 15). Mice carrying xenograft tumors [basal-like ( $n = 3$ ) and luminal-like ( $n = 3$ )] were sacrificed by cervical dislocation and tumor tissue was harvested and snap-frozen in liquid nitrogen according to the protocol below. All procedures and experiments involving animals were approved by the National Animal Research Authority and carried out according to the European Convention for the Protection of Vertebrates used for Scientific Purposes.

#### Patient Material

Breast cancer tissue samples from 14 female patients undergoing surgery at St. Olav's Hospital (Trondheim, Norway) and Molde Hospital (Molde, Norway) were included in the study. Patients were chosen without any other prior clinical information. The biopsies were snap-frozen immediately after excision during the surgical procedure and further stored in liquid nitrogen until subsequent analyses. All patients have signed a written informed consent, and the study was approved by the Regional Ethics Committee, Central Norway.

## Experimental Design and HR MAS MRS Experiments

### Effect of Freezing Delay Time

One tumor from each mouse was divided into pieces and left at room temperature for 0, 15, 30, 60, 90, and 120 min, prior to snap-freezing in liquid nitrogen. This procedure covers both realistic and extreme freezing time delays, which could occur in tissue harvesting procedures during breast cancer surgery. In addition, one sample was analyzed immediately after excision representing the metabolic profile of the tumor tissue without exposure to liquid nitrogen or freezing. The total number of samples analyzed for this study was 42.

Before HR MAS MRS experiments, 3  $\mu$ L cold sodium formate in D<sub>2</sub>O (24.29 mM) was added to a leak-proof disposable 30- $\mu$ L insert (Bruker, Biospin GmbH, Germany) as a shimming reference. Tissue samples were cut to fit the insert (mean sample weight 9.8 mg) on a dedicated work station designed to keep the samples frozen (16) during preparation. The insert containing the frozen sample was placed in a 4-mm diameter zirconium rotor (Bruker, Biospin GmbH, Germany) and kept at  $-20^{\circ}\text{C}$  for 6–8 h before the experiments to minimize degradation.

HR MAS MRS experiments were performed on a Bruker Avance DRX600 spectrometer (Bruker, Biospin GmbH, Germany) equipped with a  $^1\text{H}/^{13}\text{C}$  MAS probe with gradient aligned with the magic angle (Bruker, Biospin GmbH, Germany). Samples were spun at 5000 Hz and experiments run at 5°C. The samples were allowed 5 min temperature acclimatization before shimming and spectral acquisition.

Spin-echo spectra were recorded using a Carr–Purcell–Meiboom–Gill (cpmg) pulse sequence (cpmgpr1D; Bruker, L4 = 126).  $T_2$  filtering was obtained using a delay of 0.6 ms between each 180° pulse to suppress macromolecules and lipid signals and enhance signal from small molecules. This resulted in a total echo time (TE) of 77 ms. The total number of scans (NS) were 64 over a spectral width of 20 ppm (−5 to 15 ppm) with an acquisition time of 3.07 s.

### Degradation during Prolonged HR MAS MRS Analysis

Frozen human breast cancer tissue samples were cut to fit a leak-proof 30- $\mu\text{L}$  disposable insert (mean sample weight: 8.8 mg) added 3  $\mu\text{L}$  of phosphate-buffered saline (PBS) based on D<sub>2</sub>O with trimethylsilyl propionate (TSP, 1 mM) and sodium formate (1 mM). The insert was placed in a 4-mm diameter zirconium rotor (Bruker, Biospin GmbH, Germany). Spin-echo experiments (cpmgpr1D; Bruker, L4 = 136) were run with 2 ms delay between 180° pulses, TE of 273.5 ms, spectral width of 20 ppm (−5 to 15 ppm) and NS of 256 scans (17). To evaluate the effect of prolonged HR MAS MRS experimental time, data acquisition was repeated after 1.5 h. The sample was kept spinning (5000 Hz) within the magnet at 5°C in this time interval.

### Data Preprocessing and Statistical Analysis

The FIDs were multiplied by a 0.30 Hz exponential function and Fourier transformed into 64k real points. Phase correction was performed automatically for each spectrum using TopSpin 3.1 (Bruker). Further preprocessing of the HR MAS spectra was performed in Matlab R2013b (The Mathworks, Inc., USA). Due to unavailability of a stable internal reference, human spectra were referenced to the TSP peak (0 ppm) while xenograft spectra were referenced to formate (8.46 ppm). Baseline correction was achieved by setting the minimum value of each spectrum to 0 and subtracting the lowest value. Peak alignment was performed using icoshift (18). The spectral region of interest in the human samples (2.89–4.73 ppm), which excludes the main lipid peaks, was normalized to equal total mean area, while the total spectral region (0.62–4.70 ppm) was normalized to sample weight in the xenograft spectra. In human tissue, lipid signals mainly originate from adipose tissue, and the lipid peaks may be very dominant in samples with low tumor content. Thus, the normalization accounts for differences in sample size and tumor cell content, the latter not necessary in xenograft samples with homogenous distribution of cancer cells.

To find underlying structure and main differences in the dataset, the unsupervised multivariate method principal component analysis (PCA) was used. PCA is a powerful method to decrease

the complexity of collinear multivariate data, such as MR spectra, into a few principal components (PCs). PCA was performed (using PLS\_Toolbox 7.5.2, Matlab, Eigenvector Research, Inc., Wenatchee, WA, USA) on xenograft spectra and human breast cancer spectra to explore the metabolic variation within samples exposed to increasing delays in postsurgical freezing and prolonged experiment time respectively.

For both cohorts, metabolite assignment was based on previous published data from HR MAS MRS analyses of breast tumors (19). Furthermore, metabolite levels were determined by integrating fixed spectral regions (performed in Matlab R2013b) corresponding to the metabolites of interest and used for univariate analysis. For metabolites with baseline strongly affected by closely resonating lipids, a linear baseline ranging from the first to the last point of the integral area was used.

Linear mixed models (LMM), an extension of linear regression, can be used to model data where several measurements from the same object are available. LMM accounts for both fixed and random effects in the modeling of the metabolite levels. Fixed effects are those that are of particular interest, e.g., effect of freezing delay time, while random effects are often not of interest but cannot be adjusted for prior to the modeling, e.g., effects originating from between subjects variation. In the current study, freezing delay time as well as type of xenograft model (basal-like or luminal-like) were set as fixed effects (continuous and categorical variable respectively), while xenograft subject was set as an random effect (without interaction term). The modeling was performed in R (20) using the “nlme” package (21).

Paired *t*-test was used to find time points where the metabolic levels had changed compared to baseline and to evaluate the effect of snap-freezing. Wilcoxon signed-rank test were performed to test the effect of prolonged experiment time on metabolite levels in human tumor tissue.

To adjust for the multiple metabolites tested, calculated *p* values were corrected for using The Benjamini Hochberg false discovery rate (FDR) in Matlab R2013b (The Mathworks, Inc., USA), and the differences were considered statistically significant for adjusted *p*-values  $\leq 0.05$ .

### Histopathology and Nile Red Staining

Histopathological analysis was performed in order to evaluate the presence of viable tumor tissue and mobile lipid droplets in each individual xenograft sample. After HR MAS MRS analysis, samples were immediately frozen in liquid nitrogen. About 4 and 10  $\mu\text{m}$  frozen sections were stained with hematoxylin–eosin–saffron (HES) and Nile Red as described in Ref. (22), respectively.

## RESULTS

### Effect of Freezing Delay Time in Xenograft Tumor Tissue

To examine the metabolic effect of delayed freezing, samples from the same xenograft tumor were left in room temperature for 0, 15, 30, 60, 90, and 120 min prior to freezing. A PCA score plot of the spectra from all 42 samples revealed a clear separation of

basal-like and luminal-like xenograft model samples (**Figure 1A**). The variability between samples was predominantly attributed to the lipid content (PC1), whereas the levels of taurine, glycerocephosphocholine, and phosphocholine (PC2) contributed to discrimination between the two xenograft models (**Figure 1B**).

A trajectory PCA score plot suggests that freezing delay time had no systematic effect on metabolic profiles (**Figure 1C**).

## The Impact of Freezing Delay Time on Individual Metabolites in Xenograft Samples

The LMM result for glucose was excluded due to non-normally distributed residuals. The percentage change in levels of 15 metabolites measured by HR MAS MRS in samples subject to increasing delays before freezing ( $n = 36$ ) are shown in **Table 1**. After adjusting  $p$ -values for multiple testing, LMM revealed that three metabolites were significantly affected by type of xenograft model (basal-like and luminal-like) and four metabolites were significantly affected by delayed freezing (**Table 2**).

**Figure 2** illustrates the change in average level of ascorbate, choline, creatine, and glutathione (GS) with increasing freezing delay time. The levels of ascorbate, creatine, and GS decreased with time. Both ascorbate and creatine levels decreased with approximately 30% within the 120 min time frame, while levels of GS were approximately 40% lower. The choline levels increased with time, reaching a level approximately 110% higher than baseline at freezing delay time of 120 min.

Ascorbate, choline, and creatine levels were significantly different from baseline sample (frozen immediately) after 60 min freezing delay time while the same was observed for GS levels after 90 min (**Figure 2**).

## Metabolic Effect of Freezing

Immediately snap-frozen samples (0 min,  $n = 6$ ) were compared to samples analyzed directly after excision (not frozen, 0 min,  $n = 6$ ). A clear effect of freezing compared to unfrozen tissue was seen for 12 of 16 metabolites (**Figure 3**). Increased levels were observed for all of these metabolites after snap-freezing.

## Histopathology

Visual inspection of HES-stained sections of xenograft samples analyzed by HR MAS MRS confirmed that the samples predominantly consisted of viable tumor tissue without significant necrosis or fibrosis. No adipose tissue or normal mammary gland tissue was observed. Due to the observed heterogeneity in lipid content of samples obtained from the same xenograft, we examined whether the lipids detected were located in adipose cells lining the tumor or in lipid droplets within the tumor. Visual inspection of the Nile Red stained histological sections showed good correlation between lipid signal intensity in spectral data and the amount of lipid detected by Nile Red staining (**Figures S1** and **S2** in Supplementary Material). The lipids were also observed to be located inside tumors and were therefore considered to represent mobile lipids in the cancer cells and not adipose tissue adjacent to the tumors. No systematic difference in lipid content

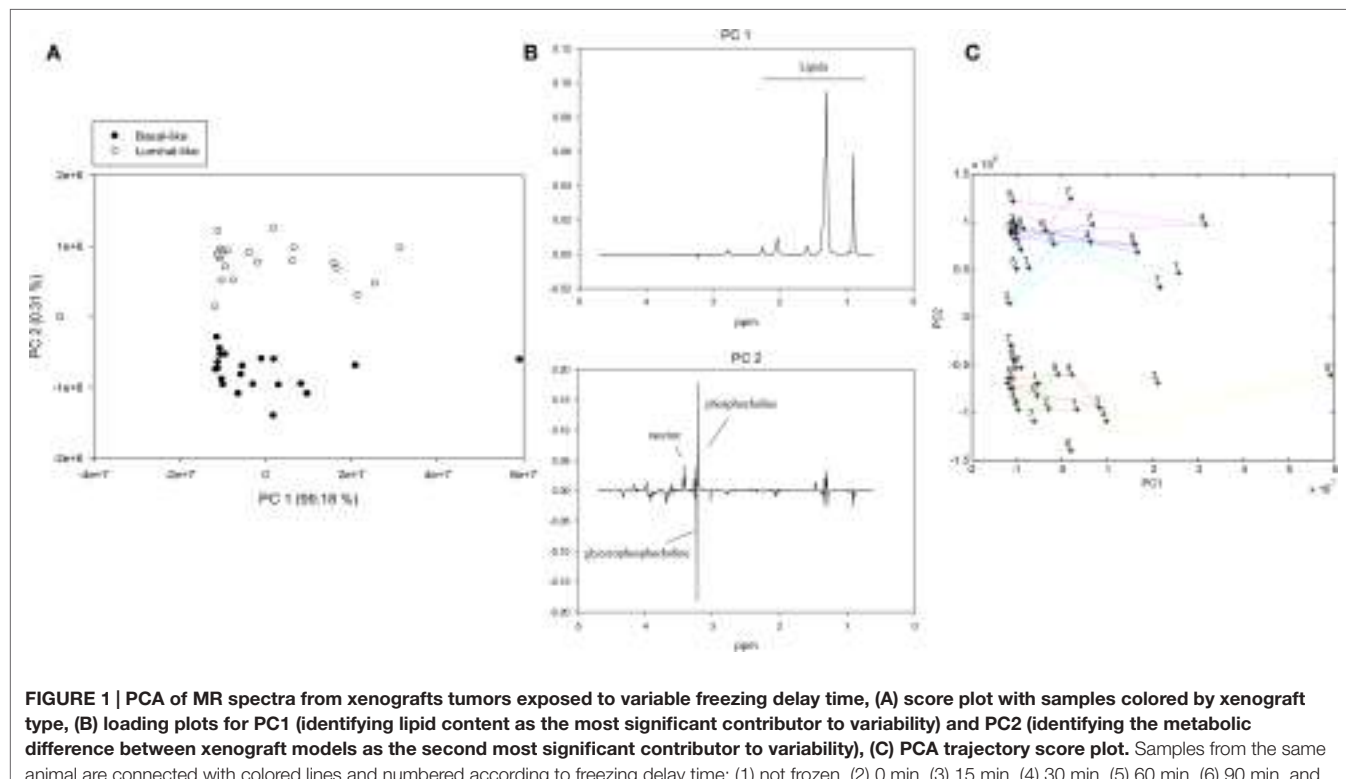


**FIGURE 1 |** PCA of MR spectra from xenograft tumors exposed to variable freezing delay time, **(A)** score plot with samples colored by xenograft type, **(B)** loading plots for PC1 (identifying lipid content as the most significant contributor to variability) and PC2 (identifying the metabolic difference between xenograft models as the second most significant contributor to variability), **(C)** PCA trajectory score plot. Samples from the same animal are connected with colored lines and numbered according to freezing delay time: (1) not frozen, (2) 0 min, (3) 15 min, (4) 30 min, (5) 60 min, (6) 90 min, and (7) 120 min.

**TABLE 1 | Metabolic effect of freezing delay time.**

Metabolite	ppm	15 min	30 min	60 min	90 min	120 min
Glucose	4.65	22 ± 107%	-8 ± 19%	31 ± 41%	6 ± 50%	26 ± 71%
Ascorbate	4.53	-18 ± 37%	-15 ± 20%	-25 ± 17%	-31 ± 22%	-31 ± 24%
Lactate	4.13	4 ± 44%	10 ± 24%	12 ± 29%	16 ± 27%	19 ± 45%
Tyrosine	3.99	-8 ± 32%	-10 ± 21%	-13 ± 19%	-15 ± 22%	-17 ± 29%
Glycine	3.55	-7 ± 45%	-4 ± 22%	-5 ± 25%	1 ± 45%	6 ± 62%
Myoinositol	3.53	12 ± 49%	11 ± 19%	26 ± 28%	26 ± 27%	43 ± 64%
Taurine	3.42	-7 ± 38%	-7 ± 15%	-8 ± 16%	-8 ± 20%	-4 ± 31%
Glycerophosphocholine	3.23	-9 ± 22%	-10 ± 18%	-3 ± 25%	0 ± 34%	28 ± 40%
Phosphocholine	3.22	-19 ± 24%	-7 ± 16%	1 ± 32%	7 ± 25%	34 ± 63%
Choline	3.21	6 ± 72%	20 ± 31%	56 ± 44%	62 ± 49%	111 ± 111%
Creatine	3.03	-16 ± 31%	-19 ± 18%	-28 ± 22%	-25 ± 22%	-29 ± 26%
Glutathione (GS)	2.55	-18 ± 32%	-19 ± 15%	-24 ± 25%	-35 ± 18%	-37 ± 26%
Succinate	2.41	-5 ± 35%	-13 ± 22%	-2 ± 33%	-13 ± 29%	-15 ± 38%
Glutamine	2.44	5 ± 49%	-1 ± 40%	28 ± 55%	-1 ± 22%	7 ± 54%
Glutamate	2.37	-10 ± 35%	-11 ± 17%	-20 ± 17%	-16 ± 25%	-14 ± 37%
Alanine	1.49	-7 ± 42%	9 ± 40%	2 ± 42%	17 ± 72%	23 ± 108%

Percentage (average ± SD) increase or decrease of metabolite level in samples exposed to freezing delay time compared to samples frozen immediately after tumor collection.

**TABLE 2 | LMM-results reporting the effect of xenograft model and freezing delay time on levels of 15 metabolites.**

Metabolite	Xenograft model			Freezing time delay		
	Adj. p-value	Est. effect	SD	Adj. p-value	Est. effect	SD
Ascorbate	0.628	1.6	2.2	<b>0.037*</b>	-1.2	0.4
Lactate	0.849	-2.5	12.2	0.281	4.5	3.0
Tyrosine	0.059	128.3	33.4	0.343	-7.1	5.6
Glycine	0.649	-9.4	16.9	0.838	1.2	2.8
Myoinositol	0.373	-4.8	3.9	0.072	2.7	1.1
Taurine	<b>0.025*</b>	240.9	37.9	0.838	-2.2	7.0
Glycerophosphocholine	<b>0.017*</b>	-477.3	56.6	0.255	23.9	14.6
Phosphocholine	<b>0.040*</b>	470.3	94.3	0.255	22.7	13.8
Choline	0.068	43.5	12.5	<b>0.002**</b>	16.2	3.7
Creatine	0.059	-41.6	10.3	<b>0.037*</b>	-8.4	3.0
Glutathione (GS)	0.649	-4.1	7.3	<b>0.005**</b>	-6.0	1.6
Succinate	0.112	8.7	3.1	0.301	-1.0	0.7
Glutamine	0.194	12.3	6.2	0.838	0.3	0.9
Glutamate	0.322	-20.9	14.4	0.348	-3.7	3.1
Alanine	0.194	17.1	8.4	0.838	0.4	1.6

The estimated effect (Est. effect) reports each fixed factors (i.e., xenograft model or freezing time delay) influence on metabolite levels. Adjusted p-values in bold indicates that the level is significantly different from the sample frozen after 0 min (\*adjusted  $p < 0.05$ , \*\*adjusted  $p < 0.01$ ).

due to delayed freezing time was observed. While Figure S1 in Supplementary Material shows a pattern of decreasing Nile Red signal with increased delay before freezing, Figure S2 in Supplementary Material shows an example where the same pattern was not observed.

## Degradation during Prolonged HR MAS Analysis

Repeated HR MAS MRS analysis of 14 human breast cancer samples was performed with 1.5 h interval to observe the metabolic effect of prolonged time in the magnet. The levels of glucose, glycine, glycerophosphocholine, and choline were found to significantly change from the first to the second acquisition (Table 3). While glucose, glycine, and choline increased, levels of glycerophosphocholine decreased with prolonged experiment time. A PCA score

plot of all spectra showed that the metabolic variation between samples was higher than variation in spectra obtained from the same sample (Figure S3 in Supplementary Material).

## DISCUSSION

In this study, we evaluated the metabolic effect of freezing delay time, snap-freezing in liquid nitrogen and prolonged experimental time using HR MAS MRS. The results show that levels of HR MAS MRS visible metabolites in breast tumors are not subject to significant degradation if snap-frozen within 30 min after surgical excision.

Principal component analysis showed that differences in lipid content explained most of the variance between the samples from the two different breast cancer xenograft models. This was

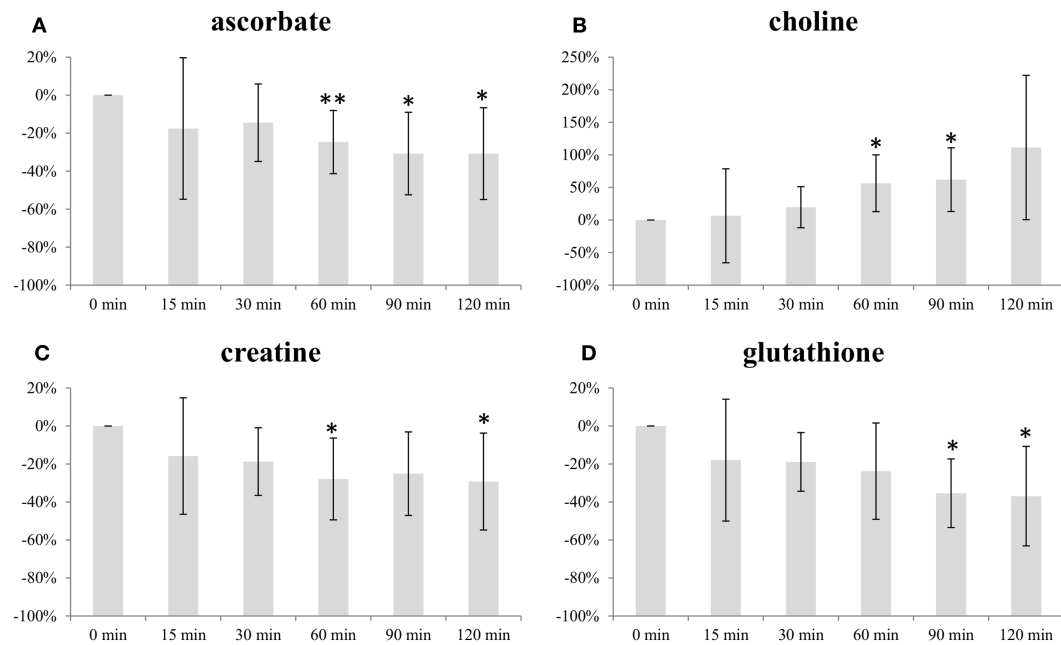


**FIGURE 2 | Impact of freezing delay time on level of (A) ascorbate, (B) choline, (C) creatine, and (D) glutathione.** Metabolite integrals from samples subject to 15, 30, 60, 90, and 120 min freezing delay time compared with samples frozen immediately (0 min). \* and \*\* indicates that the level is significantly different from the sample frozen after 0 min (\* $p < 0.05$ , \*\* $p < 0.01$ ).

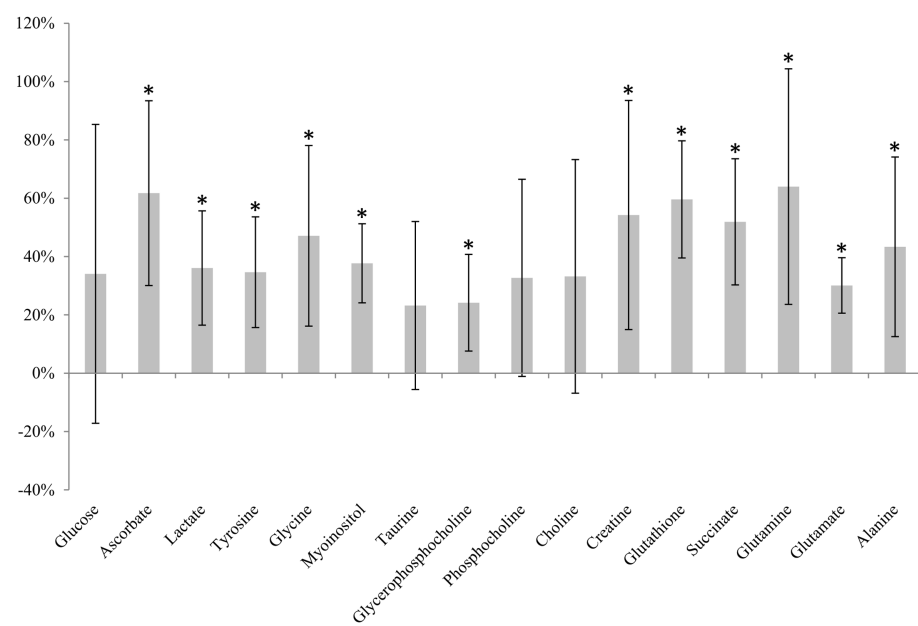


**FIGURE 3 | Metabolic effect of snap-freezing.** Percentage change in metabolite levels measured in frozen samples relative to samples not frozen prior to HR MAS MRS analysis. \* indicates that the level is significantly different from the sample not frozen (\*adjusted  $p < 0.05$ ).

further examined by histopathological staining of frozen sections with Nile Red, which showed no correlation between lipid content and freezing delay time. Hence, the variability explained by lipid content most likely reflects tumor heterogeneity rather

than the sample handling conditions. Furthermore, PCA clearly discriminated between samples from the two xenograft models (i.e., basal-like or luminal-like breast cancer subtype). Basal-like xenografts had higher levels of glycerophosphocholine, while

**TABLE 3 | Metabolic effect of prolonged experiment time.**

Metabolite	ppm	1.5 h	Adj. p-value
Glucose	4.65	21 ± 20%	<b>0.006**</b>
Ascorbate	4.53	-4 ± 6%	0.078
Lactate	4.15	0 ± 7%	0.903
Tyrosine	3.98	3 ± 6%	0.08
Glycine	3.56	8 ± 7%	<b>0.006**</b>
Myoinositol	3.54	7 ± 11%	0.08
Taurine	3.42	0 ± 5%	0.903
Glycerophosphocholine	3.23	-15 ± 12%	<b>0.001**</b>
Phosphocholine	3.22	-4 ± 6%	0.08
Choline	3.21	11 ± 13%	<b>0.011*</b>
Creatine	3.03	0 ± 6%	0.903

Percentages (average ± SD) were calculated relative to the metabolite levels (integrals) from the initial experiment. Adjusted p-values in bold indicates that the level is significantly different from the sample frozen after 0 min (\*adjusted  $p < 0.05$ , \*\*adjusted  $p < 0.01$ ).

luminal-like xenografts had higher levels of phosphocholine and taurine, in accordance with previously published data from these xenograft models (15). The same metabolic differences between the xenograft models were observed in LMM.

Discrimination between the two xenograft models based on overall metabolic profile did not depend on freezing delay time. Furthermore, no significant changes in individual metabolite levels were observed at 30 min past tumor excision. At 60 min, levels of three metabolites had significantly changed from baseline measurements. Thus, samples should be frozen within 30 min of resection, which in general should be sufficient when obtaining tissue biopsies during surgical procedures. Ascorbate, choline, creatine, and GS were the only metabolites exhibiting significant changes within the time frame (0–120 min) used in the current study. For the majority of metabolites, no systematic dependency on freezing time delay was observed, suggesting that intratumor heterogeneity is the predominant source of variability.

Ascorbate, also known as vitamin C, and GS are important antioxidants in animal cells that, together with other antioxidants, are responsible for eliminating reactive oxygen species (ROS) from oxidative stress (23, 24). As a consequence of high ROS levels in cancer cells, GS levels are often elevated compared to normal tissue (25). GS has also been reported to be increased in estrogen receptor (ER) negative tumors compared to ER-positive (26). ROS levels can increase as a consequence of ischemia, potentially leading to oxidative damage. It is therefore plausible that the decreased levels of GS and ascorbate reflect oxidative stressed caused by prolonged ischemia. Ascorbate levels obtained from samples frozen 60, 90, and 120 min after excision were significantly lower than the levels from samples frozen immediately. The same was observed for GS levels at 90 and 120 min of freezing delay. Consequently, biological interpretation of the levels of these antioxidants should only be considered if the experimental design of the study includes a controlled freezing delay time of <30 min.

The levels of choline increased with increasing freezing delay time. Although not significant, a similar trend was observed for the choline-containing metabolites phosphocholine and glycerophosphocholine, suggesting that ischemia affects choline metabolism. Studying the effect of hypoxia in human

MDA-MB-231 breast cancer cell and tumors, Jiang et al. detected higher concentrations of total choline-containing metabolites (tCho; composed of phosphocholine, glycerophosphocholine, and free choline), mainly contributed by phosphocholine, in hypoxic regions (27). Altered choline metabolism is considered an emerging hallmark in malignant transformation (28). A major component of mammalian cell membranes, phosphatidylcholine (PtdCho), is synthesized from choline, thus making choline and choline-containing intermediates essential for the increased proliferation observed in tumor cells. Several *ex vivo* breast cancer studies using HR MAS MRS have detected increased concentrations of choline, phosphocholine, and glycerophosphocholine in tumor tissue compared to non-involved breast tissue (19, 29, 30). Differences in tCho have been found to have predictive value for the 5-year survival of breast cancer patients receiving neoadjuvant chemotherapy (31) and higher choline concentrations have been found in core needle biopsies from patients that are ER- and/or PgR-negative compared to ER- and/or PgR-positive patients (10). Delays in freezing time up to 30 min had no significant impact on choline levels. While choline levels at 60 and 90 min delay were significantly increased, this was not observed at 120 min ( $p = 0.065$ ), probably due to variability within these last measurements. However, because of the biological relevance of choline metabolism in cancer, this trend of increasing levels with freezing delay time emphasize the importance of reporting and controlling sample handling to limit possible effects.

Levels of creatine significantly decreased as a result of prolonged time before freezing, where 60 min was found to be the first time point significantly different from samples frozen directly after exiting. Creatine is involved in energy storage through formation of phosphocreatine and thus functions as a carrier of energy within cells. Decreasing levels of creatine (or phosphocreatine) could be suggestive of energy depletion caused by ischemia. Several studies use creatine for calculation of metabolic ratios to allow for comparable quantities between samples (10, 32–34) and in studies of breast cancer tissue, higher level of this metabolite have been correlated to ER-positive (35) and PgR-positive tumors (15). As the tendency of decreasing levels is seen from the initial time point, it is important to keep the time before freezing minimal to allow the usage of ratios involving creatine.

Rapid metabolic phenotyping in operating theaters of unfrozen tissue has been proposed to facilitate real-time diagnostics and further aid decision making during surgery (36). To evaluate the metabolic effect of snap-freezing, tumor tissue was analyzed by HR MAS MRS without any exposure to liquid nitrogen and compared to tissue from the same xenografts that were immediately frozen after excision. Freezing was found to significantly increase the level of 12 metabolites. In previous studies, the freezing of rat kidney and liver tissue has reportedly led to increased amounts of amino acids (37, 38) and decreased contents of choline, glycerophosphocholine, glucose, myoinositol, trimethylamine N-oxide (TMAO), and taurine (38) using HR MAS MRS. The increased levels of multiple metabolites observed in the current study might be caused by intracellular lysis releasing metabolites. Metabolites bound to cellular molecules or compartments are more restricted and thus less MR-visible. If these metabolites are released as a consequence of freezing, HR MAS MRS will detect higher levels

than in unfrozen tissue as found here. The findings underpin that studies of fresh and frozen tissue are not directly comparable. Although the effect of freezing was significant for the majority of metabolites, we believe that analyzing fresh tissue samples is neither feasible nor optimal in the current clinical and research setting. Care must therefore be taken not to compare metabolic information obtained in unfrozen samples with data from frozen biobank tissue.

We also examined the effect on the metabolic profile of prolonged HR MAS MRS analysis. After the first acquisition, the sample was kept spinning inside the magnet and reanalyzed after 1.5 h. The level of four metabolites was found to differ significantly from the initial acquisition. Glucose, glycine, and choline were found to increase with time, while glycerophosphocholine decreased. Similar effects on glycine, choline, and glycerophosphocholine levels have been observed in lung cancer tissue (39) and in brain tumor tissue (40) supporting the current findings. As Rocha et al. describe, the changes might be caused by spinning effects causing release of bound metabolites or due to ongoing metabolic activity (39). Importantly, these metabolic effects should be considered for quantitative two-dimensional HR MAS MRS studies where long acquisition time is required.

In conclusion, this study confirms that HR MAS MRS metabolic profiles are robust to metabolic changes due to delayed freezing within a timeframe of 30 min. This allows biological interpretation of metabolic profiles, including metabolites involved in protection against ROS formation/oxidative stress, such as GS and ascorbate, as well as evaluation of the levels of creatine and choline-containing metabolites. Within the 30 min freezing delay time window, the effect of structural or biochemical degradation on metabolic profiles is insignificant. A clear effect of freezing was observed for most of the detected metabolites. However, this step in sample handling is considered essential for biobanking and research purposes. The study also identified moderate metabolic consequences of prolonged HR MAS experiment time, and thus, the protocol should be designed to keep experiment time to a minimum.

## REFERENCES

- Patel S, Ahmed S. Emerging field of metabolomics: big promise for cancer biomarker identification and drug discovery. *J Pharm Biomed Anal* (2015) **107**:63–74. doi:10.1016/j.jpba.2014.12.020
- Zhang A-H, Sun H, Qiu S, Wang X. Metabolomics in noninvasive breast cancer. *Clin Chim Acta* (2013) **424**:3–7. doi:10.1016/j.cca.2013.05.003
- Pan Z, Raftery D. Comparing and combining NMR spectroscopy and mass spectrometry in metabolomics. *Anal Bioanal Chem* (2007) **387**(2):525–7. doi:10.1007/s00216-006-0687-8
- Bathen TF, Sitter B, Sjøbakk TE, Tessem M-B, Gribbestad IS. Magnetic resonance metabolomics of intact tissue: a biotechnological tool in cancer diagnostics and treatment evaluation. *Cancer Res* (2010) **70**(17):6692–6. doi:10.1158/0008-5472.CAN-10-0437
- Bathen T, Geurts B, Sitter B, Fjøsne H, Lundgren S, Buydens L, et al. Feasibility of MR metabolomics for immediate analysis of resection margins during breast cancer surgery. *PLoS One* (2013) **8**(4):e61578. doi:10.1371/journal.pone.0061578
- Bertilsson H, Tessem M-B, Flatberg A, Viset T, Gribbestad I, Angelsen A, et al. Changes in gene transcription underlying the aberrant citrate and choline metabolism in human prostate cancer samples. *Clin Cancer Res* (2012) **18**(12):3261–9. doi:10.1158/1078-0432.CCR-11-2929

## AUTHOR CONTRIBUTIONS

Author contributions included: study design (TH, SM, BS, and TB), data acquisition (SM, TH, and SL), data analysis (TH, SM, RV, SL, and RS), data interpretation (TH, SM, GG, and TB), and drafting the manuscript (TH, SM, and TB). All authors contributed in revising the manuscript.

## ACKNOWLEDGMENTS

The HR MAS MRS analysis was performed at the MR Core Facility, Norwegian University of Science and Technology (NTNU). MR core facility is funded by the Faculty of Medicine at NTNU and Central Norway Regional Health Authority. The staining of histology sections was provided by the *Cellular and Molecular Imaging* Core Facility (CMIC), NTNU. CMIC is funded by the Faculty of Medicine at NTNU and Central Norway Regional Health Authority.

## FUNDING

This work was funded by K.G. Jebsen Center for Breast Cancer Research, Norwegian Cancer Society grant 2209215-2011, The Research Council of Norway grant number FRIMED-221879 and 239940/F20, the Financial Statement Grants SAF2011-23029 and SAF2014-52875R from Ministerio de Economía y Competitividad of Spain, the Liaison Committee between the Central Norway Regional Health Authority (RHA), the Norwegian University of Science and Technology grant number 46056655, and INCLIVA Foundation with funding for scholarship stay in prestigious center 2013.

## SUPPLEMENTARY MATERIAL

The Supplementary Material for this article can be found online at <http://journal.frontiersin.org/article/10.3389/fonc.2016.00017>

- Moestue S, Sitter B, Bathen T, Tessem M-B, Gribbestad I. HR MAS MR spectroscopy in metabolic characterization of cancer. *Curr Top Med Chem* (2011) **11**(1):2–26. doi:10.2174/156802611793611869
- Giskeødegård GF, Bertilsson H, Selnaes KM, Wright AJ, Bathen TF, Viset T, et al. Spermine and citrate as metabolic biomarkers for assessing prostate cancer aggressiveness. *PLoS One* (2013) **8**(4):e62375. doi:10.1371/journal.pone.0062375
- Giskeødegård G, Lundgren S, Sitter B, Fjøsne HE, Postma G, Buydens L, et al. Lactate and glycine – potential MR biomarkers of prognosis in estrogen receptor-positive breast cancers. *NMR Biomed* (2012) **25**(11):1271–9. doi:10.1002/nbm.2798
- Choi J, Baek H-M, Kim S, Kim M, Youk J, Moon H, et al. HR-MAS MR spectroscopy of breast cancer tissue obtained with core needle biopsy: correlation with prognostic factors. *PLoS One* (2012) **7**(12):e51712. doi:10.1371/journal.pone.0051712
- Bergamaschi A, Hjortland G, Triulzi T, Sørlie T, Johnsen H, Ree A, et al. Molecular profiling and characterization of luminal-like and basal-like *in vivo* breast cancer xenograft models. *Mol Oncol* (2009) **3**(5):469–82. doi:10.1016/j.molonc.2009.07.003
- Grinde MT, Moestue SA, Borgan E, Risa Ø, Engebraaten O, Gribbestad IS. <sup>13</sup>C High-resolution-magic angle spinning MRS reveals differences in glucose metabolism between two breast cancer xenograft models with different gene

- expression patterns. *NMR Biomed* (2011) **24**(10):1243–52. doi:10.1002/nbm.1683
13. Sørlie T, Perou C, Tibshirani R, Aas T, Geisler S, Johnsen H, et al. Gene expression patterns of breast carcinomas distinguish tumor subclasses with clinical implications. *Proc Natl Acad Sci U S A* (2001) **98**(19):10869–74. doi:10.1073/pnas.191367098
  14. Sørlie T, Tibshirani R, Parker J, Hastie T, Marron J, Nobel A, et al. Repeated observation of breast tumor subtypes in independent gene expression data sets. *Proc Natl Acad Sci U S A* (2003) **100**(14):8418–23. doi:10.1073/pnas.0932692100
  15. Moestue S, Borga E, Huuse E, Lindholm E, Sitter B, Børresen-Dale A-L, et al. Distinct choline metabolic profiles are associated with differences in gene expression for basal-like and luminal-like breast cancer xenograft models. *BMC Cancer* (2010) **10**(1):433. doi:10.1186/1471-2407-10-433
  16. Giskeodegård G, Cao M, Bathen T. High-resolution magic-angle-spinning NMR spectroscopy of intact tissue. In: Bjerrum, Jacob T, editor. *Metabonomics: Methods and Protocols*. New York: Springer (2015). p. 37–50.
  17. Cao M, Lamichhane S, Lundgren S, Bofin A, Fjösne H, Giskeodegård G, et al. Metabolic characterization of triple negative breast cancer. *BMC Cancer* (2014) **14**(1):941. doi:10.1186/1471-2407-14-941
  18. Savorani F, Tomasi G, Engelsen S. icoshift: a versatile tool for the rapid alignment of 1D NMR spectra. *J Magn Reson* (2010) **202**(2):190–202. doi:10.1016/j.jmr.2009.11.012
  19. Sitter B, Sonnewald U, Spraul M, Fjösne H, Gribbestad I. High-resolution magic angle spinning MRS of breast cancer tissue. *NMR Biomed* (2002) **15**(5):327–37. doi:10.1002/nbm.775
  20. R Core Team. *R: A Language and Environment for Statistical Computing*. Vienna: R Foundation for Statistical Computing (2012).
  21. Pinheiro J, Bates D, DebRoy S, Sarkar D, R Core Team. *nlme: Linear and Nonlinear Mixed Effects Models*. R Package Version 3.1-117 (2014). Available from: <http://CRAN.R-project.org/package=nlme>
  22. Opstad KS, Bell BA, Griffiths JR, Howe FA. An investigation of human brain tumour lipids by high-resolution magic angle spinning 1H MRS and histological analysis. *NMR Biomed* (2008) **21**(7):677–85. doi:10.1002/nbm.1239
  23. Gorrini C, Harris IS, Mak TW. Modulation of oxidative stress as an anticancer strategy. *Nat Rev Drug Discov* (2013) **12**(12):931–47. doi:10.1038/nrd4002
  24. Bánhegyi G, Braun L, Csala M, Puskás F, Mandl J. Ascorbate metabolism and its regulation in animals. *Free Radic Biol Med* (1997) **23**(5):793–803. doi:10.1016/S0891-5849(97)00062-2
  25. Gamcsik MP, Kasibhatla MS, Teeter SD, Colvin OM. Glutathione levels in human tumors. *Biomarkers* (2012) **17**(8):671–91. doi:10.3109/1354550X.2012.715672
  26. Tang X, Lin C-C, Spasojevic I, Iversen ES, Chi J-T, Marks JR. A joint analysis of metabolomics and genetics of breast cancer. *Breast Cancer Res* (2014) **16**(4):415. doi:10.1186/s13058-014-0415-9
  27. Jiang L, Greenwood TR, Artemov D, Raman V, Winnard PT, Heeren RM, et al. Localized hypoxia results in spatially heterogeneous metabolic signatures in breast tumor models. *Neoplasia* (2012) **14**(8):732–41. doi:10.1593/neo.12858
  28. Glunde K, Bhujwalla Z, Ronen S. Choline metabolism in malignant transformation. *Nat Rev Cancer* (2011) **11**(12):835–48. doi:10.1038/nrc3162
  29. Sitter B, Lundgren S, Bathen T, Halgunset J, Fjösne H, Gribbestad I. Comparison of HR MAS MR spectroscopic profiles of breast cancer tissue with clinical parameters. *NMR Biomed* (2006) **19**(1):30–40. doi:10.1002/nbm.992
  30. Gribbestad IS, Sitter B, Lundgren S, Krane J, Axelson D. Metabolite composition in breast tumors examined by proton nuclear magnetic resonance spectroscopy. *Anticancer Res* (1998) **19**(3A):1737–46.
  31. Cao M, Sitter B, Bathen T, Bofin A, Lønning P, Lundgren S, et al. Predicting long-term survival and treatment response in breast cancer patients receiving neoadjuvant chemotherapy by MR metabolic profiling. *NMR Biomed* (2012) **25**(2):369–78. doi:10.1002/nbm.1762
  32. Choi JS, Baek H-M, Kim S, Kim MJ, Youk JH, Moon HJ, et al. Magnetic resonance metabolic profiling of breast cancer tissue obtained with core needle biopsy for predicting pathologic response to neoadjuvant chemotherapy. *PLoS One* (2013) **8**(12):e83866. doi:10.1371/journal.pone.0083866
  33. van Asten JJ, Vettukattil R, Buckle T, Rottenberg S, van Leeuwen F, Bathen TF, et al. Increased levels of choline metabolites are an early marker of docetaxel treatment response in BRCA1-mutated mouse mammary tumors: an assessment by ex vivo proton magnetic resonance spectroscopy. *J Transl Med* (2015) **13**(1):114. doi:10.1186/s12967-015-0458-4
  34. Vettukattil R. Preprocessing of raw metabolomic data. *Methods Mol Biol* (2015) **1277**:123–36. doi:10.1007/978-1-4939-2377-9\_10
  35. Giskeodegård G, Grinde M, Sitter B, Axelson D, Lundgren S, Fjösne H, et al. Multivariate modeling and prediction of breast cancer prognostic factors using MR metabolomics. *J Proteome Res* (2010) **9**(2):972–9. doi:10.1021/pr9008783
  36. Kinross JM, Holmes E, Darzi AW, Nicholson JK. Metabolic phenotyping for monitoring surgical patients. *Lancet* (2011) **377**(9780):1817–9. doi:10.1016/S0140-6736(11)60171-2
  37. Middleton DA, Bradley DP, Connor SC, Mullins PG, Reid DG. The effect of sample freezing on proton magic-angle spinning NMR spectra of biological tissue. *Magn Reson Med* (1998) **40**(1):166–9. doi:10.1002/mrm.1910400122
  38. Waters N, Garrod S, Farrant R, Haselden J, Connor S, Connelly J, et al. High-resolution magic angle spinning 1H NMR spectroscopy of intact liver and kidney: optimization of sample preparation procedures and biochemical stability of tissue during spectral acquisition. *Anal Biochem* (2000) **282**(1):16–23. doi:10.1006/abio.2000.4574
  39. Rocha CM, Barros AS, Gil AM, Goodfellow BJ, Humpfer E, Spraul M, et al. Metabolic profiling of human lung cancer tissue by 1H high resolution magic angle spinning (HRMAS) NMR spectroscopy. *J Proteome Res* (2009) **9**(1):319–32. doi:10.1021/pr9006574
  40. Opstad KS, Bell BA, Griffiths JR, Howe FA. An assessment of the effects of sample ischaemia and spinning time on the metabolic profile of brain tumour biopsy specimens as determined by high-resolution magic angle spinning 1H NMR. *NMR Biomed* (2008) **21**(10):1138–47. doi:10.1002/nbm.1296

**Conflict of Interest Statement:** The authors declare that the research was conducted in the absence of any commercial or financial relationships that could be construed as a potential conflict of interest.

Copyright © 2016 Haukaas, Moestue, Vettukattil, Sitter, Lamichhane, Segura, Giskeodegård and Bathen. This is an open-access article distributed under the terms of the Creative Commons Attribution License (CC BY). The use, distribution or reproduction in other forums is permitted, provided the original author(s) or licensor are credited and that the original publication in this journal is cited, in accordance with accepted academic practice. No use, distribution or reproduction is permitted which does not comply with these terms.



# Metabolic Study of Breast MCF-7 Tumor Spheroids after Gamma Irradiation by $^1\text{H}$ NMR Spectroscopy and Microimaging

Alessandra Palma<sup>1,2\*</sup>, Sveva Grande<sup>1,2</sup>, Anna Maria Luciani<sup>1,2</sup>, Vladimír Mlynárik<sup>3</sup>, Laura Guidoni<sup>2</sup>, Vincenza Viti<sup>2</sup> and Antonella Rosi<sup>1,2</sup>

<sup>1</sup>Department of Technology and Health, Istituto Superiore di Sanità, Rome, Italy, <sup>2</sup>INFN Sezione di Roma, Rome, Italy,

<sup>3</sup>Department of Biomedical Imaging and Image-Guided Therapy, High-Field MR Center, Medical University of Vienna, Vienna, Austria

## OPEN ACCESS

### Edited by:

Zaver Bhujwalla,  
Johns Hopkins University  
School of Medicine, USA

### Reviewed by:

Aslam Khan,  
University of Missouri, USA  
Santosh Kumar Bharti,  
Johns Hopkins University, USA

### \*Correspondence:

Alessandra Palma  
alessandra.palma@iss.it

### Specialty section:

This article was submitted  
to Cancer Imaging and  
Diagnosis, a section of the  
journal Frontiers in Oncology

Received: 09 December 2015

Accepted: 13 April 2016

Published: 28 April 2016

### Citation:

Palma A, Grande S, Luciani AM,  
Mlynárik V, Guidoni L, Viti V and  
Rosi A (2016) Metabolic Study of  
Breast MCF-7 Tumor Spheroids after  
Gamma Irradiation by  $^1\text{H}$  NMR  
Spectroscopy and Microimaging.  
*Front. Oncol.* 6:105.  
doi: 10.3389/fonc.2016.00105

Multicellular tumor spheroids are an important model system to investigate the response of tumor cells to radio- and chemotherapy. They share more properties with the original tumor than cells cultured as 2D monolayers do, which helps distinguish the intrinsic properties of monolayer cells from those induced during cell aggregation in 3D spheroids. The paper investigates some metabolic aspects of small tumor spheroids of breast cancer and their originating MCF-7 cells, grown as monolayer, by means of high-resolution (HR)  $^1\text{H}$  NMR spectroscopy and MR microimaging before and after gamma irradiation. The spectra of spheroids were characterized by higher intensity of mobile lipids, mostly neutral lipids, and glutamine (Gln) signals with respect to their monolayer cells counterpart, mainly owing to the lower oxygen supply in spheroids. Morphological changes of small spheroids after gamma-ray irradiation, such as loss of their regular shape, were observed by MR microimaging. Lipid signal intensity increased after irradiation, as evidenced in both MR localized spectra of the single spheroid and in HR NMR spectra of spheroid suspensions. Furthermore, the intense Gln signal from spectra of irradiated spheroids remained unchanged, while the low Gln signal observed in monolayer cells increased after irradiation. Similar results were observed in cells grown in hypoxic conditions. The different behavior of Gln in 2D monolayers and in 3D spheroids supports the hypothesis that a lower oxygen supply induces both an upregulation of Gln synthetase and a downregulation of glutaminases with the consequent increase in Gln content, as already observed under hypoxic conditions. The data herein indicate that  $^1\text{H}$  NMR spectroscopy can be a useful tool for monitoring cell response to different constraints. The use of spheroid suspensions seems to be a feasible alternative to localized spectroscopy since similar effects were found after radiation treatment.

**Keywords:** MR spectroscopy, spheroids, mobile lipids, radiation, metabolism

## INTRODUCTION

Solid tumors grow in a three-dimensional (3D) spatial conformation, resulting in an heterogeneous exposure to oxygen and nutrients, which induces radio- and chemotherapy resistance with a high rate of tumor recurrence and treatment failure. Different model systems have been proposed in order to gain insight into the mechanisms that underlie induced tumor resistance (1). To investigate

the characteristics of tumors and their response to chemo–radio treatment, cells obtained from tumors are usually cultured as a monolayer, though differences with the original tumors have been observed (2). Three-dimensional *in vitro* models, such as spheroids, have been used in cancer research as an intermediate model between *in vitro* cancer cell line cultures and *in vivo* tumors. Spherical cancer models are major 3D *in vitro* models that have been mostly described over the past four decades (1). Spheroids provide an *in vitro* 3D model for studying proliferation, cell death, differentiation, and metabolism of cells in tumors and their response to different treatments (3). Spheroids above 500 µm in diameter commonly display a layer-like structure comprising a necrotic core surrounded by a viable rim, which consists of an inner layer of quiescent cells and an outer layer of proliferating cells (4). Cellular microenvironments, such as hypoxia, which has been identified as a cause of drug resistance can be modeled and created within spheroids for accurate testing of drug efficacy. In fact, the cells in the spheroid core may mimic the condition of hypoxia typical of solid tumors (5–7). Spheroids have often been proposed as a model in view of their potential use in preclinical studies (8), for example, for studying tumor stem cells, such as those growing as neurospheres from brain tumors (9) or as mammospheres from breast cancer (10). Obviously, in these systems, it is critical to distinguish between cell aggregation-related phenomena from phenomena associated to the stem nature of the cells. Spheroids have also been studied to better understand the energy metabolism of breast cancer cells, where an unexpected modulation of glycolysis and mitochondrial metabolism has been observed and used as targeted anti-mitochondrial therapy (11).

Magnetic resonance spectroscopy (MRS) and imaging (MRI) are versatile techniques to study tissues and related models, such as multicellular 3D systems (12). They may represent a useful tool to elucidate cell metabolism for they can reveal biomarker metabolites to be targeted for disease treatment without perturbing the system (11, 13). Both approaches are valid. Through high-resolution (HR) MRS, it is possible to monitor cell metabolism in systems much more complex than a single cell, whereas MRI and localized MRS allow the separate monitoring of the metabolism in the inner region and in the peripheral cell layers where DNA synthesis and mitotic activity are largely confined.

In a previous paper, <sup>1</sup>H NMR was used to reveal differences in signals of lipids and lipid metabolites during cell growth in culture. High intensity mobile lipid (ML) signals were found during the first days in culture; afterwards the same signals declined but started to increase again at late confluence in MCF-7. Spectra from suspensions of MCF-7 spheroids suggested that lipid metabolism in spheroids mimics that of confluent cultures of monolayer cells (2). In the present work, we studied small MCF-7 spheroids in suspension by HR <sup>1</sup>H NMR, and single larger MCF-7 spheroids by localized <sup>1</sup>H MR spectroscopy. Spectra were compared with those of MCF-7 cells growing as monolayer under normal and hypoxic conditions. In addition, given the well-known higher resistance of hypoxic tumor cells to radiation therapy, we investigated spheroid response to irradiation with a single acute 20 Gy dose of gamma rays to get information on the possible effects of radiation therapy on tumors. We irradiated cells and spheroids with a single high radiation dose comparable with total doses

delivered during radiation therapy in a fractionated regimen, and with single high doses used in other therapeutic modalities, such as intraoperative radiotherapy and stereotactic radiosurgery (14). In particular, NMR visible lipids and glutamine (Gln)–glutathione (GSH) metabolic pathways were examined in consideration of their role in the cell response to oxidative stress.

## MATERIALS AND METHODS

### Cells and Spheroids

MCF-7 cells were purchased from ATCC (Manassas, VA, USA) and kindly donated by Dr Stefania Meschini, Istituto Superiore di Sanità, Rome (Italy). Both monolayer cultures and spheroids were grown in RPMI 1640 medium (Hyclone, Logan, UT, USA) supplemented with 10% fetal calf serum (Hyclone, Logan, UT, USA) and 50 µg/ml gentamicin. Monolayer cells were routinely seeded in 175 cm<sup>2</sup> flasks in 50 ml medium. The medium was replaced every 72 h.

Spheroids were obtained by growing cells in a gyratory rotation system at a rate of 70 rpm, at 37°C: a suspension of MCF-7 cells was inserted in a 225-ml conical tube filled with 180 ml growth medium, at a density of 4 × 10<sup>6</sup> cells per tube and maintained during spheroids aggregation in a horizontal position.

Cells and spheroids were irradiated in culture flasks at a dose of 20 Gy with a <sup>137</sup>Cs gamma rays source [Gammacell 40 Exactor (NORDION, Canada)]. Cells were harvested and measured at 48 h after irradiation.

Hypoxia was obtained by growing cells for 24 h in 2% O<sub>2</sub>, 93% N<sub>2</sub>, and 5% CO<sub>2</sub>.

For HR spectroscopy experiments, NMR cell samples were prepared as described elsewhere (15). The pellet from monolayer cells, suspended in phosphate-buffered saline (PBS) (approximately 20 × 10<sup>6</sup> cells), was transferred into a coaxial tube system. Spheroid suspensions were centrifuged at 400 rpm for 3 min and washed in PBS, the pellet was then transferred into the coaxial tube system. In both systems, 1 mM sodium 3-(trimethyl-silyl) propionate 2,2,3,3-d (TMSP) in D<sub>2</sub>O in the external compartment was used to provide a lock signal and a frequency standard.

For microimaging and localized spectroscopy experiments, individual spheroids were selected from the spinner tube, suspended in PBS, and poured into a 1% (w/v) low-melting-point agarose solution. Agarose powder (Sigma chemicals, Type VII, low gelling temperature) was dissolved in deionized water and heated in a microwave oven, until all agarose was completely dissolved. The solution was allowed to cool to 37°C, then the spheroid suspension was added. Small amounts of the solution, containing one or more spheroids, were inserted in capillary tubes (2 mm diameter) and allowed to solidify at room temperature.

### <sup>1</sup>H NMR Spectroscopy High-Resolution <sup>1</sup>H MRS Measurements

<sup>1</sup>H MR spectra were run at 400.14 MHz on a digital Avance spectrometer (Bruker, AG, Darmstadt, Germany). One-dimensional <sup>1</sup>H NMR spectra were acquired with a 90° RF pulse, using a sweep width of 4006.4 Hz. Typically 300 scans were sufficient to obtain a good signal-to-noise ratio for intact cells.

Two-dimensional  $^1\text{H}$  correlation spectroscopy (COSY) spectra of cells were acquired using a  $90^\circ - t_1$  to  $90^\circ - t_2$  pulse sequence, by summing 16 free induction decays for each of 256 increments in  $t_1$ .

Spectra were acquired as a matrix of  $512 \times 256$  data points in the time domain. A Lorentzian–Gaussian function with LB1/4:10 Hz and GB1/4:0.1 was applied to enhance the resolution in the  $t_1$  domain before Fourier transformation. Water suppression in one- and two-dimensional  $^1\text{H}$  experiments was achieved by irradiating water signal. Measurement of cell samples lasted approximately 100 min (10 min for one dimensional and 90 min for the two-dimensional experiment) as previously reported (2). Cell viability, tested by trypan blue exclusion, was greater than 90% at the beginning of the preparation and greater than 80% at the end of the MRS measurements, in agreement with the literature for other cell samples examined with MRS under similar conditions (15). One-dimensional spectra were run before and after two-dimensional COSY to check the stability of the signals of interest. Cell spectra were run on samples containing comparable cell mass.

## Quantitative Analysis of 1D Spectra and 2D COSY Cross Peak Integration

Resonance deconvolution of one-dimensional spectra was performed using Bruker software “1D WINNMR” (Bruker, Germany). A Gauss/Lorentz ratio equal to unity for the line shape function was chosen. Nine deconvolution lines were used to obtain a good fit in the interval 0.75–1.65 ppm as previously reported (9). All peak positions were fixed, while peak intensities and line widths were fitted. No prior knowledge was imposed on  $-(\text{CH}_2)_n-$  of ML resonance. The quantitative analysis of peaks was done by measuring the fitted peak intensities. Individual integral values were normalized using the methyl group of cytosolic polypeptides at 0.94 ppm as internal reference. This signal, which is observed in cancer cells of different origin as well as in normal tissues, belongs to the methyl group of cytosolic polypeptides, and is indicative of cell mass (16).

Two-dimensional cross-peak integration was done by the Bruker “2D WINNMR” software (Bruker, Germany). The integral values were computed by summing all positive points inside the integral region. The plane baseline was evaluated and subtracted from the integrals. Besides providing spectral assignment from correlations between pairs of related resonances that overcame the problem of peak superimposition in 1D spectra, the off-diagonal elements in 2D spectra gave information on relative concentrations. Cross-peak integrals were normalized to the intensity of lysine (Lys) cross peak at 1.70–3.00 ppm. This peak is reasonably constant in a large number of cell models and tissue samples (9, 17).

## Localized $^1\text{H}$ MR Spectroscopy and Imaging

$^1\text{H}$  MR localized spectroscopy and imaging were done with a Bruker AVANCE spectrometer microimaging device, equipped with a 2 mm inner diameter resonator. Proton density weighted images were acquired using a multislice spin-echo (MSME) pulse

sequence with the following parameters: 0.5 cm field of view, 0.3 mm slice thickness, 2000 ms repetition time, 15 ms echo time, and  $256 \times 256$  acquisition matrix. Localized spectra were acquired from a volume of interest of  $0.3 \text{ mm} \times 0.3 \text{ mm} \times 0.3 \text{ mm}$  using the PRESS sequence with 15 ms echo time and 3600 acquisitions (100 min total acquisition time). Exponential line broadening was used resulting in a line width of 30 Hz.

## RESULTS

Magnetic resonance images of MCF-7 spheroids of different sizes were obtained and compared. Figure 1A depicts a representative

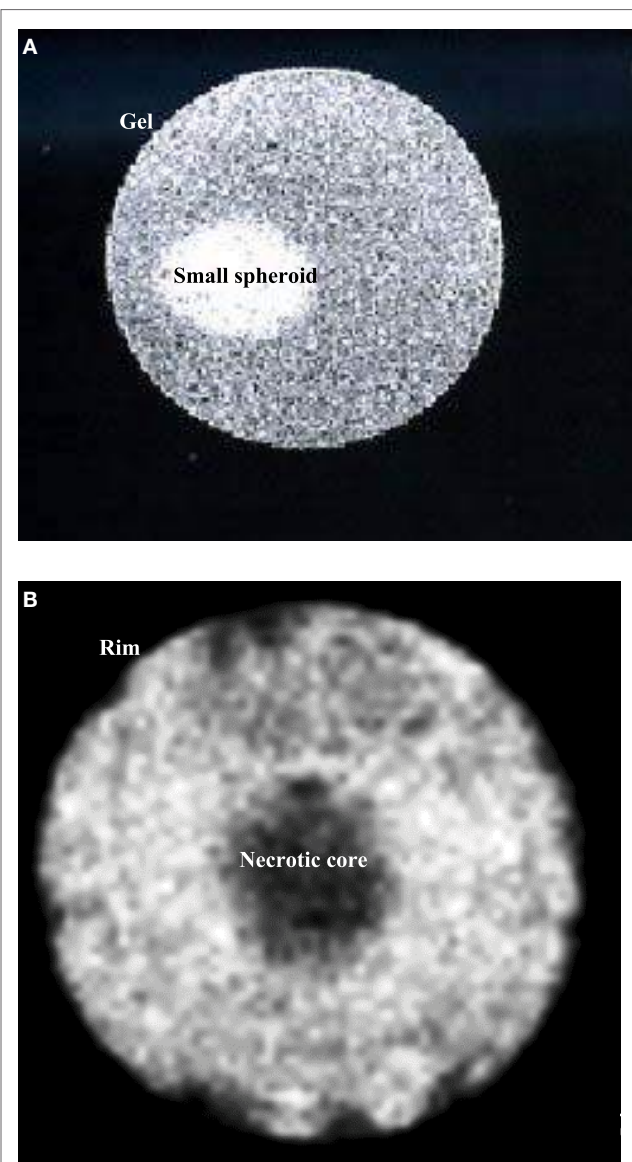


**FIGURE 1 | (A)** Sagittal image of a small spheroid with a diameter of about 0.5 mm, inserted in agarose gel. **(B)** Sagittal image of a spheroid after 10 days in culture. The diameter is about 1.8 mm. It is possible to identify two different regions: a necrotic core and a viable rim. Both images were acquired with an MSME sequence.

small spheroid, <0.5 mm diameter, usually obtained after 4 days in culture. **Figure 1B** shows a larger spheroid, 1.8 mm diameter, typically obtained after at least 10 days in culture. In this latter case, a necrotic core is clearly visible, while cells in the rim look similar to those of small spheroids.

To avoid the confounding presence of the necrotic core characterized by non-viable cells with a metabolic fingerprint substantially different from the cells in the rim, we examined only small spheroids by both localized and HR MR spectroscopy. When using an internal signal as a reference for quantification, the number of cells *per se* does not influence metabolite levels. On the other hand, different spheroid sizes, due to different number of cells, may influence spectral signals because of differences in pO<sub>2</sub> gradient within spheroids. For this reason, a lot of attention was paid to keep the spheroid size constant. The size conformity was achieved by the strict control of growth conditions and was confirmed by light microscopy and MR imaging.

Localized spectra of single small spheroids were then obtained. A representative spectrum is shown in **Figure 2A**. These spectra were compared with HR NMR spectra from a suspension of small spheroids and cells grown as monolayer. **Figures 2B,B';C,C'** show typical HR 1D and 2D COSY spectra of small spheroid suspensions and monolayer MCF-7 cells, respectively. Interestingly, the localized spectrum of the single spheroid (**Figure 2A**) showed remarkable similarities with the HR spectrum of the small spheroid suspension (**Figure 2B**); in both cases signals at 1.28 and 0.89 ppm dominated the spectra. These signals are attributed to MLs, mostly triglycerides in intracellular lipid droplets (18, 19). The greater signal linewidth in spheroid (**Figures 2A,B**) vs. monolayer cell spectra (**Figure 2C**) can be explained by a lower tumbling of lipids aggregates in spheroids due to their immobilization in the three-dimensional structure. Gln signal at 2.44 ppm was also quite different in spheroid and monolayer cell spectra.

Given the similarities between the localized and small spheroid suspension spectra, we studied the suspension by HR spectroscopy, preferentially using 2D COSY, that was recently implemented even for *in vivo* spectroscopy (19), for more precise quantification of spectral changes. In the present paper, MLs were quantified by cross-peak integrals in 2D COSY spectra deriving from the interaction of the terminal methyl group at 0.89 ppm and the proximal methylene at 1.28 ppm, excluding the contribution from ω-3 fatty acids, where methyl protons at 0.98 ppm are coupled to the allylic methylene at 2.09 ppm (18, 19). The results of the quantification of ML and Gln signals in 2D spectra are shown in **Figures 2D,E**. Assignments of the signals of interest were performed on the basis of comparison with 1D and 2D COSY spectra of total lipid extracts and of Gln pure compound, reported in Supplementary Material (Figure S1 and S2 in Supplementary Material, respectively).

The spectra of spheroid samples were characterized by higher intensity of ML (**Figure 2D**), mostly neutral lipids, and Gln signals (**Figure 2E**) as compared with their monolayer cells counterpart, most likely due to the occurrence of lower cell oxygenation in spheroids. To assess whether the behavior of these signals could be attributed to lower cell oxygenation in spheroids, we measured the spectra of MCF-7 monolayer cells grown under mild hypoxic

conditions (**Figures 2D,E**). In both spheroids and hypoxic cells spectra, higher concentrations of Gln were found with respect to the spectra of monolayer cells (**Figure 2E**). A similar effect was observed in hypoxic HeLa cells (20). Also, the ML signals were more intense in comparison with well oxygenated cells growing as monolayer (**Figure 2D**).

We then examined the effects of irradiation in this multicellular model for possible differences compared to monolayer cells. Spheroids suspension has been irradiated with a dose of 20 Gy. Under these conditions, cell proliferation is completely arrested, although maintaining metabolic activity. Monolayer MCF-7 cells were examined in the past at different times after irradiation (18). In the present paper, we examined samples 48 h after irradiation. Based on our previous experience (18), at this time interval, lipid signals in irradiated samples are much more intense than those in control samples, the latter still being in exponential growth. At later time intervals, exponential growth cannot be assured for control samples and consequently differences with irradiated samples can be deceptive. No cell killing was observed within 48 h after irradiation (21). Therefore, changes in lipid and Glx pool metabolism could be observed. **Figure 3A** shows the MR image of a typical spheroid 48 h after irradiation. Irradiated spheroids lose their regular shape, appearing larger and frayed. The effect of irradiation on ML signals is shown in **Figures 3B,B';C,C';D,D'** for a localized single spheroid, spheroid suspension, and monolayer cell spectra, respectively. The effect on single spheroid and on spheroid suspension was similar to that on monolayer cell spectra. The irradiation produced a strong increase in ML signals in all cases (**Figures 3B',C,D'**). **Figure 3E** reports relative intensities of the ML signal in 2D COSY spectra of monolayer cells and spheroid suspensions, which shows the increase of ML in irradiated samples (average of five experiments).

In addition, taking into account the oxidative stress induced by irradiation and the antioxidant properties of GSH, we analyzed the Glx pool (GSH, Gln, and Glu) region in 2D COSY spectra from spheroid suspension and monolayer cells. **Figure 4** shows the effect of irradiation on signals of the Glx pool; a representative experiment is reported in **Figures 4A,A';B,B'** and the quantification of five experiments in **Figures 4C,C'** for spheroid suspension and monolayer cells, respectively. GSH decreased in both spheroids and monolayer cells upon irradiation, the effect being very strong in spheroids, while Gln remained high in irradiated spheroids and increases in monolayer cells after irradiation.

## DISCUSSION

According to several studies and recent reviews (1, 22), some important properties of cell biology are shared by multicellular cancer spheroids and solid tumors *in vivo*, in particular growth characteristics, including growth rates (23), microenvironmental conditions, such as hypoxia, and related resistance to radiation treatments (1).

<sup>1</sup>H NMR spectroscopy has provided new insights into cell metabolism in animals and humans as it allows investigation of biologically active molecules in cells. With this respect, cell aggregates, such as spheroids, provide a system of higher complexity as compared with monolayer cells allowing better characterization

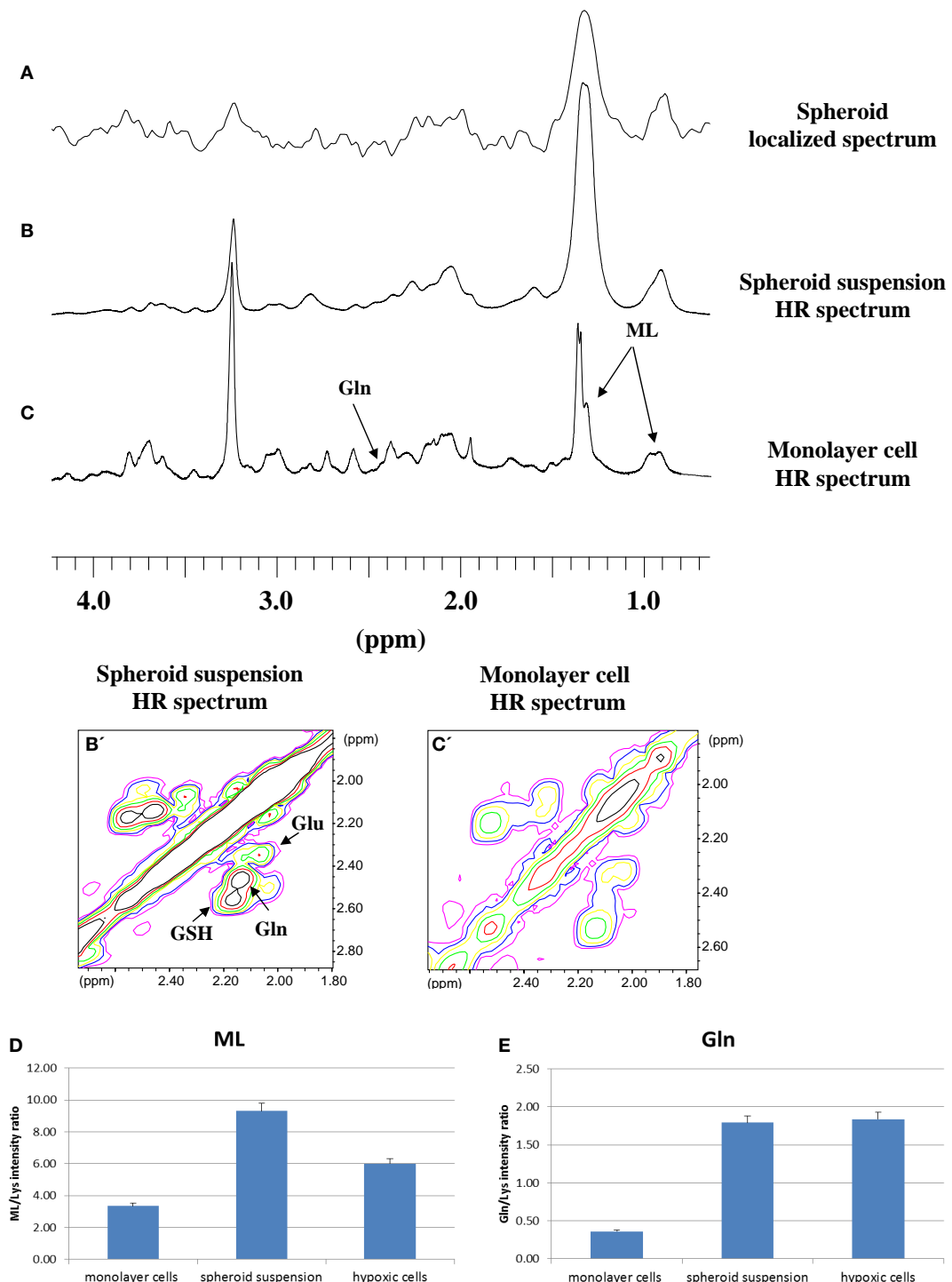


**FIGURE 2 | (A)** Localized 1D spectrum of a single small MCF-7 spheroid. 1D and 2D COSY high resolution (HR) spectra of small MCF-7 spheroid suspension (**B,B'**) and of monolayer MCF-7 cells (**C,C'**). Cross-peak labeled ML is from terminal methyl and bulk methylene coupling in mobile lipids (ML). Signal intensities of ML (**D**) and Gln (**E**) from 2D spectra of monolayer MCF-7 cells, spheroid suspension, and MCF-7 cells grown under mild hypoxia conditions (average of five experiments, error is the SD). In the figure, GSH and Glu stand for glutathione and glutamate, respectively. TMSP in  $\text{D}_2\text{O}$  in the external compartment was used to provide a lock signal and a frequency standard.

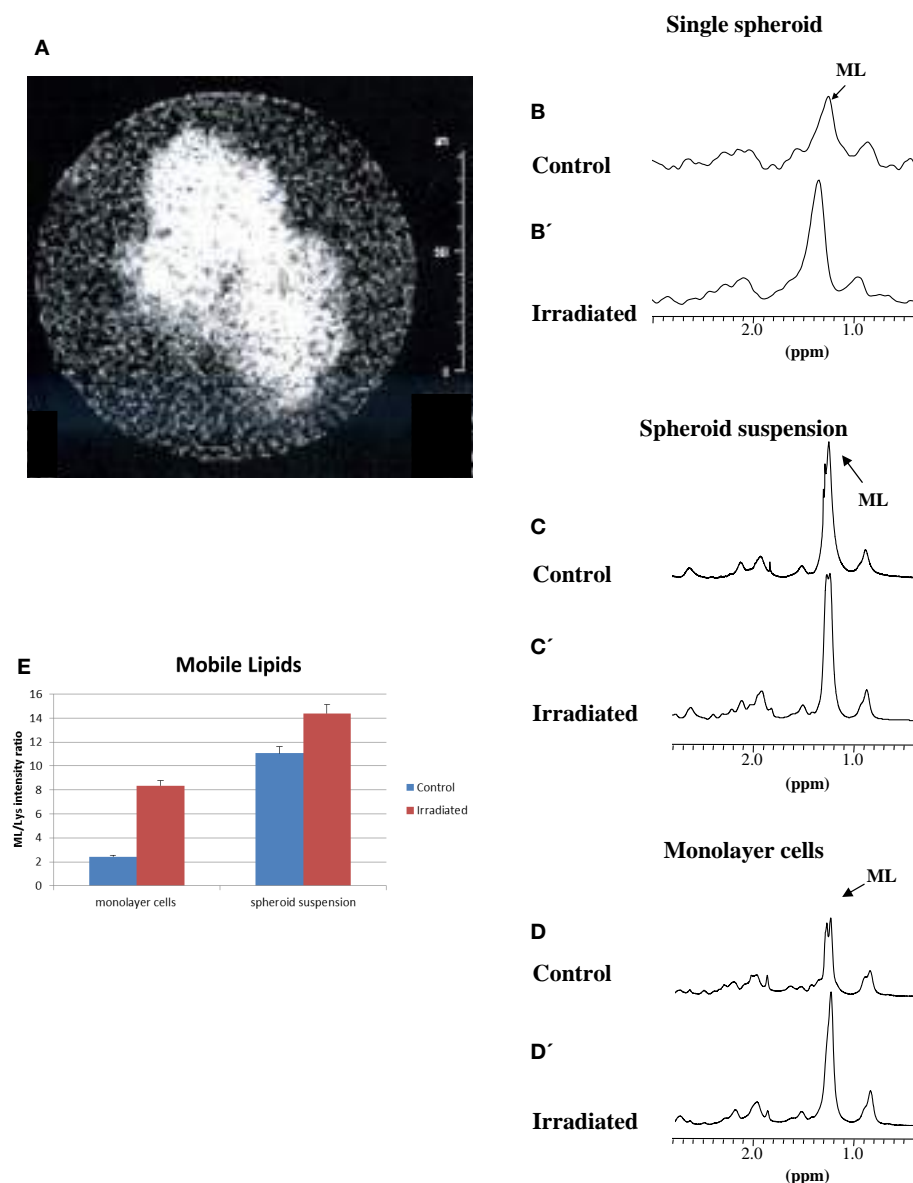


**FIGURE 3 | (A)** MR image of a typical irradiated spheroid 48 h after a 20 Gy dose irradiation. **(B,C,D)** Spectra of control and, **(B',C',D')**, spectra of an irradiated single spheroid, a spheroid suspension and monolayer cells 48 h after a 20 Gy dose irradiation. **(E)** Quantitative evaluation of ML signal intensities in 2D COSY spectra of monolayer cells and the spheroid suspension (average of five experiments, error is the SD). The most evident metabolites are labeled and abbreviated as in **Figure 2**.

of cell metabolism. In the present work, we compared the localized spectrum from a voxel in a single spheroid with NMR spectra from spheroid suspensions. A similar spectral behavior indicates that spheroid suspensions can be useful in NMR-based metabolic studies, thanks to simple sample preparation and spectra measurement.

The intense lipid signals attributed to fatty acid chains in neutral lipids (ML) have elicited much attention in the NMR community, which aims at providing new tools to improve the knowledge of lipid metabolism and correlate the spectral observations to biologically relevant events (24). Several studies

have been conducted on these signals. Some authors found ML increasing concurrently with cell death by apoptosis (25). By contrast, such correlation was not found in our previous studies (18, 26). In fact, the intense increase in lipid signals observed in the monolayer MCF-7 cells after irradiation did not correlate with the onset of consistent apoptosis. Furthermore, HeLa cells, which had undergone relevant apoptosis after irradiation, did not show any increase in ML signal (18, 26). No definitive statement on the origin of ML accumulation or degradation may be issued given the complex, interrelated reactions involving lipid synthesis and degradation in different cells, and the numerous changes

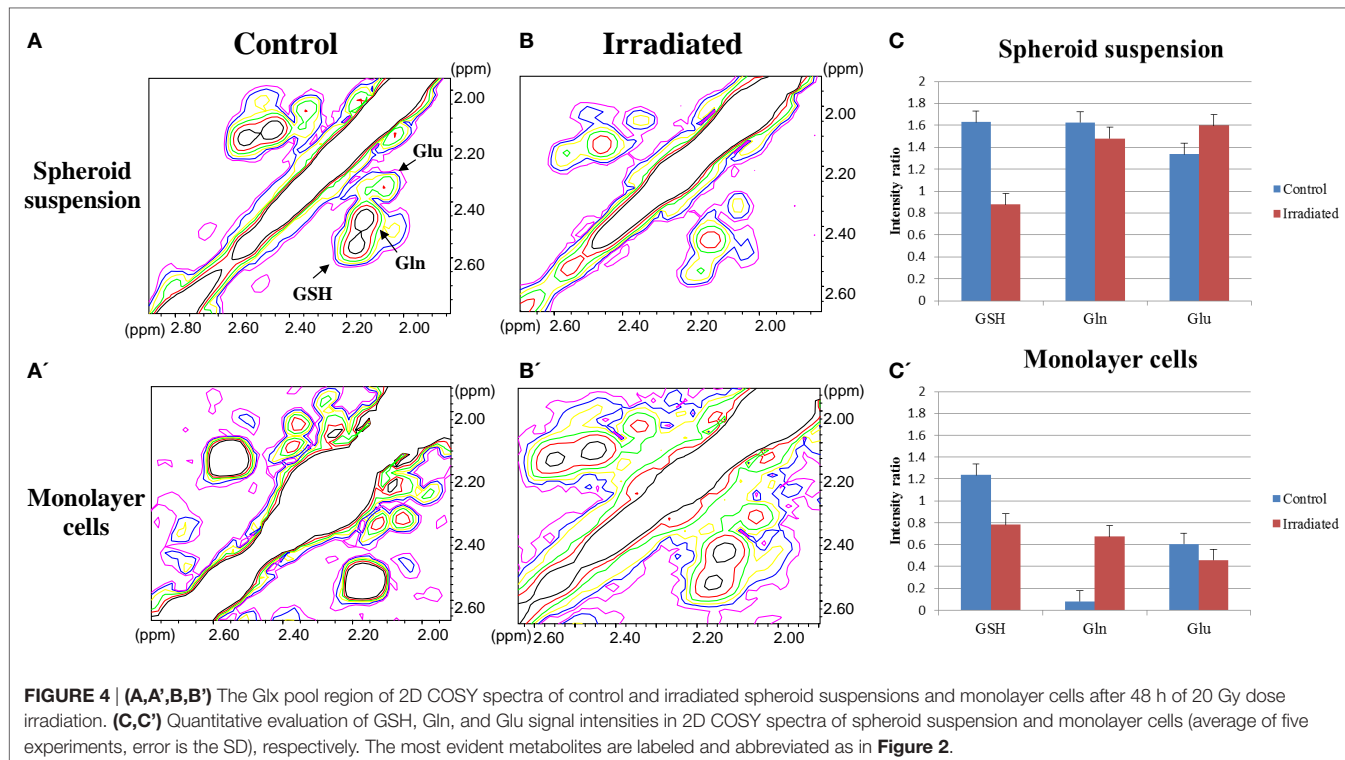


**FIGURE 4 | (A,A',B,B')** The Glx pool region of 2D COSY spectra of control and irradiated spheroid suspensions and monolayer cells after 48 h of 20 Gy dose irradiation. **(C,C')** Quantitative evaluation of GSH, Gln, and Glu signal intensities in 2D COSY spectra of spheroid suspension and monolayer cells (average of five experiments, error is the SD), respectively. The most evident metabolites are labeled and abbreviated as in Figure 2.

taking place in response to stress of different origin. On the other hand, ML signals were found to be sensitive in detecting cellular responses to microenvironmental changes, such as irradiation or treatment with anticancer drugs. Thus, they are good candidates for detecting success or resistance to treatments (27).

Lipid signals (ML) were found to be more intense in multicellular spheroids than in monolayer cells: this can be attributed to lower cell oxygenation with the ensuing decline in cell growth as that observable in solid tissues (1). A similar increase in ML signals was confirmed by growing monolayer cells under low oxygen conditions, since a relevant increase in the intense lipid signal is present in hypoxic cells, possibly related to impaired fatty acid beta-oxidation due to the shift from aerobic to anaerobic metabolism (28). Similar observations were obtained in hypoxic HeLa cells (20). In addition, the hypoxic condition has been associated with triglyceride and free fatty acid accumulation (29). Hypoxia is expected to increase lactate production, therefore, decreasing environmental pH: culturing in acidic pH produced an increase in lipid signals in C6 glioma cells (30). The ML increase may then be also related to decreased pH.

Finally, we observed an increased ML content in the cells after the radiation treatment. Interestingly, this has been reported for cells exposed at high doses, such as those used in medical treatments, not a general phenomenon though, as it is modulated by differences in radiation sensitivity (18, 31). In a previous work on MCF-7 cells grown as monolayer cultures, we had already observed more intense ML signals in the spectra of irradiated cells with respect to control samples (18). This was attributed to cell cycle-dependent impairment of phospholipid synthesis and the consequent triglyceride accumulation accompanying

the radiation-induced cell cycle block and proliferative arrest. Both in monolayer cell and in spheroid suspensions, lipid signals increased after irradiation. The effect in monolayer cells was attributed mainly to a slowing down of MCF-7 cell growth since apoptosis was not significant in these irradiated cells (21). Irradiated spheroids showed intense ML signals (likely related to the enhanced storage of lipids) and loss of their regular shape; while in monolayer cells, an altered cell growth condition was observed in the past (18).

Exposure to radiation usually affects metabolites of the Glx pool involved in antioxidant reactions of the cell response to oxidative stress. The analysis of Glx pool metabolites showed a decrease in GSH signal intensity after irradiation in both monolayer cell and spheroid spectra. The decrease of GSH in spheroids after irradiation is due to its use as an antioxidant against reactive oxygen species (ROS) produced in large quantity by irradiation. The role of GSH in the radiation response of mammalian cells is well known and a protective effect was actually demonstrated in irradiated MCF-7 cells grown as monolayers (21). Similar effects were observed in hypoxic cells (32). Gln is differently regulated in monolayers and in 3D structures, being more abundant in spheroids than in cells growing as monolayer. This effect may also be ascribed to the reduced oxygen availability in spheroids where the lower oxygen tension induces increased Gln levels, as much as it occurs in other cell aggregates, such as stem cell neurospheres (9). This behavior can be attributed to upregulation of Gln synthetase and downregulation of glutaminases found in hypoxic conditions (33).

Although it has long been known that cell radiosensitization *in vitro* is easily done by depletion of antioxidant scavengers, such

as GSH (21, 34, 35) and that this molecule may be involved in antioxidant defense in different cultured cells (25), it is still under discussion whether targeting cancer cells by ROS-mediated mechanisms may be a reasonable therapeutic approach (36, 37). Modulation of antioxidant defenses of cancer cells by radio/chemo therapies may, in principle, provide a tool to improve therapeutic effectiveness. In this context, it would be worth further exploring the role of GSH together with that of amino acids Glu and Gln involved in its synthesis during therapeutic treatments.

## CONCLUSION

The comparison between localized  $^1\text{H}$  MR spectroscopy of single spheroids and HR NMR on spheroid suspensions suggested the use of the latter for studying cell metabolism in spheroids, used as a 3D model close to solid tumors. Tumor tissues are often characterized by intense signals from fatty acids that have also been found in spheroids and, with less intensity, in the spectra of monolayer cells. These signals are also intense in irradiated and hypoxic MCF-7 cells, which is likely related to switching toward glycolytic metabolism after the radiation treatment. Gln levels are also quite high in spheroids as compared to 2D cultures. Similar Gln levels were present in different 3D aggregates, such as neurospheres. The Glx pool is strictly involved in the cell response

to the hypoxic condition and radiation treatment, showing a GSH decrease due to its antioxidant role in irradiated samples of either spheroids or monolayer cells.

## AUTHOR CONTRIBUTIONS

AP designed the work, and carried out NMR experiments and data analysis. SG carried out NMR experiments and data analysis. AL and AR carried out cell cultures and spheroid growth. VM carried out MR microimaging and localized spectroscopy experiments. LG, VV, and AR contributed to the interpretation of data for the work. All authors discussed the results, and read and approved the final manuscript.

## ACKNOWLEDGMENTS

The authors are very grateful to Monica Brocco (ISS) for the linguistic revision of the manuscript.

## SUPPLEMENTARY MATERIAL

The Supplementary Material for this article can be found online at <http://journal.frontiersin.org/article/10.3389/fonc.2016.00105>

## REFERENCES

1. Weiswald LB, Bellet D, Dangles-Marie V. Spherical cancer models in tumor biology. *Neoplasia* (2015) **17**:1–15. doi:10.1016/j.neo.2014.12.004
2. Rosi A, Grande S, Luciani AM, Barone P, Mlynarik V, Viti V, et al.  $^1\text{H}$  MRS studies of signals from mobile lipids and from lipid metabolites: comparison of the behavior in cultured tumor cells and in spheroids. *NMR Biomed* (2004) **17**:76–91. doi:10.1002/nbm.867
3. Ivascu A, Kubbies M. Rapid generation of single-tumor spheroids for high-throughput cell function and toxicity analysis. *J Biomol Screen* (2006) **11**(8):922–32. doi:10.1177/1087057106292763
4. Lin RZ, Chang HY. Recent advances in three-dimensional multicellular spheroid culture for biomedical research. *Biotechnol J* (2008) **3**:1172–84. doi:10.1002/biot.200700228
5. Kim SH, Kuh HJ, Dass CR. The reciprocal interaction: chemotherapy and tumor microenvironment. *Curr Drug Discov Technol* (2011) **8**:102–6. doi:10.2174/157016311795563875
6. Shekhar MP. Drug resistance: challenges to effective therapy. *Curr Cancer Drug Targets* (2011) **11**:613–23. doi:10.2174/156800911795655921
7. Andre F, Berrada N, Desmedt C. Implication of tumor microenvironment in the resistance to chemotherapy in breast cancer patients. *Curr Opin Oncol* (2010) **22**:547–51. doi:10.1097/CCO.0b013e32833fb384
8. Hirschhaeuser F, Menne H, Dittfeld C, West J, Mueller-Klieser W, Kunz-Schughart LA. Multicellular tumor spheroids: an underestimated tool is catching up again. *J Biotechnol* (2010) **148**:3–15. doi:10.1016/j.biote.2010.01.012
9. Guidoni L, Ricci-Vitiani L, Rosi A, Palma A, Grande S, Luciani AM, et al.  $^1\text{H}$  NMR detects different metabolic profiles in glioblastoma stem-like cells. *NMR Biomed* (2014) **27**:129–45. doi:10.1002/nbm.3044
10. Lamb R, Bonuccelli G, Ozsvári B, Peiris-Pagès M, Fiorillo M, Smith DL, et al. Mitochondrial mass, a new metabolic biomarker for stem-like cancer cells: understanding WNT/FGF-driven anabolic signaling. *Oncotarget* (2015) **6**(31):30453–71. doi:10.18632/oncotarget.5852
11. Mandujano-Tinoco EA, Gallardo-Pérez JC, Marín-Hernández A, Moreno-Sánchez R, Rodríguez-Enríquez S. Anti-mitochondrial therapy in human breast cancer multi-cellular spheroids. *Biochim Biophys Acta* (2013) **1833**(3):541–51. doi:10.1016/j.bbamcr.2012.11.013
12. Belouche-Babari M, Box C, Arunan V, Parkes HG, Valenti M, De Haven Brandon A, et al. Acquired resistance to EGFR tyrosine kinase inhibitors alters the metabolism of human head and neck squamous carcinoma cells and xenograft tumours. *Br J Cancer* (2015) **112**:1206–14. doi:10.1038/bjc.2015.86
13. Palmas MSA, Voge HJ. The future of NMR metabolomics in cancer therapy: towards personalizing treatment and developing targeted drugs? *Metabolites* (2013) **3**(2):373–96. doi:10.3390/metabo3020373
14. Eldredge-Hind HB, Rosenberg AL, Simone NL. Intraoperative radiotherapy for breast cancer: the lasting effects of a fleeting treatment. *Int J Breast Cancer* (2014) ArticleID214325. doi:10.1155/2014/214325
15. Palma A, Grande S, Rosi A, Luciani AM, Guidoni L, Viti V.  $^1\text{H}$  MRS can detect aberrant glycosylation in tumour cells a study of the HeLa cell line. *NMR Biomed* (2010) **24**:1099–110. doi:10.1002/nbm.1665
16. Behar KL, Rothman DL, Spencer DD, Petroff OAC. Analysis of macromolecule resonances in  $^1\text{H}$  NMR spectra of human brain. *Magn Reson Med* (1994) **32**:294–302. doi:10.1002/mrm.1910320304
17. Morvan D, Demidem A, Papon J, De Latour M, Madelmont JC. Melanoma tumors acquire a new phospholipid metabolism phenotype under cysteamine as revealed by high-resolution magic angle spinning proton nuclear magnetic resonance spectroscopy of intact tumor samples. *Cancer Res* (2002) **62**:1890–7.
18. Luciani AM, Grande S, Palma A, Rosi A, Giovannini C, Sapora O, et al. Characterization of  $^1\text{H}$  NMR detectable mobile lipids in cells from human adenocarcinomas. *FEBS J* (2009) **276**:1333–46. doi:10.1111/j.1742-4658.2009.06869.x
19. Mountford C, Ramadan S, Stanwell P, Malycha P. Proton MRS of the breast in the clinical setting. *NMR Biomed* (2009) **22**(1):54–64. doi:10.1002/nbm.1301
20. Grande S, Luciani AM, Palma A, Rosi A, Sapora O, Viti V, et al. Hyperammonia and hypoxia induce relevant changes in lipid signals in  $^1\text{H}$  NMR spectra from human cancer cells. *Proc Int Soc Magn Reson Med* (2009) **17**:2308.
21. Rosi A, Grande S, Luciani AM, Palma A, Giovannini C, Guidoni L, et al. Role of glutathione in apoptosis by irradiation as evidenced by  $^1\text{H}$  MR spectra of cultured tumour cells. *Radiat Res* (2007) **167**(3):268–82. doi:10.1667/RR0578.1

22. Kimlin LC, Casagrande G, Virador VM. *In vitro* three-dimensional (3D) models in cancer research: an update. *Mol Carcinog* (2013) **52**(3):167–82. doi:10.1002/mc.21844
23. Lawlor ER, Scheel C, Irving J, Sorensen PH. Anchorage independent multi-cellular spheroids as an *in vitro* model of growth signaling in Ewing tumors. *Oncogene* (2002) **21**:307–18. doi:10.1038/sj.onc.1205053
24. Di Vito M, Lenti L, Knijn A, Iorio E, D'Agostino F, Molinari A, et al. <sup>1</sup>H NMR-visible mobile lipid domains correlate with cytoplasmic lipid bodies in apoptotic T-lymphoblastoid cells. *Biochim Biophys Acta* (2001) **1530**:47–66. doi:10.1016/S1388-1981(00)00165-7
25. Santini MT, Romano R, Rainaldi G, Ferrante A, Indovina P, Motta A, et al. <sup>1</sup>H-NMR evidence for a different response to the same dose (2 Gy) of ionizing radiation of MG-63 human osteosarcoma cells and three-dimensional spheroids. *Anticancer Res* (2006) **26**:267–82.
26. Grande S, Giovannini C, Luciani AM, Palma A, Rosi A, Saporra O, et al. Radiation effects in cultured tumour cells examined by <sup>1</sup>H MRS: mobile lipids modulation and proliferative arrest. *Radiat Prot Dosimetry* (2006) **122**(1–4):202–4. doi:10.1093/rpd/ncl517
27. Delikatny EJ, Chawla S, Leung DJ, Poptan H. MR-visible lipids and the tumor microenvironment. *NMR Biomed* (2011) **24**(6):592–611. doi:10.1002/nbm.1661
28. Huang D, Li T, Li X, Zhang L, Sun L, He X, et al. HIF-1-mediated suppression of Acyl-CoA dehydrogenases and fatty acid oxidation is critical for cancer progression. *Cell Rep* (2014) **8**(6):1930–42. doi:10.1016/j.celrep.2014.08.028
29. Gordon GB, Barcza MA, Bush ME. Lipid accumulation of hypoxic tissue culture cells. *Am J Pathol* (1977) **88**(3):663–78.
30. Barba I, Cabanas ME, Arus C. The relationship between nuclear magnetic resonance-visible lipids, lipid droplets, and cell proliferation in cultured C6 cells. *Cancer Res* (1999) **59**(8):1861–8.
31. Essmann F, Engels IH, Totzke G, Schulze-Osthoff K, Jänicke RU. Apoptosis resistance of MCF-7 breast carcinoma cells to ionizing radiation is independent of p53 and cell cycle control but caused by the lack of Caspase-3 and a caffeine-inhibitable event. *Cancer Res* (2004) **64**:7065–72. doi:10.1158/0008-5472.CAN-04-1082
32. Ogunrinu TA, Sontheimer H. Hypoxia increases the dependence of glioma cells on glutathione. *J Biol Chem* (2010) **285**:37716–24. doi:10.1074/jbc.M110.161190
33. Kobayashi S, Millhorn DE. Hypoxia regulates glutamate metabolism and membrane transport in rat PC12 cells. *J Neurochem* (2001) **76**:1935–48. doi:10.1046/j.1471-4159.2001.00214.x
34. Clark EP, Epp ER, Biaglow JE, Morse-Gaudio M, Zachgo E. Glutathione depletion, radiosensitization, and misonidazole potentiation in hypoxic Chinese hamster ovary cells by buthionine sulfoximine. *Radiation Res* (1984) **98**:370–80. doi:10.2307/3576244
35. Guichard M, Lepinasse F, Malaise EP. Influence of buthionine sulfoximine and misonidazole on glutathione level and radiosensitivity of human tumor xenografts. *Radiation Res* (1986) **105**(1):115–25. doi:10.2307/3576731
36. Trachootham D, Alexandre J, Huang P. Targeting cancer cells by ROS-mediated mechanisms: a radical therapeutic approach? *Nat Rev Drug Discov* (2009) **8**(7):579–91. doi:10.1038/nrd2803
37. Abdalla MY. Glutathione as potential target for cancer therapy; more or less is good? *Jordan J Biol Sci* (2011) **4**:119–24.

**Conflict of Interest Statement:** The authors declare that the research was conducted in the absence of any commercial or financial relationships that could be construed as a potential conflict of interest.

The reviewer SB and handling Editor declared their shared affiliation, and the handling Editor states that the process nevertheless met the standards of a fair and objective review.

Copyright © 2016 Palma, Grande, Luciani, Mlynárik, Guidoni, Viti and Rosi. This is an open-access article distributed under the terms of the Creative Commons Attribution License (CC BY). The use, distribution or reproduction in other forums is permitted, provided the original author(s) or licensor are credited and that the original publication in this journal is cited, in accordance with accepted academic practice. No use, distribution or reproduction is permitted which does not comply with these terms.



# Glycerophosphocholine and Glycerophosphoethanolamine Are Not the Main Sources of the *In Vivo* $^{31}\text{P}$ MRS Phosphodiester Signals from Healthy Fibroglandular Breast Tissue at 7 T

Wybe J. M. van der Kemp<sup>1\*</sup>, Bertine L. Stehouwer<sup>1</sup>, Jurgen H. Runge<sup>2</sup>, Jannie P. Wijnen<sup>1</sup>, Aart J. Nederveen<sup>2</sup>, Peter R. Luijten<sup>1</sup> and Dennis W. J. Klomp<sup>1</sup>

<sup>1</sup> Radiology, University Medical Center Utrecht, Utrecht, Netherlands, <sup>2</sup> Radiology, Academic Medical Center, Amsterdam, Netherlands

## OPEN ACCESS

### Edited by:

Franca Podo,  
Istituto Superiore di Sanità, Italy

### Reviewed by:

Hadassa Degani,  
Weizmann Institute of Science, Israel

Sebastian Cerdan,

Instituto de Investigaciones  
Biomedicas Alberto Sols, Spain  
Jim Delikatny,  
University of Pennsylvania, USA

### \*Correspondence:

Wybe J. M. van der Kemp  
w.j.m.vanderkemp@umcutrecht.nl

### Specialty section:

This article was submitted to Cancer Imaging and Diagnosis, a section of the journal *Frontiers in Oncology*

Received: 17 September 2015

Accepted: 28 January 2016

Published: 15 February 2016

### Citation:

van der Kemp WJM, Stehouwer BL, Runge JH, Wijnen JP, Nederveen AJ, Luijten PR and Klomp DWJ (2016)

Glycerophosphocholine and Glycerophosphoethanolamine Are Not the Main Sources of the *In Vivo*

$^{31}\text{P}$  MRS Phosphodiester Signals from Healthy Fibroglandular Breast Tissue at 7 T.

Front. Oncol. 6:29.

doi: 10.3389/fonc.2016.00029

**Purpose:** The identification of the phosphodiester (PDE)  $^{31}\text{P}$  MR signals in the healthy human breast at ultra-high field.

**Methods:** *In vivo*  $^{31}\text{P}$  MRS measurements at 7 T of the PDE signals in the breast were performed investigating the chemical shifts, the transverse- and the longitudinal relaxation times. Chemical shifts and transverse relaxation times were compared with non-ambiguous PDE signals from the liver.

**Results:** The chemical shifts of the PDE signals are shifted  $-0.5$  ppm with respect to glycerophosphocholine (GPC) and glycerophosphoethanolamine (GPE), and the transverse and longitudinal relaxation times for these signals are a factor 3 to 4 shorter than expected for aqueous GPC and GPE.

**Conclusion:** The available experimental evidence suggests that GPC and GPE are not the main source of the PDE signals measured in fibroglandular breast tissue at 7 T. These signals may predominantly originate from mobile phospholipids.

**Keywords:** MRSI,  $^{31}\text{P}$ , relaxation time, 7 T, phosphodiester, breast, phospholipids

## INTRODUCTION

The phosphomonoesters (PME), phosphocholine (PC) and phosphoethanolamine (PE), and the phosphodiesters (PDEs), glycerophosphocholine (GPC) and glycerophosphoethanolamine (GPE), are involved in cell membrane metabolism. From *ex vivo* studies, it is known that the PC/GPC ratio goes up on malignant transformation of cells (1, 2), while the decrease of the PC/GPC ratio was shown to be a marker in predicting cancer treatment response in *ex vivo* NMR studies (2–4). *In vivo*, the total choline signal, which can be obtained by localized  $^1\text{H}$  MRS, has been shown to be a biomarker for malignancy and treatment response (5). In contrast to *in vivo*  $^1\text{H}$  MRS, where only

**Abbreviations:** AMESING, Adiabatic Multi-Echo Spectroscopic ImagING; CSA, chemical shift anisotropy; DPPC, dipalmitoylphosphatidylcholine (1,2-dipalmitoyl-sn-glycero-3-phosphocholine); DMPC, dimyristoylphosphatidylcholine (1,2-dimyristoyl-sn-glycero-3-phosphocholine); GPC, glycerophosphocholine; GPE, glycerophosphoethanolamine; GPTC, (diacyl-)glycerophosphatidylcholine; GPtE, (diacyl-)glycerophosphatidylethanolamine; ILA, inter-lamellar attachment; MPL, membrane phospholipids; PC, phosphocholine; PE, phosphoethanolamine; Pi, inorganic phosphate; PCr, phosphocreatine.

a total choline signal can be observed, one can easily distinguish PME from PDEs with *in vivo*  $^{31}\text{P}$  MRS and even PE from PC and GPE from GPC, with ultra-high field  $^{31}\text{P}$  MRS (6). Besides higher spectral resolution, ultra-high field MRS comes with a higher signal-to-noise ratio that can be traded off for improving spatial resolution or to shorten scan time. High *in vivo* PME/PDE ratios, as measured with  $^{31}\text{P}$  MRS, have been shown to be indicative of cancer, while treatment response is often accompanied by a reduction in PME/PDE (7–12). However, in contrast to some *ex vivo* methods, where extraction techniques are used to separate aqueous pools of metabolites from lipid pools, *in vivo* methods will also obtain signals from membrane phospholipids (MPL) (13, 14). Moreover, as these MPL have chemical shifts similar to GPC, e.g., glycerophosphatidylethanolamine (GPtE) has almost identical chemical shift as GPC (15, 16) (the molecular structures and chemical shifts are shown in Figure 1) – *in vivo* distinction of these compounds is hampered.

At lower field strength (<2.5 T), *in vivo*  $^{31}\text{P}$  spectra of various tissues, e.g., breast (17, 18), brain (19–24), liver (25–28), and kidney (29, 30), show a large signal in the PDE chemical shift range, with its top between 2 and 3 ppm with respect to phosphocreatine (PCr) at 0 ppm. The full width at half max of this signal is dependent on the field strength, and the delay between excitation and acquisition, as, for instance, caused by phase encoding. It has been suggested (21, 25) that this membrane peak disappears almost completely at high-field strength due to enhanced relaxation by chemical shift anisotropy, leaving only the signals of the aqueous-soluble metabolites GPC and GPE. Nowadays, with high magnetic field human MRI systems becoming available, the origin of the PDE  $^{31}\text{P}$  MRS signal – whether GPC and GPE, and/or GPtC and GPtE – is of renewed interest.

Here, we show that the PDE signals measured *in vivo* in fibroglandular tissue of the human breast ( $^{31}\text{P}$  signal from breast

fatty tissue is below the detection limit) at 7 T are possibly signals from MPL, although their line widths suggest aqueous small molecules, such as GPC and GPE. Measurements are performed at 7 T to distinguish GPE from GPC and GPtE from GPtC. Adiabatic multi-echo spectroscopic imaging (AMESING) (31) and progressive saturation are used to identify the mobility of the molecules as reflected in the  $T_2$ - and  $T_1$ -values, respectively, to enable a distinction between the aqueous GPE and GPC from the more restricted MPL (GPtE and GPtC). Data are obtained in breast glandular tissue and compared to GPC and GPE metabolite signals as measured in liver tissue, all in healthy human volunteers *in vivo*.

## MATERIALS AND METHODS

$^{31}\text{P}$  MRS measurements of glandular breast tissue were obtained from healthy volunteers using a dedicated breast coil (MR Coils BV, Drunen, The Netherlands) interfaced to a 7-T MRI system (Philips, Cleveland, OH, USA). Pulse-acquire and multi-echo acquisitions [AMESING (31)] were obtained with adiabatic RF pulses. Excitation was done with an adiabatic half passage (AHP) of 2 ms. For refocusing 4 ms  $B_1$  insensitive rotation pulses (BIR-4 180°) were used. The AHP excitation pulse had a frequency sweep of 10.0 kHz and the BIR-4 refocusing pulses a frequency sweep of 20.0 kHz. Both pulses had tangent frequency modulation and hyperbolic tangent amplitude modulation as described in Garwood and Ke (32). Pulses were driven with  $\gamma B_{1\max} = 1700$  Hz. Transmitter offset on the  $^{31}\text{P}$  channel was set to 600 Hz with respect to the resonance of PCr. All chemical shifts reported here are referenced to PCr as standard at a chemical shift of 0.0 ppm, which is –2.48 ppm compared to 85% phosphoric acid. Frequency calibration of the scanner is done based on the water signal (the MR system uses a fixed ratio between  $^{31}\text{P}$  and  $^1\text{H}$  carrier frequency

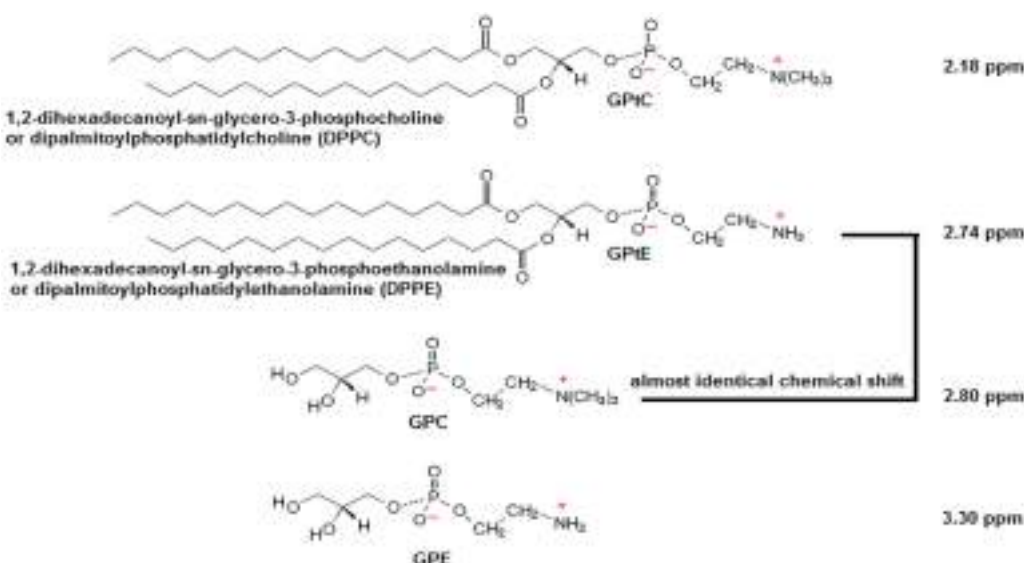


**FIGURE 1 | Molecular structures of GPC, GPE, and their membrane phospholipids GPtC and GPtE.** Chemical shift of GPC is taken as a reference at 2.80 ppm. Chemical shift differences  $\Delta\delta(\text{GPtE}-\text{GPtC}) = 0.56$  ppm and  $(\text{GPC}-\text{GPtC}) = 0.62$  ppm were calculated from high-resolution spectra (spectral resolution <0.02 ppm) by Schiller and Arnold (15), and  $\Delta\delta(\text{GPE}-\text{GPC}) = 0.50$  ppm from Payne et al. (16).

such that the proton signal for water corresponds to the  $^{31}\text{P}$  PCr signal). Measurements with the AMESING sequence were performed with a  $T_{\text{R}}$  of 6 s,  $8 \times 8 \times 8$  spherical acquired MRSI,  $2 \text{ cm} \times 4 \text{ cm} \times 4 \text{ cm}$  voxel sizes for the breast on five volunteers.

Both FID and symmetric echoes were acquired with 256 data points, and the spectral bandwidth for the acquisition of the FID was 17.0 kHz and for the echoes 8.5 kHz (echo spacing 45 ms) to maintain equal acquisition durations for FID and each half echo. Acquired data were spatially Hamming filtered and zero filled in the time domain to 8192 data points. To obtain high SNR spectra of the breast, the datasets of five volunteers (age range 24–30 years) were pooled and Pi-weighted based on the FID signal. Phosphorus metabolite  $T_1$ -values in the breast were measured for five volunteers by means of progressive saturation with an adiabatic AHP pulse-acquire 1D MRSI sequence with  $T_{\text{R}}$  values in the range of 0.5–8 s, where the scan time was kept identical for each  $T_{\text{R}}$ . The FID data were acquired with 512 data points and a spectral bandwidth of 8.2 kHz. A 1D MRSI encoded in the anterior-posterior direction was chosen to effectively suppress signals from the underlying pectoral muscles. Data were spatially Hamming filtered and subsequently zero filled in the time domain to 8192 data points. To obtain high SNR datasets for  $T_1$ -fitting, the volunteers were measured two or three times and the data per volunteer were averaged. Before averaging, all spectra were aligned for Pi. Averaged spectra were spectrally fitted in JMRUI (33) using the AMARES algorithm (34), chemical shifts for the GPtE + GPC and GPtC resonances were fixed with a soft constraint to  $2.77 \pm 0.1$  ppm and  $2.18 \pm 0.1$  ppm and free but equal line width.

$^{31}\text{P}$  MRS liver measurements were also done with the AMESING sequence with  $32 \times 10$  2D MRSI (feet-head direction unlocalized) voxel sizes  $1 \text{ cm} \times 1 \text{ cm}$  (echo spacing 40 ms) on five volunteers for the liver [data included from earlier study (35)], using a half volume coil (MR Coils BV, Drunen, The Netherlands). Other parameters and data post-processing and analysis were equal to those used in the breast measurements. Here, a 2D scheme with small AP and LR dimensions of the voxels was chosen to be able to exclude signal from muscle tissue, whereas the FH dimension is unlocalized but constrained by the coil sensitivity to encompass the liver but not beyond.

The study was approved by the local medical ethics review board (METC UMC Utrecht) and written informed consent was obtained from all volunteers.

## RESULTS

In **Figure 2**, the spectra of a voxel of the breast (average spectrum of five volunteers) and the liver (five volunteers) are shown. Due to limited bandwidth of the adiabatic pulses only the spectral range from +10 to  $-10$  ppm is shown. The chemical shifts of the GPC and GPE signals in the liver (**Figure 2C**) do not correspond to the signals observed in the breast spectra (**Figures 2A,B**), which are usually labeled GPC and GPE, while the chemical shifts of the other metabolites (PE, PC, Pi,  $\gamma$ -ATP,  $\alpha$ -ATP) in liver and breast do match. **Figures 2A,B** show, for a voxel of breast glandular tissue, the average FID and the average  $T_2$ -weighted

echo-sum spectra using a fixed  $T_2$  weighting of  $154 \pm 5$  ms (36), scaled to the same noise. Note that the signal intensities of the peaks labeled PE, PC, Pi, and (GPtE + GPC) increase, or at least do not decrease, in the echo-sum spectrum as compared

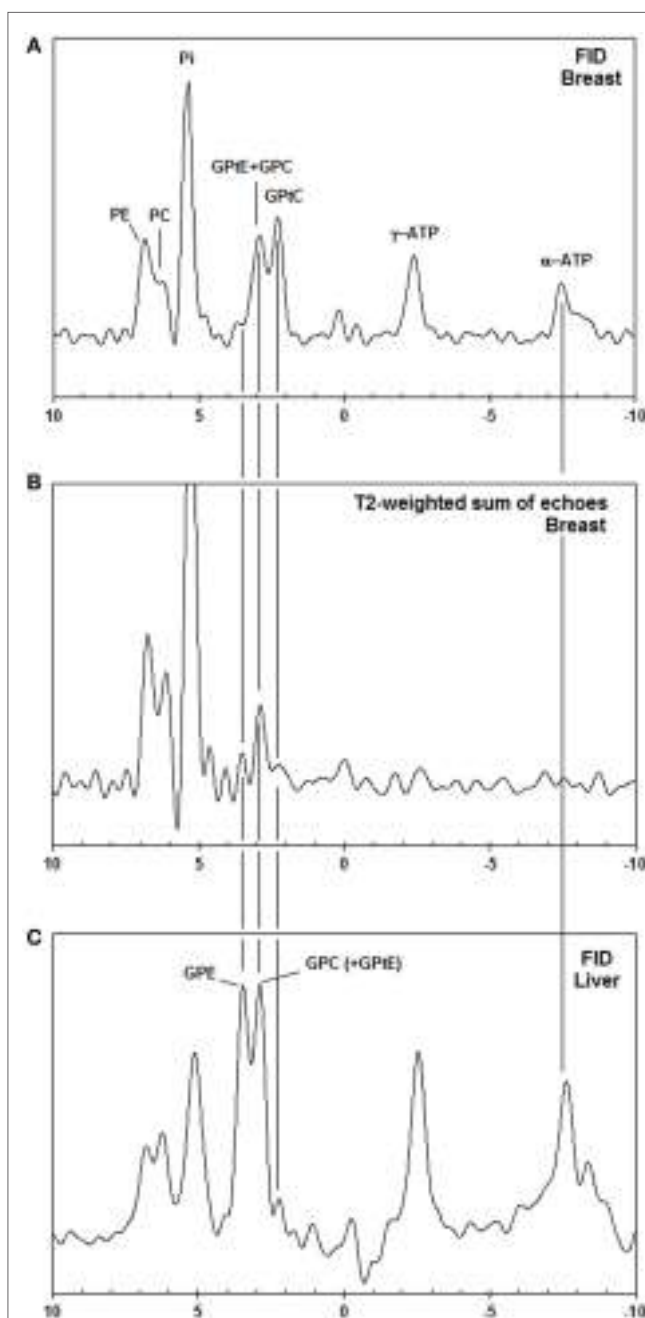


**FIGURE 2 | (A)** Pulse acquire, **(B)**  $T_2$ -weighted echo sum ( $T_2 = 154$  ms)  $^{31}\text{P}$  MR spectra [AMESING sequence (31)] from a voxel ( $2 \text{ cm} \times 4 \text{ cm} \times 4 \text{ cm}$ ) of the breast (average of five volunteers) scaled to the same noise, and **(C)** pulse-acquire  $^{31}\text{P}$  MR spectrum from the liver (average of five volunteers). Note that only the aqueous metabolites with long  $T_2$ -values, such as PE, PC, Pi, and GPC get enhanced in the  $T_2$ -weighted echo sum and that the chemical shifts of liver GPE and GPC do not match the PDE signals from the breast, but are shifted  $+0.5$  ppm.

to the FID spectrum of the breast, while the signals of GPtC and ATP, with known short  $T_2$ -values, do decrease in the echo-sum spectrum. Unlike ATP, the short apparent  $T_2$  for GPtC (and GPtE) is not the result of homonuclear coupling. In **Figure 3**, a comparison is made between  $T_2$  fits obtained for the PDE signal at 2.2 ppm (labeled GPtC) from the breast (a) and the 2.8 ppm signal from the liver (labeled GPC), showing almost a factor 3 lower  $T_2$  for the GPtC signal from the breast. **Figure 4** shows the  $T_1$ -fits for the average signals of (GPtE + GPC) and GPtC from fibroglandular breast tissue as measured in the five volunteers. The (GPtE + GPC) signal is fitted bi-exponentially with a short  $T_1$  component for GPtE (taken equal to GPtC,  $T_1 = 1.2$  s). The  $T_1$ -value that is fitted for the long  $T_1$  component GPC is 3.2 s.

## DISCUSSION

Phosphorous spectra from the breast and liver as shown in **Figure 2** do not match to the chemical shift of the PDE signals. As the chemical shift of GPC and GPE are hardly pH sensitive, but Pi and to a lesser extent also PE, PC, and  $\gamma$ -ATP are (37), pH differences between liver and breast may influence chemical shift. If we would shift the breast spectrum by +0.5 ppm to match the PDE signals between breast and liver, this would correspond to

a shift in pH of +0.4 units based on Pi chemical shift. This pH difference is unreasonably large, moreover expressing the change in chemical shift of +0.5 ppm for PE, PC, and  $\gamma$ -ATP in pH units is either not possible, or goes beyond any physiologic condition. Therefore, it seems likely that the metabolite signals in the breast that do not match those in the liver are (GPtE + GPC) and GPtC. Healthy liver is known to show high signals of GPC and GPE in  $^{31}\text{P}$  MRS *in vivo* and also in *ex vivo* perchloric acid extracts (38, 39). The peak labeled GPtC in the liver spectrum of **Figure 2C** is sometimes referenced to as (potentially) phosphoenolpyruvate (28, 40). However, it does not show up in  $^{31}\text{P}$  MRS perchloric acid liver extract studies (38, 39), even though phosphoenolpyruvate is sufficiently soluble in an aqueous phase.

The most likely reason for the nearly constant (GPtE + GPC) signal over FID and echo sum (**Figures 2A,B**) is that aqueous GPC, with a relatively long  $T_2$ , increases in the echo sum, while GPtC, just like GPtE, decreases in intensity due to short  $T_2$ .

A recent lipidomic profiling study on healthy mammary epithelial and breast cancer cells (41) has shown that in the membranes of healthy mammary epithelial cells the concentration of GPtC is approximately twice the concentration of GPtE. If we assume that the  $T_2$ -weighted echo-sum signal at the chemical shift of GPtE + GPC in **Figure 2B** is indeed all GPC and we assume

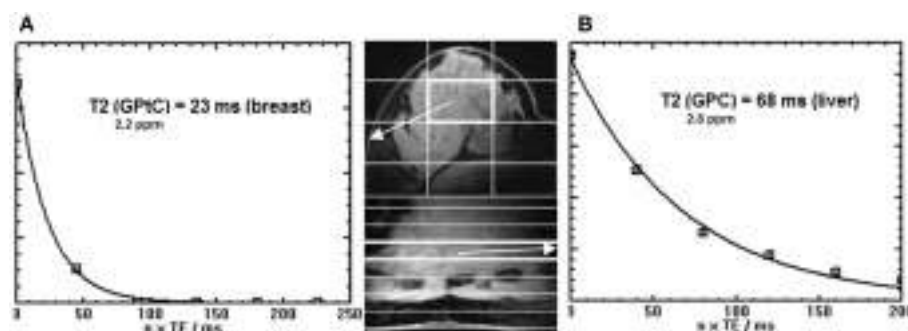


**FIGURE 3 |** Signal decay [as quantified by spectral fitting of FID and echoes with JMRUI (33)] as a function of time of the GPtC peak at 2.2 ppm obtained from (A) the breast (36) (echo spacing 45 ms) and (B) the true GPC peak from the liver (35) at 2.8 ppm (echo spacing 40 ms). Data were obtained by the AMESING sequence (31) and are averaged values for the group of volunteers. Note the threefold reduced  $T_2$  of the  $^{31}\text{P}$  spins of GPtC in the breast as compared to GPC in the liver. Images shown are (fast field echo) examples of breast and liver for one volunteer.

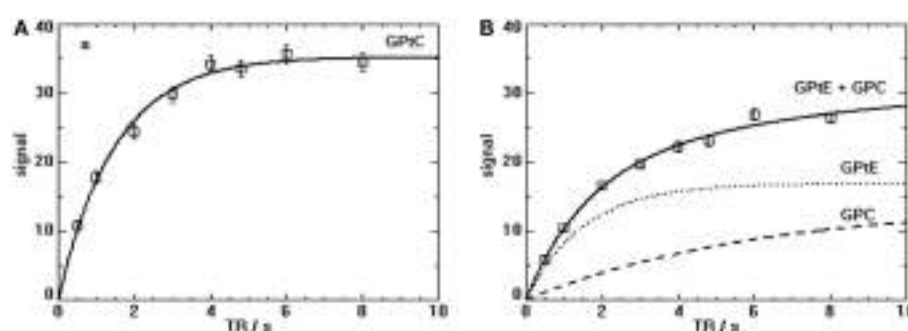


**FIGURE 4 |**  $T_1$ -fits of the progressive saturation measurements for the PDE signals (sum of five volunteers) in the breast at 7 T. (A) The  $T_1$ -value of the GPtC signal (mono-exponential decay) is  $1.2 \pm 0.3$  s. (B) The (GPtE + GPC) signal for the five volunteers was fitted bi-exponentially with a fixed short  $T_1$  component for GPtE taken equal to GPtC leading to a  $T_1$  for GPC of  $3.2 \pm 0.6$  s.

a similar  $T_2$  for GPC and PE and PC, then we can calculate the GPtC to GPtE ratio by subtraction of the GPC contribution in **Figure 2A**. This leads to a GPtC to GPtE ratio of 2, in close agreement with the lipidomic profiling study. Minor contributions from sphingomyelin and glycerophosphatidylserines, seen in the lipidomic profiling study will probably add to the *in vivo*  $^{31}\text{P}$  MR signal of GPtE and glycerophosphatidylinositol to the *in vivo*  $^{31}\text{P}$  MR signal of GPtC, not altering the ratio substantially. Chemical shift differences for these different phospholipids are reported by Schiller and Arnold (15).

The  $^{31}\text{P}$   $T_2$  values in liver can be low due to the presence of iron, for instance, in the form of ferritin, which is known to increase the relaxivity of water (42). *In vivo* values for  $T_2$  of  $^{31}\text{P}$  metabolites (PE, PC, Pi, GPE, GPC) in the liver ranging between 37 and 71 ms have recently been measured at 7 T in our hospital in a group of five healthy volunteers (35). For the breast, however, we measured that the  $T_2$  of the  $^{31}\text{P}$  spins at the chemical shift of GPtC (36) is even a factor 3 shorter than the  $T_2$  of the  $^{31}\text{P}$  spins of GPC in the liver (35), as shown in **Figure 3**. In fact, compared to the reported  $T_2$  values – measured at 7 T – of PDEs in calf muscle [ $T_2 = 314$  ms (43), 375 ms (31)] or of PC and PE in the breast, the  $T_2$  value of GPtC we measured is almost an order of magnitude lower. Spectral fitting of the FID spectrum of **Figure 2A**, simplified by equal line widths for PE, PC, Pi, and equal linewidths for the PDE signals shows an additional linewidth for the PDE signals of 9 Hz, which is close to the calculated value of 12 Hz when considering the measured  $T_2$  of  $23 \pm 1$  ms (35) and a  $T_2$  for the PMEs and Pi of  $\sim 160$  ms.

The low signals for GPE and GPC in the echo-sum spectra of the breast are corroborated by an *in vitro* extract study on breast tumors by Smith et al. (14), where it was shown that GPE and GPC concentrations are low in non-necrotic breast tumors and that, at low field, PDE signals observed *in vivo* are mainly from phospholipids. A recent LC MS study by Mimmi et al. (44) showed a very low average concentration of only 0.04 mmol/kg GPC in three healthy fibroglandular breast tissue samples.

Another reason to suspect that the dominant PDE signal we observe in the breast at 7 T originates from mobile lipid structures is based on the results of the  $T_1$ -measurements of the PDE signal in the breast, as depicted in **Figure 4**. Here, the  $T_1$  of GPtC was fitted mono-exponentially leading to  $1.5 \pm 0.1$  s and the signal of GPtE + GPC was fitted bi-exponentially with the  $T_1$  of the GPtE component fixed equal to the  $T_1$  of GPtC. For the signal of the aqueous GPC, this leads to  $6 \pm 2$  s. The fitted  $T_1$  of mobile GPtC is three- to fivefold lower than that reported for GPC and GPE in calf muscle and brain at 7 and 3 T (43, 45, 46). A value of 1.4 s for the  $T_1$  of the  $^{31}\text{P}$  MRS signal of dipalmitoylphosphatidylcholine (DPPC) vesicles with an average diameter of 100 nm has been measured by Klauda et al. (47) above the phase transition temperature. For multi-lamellar dispersions of dimyristoylphosphatidylcholine (DMPC), a value around 1 s has been measured just above the phase transition temperature by Dufourc et al. (48). The  $T_1$ -value of 6 s fitted for the GPC component, **Figure 4B**, agrees well with the  $T_1$ -values for GPC reported at 3 T and 7 T for calf muscle and brain ranging from 4 to 7.8 s (43, 45, 46).

All presented data throughout this paper is based on average spectra of the group of volunteers. This has the advantage that it maximizes signal to noise and enables the most reliable relaxation

time fitting. A short coming is that individual physiological differences between volunteers are averaged out.

The fitted linewidth of the two overlapping PDE signals of the breast spectrum depicted in **Figure 2A** is 58 Hz (i.e., 0.5 ppm). Bulk phospholipid bilayers show broad asymmetrical lineshapes (several tens of ppm) caused by large chemical shift anisotropy (49). Therefore, if the very sharp PDE resonances that we observe are from MPL, then these MPL must be highly mobile phospholipids, for which chemical shift anisotropy and dipolar couplings are sufficiently averaged out. Especially at ultra-high field, relaxation by chemical shift anisotropy that goes with the square of the field causes additional line broadening as compared to spectra recorded at lower field strength. Highly mobile phospholipids can be found in small-sized vesicles ( $<50$  nm) (50), and in large arrays of lipidic particles (51), inter-lamellar attachments (52), and inverted cubic structures (52–54) within the lipid bilayer.

A rough estimate of the percentage of *in vivo* visible mobile phospholipids at 7 T can be made as follows. The ratio of PE to PC is  $\sim 2$  and the PME to PDE ratio is  $\sim 1$  (**Figure 2A**). A weighted average of PC concentrations measured in healthy breast tissue by Mimmi et al. (44) is 0.08 mmol/kg, with PE/PC = 2 (**Figure 2A**), this leads to a PME concentration of  $\sim 0.2$  mmol/kg. Most of the PDE signal is from mobile phospholipids (**Figures 2A,B**). The total concentration of phospholipids in human tissues is in the range of 17–83 mmol/kg (55). With a signal ratio of PDEs to PMEs in breast glandular tissue of 1.4 at  $T_R = 6$  s (35) and a  $T_1$  of PMEs of 5 s (56) and a  $T_1$  of mobile phospholipids of 1.5 s, the total concentration of *in vivo* visible mobile phospholipids in the human breast at 7 T is also of the order of  $\sim 0.2$  mmol/kg. This leads to a crude estimate of the visible mobile phospholipid fraction at 7 T of 0.2–1.2%.

## CONCLUSION

The PDE signals from the breast, as measured with MRSI techniques at 7 T *in vivo*, show aberrant behavior from aqueous GPE and GPC. The  $T_1$  and  $T_2$  relaxation values for these PDE signals are too short to represent true aqueous GPC and GPE. In addition, the chemical shifts of these PDE signals do not correspond to GPE and GPC, but are shifted  $-0.5$  ppm with regard to these, and correspond to chemical shift values of GPtE and GPtC. These PDE signals could originate from mobile lipid structures such as small vesicles with diameters  $\leq 50$  nm, large arrays of ILAs or large domains of inverted cubic phases within the lipid bilayer. As the PC over GPC ratio is used as a biomarker in breast cancer research, the *in vivo* obtained value will be contaminated with signal from GPtE – having a similar chemical shift as GPC – or the GPtC peak may be erroneously assigned as GPC.

## AUTHOR CONTRIBUTIONS

WK: study design, MR measurements, data analyses, first draft of typescript; BS: MR measurements, critical revision of typescript; JR: MR measurements, data analysis, critical revision of typescript; JW: study design, critical revision of typescript; AN: study design, critical revision of typescript; PL: study design, critical revision of typescript; DK: study design, critical revision of typescript. All authors approved the final version of the manuscript.

## REFERENCES

- Aboagye EO, Bhujwalla ZM. Malignant transformation alters membrane choline phospholipid metabolism of human mammary epithelial cells. *Cancer Res* (1999) **59**(1):80–4.
- Glunde K, Ackerstaff E, Mori N, Jacobs MA, Bhujwalla ZM. Choline phospholipid metabolism in cancer: consequences for molecular pharmaceutical interventions. *Mol Pharm* (2006) **3**:496–506. doi:10.1021/mp060067e
- Podo F. Tumour phospholipid metabolism. *NMR Biomed* (1999) **12**:413–39. doi:10.1002/(SICI)1099-1492(199911)12:7<413::AID-NBM587>3.0.CO;2-U
- Podo F, Canevari S, Canese R, Pisani ME, Ricci A, Iorio E. MR evaluation of response to targeted treatment in cancer cells. *NMR Biomed* (2011) **24**:648–72. doi:10.1002/nbm.1658
- Glunde K, Jiang L, Moestue SA, Gribbestad IS. MRS and MRSI guidance in molecular medicine: targeting and monitoring of choline and glucose metabolism in cancer. *NMR Biomed* (2011) **24**:673–90. doi:10.1002/nbm.1751
- Khlebnikov V, Wijnen JP, van der Kemp WJM, Klomp DWJ.  $^{31}\text{P}$  MRSI Studies in Patients with Cancer. *Ann R NMR S* (2016) **87**:320–68. doi:10.1016/bs.arnmr.2015.08.004
- Koutcher JA, Ballon D, Graham M, Healey JH, Casper ES, Heelan R, et al.  $^{31}\text{P}$  NMR spectra of extremity sarcomas: diversity of metabolic profiles and changes in response to chemotherapy. *Magn Reson Med* (1990) **16**(1):19–34. doi:10.1002/mrm.1910160104
- Cox IJ, Bell JD, Peden CJ, Iles RA, Foster CS, Watanapa P, et al. In vivo and in vitro  $^{31}\text{P}$  magnetic resonance spectroscopy of focal hepatic malignancies. *NMR Biomed* (1992) **5**(3):114–20. doi:10.1002/nbm.1940050303
- Redmond OM, Stack JP, O'Connor NG, Carney DN, Dervan PA, Hurson BJ, et al.  $^{31}\text{P}$  MRS as an early prognostic indicator of patient response to chemotherapy. *Magn Reson Med* (1992) **25**(1):30–44. doi:10.1002/mrm.1910250104
- Dewhurst MW, Poulsom JM, Yu D, Sanders L, Lora-Michels M, Vujaskovic Z, et al. Relation between pO<sub>2</sub>,  $^{31}\text{P}$  magnetic resonance spectroscopy parameters and treatment outcome in patients with high-grade soft tissue sarcomas treated with thermoradiotherapy. *Int J Radiat Oncol Biol Phys* (2005) **61**(2):480–91. doi:10.1016/j.ijrobp.2004.06.211
- Ha DH, Choi S, Oh JY, Yoon SK, Kang MJ, Kim KU. Application of  $^{31}\text{P}$  MRspectroscopy to the brain tumors. *Korean J Radiol* (2013) **14**(3):477–86. doi:10.3348/kjr.2013.14.3.477
- van der Kemp WJ, Stehouwer BL, Luijten PR, van den Bosch MA, Klomp DW. Detection of alterations in membrane metabolism during neoadjuvant chemotherapy in patients with breast cancer using phosphorus magnetic resonance spectroscopy at 7 Tesla. *Springerplus*. (2014) **3**:634. doi:10.1186/2193-1801-3-634
- Cerdan S, Subramanian VH, Hilberman M, Cone J, Egan J, Chance B, et al.  $^{31}\text{P}$  NMR detection of mobile dog brain phospholipids. *Magn Reson Med* (1986) **3**:432–9. doi:10.1002/mrm.1910030308
- Smith TA, Glaholm J, Leach MO, Machin L, Collins DJ, Payne GS, et al. A comparison of in vivo and in vitro  $^{31}\text{P}$  NMR spectra from human breast tumours: variations in phospholipid metabolism. *Br J Cancer* (1991) **63**:514–6. doi:10.1038/bjc.1991.122
- Schiller S, Arnold K. Application of high resolution  $^{31}\text{P}$  NMR spectroscopy to the characterization of the phospholipid composition of tissues and body fluids – a methodological review. *Med Sci Monit* (2002) **8**:MT205–22.
- Payne GS, Troy H, Vaidya SJ, Griffiths JR, Leach MO, Chung Y-L. Evaluation of  $^{31}\text{P}$  high-resolution magic angle spinning of intact tissue samples. *NMR Biomed* (2006) **19**:593–8. doi:10.1002/nbm.1040
- Twelves CJ, Lowry M, Porter DA, Dobbs NA, Graves PE, Smith MA, et al. 31-phosphorus metabolism of human breast – an in vivo MRS study at 1.5 Tesla. *Br J Radiol* (1993) **67**:36–45. doi:10.1259/0007-1285-67-793-36
- Payne GS, Dowsett M, Leach MO. Hormone-dependent metabolic changes in the normal breast monitored noninvasively by  $^{31}\text{P}$  magnetic resonance (MR) spectroscopy. *The Breast* (1994) **3**:20–3. doi:10.1016/0960-9776(94)90031-0
- Sauter A, Rudin M. Effects of calcium antagonists on high-energy phosphates in ischemic rat brain measured by  $^{31}\text{P}$  NMR spectroscopy. *Magn Reson Med* (1987) **4**:1–8. doi:10.1002/mrm.1910040102
- Kilby PM, Allis JL, Radda GK. Spin-spin relaxation of the phosphodiester resonance in the  $^{31}\text{P}$  NMR spectrum of human brain. The determination of the concentrations of phosphodiester components. *FEBS Lett* (1990) **272**:163–5. doi:10.1016/0014-5793(90)80474-W
- Kilby PM, Bolas NM, Radda GK.  $^{31}\text{P}$ -NMR study of brain phospholipid structures in vivo. *Biochim Biophys Acta* (1991) **1085**:257–64. doi:10.1016/0005-2760(91)90102-N
- McNamara R, Arias-Mendoza F, Brown TR. Investigation of broad resonances in  $^{31}\text{P}$  NMR spectra of the human brain in vivo. *NMR Biomed* (1994) **7**:237–42. doi:10.1002/nbm.1940070507
- Potwarka JL, Drost DJ, Williamson PC. Quantifying  $^1\text{H}$  decoupled in vivo  $^{31}\text{P}$  brain spectra. *NMR Biomed* (1999) **12**:8–14. doi:10.1002/(SICI)1099-1492(199902)12:1<8::AID-NBM540>3.0.CO;2-#
- Jensen JE, Drost DJ, Menon RS, Williamson PC. In vivo brain  $^{31}\text{P}$ -MRS: measuring the phospholipid resonances at 4 Tesla from small voxels. *NMR Biomed* (2002) **15**:338–47. doi:10.1002/nbm.776
- Bates TE, Williams SR, Gadian DG. Phosphodiesters in the liver: the effect of field strength on the  $^{31}\text{P}$  signal. *Magn Reson Med* (1989) **12**:145–50. doi:10.1002/mrm.1910120116
- Murphy EJ, Rajagopalan B, Brindle KM, Radda GK. Phospholipid bilayer contribution to  $^{31}\text{P}$  NMR spectra in vivo. *Magn Reson Med* (1989) **12**:282–9. doi:10.1002/mrm.1910120218
- Murphy EJ, Bates TE, Williams SR, Watson T, Brindle KM, Rajagopalan B, et al. Endoplasmic reticulum: the major contributor to the PDE peak in hepatic  $^{31}\text{P}$ -NMR spectra at low magnetic field strengths. *Biochim Biophys Acta* (1992) **1111**:51–8. doi:10.1016/0005-2736(92)90273-O
- Wylezinska M, Cobbold JF, Fitzpatrick J, McPhail MJ, Crossey MM, Thomas HC, et al. A comparison of single-voxel clinical in vivo hepatic  $^{31}\text{P}$  MR spectra acquired at 1.5 and 3.0 Tesla in health and diseased states. *NMR Biomed* (2010) **24**:231–7. doi:10.1002/nbm.1578
- Ratcliffe PJ, Moonen CT, Ledingham JG, Radda GK. Timing of the onset of changes in renal energetics in relation to blood pressure and glomerular filtration in haemorrhagic hypotension in the rat. *Nephron* (1989) **51**:225–32. doi:10.1159/000185290
- Heindel W, Kugel H, Wenzel F, Stippel D, Schmidt R, Lackner K. Localized  $^{31}\text{P}$  MR spectroscopy of the transplanted human kidney in situ shows altered metabolism in resection and acute tubular necrosis. *J Magn Reson Imaging* (1997) **7**:58–64. doi:10.1002/jmri.1880070514
- van der Kemp WJ, Boer VO, Luijten PR, Stehouwer BL, Veldhuis WB, Klomp DWJ. Adiabatic multi-echo  $^{31}\text{P}$  spectroscopic imaging (AMESING) at 7 tesla for measuring transverse relaxation times and regaining sensitivity in tissues with short T2\* values. *NMR Biomed* (2013) **26**:1299–307. doi:10.1002/nbm.2952
- Garwood M, Ke Y. Symmetric pulses to induce arbitrary flip angles with compensation for RF inhomogeneity and resonance offsets. *J Magn Reson* (1991) **94**:511–25.
- Naressi A, Couturier C, Devos JM, Janssen M, Mangeat C, de Beer R, et al. Java-based graphical user interface for the MRUI quantitation package. *MAGMA* (2001) **12**:141–52. doi:10.1016/S1352-8661(01)00111-9
- Vanhamme L, van den Boogaart A, Van Huffel S. Improved method for accurate and efficient quantification of MRS data with use of prior knowledge. *J Magn Reson* (1997) **129**:35–43. doi:10.1006/jmre.1997.1244
- Runge JH, van der Kemp WJM, Klomp DWJ, Nederveen AJ, Stoker J.  $^{31}\text{P}$  MRSI of the healthy liver at 3T and 7T with AMESING-boosted SNR. In *Proceedings of the 22nd Annual Meeting of ISMRM*, Milan (2014). 2265 p.
- Stehouwer BL, van der Kemp WJM, Luijten PR, van den Bosch MA, Veldhuis WB, Wijnen JP, et al. (31)P magnetic resonance spectroscopy of the breast and the influence of the menstrual cycle. *Breast Cancer Res Treat* (2014) **144**:583–9. doi:10.1007/s10549-014-2889-7
- Robitaille P-ML, Robitaille PA, Brown GG Jr, Brown GG. An analysis of the pH-dependent chemical-shift behavior of phosphorus-containing metabolites. *J Magn Reson* (1991) **92**:73–84.
- Taylor-Robinson SD, Sargentoni J, Bell JD, Thomas EL, Marcus CD, Changani KK, et al. In vivo and in vitro hepatic phosphorus-31 magnetic resonance spectroscopy and electron microscopy in chronic ductopenic rejection of human liver allografts. *Gut* (1998) **42**:735–43. doi:10.1136/gut.42.5.735
- Taylor-Robinson SD, Thomas EL, Sargentoni J, Marcus CD, Davidson BR, Bell JD. Cirrhosis of the human liver: an in vitro  $^{31}\text{P}$  nuclear magnetic resonance study. *Biochim Biophys Acta* (1995) **1272**:113–8. doi:10.1016/0925-4439(95)00074-E
- Sebastianova K, Hakkarainen A, Kotronen A, Cornér A, Arkkila P, Arola J, et al. Nonalcoholic fatty liver disease: detection of elevated nicotinamide adenine

- dinucleotide phosphate with *in vivo* 3.0-T  $^{31}\text{P}$  MR spectroscopy with proton decoupling. *Radiology* (2010) **256**:466–73. doi:10.1148/radiol.10091351
41. Dória ML, Cotrim Z, Macedo B, Simões C, Domingues P, Helguero L, et al. Lipidomic approach to identify patterns in phospholipid profiles and define class differences in mammary epithelial and breast cancer cells. *Breast Cancer Res Treat* (2012) **133**:635–48. doi:10.1007/s10549-011-1823-5
  42. Gossuin Y, Muller RN, Gillis P, Bartel L. Relaxivities of human liver and spleen ferritin. *Magn Reson Imaging* (2005) **23**:1001–4. doi:10.1016/j.mri.2005.10.009
  43. Bogner W, Chmelik M, Schmid AI, Moser E, Trattning S, Gruber S. Assessment of  $^{31}\text{P}$  relaxation times in the human calf muscle: a comparison between 3 T and 7 T *in vivo*. *Magn Reson Med* (2009) **62**:574–82. doi:10.1002/mrm.22057
  44. Mimmi MC, Finato N, Pizzolato G, Beltrami CA, Fogolari F, Corazza A, et al. Absolute quantification of choline-related biomarkers in breast cancer biopsies by liquid chromatography electrospray ionization mass spectrometry. *Anal Cell Pathol (Amst)* (2013) **36**:71–83. doi:10.3233/ACP-130082
  45. Klomp DWJ, Wijnen JP, Scheenen TW, Heerschap A. Efficient  $^1\text{H}$  to  $^{31}\text{P}$  polarization transfer on a clinical 3T MR system. *Magn Reson Med* (2008) **60**:1298–305. doi:10.1002/mrm.21733
  46. Lei H, Zhu XH, Zhang XL, Ugurbil K, Chen W. *In vivo*  $^{31}\text{P}$  magnetic resonance spectroscopy of human brain at 7 T: an initial experience. *Magn Reson Med* (2003) **49**:199–205. doi:10.1002/mrm.10379
  47. Klauda JB, Roberts MF, Redfield AG, Brooks BR, Pastor RW. Rotation of lipids in membranes: molecular dynamics simulation,  $^{31}\text{P}$  spin-lattice relaxation, and rigid-body dynamics. *Biophys J* (2008) **94**:3074–83. doi:10.1529/biophysj.107.121806
  48. Dufourc EJ, Mayer C, Stohrer J, Althoff G, Kothe G. Dynamics of phosphate head groups in biomembranes. Comprehensive analysis using phosphorus-31 nuclear magnetic resonance lineshape and relaxation time measurements. *Biophys J* (1992) **61**:42–57. doi:10.1016/S0006-3495(92)81814-3
  49. Seelig J.  $^{31}\text{P}$  nuclear magnetic resonance and the head group structure of phospholipids in membranes. *Biochim Biophys Acta* (1978) **515**:105–40. doi:10.1016/0304-4157(78)90001-1
  50. McLaughlin AC, Cullis PR, Berden JA, Richards RE.  $^{31}\text{P}$  NMR of phospholipid membranes: effects of chemical shift anisotropy at high magnetic field strengths. *J Mag Resonance* (1975) **20**:146–65.
  51. de Kruijff B, Verkley AJ, van Echteld CJ, Gerritsen WJ, Memmers C, Noordam PC, et al. The occurrence of lipidic particles in lipid bilayers as seen by  $^{31}\text{P}$  NMR and freeze fracture electron microscopy. *Biochim Biophys Acta* (1979) **555**:200–9. doi:10.1016/0005-2736(79)90160-3
  52. Siegel DP. Inverted micellar intermediates and the transitions between lamellar, cubic, and inverted hexagonal amphiphile phases. III. Isotropic and inverted cubic state formation via intermediates in transitions between L alpha and HII phases. *Chem Phys Lipids* (1986) **42**:279–301. doi:10.1016/0009-3084(86)90087-3
  53. Jiménez-Monreal AM, Villalain J, Aranda FJ, Gómez-Fernández JC. The phase behavior of aqueous dispersions of unsaturated mixtures of diacylglycerols and phospholipids. *Biochim Biophys Acta* (1998) **1373**:209–19. doi:10.1016/S0005-2736(98)00106-0
  54. Boni LT, Hui SW. Polymorphic phase behaviour of dilinoleoylphosphatidylethanolamine and palmitoyloleoylphosphatidylcholine mixtures. Structural changes between hexagonal, cubic and bilayer phases. *Biochim. Biophys Acta* (1983) **731**:177–85.
  55. Ansell GB, Spanner S. Phosphatidylserine, phosphatidylethanolamine, and phosphatidyl-choline. In: Hawthorne JN, Ansell CB, editors. *Phospholipids, New Comprehensive Biochemistry*. (Vol. 4), Amsterdam: Elsevier Biomedical Press (1982). p. 1–41.
  56. Wijnen JP, van der Kemp WJM, Luttje MP, Korteweg MA, Luijten PR, Klomp DWJ. Quantitative  $^{31}\text{P}$  magnetic resonance spectroscopy of the human breast at 7 T. *Magn Reson Med* (2012) **68**:339–48. doi:10.1002/mrm.23249

**Conflict of Interest Statement:** The authors declare that the research was conducted in the absence of any commercial or financial relationships that could be construed as a potential conflict of interest.

Copyright © 2016 van der Kemp, Stehouwer, Runge, Wijnen, Nederveen, Luijten and Klomp. This is an open-access article distributed under the terms of the Creative Commons Attribution License (CC BY). The use, distribution or reproduction in other forums is permitted, provided the original author(s) or licensor are credited and that the original publication in this journal is cited, in accordance with accepted academic practice. No use, distribution or reproduction is permitted which does not comply with these terms.



# Potential of Diffusion-Weighted Imaging in the Characterization of Malignant, Benign, and Healthy Breast Tissues and Molecular Subtypes of Breast Cancer

Uma Sharma<sup>1</sup>, Rani G. Sah<sup>1</sup>, Khushbu Agarwal<sup>1</sup>, Rajinder Parshad<sup>2</sup>, Vurthaluru Seenu<sup>2</sup>, Sandeep R. Mathur<sup>3</sup>, Smriti Hari<sup>4</sup> and Naranamangalam R. Jagannathan<sup>1\*</sup>

<sup>1</sup>Department of Nuclear Magnetic Resonance, All India Institute of Medical Sciences, New Delhi, India, <sup>2</sup>Department of Surgical Disciplines, All India Institute of Medical Sciences, New Delhi, India, <sup>3</sup>Department of Pathology, All India Institute of Medical Sciences, New Delhi, India, <sup>4</sup>Department of Radiodiagnosis, All India Institute of Medical Sciences, New Delhi, India

## OPEN ACCESS

### Edited by:

Franca Podo,  
Istituto Superiore di Sanità, Italy

### Reviewed by:

Marie-France Penet,  
Johns Hopkins University  
School of Medicine, USA  
Rossella Canese,  
Istituto Superiore di Sanità, Italy  
Michael Albert Thomas,  
University of California-Los Angeles,  
USA

### \*Correspondence:

Naranamangalam R. Jagannathan  
jagan1954@hotmail.com,  
nrjgj@yahoo.co.in

### Specialty section:

This article was submitted to  
Cancer Imaging and Diagnosis,  
a section of the journal  
*Frontiers in Oncology*

Received: 21 January 2016

Accepted: 09 May 2016

Published: 23 May 2016

### Citation:

Sharma U, Sah RG, Agarwal K,  
Parshad R, Seenu V, Mathur SR,  
Hari S and Jagannathan NR (2016)

Potential of Diffusion-Weighted  
Imaging in the Characterization of  
Malignant, Benign, and Healthy  
Breast Tissues and Molecular  
Subtypes of Breast Cancer.

Front. Oncol. 6:126.

doi: 10.3389/fonc.2016.00126

The role of apparent diffusion coefficient (ADC) in the diagnosis of breast cancer and its association with molecular biomarkers was investigated in 259 patients with breast cancer, 67 with benign pathology, and 54 healthy volunteers using diffusion-weighted imaging (DWI) at 1.5 T. In 59 breast cancer patients, dynamic contrast-enhanced MRI (DCEMRI) was also acquired. Mean ADC of malignant lesions was significantly lower ( $1.02 \pm 0.17 \times 10^{-3} \text{ mm}^2/\text{s}$ ) compared to benign ( $1.57 \pm 0.26 \times 10^{-3} \text{ mm}^2/\text{s}$ ) and healthy ( $1.78 \pm 0.13 \times 10^{-3} \text{ mm}^2/\text{s}$ ) breast tissues. A cutoff ADC value of  $1.23 \times 10^{-3} \text{ mm}^2/\text{s}$  (sensitivity 92.5%; specificity 91.1%; area under the curve 0.96) to differentiate malignant from benign diseases was arrived by receiver operating curve analysis. In 10/59 breast cancer patients, indeterminate DCE curve was seen, while their ADC value was indicative of malignancy, implying the potential of the addition of DWI in increasing the specificity of DCEMRI data. Further, the association of ADC with tumor volume, stage, hormonal receptors [estrogen receptor (ER), progesterone receptor (PR), and human epidermal growth factor (HER2)], and menopausal status was investigated. A significant difference was seen in tumor volume between breast cancer patients of stages IIA and IIIA, IIB and IIIA, and IIB and III (B + C), respectively ( $P < 0.05$ ). Patients with early breast cancer ( $n = 52$ ) had significantly lower ADC and tumor volume than those with locally advanced breast cancer ( $n = 207$ ). No association was found in ADC and tumor volume with the menopausal status. Breast cancers with ER-, PR-, and triple-negative (TN) status showed a significantly larger tumor volume compared to ER+, PR+, and non-triple-negative (nTN) cancers, respectively. Also, TN tumors showed a significantly higher ADC compared to ER+, PR+, and nTN cancers. Patients with ER- and TN cancers were younger than those with ER+ and nTN cancers. The present study demonstrated that ADC may increase the diagnostic specificity of DCEMRI and be useful for treatment management in clinical setting. Additionally, it provides an insight into characterization of molecular types of breast cancer and may serve as an indicator of metabolic reprogramming underlying tumor proliferation.

**Keywords:** diffusion-weighted MRI, breast cancer, apparent diffusion coefficient, benign lesions, molecular biomarkers, estrogen receptor, progesterone receptor, human epidermal growth factor receptor 2

## INTRODUCTION

Breast cancer is a heterogeneous tumor exhibiting five molecular types, classified by gene profiling and the expression of hormonal receptors such as estrogen receptor (ER), progesterone receptor (PR), and human epidermal growth factor (HER2) (1). The pre-operative tumor size, nodal status, metastasis (TNM) stage, tumor grade, receptor status, lymph node status, and Ki-67 were outcome predictors of breast cancer in previous studies (2, 3). Accordingly, early diagnosis of malignancy in individual patients may be important for a successful therapy. Mammography is the primary diagnostic screening tool, despite its limitation in sensitivity and specificity, especially in regard to the dense breast (4, 5). In such cases, ultrasound is useful. However, it has limitations in detecting microcalcification and ductal carcinoma *in situ* (DCIS) (6). Breast magnetic resonance imaging (MRI) has become an important adjunct modality in the evaluation of suspicious mammographically occult breast lesions, detection of tumor recurrence, and screening of women with high-risk cancer and those with breast implants (7). It is also useful in pre-operative tumor staging and in the assessment of post-therapy residual disease in a clinical setting (7). The use of dynamic contrast-enhanced (DCE) MRI with gadolinium-based contrast agents depicts high-resolution tumor morphology and allows for contrast uptake kinetics, tumor angiogenesis, and vascularity (8). The DCEMRI has been shown to have high sensitivity (93–99%) but with variable specificity (37–85%) (9).

The rapid proliferation of cancer is associated with reprogramming both the anabolic and catabolic pathways, supporting its growth and altering the intracellular and extracellular milieu. Functional MR imaging technique – such as diffusion-weighted imaging (DWI) – is useful to monitor such changes associated with tumor proliferation (10–12). By measuring diffusion constant of water molecules, DWI provides information about the extracellular and intracellular tissue compartments as well as the altered pathologies during cancer growth. The presence of cell membranes, macromolecules, and organelles restrict the motion of water molecules, and therefore decreases the diffusion constant of water compared to free aqueous solution. This is represented as apparent diffusion coefficient (ADC) (13). ADC has been used in differentiating various tissue pathologies, and DWI has in fact been established as an important adjunct technique with many clinical applications (10, 14). Studies have documented a relationship between the cell density and ADC (12, 15). Applications of DWI include characterization of malignant, benign, and healthy breast tissues (12, 16–18), and monitoring of the therapeutic response of breast tumors (19, 20). A correlation of ADC with the histological features and the enhancement ratios using DCEMRI has been reported (21). The growth patterns of cancer and the architectural features of stroma using DWI (21) and the correlation between ADC with the molecular markers of breast cancer have been reported (22–26). The addition of DWI increases the specificity of DCEMRI (27).

The objectives of the present study were (a) to determine a cutoff value of ADC for the differentiation of malignant, benign, and healthy breast tissues in a large cohort of subjects; (b) to

evaluate the potential of quantitative DWI in differentiating various histological types of malignant and benign lesions; (c) to evaluate the potential of ADC in indeterminate DCEMRI findings in a sub-group of patients; and (d) to examine the association of ADC, stage, tumor volume, age, menopausal status, and hormonal receptors in these patients.

## PATIENTS AND METHODS

### Patients

In this prospective study, a total of 388 subjects, including 259 with breast malignancy, 67 with benign breast pathology attending the breast cancer clinic of our Institute, and 54 healthy volunteers, were recruited during the period of 2007–2015. However, data of 8 subjects [malignant ( $n = 4$ ), benign ( $n = 2$ ), and healthy volunteers ( $n = 2$ )] were excluded from analyses because of motion and other artifacts. The demographic and histological details were presented in **Table 1**. American Joint Committee on Cancer (AJCC) TNM criteria were used for clinical staging of patients, which included stage IIA, IIB, IIIA, and IIIB + C. In breast cancer patients, MR was performed prior to therapy with at least 1 week after the core biopsy. The purpose and the methodology of the study were fully explained to all the subjects. All studies were carried out as per the standard regulatory guidelines of the institute ethics committee, which approved the study, and written informed consent was obtained from each subject. Clinical history and physical examination was taken for all patients. An ultrasonography, mammogram [Breast imaging Reporting and Data System (BIRADS) IV and V lesions], and histology (fine needle aspiration cytology/core biopsy) were performed. All patients had clinically palpable lumps, and the size of tumor was measured in two dimensions using a Vernier caliper after palpation. In this study, there were no patients with non-subcutaneous tumors.

Biopsied tissues were subjected to histology and immunohistochemical examinations to determine the expression of hormonal receptors, such as ER, PR, and HER2, status according to the standard published guidelines by the American Society of Clinical Oncology/College of American Pathologists (28). Patients with HER2 expression scores of 0 and 1+ were categorized as HER2 negative (HER2-) and those with the scores of 3+ were categorized as HER2 positive (HER2+). Patients with a score of 2+ were excluded from the analysis since their data of fluorescence *in situ* hybridization were not available. Accordingly, the ER status was available for 185 patients, PR status for 182, and HER2 status for 144 patients, and other details were presented in **Table 1**.

All patients underwent metastatic workup as per the standard guidelines for clinical staging of the tumor prior to any interventional procedure such as neoadjuvant chemotherapy (NACT) or surgery. Further, the metastatic workup included liver function tests, chest roentgenogram, and ultrasound evaluation of abdomen, pelvis, and bone scan. Patients with metastasis, atypia, claustrophobic, on prior treatment, radial scar, pregnant, using contraceptive pills, metallic implants, pacemaker, etc., and also those not willing to take part in the study, were excluded.

**TABLE 1 | Demographic details of subjects.**

<b>Breast cancer (n = 259)</b>	
Age in years [mean ± SD (range)]	45.4 ± 10.5 (19–70)
<i>Histology type</i>	
Invasive ductal carcinoma (IDC)	182
IDC with ductal carcinoma <i>in situ</i> (DCIS)	8
IDC + mucinous carcinoma	6
DCIS + cribriform type	2
Papillary carcinoma	1
Ductal adenocarcinoma	2
Lobular carcinoma	3
Medullary carcinoma	1
Neuroendocrine tumor	1
Malignant phyllodes	1
Pagets disease	1
Fibrous stroma	1
AJCC stage	
IIA	52
IIB	49
IIIA	45
III (B + C)	113
<i>Hormone receptor status</i>	
ER+	93
ER-	92
PR+	82
PR-	100
HER2+	56
HER2-	84
HER2 2+	23
Triple negative (TN)	26
Non-triple negative (nTN)	155
Triple positive (TP)	13
<b>Benign lesions (n = 67)</b>	
Age in years [mean ± SD (range)]	30 ± 9.4 (13–61)
<i>Histology type</i>	
Fibroadenoma	33
Phyllodes	8
Benign ductal epithelial cells	8
Fibrocystic fibroadenoma	8
Cysts	6
Benign proliferative breast disease	1
Fibroepithelial lesion	1
Sclerosing adenosis	1
Mastitis	1
<b>Healthy volunteers (n = 54)</b>	
Age in years [mean ± SD (range)]	30 ± 9.4 (13–61)

<sup>a</sup>Histopathology available for 209 breast cancer patients only.

## MR Imaging

MR imaging was performed using a four-channel-phased array breast matrix receiver coil at 1.5 T (Magnetom AVANTO, Siemens Healthcare Sector, Germany). Subjects were positioned with head first in prone position with each breast fitting into the cup of the coil. Following the scout images, short tau inversion recovery coronal images were acquired with repetition time (TR) and time to echo (TE) of 6940 and 58 ms, respectively; slice thickness of 3 mm; and a matrix size of 320 × 256. Also, fat-suppressed MR images were acquired in transverse and sagittal planes (TR and TE of 6270 and 102 ms, respectively; slice thickness = 3 mm with no gap; matrix size = 512 × 440). DCEMRI in the axial plane was carried out for 59 breast cancer patients using a fat-saturated

3D FLASH (fast low angle shot) sequence with the following parameters: TR and TE of 5.46 and 2.53 ms, respectively; flip angle = 12°; matrix size = 305 × 448; and slice thickness = 1.4 mm with no gap. Gadolinium-diethylene triamine pentaacetic acid (Gd-DTPA) contrast agent (0.1 mmol/kg) was injected using automatic injector at a rate of 2 ml/s followed by saline flush. One pre- followed by five post-gadolinium image series were acquired with a total acquisition time of 5.5 min (6 × 55 s).

Diffusion-weighted imaging sequence calibration was carried out using a single compartment phantom for water and acetone prepared in separate containers. The mean ADC for water and acetone were  $2.25 \pm 0.03 \times 10^{-3}$  and  $4.1 \pm 0.17 \times 10^{-3} \text{ mm}^2/\text{s}$ , respectively, which were in agreement with the literature (12). Reproducibility of ADC measurements were checked with repeated measurements, and the coefficient of variance (COV) were within 1 and 4% of error limit for water and acetone, respectively. DW images were acquired in the transverse plane covering both the breasts using a single shot echo-planar imaging sequence with the diffusion gradients applied along the orthogonal direction concurrently to reduce motion artifacts (10). The parameters used for DWI were  $b = 0, 500$ , and  $1000 \text{ s/mm}^2$ ; TR = 5000 ms; TE = 87 ms; FOV = 250–350 mm; NSA = 1; EPI factor = 128; acquisition matrix = 128 × 128; and slice thickness = 4–5 mm without any inter slice gap. The total acquisition time was 42 s. A minimum of two  $b$  values are necessary for the measurement of ADC; however, the curve fitting with more than two  $b$  values reduces the error in ADC estimation by linear regression method; hence, DWI scan with three  $b$  values was acquired.

## ADC Measurement

Mean ADC values were calculated using an ADC map and by drawing contiguous circular ROIs of five pixels (size = 0.49 cm<sup>2</sup>) on the lesion (malignant and benign lesions) from each patient and from the entire healthy breast tissue in volunteers. For ADC calculation, the mean number of ROIs used for malignant cases was 20 (range 2–137), 19 (range 2–75) for benign cases, and 36 (range 8–163) for healthy volunteers.

## Tumor Volume Measurement

The tumor volume was measured from MR images by a perimeter method using the formula: volume = ST ( $A_1 + A_2, \dots, A_n$ ), where ST is the slice thickness and  $A$  is the area of the tumor (20). The subtracted axial dynamic images were used for volume calculation, while sagittal (T2 fat-saturated) images were used in patients for whom DCEMRI could not be carried out. All slices (with no inter slice gap) in which the tumor was seen were used for volume calculation using free hand ROIs. In six malignant lesions of infiltrating ductal carcinoma (IDC) type, ROIs were drawn twice to find out intra-individual variation, which was later verified by another co-author (Uma Sharma). The difference between the COV of the two measurements (inter-individual) was 0.001, and 95% confidence intervals of the difference (CI) was –1.633 to –1.341, indicating that there was no significant variation between the two measurements. The inter-observer agreement was assessed using intraclass correlation coefficient (ICC). The ICC was 0.99, indicating better reproducibility of volume measurements by two different observers.

## Statistical Analysis

One-way analysis of variance (ANOVA) followed by Bonferroni *post hoc* correction was used for comparisons of mean ADC among malignant, benign, and healthy breast tissues. Further, comparison of mean ADC values was also carried out using the analysis of covariance (ANCOVA), considering age as a covariate since mean age was significantly different among the three groups. Receiver operating curve (ROC) analysis was used to obtain cutoff values of mean ADC for the differentiation of malignant, benign, and healthy breast tissues. The sensitivity and specificity of ADC were also calculated. Student's *t*-test was used to compare the age (years), mean ADC, and tumor volume between patients with positive and negative hormonal receptor status. ANOVA with Bonferroni *post hoc* correction was used for comparisons of mean ADC and tumor volume among various tumor stages. A *P*-value of  $\leq 0.05$  was considered significant. All statistical analyses were carried out using statistical software SPSS 19.0.

## RESULTS

**Figure 1** shows the T2-weighted MR image of (A) a 28-year-old patient with IDC; (B) a 25-year-old patient with benign fibroadenoma; and (C) that from a 30-year-old normal healthy volunteer. The DWI images obtained for malignant, benign, and healthy breast tissues are shown in **Figures 1D–F**, while the respective ADC maps obtained are shown in **Figures 1G–I**. **Figure 2A** shows the representative DCE image of a 56-year-old locally advanced breast cancer (LABC) patient with IDC, and the corresponding Type III curve obtained from the ROI positioned in the lesion is shown in **Figure 2B**. T2-weighted image and the ADC map of the same patient are shown for comparison in **Figures 2C,D**. The malignant lesion was hypointense compared to the surrounding tissue on T2-weighted image, while on DCE image, the lesion was hyperintense. The time intensity curve showed a washout pattern, which was indicative of malignancy. In addition, on ADC map, the lesion was hypointense, suggestive of restricted diffusion.

## Differentiation of Malignant, Benign Lesions, and Healthy Breast Tissues

The mean ADC of malignant lesions was significantly lower ( $1.02 \pm 0.17 \times 10^{-3} \text{ mm}^2/\text{s}$ ) compared to benign ( $1.57 \pm 0.26 \times 10^{-3} \text{ mm}^2/\text{s}$ ) and healthy ( $1.78 \pm 0.13 \times 10^{-3} \text{ mm}^2/\text{s}$ ) breast tissues (**Table 2**; **Figure 1**). Also, a significant difference in the age-adjusted ADC of malignant compared to benign and healthy breast tissues of volunteers was obtained (**Table 2**). The ADC of various histological types of malignant lesions was similar as shown in **Table 3**. A comparison of ADC among various benign lesions showed that the ADC was significantly lower in fibroadenomas compared to fibrocystic with fibroadenoma and cystic lesions ( $P < 0.05$ ; **Table 4**). Further, the ADC of benign ductal epithelial was also significantly lower compared to fibrocystic with fibroadenoma and cystic lesions ( $P < 0.05$ ; **Table 4**).

Using ROC analysis, a cutoff value of  $1.23 \times 10^{-3} \text{ mm}^2/\text{s}$  [sensitivity of 92.5%; specificity of 91.1% and area under the curve (AUC) of 0.96] was determined to differentiate malignant from benign breast tissues (**Table 2**).

Furthermore, utility of ADC as an aid in the diagnosis of malignancy in patients with indeterminate DCE findings was evaluated in 59 patients with malignant lesions. Of these, 49 lesions showed a Type III washout curve indicating malignancy, while 9 showed Type II curve, and 1 patient showed Type I curve, suggestive of indeterminate DCE findings (**Table 5**). However, their ADC values were below the cutoff value ( $1.23 \times 10^{-3} \text{ mm}^2/\text{s}$ ). Three patients with IDC demonstrated an ADC that was above the cutoff value with a Type III curve on DCEMRI, indicating the false-negative finding (**Table 5**).

## Comparison of ADC, Volume, and Age in Malignant Tumors Classified Based on the Stage, Menopausal, and Hormonal Receptor Status

Significant difference in tumor volume was seen, while there was no significant difference in the mean ADC of tumors with different AJCC stages (**Table 6**). Also, ADC and the tumor volume were significantly higher in LABC patients compared to those with early breast cancer patients (EBC;  $P < 0.05$ ; **Table 6**).

Our data further showed that patients who were negative for all receptors, i.e., patients with triple negative (TN) status were of younger age, had a larger tumor volume and a higher ADC value compared to those with non-triple negative (nTN), ER+, and PR+ status. Also, ER- patients showed a larger tumor volume and were of younger age group compared to those with ER+ status (**Table 6**). The tumor volume of 13 triple positive (TP) patients (positive for all three receptors, i.e., ER+, PR+, and HER2+) was significantly lower than the TN patients, while there was no significant difference in patients' age and mean ADC value between these two groups. No association was seen between ADC, tumor volume, and the menopausal status of patients (see **Table 6**).

## DISCUSSION

Metabolic reprogramming is an important area of research that combines numerous aspects of metabolic adaptation associated with the cancer proliferation. Cancer cells upregulate their metabolism to meet their biosynthetic demands to facilitate the uncontrolled cell replication, leading to changes in the tissue characteristics and the microenvironment, and these could be monitored using DWI. Due to its potential to improve the characterization and diagnosis of breast lesions, DWI is increasingly being included in breast MRI protocols. The present study investigated its potential in the characterization of breast lesions and its association with prognostic factors, such as tumor stage and hormonal receptor status, in a large cohort of subjects. Our data showed that ADC of malignant lesions was significantly lower compared to benign lesions and healthy breast tissues of volunteers. Also, the age-adjusted ADC of healthy breast tissues was significantly higher compared to the benign breast tissues. These findings were in line with previous studies (29–34). Malignant tumors are characterized by high proliferative activity that increases the cell density and consequently restricts the diffusion of water molecules resulting in a lower ADC value (12, 29, 35). A significant relationship

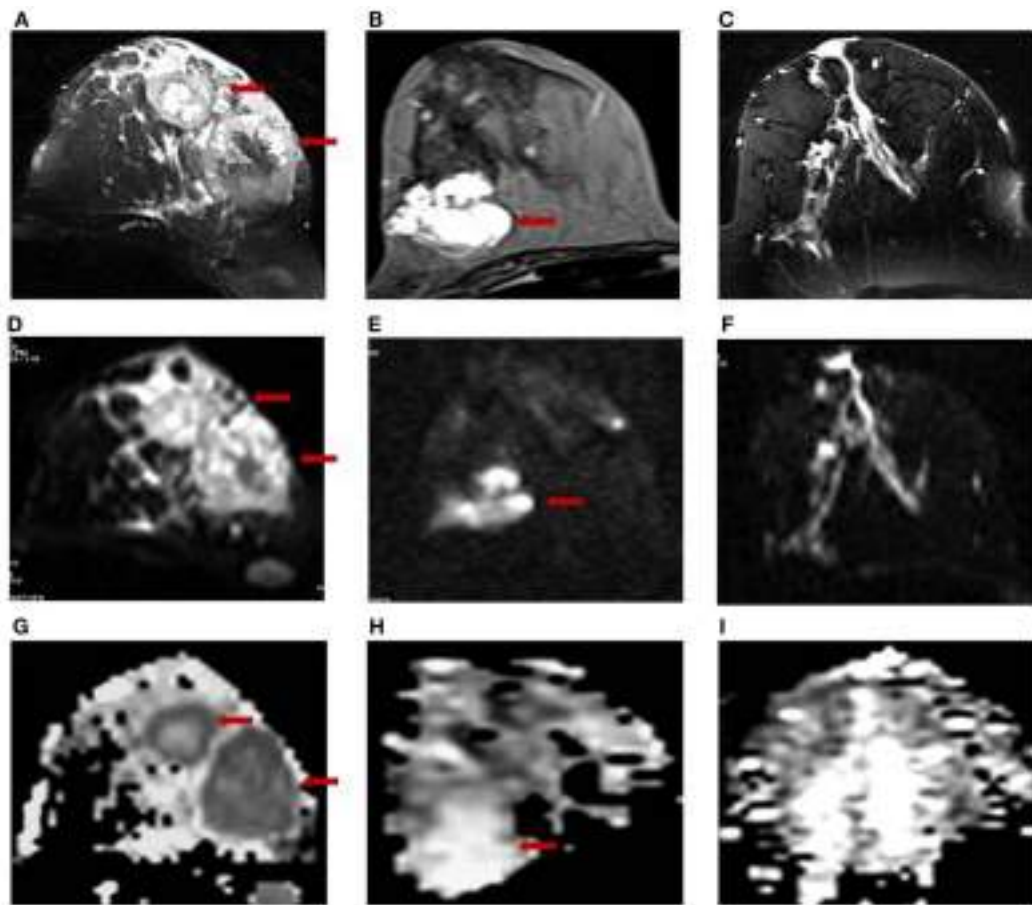


**FIGURE 1 |** T2-weighted MR images of **(A)** a 28-year-old patient with infiltrating ductal carcinoma (IDC); **(B)** a 25-year-old patient with benign fibroadenoma; and **(C)** a 30-year-old volunteer with healthy breast tissue. The respective DW images are shown in **(D–F)**, while the ADC maps obtained are shown in **(G–I)**.

has been reported between ADC and the tumor cellularity using histology (11, 18, 36, 37).

We found 12 different histological types of malignant lesions in our study cohort, which showed similar ADC values. Eight patients with IDC had components of DCIS, and the mean ADC of these lesions was similar to that of IDC lesions. This might be due to increased endoductal cellular density. Several studies have reported higher ADC in DCIS compared to IDC lesions (16, 17, 24, 25, 31, 38). Elucidation of DCIS tumors using DWI has not been consistent due to interspersed distribution of cancer cells and healthy breast parenchyma (17). Medullary invasive cancer, a rare low grade tumor, also showed a low ADC similar to IDC lesions (16, 18, 31). Further, six patients presented with mucinous carcinoma with IDC, and the mean ADC was also similar to that seen for IDC lesions. Few studies have reported a higher ADC for mucinous carcinoma compared to IDC, which has been ascribed to the presence of colloidal mucin content (18) and the relative volume of the mucin and the cellularity of lesion (17, 35). In our study, patients with invasive lobular carcinoma ( $n = 3$ ), Paget's

disease ( $n = 1$ ), fibrous stroma ( $n = 1$ ), and phyllodes ( $n = 1$ ) also showed a lower ADC, similar to that seen for IDC lesions. However, the number of patients in these histological types was less to draw any definitive conclusion.

Additionally, the ADC values were compared among the various histological types of benign lesions. Mean ADC was statistically lower in fibroadenomas and benign ductal epithelial lesions compared to fibrocystic with fibroadenoma and cystic lesions (16, 29). Cystic lesions represent a pouch filled with fluid and proteins, and therefore have less restricted water diffusion compared to that seen in fibroadenomas, which are solid lesions with relatively more cellularity. In literature, lower ADC in fibroadenoma lesions has been reported, which was attributed to the presence of fibrous component (16, 39, 40), while in our study, only one fibroadenoma and one fibrocystic with fibroadenoma lesion showed a low ADC value. Benign phyllodes, mastitis, and benign proliferative lesions showed higher ADC characteristic of benign breast disease. In contrary, a low ADC value similar to malignant tumors has been reported for mastitis (17).

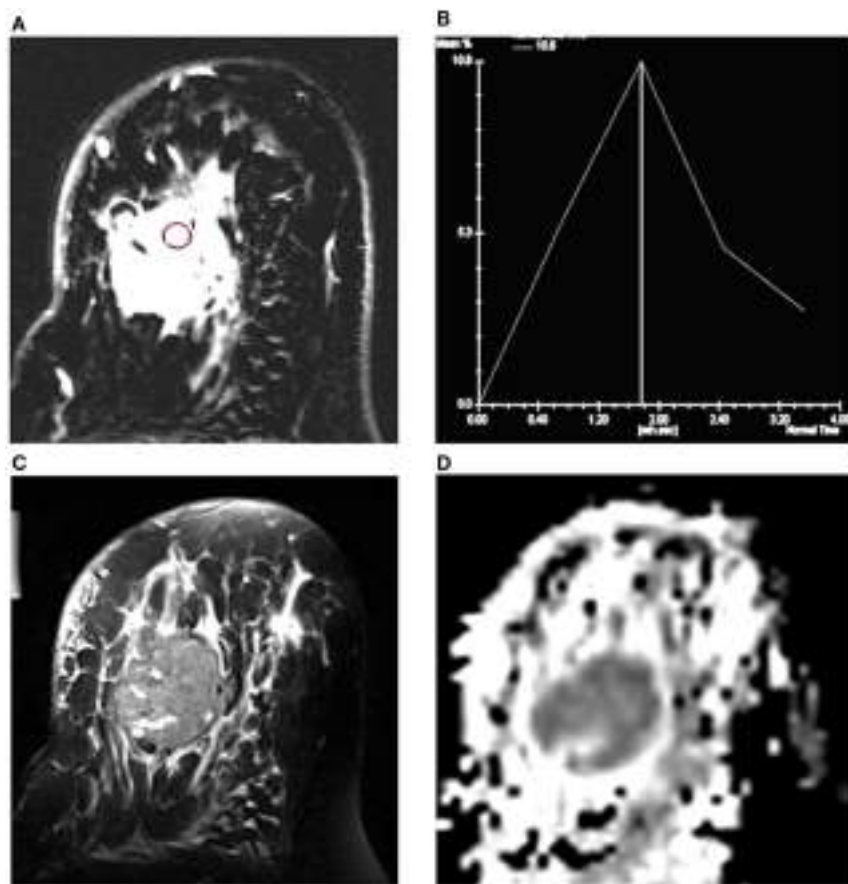


**FIGURE 2 | (A)** T1-axial DCEMR image of a 56-year-old patient with infiltrating ductal carcinoma (IDC); **(B)** Type III dynamic curve with washout pattern from the ROI shown in the lesion; **(C)** T2-weighted fat-saturated axial image; and **(D)** the ADC map of the same patient.

**TABLE 2 | Distribution of mean ADC in malignant and benign breast lesions, and healthy breast tissue of volunteers and cutoff ADC values using ROC analysis.**

	Malignant (n = 259)	Benign (n = 67)	Healthy volunteers (n = 54)
ADC ( $\times 10^{-3}$ mm $^2$ /s) (mean $\pm$ SD)	1.02 $\pm$ 0.17	1.57 $\pm$ 0.26*	1.78 $\pm$ 0.13**
<b>ANCOVA</b>			
ADC ( $\times 10^{-3}$ mm $^2$ /s)	1.06 (1.04, 1.09)	1.61 (1.55, 1.68)*	1.83 (1.76, 1.89)**
Adjusted mean (95% CI)*			
Malignant vs. benign	Malignant vs. healthy volunteers	Benign vs. healthy volunteers	
Difference between means (95% CI)	0.55 (0.55, 0.56)	0.76 (0.76, 0.77)	0.21 (0.21, 0.22)
<b>ROC analysis and ADC cutoff</b>			
Malignant vs. benign	1.23 (sensitivity 92.5%; specificity 91.1%; AUC 0.96)		
Malignant vs. healthy	1.43 (sensitivity 100%; specificity 98.1%; AUC 0.99)		
Healthy vs. benign	1.69 (sensitivity 75.9%; specificity 74.6%; AUC 0.79)		

\*Adjusted for age.

\*Denotes P < 0.05 between benign vs. malignant; malignant vs. healthy volunteers.

\*\*Denotes P < 0.05 between benign vs. healthy volunteers.

With the availability of ADC values from a large cohort of malignant, benign, and healthy breast tissues, we determined a cutoff value of mean ADC using ROC curves to predict malignancy. A cutoff value of  $1.23 \times 10^{-3}$  mm $^2$ /s was obtained to differentiate malignant from benign disease, which was similar to that reported previously (20, 30, 31, 41). However, a few studies have reported a higher cutoff, which may be due to the variability in experimental parameters used such as low b values (14, 16). Further, a meta-analysis of 13 studies that included 615 malignant and 349 benign lesions reported a sensitivity of 84% and a specificity of 79% with area under the curve (AUC) of 0.90 for ADC to differentiate between benign and malignant lesions. The sensitivity and the specificity calculated in this meta-analysis were lower than that seen in the present study (32). This was attributed to the variation in methodology and the b values used across studies (32). At low b values (<200 s/mm $^2$ ), the effect of perfusion is more, while at high b values, pure diffusion component would dominate the measured signal (42). The b values used by us emphasize on minimizing the perfusion and T2 shine-through effect. Also, a cutoff value of  $1.43 \times 10^{-3}$  mm $^2$ /s (sensitivity 100%; specificity 98.1%) was obtained to discriminate malignant from healthy breast tissue, which was similar to our earlier observation (20).

**TABLE 3 | Distribution of mean ADC, volume, and age in various histological types of breast cancer patients (*n* = 209).**

Malignant lesions (histological types)	Number ( <i>n</i> )	Age (years) (mean ± SD)	ADC (×10 <sup>-3</sup> mm <sup>2</sup> /s) (mean ± SD)	Volume (cm <sup>3</sup> ) (mean ± SD)
IDC	182	45.4 ± 10.2	1.00 ± 0.16	78.5 ± 89.7
IDC + DCIS	8	43.6 ± 12.9	1.05 ± 0.15	41.3 ± 25.9
IDC + mucinous (or colloid)	6	42.2 ± 19.2	1.05 ± 0.17	59.3 ± 64.0
Papillary	1	53	1.01	29.0
Lobular	3	53.6 ± 7.5	0.96 ± 0.09	73.4 ± 76.7
Ductal adenocarcinoma	2	51.5 ± 9.9	0.91 ± 0.19	42.9 ± 28.2
DCIS + cribriform	2	35.4 ± 14.4	0.97	31.9 ± 19.6
Neuroendocrine	1	65	0.99	15.5
Fibrous stroma	1	53	0.94	29.1
Malignant phyllodes	1	50	1.02	23.5
Paget disease	1	40	0.99	7.2
Medullary	1	57	1.08	30.6
Total	209			

**TABLE 4 | Distribution of mean ADC values and age in various histological types of benign breast lesions.**

Benign lesions	Number ( <i>n</i> )	Age (mean ± SD)	ADC (×10 <sup>-3</sup> mm <sup>2</sup> /s) (mean ± SD)
Fibroadenomas (FA)	33	29.1 ± 10.1	1.48 ± 0.17*
Benign ductal epithelial	8	30.9 ± 7.5	1.42 ± 0.18*
Benign phyllodes	8	31.3 ± 12.7	1.73 ± 0.25
Fibrocystic with FA	8	29.8 ± 4.4	1.80 ± 0.31* <sup>†</sup>
Cyst	6	33.5 ± 11.5	1.80 ± 0.30* <sup>†</sup>
Sclerosing adenosis	1	29	1.18
Mastitis	1	34	1.44
Fibroepithelial	1	32	1.66
Benign proliferative	1	20	1.79
Total	67		

\**P* < 0.05 between fibroadenoma and fibrocystic disease with FA and cyst.

†*P* < 0.05 between benign ductal epithelial cells and fibrocystic disease with FA and cyst.

Further, we compared the DCEMRI kinetics and the ADC data in detecting malignancy in 59 breast cancer patients. Of the 59 lesions in these patients, 49 showed washout curve (Type III), which was characteristic of malignancy, while 10 showed indeterminate curves [Type I (*n* = 1) and Type II (*n* = 9)]. However, the ADC values obtained in these 10 lesions were below the cutoff value ( $1.23 \times 10^{-3}$  mm<sup>2</sup>/s), indicative of positive for malignancy. Of these 10 lesions, 8 were IDC, 1 was DCIS + cribriform, and the other 1 was papilloma. Kuhl et al. also have reported DCE kinetics to be inconsistent for diagnosis of DCIS lesions (8). Thus, our findings demonstrated that addition of DWI increases the sensitivity and the diagnostic accuracy of breast cancer (17, 26, 30, 43). Also, DWI has a significant advantage over DCEMRI as diffusion is highly sensitive to changes in the cellular environment, and there is no need to use contrast agent (17). Additionally, DWI has a short scan time. It has also been reported that DWI of breast in combination with T2-weighted imaging has the potential to improve the specificity of breast cancer diagnosis (17). However in our study, three IDC patients with AJCC stage III A and with Type III curve showed an ADC value which was above the cutoff, which may be attributed to the intermingling necrotic cores seen in such large sized tumors (44).

Further, the association among ADC, age, hormonal receptor status, tumor volume, stage, and the menopausal status of patients was investigated. Tumor volume and ADC showed no association with the menopausal status. The tumor volume was significantly different among various AJCC stage tumors, while ADC was not significantly different. LABC patients had a higher ADC and a larger tumor volume compared to EBC patients. Correlation between ADC and the histologically determined tumor size has been reported (36). Higher ADC in large sized tumors may be related to the formation of intermingling necrotic regions due to non-uniform supply of nutrients in fast growing tumors. It is well recognized that by upregulating their metabolism, cancer cells eventually grow into a tumor mass, and further growth requires abundance of nutrients to support biosynthesis of nucleic acids, proteins, and lipids essential for replication. However, the nutrient supply for cancer cells varies across the tumor mass, and the cells on the surface of the tumor may get more nutrients and continue replicating, but cells at the central regions may die due to limited availability of nutrients (45, 46). Further, the gradients in nutrient availability in different regions of the tumor are an outcome of altered metabolic pathways such as glucose metabolism, glutamine synthesis, and oxygen availability (47). Thus, there will be lack of uniform availability of nutrient material affecting the metabolic activity and the viability of tumor cells. This eventually would lead to a heterogeneous mixture of dead, quiescent, and mitotic cells in large sized tumors, which is reflected in parameters such as ADC and tCho concentration determined by functional MR techniques. It was documented that ADC reflects the relative necrotic content of tumors as relative volume fraction of water in the extracellular space is increased due to cell death, leading to higher ADC (48). Further, EBC had a higher tCho concentration compared to LABC, indicating more necrotic cores in LABC (49). In an earlier study, ADC was used to delineate necrotic and viable regions using DWI in patients who cannot afford the cost of contrast (44). In the calculation of ADC, the visible hyperintense necrotic areas were avoided; however, there is a possibility that intermingling micro-sized necrotic regions might have been included in the ROIs, especially in large tumors, which might have led to higher ADC seen in LABC patients.

Triple-negative cancers showed a higher ADC compared to nTN cancers, which is in agreement with the findings of Youk et al.

**TABLE 5 | ADC value, histology, stage, volume, and BIRADS of breast cancer patients who showed Type I or II curve on DCEMRI and those patients who showed ADC above the cutoff value.**

Patient no.	Histology	Curve type	ADC ( $\times 10^{-3}$ mm $^2$ /s)	Tumor volume (cm $^3$ )	AJCC stage	BIRADS
1.	IDC	Type I	1.09	77.92	IIB	5
2.	IDC	Type II	1.16	117.6	IIB	5
3.	DCIS + cribriform	Type II	0.97	45.85	IIB	5
4.	IDC	Type II	0.95	2.38	IIIA	4b
5.	IDC	Type II	0.98	78.34	IIB	4
6.	IDC	Type II	1.08	5.26	IIIA	6
7.	Papillary carcinoma	Type II	1.02	29.06	IIB	5
8.	IDC	Type II	0.98	59.82	IIA	3
9.	IDC	Type II	0.97	29.35	IIIB + C	4
10.	IDC	Type II	0.92	44.92	IIIA	4
Breast cancer patients with Type III curve but mean ADC above cutoff						
1.	IDC	Type III	1.31	54.52	IIIA	5
2.	IDC	Type III	1.24	41.43	IIIA	5
3.	IDC	Type III	1.28	160.27	IIIA	5

**TABLE 6 | Distribution of mean ADC, age, and volume in various subgroups of breast cancer patients based on tumor stage, menopausal, and hormonal biomarker status.**

Groups	Number (n)	Age (years) (mean $\pm$ SD)	ADC ( $\times 10^{-3}$ mm $^2$ /s) (mean $\pm$ SD)	Volume (cm $^3$ ) (mean $\pm$ SD)
Premenopausal (Pre)	119	36.4 $\pm$ 5.9 <sup>§</sup>	1.02 $\pm$ 0.18	78.50 $\pm$ 80.60
Postmenopausal (Post)	140	53.0 $\pm$ 7.5 <sup>§</sup>	1.02 $\pm$ 0.17	70.45 $\pm$ 87.33
EBC	52	46.7 $\pm$ 11.9	0.98 $\pm$ 0.18 <sup>®</sup>	17.67 $\pm$ 19.12 <sup>§</sup>
LABC	207	45.0 $\pm$ 10.4	1.03 $\pm$ 0.17 <sup>®</sup>	88.17 $\pm$ 88.26 <sup>§</sup>
Stage IIA	52	46.7 $\pm$ 11.9	0.98 $\pm$ 0.18	17.67 $\pm$ 19.12 <sup>*</sup>
Stage IIB	49	43.8 $\pm$ 10.4	0.98 $\pm$ 0.12	49.34 $\pm$ 51.74 <sup>*</sup>
Stage IIIA	45	46.0 $\pm$ 9.2	1.05 $\pm$ 0.20	82.23 $\pm$ 70.04 <sup>*</sup>
Stage III (B + C)	113	45.2 $\pm$ 10.9	1.04 $\pm$ 0.17	107.21 $\pm$ 101.02 <sup>*</sup>
HER2+	56	44.7 $\pm$ 10.3	1.03 $\pm$ 0.16	94.60 $\pm$ 93.27
HER2-	84	45.1 $\pm$ 11.1	1.02 $\pm$ 0.15	84.47 $\pm$ 83.74
ER+	93	47.8 $\pm$ 10.8 <sup>®</sup>	0.99 $\pm$ 0.14	54.57 $\pm$ 50.62 <sup>§</sup>
ER-	92	43.4 $\pm$ 10.5 <sup>®</sup>	1.02 $\pm$ 0.16	97.72 $\pm$ 104.94 <sup>®</sup>
PR+	82	46.9 $\pm$ 11.4	1.00 $\pm$ 0.14	64.81 $\pm$ 61.74 <sup>†</sup>
PR-	100	44.4 $\pm$ 10.2	1.02 $\pm$ 0.16	86.71 $\pm$ 100.29 <sup>†</sup>
Triple-negative (TN)	26	40.9 $\pm$ 9.9 <sup>+</sup>	1.07 $\pm$ 0.19 <sup>#</sup>	111.21 $\pm$ 116.34 <sup>¥</sup>
Triple-positive (TP)	13	42.8 $\pm$ 12.2	1.01 $\pm$ 0.16	61.19 $\pm$ 69.51 <sup>¥</sup>
Non-triple-negative (nTN)	155	46.4 $\pm$ 10.8 <sup>+</sup>	1.00 $\pm$ 0.14 <sup>#</sup>	69.21 $\pm$ 74.06 <sup>¥</sup>

<sup>§,®</sup>Age P < 0.05: between Pre vs. Post; <sup>®</sup>ER+ vs. ER-; <sup>+</sup>TN vs. nTN.<sup>®,#</sup>ADC P < 0.05: between EBC vs. LABC; <sup>#</sup>TN vs. nTN.<sup>§,\*,†,¥</sup>Volume P < 0.05: between EBC vs. LABC; \*stages IIA, IIB, IIIA, and III (B + C); <sup>®</sup>ER+ vs. ER-; <sup>†</sup>PR+ vs. PR-; <sup>¥</sup>TN vs. nTN and TN vs. TP.

\*Significant difference in tumor volume of different tumor stages.

(23). Also, TN cancers had a larger tumor volume compared to nTN cancers due to aggressive and high proliferative activity (23). It has been established that metabolic reprogramming of both catabolic and anabolic pathways occurs to support the survival and high proliferation of cancer cells (47). This metabolic demand is fulfilled by the overexpression of several enzymes such as pyruvate kinase and glutamine fructose 6-phosphate transaminase (50). Higher glutamine utilization compared to other breast cancer types has been reported in TN cancers, indicating higher energy demand for cell proliferation (51). Further, lipid reprogramming with upregulation of genes involved in lipid biosynthesis has also been reported to be an important hallmark of cancer development and progression (52). However, TN cancers had lower concentration of tCho (membrane metabolites) compared to that seen in nTN and TP cancers (51). This observation indicates

the presence of intermingling necrotic cores in large sized TN cancers and the molecular heterogeneity of breast lesions (51). It was reported that 56% of TN cancers showed intratumoral necrosis (23) and frequent rim enhancement, suggestive of high angiogenesis in the periphery of the tumor, central necrosis, and fibrosis (53). Additionally, the TN group consisted of younger and premenopausal women as reported in literature (54, 55).

Further, our results revealed that ER- cancers had a larger volume and were of younger age compared to ER+ cancers (56, 57). Higher proliferative activity (58) and higher micro-vessel density associated with a larger volume (59) has been documented in ER- cancers. Studies have reported lower ADC in ER+ compared to ER- cancers (25, 42, 56, 60), while the value was similar for these cancers in our study. PR+ showed a lower ADC compared to PR- cancers (25, 61), while a higher ADC has been reported

in HER2+ cancers (53, 56, 60, 62). In the present study, there was no significant difference in ADC of HER2+ and PR+ compared to HER2- and PR- cancers. Many studies showed no association of ADC with the hormonal receptor status (22, 24, 63, 64). Thus, variable findings are seen in literature on the association of hormonal receptor status with the ADC values in breast cancer patients.

Several factors may be responsible for such variable findings in the ADC values and its association with the hormonal status of breast cancer patients. First, it may represent the heterogeneous nature of breast cancers, which may be related to the biological behavior of cancers in relation to the expression of various receptors. Inhibition of angiogenic pathway due to estrogen hormone has been reported in ER+ cancers, which may decrease the perfusion in ER+ cancers (22, 65). Recently, Cho et al. reported that higher ADC in ER- cancers may be related to the tumor vascularity and perfusion using intravoxel incoherent motion imaging (42). Hyder et al. have shown that progesterone may increase the angiogenesis through regulation of VEGF in breast cancer (66). Association between angiogenesis and HER2 expression has also been described (67, 68). These findings indicated that positive ER expression was associated with the inhibition of angiogenesis, while positive PR and HER2 expression was associated with the enhancement of angiogenesis. Thus, there is a need to take into account the expression status of all the three receptors while interpreting the ADC and the tumor volume data.

Additionally, the variability in results across studies might also be due to the differences in the tumor size and variations in terms of experimental procedures used such as selection of *b*-value, choice of imaging sequence, and the method used for measurement of ADC. In our study, the mean ADC calculation was carried out by drawing small circular ROIs encompassing the entire visible tumor on a slice that showed the largest tumor area but avoiding necrotic areas. However, most studies in the literature have drawn either single or only few ROIs and have reported mean ADC (24, 60, 62). The methodology adopted by us, though time consuming, may provide a more accurate determination of the ADC and tumor heterogeneity. Arponent et al. also demonstrated that ADC measurements using small ROI were more accurate than whole region ROI (61).

In spite of the clinical potential of DWI, the study has some limitations. First, the sample size was small for some histological

types to arrive at definitive conclusions and thus warrant further investigation in a large cohort. Second, multicenter studies with standardized DWI protocol across various laboratories with an appropriate algorithm are required for consistent results in ADC measurement. Third, due to poor socioeconomic status, DCEMRI could not be carried out in all patients.

## CONCLUSION

The present study on a relatively large cohort of subjects demonstrated that a low ADC value is indicative of malignancy. The sensitivity and specificity calculated from the present data indicated that ADC is a sensitive parameter for the differentiation of malignant, benign, and healthy breast tissues in a short scan time. Further, the changes seen in ADC with various hormonal receptors show its dependence on the biological features of different tumor subtypes, stage, etc. Moreover, the functional MR imaging techniques, such as quantitative DWI, provide an insight into metabolic reprogramming and the heterogeneity of breast cancers. Also, the MR imaging features of various molecular subtypes of breast cancer may aid in appropriate incorporation of non-invasive approaches for molecular characterization of breast cancer, which would be useful in treatment planning and patient management.

## AUTHOR CONTRIBUTIONS

NRJ and US conceived the hypothesis and NRJ, US, RP, and VS designed the experiments. RP and VS recruited patients and carried out clinical work-up, while SM carried out histopathological evaluation and SH helped with DCEMRI data. RS and KA performed MR experiments. RS, US, KA, and NRJ analyzed and interpreted the data. US and NRJ wrote the manuscript that was reviewed by all authors and approved.

## ACKNOWLEDGMENTS

We thank Drs. Gensicke Henrik and Chris d'Esterre for critical reading of the manuscript and for many useful corrections. The Department of Science and Technology, Government of India, is acknowledged for financial support (SP/SO/HS-80/2006 and SR/SO/HS/213/2012) and J.C. Bose Fellowship to NRJ. KA acknowledges the Indian Council of Medical Research, New Delhi, for Senior Research Fellowship [3/2/241/2014/NCD-III (OPA-31710)].

## REFERENCES

- Sørlie T, Perou CM, Tibshirani R, Aas T, Geisler S, Johnsen H, et al. Gene expression patterns of breast carcinomas distinguish tumor subclasses with clinical implications. *Proc Natl Acad Sci U S A* (2001) **98**:10869–74. doi:10.1073/pnas.191367098
- Makkat S, Luypaert R, Stadnik T, Bourgoin C, Sourbron S, Dujardin M, et al. Deconvolution-based dynamic contrast-enhanced MR imaging of breast tumors: correlation of tumor blood flow with human epidermal growth factor receptor 2 status and clinicopathologic findings – preliminary results. *Radiology* (2008) **249**:471–82. doi:10.1148/radiol.2492071147
- Bauer KR, Brown M, Cress RD, Parise CA, Caggiano V. Descriptive analysis of estrogen receptor (ER)-negative, progesterone receptor (PR)-negative, and HER2-negative invasive breast cancer, the so-called triple-negative phenotype: a population-based study from the California Cancer Registry. *Cancer* (2007) **109**:1721–8. doi:10.1002/cncr.22618
- Kerlikowske K, Grady D, Barclay J, Sickles EA, Ernster V. Effect of age, breast density, and family history on the sensitivity of first screening mammography. *JAMA* (1996) **276**:33–8. doi:10.1001/jama.276.1.33
- Kolb TM, Lichy J, Newhouse JH. Comparison of the performance of screening mammography, physical examination, and breast US and evaluation of factors that influence them: an analysis of 27,825 patient evaluations. *Radiology* (2002) **225**:165–75. doi:10.1148/radiol.2251011667
- Evans A. The diagnosis and management of pre-invasive breast disease: radiological diagnosis. *Breast Cancer Res* (2003) **5**:250–3. doi:10.1186/bcr621
- Argus A, Mahoney MC. Clinical indications for breast MRI. *Appl Radiol* (2010) **39**:10–9.

8. Kuhl C. The current status of breast MR imaging. Part I. Choice of technique, image interpretation, diagnostic accuracy, and transfer to clinical practice. *Radiology* (2007) **244**:356–78. doi:10.1148/radiol.2442051620
9. Pediconi F, Catalano C, Occhiali R, Venditti F, Fraioli F, Napoli A, et al. Breast lesion detection and characterization at contrast-enhanced MR mammography: gadobenate dimeglumine versus gadopentetate dimeglumine. *Radiology* (2005) **237**:45–56. doi:10.1148/radiol.2371041369
10. Issa B. In vivo measurement of the apparent diffusion coefficient in healthy and malignant prostatic tissues using echo-planar imaging. *J Magn Reson Imaging* (2002) **16**:196–200. doi:10.1002/jmri.10139
11. Kono K, Inoue Y, Nakayama K, Shakudo M, Morino M, Ohata K, et al. The role of diffusion weighted imaging in patients with brain tumors. *AJNR Am J Neuroradiol* (2001) **22**:1081–8.
12. Guo Y, Cai YQ, Cai ZL, Gao YG, An NY, Ma L, et al. Differentiation of clinically benign and malignant breast lesions using diffusion-weighted imaging. *J Magn Reson Imaging* (2002) **16**:172–8. doi:10.1002/jmri.10140
13. Le Bihan D. *Magnetic Resonance Imaging of Diffusion and Perfusion: Applications to Functional Imaging*. New York: Lippincott-Raven Press (1995).
14. Razek AA. Diffusion-weighted magnetic resonance imaging of head and neck. *J Comput Assist Tomogr* (2010) **34**:808–15. doi:10.1097/RCT.0b013e3181f01796
15. Anderson AW, Xie J, Pizzonia J, Bronen RA, Spencer DD, Gore JC. Effects of cell volume fraction changes on apparent diffusion in human cells. *Magn Reson Imaging* (2000) **18**:689–95. doi:10.1016/S0730-725X(00)00147-8
16. Woodhams R, Matsunaga K, Kan S, Hata H, Ozaki M, Iwabuchi K, et al. ADC mapping of benign and malignant breast tumors. *Magn Reson Med Sci* (2005) **4**:35–42. doi:10.2463/mrms.4.35
17. Woodhams R, Ramadan S, Stanwell P, Sakamoto S, Hata H, Ozaki M, et al. Diffusion-weighted imaging of the breast: principles and clinical applications. *Radiographics* (2011) **31**:1059–84. doi:10.1148/rg.314105160
18. Hatakenaka M, Soeda H, Yabuuchi H, Matsuo Y, Kamitani T, Oda Y, et al. Apparent diffusion coefficients of breast tumors: clinical application. *Magn Reson Med Sci* (2008) **7**:23–9. doi:10.2463/mrms.7.23
19. Pickles MD, Gibbs P, Lowry M, Turnbull LW. Diffusion changes precede size reduction in neoadjuvant treatment of breast cancer. *Magn Reson Imaging* (2006) **24**:843–7. doi:10.1016/j.mri.2005.11.005
20. Sharma U, Danishad KK, Seenu V, Jagannathan NR. Longitudinal study of the assessment by MRI and diffusion-weighted imaging of tumor response in patients with locally advanced breast cancer undergoing neoadjuvant chemotherapy. *NMR Biomed* (2009) **22**:104–13. doi:10.1002/nbm.1245
21. Matsabayashi RN, Fujii T, Yasumori K, Muranaka T, Momosaki S. Apparent diffusion coefficient in invasive ductal breast carcinoma: correlation with detailed histologic features and the enhancement ratio on dynamic contrast-enhanced MR images. *J Oncol* (2010). doi:10.1155/2010/821048
22. Kim SH, Cha ES, Kim HS, Kang BJ, Choi JJ, Jung JH, et al. Diffusion-weighted imaging of breast cancer: correlation of the apparent diffusion coefficient value with prognostic factors. *J Magn Reson Imaging* (2009) **30**:615–20. doi:10.1002/jmri.21884
23. Youk JH, Son EJ, Chung J, Kim JA, Kim EK. Triple-negative invasive breast cancer on dynamic contrast-enhanced and diffusion-weighted MR imaging: comparison with other breast cancer subtypes. *Eur Radiol* (2012) **22**:1724–34. doi:10.1007/s00330-012-2425-2
24. Nakajo M, Kajiyama Y, Kaneko T, Kaneko Y, Takasaki T, Tani A, et al. FDG PET/CT and diffusion-weighted imaging for breast cancer: prognostic value of maximum standardized uptake values and apparent diffusion coefficient values of the primary lesion. *Eur J Nucl Med Mol Imaging* (2010) **37**:2011–20. doi:10.1007/s00259-010-1529-7
25. Choi SY, Chang YW, Park HJ, Kim HJ, Hong SS, Seo DY. Correlation of the apparent diffusion coefficient values on diffusion-weighted imaging with prognostic factors for breast cancer. *Br J Radiol* (2012) **85**:474–9. doi:10.1259/bjrad.79381464
26. Park MJ, Cha ES, Kang BJ, Ihn YK, Baik JH. The role of diffusion-weighted imaging and the apparent diffusion coefficient (ADC) values for breast tumors. *Korean J Radiol* (2007) **8**:390–6. doi:10.3348/kjr.2007.8.5.390
27. Kul S, Cansu A, Alhan E, Dinc H, Gunes G, Reis A. Contribution of diffusion-weighted imaging to dynamic contrast-enhanced MRI in the characterization of breast tumors. *AJR Am J Roentgenol* (2011) **196**:210–7. doi:10.2214/AJR.10.4258
28. Wolff AC, Hammond ME, Schwartz JN, Hagerty KL, Allred DC, Cote RJ, et al. American Society of Clinical Oncology/College of American Pathologists guideline recommendations for human epidermal growth factor receptor 2 testing in breast cancer. *J Clin Oncol* (2007) **25**:118–45. doi:10.1200/JCO.2006.09.2775
29. Sinha S, Lucas-Quesoda FA, Sinha U, DeBruhl N, Bassett LW. *In vivo* diffusion weighted MRI of the breast: potential for lesion characterization. *J Magn Reson Imaging* (2002) **15**:693–704. doi:10.1002/jmri.10116
30. Rubesova E, Grell AS, De Maertelaer V, Metens T, Chao SL, Lemort M. Quantitative diffusion imaging in breast cancer: a clinical prospective study. *J Magn Reson Imaging* (2006) **24**:319–24. doi:10.1002/jmri.20643
31. Marin C, Iacconi C, Giannelli M, Cilotti A, Moretti M, Bartolozzi C. Quantitative diffusion-weighted MR imaging in the differential diagnosis of breast lesion. *Eur Radiol* (2007) **17**:2646–55. doi:10.1007/s00330-007-0621-2
32. Chen X, Li WL, Zhang YL, Wu Q, Guo YM, Bai ZL. Meta-analysis of quantitative diffusion-weighted MR imaging in the differential diagnosis of breast lesions. *BMC Cancer* (2010) **10**:693. doi:10.1186/1471-2407-10-693
33. Immura T, Isomoto I, Sueyoshi E, Yano H, Uga T, Abe K, et al. Diagnostic performance of ADC for non-mass-like breast lesions on MR imaging. *Magn Reson Med Sci* (2010) **9**:217–25. doi:10.2463/mrms.9.217
34. Partridge SC, Singer L, Sun R, Wilmes LJ, Klifa CS, Lehman CD, et al. Diffusion-weighted MRI: influence of intravoxel fat signal and breast density on breast tumor conspicuity and apparent diffusion coefficient measurements. *Magn Reson Imaging* (2011) **29**:1215–21. doi:10.1016/j.mri.2011.07.024
35. Woodhams R, Kakita S, Hata H, Iwabuchi K, Umeoka S, Mountford CE, et al. Diffusion-weighted imaging of mucinous carcinoma of the breast: evaluation of apparent diffusion coefficient and signal intensity in correlation with histologic findings. *AJR Am J Roentgenol* (2009) **193**:260–6. doi:10.2214/AJR.08.1670
36. Sugahara T, Korogi Y, Kochi M, Ikushima I, Shigematsu Y, Hirai T, et al. Usefulness of diffusion-weighted MRI with echo-planar technique in the evaluation of cellularity in gliomas. *J Magn Reson Imaging* (1999) **9**:53–60. doi:10.1002/(SICI)1522-2586(199901)9:1<53::AID-JMRI7>3.0.CO;2-2
37. Nonomura Y, Yasumoto M, Yoshimura R, Haraguchi K, Ito S, Akashi T, et al. Relationship between bone marrow cellularity and apparent diffusion coefficient. *J Magn Reson Imaging* (2001) **13**:757–60. doi:10.1002/jmri.1105
38. Tozaki M, Fukuma E. <sup>1</sup>H MR spectroscopy and diffusion-weighted imaging of the breast: are they useful tools for characterizing breast lesions before biopsy? *AJR Am J Roentgenol* (2009) **193**:840–9. doi:10.2214/AJR.08.2128
39. Kinoshita T, Yashiro N, Ihara N, Funatu H, Fukuma E, Narita M. Diffusion-weighted half-Fourier single-shot turbo spin echo imaging in breast tumors: differentiation of invasive ductal carcinoma from fibroadenoma. *J Comput Assist Tomogr* (2002) **26**:1042–6. doi:10.1097/00004728-200211000-00033
40. Yabuuchi H, Matsuo Y, Okafuji T, Kamitani T, Soeda H, Setoguchi T, et al. Enhanced mass on contrast-enhanced breast MR imaging: lesion characterization using combination of dynamic contrast-enhanced and diffusion-weighted MR images. *J Magn Reson Imaging* (2008) **28**:1157–65. doi:10.1002/jmri.21570
41. Baltzer PA, Renz DM, Herrmann KH, Dietzel M, Krumbein I, Gajda M, et al. Diffusion-weighted imaging (DWI) in MR mammography (MRM): clinical comparison of echo planar imaging (EPI) and half-Fourier single-shot turbo spin echo (HASTE) diffusion techniques. *Eur Radiol* (2009) **19**:1612–20. doi:10.1007/s00330-009-1326-5
42. Cho GY, Moy L, Kim SG, Baete SH, Moccaldi M, Babb JS, et al. Evaluation of breast cancer using intravoxel incoherent motion (IVIM) histogram analysis: comparison with malignant status, histological subtype, and molecular prognostic factors. *Eur Radiol* (2015). doi:10.1007/s00330-015-4087-3
43. Partridge SC, Rahbar H, Murthy R, Chai X, Kurland BF, DeMartini WB, et al. Improved diagnostic accuracy of breast MRI through combined apparent diffusion coefficients and dynamic contrast-enhanced kinetics. *Magn Reson Med* (2011) **65**:1759–67. doi:10.1002/mrm.22762
44. Sharma U, Sah RG, Parshad R, Sharma R, Seenu V, Jagannathan NR. Role of apparent diffusion coefficient values for the differentiation of viable and necrotic areas of breast cancer and its potential utility to guide voxel positioning for MRS in the absence of dynamic contrast-enhanced MRI data. *Magn Reson Imaging* (2012) **30**:649–55. doi:10.1016/j.mri.2012.02.009
45. Shangbin C. Formation of necrotic cores in the growth of tumors: analytic results. *Acta Math Sci* (2006) **26**:781–96. doi:10.1016/S0252-9602(06)60104-5

46. Sutherland RM. Cell and environmental interactions in tumor microregions: the multicell spheroid model. *Science* (1988) **240**:177–84. doi:10.1126/science.2451290
47. Boroughs LK, DeBerardinis RJ. Metabolic pathways promoting cancer cell survival and growth. *Nat Cell Biol* (2015) **17**:351–9. doi:10.1038/ncb3124
48. Maier CF, Paran Y, Bendel P, Rutt BK, Degani H. Quantitative diffusion imaging in implanted human breast tumors. *Magn Reson Med* (1997) **37**:576–81. doi:10.1002/mrm.1910370417
49. Sah RG, Sharma U, Parshad R, Seenu V, Mathur SR, Jagannathan NR. Association of estrogen receptor, progesterone receptor, and human epidermal growth factor receptor 2 status with total choline concentration and tumor volume in breast cancer patients: an MRI and in vivo proton MRS study. *Magn Reson Med* (2012) **68**:1039–47. doi:10.1002/mrm.24117
50. Dong T, Kang X, Liu Z, Zhao S, Ma W, Xuan Q, et al. Altered glycometabolism affects both clinical features and prognosis of triple-negative and neoadjuvant chemotherapy-treated breast cancer. *Tumour Biol* (2015). doi:10.1007/s13277-015-4729-8
51. Timmerman LA, Holton T, Yunева M, Louie RJ, Padró M, Daemen A, et al. Glutamine sensitivity analysis identifies the xCT antiporter as a common triple-negative breast tumor therapeutic target. *Cancer Cell* (2013) **24**:450–65. doi:10.1016/j.ccr.2013.08.020
52. Beloribi-Djeafaflia S, Vasseur S, Guillaumond F. Lipid metabolic reprogramming in cancer cells. *Oncogenesis* (2016) **5**:1–10. doi:10.1038/oncsis.2015.49
53. Jeh SK, Kim SH, Kim HS, Kang BJ, Jeong SH, Yim HW, et al. Correlation of the apparent diffusion coefficient value and dynamic magnetic resonance imaging findings with prognostic factors in invasive ductal carcinoma. *J Magn Reson Imaging* (2011) **33**:102–9. doi:10.1002/jmri.22400
54. Rhee J, Han SW, Oh DY, Kim JH, Im SA, Han W, et al. The clinicopathologic characteristics and prognostic significance of triple-negativity in node-negative breast cancer. *BMC Cancer* (2008) **8**:307. doi:10.1186/1471-2407-8-307
55. Carey LA, Perou CM, Livasy CA, Dressler LG, Cowan D, Conway K, et al. Race, breast cancer subtypes, and survival in the Carolina Breast Cancer Study. *JAMA* (2006) **295**:2492–502. doi:10.1001/jama.295.21.2492
56. Martinich L, Deantonio V, Bertotto I, Redana S, Kubatzki F, Sarotto I, et al. Correlations between diffusion-weighted imaging and breast cancer biomarkers. *Eur Radiol* (2012) **22**:1519–28. doi:10.1007/s00330-012-2403-8
57. Yu X, Liu S, Chen Z, Zhang P, Zhang J, Xu L, et al. Correlations between MRI apparent diffusion coefficient and histological grade and molecular biology of breast invasive ductal carcinoma. *Zhonghua Zhong Liu Za Zhi* (2014) **36**:606–11.
58. Fuckar D, Dekanic A, Stifter S, Mustac E, Krstulja M, Dobrila F, et al. VEGF expression is associated with negative estrogen receptor status in patients with breast cancer. *Int J Surg Pathol* (2006) **14**:49–55. doi:10.1177/106689690601400109
59. Koukourakis MI, Manolas C, Minopoulos G, Giatromanolaki A, Sivridis E. Angiogenesis relates to estrogen receptor negativity, c-erbB-2 over-expression and early relapse in node-negative ductal carcinoma of the breast. *Int J Surg Pathol* (2003) **11**:29–34. doi:10.1177/106689690301100107
60. Choi BB, Kim SH, Kang BJ, Lee JH, Song BJ, Jeong SH, et al. Diffusion-weighted imaging and FDG PET/CT: predicting the prognoses with apparent diffusion coefficient values and maximum standardized uptake values in patients with invasive ductal carcinoma. *World J Surg Oncol* (2012) **10**:126. doi:10.1186/1477-7819-10-126
61. Arponen O, Sudah M, Masarwah A, Taina M, Rautiainen S, Könönen M, et al. Diffusion-weighted imaging in 3.0 Tesla breast MRI: diagnostic performance and tumor characterization using small subregions vs. whole tumor regions of interest. *PLoS One* (2015) **10**:e0138702. doi:10.1371/journal.pone.0138702
62. Park SH, Choi HY, Hahn SY. Correlations between apparent diffusion coefficient values of invasive ductal carcinoma and pathologic factors on diffusion-weighted MRI at 3.0 Tesla. *J Magn Reson Imaging* (2013) **41**:175–82. doi:10.1002/jmri.24519
63. Tan SL, Rahmat K, Rozalli FI, Mohd-Shah MN, Aziz YF, Yip CH, et al. Differentiation between benign and malignant breast lesions using quantitative diffusion-weighted sequence on 3 T MRI. *Clin Radiol* (2014) **69**:63–71. doi:10.1016/j.crad.2013.08.007
64. Sun K, Chen X, Chai W, Fei X, Fu C, Yan X, et al. Breast cancer: diffusion kurtosis MR imaging-diagnostic accuracy and correlation with clinical-pathologic factors. *Radiology* (2015) **277**:46–55. doi:10.1148/radiol.15141625
65. Ludovini V, Sidoni A, Pistola L, Bellezza G, De Angelis V, Gori S, et al. Evaluation of the prognostic role of vascular endothelial growth factor and microvessel density in stages I and II breast cancer patients. *Breast Cancer Res Treat* (2003) **81**:159–68. doi:10.1023/A:1025755717912
66. Hyder SM, Murthy L, Stancel GM. Progestin regulation of vascular endothelial growth factor in human breast cancer cells. *Cancer Res* (1998) **58**:392–5.
67. Konecny GE, Meng YG, Untch M, Wang HJ, Bauerfeind I, Epstein M, et al. Association between HER-2/neu and vascular endothelial growth factor expression predicts clinical outcome in primary breast cancer patients. *Clin Cancer Res* (2004) **10**:1706–16. doi:10.1158/1078-0432.CCR-0951-3
68. Kumar R, Yarmand-Bagheri R. The role of HER2 in angiogenesis. *Semin Oncol* (2001) **28**:27–32. doi:10.1016/S0093-7754(01)90279-9

**Conflict of Interest Statement:** The authors declare that the research was conducted in the absence of any commercial or financial relationships that could be construed as a potential conflict of interest.

The reviewer RC and handling Editor declared their shared affiliation, and the handling Editor states that the process nevertheless met the standards of a fair and objective review.

Copyright © 2016 Sharma, Sah, Agarwal, Parshad, Seenu, Mathur, Hari and Jagannathan. This is an open-access article distributed under the terms of the Creative Commons Attribution License (CC BY). The use, distribution or reproduction in other forums is permitted, provided the original author(s) or licensor are credited and that the original publication in this journal is cited, in accordance with accepted academic practice. No use, distribution or reproduction is permitted which does not comply with these terms.



# Clinical Breast MR Using MRS or DWI: Who Is the Winner?

**Francesco Sardanelli<sup>1,2\*</sup>, Luca Alessandro Carbonaro<sup>1</sup>, Stefania Montemezzi<sup>3</sup>, Carlo Cavedon<sup>4</sup> and Rubina Manuela Trimboli<sup>1</sup>**

<sup>1</sup>Ufficio di Radiologia, IRCCS Policlinico San Donato, San Donato Milanese, Milan, Italy, <sup>2</sup>Dipartimento di Scienze Biomediche per la Salute, Università degli Studi di Milano, Milan, Italy, <sup>3</sup>Dipartimento di Radiologia, Azienda Ospedaliera Universitaria Integrata, Verona, Italy, <sup>4</sup>Dipartimento di Fisica Sanitaria, Azienda Ospedaliera Universitaria Integrata, Verona, Italy

## OPEN ACCESS

### Edited by:

Egidio Iorio,  
Istituto Superiore di Sanità, Italy

### Reviewed by:

Tariq Shah,  
Johns Hopkins University, USA  
Samata Kakkad,  
Johns Hopkins School of Medicine,  
USA

### \*Correspondence:

Francesco Sardanelli  
francesco.sardanelli@unimi.it

### Specialty section:

This article was submitted  
to Cancer Imaging and Diagnosis,  
a section of the journal  
*Frontiers in Oncology*

**Received:** 19 May 2016

**Accepted:** 30 September 2016

**Published:** 28 October 2016

### Citation:

Sardanelli F, Carbonaro LA,  
Montemezzi S, Cavedon C and  
Trimboli RM (2016) Clinical Breast  
MR Using MRS  
or DWI: Who Is the Winner?  
*Front. Oncol.* 6:217.  
doi: 10.3389/fonc.2016.00217

Magnetic resonance imaging (MRI) of the breast gained a role in clinical practice thanks to the optimal sensitivity of contrast-enhanced (CE) protocols. This approach, first proposed 30 years ago and further developed as bilateral highly spatially resolved dynamic study, is currently considered superior for cancer detection to any other technique. However, other directions than CE imaging have been explored. Apart from morphologic features on unenhanced T2-weighted images, two different *non-contrast* molecular approaches were mainly run *in vivo*: proton MR spectroscopy (1H-MRS) and diffusion-weighted imaging (DWI). Both approaches have shown aspects of breast cancer (BC) hidden to CE-MRI: 1H-MRS allowed for evaluating the total choline peak (tCho) as a biomarker of malignancy; DWI showed that restricted diffusivity is correlated with high cellularity and tumor aggressiveness. Secondary evidence on the two approaches is now available from systematic reviews and meta-analyses, mainly considered in this article: pooled sensitivity ranged 71–74% for 1H-MRS and 84–91% for DWI; specificity 78–88% and 75–84%, respectively. Interesting research perspectives are opened for both techniques, including multivoxel MRS and statistical strategies for classification of MR spectra as well as diffusion tensor imaging and intravoxel incoherent motion for DWI. However, when looking at a clinical perspective, while MRS remained a research tool with important limitations, such as relatively long acquisition times, frequent low quality spectra, difficult standardization, and quantification of tCho tissue concentration, DWI has been integrated in the standard clinical protocols of breast MRI and several studies showed its potential value as a stand-alone approach for BC detection.

**Keywords:** breast cancer, diffusion-weighted imaging, magnetic resonance imaging, proton MR spectroscopy, systematic reviews and meta-analyses

## INTRODUCTION

Valuable results of breast magnetic resonance imaging (MRI) were first obtained 30 years ago, when sequences acquired after intravenous injection of a Gd-chelate as a contrast material were added to a non-contrast protocol (1). This approach was further developed as bilateral highly spatially resolved contrast-enhanced (CE) dynamic study, which is now currently considered superior for breast cancer (BC) detection to any other imaging technique with a reported pooled sensitivity and specificity of 93.2 and 71.1%, respectively (2), as also shown by studies on MRI screening of women at increased risk of BC (3–6). In fact, CE-MRI provides a physiopathological information that correlates

with increased vascularity, vascular permeability, and interstitial space in malignant tissue, not available from mammography and ultrasound. This diagnostic modality has been shown to provide even better sensitivity for BC detection than new techniques such as digital breast tomosynthesis (7–9). As a consequence, CE-MRI has been recommended for a spectrum of indications by medical bodies such as the American College of Radiology (10), the European Society of Breast Imaging (11, 12), and the European Society of Breast Cancer Specialists (EUSOMA) (13). The debate is still open on preoperative MRI (14, 15), but new indications, such as nipple discharge (16, 17) and evaluation of lesions with uncertain malignant potential (so-called B3 lesions), are emerging (18).

However, MR directions other than dynamic CE imaging have been explored searching for a better specificity and a deeper insight into BC biology and metabolism, opening a wider and wider window for the so-called *non-contrast breast MR*. Of note, the clinical relevance of a *non-contrast* approach for breast MR has been recently fueled by the evidence of Gd accumulation in the brain after multiple administrations of contrast material (19, 20), which implies a word of caution for the use of Gd-based contrast at least in the case of screening of healthy subjects when the risk profile is not high.

Traditionally, unenhanced sequences were associated to CE sequences in a breast MRI protocol for the sake of appraising morphologic features for lesion characterization. Several signs, typically appreciated on T2-weighted images, can be associated with malignancy, the most important being peritumoral and prepectoral edema (21), hook sign, i.e., a hook-like spiculated dendrite from the lesion to the pectoral muscle (22), and necrosis sign, i.e., a hyperintense center in a hypointense lesion (23). Non-enhancing septations are instead usually associated with benign lesions such as fibroadenomas (24).

Two other non-contrast MR methods were mainly implemented for an *in vivo* study of breast tissues: proton MR spectroscopy (1H-MRS) and diffusion-weighted imaging (DWI).

Proton MR spectroscopy is a non-invasive technique assessing biochemical tissue properties. The presence of a resonance at 3.14–3.34 ppm, attributed to choline metabolites, such as free choline, phosphocholine, and glycerophosphocholine, is

usually reported as total choline (tCho). An increased tCho has been detected in malignant breast lesions (25–31), as a result of complex metabolic alteration of biosynthetic and/or catabolic phosphatidylcholine-cycle pathways: the *de novo* biosynthesis of phosphatidylcholine *via* the Kennedy pathway and three different major catabolic pathways, contributing to phosphocholine and/or tCho accumulation (31).

The other non-contrast approach – DWI – is a way for characterizing tissue properties on the basis of the difference in the movement freedom of water molecules (diffusion) along multiple spatial directions, quantified *via* the measurement of the mean diffusivity and the apparent diffusion coefficient (ADC) (32). Breast malignant tissues show restricted diffusion and significantly lower ADC values compared with those of normal and benign breast tissues (33).

Many studies were published regarding clinical breast applications of MRS and DWI showing a potential for both techniques. The aim of this review is to look at secondary evidence, published between 2010 and 2015, on 1H-MRS and DWI of the breast as well as to try to define which of the two techniques is clinically emerging as a routine tool added to CE-MRI or also potentially usable as a stand-alone approach for cancer detection.

## DIAGNOSTIC PERFORMANCE OF 1H-MRS

The diagnostic performance of 1H-MRS of the breast, performed using the single-voxel technique, was evaluated by four systematic reviews (34–37) (Table 1).

The pooled sensitivity ranged between 71 and 74%, and the pooled specificity between 78 and 88%. Baltzer and Dietzel also performed a subgroup analysis for mass and non-mass lesions on six studies obtaining a pooled sensitivity of 68 and 62%, and a pooled specificity of 88 and 69%, respectively (34), showing that especially for non-mass lesions, 1H-MRS has a too low diagnostic performance to be used in clinical practice. Another subgroup analysis was performed on seven studies by Wang et al. (37), showing that the area under the curve (AUC) at receiver operating characteristic (ROC) analysis was higher (92 vs. 89%) when tCho signal-to-noise ratio  $\geq 2$  was selected as a cutoff for malignancy.

**TABLE 1 | Diagnostic performance of proton MR spectroscopy and DWI of the breast as evaluated in systematic reviews and meta-analyses published between 2010 and 2015.**

Included studies	Lesions/patients	Pooled sensitivity		Pooled specificity		Notes	Reference
		Point estimate (%)	95% CI	Point estimate (%)	95% CI		
<b>Proton MR spectroscopy (1H-MRS)</b>							
19	1198/1183	73	64–82	88	85–91	tCho evaluation: visual, SNR, 2 or 4 cutoff values	(34)
18	1169/NR	71	68–74	85	81–88	tCho evaluation: visual, SNR, variable cutoff values	(35)
16	1049/NR	74	70–77	78	73–82	tCho evaluation: visual, SNR, variable cutoff values	(36)
10	792/NR	74	69–77	76	71–81	tCho evaluation: SNR, 2 cut off	(37)
<b>Diffusion-weighted imaging (DWI)</b>							
13	964/815	84	82–87	79	75–82	Heterogeneity among individual studies; subgroup analysis	(50)
14	1276/1140	86	80–91	76	67–83	Heterogeneity among individual studies; subgroup analysis	(2)
26	2151/2111	91	84–95	75	61–85	Including 11 studies using <i>b</i> values $\leq 600 \text{ mm}^2/\text{s}$	(51)
26	2151/2111	89	85–92	84	78–89	Including 30 studies using <i>b</i> values $> 600 \text{ mm}^2/\text{s}$	(51)

All studies included in this meta-analysis (37) showed a high heterogeneity for both sensitivity and specificity, probably due to the large variety of MRS techniques and different field strengths used. Even though improvements from newer technology (such as 3-T magnets and multiple radiofrequency sources) were expected, the authors (37) concluded that none of these innovations significantly influenced the diagnostic performance, as year of publication showed no effect on the diagnostic performance.

Notably, small masses (between 5 and 10 mm in diameter) or foci (<5 mm in diameter) are commonly encountered on CE-MRI, depending on the clinical setting, a proportion of them turning out to be false positives. As a consequence, to avoid work-up (targeted ultrasound, needle biopsy) would be a great achievement. However, in this regard, 1H-MRS is scarcely useful. The large majority of studies did not include lesions smaller than 10 mm, thus limiting the applicability of 1H-MRS for characterization of small lesions and early BC diagnosis.

One relevant technical problem for 1H-MRS, especially important for small lesions, is the need for patient's immobility during the acquisition, i.e., for 5–10 min or more (depending also on the time for the preliminary optimization checks), which also impacts on patient's throughput and cost-effectiveness. Of note, a trend for a higher sensitivity of 1H-MRS was observed when acquisition is performed before contrast injection, due to a detrimental effect of ionic-charged contrast materials in both experimental and clinical settings (38). As lesion localization (the placement of the spectroscopic volume of interest) has to be made on CE images (especially for otherwise not visible small lesions), the majority of 1H-MRS studies were performed after contrast injection, potentially implying a suboptimal sensitivity. On the other hand, a major clinical application of 1H-MRS should be lesion characterization, typically arising immediately after the detection, implying that 1H-MRS should be performed immediately after CE-MRI, which usually lasts about 15–20 min. Thus, a time prolongation of additional 10 min increases the probability of patient's movements, reducing the possibility of getting good quality spectra.

Moreover, again especially important for small lesions, to adapt the volume of interest to the lesion morphology is often not easy: cubic or anyway squared volumes of interest tend to include tissues (fat or gland) surrounding the lesion, determining volume contamination and resulting in reduced sensitivity (28). Lesion located posteriorly, close to the pectoral muscle or the thoracic wall, or superficially, near the skin, may provide spectra with low signal-to-noise ratio. Thus, even using 3-T magnets and multiple radiofrequency sources, in clinical practice about 20% of lesions finally result to be not evaluable with MRS (39).

Several of these limitations are not acting when 1H-MRS is applied for the evaluation of the response to neoadjuvant therapy (NAT), typically administered to patients with locally advanced BCs. Studies have shown that 1H-MRS enables an early prediction of the final NAT effect (40–42). This is, in our opinion, the most promising clinical application of 1H-MRS, even though it regards a relatively small fraction of patients. However, also in this field, as we will explain below, DWI is a strong competitor (**Figure 1**). Anyway, for a well-accepted application of MRS

techniques to the NAT setting, large multicenter studies using clearly standardized pathologic response classification are warranted (43–46).

Finally, we should note that 1H-MRS was mostly applied in clinical breast studies using methods not allowing for quantification of tissue tCho concentration. Both the SNR between tCho peak and noise (usually with a  $\geq 2$  threshold for malignancy) (34–37) and the integral under the tCho peak (30) have limitations and low potential for standardization. On the other hand, tissue tCho quantification using internal or external standard of reference (47) implies dedicated high technical expertise. This highlights the need for cooperation with a physicist experienced in MRS, not only for tCho tissue quantification but also generally if MRS has to be integrated in a clinical setting. This is a possibility that only large hospitals or academic facilities can afford and is another limitation for MRS effectiveness.

Highly interesting results were obtained, even at 1.5 T, by Stanwell et al. (48), carefully referencing the spectra using a special post-processing: 80% sensitivity and 100% specificity. They optimized spectral resolution from human breast tissues resolving the composite choline resonances of the tCho peak. False positives including three lactating women were distinguished by a resonance at 3.28 in contrast with the profile from BC patients consistent with phosphocholine centered at 3.22 ppm. However, a false negative rate of 20% remained unresolved, and this high spectral resolution was never reproduced, not even using 3-T magnets.

Looking at the potential prognostic value of 1H-MRS of the breast, it is worth to note that tCho levels, evaluated by 1H-MRS, were significantly higher for invasive ductal carcinoma, for cancers with high nuclear or histologic grade, and ER-negative and triple-negative status (49). This perspective deserves confirmation in future large studies with quantification of tissue tCho concentration.

## DIAGNOSTIC PERFORMANCE OF DWI

Breast MR sequences for DWI have been mainly used to try to characterize breast lesions, adding a new parameter in the algorithm for diagnosis, with the potential for avoiding unnecessary biopsy, especially for MRI-only visible lesions that should be sampled under MR-guidance, a time-demanding and high-cost procedure (11).

Studies were performed in order to understand the potential value of DWI added to CE-MRI. Two meta-analyses, from Chen et al. (50) and from Zhang et al. (2), reported an overall sensitivity of 84 and 86% and an overall specificity of 79 and 76%, respectively. However, a notable heterogeneity among individual studies was observed, and a subgroup analysis to investigate the source of this heterogeneity was performed. The two most important factors resulted to be the *b* value of diffusion gradient used and the so-called *threshold effect* (a detectable difference in sensitivities and specificities due to different thresholds used in included studies).

Different *b* values significantly affect the ADC of breast lesions and therefore confound quantitative DWI. In a large systematic

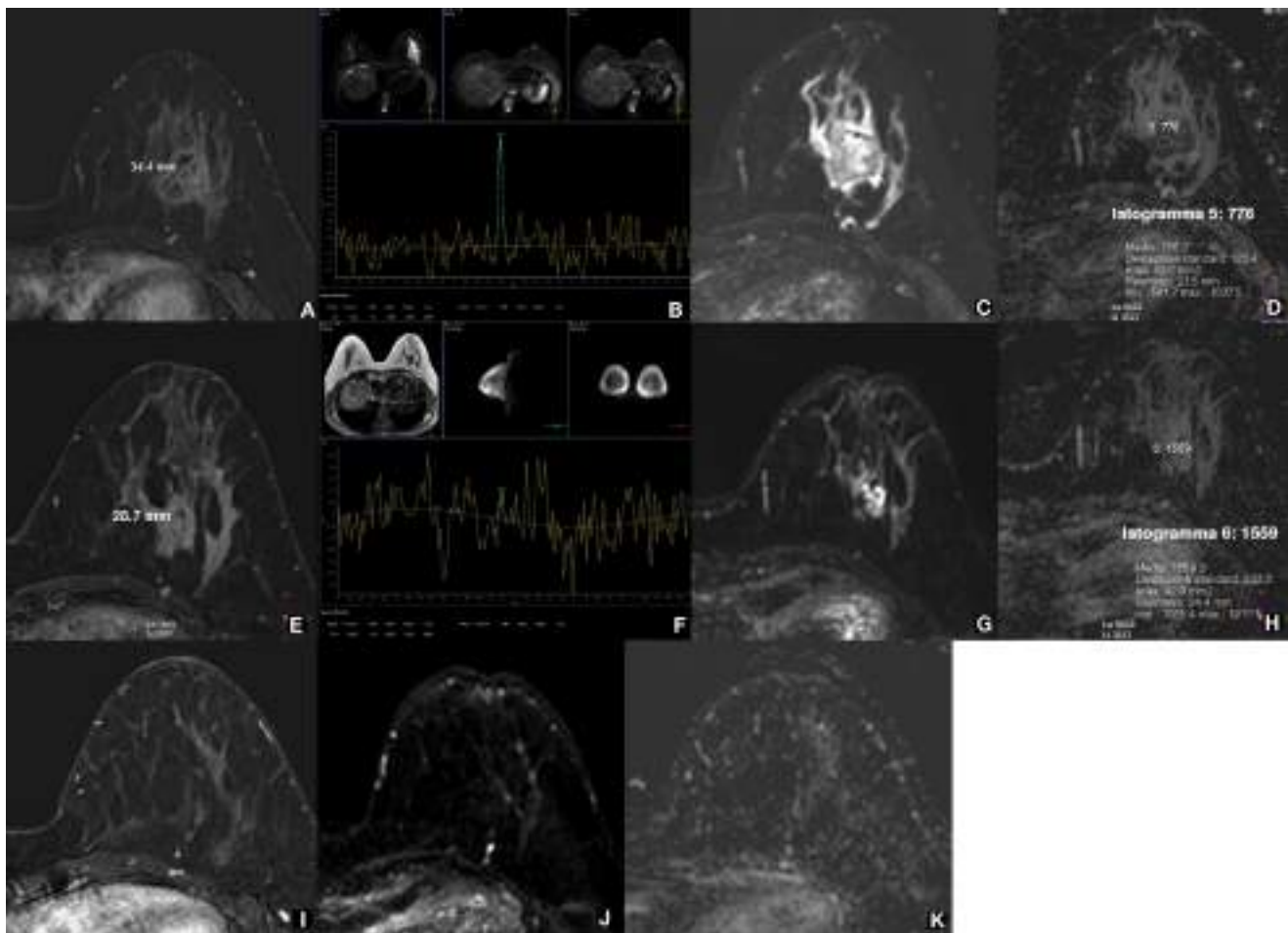


**FIGURE 1 | 1H-MRS and DWI for evaluating the response to neoadjuvant therapy (NAT) of a locally advanced breast cancer.** A 37-year-old woman with locally advanced breast cancer before, during, and after neoadjuvant therapy (NAT). Before treatment, the lesion at the lower external quadrant of the left breast is well depicted as a 34.4-mm nodule on subtracted CE-MRI with 0.1 mmol/kg of gadobenate dimeglumine (**A**), shows a high tCho peak at 1H-MRS with a signal-to-noise ratio (SNR) of 6.7 (**B**), low diffusivity as a high signal on DWI (**C**), and a low ( $0.776 \times 10^{-3}$  mm $^2$ /s) mean ADC value (**D**). After two NAT cycles, the lesion is reduced in size (28.7 mm) at CE-MRI (**E**), while the tCho peak is no longer detectable at 1H-MRS (**F**); DWI (**G**) and ADC map (**H**) show an evident increased diffusivity (mean ADC  $1.559 \times 10^{-3}$  mm $^2$ /s). After the end of treatment, the lesion is not visible at all on CE-MRI (**I**), DWI (**J**), and ADC map (**K**); therefore, MRS was not performed. The lesion was a metaplastic carcinoma with condroid differentiation (negative for estrogen, progesterone, and HER2 receptors, Ki67 80%), and after surgical removal, a complete pathological response was appreciated. Both 1H-MRS and DWI early predicted the pathological response to NAT showing an effect more pronounced than that of CE-MRI. Acquisition times: CE-MRI 9 min; 1H-MRS 8 min (including preparation); DWI 5 min (Philips Achieva STx 3.0 T, MultiTransmit radiofrequency technology; dedicated 16-channel breast coil; Azienda Ospedaliera Universitaria Integrata, Verona, Italy).

review performed on 26 studies, including a total of 2111 patients with 2151 breast lesions, Dorrius et al. (51) showed that the combination of  $b = 0$  and  $1000$  s/mm $^2$  is optimal for benign/malignant differentiation. Pooled 89% sensitivity and 84% specificity were reported for  $b$  values  $>600$  s/mm $^2$  (ROC-AUC 0.93), while using  $b$  values  $\leq 600$  s/mm $^2$ , 91% sensitivity and 75% specificity were obtained (ROC-AUC 0.92). A summary of the recently published meta-analyses on breast DWI is reported in **Table 1**.

There is no clear consensus regarding the threshold values for ADC to diagnose malignancy. A substantial variability of threshold values, ranging  $0.90$ – $1.76 \times 10^{-3}$  mm $^2$ /s has been observed (51). As a recommendation, a relatively higher threshold value may be used to minimize missing malignancy.

Of note, the studies evaluating mass lesions had a higher specificity (84%) than those evaluating non-mass lesions (70%) (2). When added to CE-MRI, DWI sequences showed a significant diagnostic gain: the summary ROC-AUC of CE-MRI combined with DWI was 0.94 compared with 0.85 for CE-MRI alone (2). Differently from 1H-MRS, contrast injection does not negatively impact on DWI performance (51); ADC measures were reported to not significantly change following DCE-MRI at 3 T, suggesting that DWI and DCE-MRI can be performed in any order without affecting diagnostic performance (52). Moreover, Janka et al. showed that DWI after contrast injection even leads to a slightly better benign/malignant discrimination (53).

Furthermore, DWI sequences are not dependent on CE-MRI. They can be performed without previous knowledge of lesion location, as the DWI field of view includes both breasts with a 4- to 5-min acquisition time.

Interestingly, some authors showed as DWI could be used as the main component of an unenhanced (*non-contrast*) MRI examinations with good sensitivity and high specificity, at least if we consider mass lesions. A reduced detection rate of small mass lesions and of non-mass lesions has to be taken into account (54, 55). However, a sensitivity theoretically comparable with that of screening mammography (54) as well as a potential for avoiding the double reading (55) candidate DWI as a sequence to be used for explorative non-contrast MRI screening studies.

Notably, DWI sequences are undergoing a progressive technical refinement. Spatial resolution and image quality are increasing, allowing also for a more detailed morphology evaluation (56, 57). As a matter of fact, authors have positively tried to integrate information coming from DWI into the Breast Imaging Reporting and Data System BI-RADS (58).

Considering the potential prognostic value of DWI, we finally highlight that a recent systematic review demonstrated that breast lesions with increased signal intensity on DWI and decreased signals on ADC are more likely associated to lymph-nodal metastases (59).

## RESEARCH TRENDS FOR 1H-MRS AND DWI OF THE BREAST

First of all, authors attempted to integrate CE-MRI, 1H-MRS, and DWI (multiparametric MRI, mpMRI) to yield significantly higher ROC-AUC (0.936) in comparison with just two of them (0.808) (60). Positron emission tomography (PET) was also added to provide an intriguing mpMRI/PET approach for lesion characterization (61), but we cannot propose this high-cost approach for characterization of breast lesions, when most cases can be solved by a needle sampling.

Regarding 1H-MRS, two interesting topics are multivoxel spectroscopy and statistical strategies for classifying MR spectra. Multivoxel 1H-MRS should overcome the need of *a priori* knowledge of lesion location (62), allowing for BC screening (or for stratifying BC risk) on the basis of tCho levels in the healthy gland tissue. However, multivoxel 1H-MRS is more technically challenging than single-voxel 1H-MRS for shimming and fat suppression (63). Statistical strategies for classification of spectra were proposed in a 2D correlated spectroscopy (COSY), where the composite resonances are separated by the use of a second frequency (63). However, this interesting approach seems to be not easy to be reproduced for clinical practice.

Finally, also 31P-MRS (64) was used to provide a direct method for the *in vivo* detection and quantification of endogenous biomarkers, yielding a new intriguing method for the non-invasive assessment of prognostic and predictive biomarkers in BC treatment.

Regarding DWI, several studies have shown that important information is lost when one relies just on the average ADC and that a higher sensitivity is given by minimum ADC instead of any metrics of the central tendency of ADC values distribution. Mori

et al. (65) indicated that a minimum ADC value  $<1.1 \times 10^{-3}$  mm<sup>2</sup>/s and that an ADC difference (maximum minus minimum ADC) greater than  $0.23 \times 10^{-3}$  mm<sup>2</sup>/s suggests the presence of invasive carcinoma in cases with only DCIS at biopsy, a crucial information for patient management.

Second, studies explored the possibility of characterizing axillary lymph nodes using DWI in BC patients. One study (66) considered only nodes with metastases  $\geq 5$  mm, obtaining 95% sensitivity and 92% specificity. More recent studies (67–69) obtained sensitivities from 72 to 85% and specificities from 80 to 88%. Future multidisciplinary researches should be placed in the context of the current rethinking of axillary dissection (70).

However, the most intriguing research areas for breast DWI are diffusion tensor imaging (DTI) and intravoxel incoherent motion (IVIM). For DTI (which adds information about tissue microstructure by addressing diffusion spatial direction), at least six DWI gradient directions should be applied, so that a symmetrical matrix, the diffusion tensor indeed, can be calculated, describing the anisotropic water diffusion in the tissue. Fractional anisotropy (FA) describes diffusion anisotropy quantitatively on a range from 1 (maximum anisotropy) to 0 (isotropy) (71). Experiences on breast DTI showed that FA does not have incremental value for differential diagnosis over ADC values (71). Eyal et al. (72) developed a breast DTI protocol at 3 T and image processing means for obtaining vector and parametric maps of the water diffusion tensor. Evaluation of the various diffusion parametric maps indicated that the prime diffusion coefficient and the maximal anisotropy are the most efficient parameters for detecting and diagnosing BC. So far, DTI turned out to be a great tool for visualizing the breast parenchyma but its clinical application remains to be investigated.

The IVIM quantifies molecular diffusion more accurately than ADC and provides additional information on microperfusion tissue properties. It separates the contribution of T2 from diffusivity using multiple *b* values, hence being less dependent on the choice of individual *b* values (73). However, IVIM as well as DTI imply longer acquisition times, and these techniques are not currently suitable for a large use in clinical practice.

## CONCLUSION

The results coming from the secondary evidence about 1H-MRS and DWI of the breast are clearly in favor of an easier and more effective use of DWI. If one of the two approaches for non-contrast breast MR has to be chosen for clinical practice, DWI is certainly the winner.

When looking at a clinical perspective, while 1H-MRS remained a tool with relevant limitations such as relatively long acquisition times, frequent low quality spectra, difficult standardization and quantification of tissue tCho concentration, DWI is feasible in almost all cases and adds diagnostic power to CE-MRI. Moreover, seminal studies showed the potential value of DWI as a stand-alone approach for BC detection.

As matter of fact, in the context of an ongoing international multicenter study exploring the value of preoperative CE-MRI with over 4500 patients enrolled so far (15), 84% of them were studied using a technical protocol including DWI among the standard sequences.

## ETHICS STATEMENT

Did the study presented in the manuscript involve human or animal subjects: Yes. The case presented in **Figure 1** comes from a prospective clinical study approved by the Ethics Committee of the Azienda Ospedaliera Universitaria Integrata, Verona, Italy. The patient gave written informed consent.

## REFERENCES

- Heywang SH, Hahn D, Schmidt H, Krischke I, Eiermann W, Bassermann R, et al. MR imaging of the breast using gadolinium-DTPA. *J Comput Assist Tomogr* (1990) 10:199–204. doi:10.1097/00004728-198603000-00005
- Zhang L, Tang M, Min Z, Lu J, Lei X, Zhang X. Accuracy of combined dynamic contrast-enhanced magnetic resonance imaging and diffusion-weighted imaging for breast cancer detection: a meta-analysis. *Acta Radiol* (2016) 57:651–60. doi:10.1177/0284185115597265
- Kuhl C, Weigel S, Schrading S, Arand B, Bieling H, König R, et al. Prospective multicenter cohort study to refine management recommendations for women at elevated familial risk of breast cancer: the EVA trial. *J Clin Oncol* (2010) 28:1450–7. doi:10.1200/JCO.2009.23.0839
- Sardanelli F, Podo F, Santoro F, Manoukian S, Bergonzi S, Trecate G, et al. Multicenter surveillance of women at high genetic breast cancer risk using mammography, ultrasonography, and contrast-enhanced magnetic resonance imaging (the high breast cancer risk Italian 1 study): final results. *Invest Radiol* (2011) 46:94–105. doi:10.1097/RLI.0b013e3181f3fcdf
- Santoro F, Podo F, Sardanelli F. MRI screening of women with hereditary predisposition to breast cancer: diagnostic performance and survival analysis. *Breast Cancer Res Treat* (2014) 147:685–7. doi:10.1007/s10549-014-3097-1
- Podo F, Santoro F, Di Leo G, Manoukian S, de Giacomi C, Corcione S, et al. Triple-negative versus non-triple-negative breast cancers in high-risk women: phenotype features and survival from the HIBCRIT-1 MRI-including screening study. *Clin Cancer Res* (2016) 22:895–904. doi:10.1158/1078-0432.CCR-15-0459
- Mariscotti G, Houssami N, Durando M, Bergamasco L, Campanino PP, Ruggieri C, et al. Accuracy of mammography, digital breast tomosynthesis, ultrasound and MR imaging in preoperative assessment of breast cancer. *Anticancer Res* (2014) 34:1219–25.
- Kim WH, Chang JM, Moon H-G, Yi A, Koo HR, Gweon HM, et al. Comparison of the diagnostic performance of digital breast tomosynthesis and magnetic resonance imaging added to digital mammography in women with known breast cancers. *Eur Radiol* (2016) 26:1556–64. doi:10.1007/s00330-015-3998-3
- Clauser P, Carbonaro LA, Pancot M, Girometti R, Bazzocchi M, Zuiani C, et al. Additional findings at preoperative breast MRI: the value of second-look digital breast tomosynthesis. *Eur Radiol* (2015) 25:2830–9. doi:10.1007/s00330-015-3720-5
- American College of Radiology. *ACR Practice Parameter for the Performance of Contrast-Enhanced Magnetic Resonance Imaging (MRI) of the Breast* (2013). Available from: <http://www.acr.org/-/media/2a0eb28eb59041e2825179af-b72ef624.pdf>
- Mann RM, Kuhl CK, Kinkel K, Boetes C. Breast MRI: guidelines from the European Society of Breast Imaging. *Eur Radiol* (2008) 18:1307–18. doi:10.1007/s00330-008-0863-7
- Mann RM, Balleyguier C, Baltzer PA, Bick U, Colin C, Cornford E, et al. Breast MRI: EUSOBI recommendations for women's information. *Eur Radiol* (2015) 25:3669–78. doi:10.1007/s00330-015-3807-z
- Sardanelli F, Boetes C, Borisch B, Decker T, Federico M, Gilbert FJ, et al. Magnetic resonance imaging of the breast: recommendations from the EUSOMA working group. *Eur J Cancer* (2010) 46:1296–316. doi:10.1016/j.ejca.2010.02.015
- Sardanelli F, Trimboli RM. Preoperative MRI: did randomized trials conclude the debate? *Eur J Radiol* (2012) 81(Suppl 1):S135–6. doi:10.1016/S0720-048X(12)0056-6
- Trimboli RM, Di Leo G, Sacchetto D, Mann R, Alvarez Benito M, Zuiani C, et al. The impact of breast MRI on surgical planning and reoperation rate: first results from the MIPA study. *Insights Imag* (2016) 7(Suppl 1):S464–5; Proceedings of the European Congress of Radiology; 2016 Mar 2–6; Vienna, Austria. doi:10.1007/s13244-016-0475-8
- Bahl M, Baker JA, Greenup RA, Ghate SV. Evaluation of pathologic nipple discharge: what is the added diagnostic value of MRI? *Ann Surg Oncol* (2015) 22(Suppl 3):S435–41. doi:10.1245/s10434-015-4792-9
- Sanders LM, Daigle M. The rightful role of MRI after negative conventional imaging in the management of bloody nipple discharge. *Breast J* (2016) 22:209–12. doi:10.1111/tbj.12551
- Lonardo V, Zuiani C, Linda A, Girometti R, Bazzocchi M, Sardanelli F. High-risk breast lesions at imaging-guided needle biopsy: usefulness of MRI for treatment decision. *AJR Am J Roentgenol* (2012) 199:W240–50. doi:10.2214/AJR.11.7869
- Kanda T, Ishii K, Kawaguchi H, Kitajima K, Takenaka D. High signal intensity in the dentate nucleus and globus pallidus on unenhanced T1-weighted MR images: relationship with increasing cumulative dose of a gadolinium-based contrast material. *Radiology* (2014) 270:834–41. doi:10.1148/radiol.13131669
- Kanda T, Fukusato T, Matsuda M, Toyoda K, Oba H, Kotoku J, et al. Gadolinium-based contrast agent accumulates in the brain even in subjects without severe renal dysfunction: evaluation of autopsy brain specimens with inductively coupled plasma mass spectroscopy. *Radiology* (2015) 276:228–32. doi:10.1148/radiol.2015142690
- Uematsu T. Focal breast edema associated with malignancy on T2-weighted images of breast MRI: peritumoral edema, prepectoral edema, and subcutaneous edema. *Breast Cancer* (2015) 22:66–70. doi:10.1007/s12282-014-0572-9
- Dietzel M, Baltzer PAT, Vag T, Gajda M, Camara O, Kaiser WA. The hook sign for differential diagnosis of malignant from benign lesions in magnetic resonance mammography: experience in a study of 1084 histologically verified cases. *Acta Radiol* (2010) 51:137–43. doi:10.3109/02841850903463638
- Dietzel M, Baltzer PAT, Vag T, Herzog A, Gajda M, Camara O, et al. The necrosis sign in magnetic resonance-mammography: diagnostic accuracy in 1,084 histologically verified breast lesions. *Breast J* (2010) 16:603–8. doi:10.1111/j.1524-4741.2010.00982.x
- Malich A, Fischer DR, Wurdinger S, Boettcher J, Marx C, Facius M, et al. Potential MRI interpretation model: differentiation of benign from malignant breast masses. *Am J Roentgenol* (2005) 185:964–70. doi:10.2214/AJR.04.1073
- Fausto A, Magaldi A, Babaei Paskeh B, Menicagli L, Lupo EN, Sardanelli F. MR imaging and proton spectroscopy of the breast: how to select the images useful to convey the diagnostic message. *Radiol Med* (2007) 112:1060–8. doi:10.1007/s11547-007-0193-x
- Bartella L, Morris EA, Dershaw DD, Liberman L, Thakur SB, Moskowitz C, et al. Proton MR spectroscopy with choline peak as malignancy marker improves positive predictive value for breast cancer diagnosis: preliminary study. *Radiology* (2006) 239:686–92. doi:10.1148/radiol.2393051046
- Katz-Bruil R, Lavin PT, Lenkinski RE. Clinical utility of proton magnetic resonance spectroscopy in characterizing breast lesions. *J Natl Cancer Inst* (2002) 94:1197–203. doi:10.1093/jnci/94.16.1197
- Sardanelli F, Fausto A, Podo F. MR spectroscopy of the breast. *Radiol Med* (2008) 113:56–64. doi:10.1007/s11547-008-0228-y
- Sardanelli F, Fausto A, Di Leo G, De Nijs R, Vorbuchner M, Podo F. In vivo proton MR spectroscopy of the breast using the total choline peak integral as a marker of malignancy. *Am J Roentgenol* (2009) 192:1608–17. doi:10.2214/AJR.07.3521
- Bartella L, Huang W. Proton (1H) MR spectroscopy of the breast. *Radiographics* (2007) 27(Suppl 1):S241–52. doi:10.1148/rg.27si075504
- Podo F, Sardanelli F, Iorio E, Canese R, Carpinelli G, Fausto A, et al. Abnormal choline phospholipid metabolism in breast and ovary cancer: molecular bases

## AUTHOR CONTRIBUTIONS

FS is responsible for the conception of the work. LC and RT searched for literature focusing on secondary evidence. FS, LC, and RT drafted multiple versions of the manuscript. SM and CC revised the manuscript adding content of intellectual importance. All authors approved the final version of the manuscript.

- for noninvasive imaging approaches. *Curr Med Imag Rev* (2007) 3:123–37. doi:10.2174/157340507780619160
32. Iima M, Le Bihan D. Clinical intravoxel incoherent motion and diffusion MR imaging: past, present, and future. *Radiology* (2016) 278:13–32. doi:10.1148/radiol.2015150244
  33. Woodhams R, Ramadan S, Stanwell P, Sakamoto S, Hata H, Ozaki M, et al. Diffusion-weighted imaging of the breast: principles and clinical applications. *Radiographics* (2011) 31:1059–84. doi:10.1148/radiol.314105160
  34. Baltzer PAT, Dietzel M. Breast lesions: diagnosis by using proton MR spectroscopy at 1.5 and 3.0 T – systematic review and meta-analysis. *Radiology* (2013) 267:735–46. doi:10.1148/radiol.13121856
  35. Cen D, Xu L. Differential diagnosis between malignant and benign breast lesions using single-voxel proton MRS: a meta-analysis. *J Cancer Res Clin Oncol* (2014) 140:993–1001. doi:10.1007/s00432-014-1605-7
  36. Tan J, Xu L, Yao W, Wan Y, Zhou S, Xin SX. In vivo post-contrast 1H-MRS evaluation of malignant and benign breast lesions: a meta-analysis. *Tumour Biol* (2015) 36:345–52. doi:10.1007/s13277-014-2635-0
  37. Wang X, Wang XJ, Song HS, Chen LH. 1H-MRS evaluation of breast lesions by using total choline signal-to-noise ratio as an indicator of malignancy: a meta-analysis. *Med Oncol* (2015) 32:160. doi:10.1007/s12032-015-0603-1
  38. Lenkinski RE, Wang X, Elian M, Goldberg SN. Interaction of gadolinium-based MR contrast agents with choline: implications for MR spectroscopy (MRS) of the breast. *Magn Reson Med* (2009) 61:1286–92. doi:10.1002/mrm.21937
  39. Montemezzi S, Caumo F, Baglio I, Camera L, Meliado G, Cavedon C. MR spectroscopy of the breast at 3 Tesla: a clinical experience. *Proceedings of the Radiological Society of North America 2013 Scientific Assembly and Annual Meeting, December 1–December 6, 2013*. Chicago, IL (2013). VSBR21-17. Available from: <http://archive.rsna.org/2013/13021676.html>
  40. Manton DJ, Chaturvedi A, Hubbard A, Lind MJ, Lowry M, Maraveyas A, et al. Neoadjuvant chemotherapy in breast cancer: early response prediction with quantitative MR imaging and spectroscopy. *Br J Cancer* (2006) 94:427–35. doi:10.1038/sj.bjc.6602948
  41. Baek H-M, Chen J-H, Nie K, Yu HJ, Bahri S, Mehta RS, et al. Predicting pathologic response to neoadjuvant chemotherapy in breast cancer by using MR imaging and quantitative 1H MR spectroscopy. *Radiology* (2009) 251:653–62. doi:10.1148/radiol.2512080553
  42. Leong KM, Lau P, Ramadan S. Utilisation of MR spectroscopy and diffusion weighted imaging in predicting and monitoring of breast cancer response to chemotherapy. *J Med Imaging Radiat Oncol* (2015) 59:268–77. doi:10.1111/jmi.12310
  43. Marinovich ML, Housami N, Macaskill P, Sardanelli F, Irwig L, Mamounas EP, et al. Meta-analysis of magnetic resonance imaging in detecting residual breast cancer after neoadjuvant therapy. *J Natl Cancer Inst* (2013) 105:321–33. doi:10.1093/jnci/djs528
  44. Marinovich ML, Macaskill P, Irwig L, Sardanelli F, von Minckwitz G, Mamounas E, et al. Meta-analysis of agreement between MRI and pathologic breast tumour size after neoadjuvant chemotherapy. *Br J Cancer* (2013) 109:1528–36. doi:10.1038/bjc.2013.473
  45. Marinovich ML, Sardanelli F, Ciatto S, Mamounas E, Brennan M, Macaskill P, et al. Early prediction of pathologic response to neoadjuvant therapy in breast cancer: systematic review of the accuracy of MRI. *Breast* (2012) 21:669–77. doi:10.1016/j.breast.2012.07.006
  46. Marinovich ML, Macaskill P, Irwig L, Sardanelli F, Mamounas E, von Minckwitz G, et al. Agreement between MRI and pathologic breast tumor size after neoadjuvant chemotherapy, and comparison with alternative tests: individual patient data meta-analysis. *BMC Cancer* (2015) 15:662. doi:10.1186/s12885-015-1664-4
  47. Bolan PJ. Magnetic resonance spectroscopy of the breast: current status. *Magn Reson Imaging Clin N Am* (2013) 21:625–39. doi:10.1016/j.mric.2013.04.008
  48. Stanwell P, Gluch L, Clark D, Tomanek B, Baker L, Giuffrè B, et al. Specificity of choline metabolites for in vivo diagnosis of breast cancer using 1H MRS at 1.5 T. *Eur Radiol* (2005) 15:1037–43. doi:10.1007/s00330-004-2475-1
  49. Shin HJ, Baek H-M, Cha JH, Kim HH. Evaluation of breast cancer using proton MR spectroscopy: total choline peak integral and signal-to-noise ratio as prognostic indicators. *AJR Am J Roentgenol* (2012) 198:W488–97. doi:10.2214/AJR.11.7292
  50. Chen X, Li W, Zhang Y, Wu Q, Guo Y, Bai Z. Meta-analysis of quantitative diffusion-weighted MR imaging in the differential diagnosis of breast lesions. *BMC Cancer* (2010) 10:693. doi:10.1186/1471-2407-10-693
  51. Dorrius MD, Dijkstra H, Oudkerk M, Sijens PE. Effect of b value and pre-admission of contrast on diagnostic accuracy of 1.5-T breast DWI: a systematic review and meta-analysis. *Eur Radiol* (2014) 24:2835–47. doi:10.1007/s00330-014-3338-z
  52. Nguyen VT, Rahbar H, Olson ML, Liu C-L, Lehman CD, Partridge SC. Diffusion-weighted imaging: effects of intravascular contrast agents on apparent diffusion coefficient measures of breast malignancies at 3 Tesla. *J Magn Reson Imaging* (2015) 42:788–800. doi:10.1002/jmri.24844
  53. Janka R, Hammon M, Geppert C, Nothelfer A, Uder M, Wenkel E. Diffusion-weighted MR imaging of benign and malignant breast lesions before and after contrast enhancement. *RöFo* (2014) 186:130–5. doi:10.1055/s-0033-1350298
  54. Baltzer PAT, Benndorf M, Dietzel M, Gajda M, Camara O, Kaiser WA. Sensitivity and specificity of unenhanced MR mammography (DWI combined with T2-weighted TSE imaging, ueMRM) for the differentiation of mass lesions. *Eur Radiol* (2010) 20:1101–10. doi:10.1007/s00330-009-1654-5
  55. Trimboli RM, Verardi N, Cartia F, Carbonaro LA, Sardanelli F. Breast cancer detection using double reading of unenhanced MRI including T1-weighted, T2-weighted STIR, and diffusion-weighted imaging: a proof of concept study. *AJR Am J Roentgenol* (2014) 203:674–81. doi:10.2214/AJR.13.11816
  56. Wisner DJ, Rogers N, Deshpande VS, Newitt DN, Laub GA, Porter DA, et al. High-resolution diffusion-weighted imaging for the separation of benign from malignant BI-RADS 4/5 lesions found on breast MRI at 3T. *J Magn Reson Imaging* (2014) 40:674–81. doi:10.1002/jmri.24416
  57. Barentsz MW, Taviani V, Chang JM, Ikeda DM, Miyake KK, Banerjee S, et al. Assessment of tumor morphology on diffusion-weighted (DWI) breast MRI: diagnostic value of reduced field of view DWI. *J Magn Reson Imaging* (2015) 42:1656–65. doi:10.1002/jmri.24929
  58. Pinker K, Bickel H, Helbich TH, Gruber S, Dubsky P, Pluschnig U, et al. Combined contrast-enhanced magnetic resonance and diffusion-weighted imaging reading adapted to the “Breast Imaging Reporting and Data System” for multiparametric 3-T imaging of breast lesions. *Eur Radiol* (2013) 23:1791–802. doi:10.1007/s00330-013-2771-8
  59. Sun J-H, Jiang L, Guo F, Zhang X-S. Diagnostic significance of apparent diffusion coefficient values with diffusion weighted MRI in breast cancer: a meta-analysis. *Asian Pac J Cancer Prev* (2014) 15:8271–7. doi:10.7314/APJCP.2014.15.19.8271
  60. Pinker K, Bogner W, Baltzer P, Gruber S, Bickel H, Brueck B, et al. Improved diagnostic accuracy with multiparametric magnetic resonance imaging of the breast using dynamic contrast-enhanced magnetic resonance imaging, diffusion-weighted imaging, and 3-dimensional proton magnetic resonance spectroscopic imaging. *Invest Radiol* (2014) 49:421–30. doi:10.1097/RLI.0000000000000029
  61. Pinker K, Bogner W, Baltzer P, Karanikas G, Magometschnigg H, Brader P, et al. Improved differentiation of benign and malignant breast tumors with multiparametric 18fluorodeoxyglucose positron emission tomography magnetic resonance imaging: a feasibility study. *Clin Cancer Res* (2014) 20:3540–9. doi:10.1158/1078-0432.CCR-13-2810
  62. Sijens PE, Dorrius MD, Kappert P, Baron P, Pijnappel RM, Oudkerk M. Quantitative multivoxel proton chemical shift imaging of the breast. *Magn Reson Imaging* (2010) 28:314–9. doi:10.1016/j.mri.2009.11.004
  63. Birdwell RL, Mountford CE, Iglesias JD. Molecular imaging of the breast. *Radiol Clin North Am* (2010) 48:1075–88. doi:10.1016/j.rcl.2010.07.017
  64. Klomp DWJ, van de Bank BL, Raaijmakers A, Korteweg MA, Possanzini C, Boer VO, et al. 31P MRSI and 1H MRS at 7 T: initial results in human breast cancer. *NMR Biomed* (2011) 24:1337–42. doi:10.1002/nbm.1696
  65. Mori N, Ota H, Mugikura S, Takasawa C, Tominaga J, Ishida T, et al. Detection of invasive components in cases of breast ductal carcinoma in situ on biopsy by using apparent diffusion coefficient MR parameters. *Eur Radiol* (2013) 23:2705–12. doi:10.1007/s00330-013-2902-2
  66. Fornasa F, Nesotti MV, Bovo C, Bonavina MG. Diffusion-weighted magnetic resonance imaging in the characterization of axillary lymph nodes in patients with breast cancer. *J Magn Reson Imaging* (2012) 36:858–64. doi:10.1002/jmri.23706
  67. Luo N, Su D, Jin G, Liu L, Zhu X, Xie D, et al. Apparent diffusion coefficient ratio between axillary lymph node with primary tumor to detect nodal metastasis in breast cancer patients. *J Magn Reson Imaging* (2013) 38:824–8. doi:10.1002/jmri.24031
  68. Rautiainen S, Könönen M, Sironen R, Masarwah A, Sudah M, Hakumäki J, et al. Preoperative axillary staging with 3.0-T breast MRI: clinical value of

- diffusion imaging and apparent diffusion coefficient. *PLoS One* (2015) 10:e0122516. doi:10.1371/journal.pone.0122516
69. Yamaguchi K, Schacht D, Nakazono T, Irie H, Abe H. Diffusion weighted images of metastatic as compared with nonmetastatic axillary lymph nodes in patients with newly diagnosed breast cancer. *J Magn Reson Imaging* (2015) 42:771–8. doi:10.1002/jmri.24829
70. Li CZ, Zhang P, Li RW, Wu CT, Zhang XP, Zhu HC. Axillary lymph node dissection versus sentinel lymph node biopsy alone for early breast cancer with sentinel node metastasis: a meta-analysis. *Eur J Surg Oncol* (2015) 41:958–66. doi:10.1016/j.ejso.2015.05.007
71. Baltzer PAT, Schäfer A, Dietzel M, Grässel D, Gajda M, Camara O, et al. Diffusion tensor magnetic resonance imaging of the breast: a pilot study. *Eur Radiol* (2011) 21:1–10. doi:10.1007/s00330-010-1901-9
72. Eyal E, Shapiro-Feinberg M, Furman-Haran E, Grobgeld D, Golan T, Itzhak Y, et al. Parametric diffusion tensor imaging of the breast. *Invest Radiol* (2012) 47:284–91. doi:10.1097/RLI.0b013e3182438e5d
73. Dijkstra H, Dorrius MD, Wielema M, Jaspers K, Pijnappel RM, Oudkerk M, et al. Semi-automated quantitative intravoxel incoherent motion analysis and its implementation in breast diffusion-weighted imaging. *J Magn Reson Imaging* (2016) 43:1122–31. doi:10.1002/jmri.25086

**Conflict of Interest Statement:** The authors declare that the research was conducted in the absence of any commercial or financial relationships that could be construed as a potential conflict of interest.

Copyright © 2016 Sardanelli, Carbonaro, Montemezzi, Cavedon and Trimboli. This is an open-access article distributed under the terms of the Creative Commons Attribution License (CC BY). The use, distribution or reproduction in other forums is permitted, provided the original author(s) or licensor are credited and that the original publication in this journal is cited, in accordance with accepted academic practice. No use, distribution or reproduction is permitted which does not comply with these terms.



# Choline Metabolism Alteration: A Focus on Ovarian Cancer

**Marina Bagnoli<sup>1\*</sup>, Anna Granata<sup>1</sup>, Roberta Nicoletti<sup>1</sup>, Balaji Krishnamachary<sup>2</sup>, Zaver M. Bhujwalla<sup>2</sup>, Rossella Canese<sup>3</sup>, Franca Podo<sup>3</sup>, Silvana Canevari<sup>1,4</sup>, Egidio Iorio<sup>3</sup> and Delia Mezzanzanica<sup>1\*</sup>**

<sup>1</sup>Unit of Molecular Therapies, Department of Experimental Oncology and Molecular Medicine, Fondazione IRCCS Istituto Nazionale dei Tumori, Milan, Italy, <sup>2</sup>Russell H. Morgan Department of Radiology and Radiological Science, Division of Cancer Imaging Research, In Vivo Cellular and Molecular Imaging Center, The Johns Hopkins University School of Medicine, Baltimore, MD, USA, <sup>3</sup>Department of Cell Biology and Neurosciences, Istituto Superiore di Sanità, Rome, Italy, <sup>4</sup>Functional Genomics and Informatics, Department of Experimental Oncology and Molecular Medicine, Fondazione IRCCS Istituto Nazionale dei Tumori, Milan, Italy

## OPEN ACCESS

### Edited by:

Giuseppe Esposito,  
Medstar Georgetown University  
Hospital, USA

### Reviewed by:

Orazio Schillaci,  
University of Rome Tor Vergata, Italy  
Luigi Aloj,  
Cambridge University Hospitals, UK  
Corina Millo,  
National Institutes of Health, USA

### \*Correspondence:

Marina Bagnoli  
[marina.bagnoli@istitutotumori.mi.it](mailto:marina.bagnoli@istitutotumori.mi.it);  
Delia Mezzanzanica  
[delia.mezzanzanica@istitutotumori.mi.it](mailto:delia.mezzanzanica@istitutotumori.mi.it)

### Specialty section:

This article was submitted to  
Cancer Imaging and  
Diagnosis, a section of the  
journal Frontiers in Oncology

**Received:** 10 March 2016

**Accepted:** 07 June 2016

**Published:** 22 June 2016

### Citation:

Bagnoli M, Granata A, Nicoletti R, Krishnamachary B, Bhujwalla ZM, Canese R, Podo F, Canevari S, Iorio E and Mezzanzanica D (2016)

Choline Metabolism Alteration:  
A Focus on Ovarian Cancer.

*Front. Oncol.* 6:153.

doi: 10.3389/fonc.2016.00153

Compared with normal differentiated cells, cancer cells require a metabolic reprogramming to support their high proliferation rates and survival. Aberrant choline metabolism is a fairly new metabolic hallmark reflecting the complex reciprocal interactions between oncogenic signaling and cellular metabolism. Alterations of the involved metabolic network may be sustained by changes in activity of several choline transporters as well as of enzymes such as choline kinase-alpha (ChoK- $\alpha$ ) and phosphatidylcholine-specific phospholipases C and D. Of note, the net outcome of these enzymatic alterations is an increase of phosphocholine and total choline-containing compounds, a “cholinic phenotype” that can be monitored in cancer by magnetic resonance spectroscopy. This review will highlight the molecular basis for targeting this pathway in epithelial ovarian cancer (EOC), a highly heterogeneous and lethal malignancy characterized by late diagnosis, frequent relapse, and development of chemoresistance. Modulation of ChoK- $\alpha$  expression impairs only EOC but not normal ovarian cells, thus supporting the hypothesis that “cholinic phenotype” is a peculiar feature of transformed cells and indicating ChoK- $\alpha$  targeting as a novel approach to improve efficacy of standard EOC chemotherapeutic treatments.

**Keywords:** choline kinase, ovarian cancer, phosphocholine metabolism, reversal of drug resistance, antioxidant defense

## INTRODUCTION

The uncontrolled cell growth characteristic of neoplastic diseases, besides involving deregulated control of cell proliferation, requires an adjustment of energy metabolism to sustain cell growth and division. Altered energy metabolism is considered as widespread in cancer cells as other cancer-associated characteristics. Reprograming of cell metabolism has been therefore included among cancer hallmarks (1), a series of biological properties acquired by tumor cells during transformation and disease progression. Metabolites themselves can interfere with oncogenic-driven cell signaling (2) and, since cancer cells are dependent on these changes in metabolism, these altered pathways represent attractive sources of promising therapeutic targets (3, 4). Furthermore, the differential uptake in some human cancers of glucose, choline, acetate, methionine, and aminoacid analogs, when used

as radiotracers in positron emission tomography (PET) imaging, is considered a clinically useful diagnostic/staging tool (4).

## CHOLINE METABOLISM ALTERATION IN HUMAN CANCER

Aberrant choline metabolism, characterized by increased phosphocholine (PCho) and total choline-containing compounds (tChos), is a fairly new metabolic hallmark that can be monitored in cancer by magnetic resonance spectroscopy (MRS) and that reflects the complex reciprocal interactions between oncogenic signaling and cellular metabolism (5, 6). PCho is both a precursor and a breakdown product of phosphatidylcholine (PC), one of the major components of cellular membranes. Indeed, the PCho content is sustained by activation of enzymes involved in PC biosynthetic and catabolic pathways: choline kinase (ChoK) and PC-specific phospholipase C (PC-PLC) (Figure 1A). ChoK is the first enzyme of the Kennedy pathway responsible for catalyzing the phosphorylation of free choline to form PCho in the biosynthesis of PC (7). Three isoforms of ChoK are present in mammalian cells encoded by two different genes: choline kinase-alpha (*CHKA*) and choline kinase-beta (*CHKB*). However, only ChoK-alpha (ChoK- $\alpha$ ) has a central role in sustaining PC biosynthesis required for the uncontrolled growth of cancer cells, and ChoK- $\beta$  alone cannot compensate this activity (8). In addition to its metabolic function, ChoK- $\alpha$  has been proven to play a critical role in oncogenesis, tumor progression, and metastasis of several cancers being required for the activation of growth factor-triggered signaling pathways (Ras activation, PI3K signaling), roles that proposed CHKA as an oncogene (5, 9–11). Indeed, an altered choline metabolism, sustained by increased expression and activity of ChoK- $\alpha$ , has been reported in various human malignancies (12–19). Furthermore, in the case of early stage non-small cell lung cancer (20), early stage hepatocellular

carcinoma (21), and prostate cancer (22), a prognostic role of ChoK- $\alpha$  overexpression has been revealed. These observations provided the molecular basis for the development of non-invasive imaging approaches based on choline phosphorylation for the characterization of tumor growth and response to therapy (23–26) as well as the rationale for developing specific inhibitors for this metabolic pathway even in diseases other than cancer (27, 28).

## CHOLINE KINASE AS A POTENTIALLY NEW THERAPEUTIC TARGET FOR CANCER TREATMENT

Choline kinase- $\alpha$  is an enzyme of particular interest being at the crossroad of the main survival signaling pathways with its overexpression contributing, through a positive feedback loop, to increased MAPK and PI3K signaling (5, 29). A large body of work in cancer cells suggests that ChoK- $\alpha$  expression and activity is directly associated not only with increased cancer cell proliferation but also with malignancy, making it a potential novel target for image-guided cancer therapy. In fact, the targeting of ChoK- $\alpha$  by RNA interference (RNAi) results in decreased PCho and tCho levels in human breast cancer cells while leaving human mammary epithelial cells unaffected (30, 31), thus opening an important therapeutic window for the development of a pharmacological intervention directed to this enzyme (32, 33). Indeed, the antitumor effects of ChoK- $\alpha$  inhibition have been reported in various cancers (34–40). Different compounds are at the moment available for ChoK- $\alpha$  pharmacological inhibition: hemicholinium-3 (HC-3), a competitive inhibitor with a ChoK- $\alpha$  mimetic structure able to block also choline transport, is very efficient *in vitro* but highly toxic *in vivo* (41); MN-58b, not commercially available, is a

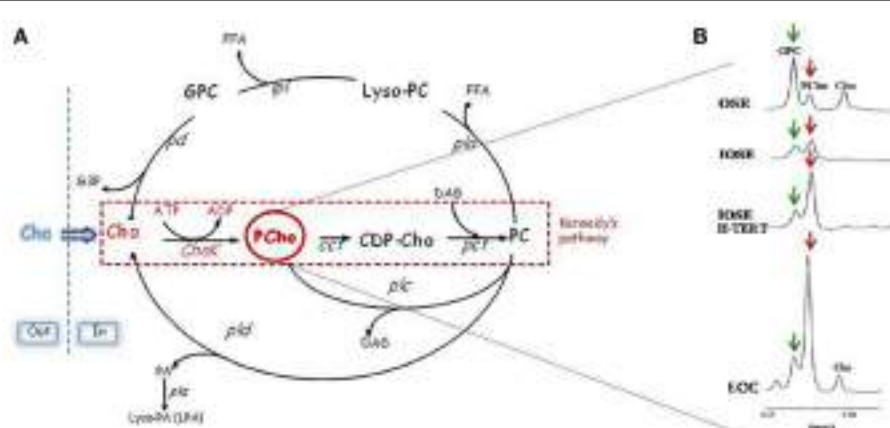


**FIGURE 1 | Schematic representation of PC cycle and routes of PCho accumulation. (A)** Kennedy's pathway: Cho, choline; Chok, choline kinase; PCho, phosphocholine; CCT, cytidylyltransferase; CDP-Cho, cytidine diphosphate-choline; PCT, phosphocholine phosphotransferase; DAG, diacylglycerol; PC, phosphatidylcholine. Catabolic pathways: PLC, PC-specific phospholipase C; PLD, PC-specific phospholipase D; PLA, PC-specific phospholipases A2 and A1; PD, phosphodiesterase; GPC, glycerophosphocholine; PA, phosphatidate. **(B)** In the progression from non-tumoral ovarian surface epithelial cells (OSE) or immortalized cell variants (IOSE with an increased replicative potential and IOSE-HTERT with unlimited replicative potential) to EOC cells, there is an evident accumulation of PCho (red arrows) and a decrease of GPC (green arrows).

less toxic HC-3 derivative able to inhibit cell growth *in vivo* in animal models (42); RSM-932A, a ChoK- $\alpha$  inhibitor selected for further clinical development due to its potent *in vivo* anticancer activity and lack of toxicity at the effective doses (43); CK37, a small molecule able to inhibit tumor growth in preclinical models (44); and new small molecule inhibitors identified by fragment-based drug discovery (45). These data suggest that inhibiting ChoK- $\alpha$ , even in combination with standard chemotherapeutic treatments, might represent a new anticancer approach particularly in tumors such as ovarian cancer with a still open clinical need for the identification of more efficient therapeutic modalities.

## OVARIAN CANCER

Epithelial ovarian cancer (EOC) is a life-threatening disease characterized by late-stage presentation and a distinctive ability to heavily invade the abdominal cavity (46). The yearly worldwide incidence of this cancer is of 238,700 new cases with a global mortality of 151,900 deaths per year (47), which make EOC the leading cause of death for gynecological cancers. Standard treatment for EOC patients is an aggressive primary surgery followed by platinum-based chemotherapy. However, around 30% of the patients undergo chemotherapeutic treatments before being identified as chemoresistant, and even for patients who achieve a pathological complete response, maintaining disease-free status remains a challenge. Indeed, most of the patients develop platinum-resistant recurrent disease, a largely incurable state. Despite the impressive improvement of surgical approaches and drug development, survival rate has changed little in the last decades (48), and 5-year survival rate for advanced stage patients is still around 30% (49).

It is well known that resistance to chemotherapy is one of the tumor “hallmarks” that also includes tumor ability to modify/reprogram cellular metabolism (1) to face with the biosynthetic demand of rapid proliferation and to overcome metabolic stress imposed by the microenvironment. As for many other cancer types, also EOC cells become dependent on these metabolic changes, which could be possibly exploited to identify therapeutic targets for overcoming chemoresistance.

## TARGETING THE ALTERED CHOLINE METABOLISM TO EVADE/CIRCUMVENT EOC CHEMORESISTANCE

Aberrant choline metabolism has been recently defined also in EOC. Analysis of expanded tCho MR spectral profiles showed that the relative areas of signal components due to individual choline metabolites [glycerophosphocholine (GPC), PCho, and free choline] changed in the progression from non-tumoral ovarian surface epithelial cells (OSE) or immortalized cell variants to EOC cells (15), with the PCho relative signal becoming predominant in carcinoma cells (**Figure 1B**).

A large body of work demonstrated that, in EOC, these alterations are sustained by the activation of two enzymes ChoK- $\alpha$  and PC-PLC, respectively, involved in the PC biosynthetic and

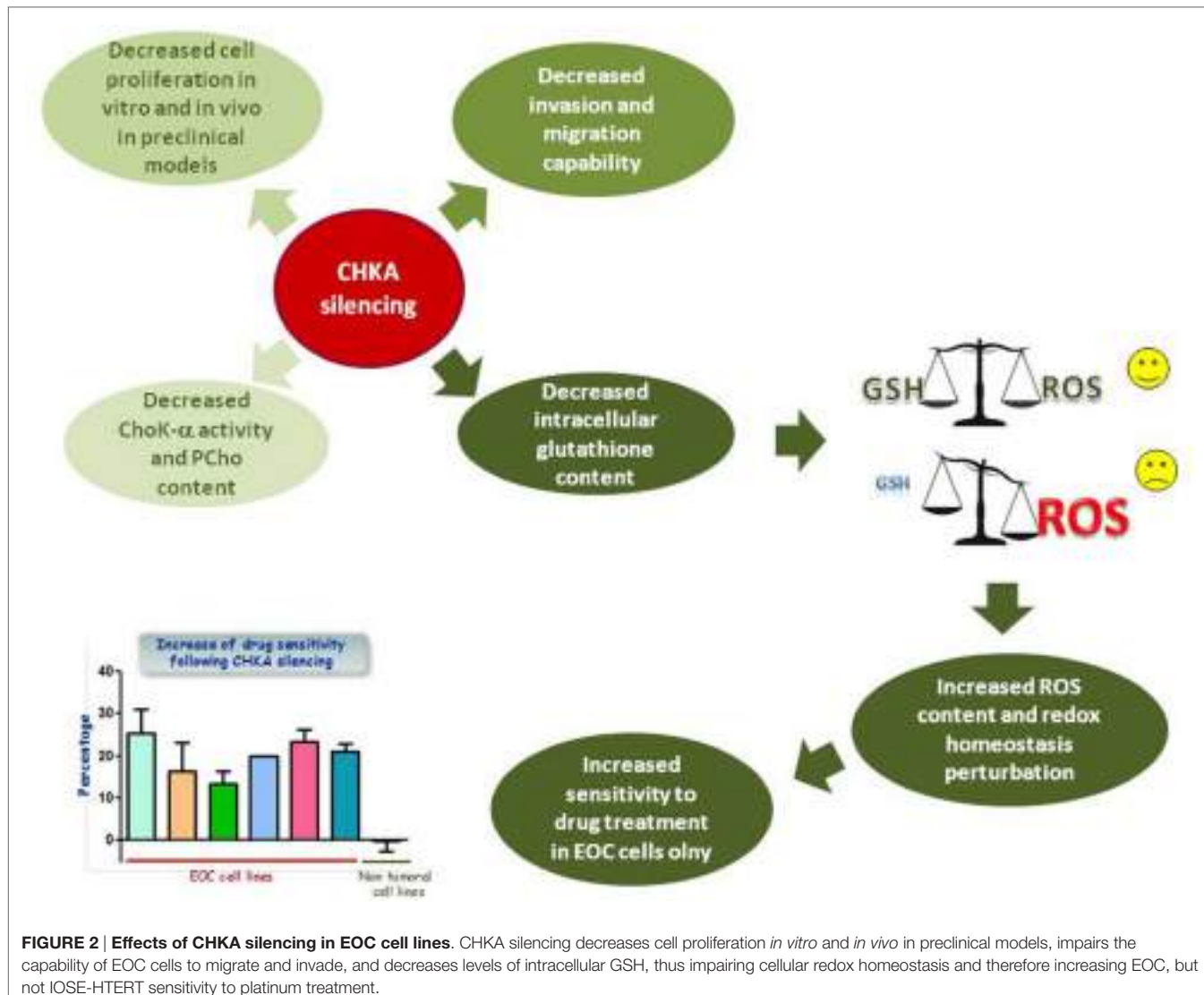
catabolic pathway. ChoK- $\alpha$  has a major role in increasing PCho content. Indeed, ChoK- $\alpha$  is overexpressed and hyperactivated in EOC cells as compared with the normal counterpart, accounting for up to the 70–80% of the total intracellular PCho content (16, 37). Gene expression analysis of the enzymes involved in the PC anabolic pathway showed that only CHKA was overexpressed, whereas the expression of other enzymes involved in the Kennedy pathway, as well as the beta isoform of choline kinase (CHKB), choline transporters, and enzymes involved in some catabolic pathways (mediated by PLD, PLA1, and PLA2) remained essentially unchanged (16). Among the enzymes involved in catabolic pathways, only PC-PLC is directly involved in PCho production. Although the mammalian PC-PLC has not been currently cloned and its sequence is unknown, this enzyme has been shown to be overexpressed and hyperactivated in EOC cells compared with normal counterparts (16, 50). EOC cells exposure to the PC-PLC inhibitor D609 abolished the activity of this enzyme and reduced the intracellular PCho level (without altering GPC and free choline contents), suggesting that also PC-PLC partially contributes to the intracellular PCho pool in EOC (16, 50).

To define the role of the abnormal expression and increased activation of ChoK- $\alpha$  in EOC biology, the enzyme was inactivated by transient and stable RNA interference in EOC cell lines and in non-tumoral immortalized cell variants. ChoK- $\alpha$  inhibition resulted in a less aggressive phenotype (36, 37), causing a decreased cell proliferation both *in vitro* and in preclinical *in vivo* models of Nu/Nu mice, an impaired capability to migrate and invade, together with an increased sensitivity to drug treatment of EOC cells (**Figure 2**).

The effects related to CHKA targeting in EOC appeared to induce a perturbation on EOC cell behavior different than that observed in other cellular models. In fact, neither previously described reduction of Akt phosphorylation in a PI3K-independent way (51) nor an attenuation of MAPK and PI3K/AKT signaling (29) was observed. Furthermore, in spite of a reduced cell proliferation, neither a decrease of cell viability nor apoptosis was detected in CHKA-silenced EOC cells.

On the other hand, the analysis of global metabolic profiling identified an altered glutathione (GSH) metabolism characterized by a decreased cysteine and GSH content (37). GSH is a thiol peptide involved in regulation of cell redox status through its antioxidant activities (52). Reduction of GSH content, perturbing redox homeostasis, is expected to render tumor cells more susceptible to chemotherapeutic treatment (**Figure 2**), and high intracellular levels of reduced GSH have been shown to contribute in developing resistance to chemotherapeutic drugs including platinum and doxorubicin (53–55). Accordingly, CHKA targeting in different EOC cellular models increased reactive oxygen species (ROS) intracellular levels and sensitivity to platinum and doxorubicin treatment. These effects were mediated by the reduction of GSH content, even in a drug resistant EOC model, while leaving unaffected the non-tumoral immortalized epithelial ovarian cells (37) (**Figure 2**).

Interestingly, the critical enzyme cleaving GPC to produce choline, the initial step in the pathway controlling the GPC/PC ratio, has been recently identified (56). The enzyme, named



endometrial differential 3 (EDI3), was initially described in a breast cancer cell line, where its inhibition corrected the GPC/PC ratio and reduced migratory activity of tumor cells. Also, EDI3 overexpression was associated with higher risk of developing metastasis and decreased survival in endometrial and ovarian cancer (56). The recent finding that EDI3 links choline metabolism to integrin expression, cell adhesion, and spreading also in an EOC cell line (57), suggests EDI3 as a new possible target to be explored, further confirming the value of the choline metabolism for therapeutic intervention in EOC.

The EOC “cholinic phenotype” is a peculiar feature of transformed cells that recapitulates the addiction of EOC cells to GSH content for the maintenance of their antioxidant defense. Targeting mechanisms upon which cancer cells are expected to be dependent (CHKA expression and cellular ROS homeostasis) could explain the differential response of cancer and non-transformed cells to CHKA knockdown. As well known, cancer cells acquire specific genetic and epigenetic alterations

that involve hyperactivation of oncogenes and/or inactivation of oncosuppressor genes. Some genetic changes support survival of cancer cells by creating specific signaling, which sustain metabolic pathways. However, the overall deregulation of cellular processes and functions is frequently associated with enhanced cellular stress, and malignant cells have to adapt to this phenotype, becoming dependent on a number of non-oncogenic functions to survive (3). Similarly, a dependency associated with ROS homeostasis has been shown to constitute a selective liability of malignant cells also in xenograft tumor models (58). Identifying such dependencies represent a promising alternative for the development of new therapeutic strategies to successfully target metabolic enzymes minimizing adverse effects on normal tissues. Synergisms of choline metabolism knockdown with conventional treatment might open an interesting clinical perspective, as it could represent an alternative strategy to increase the treatment efficacy also by reducing the clinical dose of drugs and limiting the damage of normal cells.

## EXPLOITING THE ALTERED CHOLINE METABOLISM FOR THE *IN VIVO* IMAGING OF TUMOR RESPONSE TO THERAPIES

Due to the increased metabolic activity, tumors are expected to intake greater amounts of a radioactive tracer than the adjacent normal tissues, justifying the use of PET imaging to monitor response to treatment and disease recurrence (59). Accordingly, the increased expression and activity of ChoK- $\alpha$  and choline transporters in tumor cells promoted a rapid development of radiolabeled choline analogs, as PET imaging tracers and  $^{11}\text{C}$ - or  $^{18}\text{F}$ -choline were proven to be more effective than  $^{18}\text{F}$ -fluorodeoxyglucose (FDG), whose abundant radioactivity excretion into the bladder could hamper image interpretation. Indeed, in the case of radiolabeled choline analogs, their incorporation mainly reflects the total amount of radiotracer that enters the cell by choline transport and accumulates, by efficient phosphorylation mainly due to ChoK activation, in the pool of water-soluble intermediates of the Kennedy pathway (24). Within the time window of choline PET examinations, the contributions given by PC catabolic enzymes (such as phospholipases C and D) to the pool of these radiolabeled choline derivatives are instead negligible (6).

The large proportion of studies evaluating choline radiotracers has been conducted in prostate cancer where choline PET gave a clinical contribution in the diagnosis and monitoring of response to therapy; however, the utility of  $^{11}\text{C}$ - or  $^{18}\text{F}$ -choline as radiotracers has been extensively reported also in non-prostate

histotypes (24, 59). Although studies on  $^{11}\text{C}$ - or  $^{18}\text{F}$ -choline as radiotracers in PET examinations of genitourinary tract cancers are currently under active evaluation as an alternative to  $^{18}\text{F}$ -FDG, few studies are currently available on the use of choline-based tracer in ovarian cancer, even at preclinical level (60, 61).

In spite of the EOC cholinic phenotype, a choline-based non-invasive detection and management is still a relatively unexplored field in this disease. An improvement in instrumentation and the integration of different imaging approaches, such as PET, magnetic resonance imaging (MRI), and computed tomography (CT), could provide the unique opportunity to monitor both morphologic and metabolic changes in tumor to improve diagnosis and the assessment of therapeutic efficacy.

## AUTHOR CONTRIBUTIONS

All the authors have contributed in writing this mini review and have been directly involved in obtaining the results described in the chapter dedicated to ovarian cancer and choline metabolism. All the authors reviewed the manuscript and approved the final version.

## ACKNOWLEDGMENTS

The authors are grateful to the Associazione Italiana per la Ricerca sul Cancro (AIRC, IG-9147, IG-12976, and IG-17475) and to the Ministero della Salute grant RF-2010-2313497 for partially supporting these studies.

## REFERENCES

1. Hanahan D, Weinberg RA. Hallmarks of cancer: the next generation. *Cell* (2011) 144:646–74. doi:10.1016/j.cell.2011.02.013
2. Ward PS, Thompson CB. Metabolic reprogramming: a cancer hallmark even Warburg did not anticipate. *Cancer Cell* (2012) 21:297–308. doi:10.1016/j.ccr.2012.02.014
3. Galluzzi L, Kepp O, Vander Heiden MG, Kroemer G. Metabolic targets for cancer therapy. *Nat Rev Drug Discov* (2013) 12:829–46. doi:10.1038/nrd4145
4. Vander Heiden MG. Targeting cancer metabolism: a therapeutic window opens. *Nat Rev Drug Discov* (2011) 10:671–84. doi:10.1038/nrd3504
5. Glunde K, Bhujwalla ZM, Ronen SM. Choline metabolism in malignant transformation. *Nat Rev Cancer* (2011) 11:835–48. doi:10.1038/nrc3162
6. Podo F, Canevari S, Canese R, Pisano ME, Ricci A, Iorio E. MR evaluation of response to targeted treatment in cancer cells. *NMR Biomed* (2011) 24:648–72. doi:10.1002/nbm.1658
7. Wu G, Vance DE. Choline kinase and its function. *Biochem Cell Biol* (2010) 88:559–64. doi:10.1139/O09-160
8. Wu G, Aoyama C, Young SG, Vance DE. Early embryonic lethality caused by disruption of the gene for choline kinase alpha, the first enzyme in phosphatidylcholine biosynthesis. *J Biol Chem* (2008) 283:1456–62. doi:10.1074/jbc.M708766200
9. Ramirez de Molina A, Gallego-Ortega D, Sarmentero J, Banez-Coronel M, Martin-Cantalejo Y, Lacal JC. Choline kinase is a novel oncogene that potentiates RhoA-induced carcinogenesis. *Cancer Res* (2005) 65:5647–53. doi:10.1158/0008-5472.CAN-04-4416
10. Gallego-Ortega D, Ramirez de Molina A, Ramos MA, Valdes-Mora F, Barderas MG, Sarmentero-Estrada J, et al. Differential role of human choline kinase alpha and beta enzymes in lipid metabolism: implications in cancer onset and treatment. *PLoS One* (2009) 4:e7819. doi:10.1371/journal.pone.0007819
11. Gallego-Ortega D, del PT, Valdes-Mora F, Cebrian A, Lacal JC. Involvement of human choline kinase alpha and beta in carcinogenesis: a different role in lipid metabolism and biological functions. *Adv Enzyme Regul* (2011) 51:183–94. doi:10.1016/j.advenzreg.2010.09.010
12. Nakagami K, Uchida T, Ohwada S, Koibuchi Y, Suda Y, Sekine T, et al. Increased choline kinase activity and elevated phosphocholine levels in human colon cancer. *Jpn J Cancer Res* (1999) 90:419–24. doi:10.1111/j.1349-7006.1999.tb00698.x
13. Ramirez de Molina A, Rodriguez-Gonzalez A, Gutierrez R, Martinez-Pineiro L, Sanchez J, Bonilla F, et al. Overexpression of choline kinase is a frequent feature in human tumor-derived cell lines and in lung, prostate, and colorectal human cancers. *Biochem Biophys Res Commun* (2002) 296:580–3. doi:10.1016/S0006-291X(02)00920-8
14. Ramirez de Molina A, Gutierrez R, Ramos MA, Silva JM, Silva J, Bonilla F, et al. Increased choline kinase activity in human breast carcinomas: clinical evidence for a potential novel antitumor strategy. *Oncogene* (2002) 21:4317–22. doi:10.1038/sj.onc.1205556
15. Iorio E, Mezzanzanica D, Alberti P, Spadaro F, Ramoni C, D'Ascenzo S, et al. Alterations of choline phospholipid metabolism in ovarian tumor progression. *Cancer Res* (2005) 65:9369–76. doi:10.1158/0008-5472.CAN-05-1146
16. Iorio E, Ricci A, Bagnoli M, Pisano ME, Castellano G, Di Vito M, et al. Activation of phosphatidylcholine cycle enzymes in human epithelial ovarian cancer cells. *Cancer Res* (2010) 70:2126–35. doi:10.1158/0008-5472.CAN-09-3833
17. Hernando E, Sarmentero-Estrada J, Koppie T, Belda-Iniesta C, Ramirez de Molina V, Cejas P, et al. A critical role for choline kinase-alpha in the aggressiveness of bladder carcinomas. *Oncogene* (2009) 28:2425–35. doi:10.1038/onc.2009.91
18. Trousil S, Lee P, Pinato DJ, Ellis JK, Dina R, Aboagye EO, et al. Alterations of choline phospholipid metabolism in endometrial cancer are caused by choline kinase alpha overexpression and a hyperactivated deacylation pathway. *Cancer Res* (2014) 74:6867–77. doi:10.1158/0008-5472.CAN-13-2409

19. Xiong J, Bian J, Wang L, Zhou JY, Wang Y, Zhao Y, et al. Dysregulated choline metabolism in T-cell lymphoma: role of choline kinase-alpha and therapeutic targeting. *Blood Cancer J* (2015) 5:287. doi:10.1038/bcj.2015.10
20. Ramirez de Molina A, Sarmentero-Estrada J, Belda-Iniesta C, Taròn M, Ramirez de Molina V, Cejas P, et al. Expression of choline kinase alpha to predict outcome in patients with early-stage non-small-cell lung cancer: a retrospective study. *Lancet Oncol* (2007) 8:889–97. doi:10.1016/S1470-2045(07)70279-6
21. Kwee SA, Hernandez B, Chan O, Wong L. Choline kinase alpha and hexokinase-2 protein expression in hepatocellular carcinoma: association with survival. *PLoS One* (2012) 7:e46591. doi:10.1371/journal.pone.0046591
22. Challapalli A, Trousil S, Hazell S, Kozlowski K, Gudi M, Aboagye EO, et al. Exploiting altered patterns of choline kinase-alpha expression on human prostate tissue to prognosticate prostate cancer. *J Clin Pathol* (2015) 68:703–9. doi:10.1136/jclinpath-2015-202859
23. Podo F, Sardanelli F, Iorio E, Canese R, Carpinelli G, Fausto A. Abnormal choline phospholipid metabolism in breast and ovary cancer: molecular bases for noninvasive imaging approaches. *Curr Med Imaging Rev* (2007) 3:123–37. doi:10.2174/157340507780619160
24. Glunde K, Penet MF, Jiang L, Jacobs MA, Bhujwalla ZM. Choline metabolism-based molecular diagnosis of cancer: an update. *Expert Rev Mol Diagn* (2015) 15:735–47. doi:10.1586/14737159.2015.1039515
25. Kumar M, Arlauckas SP, Saksena S, Verma G, Ittyerah R, Pickup S, et al. Magnetic resonance spectroscopy for detection of choline kinase inhibition in the treatment of brain tumors. *Mol Cancer Ther* (2015) 14:899–908. doi:10.1158/1535-7163.MCT-14-0775
26. Mignion L, Danhier P, Magat J, Porporato PE, Masquelier J, Gregoire V, et al. Non-invasive in vivo imaging of early metabolic tumor response to therapies targeting choline metabolism. *Int J Cancer* (2015) 138:2043–9. doi:10.1002/ijc.29932
27. Bernard NJ. Rheumatoid arthritis: choline kinase-more than a cancer therapy target? *Nat Rev Rheumatol* (2014) 10:699. doi:10.1038/nrrheum.2014.180
28. Guma M, Sanchez-Lopez E, Lodi A, Garcia-Carbonell R, Tiziani S, Karin M, et al. Choline kinase inhibition in rheumatoid arthritis. *Ann Rheum Dis* (2014) 74:1399–407. doi:10.1136/annrheumdis-2014-205696
29. Yalcin A, Clem B, Makoni S, Clem A, Nelson K, Thornburg J, et al. Selective inhibition of choline kinase simultaneously attenuates MAPK and PI3K/AKT signaling. *Oncogene* (2010) 29:139–49. doi:10.1038/onc.2009.317
30. Glunde K, Raman V, Mori N, Bhujwalla ZM. RNA interference-mediated choline kinase suppression in breast cancer cells induces differentiation and reduces proliferation. *Cancer Res* (2005) 65:11034–43. doi:10.1158/0008-5472.CAN-05-1807
31. Mori N, Glunde K, Takagi T, Raman V, Bhujwalla ZM. Choline kinase down-regulation increases the effect of 5-fluorouracil in breast cancer cells. *Cancer Res* (2007) 67:11284–90. doi:10.1158/0008-5472.CAN-07-2728
32. Lacal JC. Choline kinase: a novel target for antitumor drugs. *IDrugs* (2001) 4:419–26.
33. Janardhan S, Srivani P, Sastry GN. Choline kinase: an important target for cancer. *Curr Med Chem* (2006) 13:1169–86. doi:10.2174/092986706776360923
34. de la Cueva A, Ramirez de Molina A, Alvarez-Ayerza N, Ramos MA, Cebrian A, Del Pulgar TG, et al. Combined 5-FU and ChoKalpah inhibitors as a new alternative therapy of colorectal cancer: evidence in human tumor-derived cell lines and mouse xenografts. *PLoS One* (2013) 8:e64961. doi:10.1371/journal.pone.0064961
35. Sanchez-Lopez E, Zimmerman T, del PT, Moyer MP, Lacal Sanjuan JC, Cebrian A. Choline kinase inhibition induces exacerbated endoplasmic reticulum stress and triggers apoptosis via CHOP in cancer cells. *Cell Death Dis* (2013) 4:e933. doi:10.1038/cddis.2013.453
36. Granata A, Nicoletti R, Tinaglia V, De Cecco L, Pisanu ME, Ricci A, et al. Choline kinase-alpha by regulating cell aggressiveness and drug sensitivity is a potential druggable target for ovarian cancer. *Br J Cancer* (2014) 110:330–40. doi:10.1038/bjc.2013.729
37. Granata A, Nicoletti R, Perego P, Iorio E, Krishnamachary B, Benigni F, et al. Global metabolic profile identifies choline kinase alpha as a key regulator of glutathione-dependent antioxidant cell defense in ovarian carcinoma. *Oncotarget* (2015) 6:11216–30. doi:10.18632/oncotarget.3589
38. Kim HS, Tian L, Jung M, Choi SK, Sun Y, Kim H, et al. Downregulation of choline kinase-alpha enhances autophagy in tamoxifen-resistant breast cancer cells. *PLoS One* (2015) 10:e0141110. doi:10.1371/journal.pone.0141110
39. Mazarico JM, Sanchez-Arevalo Lobo V, Favicchio R, Greenhalf W, Costello E, Carrillo-de Santa PE, et al. Choline kinase alpha (CHKalpha) as a therapeutic target in pancreatic ductal adenocarcinoma: expression, predictive value, and sensitivity to inhibitors. *Mol Cancer Ther* (2016) 15:323–33. doi:10.1158/1535-7163.MCT-15-0214
40. Asim M, Massie CE, Orafidiya F, Pertega-Gomes N, Warren AY, Esmaeili M, et al. Choline kinase alpha as an androgen receptor chaperone and prostate cancer therapeutic target. *J Natl Cancer Inst* (2016) 108:iidjv371. doi:10.1093/jnci/djv371
41. Hernandez-Alcoceba R, Saniger L, Campos J, Nunez MC, Khalees F, Gallo MA, et al. Choline kinase inhibitors as a novel approach for antiproliferative drug design. *Oncogene* (1997) 15:2289–301. doi:10.1038/sj.onc.1201414
42. Hernandez-Alcoceba R, Fernandez F, Lacal JC. In vivo antitumor activity of choline kinase inhibitors: a novel target for anticancer drug discovery. *Cancer Res* (1999) 59:3112–8.
43. Lacal JC, Campos JM. Preclinical characterization of RSM-932A, a novel anti-cancer drug targeting the human choline kinase alpha, an enzyme involved in increased lipid metabolism of cancer cells. *Mol Cancer Ther* (2015) 14:31–9. doi:10.1158/1535-7163.MCT-14-0531
44. Clem BF, Clem AL, Yalcin A, Goswami U, Arumugam S, Telang S, et al. A novel small molecule antagonist of choline kinase-alpha that simultaneously suppresses MAPK and PI3K/AKT signaling. *Oncogene* (2011) 30:3370–80. doi:10.1038/onc.2011.51
45. Zech SG, Kohlmann A, Zhou T, Li F, Squillace RM, Parillon LE, et al. Novel small molecule inhibitors of choline kinase identified by fragment-based drug discovery. *J Med Chem* (2016) 59:671–86. doi:10.1021/acs.jmedchem.5b01552
46. Jayson GC, Kohn EC, Kitchener HC, Ledermann JA. Ovarian cancer. *Lancet* (2014) 384:1376–88. doi:10.1016/S0140-6736(13)62146-7
47. Torre LA, Bray F, Siegel RL, Ferlay J, Loriet-Tieulent J, Jemal A. Global cancer statistics, 2012. *CA Cancer J Clin* (2015) 65:87–108. doi:10.3322/caac.21262
48. Vaughan S, Coward JI, Bast RC Jr, Berchuck A, Berek JS, Brenton JD, et al. Rethinking ovarian cancer: recommendations for improving outcomes. *Nat Rev Cancer* (2011) 11:719–25. doi:10.1038/nrc3144
49. Siegel RL, Miller KD, Jemal A. Cancer statistics, 2015. *CA Cancer J Clin* (2015) 65:5–29. doi:10.3322/caac.21254
50. Spadaro F, Ramoni C, Mezzanzanica D, Miotti S, Alberti P, Cecchetti S, et al. Phosphatidylcholine-specific phospholipase C activation in epithelial ovarian cancer cells. *Cancer Res* (2008) 68:6541–9. doi:10.1158/0008-5472.CAN-07-6763
51. Chua BT, Gallego-Ortega D, de Molina A, Ullrich A, Lacal JC, Downward J. Regulation of Akt(ser473) phosphorylation by Choline kinase in breast carcinoma cells. *Mol Cancer* (2009) 8:131. doi:10.1186/1476-4598-8-131
52. Singh S, Khan AR, Gupta AK. Role of glutathione in cancer pathophysiology and therapeutic interventions. *J Exp Ther Oncol* (2012) 9:303–16.
53. Godwin AK, Meister A, O'Dwyer PJ, Huang CS, Hamilton TC, Anderson ME. High resistance to cisplatin in human ovarian cancer cell lines is associated with marked increase of glutathione synthesis. *Proc Natl Acad Sci USA* (1992) 89:3070–4. doi:10.1073/pnas.89.7.3070
54. Chen HH, Kuo MT. Role of glutathione in the regulation of cisplatin resistance in cancer chemotherapy. *Met Based Drugs* (2010) 2010:430939. doi:10.1155/2010/430939
55. Shim GS, Manandhar S, Shin DH, Kim TH, Kwak MK. Acquisition of doxorubicin resistance in ovarian carcinoma cells accompanies activation of the NRF2 pathway. *Free Radic Biol Med* (2009) 47:1619–31. doi:10.1016/j.freeradbiomed.2009.09.006
56. Stewart JD, Marchan R, Lesjak MS, Lambert J, Hergenroeder R, Ellis JK, et al. Choline-releasing glycerophosphodiesterase EDI3 drives tumor cell migration and metastasis. *Proc Natl Acad Sci USA* (2012) 109:8155–60. doi:10.1073/pnas.1117654109
57. Lesjak MS, Marchan R, Stewart JD, Rempel E, Rahnenführer J, Hengstler JG. EDI3 links choline metabolism to integrin expression, cell adhesion and spreading. *Cell Adh Migr* (2014) 8:499–508. doi:10.4161/cam.29284

58. Raj L, Ide T, Gurkar AU, Foley M, Schenone M, Li X, et al. Selective killing of cancer cells by a small molecule targeting the stress response to ROS. *Nature* (2011) 475:231–4. doi:10.1038/nature10167
59. Challapalli A, Aboagye EO. Positron emission tomography imaging of tumor cell metabolism and application to therapy response monitoring. *Front Oncol* (2016) 6:44. doi:10.3389/fonc.2016.00044
60. Fanti S, Nanni C, Ambrosini V, Gross MD, Rubello D, Farsad M. PET in genitourinary tract cancers. *Q J Nucl Med Mol Imaging* (2007) 51(3):260–71.
61. Torizuka T, Kanno T, Futatsubashi M, Okada H, Yoshikawa E, Nakamura F, et al. Imaging of gynecologic tumors: comparison of (11)C-choline PET with (18)F-FDG PET. *J Nucl Med* (2003) 44(7):1051–6.

**Conflict of Interest Statement:** The authors declare that the research was conducted in the absence of any commercial or financial relationships that could be construed as a potential conflict of interest.

Copyright © 2016 Bagnoli, Granata, Nicoletti, Krishnamachary, Bhujwalla, Canese, Podo, Canevari, Iorio and Mezzanzanica. This is an open-access article distributed under the terms of the Creative Commons Attribution License (CC BY). The use, distribution or reproduction in other forums is permitted, provided the original author(s) or licensor are credited and that the original publication in this journal is cited, in accordance with accepted academic practice. No use, distribution or reproduction is permitted which does not comply with these terms.



# In vivo Magnetic Resonance Metabolic and Morphofunctional Fingerprints in Experimental Models of Human Ovarian Cancer

Rossella Canese<sup>1\*</sup>, Delia Mezzanzanica<sup>2</sup>, Marina Bagnoli<sup>2</sup>, Stefano Indraccolo<sup>3</sup>, Silvana Canevari<sup>2</sup>, Franca Podo<sup>1</sup> and Egidio Iorio<sup>1</sup>

<sup>1</sup>Department of Cell Biology and Neurosciences, Istituto Superiore di Sanità, Rome, Italy, <sup>2</sup>Department of Experimental Oncology and Molecular Medicine, Fondazione IRCCS Istituto Nazionale dei Tumori, Milan, Italy, <sup>3</sup>Immunology and Molecular Oncology Unit, IOV – Istituto Oncologico Veneto – I.R.C.C.S, Padova, Italy

## OPEN ACCESS

### Edited by:

Cicero Matthew R. Habito,  
Massachusetts  
General Hospital, USA

### Reviewed by:

Orazio Schillaci,  
University of Rome Tor Vergata, Italy  
Angelo Don Il Santos Grasparil,  
Cardinal MRI Center, Philippines

### \*Correspondence:

Rossella Canese  
rossella.canese@iss.it

### Specialty section:

This article was submitted  
to *Cancer Imaging  
and Diagnosis*,  
a section of the journal  
*Frontiers in Oncology*

**Received:** 22 March 2016

**Accepted:** 17 June 2016

**Published:** 29 June 2016

### Citation:

Canese R, Mezzanzanica D, Bagnoli M, Indraccolo S, Canevari S, Podo F and Iorio E (2016) In vivo Magnetic Resonance Metabolic and Morphofunctional Fingerprints in Experimental Models of Human Ovarian Cancer. *Front. Oncol.* 6:164.  
doi: 10.3389/fonc.2016.00164

Epithelial ovarian cancer (EOC) is the gynecological malignancy with the highest death rate, characterized by frequent relapse and onset of drug resistance. Disease diagnosis and therapeutic follow-up could benefit from application of molecular imaging approaches, such as magnetic resonance imaging (MRI) and magnetic resonance spectroscopy (MRS), able to monitor metabolic and functional alterations and investigate the underlying molecular mechanisms. Here, we overview the quantitative alterations that occur during either orthotopic or subcutaneous growth of preclinical EOC models. A common feature of <sup>1</sup>H MR spectra is the presence of a prominent peak due to total choline-containing metabolites (tCho), together with other metabolic alterations and MRI-detected morphofunctional patterns specific for different phenotypes. The tCho signal, already present at early stages of tumor growth, and changes of diffusion-weighted MRI parameters could serve as markers of malignancy and/or tumor response to therapy. The identification by MRS and MRI of biochemical and physiopathological fingerprints of EOC disease in preclinical models can represent a basis for further developments of non-invasive MR approaches in the clinical setting.

**Keywords:** MRI, magnetic resonance spectroscopy, DWI, ADC, epithelial ovarian cancer, target therapy, animal model

## INTRODUCTION

Epithelial ovarian cancer (EOC) is the fifth cause of cancer-related deaths among women (1), leading to about 140,000 deaths worldwide per year. Standard treatment for advanced-stage EOC is debulking surgery followed by platinum-based chemotherapy, with high response rates, but most of these patients will eventually relapse. Several drugs are available to treat recurrences; however, clinical responses remain short-lived and lead to only marginal improvements in survival of patients with platinum-resistant disease (2).

Prognostic and predictive biomarkers of therapy response need to be identified, and novel approaches of drug response assessment need to be developed to validate additional biological end points.

Early detection of response to cancer treatment frequently presents a challenge, as many new therapies lead to inhibition of tumor growth rather than to tumor shrinkage. Among the new therapeutic

agents under clinical development, those with relative late effects could strongly benefit from an early indication of tumor response to treatment. Novel non-invasive methods to monitor or predict response to treatment, therefore, need to be developed.

Magnetic resonance spectroscopy (MRS) is a non-invasive imaging method that can be employed to monitor metabolism alterations that are associated with early drug target modulation (3) and can be predictive of cancer response to treatment (4). After controversial results in the differentiation of benign vs. malignant lesions in EOC patients, probably due to the heterogeneous nature of this disease (5), recent clinical studies are evaluating the role of the altered spectral pattern as an indicator of response during treatment of malignant disease rather than as initial diagnostic tool.

Magnetic resonance imaging (MRI) is the standard modality for the local staging of gynecological malignancies but has several limitations, particularly for lymph node staging and evaluation of peritoneal carcinomatosis. Recent growing interest is addressed to functional imaging modalities, such as diffusion-weighted MRI (DWI), a unique technique that provides tissue contrast by exploiting the restricted water mobility within hypercellular tumors to increase the contrast between these lesions and surrounding tissues. Using quantitative measurement of apparent diffusion coefficient (ADC) or other perfusion-related parameters, DWI provides a new tool for better distinguishing malignant tissues from benign tumors (6) and can aid in early monitoring of treatment efficacy in patients with advanced EOC (7). Moreover, the capability of DWI to detect alterations at cellular level rather than in the entire tumor mass could be crucial in the assessment of early response to a targeted therapy.

Important advances in our understanding of the molecular EOC pathogenesis and tissue heterogeneity were achieved by using appropriate preclinical models that approach the complexity of this disease in humans. Proper preclinical models that mimic tumor behavior and microenvironment involvement in patients are also essential for the evaluation of novel treatments (8, 9). Among these, models of spontaneous EOC in experimental animals (10, 11) or genetically modified animals (12, 13) have been developed, but their use remains limited because of the long latency to tumorigenesis and the heterogeneity in the timing of tumor development. EOC cell lines derived from ascites or primary ovarian tumors have been extensively used for studying tumor growth and response to treatment (14). Xenografts derived from intraperitoneal (i.p.) injection of human EOC cells in immunodeficient mice are relatively rapid to generate and develop tumor masses mimicking tumor diffusion in patients; together with subcutaneous (s.c.) xenografts, these models have been widely used for studying the mechanisms controlling tumor growth and chemosensitivity. An alternative orthotopic EOC model can be generated by directly engrafting onto the ovary of female mice a piece of tumor tissue derived from an ovarian tumor xenograft (15).

In this short review, we will discuss the significance of metabolic and functional features, respectively, detected by MRS and DWI in different EOC preclinical models, focusing on aspects of metabolic reprogramming occurring in response to anticancer

treatment strategies. In spite of the growing interest in the use of MRI (especially DWI) techniques in ovarian cancer clinical studies (16–18), a still limited number of papers have been published on *in vivo* experimental EOC models, mainly due to inherent experimental difficulties. For this reason, we decided to also include, in this review, some reports presented at prestigious peer reviewed international conferences (with abstracts published in copyrighted proceedings), although not yet translated into *in extenso* articles.

## METABOLIC FEATURES DETECTED BY *IN VIVO* $^1\text{H}$ MRS IN EOC XENOGRAFTS

Typical  $^1\text{H}$  MR spectra acquired from vital areas of EOC models obtained by either s.c. or i.p. implantation of human EOC cell lines of different origins (19, 20) in immunocompromised mice (21, 22) are reported in Figures 1A–F. The choice of an s.c. implant relies on its simplicity and the short time (about 2 weeks) required to develop solid masses. The i.p. model, instead, recapitulates peritoneal spread, mimicking typical features of EOC growth and dissemination observed in patients. As shown in Figure 1, a prominent  $^1\text{H}$  MRS signal at 3.2 parts per million (ppm) arises from the trimethylammonium headgroups of the total choline-containing metabolites (tCho). This peak could be clearly detected and quantitated in all investigated EOC models at different times of tumor growth. A complete set of MRS analyses at different echo times and at different time points during tumor growth, together with the application of a quantitative method including measurements of water T2 and content (21), allowed quantification of the spectral changes occurring over time. The tCho level was found to range between 2 and 6 mM in all analyzed xenografts (Figures 1A–F).

According to high resolution  $^1\text{H}$  MRS analyses of cancer cell (23) and tissue extracts (21, 24), the tCho peak mainly comprises contributions from phosphocholine (PCho), glycerophosphocholine (GPCho), and free choline (Cho). These analyses showed that the PCho/tCho ratio in all cells used for implants shown in Figure 1 was greater than 0.70 (21, 24).

Besides tCho, multiple signals arising from the glutamine and glutamate pool (Glx), myo-inositol (Ins), and taurine (Tau) are also detected in the spectra of EOC xenografts (Figures 1A–D). Xenografts obtained from s.c. implantation of SKOV3.ip cells [a highly tumorigenic cell variant of the ATCC SKOV3 cell line, endowed with a twofold higher HER2 overexpression level (14)], showed that the mean tCho content ranged from 2.9 to 4.5 mM (with a PCho/tCho ratio of 0.90). In the SKOV3.ip s.c. model, the Glx signal was detected at early stages of tumor growth and decreased at later stages, while Ins increased in vital areas of the tumors (21). When the tumor reached a size larger than 400 mm<sup>3</sup>, an increase in lipid (Lip) signal at 1.3 ppm was also observed in “normal appearing” areas in which the presence of micronecrosis was detected. Spectral editing ensured that this signal was mainly due to lipids rather than to lactate (Lac) (21).

An increased Lip resonance was also observed in the viable part of i.p. implants, either OVCA432 (Figure 1B) or SKOV3.ip models (Figure 1D), compared with the corresponding s.c. implants (Figures 1A,C, respectively). This was due to the

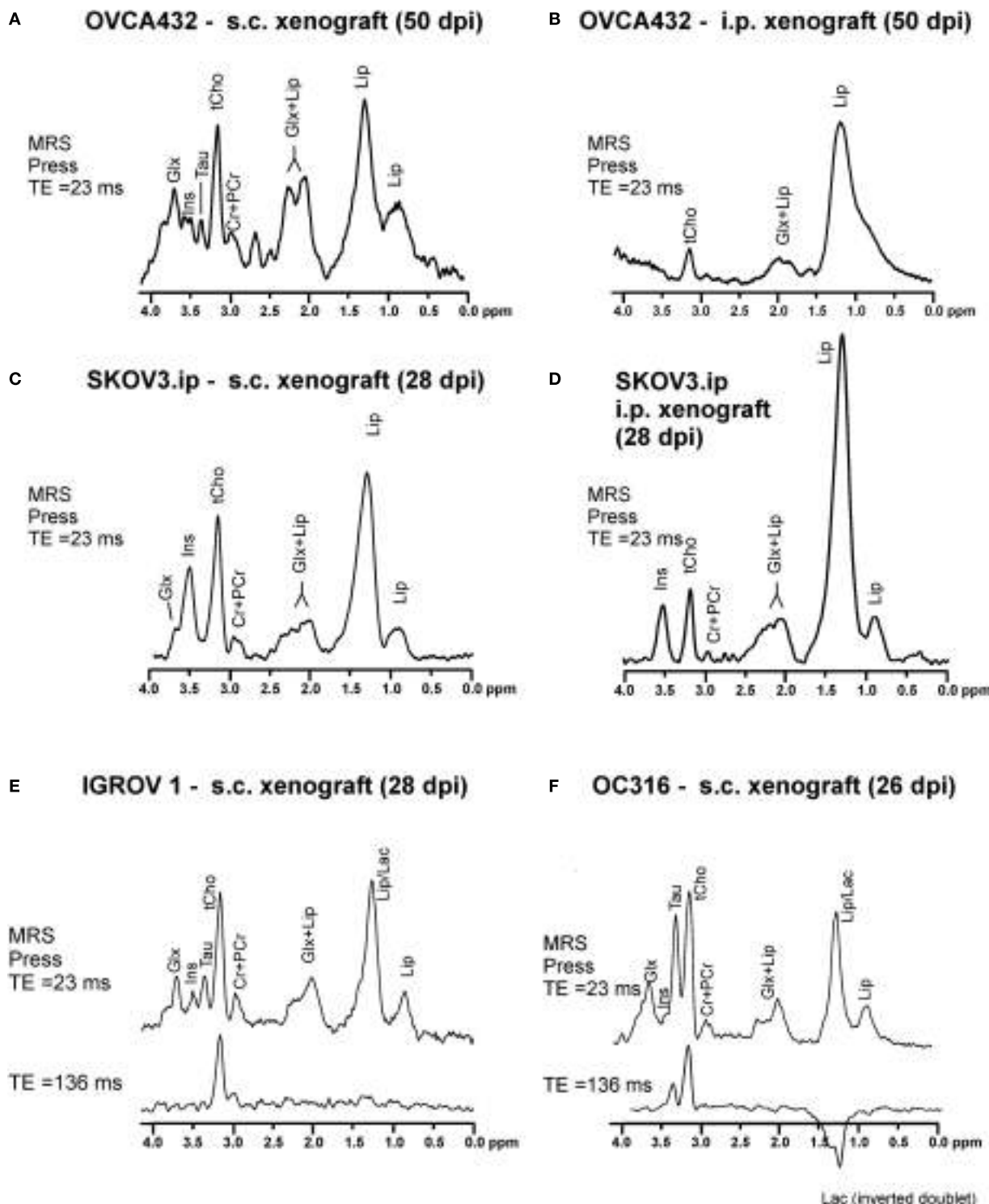


**FIGURE 1 |** Typical *in vivo*  $^1\text{H}$  MRS spectra acquired at 4.7 T from vital areas (as detected by T2-weighted MRI) of xenografts of about 400–600  $\text{mm}^3$  obtained in SCID mice by (A) subcutaneous (s.c.) implantation of OVCA432 cells (ATTC cell line derived from patient ascite), (B) intraperitoneal (i.p.) implantation of OVCA432 cells, (C) s.c. implantation of the SKOV3.ip cells [a cell line obtained by *in vivo* passage and subsequent *in vitro* culture of the HER2-positive ATTC SKOV3 cell line (14)], (D) i.p. implantation of SKOV3.ip cells, (E) s.c. implantation of IGROV1 cells (ATTC cell line derived from human primary ovarian cancer), and (F) s.c. implantation of OC316 cells (cell line derived from patient ascite). All these EOC models were examined between 26 and 50 days post implantation (dpi). Peak assignment: Glx, glutamine plus glutamate; Ins, myo-inositol; Tau, taurine; tCho, total choline-containing compounds; Cr + PCr, creatine plus phosphocreatine; Lip, lipids; Lac, lactate. Abbreviation: ppm, part per million. Further details in Ref. (22) for spectra in (A,B), Ref. (21) for spectra in (C,D), and Ref. (24) for spectra in (E,F).

presence of round-shaped structures compatible with lipid aggregates detected by H&E staining in *ex vivo* analyses (21).

Peculiar spectral profiles have also been observed in s.c. xenografts derived from OC316 and IGROV1 cells (**Figures 1E,F**). These patient-derived EOC cell lines have been identified as prototypes of highly and poorly glycolytic EOC cells, respectively (25), based on measurements of glucose consumption and lactate production rates *in vitro*, as well as assessment of expression levels of glycolysis-associated genes. Besides the tCho and lipid signals, high resonances arising from Tau and Lac were detected in the spectra of “glucose addicted” EOC xenografts (OC316) – but not in those of the low glycolytic IGROV1 EOC model. The Lac resonance could be isolated from the partially overlapping Lip resonance in the *in vivo* <sup>1</sup>H MR spectra of the OC316 model by exploiting the property of the Lac signal to be reversed when acquired with an echo time (TE) of 136 ms and the property of Lip signal to be decayed at TE = 136 ms due to its short T2 value, as shown in the lower spectrum of **Figure 1F** and confirmed by bioluminescence metabolic imaging (24).

Overall, this body of evidence showed that an elevated tCho peak was the most common feature of *in vivo* <sup>1</sup>H MR spectra of the investigated EOC models, in agreement with similar findings reported for clinical EOC lesions (26–28). Moreover, thanks to the shorter echo times achievable in preclinical studies [about 20 ms vs. 135 ms typically used for clinical MRS and <sup>31</sup>P MRS and spectroscopic imaging (MRSI) examinations], we could observe and quantify several other metabolites, which give a more detailed picture of tumor metabolism and may allow for a more extensive “metabolic targeting.”

## THE tCHO PEAK AS A MARKER OF MALIGNANCY AND RESPONSE TO THERAPY

The concentration levels of the tCho peak components depend on the activity rates of multiple enzymes involved in anabolic and catabolic pathways of the agonist-activated phosphatidylcholine cycle (29). Alterations in the levels of the tCho components in cancer may result from changes occurring in the activity rates of multiple enzymes of this cycle under the dysregulated control exerted by oncogene-driven cell signaling cascades (23, 30). An increase in the tCho content has been indicated as a biomarker for distinguishing malignant from benign lesions in the breast (31, 32) and has been detected in a variety of other cancer cells and tissues (23), including EOC cells (19, 20) and clinical lesions (19, 20, 33). In particular, a 4- to 7-fold increase in PCho detected in a series of human EOC cell lines was associated with a 12- to 25-fold activation of choline kinase (ChoK) and a 5- to 17-fold activation of phosphatidylcholine-specific phospholipase C (PC-PLC) (20).

A number of preclinical studies have been addressed to evaluate the role of tCho and its components (especially PCho) as possible markers of tumor progression and response to therapies in different types of cancers (23). Among these, recent investigations also focused on MRS-detected metabolic effects induced on EOC models by anticancer treatments.

Reduction of the tCho content of SKOV3.ip xenograft after cytotoxic treatments suggests that this signal could be a potential biomarker of treatment response. Decreased tCho levels and increased Lac content, associated with an increase in diffusion parameters (both diffusion and perfusion components), were found to be induced in a SKOV3.ip xenograft model by trabectedin (a new marine-derived antitumor agent, which has shown activity in multiple tumor types, including EOC). The detected tCho reduction suggests that this signal could be a potential biomarker of trabectedin response, while the Lac increase likely reflects the activation of lactic dehydrogenase (LDH) as a consequence of a cytotoxic damage to the cancer cells (34).

The effects exerted on tumor growth and metabolism by pantethine, a derivative of vitamin B5 and precursor of coenzyme A, were investigated by Penet et al. (35) using MRI/MRS in an orthotopic model of ovarian cancer obtained by engrafting a piece of OVCAR3 tumor tissue onto the ovary of SCID female mice. Pantethine treatment resulted in slower tumor progression, decreased levels of PCho and phosphatidylcholine, and reduced metastases and ascites occurrence.

A marked tCho reduction has also been observed *in vitro* (in SKOV3.ip cells) and *in vivo* (in SKOV3.ip s.c. xenografts) upon treatment with the competitive PC-PLC inhibitor tricyclodecan-9-yl-potassium xanthate (D609). The *in vivo* tCho reduction was associated with increases in the T2 and ADC mean values, along with reduced Ki67 index and HER2 content, suggesting that PC-PLC plays an important role in HER2-driven EOC cell signaling and tumorigenicity (36).

## pH ALTERATIONS IN EOC MODELS AND ITS POTENTIAL EFFECTS ON CANCER TREATMENT

The tumor microenvironment plays a key role in tumor malignancy (37). In particular, microenvironment acidity has been shown to have a role in the resistance to chemotherapy, proliferation, and tumor progression. The causes of acidic extracellular pH in tumors have not yet been fully elucidated, although important contributions probably arise from deficiencies in blood perfusion, metabolic abnormalities associated with transformation, and an increased capability for transmembrane pH regulation (23).

<sup>31</sup>P MRS and spectroscopic imaging offers the most powerful approaches currently available to non-invasively measure extracellular pH (pHe) and intracellular/extracellular pH gradient ( $\Delta$ pH) in intact cancer cells and tissues (38, 39). In fact, by measuring the chemical shift difference between the exogenous cell-impermeant <sup>31</sup>P reporter 3-aminopropyl phosphonate resonance (3-APP, administered i.p. immediately prior to the MRI/MRS analyses) and that of  $\alpha$ -ATP, the acidic pHe (6.7–6.8) for s.c. and i.p. SKOV3.ip models has been measured at 30–35 dpi. The intracellular pH (pHi) measured from the chemical shift difference between Pi and  $\alpha$ -ATP was 7.3 in s.c. and 7.1 in i.p. xenografts (21).

An emerging technique, acidocEST-MRI, utilizes iopromide, a contrast agent that contains two chemical exchange saturation transfer (CEST) effects and can assess *in vivo* pHe more accurately and with a higher spatial resolution than <sup>31</sup>P MRS (40).

AcidoCEST-MRI was applied to the orthotopic (i.p.) SKOV3 model to investigate the relationship between pHe, vascular perfusion, and tumor volume (40). This tumor model was mildly acidic, with an average pH of 6.88, in agreement with our findings. Additionally, larger tumors were found to be more acidic. A lower vascular perfusion allowed for an elevated lactic acid production, thus causing an increase in tumor acidosis.

These pH alterations observed in EOC models can reflect microenvironment alteration in EOC patients' cancer lesions and may modulate their response to conventional or targeted therapies. The negative pH gradient detected in EOC models impairs the uptake of weakly basic drugs but can facilitate a selective retention by tumor tissues of drugs behaving as weak acids. MR techniques provide unique tools to selectively investigate these aspects *in vivo*.

## DIFFERENCES IN CYTOTOXIC AND CYTOSTATIC DRUGS' EFFECTS AS DETECTED BY *IN VIVO* DWI AND MRS

Early monitoring of treatment efficacy in patients with advanced EOC can be achieved using DWI and ADC mean values and distributions. In particular, the shape of the ADC distribution (in terms of skewness and kurtosis) has been proven to reflect chemotherapy response in patients (7, 41), as well as in EOC models (14, 24).

By analyzing ADC mean values and distributions, differences in cytotoxic and cytostatic effect can be observed largely before tumor shrinkage. In fact, cytostatic treatment effects can be observed during or up to 48 h after the end of treatment due to cell swelling, which results in an ADC decrease during the treatment, in absence of any detectable alteration in tCho level. Although cell swelling is a phenomenon that occurs during all treatments (it is in fact the first manifestation of almost all forms of injury

to cells), it is dominated by cell death when a cytotoxic agent is administered resulting in an increased extracellular space, which can be observed as an increased ADC, associated with a tCho reduction. Notably, the effect of a cisplatin-based treatment on the SKOV3.ip model (s.c. implant) was to reduce the ADC mean value (14). On the same EOC model, cytotoxic agents, such as D609 or trabectedin, induced a marked mean ADC increase associated with tCho reduction (34, 36).

## EOC MODELS WITH DIFFERENT GLYCOLYTIC PHENOTYPES HAVE DIFFERENT RESPONSES TO A HUMAN VEGF NEUTRALIZING mAB AS DETECTED BY *IN VIVO* MRS AND DWI

Xenografts obtained from OC316 and IGROV1 patient-derived EOC cells (described in paragraph 2) were used to investigate the effects on glucose metabolism of A4.6.1, a human VEGF neutralizing mAb bearing the same CDR region as bevacizumab (24).

In the "glucose addicted" OC316 xenografts, A4.6.1 caused a dramatic depletion of glucose and an exhaustion of ATP levels in tumors associated with the presence of large necrotic areas and partial tumor regression. Different behavior was observed in the IGROV1 xenograft where metabolism remained unaltered after anti-VEGF treatment associated with a minor effect on tumor growth. Functional links between AMPK pathway and therapeutic responses to VEGF neutralization have also been detected in EOC models.

Different ADC distributions characterized the response to VEGF neutralization of those two EOC models. In fact, as early as after 1 week of treatment, in the "glucose addicted" OC316 model, a cytotoxic effect of the anti-VEGF treatment could be observed as increased mean ADC (Figure 2A). This effect could

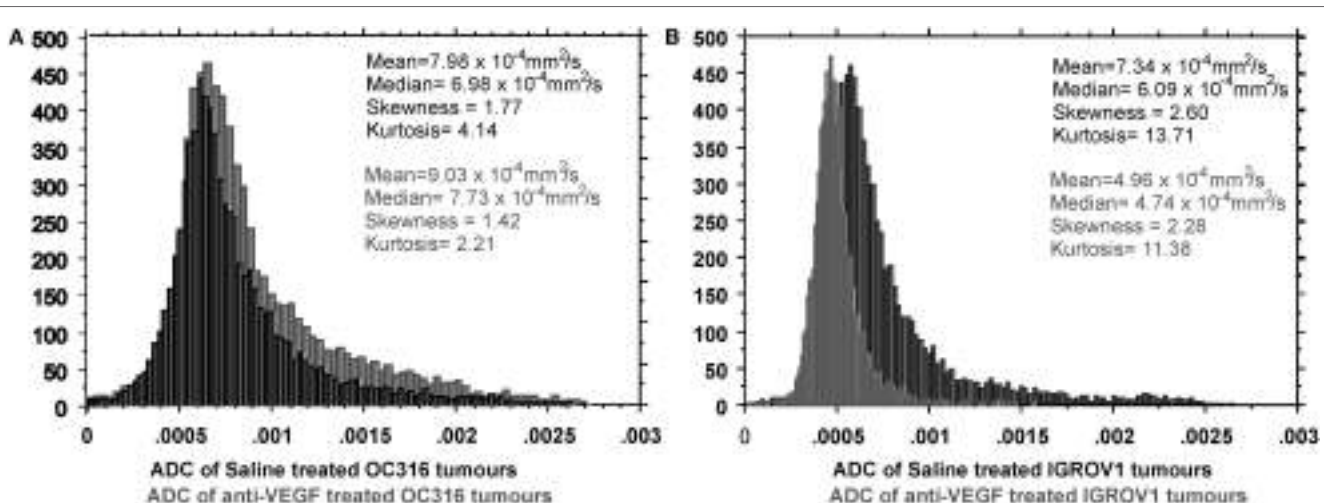


**FIGURE 2 |** Differential response to VEGF neutralization of two EOC models (OC316 and IGROV1) characterized by *in vitro* different glucose consumption and lactate production rates. In the "glucose addicted" model, (A) an average increase of ADC is present corresponding to increased necrotic areas. In the IGROV1 model, (B) the A4.6.1 mAb induces a cell damage that can be observed as "cell swelling," which causes the ADC reduction in the mean value and the right-hand shift of the ADC peak. Further details in Ref. (24).

be attributed to an increase in the extracellular space in agreement with microscopic or macroscopic areas of necrosis detected by histology (24) and associated with a significant delay in tumor growth. Opposite effect (ADC reduction) can be detected in the IGROV1 xenografts, where anti-VEGF treatment probably induces a cytostatic effect associated with a minor delay in tumor growth (**Figure 2B**). Moreover, the perfusion component [in terms of vascular signal fraction (VSF)], i.e., the component of fast diffusing spins (42), is reduced after anti-VEGF therapy, more pronounced in the OC316 than in the IGROV1 xenografts.

Prospectively, *in vivo* lactate and ADC quantitation and their monitoring following anti-VEGF treatment by MRI/MRS could represent non-invasive tools for the identification of “glucose addicted” EOC tumors and for predicting their clinical responses to bevacizumab and/or other antiangiogenic drugs.

## FUTURE PROSPECTIVES WITH RADIOLABELED COMPOUNDS FOR POSITRON EMISSION TOMOGRAPHY

Positron emission tomography (PET) imaging is mainly used to visualize general tumor processes, such as glucose metabolism using <sup>18</sup>F-fluorodeoxyglucose (<sup>18</sup>F-FDG) and DNA synthesis using <sup>18</sup>F-fluorodeoxythymidine (<sup>18</sup>F-FLT), as tools to predict prognosis and response to therapies (43, 44). More specific labeled ligands have been evaluated for specific targets, including immunotherapy components (<sup>64</sup>Cu-labeled anti-CA125 monoclonal antibody in SKOV3 and OVCAR3 xenografts) (45) and cell surface receptors (HER2 expression in SKOV3 xenografts) (46).

Despite the success in other cancers, the use of <sup>11</sup>C-Cho-PET has been rarely applied to EOC with limited results (47), and to the best of our knowledge, there are no papers on preclinical

## REFERENCES

- Siegel R, Naishadham D, Jemal A. Cancer statistics, 2013. *CA Cancer J Clin* (2013) 63(1):11–30. doi:10.3322/caac.21166
- Luvero D, Milani A, Ledermann JA. Treatment options in recurrent ovarian cancer: latest evidence and clinical potential. *Ther Adv Med Oncol* (2014) 6(5):229–39. doi:10.1177/1758834014544121
- Lodi A, Ronen SM. Magnetic resonance spectroscopy detectable metabolic fingerprint of response to antineoplastic treatment. *PLoS One* (2011) 6(10):e26155. doi:10.1371/journal.pone.0026155
- Wei L, Hong S, Yoon Y, Hwang SN, Park JC, Zhang Z, et al. Early prediction of response to Vorinostat in an orthotopic rat glioma model. *NMR Biomed* (2012) 25(9):1104–11. doi:10.1002/nbm.2776
- Ma FH, Qiang JW, Cai SQ, Zhao SH, Zhang GF, Rao YM. MR spectroscopy for differentiating benign from malignant solid adnexal tumors. *AJR Am J Roentgenol* (2015) 204(6):W724–30. doi:10.2214/AJR.14.13391
- Levy A, Medjoul A, Caramella C, Zareski E, Berges O, Chargari C, et al. Interest of diffusion-weighted echo-planar MR imaging and apparent diffusion coefficient mapping in gynecological malignancies: a review. *J Magn Reson Imaging* (2011) 33(5):1020–7. doi:10.1002/jmri.22546
- Kyriazi S, Collins DJ, Messiou C, Pennert K, Davidson RL, Giles SL, et al. Metastatic ovarian and primary peritoneal cancer: assessing chemotherapy response with diffusion-weighted MR imaging – value of histogram analysis of apparent diffusion coefficients. *Radiology* (2011) 261(1):182–92. doi:10.1148/radiol.11110577
- Konstantinopoulos PA, Matulonis UA. Current status and evolution of pre-clinical drug development models of epithelial ovarian cancer. *Front Oncol* (2014) 3:296. doi:10.3389/fonc.2013.00296
- Hasan N, Ohman AW, Dinulescu DM. The promise and challenge of ovarian cancer models. *Transl Cancer Res* (2015) 4(1):14–28. doi:10.3978/j.issn.2218-676X.2015.01.02
- Vanderhyden BC, Shaw TJ, Ethier JF. Animal models of ovarian cancer. *Reprod Biol Endocrinol* (2003) 1:67. doi:10.1186/1477-7827-1-67
- Connolly DC, Hensley HH. Xenograft and transgenic mouse models of epithelial ovarian cancer and non invasive imaging modalities to monitor ovarian tumor growth in situ-applications in evaluating novel therapeutic agents. *Curr Protoc Pharmacol* (2009) 45:1421–226.
- Hensley H, Quinn BA, Wolf RL, Litwin SL, Mabuchi S, Williams SJ, et al. Magnetic resonance imaging for detection and determination of tumor volume in a genetically engineered mouse model of ovarian cancer. *Cancer Biol Ther* (2007) 6(11):1717–25. doi:10.4161/cbt.6.11.4830
- Ince TA, Quade BJ, Shafer SA, Crowley D, Jacks T. Role of K-ras and Pten in the development of mouse models of endometriosis and endometrioid ovarian cancer. *Nat Med* (2005) 11(1):63–70. doi:10.1038/nm1173
- Pisanu ME, Ricci A, Paris L, Surrentino E, Liliac L, Bagnoli M, et al. Monitoring response to cytostatic cisplatin in a HER2(+) ovary cancer model by MRI and in vitro and *in vivo* MR spectroscopy. *Br J Cancer* (2014) 110(3):625–35. doi:10.1038/bjc.2013.758
- Penet M-F, Glunde K, Artemov D, Podo F, Bhujwalla ZM. Magnetic resonance spectroscopic imaging of orthotopic ovarian cancer. *Proc Int Soc Mag Reson Med* (2011) 19:560.

models. Deuterium-substituted <sup>18</sup>F-fluoromethyl-[1,2-<sup>2</sup>H<sub>4</sub>]choline is a recently developed stable radiotracer that overcomes the short physical half-life of <sup>11</sup>C and seems to be a promising tool for choline metabolism imaging for tumors with high PCho level such as ovarian cancer (48).

## CONCLUSION ON THE USEFULNESS OF MRS AND DWI IN THE MANAGEMENT OF EOC MODELS

The use of multidisciplinary approaches including MRI and MRS in suitable EOC preclinical models may enhance understanding of molecular mechanisms of disease progression and response to therapy, eventually leading to the design of improved treatment strategies.

## AUTHOR CONTRIBUTIONS

The manuscript was written by RC; revised by EI, FP, SC, DM, SI, and RC. All co-authors have been directly involved in obtaining part of the results described in the manuscript and read and approved it.

## FUNDING

We acknowledge partial support by: Associazione Italiana per la Ricerca sul Cancro (AIRC) 2007–2010; Integrated Oncology Program RO 06.5/N.ISS/Q0, Oncology Program OncOrd 37/07/N. ISS/70CF/4 and Special Program Alleanza Contro il Cancro 2006, ACC3-AC5/D, Ministry of Health, Italy; Accordo di Collaborazione Italia-USA ISS/530F/0F29; AIRC 2009–2011, IG N. 9147 and AIRC IG 12976 2012 and Programma Oncotecnologico ISS/13ONC/5.

16. Sala E, Kataoka MY, Priest AN, Gill AB, McLean MA, Joubert I, et al. Advanced ovarian cancer: multiparametric MR imaging demonstrates response- and metastasis-specific effects. *Radiology* (2012) 263(1):149–59. doi:10.1148/radiol.11110175
17. Sala E, Rockall AG, Freeman SJ, Mitchell DG, Reinhold C. The added role of MR imaging in treatment stratification of patients with gynecologic malignancies: what the radiologist needs to know. *Radiology* (2013) 266(3):717–40. doi:10.1148/radiol.12120315
18. Fan X, Zhang H, Meng S, Zhang J, Zhang C. Role of diffusion-weighted magnetic resonance imaging in differentiating malignancies from benign ovarian tumors. *Int J Clin Exp Med* (2015) 8(11):19928–37.
19. Iorio E, Mezzanzanica D, Alberti P, Spadaro F, Ramoni C, D'Ascenzo S, et al. Alterations of choline phospholipid metabolism in ovarian tumor progression. *Cancer Res* (2005) 65(20):9369–76. doi:10.1158/0008-5472.CAN-05-1146
20. Iorio E, Ricci A, Bagnoli M, Pisano ME, Castellano G, Di Vito M, et al. Activation of phosphatidylcholine cycle enzymes in human epithelial ovarian cancer cells. *Cancer Res* (2010) 70(5):2126–35. doi:10.1158/0008-5472.CAN-09-3833
21. Canese R, Pisano ME, Mezzanzanica D, Ricci A, Paris L, Bagnoli M, et al. Characterisation of in vivo ovarian cancer models by quantitative <sup>1</sup>H magnetic resonance spectroscopy and diffusion-weighted imaging. *NMR Biomed* (2012) 25(4):632–42. doi:10.1002/nbm.1779
22. Podo F, Sardanelli F, Iorio E, Canese R, Carpinelli G, Fausto A, et al. Abnormal choline phospholipid metabolism in breast and ovary cancer: molecular bases for noninvasive imaging approaches. *Curr Med Imaging Rev* (2007) 3:123–37. doi:10.2174/157340507780619160
23. Podo F, Canevari S, Canese R, Pisano ME, Ricci A, Iorio E. MR evaluation of response to targeted treatment in cancer cells. *NMR Biomed* (2011) 24(6):648–72. doi:10.1002/nbm.1658
24. Nardo G, Favaro E, Curtarello M, Moserle L, Zulato E, Persano L, et al. Glycolytic phenotype and AMP kinase modify the pathologic response of tumor xenografts to VEGF neutralization. *Cancer Res* (2011) 71(12):4214–25. doi:10.1158/0008-5472.CAN-11-0242
25. Fabian C, Koetz L, Favaro E, Indraccolo S, Mueller-Klieser W, Sattler UG. Protein profiles in human ovarian cancer cell lines correspond to their metabolic activity and to metabolic profiles of respective tumor xenografts. *FEBS J* (2012) 279(5):882–91. doi:10.1111/j.1742-4658.2012.08479.x
26. Booth SJ, Pickles MD, Turnbull LW. In vivo magnetic resonance spectroscopy of gynaecological tumours at 3.0 Tesla. *BJOG* (2009) 116(2):300–3. doi:10.1111/j.1471-0528.2008.02007.x
27. McLean MA, Priest AN, Joubert I, Lomas DJ, Kataoka MY, Earl H, et al. Metabolic characterization of primary and metastatic ovarian cancer by <sup>1</sup>H-MRS in vivo at 3T. *Magn Reson Med* (2009) 62(4):855–61. doi:10.1002/mrm.22067
28. Stanwell P, Russell P, Carter J, Pather S, Heintze S, Mountford C. Evaluation of ovarian tumors by proton magnetic resonance spectroscopy at three Tesla. *Invest Radiol* (2008) 43(10):745–51. doi:10.1097/RLI.0b013e31817e9104
29. Pelech SL, Vance DE. Regulation of phosphatidylcholine biosynthesis. *Biochim Biophys Acta* (1984) 779(2):217–51. doi:10.1016/0304-4157(84)90010-8
30. Glunde K, Bhujwalla ZM, Ronen SM. Choline metabolism in malignant transformation. *Nat Rev Cancer* (2011) 11(12):835–48. doi:10.1038/nrc3162
31. Sardanelli F, Fausto A, Di Leo G, de Nijs R, Vorbuchner M, Podo F. In vivo proton MR spectroscopy of the breast using the total choline peak integral as a marker of malignancy. *AJR Am J Roentgenol* (2009) 192(6):1608–17. doi:10.2214/AJR.07.3521
32. Katz-Brull R, Lavin PT, Lenkinski RE. Clinical utility of proton magnetic resonance spectroscopy in characterizing breast lesions. *J Natl Cancer Inst* (2002) 94(16):1197–203. doi:10.1093/jnci/94.16.1197
33. Esseridou A, Di Leo G, Sconfienza LM, Caldiera V, Raspagliesi F, Grijuela B, et al. In vivo detection of choline in ovarian tumors using 3D magnetic resonance spectroscopy. *Invest Radiol* (2011) 46(6):377–82. doi:10.1097/RLI.0b013e31821690ef
34. Iorio E, Ginnari Satriani F, Ricci A, Surrentino E, Bagnoli M, Alberti P, et al. Effects of Trabectedin on tumour growth and metabolism in preclinical models of HER-2 overexpressing ovarian cancer. *Proc Int Soc Mag Reson Med* (2014) 22:1526.
35. Penet M-F, Mezzanzanica D, Podo F, de Reggi M, Gharib B, Bhujwalla ZM. Effect of pantethine on ovarian tumor progression and choline metabolism. *Proc Int Soc Mag Reson Med* (2014) 22:912.
36. Canese R, Ricci A, Pisano ME, Paris L, Altabella L, Surrentino E, et al. Effects of PtdCho-PLC inhibition on tumour growth, metabolism and HER2 expression in preclinical models of HER-2 overexpressing ovarian cancer. *Proc Int Soc Mag Reson Med* (2013) 21:807.
37. De Milito A, Fais S. Tumor acidity, chemoresistance and proton pump inhibitors. *Future Oncol* (2005) 1(6):779–86. doi:10.2217/14796694.1.6.779
38. Gillies RJ, Raghunand N, Garcia-Martin ML, Gatenby RA. pH imaging: A review of pH measurement methods and applications in cancers. *IEEE Eng Med Biol Mag* (2004) 23(5):57–64. doi:10.1109/EMB.2004.1360409
39. De Milito A, Canese R, Marino ML, Borghi M, Iero M, Villa A, et al. pH-dependent antitumor activity of proton pump inhibitors against human melanoma is mediated by inhibition of tumor acidity. *Int J Cancer* (2009) 127(1):207–19. doi:10.1002/ijc.25009
40. Chen LQ, Howison CM, Jeffery JJ, Robey IF, Kuo PH, Pagel MD. Evaluations of extracellular pH within in vivo tumors using acidCEST MRI. *Magn Reson Med* (2014) 72(5):1408–17. doi:10.1002/mrm.25053
41. Orton MR, Messiou C, Collins D, Morgan VA, Tessier J, Young H, et al. Diffusion-weighted MR imaging of metastatic abdominal and pelvic tumours is sensitive to early changes induced by a VEGF inhibitor using alternative diffusion attenuation models. *Eur Radiol* (2015) 26(5):1412–9. doi:10.1007/s00330-015-3933-7
42. Sala E, Priest AN, Kataoka M, Graves MJ, McLean MA, Joubert I, et al. Apparent diffusion coefficient and vascular signal fraction measurements with magnetic resonance imaging: feasibility in metastatic ovarian cancer at 3 Tesla: technical development. *Eur Radiol* (2010) 20(2):491–6. doi:10.1007/s00330-009-1543-y
43. Jensen MM, Erichsen KD, Johnbeck CB, Bjorkling F, Madsen J, Jensen PB, et al. [18F]FDG and [18F]FLT positron emission tomography imaging following treatment with belinostat in human ovary cancer xenografts in mice. *BMC Cancer* (2013) 13:168. doi:10.1186/1471-2407-13-168
44. Jensen MM, Erichsen KD, Johnbeck CB, Bjorkling F, Madsen J, Bzorek M, et al. [18F]FLT and [18F]FDG PET for non-invasive treatment monitoring of the nicotinamide phosphoribosyltransferase inhibitor APO866 in human xenografts. *PLoS One* (2013) 8(1):e53410. doi:10.1371/journal.pone.0053410PONE-D-12-17807
45. Sharma SK, Wuest M, Wang M, Glubrecht D, Andrais B, Lapi SE, et al. Immuno-PET of epithelial ovarian cancer: harnessing the potential of CA125 for non-invasive imaging. *EJNMMI Res* (2014) 4(1):60. doi:10.1186/s13550-014-0060-4
46. Wallberg H, Grafstrom J, Cheng Q, Lu L, Martinsson Ahlzen HS, Samen E, et al. HER2-positive tumors imaged within 1 hour using a site-specifically <sup>11</sup>C-labeled Sel-tagged affibody molecule. *J Nucl Med* (2012) 53(9):1446–53. doi:10.2967/jnumed.111.102194
47. Torizuka T, Kanno T, Futatsubashi M, Okada H, Yoshikawa E, Nakamura F, et al. Imaging of gynecologic tumors: comparison of (11)C-choline PET with (18)F-FDG PET. *J Nucl Med* (2003) 44(7):1051–6.
48. Challapalli A, Aboagye EO. Positron emission tomography imaging of tumor cell metabolism and application to therapy response monitoring. *Front Oncol* (2016) 6:44. doi:10.3389/fonc.2016.00044

**Conflict of Interest Statement:** The authors declare that the research was conducted in the absence of any commercial or financial relationships that could be construed as a potential conflict of interest.

Copyright © 2016 Canese, Mezzanzanica, Bagnoli, Indraccolo, Canevari, Podo and Iorio. This is an open-access article distributed under the terms of the Creative Commons Attribution License (CC BY). The use, distribution or reproduction in other forums is permitted, provided the original author(s) or licensor are credited and that the original publication in this journal is cited, in accordance with accepted academic practice. No use, distribution or reproduction is permitted which does not comply with these terms.



# Effect of Pantethine on Ovarian Tumor Progression and Choline Metabolism

**Marie-France Penet<sup>1,2\*</sup>, Balaji Krishnamachary<sup>1</sup>, Flonne Wildes<sup>1</sup>, Yelena Mironchik<sup>1</sup>, Delia Mezzanzanica<sup>3</sup>, Franca Podo<sup>4</sup>, Max de Reggi<sup>5</sup>, Bouchra Gharib<sup>5</sup> and Zaver M. Bhujwalla<sup>1,2</sup>**

<sup>1</sup>JHU ICMIC Program, Russell H. Morgan, Division of Cancer Imaging Research, Department of Radiology and Radiological Science, The Johns Hopkins University School of Medicine, Baltimore, MD, USA, <sup>2</sup>Sidney Kimmel Comprehensive Cancer Center, The Johns Hopkins University School of Medicine, Baltimore, MD, USA, <sup>3</sup>Unit of Molecular Therapies, Department of Experimental Oncology and Molecular Medicine, Fondazione IRCCS Istituto Nazionale dei Tumori, Milan, Italy, <sup>4</sup>Section of Molecular and Cellular Imaging, Department of Cell Biology and Neurosciences, Istituto Superiore di Sanità, Rome, Italy, <sup>5</sup>Neurobiology of Cellular Interactions and Neurophysiopathology (NICN), Aix Marseille Univ, CNRS, Marseille, France

## OPEN ACCESS

**Edited by:**

Cicero Matthew R. Habito,  
Massachusetts General  
Hospital, USA

**Reviewed by:**

Goutam Chakraborty,  
Memorial Sloan Kettering Cancer  
Center, USA  
Johanna Patricia Adevoso Canal,  
University of the Philippines  
Manila, Philippines

**\*Correspondence:**  
Marie-France Penet  
mpenet@mri.jhu.edu

**Specialty section:**

This article was submitted to Cancer Imaging and Diagnosis, a section of the journal Frontiers in Oncology

**Received:** 22 March 2016

**Accepted:** 02 November 2016

**Published:** 16 November 2016

**Citation:**

Penet MF, Krishnamachary B,  
Wildes F, Mironchik Y,  
Mezzanzanica D, Podo F,  
de Reggi M, Gharib B and  
Bhujwalla ZM (2016) Effect of  
Pantethine on Ovarian Tumor  
Progression and Choline Metabolism.  
*Front. Oncol.* 6:244.  
doi: 10.3389/fonc.2016.00244

Epithelial ovarian cancer remains the leading cause of death from gynecologic malignancy among women in developed countries. New therapeutic strategies evaluated with relevant preclinical models are urgently needed to improve survival rates. Here, we have assessed the effect of pantethine on tumor growth and metabolism using magnetic resonance imaging and high-resolution proton magnetic resonance spectroscopy (MRS) in a model of ovarian cancer. To evaluate treatment strategies, it is important to use models that closely mimic tumor growth in humans. Therefore, we used an orthotopic model of ovarian cancer where a piece of tumor tissue, derived from an ovarian tumor xenograft, is engrafted directly onto the ovary of female mice, to maintain the tumor physiological environment. Treatment with pantethine, the precursor of vitamin B5 and active moiety of coenzyme A, was started when tumors were ~100 mm<sup>3</sup> and consisted of a daily i.p. injection of 750 mg/kg in saline. Under these conditions, no side effects were observed. High-resolution <sup>1</sup>H MRS was performed on treated and control tumor extracts. A dual-phase extraction method based on methanol/chloroform/water was used to obtain lipid and water-soluble fractions from the tumors. We also investigated effects on metastases and ascites formation. Pantethine treatment resulted in slower tumor progression, decreased levels of phosphocholine and phosphatidylcholine, and reduced metastases and ascites occurrence. In conclusion, pantethine represents a novel potential, well-tolerated, therapeutic tool in patients with ovarian cancer. Further *in vivo* preclinical studies are needed to confirm the beneficial role of pantethine and to better understand its mechanism of action.

**Keywords:** choline metabolism, pantethine, ovarian cancer, orthotopic model, ascites, metastasis, high-resolution MRS

**Abbreviations:** FAS, fatty acid synthase; IHC, immunohistochemistry; MRI, magnetic resonance imaging; MRS, magnetic resonance spectroscopy; PC, phosphocholine; PtCh, phosphatidylcholine.

## INTRODUCTION

Ovarian cancer is the leading cause of death from gynecological malignancies with an incidence of 220,000 cases worldwide per year (1). Although the prognosis in cases detected at an early stage is quite favorable, the vast majority of cases are diagnosed at an advanced stage, when 5-year survival rates are only 30–40%. Median life expectancy for ovarian cancer patients is 5 years, and about 80% of diagnosed patients will eventually succumb to it (2). The poor prognosis of epithelial ovarian cancer (EOC) is due to a combination of the aggressive characteristics of the disease and an unpredictable response to front-line therapy, further compounded by late detection of the disease and resistance of ovarian cancers to current treatments (3). The primary treatment for EOC consists of aggressive cytoreductive surgery, followed by chemotherapy with platinum and taxane (4). Although platinum and taxane combination remains the standard treatment for EOC, new drug combinations (5) as well as different administration schedules (6) are being tested and might be reasonable options for first-line treatment of women with advanced EOC. Recently, the introduction of anti-angiogenic drug combined to front-line treatment has been also proposed (7, 8). Current first-line chemotherapies for advanced diseases are listed in **Table 1**.

Metastases and malignant ascites are complications frequently observed in late-stage ovarian cancer. Intraperitoneal seeding is the most common route of dissemination (9), although direct invasion or dissemination through the lymphatics and vasculature also occur. Malignant ascites function as a permissive reactive tumor-host microenvironment and provides sustenance for floating tumor cells (10). This results in an abnormal build-up of fluid in the abdomen, causing discomfort, pain, problems with mobility and breathing, and other symptoms that decrease the quality of life. Despite the improvement of surgical approaches and drug development, EOC patients have experienced little improvement in overall survival in the last 30 years (11). New therapeutic strategies exploiting novel targets are urgently needed to minimize morbidity, improve survival rates, and to eventually cure patients.

In the present study, we applied magnetic resonance imaging (MRI) and high-resolution magnetic resonance spectroscopy (MRS) to assess the use of pantethine as a therapeutic agent in an orthotopic model of ovarian cancer. We used an orthotopic model in which the relevant tumor physiological environment is maintained and that frequently forms metastases and

malignant ascites. Pantethine is the stable disulfide form of pantetheine, the precursor of vitamin B5 (pantothenic acid). As a part of the active moiety of coenzyme A (CoA), it is a key regulator in lipid metabolism (12–14). Pantethine has the advantage of being an anti-inflammatory and hypolipidemic agent with very few side effects. Pantethine has been shown to prevent the perivascular inflammation and to protect mice against the cerebral syndrome associated with malaria (15); the protection was associated with a significantly lower level of circulating tumor necrosis factor (TNF)- $\alpha$  (15). TNF- $\alpha$  has been linked to multiple steps of tumorigenesis, including cellular transformation, promotion, survival, proliferation, invasion, angiogenesis, and metastasis (16). Pantethine has also been shown to inhibit CXCL12/CXCR4-induced cell transendothelial migration (17). With its anti-inflammatory and hypolipidemic properties, pantethine appeared to be a good novel candidate against ovarian cancer progression, metastases, and ascites formation.

## MATERIALS AND METHODS

### Cell Line and Tumor Implantation

NIH: OVCAR3 cells from American Type Culture Collection (ATCC, VA, USA) were used in the present study. OVCAR3 cells are human epithelial ovary adenocarcinoma cells originally isolated from a malignant effusion. Cells were cultured in RPMI 1640 (Sigma Chemical Co., St. Louis, MO, USA) with 10% fetal bovine serum (Sigma Chemical Co., St. Louis, MO, USA). Tumor implantation was performed using 6- to 8-week-old severe combined immunodeficient (SCID) female mice. We used a two-step process for orthotopic tumor implantation (Supplementary Material). We first generated subcutaneous tumors by inoculating a cell suspension of  $2 \times 10^6$  cells in 0.05 ml of Hanks balanced salt solution in the flank of SCID female mice. Once the tumor reached a size of 100–200 mm<sup>3</sup>, it was excised and cut into small pieces under sterile conditions. Orthotopic implantation was then performed by surgically transplanting a piece of tumor tissue onto the ovaries of a separate group of SCID mice. All surgical procedures and animal handling were performed in accordance with protocols approved by the Johns Hopkins University Institutional Animal Care and Use Committee and conformed to the Guide for the Care and Use of Laboratory Animals published by the NIH.

### Treatment Protocol

The treatment was started when the tumors reached about 100 mm<sup>3</sup> with a daily i.p. injection of saline for the control group, and pantethine (Sigma Chemical Co., St. Louis, MO, USA) diluted in saline for the treated group (750 mg/kg).

### In Vivo MR Examination

Non-invasive MRI was used to assess tumor growth in deep-seated tissue using T<sub>1</sub>-weighted imaging and diffusion-weighted imaging. All imaging studies were performed on a 4.7-T BrukerAvance (Bruker, Billerica, MA, USA) spectrometer

**TABLE 1 |** Front-line treatment for ovarian cancer patients.

Carboplatinum + paclitaxel (1)	Platinum-based chemotherapy + anti-mitotic chemotherapy
Carboplatinum and pegylated doxorubicin (5)	Platinum-based chemotherapy + intercalating DNA chemotherapy
Carboplatinum + weekly paclitaxel (6)	Platinum-based chemotherapy + anti-mitotic chemotherapy
Carboplatinum and taxol + bevacizumab (7, 8)	Platinum-based chemotherapy + anti-mitotic chemotherapy + angiogenesis inhibitor

using a home-built volume coil placed around the torso of the anesthetized mice. Animals were anesthetized with a mixture of ketamine (6.25 mg/kg) and acepromazine (62.5 mg/kg) administered i.p. A pad circulated with warm water was used to maintain animal body temperature. Multi-slice T<sub>1</sub>-weighted images and multi-slice diffusion-weighted images, with an in-plane spatial resolution of 250 μm × 250 μm (128 × 128 matrix, 32 mm field of view, *b*-value of 100 mT/m), were acquired to localize the orthotopic tumors that appear hyperintense on these images.

## MR Spectroscopy of Dual Phase Extracts

High-resolution proton MRS of tumor tissue extracts was applied to assess water phase and lipid phase metabolites in tumor extracts. Lipid- and water-soluble fractions were obtained from tumors using a dual-phase extraction method with methanol/chloroform/water (1/1/1) (18). Briefly, tissues were freeze-clamped and ground to powder. Ice-cold methanol was added to the powder, and the samples were homogenized. Ice-cold chloroform, followed by ice-cold water, was added, and the samples were kept at 4°C overnight for phase separation. Samples were centrifuged for 30 min at 15,000 g at 4°C to separate the phases. The water/methanol phase containing the water-soluble metabolites was treated with chelex (Sigma Chemical Co., St. Louis, MO, USA) for 10 min on ice to remove divalent cations. Methanol was removed by rotary evaporation, and the remaining water phase was lyophilized and stored at -20°C. The chloroform phase containing the lipids was dried in a stream of N<sub>2</sub> and stored at -20°C. Water-soluble samples were dissolved in 0.5 ml of D<sub>2</sub>O (Sigma Chemical Co., St. Louis, MO, USA) containing 3-(trimethylsilyl) propionic-2,2,3,3-d4 acid (Sigma Chemical Co., St. Louis, MO, USA) as an internal concentration standard (sample pH of 7.4). Lipid samples were dissolved in 0.6 ml of CDCl<sub>3</sub>/CD<sub>3</sub>OD (2/1) containing tetramethylsilane as an internal concentration standard (CDCl<sub>3</sub> and CD<sub>3</sub>OD premixed with tetramethylsilane by the manufacturer, Cambridge Isotope Laboratories, Inc.). Fully relaxed <sup>1</sup>H MR spectra of the extracts were acquired on a BrukerAvance 500 spectrometer operating at 11.7 T (BrukerBioSpin Corp., Billerica, MA, USA) using a 5-mm HX inverse probe and the following acquisition parameters: 30° flip angle, 6,000 Hz sweep width, 12.7 s repetition time, time-domain data points of 32k, and 128 transients (18). Spectra were analyzed using the Bruker XWIN-NMR 3.5 software (BrukerBioSpin). Integrals of the metabolites of interest were determined and normalized to the tumor weight. To determine concentrations, peak integration from <sup>1</sup>H spectra for all metabolites studied was compared to the internal standard.

## Metastases and Ascites

Presence of ascites was recorded at necropsy. Lymph nodes, lungs, and livers were fixed in formalin, paraffin embedded, sectioned, and stained with hematoxylin and eosin (H&E) for further analysis. The presence of metastases was checked on H&E stained sections of the lymph nodes, liver, and lungs.

## Immunohistochemistry

The 5-μm thick formalin fixed sections were used for Immunohistochemistry (IHC) analysis. Antigen retrieval was achieved by boiling sections in citrate buffer solution (pH 6) for 20 min. Sections were stained for proliferation using Ki-67 (rabbit polyclonal, Thermo Fisher, Rockford, IL, USA, 1:100 dilution), and for apoptosis using Caspase-3 (8G10, rabbit polyclonal, Cell Signaling, Danvers, MA, USA, 1:100 dilution) following standard protocols, and further processed by addition of biotinylated anti-rabbit IgG and ABC reagent (PK-4001, Vector laboratories, Burlingame, CA, USA). Detection was achieved by addition of the chromogen DAB (3,3'-diaminobenzidine, Dako, Carpinteria, CA, USA). Images were captured by scanning the immunostained sections at high resolution on an Aperio ScanScope® CS System at 20 × resolution (Leica Biosystems Inc., Buffalo Grove, IL, USA). Analysis of the slides was performed using the algorithms and protocols developed by the company.

## Toxicity Analysis

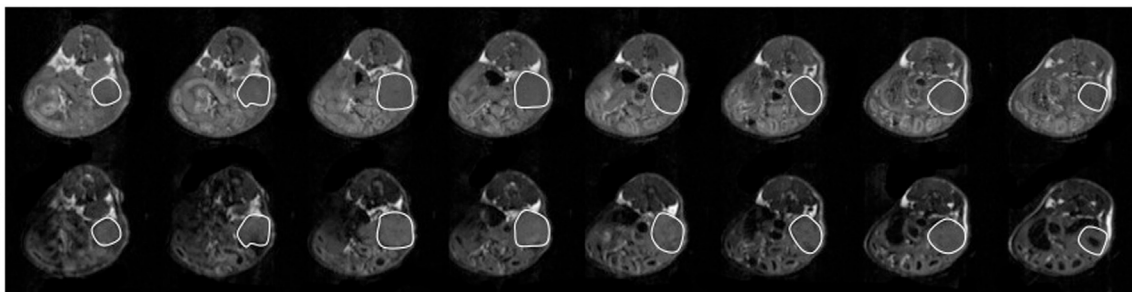
The toxicity analyses were performed in MDA-MB-231 tumor-bearing mice. The 2 × 10<sup>6</sup> cells were injected orthotopically into the mammary fat pad of 6- to 8-week-old female SCID mice. The treatment was started when the tumors reached about 100 mm<sup>3</sup> with a daily i.p. injection of saline for the control group and pantethine for the treated group (750 mg/kg) (*n* = 5). Mice were treated for 3 weeks and weighed once a week. At the end of the treatment period, mice were sacrificed. Kidney and liver function were evaluated from serum creatinine, blood urea nitrogen (BUN), serum alanine aminotransferase (ALT), and aspartate aminotransferase (AST) levels obtained at the Johns Hopkins University School of Medicine Phenotyping Core Facility, using spectrophotometric measurements obtained with an automated Vet Ace Clinical Chemistry system (Alfa Wasserman Diagnostic Technologies LLC, NJ, USA).

## Statistical Analysis

Values were displayed as mean ± SEM. Statistical significance was evaluated using the Student's *t*-test; *p* < 0.05 was considered significant.

## RESULTS

To assess the efficacy of pantethine on tumor progression, metastases, and ascites formation, we used an orthotopic model of ovarian cancer. The orthotopic implantation was performed to maintain the relevant tumor physiological environment. Ovarian cancer cells are typically injected into the peritoneal cavity, inducing ascites and peritoneal spread of tumor, but most cell lines do not form solid tumors. Instead, here we performed microsurgical orthotopic implantation of ovarian cancer tissue onto the ovary of female SCID mice. In our model, ascites and metastases in the peritoneal cavity, in the liver, on the diaphragm, and in distal lymph nodes are frequent, similar to human disease. Tumor growth was measured following implantation by imaging the mice weekly with MRI (Figure 1). The treatment consisting of daily i.p. injections of pantethine at a dose of 750 mg/kg

**T<sub>1</sub>-weighted Images**

**FIGURE 1 | Representative adjacent T<sub>1</sub>-weighted images (top row) and diffusion-weighted images (bottom row) of an orthotopically implanted OVCAR3 tumor-bearing mouse.** The tumor is highlighted by a white line. The tumor volume was measured by determining the tumor area on each 1-mm thick slice and by adding the areas to calculate the total tumor volume.

commenced when tumors were ~100 mm<sup>3</sup>. Under these conditions, no side effects and no significant weight loss were observed in the treated group compared to the control group ( $20.8 \pm 0.9$  versus  $22.2 \pm 2.8$  g, respectively). The control group was injected daily with saline. Tumor growth was followed weekly non-invasively by MRI on a 4.7-T spectrometer. Tumor areas were measured for each 1-mm thick slice, and the values were added to assess the total tumor volume. We observed a significant reduction of tumor growth in the treated group compared to the control group (Figure 2).

When we sacrificed the mice after 4 weeks of treatment, we observed liver metastases in 86% of control mice (6/7), but only in 43% of treated mice (2/7), lungs metastases in 29% of control mice (2/7), and none in treated mice and ascites in 86% of control mice (6/7), and 29% of treated mice (2/7) (Figure 3). IHC analysis of tumor sections did not show any statistically significant differences in proliferation rates (Figures 4A,C). Higher levels of caspase-3 were measured in the treated tumors compared to control tumors (Figures 4B,C).

To assess the effect of the treatment on the tumor metabolism, we analyzed tumor extracts with high-resolution <sup>1</sup>H MRS. We performed dual-phase extraction of the tumors to assess the lipid phase and the water phase. Representative water phase <sup>1</sup>H MR spectra centered around the 3.2 ppm region of a control tumor and a pantethine-treated tumor are shown in Figures 5A,B, respectively. A significant decrease of phosphocholine (PC) in the treated tumors was observed (Figure 5C). No differences were observed in the other metabolites measured, including lactate.

We next measured the lipid concentration in the lipid phase. Representative spectra of a control tumor and a treated tumor are shown in Figures 6A,B, respectively. Analysis of the spectra revealed a significant decrease of phosphatidylcholine (PtCho) in the pantethine-treated tumors compared to the controls (Figure 6C). No differences were observed in the other lipids assessed (Figures 6C,D).

Renal and hepatic cytotoxicity studies were conducted in MDA-MB-231 tumor-bearing mice. We did not observe any weight loss following 3 weeks of pantethine treatment (Figure 7A). Blood analysis performed at the end of the treatment

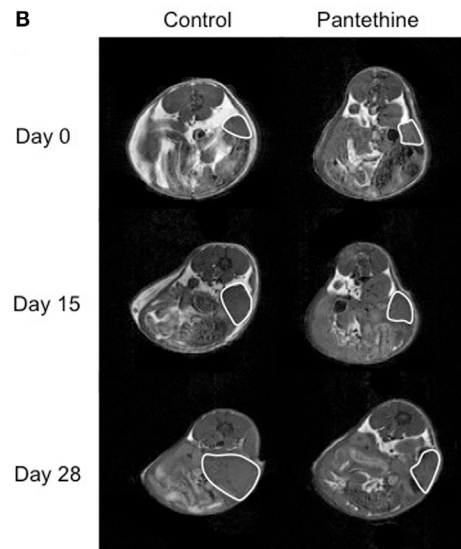
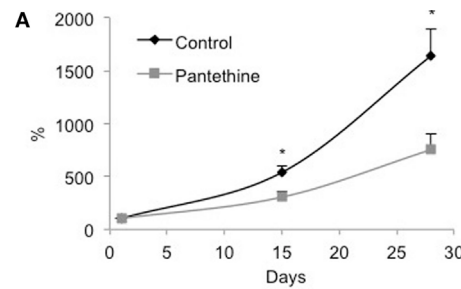


**FIGURE 2 | Normalized tumor growth curves from control mice and pantethine-treated mice (A) and representative T<sub>1</sub>-weighted images of a central slice of tumors imaged at days 0, 15, and 28 of a control mouse (left column) and a treated mouse (right column) (B).**  $n = 13$  and 14, respectively; \* $P < 0.05$ .

period revealed neither hepatic (Figure 7B) nor renal toxicity (Figure 7C), as shown by the absence of significant differences in the levels of BUN, creatinine, AST, and ALT between the control mice and the pantethine-treated mice.

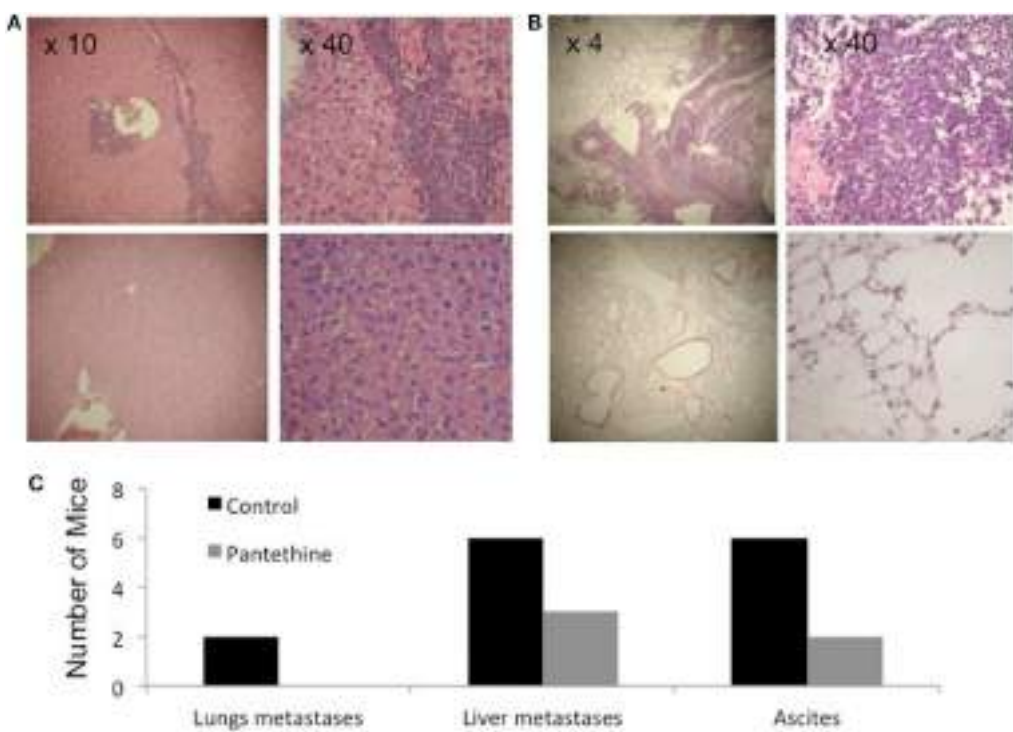


**FIGURE 3 | Representative H&E stained sections of liver (A) and lungs (B) from a control mouse (top row) and a treated mouse (bottom row). (C)** Histogram representing the number of control and treated mice with metastases in the lungs, in the liver, and with ascites ( $n = 7$ ).

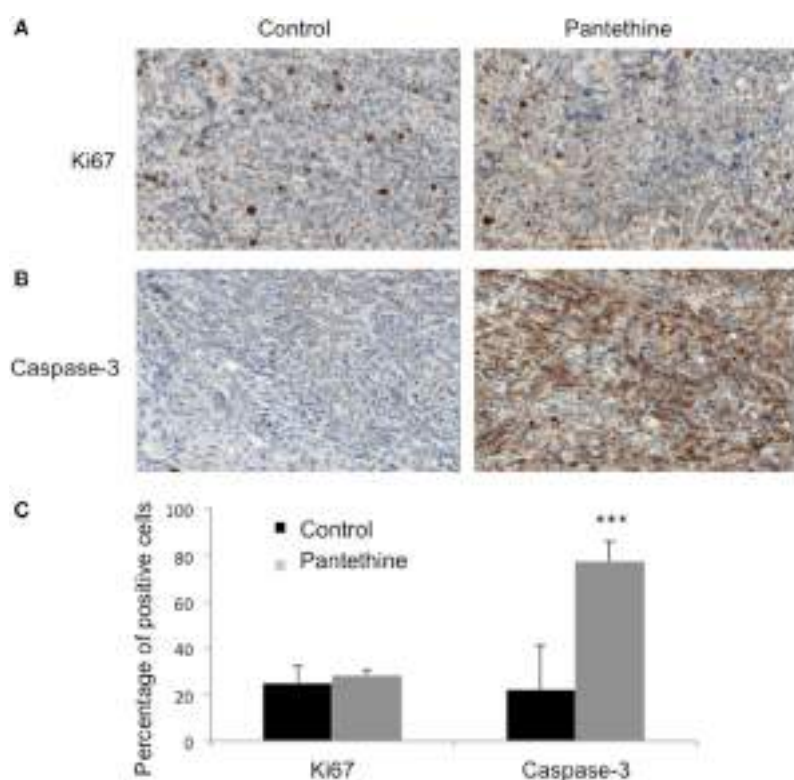


**FIGURE 4 | Representative IHC stained sections of control and treated tumors for Ki-67 (A) and Caspase-3 (B). (C)** Histogram representing the percentage of positive cells for each marker in control and treated tumors ( $n = 3$ ; mean  $\pm$  SD are represented; \*\*\* $P < 0.001$ ).

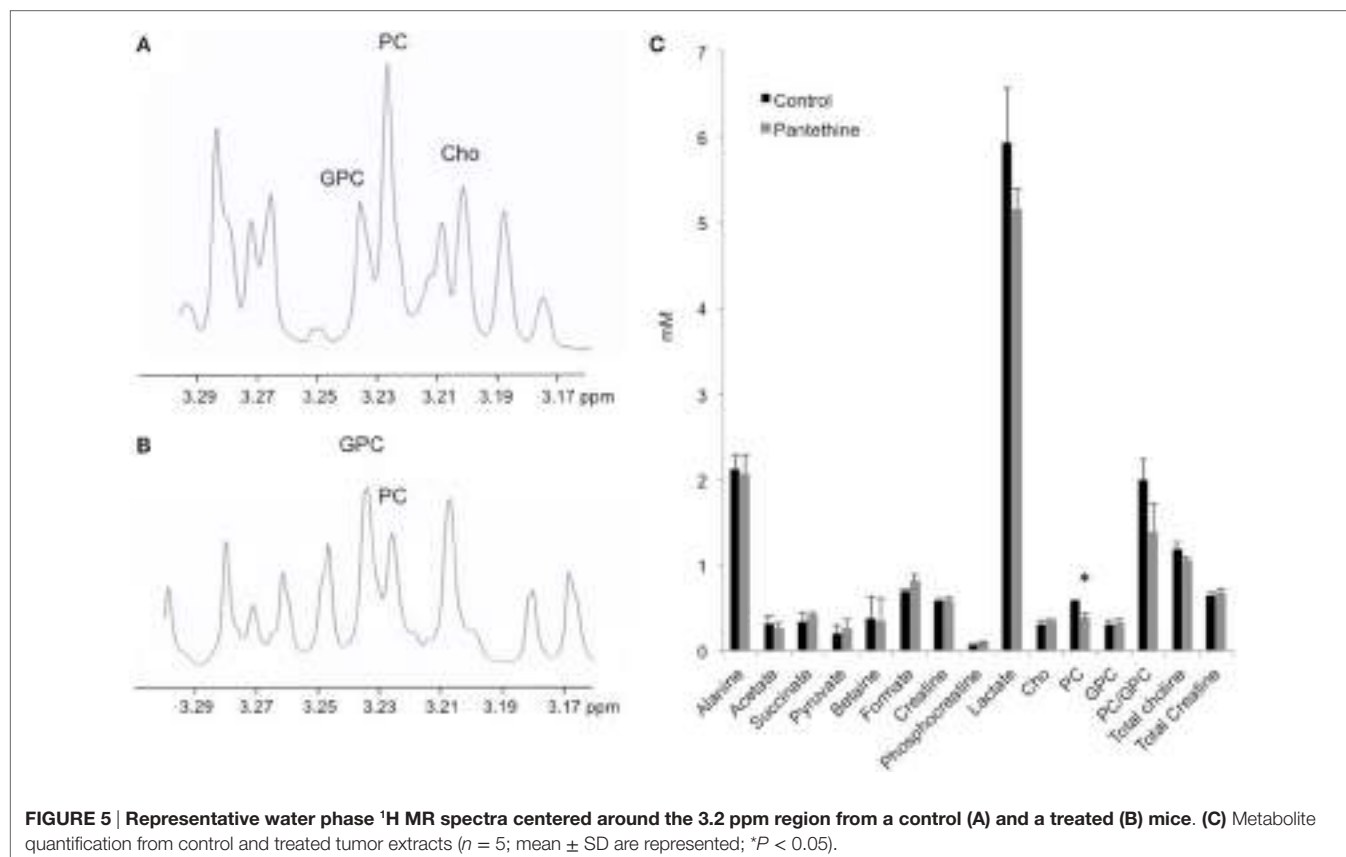


**FIGURE 5 | Representative water phase  $^1\text{H}$  MR spectra centered around the 3.2 ppm region from a control (A) and a treated (B) mice. (C) Metabolite quantification from control and treated tumor extracts ( $n = 5$ ; mean  $\pm$  SD are represented;  $*P < 0.05$ ).**

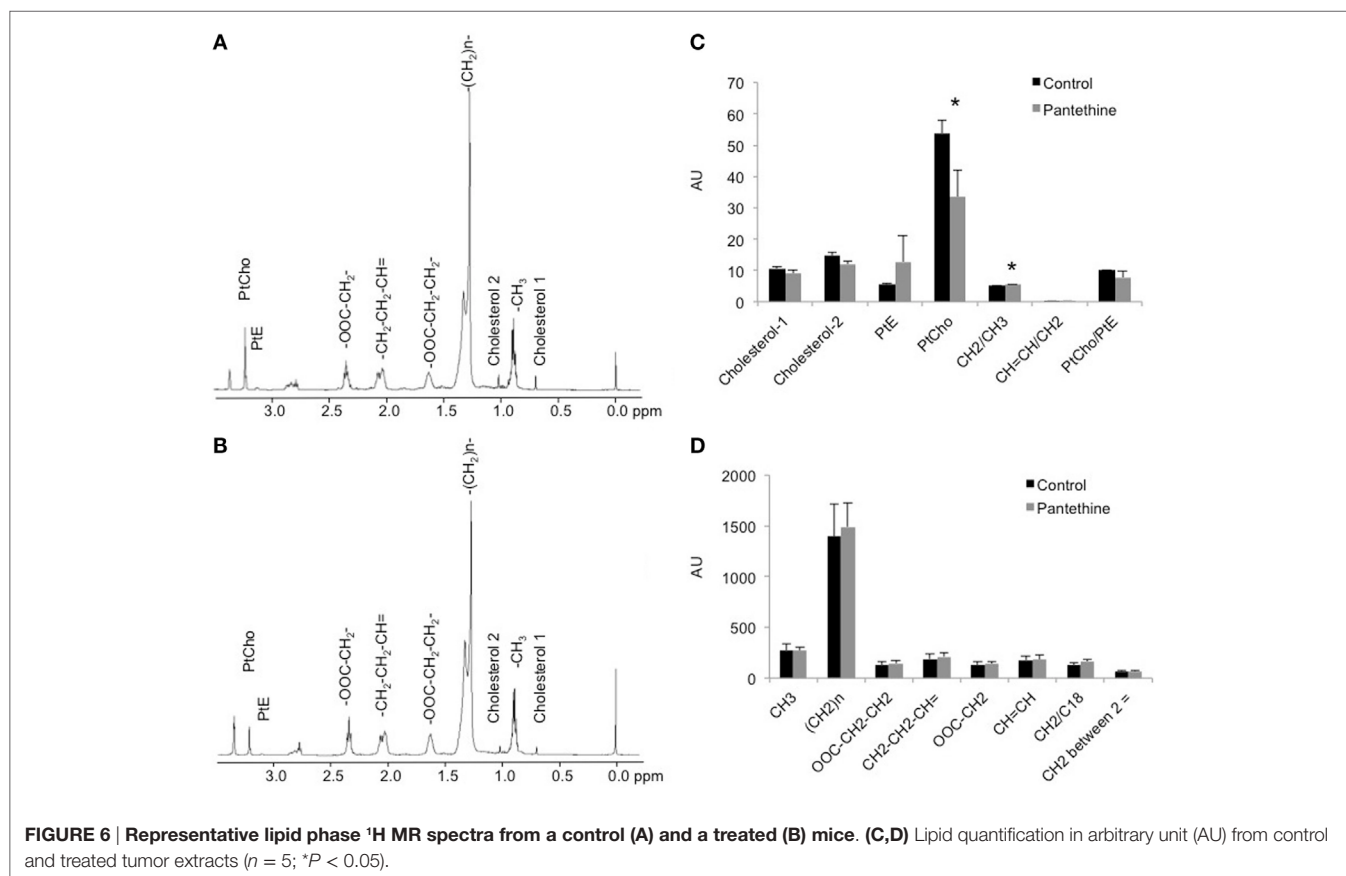
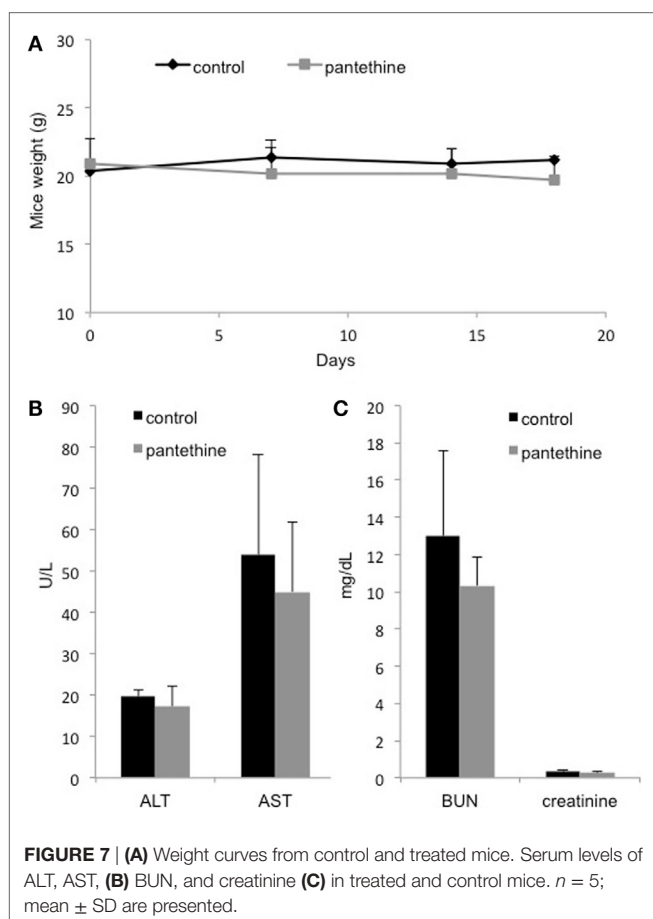


**FIGURE 6 | Representative lipid phase  $^1\text{H}$  MR spectra from a control (A) and a treated (B) mice. (C,D) Lipid quantification in arbitrary unit (AU) from control and treated tumor extracts ( $n = 5$ ;  $*P < 0.05$ ).**



## DISCUSSION

The majority of ovarian cancer studies in mouse models use xenografts that are obtained either after subcutaneous implantation (19) or intraperitoneal injection of cancer cells (20). To mimic the tumor microenvironment, more recent models involved direct injection of cells into the ovarian intrabursa (21, 22). Another technique involving the implantation of a preparation of tumor solid pellets into the ovarian bursa was recently described (23). In this model, a pellet was prepared by embedding tumor cells into a collagen matrix to control the number of cells, and to limit their leakage during the injection (23). In the present study, we engrafted a piece of tumor tissue onto the ovary to avoid spilling of cancer cells and to maintain the tumor tissue microenvironment. We have used this technique in the past for prostate cancer (24) and for pancreatic cancer (25). In our model, ascites and metastases in the peritoneal cavity, in the liver, on the diaphragm, and in distal lymph nodes are frequent, similar to human disease, since ovarian carcinoma usually metastasizes along the peritoneum throughout the pelvic and abdominal cavity. In ovarian cancer patients, metastases can be found in lung, skin, pleura, mediastinal, and lymph nodes, and also in bone, brain, or gastrointestinal track (26).

Using our orthotopic model, we identified pantethine as a promising new drug against ovarian cancer, targeting not only

tumor progression but also metastases occurrence, and ascites formation. The orthotopic tumor growth could be followed non-invasively using MRI, and we observed slower tumor progression in the treated mice compared to the non-treated ones. While there were no differences in cell proliferation, increased caspase-3 was observed in the treated tumors, linking the tumor growth reduction to an increase in apoptosis. High-resolution  $^1\text{H}$  MRS analysis of tumor extracts revealed a significant decrease of PC and PtCho concentrations in the tumors from treated mice compared to the untreated controls. We used a high dose of pantethine and did not observe any side effects. Pantethine is rapidly eliminated into the urine allowing its administration in humans at a reasonable dose using a slow dispensing device.

Abnormal choline metabolism continues to be identified as one of the most consistent hallmarks of cancer (27). The molecular causes are being gradually unraveled and are providing potential novel targets in the treatment of cancer. Iorio et al. demonstrated that EOC possessed an altered MRS-choline profile, characterized by increased PC content (28). Several studies have demonstrated that targeting choline kinase resulted in a decrease of PC and a reduction of tumor growth (29, 30). Here, we observed a reduction of tumor progression that was associated with a decrease of PC and PtCho.

Several known properties of pantethine may explain these results. A previous study described the inhibition of PtCho synthesis *in vitro* in rat liver microsomal preparations with pantetheine and CoA (31). Here, we observed an *in vivo* effect of pantethine on PtCho level in orthotopically implanted OVCAR3 tumor. Pantethine inhibited fatty acid synthase (FAS), as demonstrated in isolated rat hepatocytes by Bocos and Herrera (32). FAS synthesizes fatty acids using 4'-phospho-pantetheine, which acts as a universal mechanism of transport of intermediates (33–35). Pantethine may inhibit FAS activity through the alteration of the thiol group of the 4'-phospho-pantetheine arm, which covalently carries the pathway intermediates. High FAS activity has been observed in most ovarian cancers and is strongly associated with high aggressiveness and poor patient survival. Inhibition of FAS activity has been shown to be cytotoxic to human cancer cells *in vitro* and *in vivo* (36). Pantethine not only affects cellular fatty acid metabolism but also displays anti-inflammatory properties by maintaining the asymmetric distribution of cell membrane phosphatidylserine, resulting in the inhibition of cellular response to proinflammatory factors (15).

It was recently shown that pantethine affects lipid raft composition causing a decline of the proportion of saturated fatty acid, an increase in mono- and polyunsaturated fatty acid, and a decrease of cholesterol content (17). These changes in raft composition led to an impairment of CXCL12 to bind to its target (17). The CXCL12–CXCR4 axis promotes proliferation, migration, invasion, and metastasis in ovarian cancer (37), therefore its alteration by pantethine may be a mechanism for the reduction of metastases observed in our study.

Finally, it was recently shown that obesity contributes to ovarian cancer metastases formation (38). Adipose tissue is a key component of the ovarian cancer metastatic microenvironment (39, 40). Increased body fat enhances tumor cell–mesothelial cell adhesion and promotes intraperitoneal metastatic dissemination (38).

As a known hypolipidemic agent, pantethine may influence metastases formation through its hypolipidemic effects.

In conclusion, pantethine represents a novel potential therapeutic option in patients with ovarian cancer, since it is a well-known and well-tolerated molecule. Further *in vivo* preclinical studies are needed to confirm the beneficial role of pantethine in ovarian cancer and to better understand its mechanism of action.

## AUTHOR CONTRIBUTIONS

MP: conception and design of the work; acquisition, analysis, and interpretation of data; drafting the work; final approval of the version to be published; and agreement to be accountable for all aspects of the work. BK, FW, and YM: acquisition, analysis, and interpretation of data; final approval of the version to be

published; and agreement to be accountable for all aspects of the work. DM, FP, MD, BG, and ZB: design of the work; revising the work; final approval of the version to be published; and agreement to be accountable for all aspects of the work.

## FUNDING

This work was supported by NIH P50CA103175, P30CA006973, The HERA Foundation, and The Tina's Wish Foundation.

## SUPPLEMENTARY MATERIAL

The Supplementary Material for this article can be found online at <http://journal.frontiersin.org/article/10.3389/fonc.2016.00244/full#supplementary-material>.

## REFERENCES

1. Jayson GC, Kohn EC, Kitchener HC, Ledermann JA. Ovarian cancer. *Lancet* (2014) 384(9951):1376–88. doi:10.1016/S0140-6736(13)62146-7
2. Schmidt C. Ovarian cancer treatments on the horizon. *J Natl Cancer Inst* (2011) 103(17):1284–5. doi:10.1093/jnci/djr343
3. Bast RC Jr. Molecular approaches to personalizing management of ovarian cancer. *Ann Oncol* (2011) 22(Suppl 8):viiii–15. doi:10.1093/annonc/mdr516
4. Krivak TC, Lele S, Richard S, Secord AA, Leath CA III, Brower SL, et al. A chemoresponse assay for prediction of platinum resistance in primary ovarian cancer. *Am J Obstet Gynecol* (2014) 211(1):e61–8. doi:10.1016/j.ajog.2014.02.009
5. Pignata S, Scambia G, Ferrandina G, Savarese A, Sorio R, Breda E, et al. Carboplatin plus paclitaxel versus carboplatin plus pegylated liposomal doxorubicin as first-line treatment for patients with ovarian cancer: the MITO-2 randomized phase III trial. *J Clin Oncol* (2011) 29(27):3628–35. doi:10.1200/JCO.2010.33.8566
6. Pignata S, Scambia G, Katsaros D, Gallo C, Pujade-Lauraine E, De Placido S, et al. Carboplatin plus paclitaxel once a week versus every 3 weeks in patients with advanced ovarian cancer (MITO-7): a randomised, multicentre, open-label, phase 3 trial. *Lancet Oncol* (2014) 15(4):396–405. doi:10.1016/S1470-2045(14)70049-X
7. Burger RA, Brady MF, Bookman MA, Fleming GF, Monk BJ, Huang H, et al. Incorporation of bevacizumab in the primary treatment of ovarian cancer. *N Engl J Med* (2011) 365(26):2473–83. doi:10.1056/NEJMoa1104390
8. Perren TJ, Swart AM, Pfisterer J, Ledermann JA, Pujade-Lauraine E, Kristensen G, et al. A phase 3 trial of bevacizumab in ovarian cancer. *N Engl J Med* (2011) 365(26):2484–96. doi:10.1056/NEJMoa1103799
9. Kyriazi S, Kaye SB, Desouza NM. Imaging ovarian cancer and peritoneal metastases-current and emerging techniques. *Nat Rev Clin Oncol* (2010) 7(7):381–93. doi:10.1038/nrclinonc.2010.47
10. Said N, Socha MJ, Olearczyk JJ, Elmarakby AA, Imig JD, Motamed K. Normalization of the ovarian cancer microenvironment by SPARC. *Mol Cancer Res* (2007) 5(10):1015–30. doi:10.1158/1541-7786.MCR-07-0001
11. Vaughan S, Coward JI, Bast RC Jr, Berchuck A, Berek JS, Brenton JD, et al. Rethinking ovarian cancer: recommendations for improving outcomes. *Nat Rev Cancer* (2011) 11(10):719–25. doi:10.1038/nrc3144
12. Branca D, Scutari G, Siliprandi N. Pantethine and pantothenate effect on the CoA content of rat liver. *Int J Vitam Nutr Res* (1984) 54(2–3):211–6.
13. Wittwer CT, Graves CP, Peterson MA, Jorgensen E, Wilson DE, Thoene JG, et al. Pantethine lipomodulation: evidence for cysteamine mediation *in vitro* and *in vivo*. *Atherosclerosis* (1987) 68(1–2):41–9. doi:10.1016/0021-9150(87)90092-X
14. Cighetti G, Del Puppo M, Paroni R, Galli Kienle M. Modulation of HMG-CoA reductase activity by pantetheine/pantethine. *Biochim Biophys Acta* (1988) 963(2):389–93. doi:10.1016/0005-2760(88)90306-2
15. Penet MF, Abou-Hamdan M, Coltel N, Cornille E, Grau GE, de Reggi M, et al. Protection against cerebral malaria by the low-molecular-weight thiol pantethine. *Proc Natl Acad Sci U S A* (2008) 105(4):1321–6. doi:10.1073/pnas.0706867105
16. Aggarwal BB, Shishodia S, Sandur SK, Pandey MK, Sethi G. Inflammation and cancer: how hot is the link? *Biochem Pharmacol* (2006) 72(11):1605–21. doi:10.1016/j.bcp.2006.06.029
17. van Gijsel-Bonnello M, Acar N, Molino Y, Bretillon L, Khrestchatsky M, de Reggi M, et al. Pantethine alters lipid composition and cholesterol content of membrane rafts, with down-regulation of CXCL12-induced T cell migration. *J Cell Physiol* (2015) 230(10):2415–25. doi:10.1002/jcp.24971
18. Glunde K, Raman V, Mori N, Bhujwalla ZM. RNA interference-mediated choline kinase suppression in breast cancer cells induces differentiation and reduces proliferation. *Cancer Res* (2005) 65(23):11034–43. doi:10.1158/0008-5472.CAN-05-1807
19. Pisani ME, Ricci A, Paris L, Surrentino E, Liliac L, Bagnoli M, et al. Monitoring response to cytostatic cisplatin in a HER2(+) ovary cancer model by MRI and *in vitro* and *in vivo* MR spectroscopy. *Br J Cancer* (2014) 110(3):625–35. doi:10.1038/bjc.2013.758
20. Canese R, Pisani ME, Mezzanzanica D, Ricci A, Paris L, Bagnoli M, et al. Characterisation of *in vivo* ovarian cancer models by quantitative 1H magnetic resonance spectroscopy and diffusion-weighted imaging. *NMR Biomed* (2012) 25(4):632–42. doi:10.1002/nbm.1779
21. Cordero AB, Kwon Y, Hua X, Godwin AK. In vivo imaging and therapeutic treatments in an orthotopic mouse model of ovarian cancer. *J Vis Exp* (2010) (42):e2125. doi:10.3791/2125
22. Zhang H, Gao X, Yang Y, Wang W, Liu J, Liang Y, et al. New construction of an animal model for the orthotopic transplantation of an ovarian tumor. *J Ovarian Res* (2014) 7:64. doi:10.1186/1757-2215-7-64
23. Xu X, Ayub B, Liu Z, Serna VA, Qiang W, Liu Y, et al. Anti-miR182 reduces ovarian cancer burden, invasion, and metastasis: an *in vivo* study in orthotopic xenografts of nude mice. *Mol Cancer Ther* (2014) 13(7):1729–39. doi:10.1158/1535-7163.MCT-13-0982
24. Penet MF, Pathak AP, Raman V, Ballesteros P, Artemov D, Bhujwalla ZM. Noninvasive multiparametric imaging of metastasis-permissive microenvironments in a human prostate cancer xenograft. *Cancer Res* (2009) 69(22):8822–9. doi:10.1158/0008-5472.CAN-09-1782
25. Penet MF, Shah T, Bharti S, Krishnamachary B, Artemov D, Mironchik Y, et al. Metabolic imaging of pancreatic ductal adenocarcinoma detects altered choline metabolism. *Clin Cancer Res* (2015) 21(2):386–95. doi:10.1158/1078-0432.CCR-14-0964
26. Thibault B, Castells M, Delord JP, Couderc B. Ovarian cancer microenvironment: implications for cancer dissemination and chemoresistance acquisition. *Cancer Metastasis Rev* (2013) 33(1):17–39. doi:10.1007/s10555-013-9456-2
27. Glunde K, Penet MF, Jiang L, Jacobs MA, Bhujwalla ZM. Choline metabolism-based molecular diagnosis of cancer: an update. *Expert Rev Mol Diagn* (2015) 15(6):735–47. doi:10.1586/14737159.2015.1039515
28. Iorio E, Mezzanzanica D, Alberti P, Spadaro F, Ramoni C, D'Ascenzo S, et al. Alterations of choline phospholipid metabolism in ovarian tumor progression. *Cancer Res* (2005) 65(20):9369–76. doi:10.1158/0008-5472.CAN-05-1146

29. Krishnamachary B, Glunde K, Wildes F, Mori N, Takagi T, Raman V, et al. Noninvasive detection of lentiviral-mediated choline kinase targeting in a human breast cancer xenograft. *Cancer Res* (2009) 69(8):3464–71. doi:10.1158/0008-5472.CAN-08-4120
30. Granata A, Nicoletti R, Perego P, Iorio E, Krishnamachary B, Benigni F, et al. Global metabolic profile identifies choline kinase alpha as a key regulator of glutathione-dependent antioxidant cell defense in ovarian carcinoma. *Oncotarget* (2015) 6(13):11216–30. doi:10.18632/oncotarget.3589
31. Sribney M, Knowles CL, Lyman EM. Regulation of phosphatidylcholine synthesis in rat liver endoplasmic reticulum. *Biochem J* (1976) 156(3):507–14. doi:10.1042/bj1560507
32. Bocos C, Herrera E. Pantethine stimulates lipolysis in adipose tissue and inhibits cholesterol and fatty acid synthesis in liver and intestinal mucosa in the normolipidemic rat. *Environ Toxicol Pharmacol* (1998) 6(1):59–66. doi:10.1016/S1382-6689(98)00020-9
33. Kleinkauf H, Von Dohren H. A nonribosomal system of peptide biosynthesis. *Eur J Biochem* (1996) 236(2):335–51. doi:10.1111/j.1432-1033.1996.00335.x
34. Marahiel MA, Stachelhaus T, Mootz HD. Modular peptide synthetases involved in nonribosomal peptide synthesis. *Chem Rev* (1997) 97(7):2651–74. doi:10.1021/cr960029e
35. Quadri LE, Weinreb PH, Lei M, Nakano MM, Zuber P, Walsh CT. Characterization of Sfp, a *Bacillus subtilis* phosphopantetheinyl transferase for peptidyl carrier protein domains in peptide synthetases. *Biochemistry* (1998) 37(6):1585–95. doi:10.1021/bi9719861
36. Ross J, Najjar AM, Sankaranarayananpillai M, Tong WP, Kaluarachchi K, Ronen SM. Fatty acid synthase inhibition results in a magnetic resonance-detectable drop in phosphocholine. *Mol Cancer Ther* (2008) 7(8):2556–65. doi:10.1158/1535-7163.MCT-08-0015
37. Guo Q, Gao BL, Zhang XJ, Liu GC, Xu F, Fan QY, et al. CXCL12-CXCR4 axis promotes proliferation, migration, invasion, and metastasis of ovarian cancer. *Oncol Res* (2015) 22(5):247–58. doi:10.3727/096504015X14343704124430
38. Liu Y, Metzinger MN, Lewellen KA, Cripps SN, Carey KD, Harper EI, et al. Obesity contributes to ovarian cancer metastatic success through increased lipogenesis, enhanced vascularity, and decreased infiltration of M1 macrophages. *Cancer Res* (2015) 75(23):5046–57. doi:10.1158/0008-5472.CAN-15-0706
39. Lengyel E. Ovarian cancer development and metastasis. *Am J Pathol* (2010) 177(3):1053–64. doi:10.2353/ajpath.2010.100105
40. Nieman KM, Kenny HA, Penicka CV, Ladanyi A, Buell-Gutbrod R, Zillhardt MR, et al. Adipocytes promote ovarian cancer metastasis and provide energy for rapid tumor growth. *Nat Med* (2011) 17(11):1498–503. doi:10.1038/nm.2492

**Conflict of Interest Statement:** The authors declare that the research was conducted in the absence of any commercial or financial relationships that could be construed as a potential conflict of interest.

Copyright © 2016 Penet, Krishnamachary, Wildes, Mironchik, Mezzanzanica, Podo, de Reggi, Gharib and Bhujwalla. This is an open-access article distributed under the terms of the Creative Commons Attribution License (CC BY). The use, distribution or reproduction in other forums is permitted, provided the original author(s) or licensor are credited and that the original publication in this journal is cited, in accordance with accepted academic practice. No use, distribution or reproduction is permitted which does not comply with these terms.



# Tissue Microstructure Is Linked to MRI Parameters and Metabolite Levels in Prostate Cancer

Kirsten Margrete Selvæs<sup>1,2\*</sup>, Riyas Vettukattil<sup>1</sup>, Helena Bertilsson<sup>3,4</sup>, Alan J. Wright<sup>5</sup>, Arend Heerschap<sup>6</sup>, Anders Angelsen<sup>1</sup>, May-Britt Tessem<sup>1</sup> and Tone Frost Bathen<sup>1</sup>

<sup>1</sup>Department of Circulation and Medical Imaging, Norwegian University of Science and Technology, Trondheim, Norway

<sup>2</sup>St. Olavs Hospital, Trondheim, Norway, <sup>3</sup>Department of Cancer Research and Molecular Medicine, Norwegian University of Science and Technology, Trondheim, Norway, <sup>4</sup>Department of Urology, St. Olavs Hospital, Trondheim, Norway, <sup>5</sup>Cancer Research UK Cambridge Institute, University of Cambridge, Cambridge, UK, <sup>6</sup>Department of Radiology and Nuclear Medicine, Radboud University Medical Center, Nijmegen, Netherlands

## OPEN ACCESS

### Edited by:

Franca Podo,  
Istituto Superiore di Sanità, Italy

### Reviewed by:

Ellen Ackerstaff,  
Memorial Sloan Kettering  
Cancer Center, USA  
Dmitri Artemov,  
Johns Hopkins University, USA

### \*Correspondence:

Kirsten Margrete Selvæs  
kirsten.m.selvas@ntnu.no

### Specialty section:

This article was submitted  
to Cancer Imaging and Diagnosis,  
a section of the journal  
*Frontiers in Oncology*

Received: 18 March 2016

Accepted: 30 May 2016

Published: 14 June 2016

### Citation:

Selvæs KM, Vettukattil R,  
Bertilsson H, Wright AJ,  
Heerschap A, Angelsen A,  
Tessem M-B and Bathen TF (2016)  
Tissue Microstructure Is Linked  
to MRI Parameters and Metabolite  
Levels in Prostate Cancer.  
*Front. Oncol.* 6:146.  
doi: 10.3389/fonc.2016.00146

**Introduction:** Magnetic resonance imaging (MRI) can portray spatial variations in tumor heterogeneity, architecture, and its microenvironment in a non-destructive way. The objective of this study was to assess the relationship between MRI parameters measured on patients *in vivo*, individual metabolites measured in prostatectomy tissue *ex vivo*, and quantitative histopathology.

**Materials and methods:** Fresh frozen tissue samples ( $n = 53$  from 15 patients) were extracted from transversal prostate slices and linked to *in vivo* MR images, allowing spatially matching of *ex vivo* measured metabolites with *in vivo* MR parameters. Color-based segmentation of cryosections of each tissue sample was used to identify luminal space, stroma, and nuclei.

**Results:** Cancer samples have significantly lower area percentage of lumen and higher area percentage of nuclei than non-cancer samples ( $p \leq 0.001$ ). Apparent diffusion coefficient is significantly correlated with percentage area of lumen ( $p = 0.6$ ,  $p < 0.001$ ) and percentage area of nuclei ( $p = -0.35$ ,  $p = 0.01$ ). There is a positive correlation ( $p = 0.31$ ,  $p = 0.053$ ) between citrate and percentage area of lumen. Choline is negatively correlated with lumen ( $p = -0.38$ ,  $p = 0.02$ ) and positively correlated with percentage area of nuclei ( $p = 0.38$ ,  $p = 0.02$ ).

**Conclusion:** Microstructures that are observed by histopathology are linked to MR characteristics and metabolite levels observed in prostate cancer.

**Keywords:** ADC, magnetic resonance imaging, citrate, choline, HR-MAS MRS, color-based segmentation

## INTRODUCTION

Magnetic resonance imaging (MRI) plays an important role in the diagnostic work-up of prostate cancer patients (1). MRI can portray spatial variations in tumor heterogeneity, architecture, and its microenvironment in a non-destructive way. Metabolic and morphologic changes in prostate cancer tissue lead to changes in MRI and MR spectroscopy (MRS) parameters. In cancer areas of the prostate's peripheral zone, T<sub>2</sub> intensity and apparent diffusion coefficient (ADC) are reduced,

while the choline and creatine-to-citrate ratio is increased compared to non-cancer areas (2, 3). These cancer-related changes in MR imaging parameters may be caused by a combination of increased cellularity, reduced luminal space, and altered metabolism.

Attempts have been made to elucidate the relationship between MR visible metabolites and MR imaging parameters. A negative correlation between ADC and the metabolite ratio choline plus creatine-to-citrate has been demonstrated (4). Due to low spectral resolution *in vivo*, correlation between MRI parameters and individual metabolites (such as choline-containing compounds and citrate) has not yet been investigated. *Ex vivo* high-resolution spectroscopy data from magic angle spinning (HR-MAS) MRS from prostate cancer can be linked to *in vivo* MR parameters as previously described (5), and individual metabolites can therefore be correlated with MRI parameters.

In the prostate, healthy peripheral zone has heterogeneous tissue architecture and consists primarily of glandular lumen lined with secretory epithelium embedded within a stromal matrix (6). Healthy prostate tissue is characterized by high levels of citrate since the glandular secretory epithelial cells have the ability to produce, accumulate, and secrete citrate (7). The water content is low in stroma, but high in luminal space resulting in a relatively long  $T_2$  and unrestricted water diffusion. As a result, healthy peripheral zone shows high signal intensity in  $T_2$ -weighted images and on ADC maps, while  $T_2$  intensity and ADC are reduced in cancer (8–14). However, it has been demonstrated by Bourne et al. that the secretory epithelia within healthy peripheral zone represent a compartment of highly restricted water diffusion (6) and that healthy peripheral zone in general displays two  $T_2$  components, one liquid-like component with long  $T_2$  time originating from the luminal space and one component with a short  $T_2$  time originating from stromal and epithelial tissues (15). Further, significant correlations between imaging parameters and histological features, such as luminal space, cell density, percentage of nuclei, and cytoplasm, have been demonstrated (16–18).

The objective of this study was to assess the relationship between MRI parameters ( $T_2$  intensity and ADC) measured on patients *in vivo*, individual metabolites measured in prostatectomy tissue *ex vivo* and quantitative histopathological features (percentage nuclei, stroma, and luminal space). An overview of these relationships could give a better insight into the origin of the observed MRI and MRS signals and contribute to better understanding of the similarities and differences of these parameters.

## MATERIALS AND METHODS

### Patients and Tissue Samples

The Regional Committee for Medical Research Ethics approved the study, and patients gave informed written consent to participate. Fresh frozen tissue samples [ $n = 53$  from 15 patients, median 3 (range 2–6) per patient] were extracted from transversal prostate slices and linked to *in vivo* MR parameters as previously described (5, 19). In short, a full transversal, fresh tissue slice (2 mm thick) was resected from the middle of the prostate and

snap-frozen. Tissue samples (3 mm in diameter) were thereafter drilled out of the frozen tissue slice, and locations of removed samples were documented on a photo. Preoperative MR images best corresponding to the level of the resected tissue slice were identified, and circular regions of interest were outlined according to the location of the removed tissue samples. Patient and tissue sample characteristics are listed in Table 1.

### MR Imaging

Magnetic resonance imaging was performed as previously described (2). In short, patients with biopsy proven prostate cancer underwent a preoperative multiparametric MR examination including  $T_2$ -weighted imaging ( $T_2$ WI), diffusion-weighted imaging (DWI), MR spectroscopic imaging [MRSI; results previously reported in Ref. (2, 5) and not shown here], and dynamic contrast-enhanced magnetic resonance imaging [DCE-MRI; results previously reported in Ref. (2) and not shown here] on a 3-T system (Magnetom Trio, Siemens Medical Solutions, Erlangen, Germany). Phased array body coil and spine coil elements were used for signal detection.  $T_2$ -weighted turbo spin echo images were obtained in three orthogonal planes. The transversal  $T_2$ -weighted images [TR/TE 4210 ms/104 ms, FOV 160 mm × 160 mm, matrix 320 × 256, slice thickness 3 mm, and acquisition time 5 min 47 s] were angulated perpendicular to the urethra to replicate the angle of slicing for histopathological analysis. Diffusion-weighted images [TR/TE 3500 ms/77 ms, FOV 340 mm × 168 mm, matrix 170 × 170, slice thickness 4 mm, four  $b$ -values (50, 300, 600, and 800 s/mm<sup>2</sup>), and acquisition time 2 min 59 s] and dynamic contrast-enhanced images (TR/TE 4 ms/1.34 ms, FOV 280 mm × 227.6 mm, matrix 256 × 230.4, slice thickness 2 mm, temporal resolution 12.9 s, and total acquisition time 5 min 32 s) were equally angulated.  $T_2$ -weighted images and ADC maps were used to calculate  $T_2$  intensities and ADC in regions of interest corresponding to tissue resection areas.

### HR-MAS MRS Experiment

<sup>1</sup>H HR-MAS MR spectra of the tissue samples were obtained using a 14.1-T spectrometer (Bruker Avance DRX 600, Bruker BioSpin

**TABLE 1 | Characteristics of patients ( $N = 15$ ) and tissue samples ( $n = 53$ ).**

Patient characteristics	Value, median (range)
Age (years)	63.7 (48.0–69.5)
sPSA (ng/ml)	12.0 (5.9–21.4)
Tissue sample characteristics	<i>n</i>
Peripheral zone	33
Transition zone	20
Gleason score	
Non-cancer	14
6 (3 + 3)	11
7 (3 + 4, 4 + 3)	12 (8, 4)
8 (3 + 5, 4 + 4)	8 (2, 6)
9 (4 + 5, 5 + 4)	8 (5, 3)
Tumor load (%) <sup>a</sup> , median (range)	60 (10–90)

sPSA, serum prostate-specific antigen at time of surgery;  $n$  = number of patients tissue samples.

<sup>a</sup>Percentage tumor in tumor-containing tissue samples.

GmbH, Karlsruhe, Germany) and post-processed as previously described (20). Quantification of metabolites was performed by LC Model (21), as described by Giskeødegård et al. (20).

## Histopathology and Color-Based Segmentation

A cryosection was taken from each tissue sample and stained with hematoxylin and eosin (H&E). These H&E-stained slides were digitized with 4 $\times$  magnification, and color-based segmentation (Positive Pixel Count algorithm in ImageScope v.11, Aperio Technologies) was used to identify luminal space, stroma, and nuclei, as described by Langer et al. (16). In short, two hue and windows settings were used (setting 1: 0.1 for hue, 0.5 for window; setting 2: 0.7 for hue, 0.35 for window) and optimized for each histologic slide by adjusting the window on a test region such that negative pixels in setting 1 represented nuclei, negative pixels in setting 2 represented stroma, and positive pixels in setting 2 represented cytoplasm and nuclei. Lumen was calculated as total area minus positive and negative pixels in setting 2 (**Figure 1**). For all the components (lumen, stroma, and nuclei), percentage of total area was used in the calculations. One tissue sample (GS 4 + 4) was excluded from color-based segmentation due to poor quality of the H&E slide. The metabolite concentrations from this tissue sample were included in the analyses when metabolites were correlated with MR parameters.

## Statistics

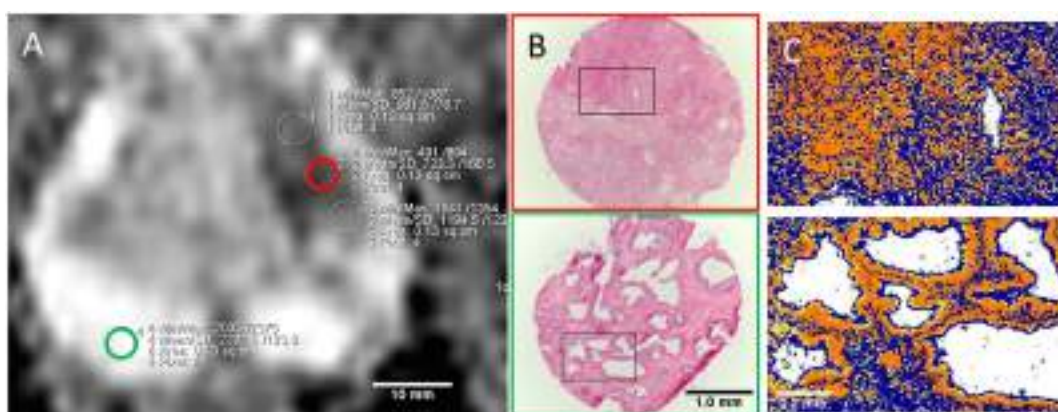
The Kolmogorov-Smirnov test was used to test data normality. Linear mixed model was used for pairwise comparison of histological components and different Gleason scores. Linear mixed model was also used to evaluate the association between MR parameters, metabolites, and histological features. Parameters that were not normally distributed were log-transformed before being entered in the linear mixed model. To account for multiple samples per patient, patient identification was entered as a random effect on the intercept in the model. Spearman's rank

correlation ( $\rho$ ) was calculated between *in vivo* MR parameters, *ex vivo* metabolite concentrations, and histological features since they were not all normally distributed. This measure does not take into account multiple samples per patient. Multiple comparisons were corrected for with the Benjamini and Hochberg false discovery rate. Adjusted  $p$  values  $<0.05$  were considered significant. All statistical analyses were performed using SPSS (IBM SPSS Statistics 22.0), except Benjamini and Hochberg corrections, which were performed in Matlab (MATLAB R2009a, The MathWorks Inc., Natick, MA, USA).

## RESULTS

An overview of histological components in cancer and non-cancer samples is given in **Table 2**. Cancer samples have significantly lower area percentage of lumen and higher area percentage of nuclei than non-cancer samples ( $p \leq 0.001$ ). Percentage area of stroma is not significantly different between cancer and non-cancer samples ( $p = 0.3$ ). There are no significant differences between histological parameters in tissue samples with different Gleason scores except for percentage area of lumen in Gleason score 9 samples, which are significantly lower than for Gleason scores 6 and 7 (**Figure 2**).

The *in vivo*-measured MR parameters,  $T_2$  intensity and ADC, are reduced in areas of cancer compared to non-cancer (**Table 3**) ( $p < 0.001$ ). There is a trend toward reduced ADC and  $T_2$  intensity with higher Gleason score and a significantly lower ADC in Gleason score 9 samples compared to Gleason score 6 samples ( $p = 0.02$ ). The *ex vivo*-measured metabolite concentrations of citrate and choline is reduced and increased, respectively, in cancer samples compared to non-cancer samples (**Table 3**). There is a trend toward increased choline and decreased citrate with increased Gleason score and significantly lower citrate in Gleason score 9 samples compared to Gleason score 6 samples ( $p = 0.01$ ). There are no significant differences in choline between samples with different Gleason scores.

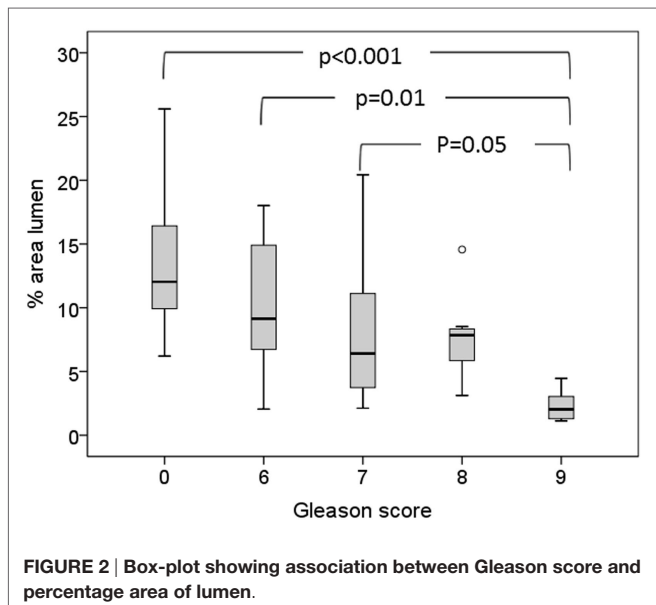


**FIGURE 1 | (A)** ADC map with ROIs from cancer (red outline) and non-cancer peripheral zone (green outline) areas corresponding to extracted tissue samples. **(B)** H&E stained slides (4 $\times$  objective) of cryosections with Gleason 5 + 4 (red) and non-cancer (green) tissue. Red and green outline refer to tissue location in **(A)**. **(C)** Close-up view of corresponding color-based segmentation with setting 2. Negative pixels (blue color) correspond to stroma; positive pixels (yellow and orange color) correspond to cytoplasm and nuclei; lumen is calculated as total number of pixels minus positive and negative (white color).

**TABLE 2 | Area percentage of histological components.**

Tissue type	Lumen (%)	Stroma (%)	Nuclei (%)	No. of samples
Non-cancer	13.8 ± 1.6	54.8 ± 1.9	23.3 ± 1.9	14
Cancer	<b>7.5 ± 0.9</b>	50.7 ± 1.2	<b>30.3 ± 1.0</b>	38
GS 6	10.4 ± 1.5	50.2 ± 1.7	28.5 ± 1.6	11
GS 7	<b>8.2 ± 1.7</b>	47.9 ± 2.1	<b>31.2 ± 2.0</b>	12
GS 8	<b>7.7 ± 1.4</b>	52.0 ± 3.1	<b>31.5 ± 2.4</b>	7
GS 9	<b>2.3 ± 0.4</b>	54.4 ± 3.1	<b>30.5 ± 2.2</b>	8

Numbers are mean ± SE. Bold font indicates a significant difference from non-cancer samples ( $p < 0.05$  after correction for multiple comparisons).

**FIGURE 2 | Box-plot showing association between Gleason score and percentage area of lumen.****TABLE 3 | MR parameters.**

Tissue type	ADC ( $\times 10^{-6}$ mm $^2$ /s)	T <sub>2</sub> intensity	Choline <sup>a</sup> (mmol/kg <sup>b</sup> )	Citrate (mmol/kg <sup>b</sup> )	No. of samples
Non-cancer	1572 ± 95	353 ± 31	1.19 ± 0.1	9.8 ± 1.4	14
Cancer	<b>1146 ± 44</b>	<b>250 ± 11</b>	<b>2.8 ± 0.3</b>	<b>6.6 ± 0.7</b>	39
GS 6	<b>1265 ± 97</b>	281 ± 18	<b>2.0 ± 0.5</b>	9.7 ± 1.4	11
GS 7	<b>1164 ± 70</b>	<b>254 ± 22</b>	<b>3.0 ± 0.5</b>	<b>5.4 ± 1.1</b>	12
GS 8	<b>1180 ± 88</b>	<b>232 ± 21</b>	<b>2.8 ± 0.5</b>	<b>7.1 ± 1.6</b>	8
GS 9	<b>921 ± 60</b>	<b>220 ± 21</b>	<b>3.7 ± 0.8</b>	<b>3.6 ± 0.9</b>	8

Numbers are mean ± SE. Bold font indicates a significant difference from non-cancer samples ( $p < 0.05$  after correction for multiple comparisons).

<sup>a</sup>Sum of all choline-containing compounds.

<sup>b</sup>Choline and citrate concentrations are reported as millimoles per kilogram wet weight.

T<sub>2</sub> intensity, total choline, and citrate levels were not normally distributed and thus were log-transformed before being entered into the linear mixed model.

There is an intermediate to strong positive correlation between ADC and percentage area of lumen ( $\rho = 0.6$ ,  $p < 0.001$ ). There is a weaker, but significant, negative correlation between ADC and percentage area of nuclei ( $\rho = -0.35$ ,  $p = 0.01$ ) (Table 4; Figure 3). ADC, percentage area of lumen, and percentage area of nuclei are all correlated with Gleason score in the tissue sample ( $\rho = -0.58$ ,  $p < 0.001$ ;  $\rho = -0.62$ ,  $p < 0.001$ ; and  $\rho = 0.4$ ,  $p = 0.01$ , respectively) (Table 4). When only non-cancer samples ( $n = 14$ ) are considered, there is still a strong correlation between ADC

**TABLE 4 | Correlation coefficients between MR parameters and histological features.**

	Lumen (%)	Nuclei (%)	Stroma (%)	Gleason score
ADC ( $\times 10^{-6}$ mm $^2$ /s)	<b>0.60</b> (<0.001)	<b>-0.35</b> (0.03)	-0.01 (0.99)	<b>-0.58</b> (<0.001)
Citrate (mmol/kg <sup>b</sup> )	0.31 (0.05)	0.09 (0.71)	-0.01 (0.99)	<b>-0.46</b> (0.002)
Choline (mmol/kg <sup>b</sup> )	<b>-0.38</b> (0.01)	<b>0.38</b> (0.01)	-0.19 (0.31)	<b>0.55</b> (<0.001)
Spermine (mmol/kg <sup>b</sup> )	0.18 (0.37)	0.12 (0.67)	0.004 (0.99)	-0.31 (0.05)
Creatine (mmol/kg <sup>b</sup> )	-0.09 (0.71)	0.07 (0.57)	0.08 (0.71)	-0.07 (0.71)
(cho + spm + cre)/citrate	<b>-0.49</b> (0.001)	0.07 (0.71)	0.003 (0.99)	<b>0.60</b> (<0.001)
(cit + spm + cre)/cho	<b>0.45</b> (0.003)	-0.22 (0.24)	0.13 (0.55)	<b>-0.69</b> (<0.001)
Gleason score	<b>-0.62</b> (<0.001)	<b>0.40</b> (0.01)	-0.14 (0.51)	

Denoted in brackets are the  $p$ -values corrected for multiple testing with Benjamini and Hochberg false discovery rate approach.

cho, choline; spm, spermine; cre, creatine; cit, citrate.

Bold font indicates a significant correlation (<0.05 after correction from multiple comparisons)

<sup>a</sup>Metabolite concentrations are reported as millimoles per kilogram wet weight.

and lumen ( $\rho = 0.7$ ,  $p = 0.005$ ), while the correlation between ADC and nuclei is no longer significant ( $\rho = -0.007$ ,  $p = 0.982$ ). In linear mixed model analysis, percentage area of lumen, nuclei, and Gleason score are significant covariates of ADC ( $p < 0.001$ ,  $p = 0.014$ , and  $p < 0.001$ , respectively). Percentage area of stroma is not significantly correlated with ADC or Gleason score (Table 4).

There is a positive correlation ( $\rho = 0.31$ ) between Citrate and percentage area of lumen, however after correcting for multiple testing, it is only borderline significant at the 0.05 level ( $p = 0.053$ ). With linear mixed model, lumen is a significant covariate of citrate ( $p = 0.005$ ). Choline is negatively correlated with lumen ( $\rho = -0.38$ ,  $p = 0.02$ ) and positively correlated with percentage area of nuclei ( $\rho = 0.38$ ,  $p = 0.02$ ). Both citrate and choline are significantly correlated with Gleason score ( $\rho = -0.46$ ,  $p = 0.002$ ;  $\rho = 0.55$ ,  $p < 0.001$ , respectively). When only non-cancer samples are considered ( $n = 14$ ) citrate is not significantly correlated with percentage area of lumen ( $\rho = 0.15$ ,  $p = 0.65$ ) and choline is not significantly correlated with lumen or nuclei ( $\rho = 0.01$ ,  $p = 0.95$ ;  $\rho = 0.24$ ,  $p = 0.41$ , respectively). The relationship between percentage area of lumen, citrate, choline, and Gleason score is visualized in Figure 4. Spermine and creatine are not significantly correlated with any of the glandular components, but the ratios (choline + spermine + creatine)/citrate and (citrate + spermine + creatine)/choline are significantly correlated with percentage area of lumen ( $\rho = 0.49$ ,  $p = 0.002$ ;  $\rho = -0.45$ ,  $p = 0.004$ , respectively) (Table 4).

## DISCUSSION

In this study, we have explored the relationship between MR parameters measured *in vivo* (ADC and T<sub>2</sub> intensity), metabolite concentrations (citrate, choline, creatine, and spermine) measured *ex vivo* with HR-MAS MRS, and histological gland components (percentage area of lumen, nuclei, and stroma) extracted from histopathology with color-based segmentation.

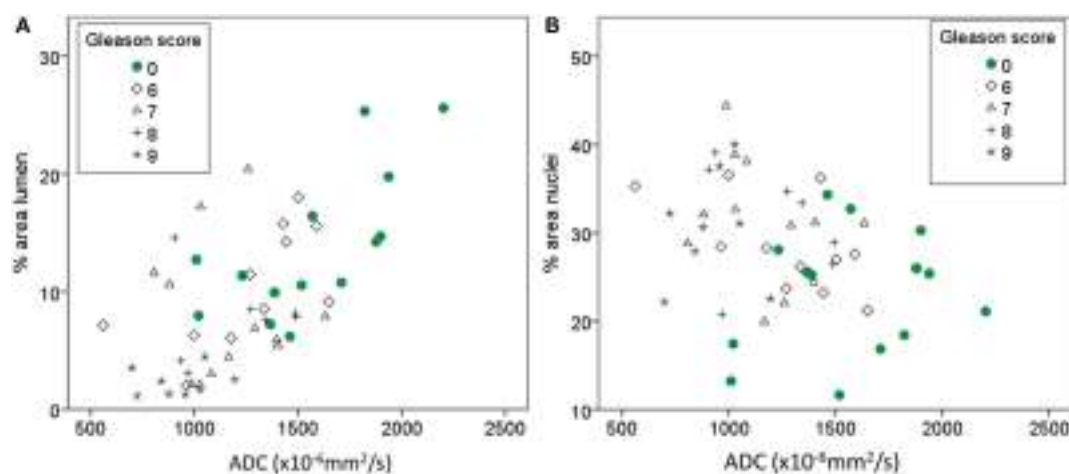


**FIGURE 3 |** Scatterplot showing the relationship between ADC and percentage area of lumen (A) and percentage area of nuclei (B), respectively.

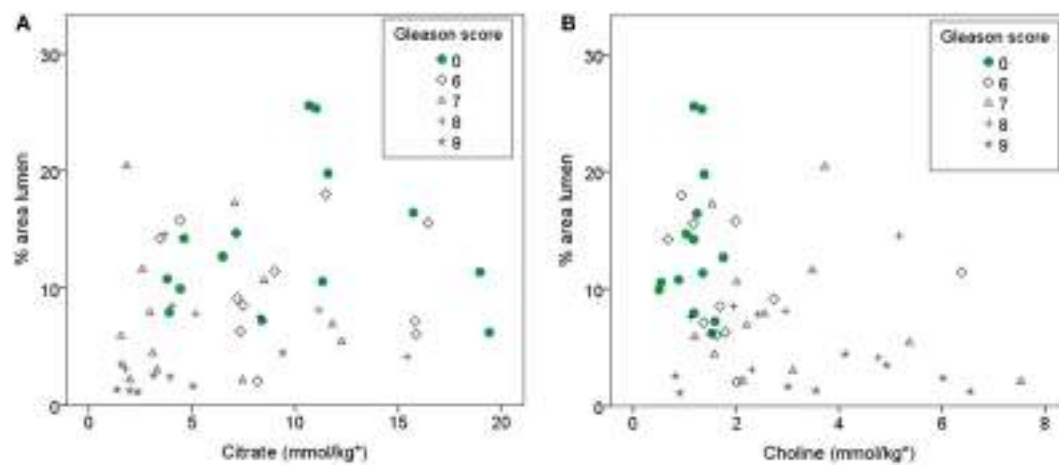


**FIGURE 4 |** Scatterplot showing the relationship between percentage area of lumen and citrate (A) and choline (B), respectively. \*Citrate and choline concentrations are reported as millimoles per kilogram wet weight.

As expected, we find a clear difference in histological features between cancer and non-cancer samples. The decrease in percentage of luminal space and increase in percentage area of nuclei in cancer samples compared to non-cancer samples is in line with previous reported findings by several groups (16, 22, 23). The percentage area of lumen in healthy prostate tissue has previously been reported to be in the range of 20–30% (16, 22), which is higher than we observed. Previous studies have performed color-based segmentation on H&E-stained whole mount sections while we used H&E-stained cryosections. H&E staining of cryosections can be of lower quality than staining of paraffin-embedded tissue, and this might explain some of the discrepancy. Further, our samples were 3 mm in diameter, and luminal space on the edges was omitted in the segmentation, which could also result in lower values. However, we observed a trend toward decreased percentage area of lumen with increased Gleason score, consistent with previous findings (16, 23). The literature is inconsistent regarding stroma content in cancer versus non-cancer tissue (16, 22, 23);

however, there was no evidence of differences in percentage area of stroma in our data.

We find a significantly increased percentage area of nuclei in cancer samples compared to non-cancer samples. In cancer samples, we see a weak trend toward increased area of nuclei with increased Gleason score; however, there is no significant difference between different Gleason scores. A trend toward increasing cellular metrics with increasing Gleason pattern is described in numerous articles, but most of them lack significant differences between Gleason groups (16, 17, 22–24). This has often been attributed to the limited range of Gleason scores in the study cohorts. However, in our study, we have tissue samples ranging from non-cancer to Gleason score 9 with approximately equal number of samples in each group and still find no significant differences. This might be a result of the nature of the Gleason scoring system, where each pattern is based on tissue architecture rather than cellularity *per se*. This finding might also explain the lack of significant differences in choline between different Gleason

scores, although there is a positive correlation between choline and percentage area of nuclei ( $\rho = 0.38, p = 0.021$ ) in our data.

The basis for the widespread use of MR imaging in prostate cancer diagnostics is the reduced  $T_2$  intensity and ADC in cancer compared to healthy prostate (2, 3, 9), which this study also confirms. The observed trend toward decreased ADC and  $T_2$  intensity with increased Gleason score is also in line with previous findings (25, 26). It is likely that observed changes in tissue composition in cancer compared to non-cancer areas are responsible for the observed changes in MRI parameters. A more detailed investigation of the correlations between MR parameters and glandular components could help us to understand what underlying structural changes have the strongest effect on the observed changes in the MR images. Bourne et al. highlight that there are three diffusion compartments in prostate tissue: ductal lumen with close to free diffusion, stromal tissue with intermediate diffusion, and epithelium with highly restricted diffusion (6). In our data, we see a positive correlation between ADC and percentage area of lumen. Since there is also a trend toward decreasing ADC with increasing Gleason score, we also tested the correlation between ADC and lumen in the non-cancer samples with a strong significant correlation also in that cohort. The percentage area of nuclei was negatively correlated with ADC; however, there was no correlation between ADC and nuclei when only non-cancer samples were investigated. Combined, these results indicate that in low resolution clinical DW images, the amount of luminal space is the main contributor to the measured ADC value, rather than increased cellularity, which is often used as the default explanation for reduced ADC in cancer imaging.

Altered tissue metabolism is an emerging hallmark of cancer (27). Although it is likely that metabolites that are stored in the luminal space, such as citrate and spermine, will be reduced when the lumen is invaded by cancer tissue, the observed change in metabolites between cancer and non-cancer tissue could also be due to cancer-related changes in metabolism. In our cohort, both citrate and luminal space were decreasing with increasing Gleason score. A weak correlation between citrate and luminal space was observed, but there was not a significant correlation when only normal samples were investigated. This could be due to the low number of non-cancer samples; however, it could also indicate that the correlation between citrate and luminal space is an indirect effect of their association with Gleason score. This could further indicate that the changes in metabolites, seen in cancer on MRSI, are not solely dependent on tissue composition and that citrate and choline measurements from MRSI give complementary information to ADC and  $T_2$ WI.

*In vivo* MRSI has lower spectral resolution than *ex vivo* HR-MAS MRS, and metabolite ratios, rather than individual metabolites, are therefore often reported for MRSI studies. The ratio of choline, polyamines (mainly spermine), and creatine-to-citrate is often used, since the resonances of choline, polyamines, and creatine can be difficult to separate in a reliable way (2). We expected to see a better correlation between individual metabolites and glandular features than by using metabolite ratios; however, this was not the case. The metabolites citrate and spermine are both stored in the prostatic fluid in the lumen, and it would therefore make sense to calculate a metabolite ratio where

citrate and spermine are added. Kobus et al. (22) focused on the metabolite ratio citrate, spermine, and creatine-to-choline and found a positive correlation with lumen with correlation coefficient of 0.5. We find a correlation in the same range between this ratio and percentage area of lumen ( $\rho = 0.45$ ), even though the individual metabolites are weaker correlated with lumen.

This study has some limitations. The low number of tissue samples hampered subdivision into peripheral zone and transition zone samples. There are also some inherent difficulties in the matching between *in vivo* MR images and tissue samples resected for HR-MAS NMR experiments and histopathology; however, the tissue harvesting method used in this study contributes to minimize the matching uncertainty (19). Previous studies have shown that there is a good correlation between *in vivo* and *ex vivo* measured metabolite ratios by using the harvesting and matching technique used in this study (5).

The acquired  $T_2$ -weighted MR images did not allow for quantitative  $T_2$  measurements, and we therefore used  $T_2$  intensity, rather than  $T_2$  relaxation, in our analysis. Since  $T_2$  intensity can be affected by other factors than pure  $T_2$  relaxation, we chose to only do brief descriptive statistics of the  $T_2$  intensity. Further for ADC calculations, we used a monoexponential diffusion model, since this is the model which is available for ADC calculation in our clinical scanners. The monoexponential diffusion model assumes Gaussian diffusion conditions. This could affect the correlation between ADC and percentage area lumen, since the lumen contains freely diffusing liquid. Bourne et al. suggest that the distinct stromal and glandular diffusion compartments are the origin of the biexponential diffusion decay seen *in vivo* (6). Therefore, application of a biexponential diffusion model might have resulted in a higher correlation of ADC with area of nuclei or stroma.

All samples in this study were taken from patients with prostate cancer. The non-cancer samples were taken from a transversal prostate slice that contained prostate cancer elsewhere, and it is not yet fully understood how the metabolism in normal-appearing tissue is affected by the adjacent cancer (field effect). The citrate production in the histopathologically normal-appearing areas could already have been altered and therefore preclude the expected correlation between citrate and percentage of lumen in non-cancer samples.

## CONCLUSION

This study adds to the literature of associations between alterations in tissue composition, metabolism, and observed MR imaging parameters. The microstructures that are observed by histopathology are linked to MR characteristics in prostate cancer, and ADC appears to mainly reflect luminal space rather than dense tumor structures.

## AUTHOR CONTRIBUTIONS

KS: study design, data collection, data analysis and interpretation, drafting the manuscript, and critical revision of the manuscript.  
RV: data analysis and interpretation, drafting the manuscript, and critical revision of the manuscript.  
HB: data collection and

critical revision of the manuscript. AW: data analysis and interpretation and critical revision of the manuscript. AH and AA: study design and critical revision of the manuscript. M-BT: study design, data collection, data analysis and interpretation, and critical revision of the manuscript. TB: study design, data analysis and interpretation, and critical revision of the manuscript.

## REFERENCES

- Heidenreich A, Bastian PJ, Bellmunt J, Bolla M, Joniau S, van der Kwast T, et al. EAU guidelines on prostate cancer. Part 1: screening, diagnosis, and local treatment with curative intent-update 2013. *Eur Urol* (2014) 65(1):124–37. doi:10.1016/j.euro.2013.09.046
- Selnaes KM, Heerschap A, Jensen LR, Tessem MB, Schweder GJ, Goa PE, et al. Peripheral zone prostate cancer localization by multiparametric magnetic resonance at 3 T: unbiased cancer identification by matching to histopathology. *Invest Radiol* (2012) 47(11):624–33. doi:10.1097/RLI.0b013e318263f0fd
- Hoeks CM, Barentsz JO, Hambrock T, Yakar D, Somford DM, Heijmink SW, et al. Prostate cancer: multiparametric MR imaging for detection, localization, and staging. *Radiology* (2011) 261(1):46–66. doi:10.1148/radiol.11091822
- Kobus T, Vos PC, Hambrock T, De Rooij M, Hulsbergen-van de Kaa CA, Barentsz JO, et al. Prostate cancer aggressiveness: in vivo assessment of MR spectroscopy and diffusion-weighted imaging at 3 T. *Radiology* (2012) 265(2):457–67. doi:10.1148/radiol.12111744
- Selnaes KM, Gribbestad IS, Bertilsson H, Wright A, Angelsen A, Heerschap A, et al. Spatially matched in vivo and ex vivo MR metabolic profiles of prostate cancer – investigation of a correlation with Gleason score. *NMR Biomed* (2013) 26(5):600–6. doi:10.1002/nbm.2901
- Bourne R, Kurniawan N, Cowin G, Sved P, Watson G. 16 T diffusion micro-imaging of fixed prostate tissue: preliminary findings. *Magn Reson Med* (2011) 66(1):244–7. doi:10.1002/mrm.22778
- Costello LC, Franklin RB. Citrate metabolism of normal and malignant prostate epithelial cells. *Urology* (1997) 50(1):3–12. doi:10.1016/S0090-4295(97)00124-6
- Hegde JV, Mulkern RV, Panych LP, Fennessy FM, Fedorov A, Maier SE, et al. Multiparametric MRI of prostate cancer: an update on state-of-the-art techniques and their performance in detecting and localizing prostate cancer. *J Magn Reson Imaging* (2013) 37(5):1035–54. doi:10.1002/jmri.23860
- deSouza NM, Reinsberg SA, Scurr ED, Brewster JM, Payne GS. Magnetic resonance imaging in prostate cancer: the value of apparent diffusion coefficients for identifying malignant nodules. *Br J Radiol* (2007) 80(950):90–5. doi:10.1259/bjr/24232319
- Hosseinzadeh K, Schwarz SD. Endorectal diffusion-weighted imaging in prostate cancer to differentiate malignant and benign peripheral zone tissue. *J Magn Reson Imaging* (2004) 20(4):654–61. doi:10.1002/jmri.20159
- Issa B. In vivo measurement of the apparent diffusion coefficient in normal and malignant prostatic tissues using echo-planar imaging. *J Magn Reson Imaging* (2002) 16(2):196–200. doi:10.1002/jmri.10139
- Kozlowski P, Chang SD, Jones EC, Berean KW, Chen H, Goldenberg SL. Combined diffusion-weighted and dynamic contrast-enhanced MRI for prostate cancer diagnosis – correlation with biopsy and histopathology. *J Magn Reson Imaging* (2006) 24(1):108–13. doi:10.1002/jmri.20626
- Mazaheri Y, Shukla-Dave A, Hricak H, Fine SW, Zhang J, Inurriigarro G, et al. Prostate cancer: identification with combined diffusion-weighted MR imaging and 3D <sup>1</sup>H MR spectroscopic imaging – correlation with pathologic findings. *Radiology* (2008) 246(2):480–8. doi:10.1148/radiol.2462070368
- Sato C, Naganawa S, Nakamura T, Kumada H, Miura S, Takizawa O, et al. Differentiation of noncancerous tissue and cancer lesions by apparent diffusion coefficient values in transition and peripheral zones of the prostate. *J Magn Reson Imaging* (2005) 21(3):258–62. doi:10.1002/jmri.20251
- Storås TH, Gjesdal KI, Gadmar ØB, Geitung JT, Kløw NE. Prostate magnetic resonance imaging: multiexponential  $T_2$  decay in prostate tissue. *J Magn Reson Imaging* (2008) 28(5):1166–72. doi:10.1002/jmri.21534
- Langer DL, van der Kwast TH, Evans AJ, Plotkin A, Trachtenberg J, Wilson BC, et al. Prostate tissue composition and MR measurements: investigating the relationships between ADC,  $T_2$ ,  $K_{trans}$ ,  $v_e$ , and corresponding histologic features. *Radiology* (2010) 255(2):485–94. doi:10.1148/radiol.10091343
- Gibbs P, Liney GP, Pickles MD, Zelhof B, Rodrigues G, Turnbull LW. Correlation of ADC and  $T_2$  measurements with cell density in prostate cancer at 3.0 Tesla. *Invest Radiol* (2009) 44(9):572–6. doi:10.1097/RLI.0b013e3181b4c10e
- Wang XZ, Wang B, Gao ZQ, Liu JG, Liu ZQ, Niu QL, et al. Diffusion-weighted imaging of prostate cancer: correlation between apparent diffusion coefficient values and tumor proliferation. *J Magn Reson Imaging* (2009) 29(6):1360–6. doi:10.1002/jmri.21797
- Bertilsson H, Angelsen A, Viset T, Skogseth H, Tessem MB, Halgunset J. A new method to provide a fresh frozen prostate slice suitable for gene expression study and MR spectroscopy. *Prostate* (2011) 71(5):461–9. doi:10.1002/pros.21260
- Giskeodgård GF, Bertilsson H, Selnaes KM, Wright AJ, Bathen TF, Viset T, et al. Spermine and citrate as metabolic biomarkers for assessing prostate cancer aggressiveness. *PLoS One* (2013) 8(4):e62375. doi:10.1371/journal.pone.0062375
- Provencher SW. Estimation of metabolite concentrations from localized in vivo proton NMR spectra. *Magn Reson Med* (1993) 30(6):672–9. doi:10.1002/mrm.1910300604
- Kobus T, van der Laak JA, Maas MC, Hambrock T, Bruggink CC, Hulsbergen-van de Kaa CA, et al. Contribution of histopathologic tissue composition to quantitative MR spectroscopy and diffusion-weighted imaging of the prostate. *Radiology* (2016) 278(3):801–11. doi:10.1148/radiol.2015142889
- Chatterjee A, Watson G, Myint E, Sved P, McEntee M, Bourne R. Changes in epithelium, stroma, and lumen space correlate more strongly with gleason pattern and are stronger predictors of prostate ADC changes than cellularity metrics. *Radiology* (2015) 277(3):751–62. doi:10.1148/radiol.2015142414
- Zelhof B, Pickles M, Liney G, Gibbs P, Rodrigues G, Kraus S, et al. Correlation of diffusion-weighted magnetic resonance data with cellularity in prostate cancer. *BJU Int* (2009) 103(7):883–8. doi:10.1111/j.1464-410X.2008.08130.x
- Wang L, Mazaheri Y, Zhang J, Ishill NM, Kuroiwa K, Hricak H. Assessment of biologic aggressiveness of prostate cancer: correlation of MR signal intensity with Gleason grade after radical prostatectomy. *Radiology* (2008) 246(1):168–76. doi:10.1148/radiol.2461070057
- Hambrock T, Somford DM, Huisman HJ, van Oort IM, Witjes JA, Hulsbergen-van de Kaa CA, et al. Relationship between apparent diffusion coefficients at 3.0-T MR imaging and Gleason grade in peripheral zone prostate cancer. *Radiology* (2011) 259(2):453–61. doi:10.1148/radiol.11091409
- Hanahan D, Weinberg RA. Hallmarks of cancer: the next generation. *Cell* (2011) 144(5):646–74. doi:10.1016/j.cell.2011.02.013

## FUNDING

This work has been funded by the Norwegian Cancer Society and the Liaison Committee between the Central Norway Regional Health Authority (RHA) and the Norwegian University of Science and Technology (NTNU).

**Conflict of Interest Statement:** The authors declare that the research was conducted in the absence of any commercial or financial relationships that could be construed as a potential conflict of interest.

Copyright © 2016 Selnaes, Vettukattil, Bertilsson, Wright, Heerschap, Angelsen, Tessem and Bathen. This is an open-access article distributed under the terms of the Creative Commons Attribution License (CC BY). The use, distribution or reproduction in other forums is permitted, provided the original author(s) or licensor are credited and that the original publication in this journal is cited, in accordance with accepted academic practice. No use, distribution or reproduction is permitted which does not comply with these terms.



# Metabolic Imaging in Prostate Cancer: Where We Are

**Claudia Testa<sup>1\*</sup>, Cristian Pultrone<sup>2</sup>, David Neil Manners<sup>1</sup>, Riccardo Schiavina<sup>2</sup> and Raffaele Lodi<sup>1</sup>**

<sup>1</sup>Functional MR Unit, Department of Biomedical and Neuromotor Sciences, S. Orsola-Malpighi Hospital, University of Bologna, Bologna, Italy, <sup>2</sup>Urologic Unit, Experimental, Diagnostic and Specialty Medicine, Department of Urology, S. Orsola-Malpighi Hospital, University of Bologna, Bologna, Italy

## OPEN ACCESS

### Edited by:

Franca Podo,  
Istituto Superiore di Sanità, Italy

### Reviewed by:

Balaji Krishnamachary,  
Johns Hopkins University, USA  
Tone Frost Bathen,  
Norwegian University of Science  
and Technology, Norway

### \*Correspondence:

Claudia Testa  
claudia.testa@unibo.it

### Specialty section:

This article was submitted to  
Cancer Imaging and Diagnosis,  
a section of the journal  
*Frontiers in Oncology*

**Received:** 05 July 2016

**Accepted:** 10 October 2016

**Published:** 09 November 2016

### Citation:

Testa C, Pultrone C, Manners DN,  
Schiavina R and Lodi R (2016)  
Metabolic Imaging in Prostate  
Cancer: Where We Are.  
*Front. Oncol.* 6:225.  
doi: 10.3389/fonc.2016.00225

In recent years, the development of diagnostic methods based on metabolic imaging has been aimed at improving diagnosis of prostate cancer (PCa) and perhaps at improving therapy. Molecular imaging methods can detect specific biological processes that are different when detected within cancer cells relative to those taking place in surrounding normal tissues. Many methods are sensitive to tissue metabolism; among them, positron emission tomography (PET) and magnetic resonance spectroscopic imaging (MRSI) are widely used in clinical practice and clinical research. There is a rich literature that establishes the role of these metabolic imaging techniques as valid tools for the diagnosis, staging, and monitoring of PCa. Until recently, European guidelines for PCa detection still considered both MRSI/MRI and PET/CT to be under evaluation, even though they had demonstrated their value in the staging of high risk PCa, and in the restaging of patients presenting elevated prostatic-specific antigen levels following radical treatment of PCa, respectively. Very recently, advanced methods for metabolic imaging have been proposed in the literature: multiparametric MRI (mpMRI), hyperpolarized MRSI, PET/CT with the use of new tracers and finally PET/MRI. Their detection capabilities are currently under evaluation, as is the feasibility of using such techniques in clinical studies.

**Keywords:** metabolic imaging, prostate cancer, MRSI, PET/CT, multiparametric MRI

Prostate cancer (PCa) is the most common cancer in American men and in European elderly males (beyond 70 years of age). About one American man in seven and one European in eight will be diagnosed with PCa during his lifetime.

Although imaging has played a major role in PCa, many challenges still remain in the different phases of the disease: initial assessment during diagnosis, and re-assessment after radical treatment in cases of biochemical relapse and disease progression.

Currently, prostate biopsy remains the only procedure that provides a definitive diagnosis. The decision to perform a biopsy is based on information gathered from serum prostatic-specific antigen (PSA) level, digital rectal examination (DRE), ultra sound (US), and magnetic resonance (MR) imaging, along with family history of PCa. In the era of active, multimodal surveillance of PCa, clinicians are presented with challenge of improving the accuracy of biopsy during the diagnostic phase and detecting only the aggressive diseases that require treatment, to avoid overdiagnosis and overtreatment. Another significant challenge for imaging is PCa staging (1). Currently, lymph node

staging is based on surgery. A greater accuracy of imaging for staging may avoid unnecessary lymph nodes dissections reducing related complications (2).

Last but not least, accurate imaging during restaging of PCa following radical treatment presents an unsolved challenge. Currently, when conventional imaging detects disease relapse, PSA and PSA kinetics are too high and patients are often outside the window of curability. A greater accuracy of metabolic imaging techniques should improve the efficacy of salvage treatments (3).

## CELL METABOLISM IN PROSTATE

Prostate gland metabolism, in both its healthy and malignant forms, can be considered a “model” that has improved our understanding of the mechanisms and factors occurring when normal cells transform themselves into malignant cells. The metabolic profile of normal and cancerous prostate cells has provided a window into the carcinogenesis process, highlighting the importance of cellular metabolism in this process.

Studies of prostate metabolism clearly demonstrate that a combined knowledge of metabolic processes, genomics, and proteomics is fundamental for a proper understanding of the cancer process.

An expanded metabolic repertoire supports the reprogramming of glucose, lipid, hormone, amino acid, and glycoprotein metabolic pathways during malignant transformation and tumor development in both the prostate gland and cancer cells in general.

Some of these pathways, especially those involving glucose, lipids, and amino acids, have been extensively studied by metabolic imaging. Normal prostate glucose pathways are characterized by low oxygen consumption (4) and minimal oxidation of citrate, both suggestive of a typical tumor cell metabolic profile (5), but caused by a normal accumulation of zinc that inhibits m-aconitase activity (6). The observed metabolic transformation in PCa is an increase in citrate oxidation of malignant cells, which has led to the hypothesis of increased m-aconitase activity compared to the normal epithelial cells. However, as highlighted by Singh et al. (7), proteomic analyses has shown that the level of m-aconitase does not change in cancerous prostate tissue, although the elevated zinc level inhibits its activity in normal tissue. As a consequence, *in vivo* non-invasive metabolic imaging has shown a high level of citrate in normal prostate gland that significantly decreases in regions of cancer associated with a significant choline (Cho) increase (8).

In fact, metabolic pathways of lipids, and in particular phospholipids, are altered, as shown by *in vivo* 1H-MR spectroscopy imaging (MRSI) studies that detect elevated total Cho in regions of PCa and by *ex vivo* (9) and tissue (10) 1H-MR spectroscopy studies that detect the total Cho peak due to significant increases of free Cho, phosphocholine (PC), and glycerophosphocholine (GPC). The altered lipid pathway in PCa has also been studied using positron emission tomography (PET) imaging (11) with radiotracers, such as 11C-Cho (and 18F-Fluorocholine) and 11C-acetate.

The amino acid metabolic pathway has also been studied by PET, exploiting the fact that amino acid transport is upregulated in PCa cells.

The metabolic peculiarities of prostate gland metabolism have driven the development of the techniques for its study *in vivo*.

## IN VIVO TECHNIQUES FOR METABOLIC IMAGING

Metabolic imaging refers to a set of molecular imaging methods that provide direct information about tissue metabolism. Molecular imaging may be defined as the visualization, characterization, and measurement of biologic processes at the molecular and cellular levels (12). Molecular imaging methods can detect specific biologic processes that change in cancer relative to surrounding normal tissue. Of course, it is desirable to have non-invasive instruments able to map the metabolism of various organs *in vivo*.

Many research methods are sensitive to tissue metabolism, and of these MRSI and PET are widely used in clinical practice and clinical research. Since the late 90s, both MRSI/MRI and PET/CT have been evaluated for PCa detection (8, 13, 14).

An MRSI exam is always associated with an MRI scan in order to have both metabolic and anatomical data. It is a non-invasive technique since non-ionizing radiation is used. Using MRSI, multiple metabolites can be spatially resolved in a single imaging protocol with a spatial resolution that can be reduced below 0.5 cm<sup>3</sup>; nevertheless with clinical systems, usually only a limited number of metabolites are present at concentrations that allow useful spatial mapping. This significantly limits the metabolic characterization of tumors. In prostate gland citrate, creatine, polyamine, and Cho-group resonances are detectable on 1.5- to 3-T scanners and the (choline + creatine)/citrate ratio is known to increase with tumor aggressiveness (15, 16). In a systematic review and meta-analysis of the use of combined MRI and MRSI in PCa pooled sensitivity for the evaluation of primary tumor was 68% (95% CI, 56–78%) with and pooled specificity 85% (95% CI, 78–90%). Subdividing patient into low and high risk subgroups, the sensitivity was lower in low-risk patients [58% (46–69%) vs. 74% (58–85%);  $p > 0.05$ ] but higher for specificity [91% (86–94%) vs. 78% (70–84%);  $p < 0.01$ ] (17).

Recently, developments in pulse sequences for MRSI have increased spectral resolution (18), and improved signal-to-noise (SNR) and volume selection (19).

Magnetic resonance spectroscopic imaging, unlike PET, detects static concentrations of endogenous molecules rather than tracer uptake. PET imaging is mostly used in association with a CT scan to sum up metabolic and anatomical information. A PET-CT scan involves exposure to ionizing radiation. PET is characterized by a high sensitivity in the detection of gamma radiation but with a spatial resolution which is not below a few millimeters. One of the drawbacks of PET for metabolic imaging is the absence of chemical information. The most commonly used tracer for PET imaging is [18F]-fluoro-2-deoxyglucose (FDG) but not all tumors consume glucose, so specific tracers have to be found for different tumors. The use of Cho radiotracers (11C-Cho and 18F-fluorocholine) and 11C-acetate is based on increased cellular membrane synthesis in PCa. Cho is overexpressed in cancer cells and is used for the synthesis of phosphatidylcholine, a prerequisite for cell membrane formation. Like Cho, acetate

is a substrate needed for lipogenesis and hence important for increased cell membrane synthesis during PCa. Just as with FDG, uptake level of lipogenesis tracers in benign tissue and PCa can overlap, determining the low specificity of these tracers for primary PCa detection (20). In a systematic review and meta-analysis of <sup>11</sup>C-acetate PET/CT in PCa, pooled sensitivity and pooled specificity for evaluation of primary tumor were 75.1% (95% CI: 69.8–79.8%) and 75.8% (95% CI: 72.4–78.9%), respectively (21). <sup>11</sup>C-Cho showed a sensitivity of 66% and specificity of 81% for localization of primary PCa on a sextant histopathologic analysis (22). Although lipogenesis tracers present limitations for detection of primary PCa, they might be useful for a minority of newly diagnosed patients in whom distant metastatic disease is highly suspected on the basis of clinical data (serum PSA level >20 ng/ml, Gleason score 8–10, locally advanced tumor). In a systematic review, Evangelista et al. reported a sensitivity and a specificity of 19–90 and 88–98%, respectively, for detection of metastatic lymph nodes (2). These results are linked to a high false-positive rate due to inflammation and a high false-negative rate linked to micrometastatic lymph node disease undetectable by the majority of PET/CT scanners. More rigorous imaging trials are required to validate methods, and determine their sensitivity, to reduce the extreme variability of these results. The role of Cho PET/CT for restaging of biochemically recurrent PCa has been confirmed, particularly when the PSA level becomes elevated. One systematic review and meta-analysis including 19 selected studies with a total of 1555 patients revealed a pooled sensitivity of 85.6% and pooled specificity of 92.6% (23). In a recent study with a large cohort of patients, the accuracy of <sup>11</sup>C-Cho PET/CT for the detection of sites of metastatic disease in PCa patients with biochemical relapse was confirmed. The authors also showed that in their series the PSA level was the main predictor of a positive scan with 1.16 ng/ml as the optimal cut-off value. They asserted that in the majority of positive scans they detected oligometastatic disease, potentially treatable with salvage therapies (3).

Other tracers have been and are currently being investigated (see Advanced Protocol and Perspectives) but only Cho and very recently <sup>18</sup>F-FACBC have FDA approval for clinical use.

One of the latest molecular imaging modalities is hyperpolarized <sup>13</sup>C-MRSI. It combines the advantages of MRSI with an enormous gain in sensitivity in <sup>13</sup>C detection due to the method of hyperpolarizing the molecules.

The dynamic nuclear polarization technique has been applied to <sup>13</sup>C-MRSI (24): it is based on the transfer of polarization from the electron spins of paramagnetic centers embedded in a glassy frozen solution to neighboring nuclear spins (i.e., <sup>13</sup>C nuclei of an informative biomolecule) through dipolar interactions. The solid solution is then rapidly dissolved and prepared for an intravenous injection. MRSI data must be obtained as rapidly as possible after dissolution because the enhancement is lost with the spin-lattice relaxation of the biomolecule. With hyperpolarized <sup>13</sup>C-MRSI, it is possible to monitor substrate uptake and the metabolism of endogenous biomolecules (25) by studying metabolic fluxes *in vivo*. Polarization methods, sequences, coils, and substrates (26, 27) have all been developed since 2007 with the aim of improving the accuracy of PCa evaluation.

## CURRENT USE OF METABOLIC IMAGING IN CLINICAL PRACTICE

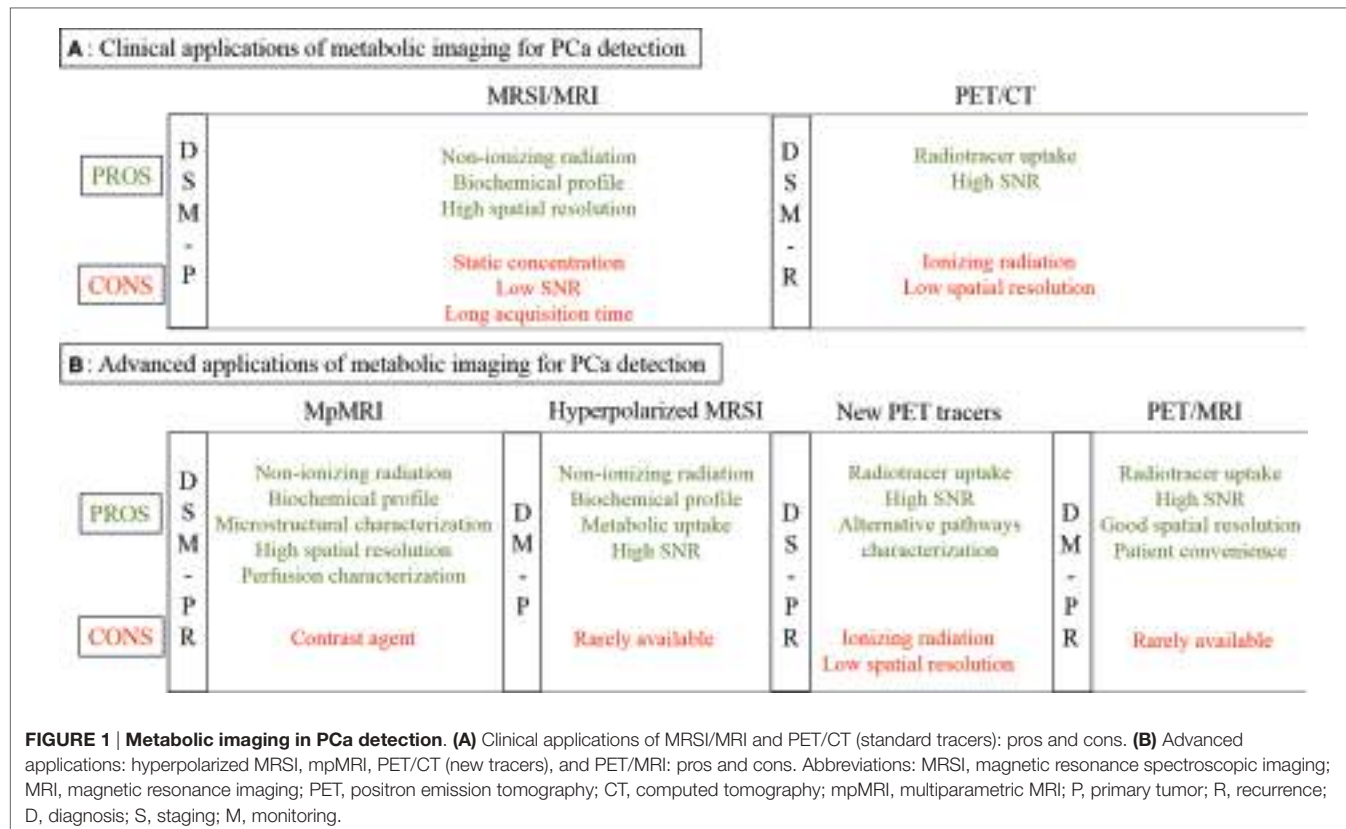
**Figure 1A** outlines the most common methods used for metabolic imaging in clinical practice. Their main technical characteristics are highlighted, divided into pros and cons. The utility of each technique for diagnosis, staging, and/or monitoring of therapy is indicated in vertical columns, subdivided into primary detection or recurrence. **Figure 2A** shows example images for these techniques.

Although an extensive literature shows how much these non-invasive imaging techniques are used to assess PCa in Europe, guidelines for PCa staging still indicate MRSI/MRI and PET/CT (32) as being under evaluation. The accuracy of MRSI/MRI aids in tumor localization within the peripheral zone, increasing the accuracy of extracapsular extension detection among less-experienced readers, and decreasing inter-observer variability. Nevertheless, given difficulties in interpreting signal changes related to post-biopsy hemorrhage and inflammatory changes of the prostate, and the unquantifiable but significant inter- and intra-observer variability seen between both non-dedicated and dedicated radiologists, that may lead to under- or overestimation of tumor presence and the local extent of disease, this technique is appropriate only for a limited number of cases. The overall accuracy of <sup>11</sup>C-Cho PET in defining local tumor stage has been reported to be around 70% (33). PET tends to understage PCa, and has a limited value for making treatment decisions in patients with clinically localized PCa. Thus, routine clinical use of <sup>11</sup>C-Cho PET cannot be recommended for detecting and staging primary PCa. By contrast, <sup>11</sup>C-Cho PET/CT is regarded as a well investigated modality for the restaging patients presenting with elevated PSA levels following radical treatment of PCa (34).

The ACRIN study on PCa localization by MRI and MRSI (35) showed that the accuracy of combined 1.5-T endorectal MR imaging–MR spectroscopic imaging for sextant localization of peripheral zone PCa is equal to that of MR imaging alone. Nevertheless, many publications have shown that the combination of MRI and MRSI even in selected applications (such as diagnosis of cancer in men with more than one previous negative biopsy) really improves MRI performance (8, 21, 36, 37). This disagreement with the ACRIN study is explained by the expertise of radiological staff (together with physicists, chemists, and biologists) in acquisition of MR spectra, in post-processing and by the close collaboration with urologists in approaching the diagnosis of each single patient. To overcome this methodological problem, fully automated procedures to assess MR spectra have been proposed; the classification capabilities of automated pattern recognition approaches are equal to or better than manual methods (38, 39).

With regard to PET, its diagnostic power lies in its ability to stage disease, monitor treatment response, and detect recurrence, rather than in initial diagnosis (40); hence, PET is still prescribed only for equivocal cases and not for clinical routine.

It remains an open question whether, in the light of the existing literature and current diagnostic guidelines, MRI/MRSI and



PET are needed to increase accuracy in PCa detection in clinical practice.

## ADVANCED PROTOCOLS AND PERSPECTIVES

**Figure 1B** outlines the most recent advanced approaches for metabolic imaging. As for **Figure 1A**, their main technical characteristics are highlighted, dividing between pros and cons. The utility of each technique for diagnosis, staging and/or monitoring of therapy is indicated in vertical columns. **Figure 2** shows example images of these advanced metabolic imaging approaches.

Multiparametric MRI (mpMRI) refers to the use of complementary MR techniques to improve the detection, characterization and staging of PCa by T2-weighted MRI, MRSI, DTI, and dynamic contrast-enhanced MRI scans in the same session. The combination of such acquisitions gives anatomical, microstructural, functional, and metabolic information with the high spatial resolution of MRI. MpMRI data appears to be the most accurate imaging method for localizing primary PCa and staging primary or recurrent PCa (28, 41, 42). An mpMRI acquisition has no particular technical limitation apart from the use of a contrast agent for DCE imaging. Nevertheless, the challenge to the diffusion of mpMRI is the need for specialized clinical staff and the need to present data to clinical colleagues in a simple but meaningful way in spite of its complexity. Shared acquisition, post-processing, and interpretative protocols become essential. This requirement has

inspired the definition of the PI-RAD score, specifically formalized for predicting the presence of cancer by mpMRI findings from of T2w, T1w, DWI, and DCE acquisitions (43). The use of this score provides a combined evaluation of all functional and structural MR imaging scans; nevertheless a quantitative score for all techniques is still lacking. On the contrary, a quantitative evaluation for MRSI, which could be part of mpMRI protocol but is absent from the PI-RAD scoring system, has already been evaluated (44) and applied (14, 45).

Magnetic resonance spectroscopic imaging of hyperpolarized nuclei is a relatively new and sophisticated approach, which offers the possibility of monitoring tumor metabolism by the injection of labeled substrates and observation of their metabolic products without the use of ionizing radiation. Metabolic imaging with hyperpolarized <sup>13</sup>C pyruvate, which provides information about tissue biochemistry, has been demonstrated to greatly increase the sensitivity of MRI in detecting PCa (46). Nevertheless, hyperpolarization is a highly demanding procedure due to both the process that drives nuclei to a non-stable but more sensitive condition and the rate of the exponential decay process, which limits acquisition time to a few tens of seconds. Thus, a number of hurdles must be overcome to transfer these methods to a clinical setting; the major one are technical, and regard the MR scanner and the polarizer, but there is the important matter of the safety of the substrate: to date no significant adverse effect have been observed in tolerability studies performed in test animals and the first application in human patients has shown no dose limit toxicity (29).

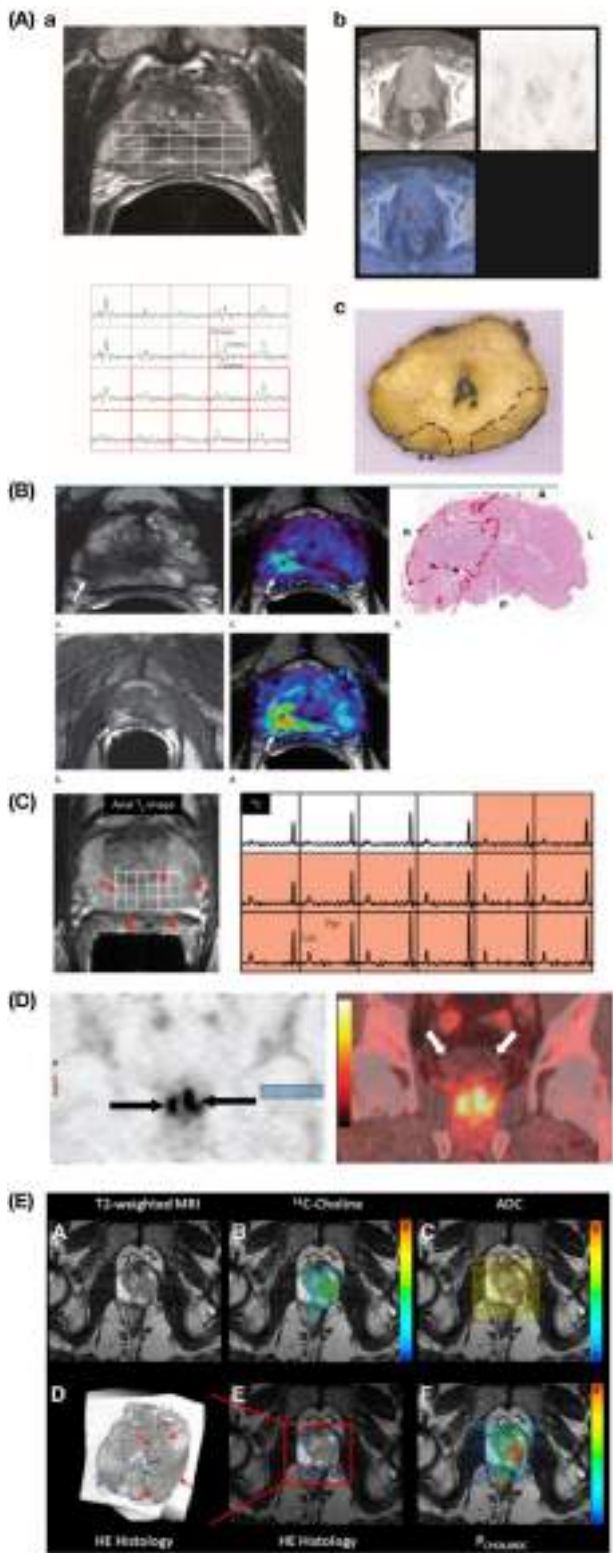


**FIGURE 2 | Example images showing advanced metabolic imaging approaches to PCa detection.**

(Continued)

#### FIGURE 2 | Continued

**(A)** MRSI/MRI and PET/CT. Transverse T2-weighted MR image (*upper left*) shows bilateral signal hypointensities and corresponding 3D MR spectroscopic spectra (*lower left*) show bilateral abnormalities [mean (Choline + Creatine)/Citrate ratio = 0.95 on right side and 1.10 on left] indicative of cancer, while corresponding PET/CT transverse images (*upper right*) do not show any relevant pathologic focal accumulation of <sup>11</sup>C-choline [background maximum SUV (standardized uptake value) = 2.5]. Corresponding pathologic specimen (hematoxylin–eosin stain; original magnification,  $\times 1$ ) (*lower right*) shows bilateral posterior adenocarcinoma (T3aNMX, Gleason score 4 + 3) with right extracapsular extension (\*\*). Reproduction with permission from Ref. (14) (RSNA).

**(B)** mpMRI in a 62-year-old man with PCa. Axial T2-weighted MR image (*upper left*) demonstrates a low-signal intensity focus (arrow) at right apex mid peripheral zone suspicious for PCa. Raw dynamic contrast-enhanced MR image (*lower left*) and  $k_{trans}$  (wash in) (*upper middle*) and  $k_{ep}$  (wash out) (*lower middle*) maps help localize tumor (arrow). Histopathologic slide at apex mid prostate level (*upper right*) confirms presence of tumor (Gleason score, 8) more anteriorly (red line), secondary to distortion and shrinkage of specimen. A, anterior; L, left; P, posterior; R, right. Reproduction with permission from Ref. (28) (RSNA).

**(C)** <sup>13</sup>C-hyperpolarized MRSI in a patient, who had a serum PSA of 4.5 ng/ml, was originally diagnosed with bilateral biopsy-proven Gleason grade 3 + 3 PCa, and received the highest dose of hyperpolarized [<sup>1</sup>-<sup>13</sup>C]pyruvate (0.43 ml/kg). On the *left*, an axial T2-weighted images and on the *right* the corresponding spectral array with the area of putative tumor highlighted by pink shading. A region of tumor was observed on the T2-weighted images (red arrows). From Ref. (29) (Nelson SJ, Kurhanewicz J, Vigneron DB, Larson PE, Harzstark AL, Ferrone M, et al. Metabolic imaging of patients with prostate cancer using hyperpolarized [<sup>1</sup>-<sup>13</sup>C]pyruvate. *Sci Transl Med* (2013) 5(198):198ra108. Reprinted with permission from AAAS.)

**(D)** Coronal PET (*left*) and CT fused (*right*) anti-<sup>18</sup>F-FACBC images of 63-year-old male patient with pathologically proven bilateral prostate carcinoma (arrows on the *left*). Note little bladder activity (white arrows on the *right*). This research was originally published in JNM (30). Schuster et al. © by the Society of Nuclear Medicine and Molecular Imaging, Inc.

**(E)** PET/MRI fusion imaging in high-grade PCa. Specific image information derived from <sup>11</sup>C-choline PET (*upper middle*), ADC (apparent diffusion coefficient) DWI (*upper right*), hematoxylin–eosin (HE) histology (*lower left*), and parametric fusion PET/MRI using PCHOL/ADC\* (*lower right*) is coregistered with transaxial T2-weighted MRI (*upper right*). Color bars indicate <sup>11</sup>C-choline SUV (standardized uptake value) (*upper middle*), PCHOL/ADC\* (*lower right*), and inverted ADC (*upper right*). Zoomed registered HE histology slice is shown for increased clarity (*lower left*). At histology, Gleason 4 + 3 lesion is located in left lobe of prostate (red arrows) in peripheral and central zone, which is identified on registered imaging, whereas additional low-volume Gleason 3 + 3 lesion in right lobe is not identified (blue arrows). \*PCHOL/ADC =  $\frac{11\text{C} - \text{Choline SUV}}{\text{ADC} + 0.001}$ .

research was originally published in JNM. Park et al. (31) © by the Society of Nuclear Medicine and Molecular Imaging, Inc.

In PET imaging, several promising radiotracers are currently being investigated for the evaluation of PCa but not based on the detection of glucose or fatty acid metabolism since glucose and lipogenesis tracers have demonstrated limitations for detection of primary PCa. These new radiotracers aim to monitor amino acid metabolism (anti-<sup>18</sup>F-FACBC), DNA synthesis, and the expression and activity levels of a variety of receptors, enzymes, and other cancer-specific and non-specific biomarkers.

The radiotracer 1-amino-3-fluorine-18-fluorocyclobutane-1-carboxylic acid (18-FACBC) exploits the fact that amino acid transport is upregulated in PCa cells. The low urinary excretion of this radiotracer also allows 18-FACBC uptake in malignant

tumor cells to be detected more accurately. Few papers have been published on the role of 18F-FACBC for the evaluation of primary or recurrent PCa. Schuster et al. compared the diagnostic performance of 18F-FACBC and 111In-capromab in 93 patients reporting a higher accuracy for 18F-FACBC and an upstaging of recurrent disease in at least 25% of patients (30). Nanni et al. recently confirmed the higher accuracy of 18F-FACBC compared to 11C-Cho in restaging of PCa, particularly in patients with low PSA levels (<1 ng/ml) (47).

To date, about 1000 patients have been studied with 68Ga-PSMA (prostate-specific membrane antigen) in different clinical indications, such as initial staging and restaging of disease and in comparison with other common radiopharmaceutical agents for PET imaging, such as radiolabeled Cho. PSMA is a membrane glycoprotein with an extensive extracellular domain, a transmembrane segment, and an intracellular domain. PSMA is normally expressed in epithelial cells within the prostate and is strongly upregulated at all stages of PCa. An increase in PSMA expression has been associated with tumor aggressiveness, metastasis, and disease recurrence, providing a rational target for ligand–receptor-based imaging and therapy. Two groups have demonstrated that 68Ga-PSMA PET/CT is superior to 18F-Cho PET/CT and conventional imaging modalities (48, 49). Eiber et al. evaluated the accuracy of 68Ga-PSMA PET/CT in 248 patients with biochemical relapse and showed a patient-based detection rate of 89.5% with a detection rates for PSA levels of  $\geq 2$ , 1 to <2, 0.5 to <1, and 0.2 to <0.5 ng/ml were 96.8, 93.0, 72.7, and 57.9%, respectively (50). Clinically, it is very important that 68Ga-PSMA PET/CT has a high detection rate for low values of PSA allowing the site of recurrence to be detected within the windows of curability. Further studies are required to confirm these data.

## REFERENCES

- Mottet N, Bellmunt J, Bolla M, Briers E, Cumberbatch MG, De Santis M, et al. EAU-ESTRO-SIOG guidelines on prostate cancer. Part 1: screening, diagnosis, and local treatment with curative intent. *Eur Urol* (2016). doi:10.1016/j.euro.2016.08.003
- Evangelista L, Briganti A, Fanti S, Joniau S, Reske S, Schiavina R, et al. New clinical indications for (18)F/(11)C-choline, new tracers for positron emission tomography and a promising hybrid device for prostate cancer staging: a systematic review of the literature. *Eur Urol* (2016) 70(1):161. doi:10.1016/j.euro.2016.01.029
- Graziani T, Ceci F, Castellucci P, Polverari G, Lima GM, Lodi F, et al. 11C-Choline PET/CT for restaging prostate cancer. Results from 4,426 scans in a single-centre patient series. *Eur J Nucl Med Mol Imaging* (2016) 43(11):1971. doi:10.1007/s00259-016-3428-z
- Costello LC, Guan Z, Kukoyi B, Feng P, Franklin RB. Terminal oxidation and the effects of zinc in prostate versus liver mitochondria. *Mitochondrion* (2004) 4(4):331. doi:10.1016/j.mito.2004.07.031
- Costello LC, Franklin RB, Feng P. Mitochondrial function, zinc, and intermediary metabolism relationships in normal prostate and prostate cancer. *Mitochondrion* (2005) 5(3):143. doi:10.1016/j.mito.2005.02.001
- Costello LC, Franklin RB. The clinical relevance of the metabolism of prostate cancer; zinc and tumor suppression: connecting the dots. *Mol Cancer* (2006) 5:17. doi:10.1186/1476-4598-5-17
- Singh KK, Desouki MM, Franklin RB, Costello LC. Mitochondrial aconitase and citrate metabolism in malignant and nonmalignant human prostate tissues. *Mol Cancer* (2006) 5:14. doi:10.1186/1476-4598-5-14
- Scheidler J, Hricak H, Vigneron DB, Yu KK, Sokolov DL, Huang LR, et al. Prostate cancer: localization with three-dimensional proton MR spectroscopic imaging – clinicopathologic study. *Radiology* (1999) 213(2):473. doi:10.1148/radiology.213.2.r99nv23473
- Ackerstaff E, Pflug BR, Nelson JB, Bhujwalla ZM. Detection of increased choline compounds with proton nuclear magnetic resonance spectroscopy subsequent to malignant transformation of human prostatic epithelial cells. *Cancer Res* (2001) 61(9):3599.
- Swanson MG, Zektzer AS, Tabatabai ZL, Simko J, Jarso S, Keshari KR, et al. Quantitative analysis of prostate metabolites using 1H HR-MAS spectroscopy. *Magn Reson Med* (2006) 55(6):1257. doi:10.1002/mrm.20909
- Brogsitter C, Zophel K, Kotzerke J. 18F-Choline, 11C-choline and 11C-acetate PET/CT: comparative analysis for imaging prostate cancer patients. *Eur J Nucl Med Mol Imaging* (2013) 40(1):S18. doi:10.1007/s00259-013-2358-2
- Mankoff DA. A definition of molecular imaging. *J Nucl Med* (2007) 48(6):18N,21N.
- Hara T, Kosaka N, Kishi H. PET imaging of prostate cancer using carbon-11-choline. *J Nucl Med* (1998) 39:990.
- Testa C, Schiavina R, Lodi R, Salizzoni E, Corti B, Farsad M, et al. Prostate cancer: sextant localization with MR imaging, MR spectroscopy, and 11C-choline PET/CT. *Radiology* (2007) 244(3):797. doi:10.1148/radiol.2443061063
- Costello LC, Franklin RB. The intermediary metabolism of the prostate: a key to understanding the pathogenesis and progression of prostate malignancy. *Oncology* (2000) 59:269. doi:10.1159/000012183
- Tran TK, Vigneron DB, Sailasuta N, Tropp J, Le Roux P, Kurhanewicz J, et al. Very selective suppression pulses for clinical MRSI studies of brain

Finally, the role of PET/MR has not yet been established: it offers the possibility of enhancing patient convenience by providing a single metabolic imaging session to replace separate MRI and PET/CT scans, reducing patient anxiety, total scan time, and recalls for repeated scanning. Although preliminary results are encouraging (31, 51, 52), it is unknown whether this sophisticated modality will demonstrate the high performance of MRI in the staging of the primary cancer and the metabolic profiling of lesions offered by 11C-Cho PET. It would be interesting to evaluate the inclusion of MRSI in PET/MR protocols.

In conclusion, the challenge for researchers is to improve the accuracy of metabolic imaging techniques for the diagnosis of PCa, and in consequence to allow improvements in therapy. MpMRI, 13C hyperpolarization for *in vivo* 13C-MRI, new tracers for PET scan, and the combination of PET with MRI are all new metabolic imaging tools that show promise in meeting this challenge.

However, all the cited advanced metabolic techniques have to be evaluated considering both their potential capabilities and their clinical applicability. The most promising technique can then be integrated in multiparametric protocols that must be standardized if they are to be applied in a clinical context.

## AUTHOR CONTRIBUTIONS

CT: literature research, manuscript draft, and manuscript revision. CP: literature research and manuscript draft. DNM: manuscript revision and English revision. RS: literature research and manuscript revision. RL: literature research and manuscript revision.

- and prostate cancer. *Magn Reson Med* (2000) 43(1):23. doi:10.1002/(SICI)1522-2594(200001)43:1<23::AID-MRM4>3.0.CO;2-E
17. Umbehr M, Bachmann LM, Held U, Kessler TM, Sulser T, Weishaupt D, et al. Combined magnetic resonance imaging and magnetic resonance spectroscopy imaging in the diagnosis of prostate cancer: a systematic review and meta-analysis. *J Eur Urol* (2009) 55(3):575. doi:10.1016/j.eururo.2008.10.019
  18. Nagarajan R, Iqbal Z, Burns B, Wilson NE, Sarma MK, Margolis DA, et al. Accelerated echo planar J-resolved spectroscopic imaging in prostate cancer: a pilot validation of non-linear reconstruction using total variation and maximum entropy. *NMR Biomed* (2015) 28(11):1366. doi:10.1002/nbm.3373
  19. Steinseifer IK, van Asten JJ, Weiland E, Scheenen TW, Maas MC, Heerschap A. Improved volume selective (1) H MR spectroscopic imaging of the prostate with gradient offset independent adiabaticity pulses at 3 tesla. *Magn Reson Med* (2015) 74(4):915. doi:10.1002/mrm.25476
  20. Mena E, Turkbey B, Mani H, Adler S, Valera VA, Bernardo M, et al. 11C-acetate PET/CT in localized prostate cancer: a study with MRI and histopathologic correlation. *J Nucl Med* (2012) 53:538. doi:10.2967/jnumed.111.096032
  21. Mohsen B, Giorgio T, Rasoul ZS, Werner L, Ali GR, Reza DK, et al. Application of C-11-acetate positron emission tomography (PET) imaging in prostate cancer: systematic review and meta-analysis of the literature. *BJU Int* (2013) 112:1062. doi:10.1111/bju.12279
  22. Farsad M, Schiavina R, Castellucci P, Nanni C, Corti B, Martorana G, et al. Detection and localization of prostate cancer: correlation of (11C) C-choline PET/CT with histopathologic step-section analysis. *J Nucl Med* (2005) 46:1642.
  23. Evangelista L, Zattoni F, Guttilla A, Saladini G, Zattoni F, Colletti PM, et al. Choline PET or PET/CT and biochemical relapse of prostate cancer: a systematic review and meta-analysis. *Clin Nucl Med* (2013) 38:305. doi:10.1097/RLU.0b013e3182867f3c
  24. Ardenkjær-Larsen JH, Fridlund B, Gram A, Hansson G, Hansson L, Lerche MH, et al. Increase in signal-to-noise ratio of >10,000 times in liquid-state NMR. *Proc Natl Acad Sci U S A* (2003) 100(18):10158. doi:10.1073/pnas.1733835100
  25. Golman K, Petersson JS. Metabolic imaging and other applications of hyperpolarized 13C. *Acad Radiol* (2006) 13(8):932. doi:10.1016/j.acra.2006.06.001
  26. Kurhanewicz J, Vigneron DB. Advances in MR spectroscopy of the prostate. *Magn Reson Imaging Clin N Am* (2008) 16(4):697. doi:10.1016/j.mric.2008.07.005
  27. Kurhanewicz J, Vigneron DB, Brindle K, Chekmenev EY, Comment A, Cunningham CH, et al. Analysis of cancer metabolism by imaging hyperpolarized nuclei: prospects for translation to clinical research. *Neoplasia* (2011) 13(2):81. doi:10.1593/neo.101102
  28. Turkbey B, Pinto PA, Mani H, Bernardo M, Pang Y, McKinney YL, et al. Prostate cancer: value of multiparametric MR imaging at 3 T for detection – histopathologic correlation. *Radiology* (2007) 255(1):89. doi:10.1148/radiol.09090475
  29. Nelson SJ, Kurhanewicz J, Vigneron DB, Larson PE, Harzstark AL, Ferrone M, et al. Metabolic imaging of patients with prostate cancer using hyperpolarized [1-13C]pyruvate. *Sci Transl Med* (2013) 5(198):198ra108. doi:10.1126/scitranslmed.3006070
  30. Schuster DM, Votaw JR, Nieh PT, Yu W, Nye JA, Master V, et al. Initial experience with the radiotracer anti-1-amino-3-18 F-fluorocyclobutane-1-carboxylic acid with PET/CT in prostate carcinoma. *J Nucl Med* (2007) 48:56.
  31. Park H, Wood D, Hussain H, Meyer CR, Shah RB, Johnson TD, et al. Introducing parametric fusion PET/MRI of primary prostate cancer. *J Nucl Med* (2012) 53(4):546. doi:10.2967/jnumed.111.091421
  32. Heidenreich A, Bastian PJ, Bellmunt J, Bolla M, Joniau S, van der Kwast T, et al. EAU guidelines on prostate cancer. Part 1: screening, diagnosis, and local treatment with curative intent – update 2013. *Eur Urol* (2014) 65(1):124. doi:10.1016/j.eururo.2013.09.046
  33. Rinnab L, Blumstein NM, Mottaghy FM, Hautmann RE, Küfer R, Hohl K, et al. 11C-choline positron-emission tomography/computed tomography and transrectal ultrasonography for staging localized prostate cancer. *BJU Int* (2007) 99(6):1421–6. doi:10.1111/j.1464-410X.2007.06776.x
  34. Picchio M, Briganti A, Fanti S, Heidenreich A, Krause BJ, Messa C, et al. The role of choline positron emission tomography/computed tomography in the management of patients with prostate specific antigen progression after radical treatment of prostate cancer. *Eur Urol* (2011) 59:51. doi:10.1016/j.eururo.2010.09.004
  35. Weinreb JC, Blume JD, Coakley FV, Wheeler TM, Cormack JB, Sotto CK, et al. Prostate cancer: sextant localization at MR imaging and MR spectroscopic imaging before prostatectomy – results of ACRIN prospective multi-institutional clinicopathologic study. *Radiology* (2009) 251(1):122. doi:10.1148/radiol.2511080409
  36. Kurhanewicz J, Swanson MG, Nelson SJ, Vigneron DB. Combined magnetic resonance imaging and spectroscopic imaging approach to molecular imaging of prostate cancer. *J Magn Reson Imaging* (2002) 16:451. doi:10.1002/jmri.10172
  37. Testa C, Schiavina R, Lodi R, Salizzoni E, Tonon C, D'Errico A, et al. Accuracy of MRI/MRSI-based transrectal ultrasound biopsy in peripheral and transition zones of the prostate gland in patients with prior negative biopsy. *NMR Biomed* (2010) 23(9):1017. doi:10.1002/nbm.1522
  38. Zechmann CM, Menze BH, Kelm BM, Zamecnik P, Ikinger U, Giesel FL, et al. Automated vs. manual pattern recognition of 3D (1)H MRSI data of patients with prostate cancer. *Acad Radiol* (2012) 19(6):675. doi:10.1016/j.acra.2012.02.014
  39. Kelm BM, Menze BH, Zechmann CM, Baudendistel KT, Hamprecht FA. Automated estimation of tumor probability in prostate magnetic resonance spectroscopic imaging: pattern recognition vs quantification. *Magn Reson Med* (2007) 57(1):150. doi:10.1002/mrm.21112
  40. Blodgett TM, Meltzer CC, Townsend DW. PET/CT: form and function. *Radiology* (2007) 242(2):360. doi:10.1148/radiol.2422051113
  41. Panebianco V, Sciarra A, Marcantonio A, Forte V, Biondi T, Laghi A, et al. Conventional imaging and Multiparametric Magnetic Resonance (MRI, MRS, DWI, MRP) in the diagnosis of prostate cancer. *Q J Nucl Med Mol Imaging* (2012) 56:331.
  42. Flavell RR, Westphalen AC, Liang C, Sotto CC, Noworolski SM, Vigneron DB, et al. Abnormal findings on multiparametric prostate magnetic resonance imaging predict subsequent biopsy upgrade in patients with low risk prostate cancer managed with active surveillance. *Abdom Imaging* (2014) 39(5):1027. doi:10.1007/s00261-014-0136-7
  43. Barentsz JO, Richenberg J, Clements R, Choyke P, Verma S, Villeirs G, et al. ESUR prostate MR guidelines 2012. *Eur Radiol* (2012) 22(4):746. doi:10.1007/s00330-011-2377-y
  44. Jung JA, Coakley FV, Vigneron DB, Swanson MG, Qayyum A, Weinberg V, et al. Prostate depiction at endorectal MR spectroscopic imaging: investigation of a standardized evaluation system. *Radiology* (2004) 233:701. doi:10.1148/radiol.2333030672
  45. Fütterer JJ, Scheenen TW, Heijmink SW, Huisman HJ, Hulsbergen-Van de Kaa CA, Witjes JA, et al. Standardized threshold approach using three-dimensional proton magnetic resonance spectroscopic imaging in prostate cancer localization of the entire prostate. *Invest Radiol* (2007) 42:116–22. doi:10.1097/01.rli.0000251541.03822.bb
  46. Albers MJ, Bok R, Chen AP, Cunningham CH, Zierhut MI, Zhang VY, et al. Hyperpolarized 13C lactate, pyruvate and alanine: noninvasive biomarkers for prostate cancer detection and grading. *Cancer Res* (2008) 68(20):8607. doi:10.1158/0008-5472.CAN-08-0749
  47. Nanni C, Zanoni L, Pultrone C, Schiavina R, Brunocilla E, Lodi F, et al. 18F-FACBC (anti-1-amino-3-18F-fluorocyclobutane-1-carboxylic acid) versus 11C-choline PET/CT in prostate cancer relapse: results of a prospective trial. *Eur J Nucl Med Mol Imaging* (2016) 43(9):160. doi:10.1007/s00259-016-3329-1
  48. Morigi JJ, Stricker PD, van Leeuwen PJ, Tang R, Ho B, Nguyen Q, et al. Prospective comparison of 18F-fluoromethylcholine versus 68Ga-PSMA PET/CT in prostate cancer patients who have rising PSA after curative treatment and are being considered for targeted therapy. *J Nucl Med* (2015) 56:1185. doi:10.2967/jnumed.115.160382
  49. Afshar-Oromieh A, Zechmann CM, Malcher A, Eder M, Eisenhut M, Linhart HG, et al. Comparison of PET imaging with a 68Ga-labelled PSMA ligand and

- 18F-choline-based PET/CT for the diagnosis of recurrent prostate cancer. *Eur J Nucl Med Mol Imaging* (2014) 41:11. doi:10.1007/s00259-013-2525-5
50. Eiber M, Maurer T, Souvatzoglou M, Beer AJ, Ruffani A, Haller B, et al. Evaluation of hybrid 68Ga-PSMA ligand PET/CT in 248 patients with biochemical recurrence after radical prostatectomy. *J Nucl Med* (2015) 56:668. doi:10.2967/jnumed.115.154153
51. Wetter A, Lipponer C, Nensa F, Heusch P, Rübben H, Altenbernd JC, et al. Evaluation of the PET component of simultaneous [(18)F]choline PET/MRI in prostate cancer: comparison with [(18)F]choline PET/CT. *Eur J Nucl Med Mol Imaging* (2014) 41(1):79. doi:10.1007/s00259-013-2560-2
52. Takei T, Souvatzoglou M, Beer AJ, Drzezga A, Ziegler S, Rummel EJ, et al. A case of multimodality multiparametric 11C-choline PET/MR for biopsy targeting in prior biopsy-negative primary prostate cancer. *Clin Nucl Med* (2012) 37(9):918. doi:10.1097/RLU.0b013e31825b23a6

**Conflict of Interest Statement:** The authors declare that the research was conducted in the absence of any commercial or financial relationships that could be construed as a potential conflict of interest.

Copyright © 2016 Testa, Pultrone, Manners, Schiavina and Lodi. This is an open-access article distributed under the terms of the Creative Commons Attribution License (CC BY). The use, distribution or reproduction in other forums is permitted, provided the original author(s) or licensor are credited and that the original publication in this journal is cited, in accordance with accepted academic practice. No use, distribution or reproduction is permitted which does not comply with these terms.

# Advantages of publishing in Frontiers



## OPEN ACCESS

Articles are free to read,  
for greatest visibility



## COLLABORATIVE PEER-REVIEW

Designed to be rigorous  
– yet also collaborative,  
fair and constructive



## FAST PUBLICATION

Average 85 days from  
submission to publication  
(across all journals)



## COPYRIGHT TO AUTHORS

No limit to article  
distribution and re-use



## TRANSPARENT

Editors and reviewers  
acknowledged by name  
on published articles



## SUPPORT

By our Swiss-based  
editorial team



## IMPACT METRICS

Advanced metrics  
track your article's impact



## GLOBAL SPREAD

5'100'000+ monthly  
article views  
and downloads



## LOOP RESEARCH NETWORK

Our network  
increases readership  
for your article

## Frontiers

EPFL Innovation Park, Building I • 1015 Lausanne • Switzerland  
Tel +41 21 510 17 00 • Fax +41 21 510 17 01 • info@frontiersin.org  
[www.frontiersin.org](http://www.frontiersin.org)

## Find us on

